

# THE DINKIDI CU-AU PORPHYRY

## GEOLOGY OF THE DIDIPIO REGION AND PARAGENESIS OF THE DINKIDI CU-AU PORPHYRY DEPOSIT

by

Rohan C. Wolfe B.Sc.(Hons)



UNIVERSITY OF TASMANIA

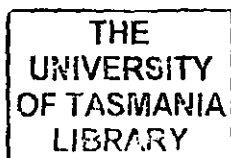
Submitted in fulfillment of the requirements for the degree  
of Doctor of Philosophy

November, 2001



**CODES SRC**  
Centre for Ore Deposit Research

Cont  
Thesis  
WOLFE  
PhD  
2002



## STATEMENTS

This thesis may be made available for loan and limited copying in accordance with the Copyright Act 1968.

This thesis contains no material which has been accepted for the award of any other degree or diploma in any university and, to the best of my knowledge and belief, contains no copy or paraphrase of material previously published or written by another person, except where due reference is made in the text of this thesis.

A handwritten signature in black ink, appearing to read 'Roh Wolfe', with a stylized, flowing script.

Rohan Wolfe  
University of Tasmania  
November, 2001.

## ABSTRACT

The Dinkidi Cu-Au porphyry deposit is located in northern Luzon, Philippines. The 110 Mt deposit is characterised by high gold grades (ave. 1.2 g/t Au and 0.5% Cu) and is one of only a few alkaline porphyry deposits to have been discovered outside British Columbia.

Alkaline magmatism in northern Luzon is related to the Late Oligocene rifting event that formed the Cagayan Valley Basin, and to the final stages of west-directed subduction along the East Luzon trench. Subalkaline andesitic and trachytic lavas and minor volcanoclastic rocks of the Mamparang Formation were emplaced along the southwest margin of the Cagayan Valley Basin, and have been intruded by a series of alkaline plutons and stocks. The Dinkidi deposit is hosted within the multiphase Dinkidi Stock, which is in turn part of a larger alkaline intrusive body, the Didipio Igneous Complex.

The Didipio Igneous Complex consists of: (1) an early composite clinopyroxene-gabbro-diorite-monzodiorite pluton; (2) the Surong clinopyroxene to biotite monzonite pluton; (3) the Cu-Au mineralised Dinkidi Stock, which comprises an early equigranular biotite-monzonite stock (Tunja Monzonite), a thin, variably-textured clinopyroxene-syenite (the Balut Dyke), and a monzosyenite porphyry (Quan Porphyry) that grades, in its core, into a crystal-crowded leucocratic quartz-syenite (Bufu Syenite); and (4) post-mineralisation andesite dykes.

Whole-rock chemistry indicates that the volcanic formations in the Didipio region become progressively more alkaline up stratigraphy, indicating that Late Oligocene rifting intermittently tapped an LILE-enriched mantle source that became progressively more LILE-enriched over time. Whole rock and mineral compositions indicate that all intrusions in the Didipio region were sourced from a common magma chamber, and were related by shallow level fractional crystallisation.

Five main hydrothermal events are recognised in the Didipio region: (1) contact metamorphism and weak biotite-cordierite alteration is associated with emplacement of the early diorite phase; (2) K-silicate magnetite-biotite alteration, and subeconomic Cu-Au mineralisation associated with the emplacement of the Surong monzonite pluton; (3) intensely developed porphyry-style alteration and ore-grade Cu-Au mineralisation which is spatially and temporally associated with emplacement of the Dinkidi Stock; (4) an advanced argillic alteration assemblage, which has overprinted the Didipio Igneous Complex and is associated with subeconomic high-sulphidation style Cu-Au mineralisation; (5) late-stage unmineralised zeolite-carbonate veins, which are associated with post-mineral strike-slip faulting.

At Dinkidi, emplacement of the Tunja Monzonite was temporally and spatially associated with the formation of a pervasive biotite-magnetite K-silicate alteration assemblage in the pre-mineral diorites. Emplacement of the Balut Dyke was associated with a calc-potassic style diopside-actinolite-K-feldspar-bornite alteration assemblage and associated vein stockwork. This quartz-free mineral assemblage is associated with high gold grades (2-8 g/t Au) and is typical of alteration assemblages found in quartz-undersaturated alkaline porphyry systems. Intrusion of the Bufu Syenite led to the formation of a quartz-sericite-calcite-chalcopyrite stockwork vein and alteration assemblage, which has overprinted the calc-potassic assemblage. The quartz stockwork



hosts the bulk of low grade mineralisation (1-2g/t Au) at Dinkidi and is typical of silica-saturated alkaline porphyry systems. A coarse-grained assemblage of quartz-actinolite-perthite (the 'Bugoy Pegmatite') formed as an apophysis on the Bufu Syenite, and was subsequently brecciated by late-stage faulting. High-level argillic and late-stage fault-related zeolite mineral assemblages have overprinted the porphyry-style hydrothermal assemblages.

The calc-potassic assemblage is inferred to have formed at temperatures in excess of  $>600^{\circ}\text{C}$  from a silica-undersaturated K-Ca-Fe brine. Fluid inclusion studies indicate that the quartz stockwork was emplaced at submagmatic temperatures ( $>600^{\circ}\text{C}$ ) from a quartz-saturated Na-K-Fe brine ( $>68$  wt. % eq. NaCl) that contained up to 0.6 wt. % Cu and 4 wt. % Fe. Cooling to  $\sim 420^{\circ}\text{C}$  and neutralisation by wall rock interaction lead to the precipitation of sulphides within the quartz stockwork. The quartz-bearing assemblage was emplacement at 2.9 to 3.5 km paleodepth, and was associated periods of overpressurisation and quartz growth disrupted by episodic depressurisation to near hydrostatic pressure conditions.

The hydrothermal mineral assemblages at Dinkidi reflect the composition and degree of fractionation of the associated intrusions. Extensive fractionation within a feldspathoid-normative dioritic magma chamber is interpreted to have ultimately caused quartz saturation and the development of the late-stage syenite intrusions and related quartz stockwork mineralisation. The calcic, silica-undersaturated Balut Dyke (associated with the calc-potassic stockwork) does not fit this fractionation trend, and is interpreted to have formed by interaction between the late-stage syenitic melt and a co-magmatic mafic melt that underplated the siliceous magma chamber prior to formation of the Balut Dyke. A reversion to fractionation-dominated magmatic processes in the silicic magma chamber then lead to the intrusion of the quartz-saturated Quan Porphyry and Bufu Syenite. Ultimately, the residual mafic melt was emplaced as a series of late-stage andesite dykes.

The Dinkidi porphyry Cu-Au deposit shows that it is possible for silica-undersaturated and silica-saturated styles of alkaline porphyry mineralisation to form in the same magmatic-hydrothermal system, given the right conjunction of geological processes. Exploration models for alkaline porphyry systems therefore need to be flexible enough to accommodate the possibility of silica-undersaturated and saturated mineralised zones forming in the same deposit. The strongly mineralised, variably textured Balut Dyke shares textural and genetic similarities with mineralised pegmatite dykes from mid-crustal granitic environments. Highly Cu-Au mineralised 'pegmatitic' dykes should therefore also be considered as a viable exploration target in alkaline porphyry systems.

# CONTENTS

	page
Abstract .....	i
Contents .....	iii
List of Tables .....	vi
List of Figures .....	vii
List of Plates .....	viii
Acknowledgments .....	ix
<b>CHAPTER ONE – INTRODUCTION</b>	
LOCATION .....	1
EXPLORATION HISTORY .....	2
PAST WORK .....	4
METHODS EMPLOYED .....	4
<b>CHAPTER TWO – REGIONAL GEOLOGY</b>	
TECTONIC SETTING .....	8
REGIONAL GEOLOGY OF THE CARABALLO MOUNTAINS .....	8
REGIONAL UNITS .....	12
Basement Complex .....	12
Caraballo Formation .....	12
Mamparang and Upper Mamparang Formation .....	13
Late Oligocene to Middle Eocene limestones .....	14
Mid-Miocene Palali Formation .....	15
Cagayan Valley Basin and other post-Palali Formation sediments .....	15
Intrusive Units .....	16
Eocene Intrusive (Coastal Batholith) .....	16
Oligocene Intrusives (Dupax and Northern Sierra Madre Batholiths) .....	17
Cordon Syenite Complex .....	18
Palali Batholith .....	18
Alkaline Dykes .....	19
Central Cordilleran Magmatism .....	19
SUMMARY .....	20
<b>CHAPTER THREE – LOCAL GEOLOGY</b>	
VOLCANIC UNITS .....	24
Mamparang Formation .....	24
Andesite lavas .....	24
Volcaniclastic breccias .....	28
Volcaniclastic sandstones .....	30
Upper Mamparang Formation .....	30
Trachyte and trachyandesites .....	32
Trachytic volcaniclastic breccias .....	33
DIDIPIO IGNEOUS COMPLEX .....	33
Early dioritic units .....	34
Clinopyroxenites and anorthosite .....	34
Clinopyroxene gabbro .....	34
Clinopyroxene diorite .....	36
Clinopyroxene-monzodiorite .....	36
Dinkidi Stock .....	42
Andesite Dykes .....	42
STRUCTURE .....	42
ENVIRONMENT OF DEPOSITION .....	45
SYNTHESIS .....	46

## CHAPTER FOUR – DEPOSIT GEOLOGY

INTRODUCTION.....	50
METHOD .....	50
INTRUSIVE UNITS.....	50
<b>Tunja Monzonite</b> .....	50
<b>Balut Dyke</b> .....	52
<b>Quan Porphyry</b> .....	54
<b>Bufu Syenite</b> .....	54
<b>The Bugoy 'pegmatite' and Bugoy breccia</b> .....	56
STRUCTURE.....	60
SUMMARY AND DISCUSSION .....	60

## CHAPTER FIVE – GEOCHEMISTRY

INTRODUCTION .....	66
METHOD .....	66
<b>Effect of alteration on analyses</b> .....	67
TOTAL ALKALINE CLASSIFICATIONS.....	68
BIVARIATE VARIATION DIAGRAMS .....	70
<b>Tectonic Discrimination Diagrams</b> .....	72
<b>Multi-element Variation Diagrams</b> .....	74
<b>REE Patterns</b> .....	76
<b>Mineral Chemistry</b> .....	80
<i>Clinopyroxene</i> .....	80
<i>Feldspars</i> .....	82
PETROGENETIC MODELLING.....	83
CONCLUSIONS.....	84

## CHAPTER SIX – ALTERATION AND MINERALISATION

INTRODUCTION .....	88
METHOD .....	88
ALTERATION AND MINERALISATION AT DINKIDI.....	89
<b>Stage 1 K-silicate alteration</b> .....	91
<i>Stage 1 Propylitic alteration</i> .....	92
<b>Stage 2 Calc-potassic assemblage</b> .....	94
<i>Stage 2A 'Pegmatitic' veins</i> .....	94
<i>Stage 2B &amp; 2C actinolite-perthite veins</i> .....	96
<i>Stage 2D</i> .....	98
<b>Stage 3 Quartz-stockwork assemblage</b> .....	100
<i>Pre-Quan Porphyry magnetite-sulphide trails and quartz veins</i> .....	100
<i>Stage 3A</i> .....	102
<i>Stage 3A quartz-actinolite veins</i> .....	102
<i>Stage 3A Bugoy Pegmatite</i> .....	104
<i>Stage 3A pervasive and selectively pervasive alteration assemblages</i> .....	104
<i>Stage 3B Potassic</i> .....	104
<i>Stage 3B Potassic quartz-perthite veins</i> .....	106
<i>Stage 3B Potassic pervasive and selectively pervasive alteration</i> .....	106
<i>Stage 3B Main quartz stockwork</i> .....	108
<i>Stage 3B sericite-sulphide-carbonate alteration</i> .....	108
<i>Stage 3C</i> .....	108
<i>Late Stage 3C sericite-quartz brecciation</i> .....	110
<b>Stage 4 Argillic alteration</b> .....	112
<b>Stage 5 Zeolite assemblage</b> .....	112
<i>Zeolite veins</i> .....	112
<i>'Mud veins'</i> .....	114
<i>Zeolite-matrix lithic breccias</i> .....	114

<i>Retrograde calcite-chlorite alteration</i> .....	116
REGIONAL ALTERATION ASSEMBLAGES .....	116
<b>Contact metamorphism</b> .....	116
<b>Surong Monzonite K-silicate alteration</b> .....	116
<b>Porphyry-style mineralisation</b> .....	118
<b>Argillic alteration</b> .....	118
DISCUSSION .....	122
SUMMARY .....	126

## CHAPTER SEVEN – FLUID INCLUSIONS & SULPHUR ISOTOPES

INTRODUCTION .....	128
FLUID INCLUSIONS.....	128
<b>Methods</b> .....	128
<b>Classification of Inclusions</b> .....	129
<b>Microthermometry Results</b> .....	132
<i>Stage 2</i> .....	132
<i>Stage 3</i> .....	132
<i>Stage 3A Bugoy Pegmatite</i> .....	132
<i>Stage 3B Potassic</i> .....	134
<i>Stage 3A &amp; B quartz stockwork</i> .....	134
<b>PIXE Results</b> .....	135
<b>Melt Inclusion Results</b> .....	138
<b>Discussion</b> .....	138
<i>Fluid compositions</i> .....	138
<i>Evidence for phase separation</i> .....	141
<i>Pressure estimates</i> .....	142
<i>Trapping temperatures</i> .....	144
<b>Conclusions</b> .....	144
SULPHUR ISOTOPES .....	145
<b>Introduction</b> .....	145
<b>Method</b> .....	146
<b>Sulphur Isotope Results</b> .....	146
<b>Sulphur Isotope Discussion</b> .....	148
<i>Sources of sulphur</i> .....	148
<i>Development of light <math>\delta_{34}S</math> values</i> .....	150
<i>Formation of the heavy <math>\delta_{34}S</math> zone</i> .....	150

## CHAPTER EIGHT – GENETIC MODEL

OVERVIEW: GEOLOGY AND MINERALISATION OF THE DIDIPIO REGION.....	154
TECTONIC SETTING AND THE GENESIS OF THE ALKALINE MELTS .....	155
VOLCANIC ENVIRONMENT: MAMPARANG & UPPER MAMPARANG FORMATIONS.....	155
EMPLACEMENT OF THE DIDIPIO IGNEOUS COMPLEX .....	156
<b>The first intrusion: diorites and monzodiorites</b> .....	156
<b>The Surong Monzonite and the start of volatile exsolution</b> .....	157
<b>Model for the emplacement of the Dinkidi Stock</b> .....	157
<b>The Tunja Monzonite and Stage 1 K-silicate alteration</b> .....	161
<b>The Balut Dyke and Stage 2 calc-potassic alteration</b> .....	162
<b>The Quan Porphyry, Bufu Syenite and Stage 3 quartz stockwork</b> .....	167
<b>Andesite dykes and retrograde assemblages</b> .....	171
<b>Possible sources of gold enrichment in the alkaline melts at Dinkidi</b> .....	172

CHAPTER NINE – CONCLUSIONS.....	176
---------------------------------	-----

REFERENCES.....	184
-----------------	-----

APPENDICES .....	201
------------------	-----

Appendix A – List of all drill holes logged

Appendix B – Geochemical data:

B1-1 – Whole rock major, trace and REE data (this study)

B1-2 – Whole rock data for regional alkaline intrusions (various sources)

B1-3 – Whole rock data for regional batholiths (various sources)

B1-4 – Whole rock data for regional volcanic units (various sources)

B2-1 – Electron microprobe analyses of primary igneous minerals (this study)

B2-2 – Electron microprobe analyses of alteration minerals (this study)

B3 – Results of least squares fractionation modeling

Appendix C – Fluid inclusion microthermometric data

Appendix D – Sulphur isotope results

## LIST OF TABLES

	<i>Page</i>
INTRODUCTION	
1.1 – Geological & hydrothermal characteristics of porphyry deposits.....	3
GEOCHEMISTRY	
5.1 – Representative analyses .....	67
5.2 – Major element modeling of fractionation .....	83
FLUID INCLUSIONS & SULPHUR ISOTOPES	
7.1 – PIXE analyses of inclusions from a Stage 3 quartz vein .....	136

# LIST OF FIGURES

	<i>Page</i>
INTRODUCTION	
1.1 – Location of the Dinkidi Cu-Au porphyry deposit.....	3
1.2 – Copper-gold contents for the Dinkidi Cu-Au porphyry deposit .....	5
REGIONAL GEOLOGY	
2.1 – Tectonic setting of the Philippines .....	9
2.2 – Regional geology .....	11
2.3 – Simplified stratigraphic sections for the Caraballo Mountains .....	10
2.4 – Tectonic history of Northern Luzon .....	21
LOCAL GEOLOGY	
3.1 – Geology of the Didipio region .....	24A3
3.2 – Simplified stratigraphic sections, Mamparang & Upper Mamparang Formations.....	25
3.3 – Simplified cross section through the Didipio Igneous Complex .....	26
3.4 – Geological history of the Didipio region .....	48-49
DEPOSIT GEOLOGY	
4.1 – Geology of the Dinkidi Cu-Au porphyry deposit .....	51
4.2 – Magmatic evolution of the Dinkidi composite stock.....	63
4.3 – Comparison of mineralized intrusions in shallow and mid-crustal environments.....	65
GEOCHEMISTRY	
5.1 – Classification diagrams for volcanic and igneous units .....	69
5.2 – Major element harker diagram.....	71
5.3 – Trace element harker diagram .....	73
5.4 – Discrimination diagrams derived for potassic rocks.....	75
5.5 – Discrimination diagrams derived for granitic rocks .....	75
5.6 – MORB-normalised spidergram, with Didipio Igneous Complex intrusions .....	77
5.7 – MORB-normalised REE plots for the Didipio Igneous Complex .....	79
5.8 – Composition of clinopyroxenes, Didipio Igneous Complex & surrounding units .....	81
5.9 – Clinopyroxene magnesium-iron ratio .....	81
5.10 – Anorthite content, Didipio Igneous Complex plagioclase.....	81
ALTERATION AND MINERALISATION	
6.1 – Time-space diagram and paragenesis for the Dinkidi Cu-Au porphyry deposit.....	88A3
6.2 – Mineral paragenesis in the core of the Dinkidi deposit .....	89
6.3 – Distribution of mineralisation at the Dinkidi porphyry deposit.....	90
6.4 – Schematic distribution of Stage 1 hydrothermal assemblages.....	91
6.5 – Approximate distribution of Stage 2 hydrothermal assemblages .....	95
6.6 – Approximate distribution of Stage 3 hydrothermal assemblages .....	103
6.7 – Approximate distribution of Stage 4 and 5 hydrothermal assemblages .....	117
6.8 – Schematic distribution of alteration in the Didipio region .....	123
FLUID INCLUSIONS & SULPHUR ISOTOPES	
7.1 – Classification of fluid inclusion types at the Dinkidi Cu-Au porphyry deposit .....	130
7.2 – Homogenisation temp. & salinities for hydrothermal Stages 2 & 3 fluid inclusions ..	133
7.3 – PIXE spectra for fluid inclusions within a Stage 3B quartz vein .....	135
7.4 – Temperature-pressure diagram, NaCl-H <sub>2</sub> O.....	143
7.5 – Range of $\delta^{34}\text{S}$ isotope values for sulphides at the Dinkidi porphyry deposit .....	147
7.6 – Distribution of sulphur isotope values, 5750 cross-section, Dinkidi Cu-Au deposit ..	149
7.7 – Interpretation of sulphur isotope values, plotted on 5750 cross section.....	152
SYNTHESIS AND GENETIC MODEL	
8.1 – Schematic model for the emplacement of the Didipio Igneous Complex .....	159
8.2 – Model for the generation and emplacement of the Balut Dyke melt.....	163
8.3 – Model for the emplacement of the Quan Porphyry and Bufu Syenite.....	169
8.4 – Model for the post-mineralisation stages in the Didipio region .....	173

# LIST OF PLATES

	<i>Page</i>
INTRODUCTION:	
1.1 – Dinkidi Ridge and Climax Mining staff .....	6
1.2 – Didipio field area .....	7
LOCAL GEOLOGY	
3.1 – Mamparang Formation: Andesites.....	27
3.2 – Mamparang Formation: Volcaniclastic Breccias.....	29
3.3 – Upper Mamparang Formation: Trachytes.....	31
3.4 – Didipio Igneous Complex: Gabbros .....	35
3.5 – Didipio Igneous Complex: Diorites.....	37
3.6 – Didipio Igneous Complex: Monzodiorites .....	39
3.7 – Didipio Igneous Complex: Monzonites.....	41
3.8 – Didipio Igneous Complex: Andesite Dykes.....	43
DEPOSIT GEOLOGY	
4.1 – Dinkidi Stock: Geological units.....	53
4.2 – Dinkidi Stock: Photomicrographs (Tunja & Balut Dykes).....	55
4.3 – Dinkidi Stock: layering in the Balut Dyke.....	57
4.4 – Dinkidi Stock: Quan Porphyry & Bufu Syenite.....	59
4.5 – Dinkidi Stock: Bugoy ‘Pegmatite’ and late-stage breccias.....	61
ALTERATION & MINERALISATION	
6.1 – Stage 1: K-silicate alteration.....	93
6.2 – Coarse-grained Stage 2A veins.....	97
6.3 – Stage 2B and 2C veins.....	99
6.4 – Stage 2 K-feldspar-sulphide.....	101
6.5 – Stage 3A.....	105
6.6 – Stage 3A veins and photomicrographs .....	107
6.7 – Stage 3B-Potassic quartz-perthite-magnetite.....	109
6.8 – Stage 3 quartz stockwork.....	111
6.9 – Stage 3 mineralisation.....	113
6.10 – Late Stage 3 assemblages.....	115
6.11 – Stage 4 argillic alteration .....	119
6.12 – Stage 5 Zeolite Assemblage.....	121
FLUID INCLUSIONS & SULPHUR ISOTOPES	
7.1 – Fluid Inclusions.....	131
7.2A– PIXE element distribution for fluid inclusions 1A .....	136
7.2B-C – PIXE element distribution for fluid inclusions 1B and 6B .....	137
7.2D-E – PIXE element distribution for fluid inclusions 6D and 8A.....	139

## ACKNOWLEDGEMENTS

I wish to thank Climax Mining for allowing this study on the Dinkidi Porphyry deposit, and for providing the logistical and financial support for this study. Special thanks go to PJ, John, George and all the staff at Didipio, Cordon and D'Beu for their invaluable assistance and company during the fieldwork periods for this study.

I wish to thank the staff at CODES and the Geology Department over the years for their assistance with this project. In particular I wish like to thank my supervisor Dr David Cooke for showing so little restraint when it came to lavishing red ink over my drafts, for his rigorous enforcement of the rudiments of the English language, and for his remarkable patience displayed over the last few years. This thesis has benefited from discussion with numerous people, both inside and out of the department, including Garry Davidson, Tony Crawford, Vadim Kamenetsky, and Ulrich Knittel. Ulrich is also thanked for providing a large number of unpublished reports and geochemical data on the region. Technical staff, including Phil Robinson and Nilar Hlaing (XRF), Keith Harris and Christine Cook (Sulphur isotopes), David Steele (Probe), Simon Stevens (Lapidary), Peter Cornish (logistics) and June Pongratz (just about everything) have all been involved with this project at various stages.

It would be fair to say that if it was not for a large group of friends at the department, and their distracting, subversive influences, I may have completed this thesis in half the time - however I wouldn't of had a such a great time during my candidature. The number of people over the few years who have succeeded in tearing me away from my chaste pursuit of academic knowledge is too large too list here (or even place on CD-ROM), but I wish to thank the old room 338 and the Friday night beers groups in particular. Special thanks go to Catherine Reid, Sarah Jones and James Cannell for assisting with the last moment production of this thesis.

*Thank You All!*



# INTRODUCTION

The Dinkidi Cu-Au Porphyry deposit is located in northern Luzon, Philippines (Figure 1.1) and is currently being developed by Australian company Climax Mining. The 110 Mt deposit is an alkaline, gold-rich Cu porphyry system, as is the nearby Marian Cu-Au porphyry deposit located nearby in Cordon (Figure 1.1; Baquiran, 1975; Alapan, 1981; Knittel, 1989). These deposits are two of the few known alkaline porphyry deposits that are located outside of British Columbia (eg., Jensen & Barton, 2000). Dinkidi, and the surrounding Didipio region, have not been the subject of any previous academic study and provide an excellent opportunity to increase our understanding of the diversity of Au-Cu porphyry systems in the Philippines, and of characteristics and formation of alkaline porphyry systems in general. By investigating a newly discovered porphyry deposit in a region that has not previously been mapped, this doctorate study had three main aims:

- Document the geology of the region and produce the first detailed geological map of the Didipio region.
- Establish the geology and paragenesis of the Dinkidi deposit, based on graphic drillcore logging.
- Use the geological framework developed above to develop a genetic model for mineralisation at Dinkidi.

Porphyry deposits may be subdivided into four broad classes based on the total alkali contents of the related intrusions: calc-alkaline, high-K calc alkaline, silica-saturated alkaline and silica-undersaturated alkaline (Barr *et al.*, 1976; Hollister 1978; Lang *et al.*, 1995a). The geological and hydrothermal characteristics of porphyry deposits tend to vary systematically within this classification scheme (Table 1.1). As will be described within this thesis, although it is classified here as alkaline, the Dinkidi deposit has characteristics that are compatible with more than one of these classes of porphyry deposits. This makes the Dinkidi deposit an ideal case study in which to investigate the magmatic and hydrothermal processes that control the development of porphyry mineralisation across part of the igneous compositional spectrum associated with porphyry-style mineralised systems.

## LOCATION

Northern Luzon can be subdivided into 4 main physiographic domains (Figure 1.1). The north-south trending Cagayan Valley Basin is flanked to the east, south and west by the Northern Sierra Madre Mountains, the Caraballo Mountains and the Central Cordillera respectively. Dinkidi is associated with Late Oligocene to Early Miocene alkaline rocks that are exposed

## INTRODUCTION

along the southwestern margin of the Cagayan Valley Basin in the Mamparang Mountains, a northern extension of the Caraballo Mountains. The deposit is situated on the boundary of the Quirino and Neuva Vizcaya local government districts. Access to the deposit, and the Climax Mining Didipio base camp, is by logging road from Cabarroguis (Figure 1.1; Plates 1.1A & C).

The Dinkidi deposit is located at an elevation of ~700 m in the steep, partially cultivated land of the Didipio barangay (population ~2000). Local inhabitants in the Didipio region are predominately Ifugao migrants from the Central Cordillera region, who settled in the previously unpopulated Didipio valley in the 1970's. Rice and banana are cultivated on the valley floors while primary tropical rainforest remains on the surrounding peaks (Plate 1.2A & B). The area has a wet-dry climate with a July-November typhoon season. Streams, paths and IP survey lines provide access and outcrop throughout the densely vegetated map area.

## EXPLORATION HISTORY

The surface expression of the Dinkidi deposit is a distinct topographic and vegetation anomaly, forming a grass-covered ridge 100 meters high, 150 meters wide and 400 meters long (Plate 1.1A). This ridge consists of strongly sericitised and argillically altered monzonite. Alluvial gold on the slopes of the ridge attracted the attention of Ifugao gold prospectors in the 1970's, triggering a gold rush to the region and the settlement of the Didipio valley. Native gold was recovered from adits tunneled into the ridge and from the panning and sluicing of soft, argillically altered zones on the ridge and from the surrounding alluvial gravels. At the height of the gold rush in the late 1970's over one thousand prospectors worked in the Didipio region.

Climax Mining acquired the Dinkidi prospect from Geophilippines and local claim owners in 1989, with encouraging geochemical, IP and magnetic surveys over the deposit leading to the commencement of drilling in April 1989. The awarding of the first Philippine FTAA agreement to Climax Mining in 1994 allowed 100% foreign ownership of the venture. Climax Mining has since tested the Dinkidi orebody with 128 diamond drill holes, totaling 38,000 meters.

Although initially planned to be an open pit mine, the downturn in metal prices that occurred in the mid-1990's lead to the reappraisal of the project, with the plan for an open pit replaced by an underground block caving operation designed to exploit the high grade core, producing a resource of 121 Mt at 1.49 g/t equivalent Au, containing 4 million ounces gold and 0.45 Mt copper and with a cut off grade at 0.5 g/t eqAu. This resource included a high-grade core of 17.8 Mt at 2.37 g/t eqAu and 0.67% Cu with a 2 g/t eqAu cut off grade. The project was expected to cost \$US 133 million (with most capital obtained from a syndicated US \$90 million loan). However recent political uncertainty in the Philippines, combined with further downturns in copper and gold prices, has precluded the raising of such a large sum of capital,

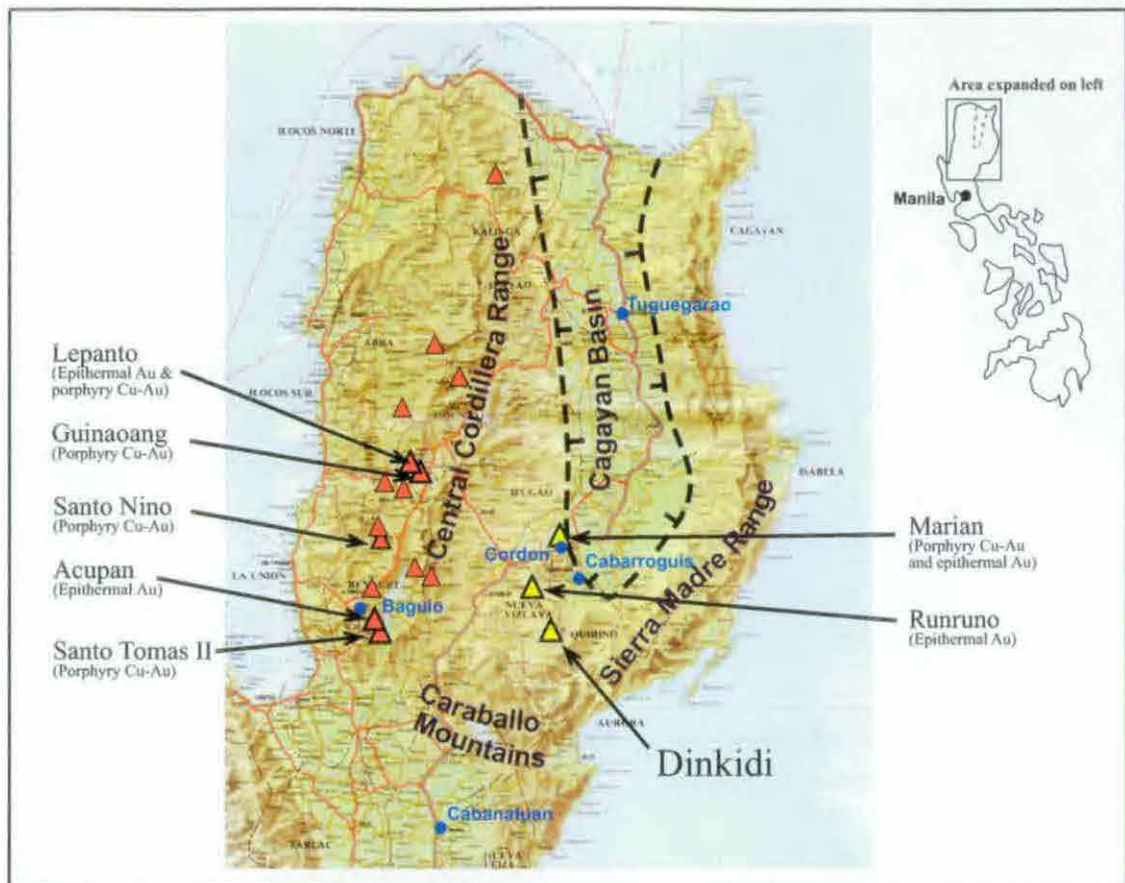


**Figure 1.1:** Location of the Dinkidi Cu-Au porphyry deposit and selected Cu-Au deposits of northern Luzon (red triangles for deposits associated with calc-alkaline intrusions; Sillitoe & Gappe, 1984; yellow triangles for deposits associated with alkaline to ultrapotassic intrusions).

Style	Related intrusions	Ore Metals	Hydrothermal assemblage	Examples
<b>Calc-alkaline</b>	Granodiorites to quartz monzonites Extensive fractionation?	Cu-Mo	Extensive potassic & propylitic Phyllic and argillic may be present Abundant pyrite	Chuquibambilla (Chile) San Manuel (USA) El Salvador (Chile) Sar Cheshmeh (Iran)
<b>High-K calc-alkaline</b>	Diorites to quartz diorites Extensive fractionation	Cu-Au-Mo	Extensive potassic, phyllic & propylitic Common late argillic alteration Abundant pyrite or magnetite	Bajo de Alumbra (Arg.) Dizon (Phil.) Batu Hijau
<b>Silica-saturated alkaline/'shoshonitic'</b>	Diorites to monzonites Extensive fractionation	Cu-Au	Extensive potassic; common sodic Argillic alteration typically absent Quartz veining and phyllic alteration may be absent (in 'Si-saturated alkaline' deposits) to abundant (in 'shoshonitic' deposits) Abundant magnetite	North Parkes (Aus.) Dinkidi (Phil.) Ajax (BC)
<b>Silica-undersaturated alkaline</b>	Syenites Associated with feldspathoid-bearing units and clinopyroxenites. No strong fractionation required?	Cu-Au	Common sodic, calc-sodic and potassic Phyllic and argillic alteration and quartz veining typically absent Abundant magnetite	Marian (Phil.) Galore Creek (BC)

**Table 1.1:** Geological and hydrothermal characteristics for the four main categories of porphyry deposit, compiled from Barr *et al.*, 1976; Hollister, 1978; Titley & Beane, 1981; Lang *et al.*, 1995a & Kirkham & Dunne, 2000). The subdivision of alkaline porphyry deposits into silica-saturated and undersaturated deposits is based on Lang *et al.*, 1995a. 'Shoshonitic' porphyry deposits (eg Heathersay & Walshe, 1995) have also been added to the silica-saturated class.

## INTRODUCTION

and the capitalization process has been postponed until there are more favorable commodity prices. Climax Mining is also currently reappraising the project, with a smaller scale, staged development of the resource considered to be appropriate in the current economic conditions and political climate, aiming at the extraction of the high grade core by cut and fill methods with a small open pit. Under this model the high grade core has a resource of 1.8 Mt underground ore at 8.68 g/t Au and 1.28% Cu at cut off at 5 g/t Au, combined with 600,000 tonnes from an open pit, at 1.92 g/t Au and 1.6% Cu, yielding 540,000 oz Au and 32,000 tonnes Cu. The estimated cost for development of this smaller scale operation is US\$32 million. The company is currently seeking third parties to develop the Dinkidi deposit and the Didipio region.

## PAST WORK

There has been little work published on the Didipio region. Garrett (1996) outlined the geology of Dinkidi. Haggman (1997) provided a description of Climax Mining's exploration effort in the Didipio region. Wolfe *et al.* (1999) summarised the geology of the Didipio region and the paragenesis of the Dinkidi deposit. Kamenetsky *et al.* (1999) described the results of a melt inclusion study on an intrusion from within the Dinkidi deposit. Several unpublished company reports have been compiled by Climax Mining on the Dinkidi prospect and the surrounding region.

Several unpublished works address the geology of the Caraballo and Northern Sierra Madre Mountains. The R.P. Japan project (1976) described the geology of Caraballo Mountains. Ringenbach (1992) and Billedo (1994) described the geology of the Northern Sierra Madre Mountains and sections of the Caraballo Mountains. Knittel (1987) and Knittel & Defant (1990) described the potassic rocks of the Cordon Syenite Complex, located 30 km to the north of Dinkidi. Albrecht & Knittel (1990) described the potassic rocks of the Palali Batholith, located 15 Km to the northwest of Dinkidi.

## METHODS EMPLOYED

Because the Didipio area had not been mapped previously, as part of this PhD study it has been necessary to describe the geology of the surrounding region in detail, in order to provide the geological context for the mineralised system. Chapter 2 is a synthesis of the regional geology, whereas Chapter 3 provides the first detailed description of the geology of the Didipio region. Chapter 4 provides a description of the geology of the Dinkidi orebody. Relationships between lithological units within the ore body and rock units exposed both within the Didipio area and regionally has been investigated using whole rock and mineral chemistry (Chapter 5). The hydrothermal vein and alteration assemblages within the Dinkidi orebody and in the region are

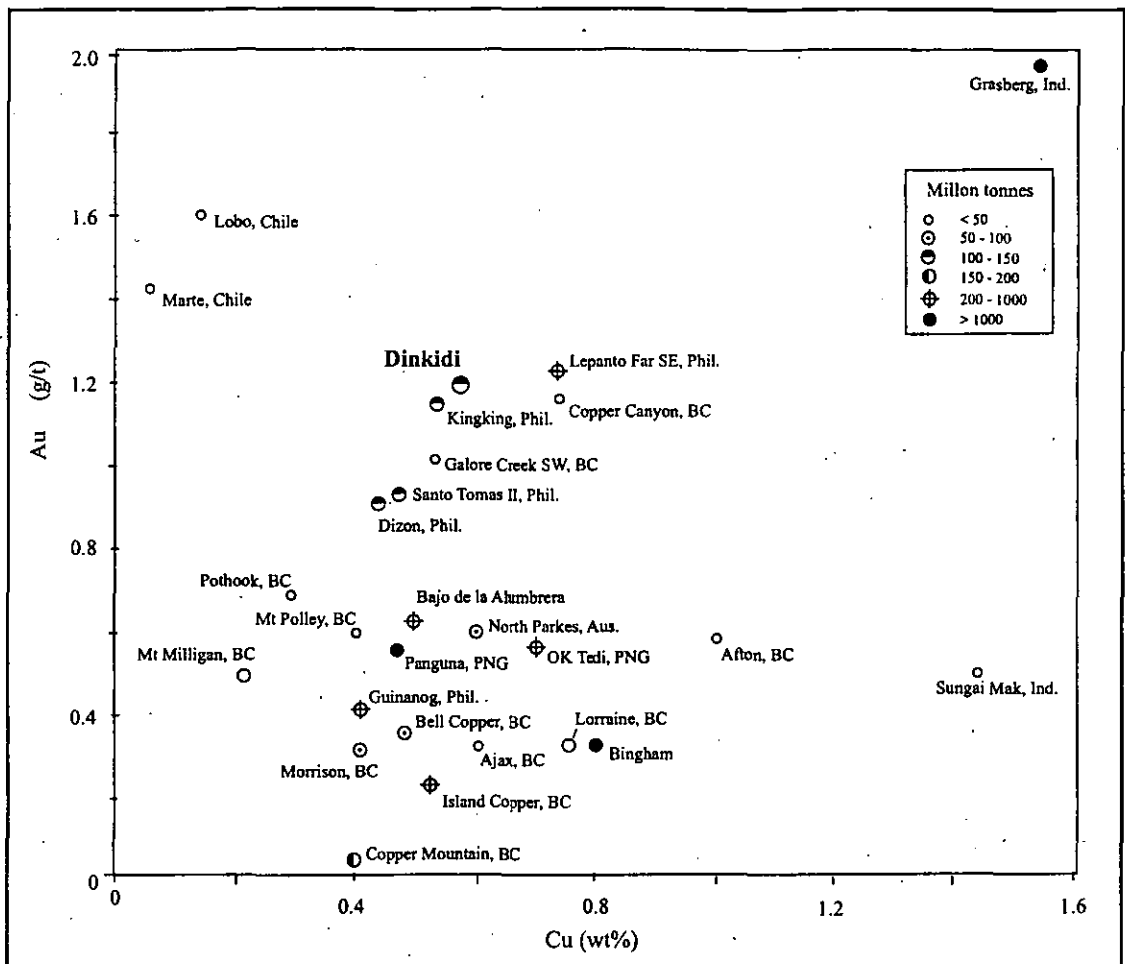


**Figure 1.2:** Copper-gold contents for the Dinkidi Cu-Au porphyry deposit and selected Au-rich porphyry Cu-Au deposits (from Sillitoe, 1990, modified with data for alkaline porphyry deposits from Stanley *et al.*, 1995; Ross *et al.*, 1995; Fraser *et al.*, 1995; Bishop *et al.*, 1995; Bottomer & Leary, 1995).

documented in Chapter 6. The physiochemical conditions for mineralisation at Dinkidi were investigated using both fluid inclusion and sulphur isotopes (Chapter 7). Chapter 8 provides a synthesis of the geological history of the Didipio region, with special emphasis on the link between the magmatic evolution of the region and the styles of hydrothermal alteration that developed.





**Plate 1.1 A:** View, looking south, of Dinkidi Ridge. The deposit forms a distinctive topographic and vegetation anomaly. The Climax Mining base camp is in the lower left hand corner.

**Plate 1.2 B:** Climax Mining's Didipio staff tee off at the Royal Didipio Golf Course. From left to right: Sadik, Bong (geologist), Johny, Reggie (geologist), Bert, Paul Joyce (Exploration Manager, Climax Mining), John Haggman (Exploration Manager, Philippines), Fred, George (Manager, Cordon base), Jimmy (holding traditional Ifugao steel golf club), and Carlos (liaison officer).

**Plate 1.3 C:** The company vehicle on route between Didipio and Cordon (with several passengers from the local community). The daily trips between Cordon and Didipio provide the main form of transport for local Didipio villagers. Before the road was upgraded, the 30 km one-way trip could take up to 6 hours to complete.



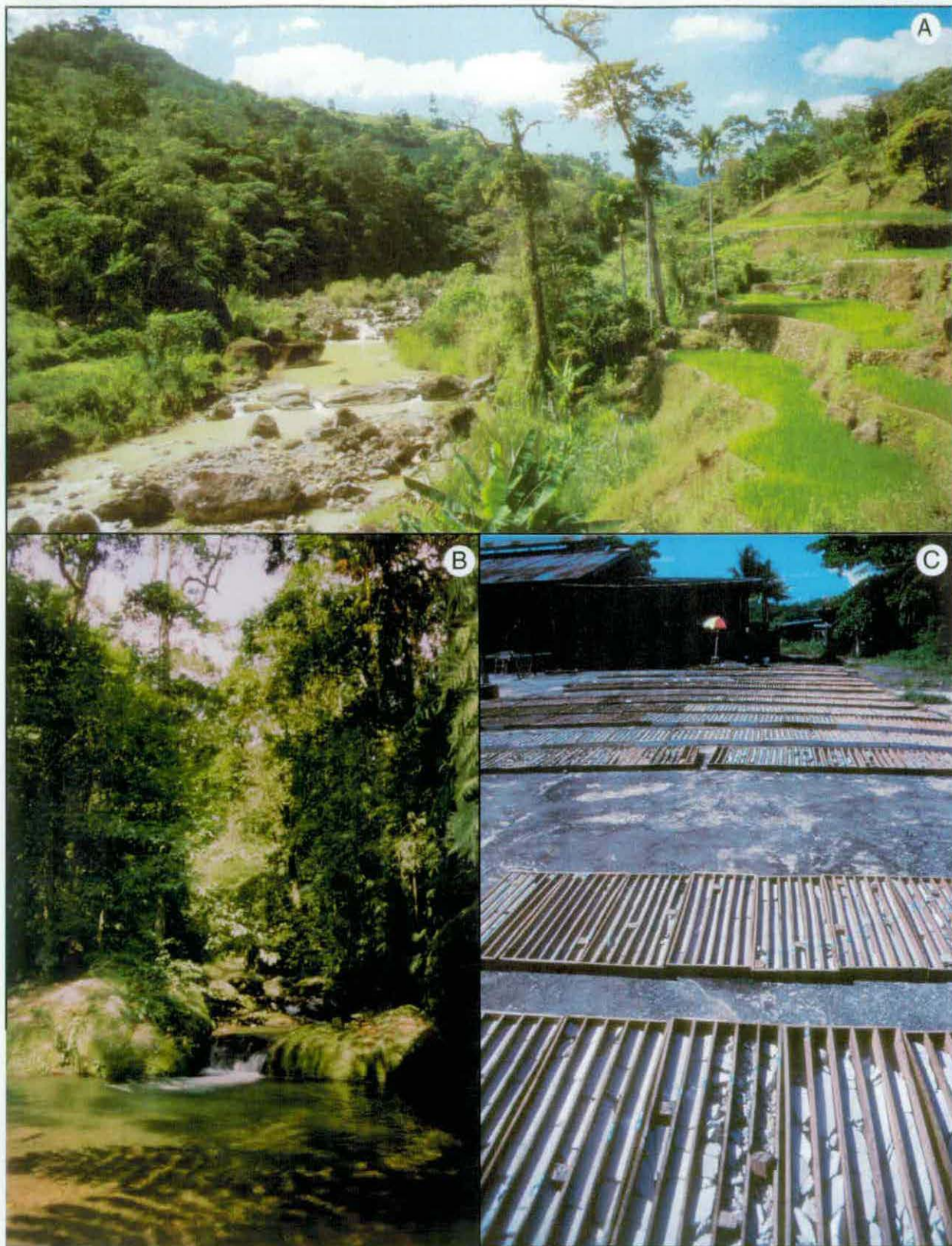


**Plate 1.2 A:** Typical terrain in the Didipio region. Rice is grown in the valley floors, and rainforest is preserved on the surrounding slopes.

**Plate 1.2 B:** Typical rock outcrops in the Didipio region. Stream beds provided the best outcrop within the densely vegetated and deeply weathered environment.

**Plate 1.2 C:** Cordon drillcore storage facility. Conditions on the concrete slab commonly exceeded 35C and >90% humidity.

# REGIONAL GEOLOGY

## TECTONIC SETTING

The Philippine Archipelago has formed where the Philippine Sea Plate obliquely collides with the rifted margin of Eurasia. It is a north-south orientated mobile belt flanked on either side by convergent zones, indicating decoupling from the surrounding Eurasian and Philippine Sea plates (Figure 2.1; Gervasio, 1971; Rangin, 1991). The mobile belt is thought to have begun forming in the Cretaceous (de Boer *et al.*, 1980; Rangin, 1991) and consisted of a collage of terrains that include two or more Early to Middle Tertiary arcs (Hamilton, 1979; Cardwell *et al.*, 1980), old continental fragments sourced from the Eurasian Plate, and ophiolite slabs that have all been tectonically juxtaposed by strike-slip displacement. Oblique movement within this mobile belt is taken up by the Philippine Fault (Fitch, 1972), a left-lateral strike-slip fault that cuts the Philippine Mobile Belt lengthwise for over 1500 km from Mindanao in the south to North Luzon, where it forms a complex array of anastomosing faults (Ringebach, 1992).

The North Luzon Terrain is located at the northern end of the Philippine Mobile Belt, where it has been juxtaposed against terrains to the west and south by splays of the Philippine Fault (Figure 2.1A). The North Luzon Terrain can be subdivided into 4 main physiographic domains (Figure 2.1B). The north-south trending Cagayan Valley Basin is located in the centre of north Luzon and is filled by post-Oligocene sediments. To the east, south and west of the Cagayan Valley Basin are the Northern Sierra Madre Mountains, the Caraballo Mountains and the Central Cordillera respectively. All three ranges consist of Eocene volcanics intruded by dioritic Oligocene to Miocene Batholiths, with the Central Cordillera overprinted by a second Late Miocene to Quaternary period of magmatism. The Didipio Igneous Complex is associated with Late Oligocene to Early Miocene alkaline rocks exposed along the south-western margin of the Cagayan Valley Basin. The Didipio Igneous Complex crops out in the Mamparang Mountains, a northern extension of the Caraballo Mountains (Figure 2.1B; Knittel, 1987; Albrecht & Knittel, 1990).

## REGIONAL GEOLOGY OF THE CARABALLO MOUNTAINS

The geology of the Caraballo and Northern Sierra Madre ranges is shown in Figure 2.2. The oldest units preserved in the area are schists and Cretaceous ophiolite that have been tectonically amalgamated, forming the basement to the Caraballo Mountains and Northern Sierra Madre. A thick pile of Eocene primitive island arc volcanics (Caraballo Group; MMAJ, 1977; Sajona *et al.*, 1999) overlies the basement and has been intruded by an Eocene tonalite batholith (Coastal Batholith; MMAJ, 1977). The Eocene units have been intruded by Oligocene tholeiitic to calc alkaline diorite batholiths (Dupax and Northern Sierra Madre Batholiths; MMAJ, 1977, 1987; Sajona *et al.*, 1999). Along the southwestern margin of the Cagayan Valley Basin, the Eocene rocks are overlain by the volcanic units of the alkaline Late Oligocene Mamparang Formation (MMAJ, 1977). The Mamparang Formation have been intruded by three



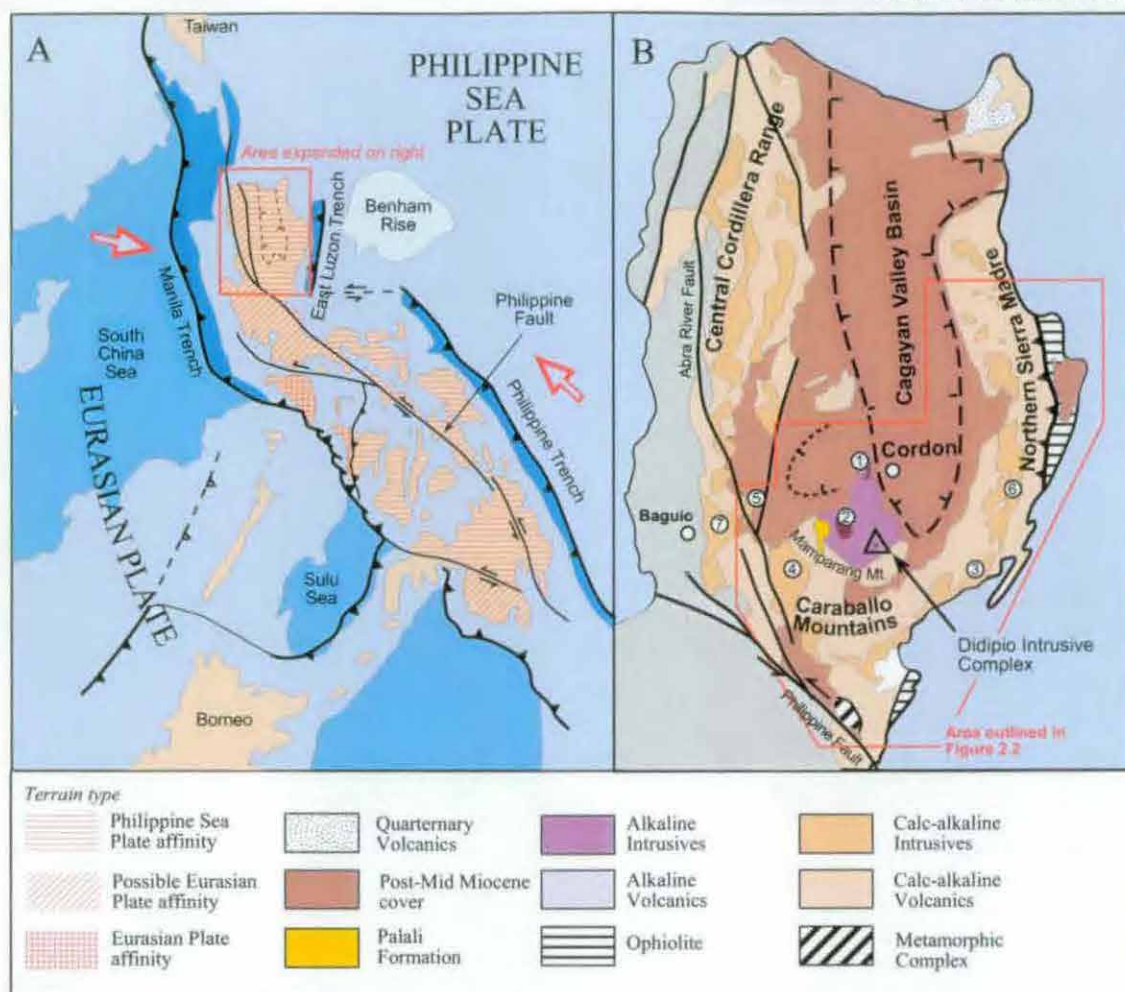


**Figure 2.1:** Tectonic setting of the Philippines (A) and physiographic domains of the Northern Luzon Terrain (B). Numbers: 1-Cordon Syenite Complex, 2-Palali Batholith, 3-Coastal Batholith, 4-Dupax Batholith, 5-Bokod Intrusions, 6-Northern Sierra Madre Batholith, 7-'Ago Batholith' (after Lewis & Hayes, 1983; Knittel, 1987; Ranglin, 1991 & Florendo, 1994;).

main Late Oligocene to Early Miocene alkaline intrusive centres: the Didipio Igneous Complex (Wolfe *et al.*, 1999), the Cordon Syenite Complex (Knittel, 1987) and the Palali Batholith (Albrecht & Knittel, 1990). All of the above formations are unconformably overlain by Oligocene to Middle Miocene shallow water carbonates (Santa Fe, Aglipay, Ibulao, Callo and Columbus Formations; Corby, 1951; Durkee & Pederson, 1961; Christian, 1964; MMAJ, 1977; Caagusan, 1977), which are interdigitated with the youngest volcanic units preserved in the region, the alkaline Palali Formation (MMAJ, 1977). The Cagayan Valley Basin began to subside in the Late Oligocene and is filled by a thick sequence of Miocene to Plio-Pleistocene carbonates and clastic sediments (Maddela, Matuno and Pantabangan Formations; Christian, 1964; Caagusan, 1977; MMAJ, 1977).

Only limited work has been conducted on the geology of the Caraballo and Northern Sierra Madre ranges. The first major study of the region was provided by a three-year joint venture between the Metal Mining Agency of Japan and the Philippine Bureau of Mines (MMAJ, 1977), with the aim of targeting mineralised areas. MMAJ (1977) established the basic stratigraphy of the Caraballo Mountains and the southern section of the Northern Sierra Madre, and also provided the first radiometric age determinations for the region, which were

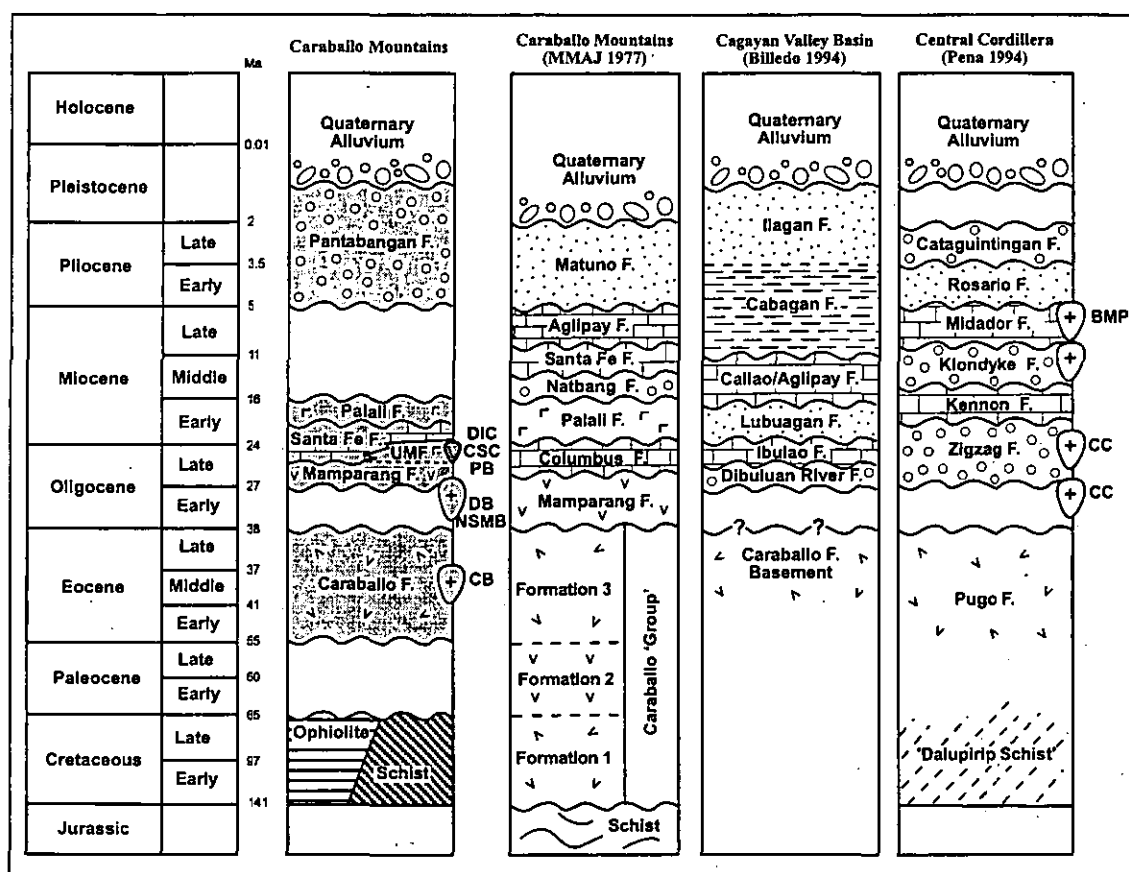


**Figure 2.3:** Simplified stratigraphic sections for the Caraballo Mountains, Cagayan Valley Basin and the Central Cordillera. UMF-Upper Mamparang Formation, DIC-Didipio Igneous Complex, CSC-Cordon Syenite Complex, PB-Palali Batholith, DB-Dupax Batholith, NSMB-Northern Sierra Madre Batholith, CB-Coastal Batholiths, BMP-Black Mountain Porphyry, CC-Cordilleran Batholiths (MMAJ, 1977; Billedo, 1994; Pena, 1994).

subsequently reclassified by Wolfe (1981). Hashimoto (1980) revised the MMAJ stratigraphy based largely on palaeontological ages for samples of Late Oligocene to Middle Miocene limestones (Hashimoto, 1980). MMAJ (1987) documented the stratigraphy for the northern section of the Northern Sierra Madre. Ringenbach (1992) clarified the stratigraphy of the Caraballo and Northern Sierra Madre Mountains, and provided new radiometric age determinations as part of his study on the evolution of the Philippine Fault. Billedo (1994) provided detailed descriptions of the regional geological units, and additional age determinations and mapping of key sections in the Northern Sierra Madre and Polillo Islands. The Cordon Syenite Complex was studied by Knittel (1983, 1987), and the Palali Batholith by Albrecht & Knittel (1990). Sajona *et al.* (1999) compiled the existing geochronological coverage of Luzon and provided new radiometric age determinations in their description of Luzon magmatism.

The geology of the Central Cordillera range, especially the Baguio district, has received a great deal of attention over the past 20 years due to the presence of Cu-Au mineralisation, but no consensus has yet been reached on the geological relationships of the region. Balce *et al.* (1980) and Pena (1994), among others, provide an overview on the stratigraphy for the region. In contrast the stratigraphy of the Cagayan Valley Basin is well developed, largely due to the work undertaken during oil and gas exploration (Durkee & Peterson, 1961; Christian, 1964; Caagusan, 1977, 1981).

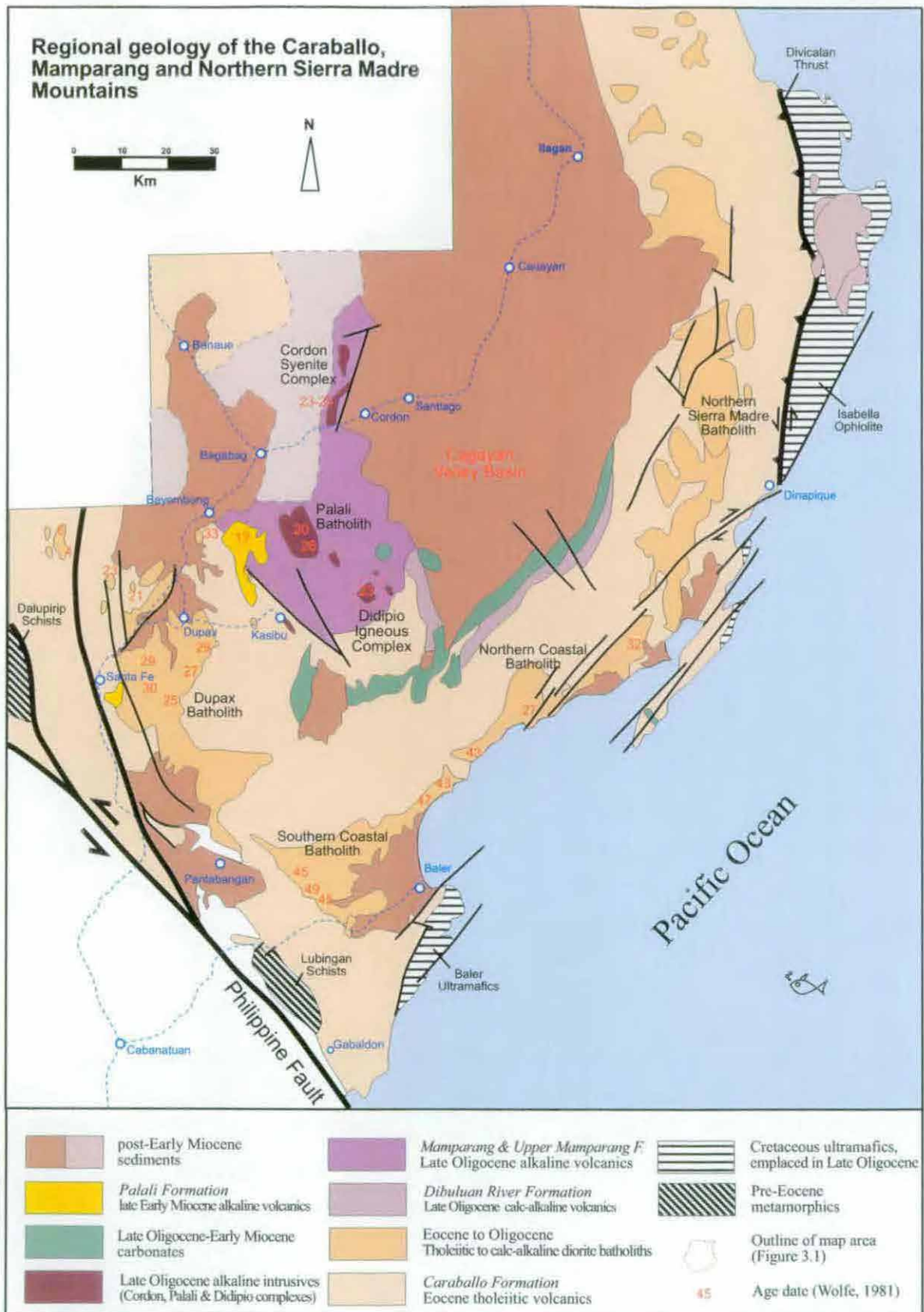


**Figure 2.2:** Regional geology. Map compiled from MMAJ, 1977; Knittel, 1983; MMAJ, 1987; Ringenbach, 1992 and Billedo, 1994. Stratigraphy for each region is described in Figure 2.3.



***Basement Complex***

The basement of the Caraballo and Northern Sierra Madre ranges consists of Cretaceous ophiolitic sequences, exposed along the east coast of Luzon (the Isabella Ophiolite) and Cretaceous (?) metamorphic units, such as the schists exposed in the Lubingan River, north of Gabaldon (Lubingan Schists; Rutland, 1968), and north of Santa Fe (Figure 2.2; MMAJ, 1979; Ringenbach, 1992). The metamorphic complexes have been tectonically amalgamated with ultramafic units (Ringenbach, 1992) along subvertical shears (Billedo, 1994), forming a metamorphic and ophiolite belt that runs the full length of eastern Luzon (Karig, 1983; Ringenbach, 1992; Billedo, 1994).

The metamorphic units consist of highly schistose but only weakly greenschist metamorphosed chlorite-mica schists, grey to black phyllites, alternating black to red calcareous sandstones and siltstones, basalts with rare pillow structures, rare volcanoclastic breccias and pink to green coloured marble interbeds (Lubingan Schists; Rutland, 1968; Ringenbach, 1992; Billedo, 1994). The metamorphic units are considered to be Late Cretaceous to Paleogene in age (BMG, 1981). The ultramafic units of the Isabella Ophiolite consist of coarse-grained peridotites, gabbros, basalts (with a N-MORB geochemical signature; Sajona *et al.*, 1999) and a dyke complex (Aurelio & Billedo, 1987; MMAJ, 1987). Palaeontological and radiometric age determinations indicate an Early Cretaceous age for the ophiolite and a Late Cretaceous age for the overlying series of basalts, limestones and claystones (MMAJ, 1987; Sajona *et al.* 1999). The ultramafic units are locally in strike-slip contact, or overthrust, by the Caraballo Group and other Eocene-Oligocene island arc sequences along the Divicalan Thrust (Figure 2.2; MMAJ, 1990), with ophiolite emplacement considered to have occurred some time between the Late Oligocene and the Early Miocene (MMAJ, 1990; Sajona *et al.* 1999).

***Caraballo Formation***

The volcanic rocks of the Caraballo Formation (Ringenbach, 1992; Billedo, 1994; Caraballo Group of MMAJ, 1977) have the largest areal extent of any rock unit in Caraballo and Northern Sierra Madre mountains (Figure 2.2). The Caraballo Group has a maximum stratigraphic thickness of at least 6000 meters (MMAJ, 1977; Sajona *et al.* 1999). The Caraballo Formation consists of two main facies, a proximal lava-dominated facies and a distal pelagic volcanoclastic facies (Billedo, 1994). The proximal facies is composed of dark green to grey or black, typically aphanitic basalts and andesites with associated coarse volcanoclastic deposits and sandstones (MMAJ, 1977; Ringenbach, 1992; Billedo, 1994). Most of the lavas appear to have been emplaced subaqueously (MMAJ, 1977; Billedo, 1994). Minor pelagic sedimentary horizons, including red and green mudstones, cherts and limestones are interbedded with the volcanic rocks (Billedo, 1994). The distal facies is composed of thinly bedded, hard, well stratified red and green mudstones, siltstones, rare cherts and volcanoclastic to siliceous sandstones with interbedded basalt flows and volcanoclastic conglomerates (Billedo, 1994). The proximal volcanic facies is best exposed along the axis of the Caraballo Mountains and the Northern

Sierra Madre while the best exposures of the distal pelagic facies crop out along the eastern coastline of the Northern Sierra Madre.

Both the proximal and distal facies of the Caraballo Formation have been weakly metamorphosed to pumpellyite-prehnite to greenschist facies. The formation is typically strongly faulted and contains open folds with NNW-trending fold axes (MMAJ, 1977; Billedo, 1994). The Caraballo Formation is based on Cretaceous to Late Eocene in age based on a K/Ar age of  $39 \pm 2$  Ma for a basalt, together with the presence of Middle Eocene fossils in inter-pillow pelagic sediments, and Late Eocene fauna in a limestone (Ringebach, 1992). The Caraballo Formation is correlatable to the Eocene volcanics of the Abuan River Formation, which are exposed along the axis of the northern end of the Northern Sierra Madre (MMAJ, 1987), and can also be tentatively correlated with the Cretaceous to Eocene Pugo Formation of the Baguio region (Figure 2.3; MMAJ, 1977). The basalts of the proximal facies have a primitive island arc composition (Sajona *et al.*, 1999).

#### ***Mamparang and Upper Mamparang Formation***

The volcanic and volcanoclastic rocks of the Mamparang Formation (MMAJ, 1977) unconformably overlie the Caraballo Formation in the Mamparang Mountains (Figure 2.2; MMAJ, 1977; Hashimoto *et al.*, 1980). In the Didipio region, the Mamparang Formation hosts the Didipio Intrusive Complex. The Mamparang Formation has a maximum stratigraphic thickness of at least 4000 metres (MMAJ, 1977) and consists of greenish grey to dark grey subalkaline to alkaline andesitic lavas and conglomerates, alkaline to subalkaline basalt flows, alkaline dacite and trachyte lavas and minor volcanoclastic sandstones, mudstones, reworked pyroclastics and rare limestones (MMAJ, 1976, 1977). The Mamparang Formation is considered to be a stratigraphic equivalent of the Zigzag Formation in the Baguio district (Figure 2.3; MMAJ, 1977), and of the Dibuluan River Formation, which crops out along the western flank of the Northern Sierra Madre (Billedo, 1994).

The Mamparang Formation is gently folded with NNW-trending fold axes (Hashimoto, 1980). Zeolite facies metamorphism has occurred, and intensely developed domains of hydrothermal alteration are common throughout the formation (MMAJ, 1977; Hashimoto *et al.*, 1980). The Mamparang Formation has not been radiometrically dated. The formation is unconformably overlain by the Late Oligocene Santa Fe Formation and other Late Oligocene to Middle Miocene limestones. It was originally considered to be Middle to Late Oligocene on the basis of the fauna in interbedded limestone lenses (MMAJ, 1977), although Hashimoto *et al.* (1978) attributed a Late Eocene to Early Oligocene age to the formation. A basaltic dyke from the Dibuluan River Formation, a possible Mamparang Formation correlate, returned a K/Ar age of  $28.85 \pm 1.99$  Ma (middle Oligocene) and a basaltic flow returned a K/Ar age of  $28.58 \pm 1.06$  Ma (Billedo, 1994). The Dibuluan River and Mamparang Formations could therefore be tentatively assigned an age of early Late Oligocene, or more strictly, pre-Ibulao limestone (Billedo, 1994).

## REGIONAL GEOLOGY

In the Didipio region, the Mamparang Formation consists of subalkaline andesite lavas and volcanoclastic conglomerates that are overlain conformably (?) by trachytic lavas and volcanoclastic units. These units are described in detail in the next chapter. The trachytic lavas are part of a belt of potassic, coarsely porphyritic dacites, trachytes, and feldspathoid-bearing trachytes (phonolites) that extends from Didipio to Cordon. These felsic units have been intruded by the co-magmatic Didipio ( $23.2 \pm 0.6$  Ma; Wolfe, 1999), Palali (25 to 17 Ma; Albrecht & Knittel, 1990) and Cordon (25 to 23 Ma; Knittel, 1983) igneous complexes. The trachytes are considered to be an Early Miocene extension of the Mamparang Formation, and are informally termed the 'Upper Mamparang Formation' to distinguish them from the underlying andesitic units of the Mamparang Formation.

Hashimoto *et al.* (1980) described a conglomeratic member of the Mamparang Formation that he considered, based on structural characteristics, to be a younger facies that was partially coeval with deposition of the Late Oligocene Columbus Formation limestone. The volcanoclastic sandstones and conglomerates of this unit were informally designated the 'Didipio Formation' by Hashimoto *et al.* (1980) and were interpreted to be the uppermost, post volcanic part of the Mamparang Formation. However, despite its name, this unit does not crop out in Didipio, but is exposed several kilometres to the east in a region mistakenly identified as Didipio on old topographic maps. The unit is possibly a member of the Dibulan River Formation, which crops out in the area.

### *Late Oligocene to Middle Miocene limestones*

In the Late Oligocene to Middle Miocene, a series of limestone formations with overlapping faunal assemblages were deposited throughout northern Luzon (Figures 2.2 & 2.3). These limestones unconformably overlie the Caraballo Formation, Mamparang Formation and the Oligocene Dupax Batholith, but are disrupted by Mid-Miocene (17 Ma) alkaline volcanism (Palali Formation) in the Mamparang Mountains (MMAJ, 1977; Ringenbach, 1992; Billedo, 1994). The limestone packages have been given several local names (Figure 2.3). Along the south east edge of the Cagayan Valley Basin, the late Late Oligocene to Early Miocene Ibulo Limestone (Christian, 1964) and Middle Miocene Callao Limestone (Durkee & Peterson, 1961) are exposed. At the southern tip of the Cagayan Valley Basin, the Middle Miocene Aglipay Limestone (MMAJ, 1977) was deposited, which is inferred to be a correlate of the Callao Limestone. The late Early to early Middle Miocene Kennon Limestone formed in the Central Cordillera (Balce *et al.*, 1980; Maletterre, 1989). The Late Oligocene Columbus Formation (MMAJ, 1977) was deposited in the Mamparang Mountains. In the Caraballo Mountains and southern parts of the Northern Sierra Madre shallow marine sedimentation resulted in the deposition of the Late Oligocene to Early Miocene Santa Fe Formation (MMAJ, 1977).

The limestones consist mostly of pure white to pale grey, massive to thickly bedded coralline limestones, typically a biosparite or biomicrite, with common interbedded calcarenites and calcirudite lenses. The formations have a typical stratigraphic thickness of approximately 300 meters. They were deposited in a shallow marine environment, with the Ibulo Limestone

containing fore-reef, back reef, lagoon and main reef facies (Billedo 1994). The deposition of these limestones is probably related to the Binangoan inundation, a world-wide sea level rise that occurred during the Late Oligocene to Middle Miocene (Vail *et al.*, 1977).

The Santa Fe Formation consists of massive pure white to pale grey limestones of different ages spanning Late Oligocene to Early Miocene that are distributed throughout the Caraballo Mountains (Hashimoto *et al.*, 1980; Ringenbach, 1992). The stratigraphic thickness is at least 300 meters (Hashimoto *et al.*, 1980). The limestones unconformably overlie the Dupax Batholith, Caraballo Formation and the Mamparang Formation (Hashimoto *et al.*, 1980; Billedo, 1994). Billedo (1994) considered the Santa Fe Formation to be at least in part intercalated with the late Oligocene Dibuluan River Formation. Ringenbach (1992) observed andesitic to dacitic volcanics, assumed to belong to the Middle Miocene Palali Formation, overlying the Santa Fe Formation in the Dalton Pass region. Hashimoto *et al.* (1980) correlated the Late Oligocene Columbus Formation of the Caraballo Mountains to the Santa Fe Formation based on similarities in faunal assemblage.

#### ***Mid-Miocene Palali Formation***

The Palali Formation consists of hornblende-bearing dacites and andesites, minor basalt lava, reworked pyroclastic deposits and interbedded mudstones and sandstones. It crops out around Mt. Palali and Santa Fe (Figure 2.2; MMAJ, 1977). The extrusive units have a high-K calc-alkaline to shoshonitic geochemical signature (MMAJ, 1977). Welded 'tuffs' within the formation suggest that volcanism was, in part, subaerial (MMAJ, 1977). The Palali Formation has a stratigraphic thickness of at least 300 meters (MMAJ, 1977), and unconformably overlies the Dupax Batholith and the Caraballo, Mamparang, Santa Fe and Columbus Formations (Figure 2.3). Syenite clasts sourced from the Palali Batholith have also been noted (MMAJ, 1977; Ringenbach, 1992). This formation is in turn overlain by the Plio-Pleistocene conglomerates of the Pantabangan Formation, and by limestones considered to be part of the Santa Fe Formation by MMAJ (1977) but more likely to be a Middle-Miocene correlate of the Aglipay Formation.

MMAJ (1977) provided a single K/Ar age on the Palali Formation of  $17.6 \pm 1.0$  Ma (late Early Miocene). This is consistent with the  $17.1 \pm 0.5$  Ma and  $17.3 \pm 0.4$  Ma K/Ar ages obtained from a basalt dyke and a basalt cobble from the Pantabangan Formation respectively (Ringenbach, 1992).

#### ***Cagayan Valley Basin and other post-Palali Formation Sediments***

The Cagayan Valley Basin is filled by a thick sequence of post-Oligocene carbonate and clastic sediments that have a total stratigraphic thickness of at least 7 km (Caagusan, 1977). The sediments were deposited on a basement of basaltic volcanics (Christian, 1964), and they onlap the flanks of the Northern Sierra Madre and Central Cordillera Ranges. The sediments progressed with time from marine (Late Oligocene Ibulo Formation, Late Oligocene to Middle Miocene Lubuagan Formation and the Middle Miocene Callao and Aglipay Formations; Corby *et al.*, 1951; Durkee & Pederson, 1961; Tamesis, 1976; Billedo, 1994; Figure 2.3), through

## REGIONAL GEOLOGY

marine-brackish (Miocene-Pliocene Cabagan Formation; Billedo, 1994) to alluvial (Upper Pliocene-Pleistocene Iiagan Formation and Quaternary gravels; Corby *et al.*, 1951; Billedo, 1994). The Iiagan Formation is a correlate of the Pliocene to early Pleistocene Pantabangan Formation that crops out in the Caraballo Mountains (Ringebach, 1992; Billedo, 1994; Figure 2.3). The eastward migration of the Cagayan Valley depocentre in the Middle Miocene (Christian, 1964; Caagusan, 1977), and Pleistocene slumping of sediments along the western margin of the Cagayan Valley Basin, are attributed to uplift of the Central Cordillera range, which began in the Middle Miocene (Christian, 1964; Caagusan, 1980). Prior to the Middle Miocene, the Cagayan Valley Basin and Central Luzon Valley Basin are thought to have been connected (Ringebach, 1992), whereas the Northern Sierra Madre and the axis of the Central Cordillera range were the main landmasses (Ringebach, 1992). The Caraballo Mountains and Southern Sierra Madre ranges emerged after the Middle Miocene (Ringebach, 1992). The sea retreated from the Cagayan Valley Basin and uplift of the Central Cordillera produced the present physiography in the Late Pleistocene (Ringebach, 1992).

### Intrusive Units

Geochemical and geochronological studies have defined four main periods of magmatism in northern Luzon: Eocene, Oligocene, Late Oligocene to Early Miocene and Middle Miocene to Quaternary (MMAJ, 1977; Wolfe, 1981; Sajona *et al.*, 1999). Primitive island arc Eocene magmatism (47 to 43 Ma) produced the tonalites that are exposed in the southern section of the Coastal Batholith, along the east coast of Luzon (Sajona *et al.*, 1999).

Extensive tholeiitic to calc alkaline magmatism occurred during the Oligocene, with emplacement of the batholiths of the Caraballo Mountains (Dupax Batholith, 33-23 Ma), Northern Sierra Madre Range (Northern Sierra Madre Batholith, 31-22 Ma; the northern section of the Coastal Batholith, 32-27 Ma), and Central Cordillera range (32-17 Ma 'Cordilleran Batholith'; Sajona *et al.*, 1999). The Oligocene intrusions are aligned north-south, parallel to the axis of the Sierra Madre arc.

There was a distinct change in magmatic compositions from the Late Oligocene to Early Miocene, with emplacement of small alkaline to ultrapotassic intrusive centres at the tip of the Cagayan Rift Valley, and shoshonitic dykes intruded throughout the Caraballo Mountains and Northern Sierra Madre (Knittel, 1987; Billedo, 1994). No magmatism younger than 20 Ma for the Northern Sierra Madre or 17 Ma for the Caraballo Mountains has been identified. However, after a hiatus, magmatism resumed in the Central Cordillera, continuing intermittently from Middle Miocene to Quaternary times. Compositions varied from initial tholeiitic to dominantly calc-alkaline with time (Sajona *et al.*, 1999).

### *Eocene Intrusives (Coastal Batholith)*

The diorites and tonalites of the Coastal Batholith (MMAJ, 1977) have intruded the Caraballo Formation (Billedo, 1994) and are exposed along the east coast of Luzon, north of Baler (Figure 2.2). In the south, the batholith consists of dark greenish grey medium- to coarse-grained



tonalite (MMAJ, 1977; Billedo, 1994). The northern section of the batholith consists of diorite and gabbro (MMAJ, 1977; Billedo, 1994). Age dating by MMAJ (1977) was reinterpreted by Wolfe (1981) and when combined with the geochemistry of Sajona *et al.* (1999) shows that the northern and southern intrusions have different ages and geochemical compositions. The southern tonalite is Eocene (49-43 Ma; MMAJ, 1977; Wolfe, 1981) and has a primitive island arc composition (Sajona *et al.*, 1999). The northern diorite is related to Oligocene magmatism (32-27 Ma; MMAJ, 1977; Wolfe, 1981). Although Florendo (1994) suggested that the southern tonalite is a fault-bound allochthonous block, Ringenbach (1992) and Billedo (1994) found that the southern mass of the Coastal Batholith has intruded the surrounding Caraballo Formation.

#### ***Oligocene Intrusives (Dupax and Northern Sierra Madre Batholiths)***

Oligocene tholeiitic to calc-alkaline magmatism produced the Dupax Batholith (MMAJ, 1977), which is exposed in the Caraballo Mountains south west of Didipio. At this time the northern section of the Coastal Batholith (MMAJ, 1977; Wolfe, 1981) and the Northern Sierra Madre Batholith (MMAJ, 1987), exposed along the axis of the Northern Sierra Madre mountain range, intruded to the north of the Coastal Batholith (Figure 2.2).

The Dupax Batholith intruded the Eocene Caraballo Formation in the Dupax-Santa Fe region (Figure 2.2). The batholith consists of dark green-grey, fine- to medium-grained tonalites, diorites and gabbros with a mineralogy identical to the coastal and cordilleran batholiths (MMAJ, 1977). K/Ar age dating of tonalites from the Dupax Batholith by MMAJ (1977) returned ages of 33 to 23 Ma (Early Oligocene to early Early Miocene) while Ringenbach (1992) obtained a K-Ar date of  $28.5 \pm 1.2$  Ma for a gabbro.

The northern section of the Coastal Batholith (Figure 2.2) consists of dark-coloured fine to medium-grained diorite and minor dark green grey medium- to coarse-grained gabbro. The diorite has an Oligocene age (32-27 Ma; MMAJ, 1977; Wolfe, 1981) and a primitive island arc to tholeiitic geochemical composition (Sajona *et al.*, 1999). These compositions and ages are similar to other Oligocene batholiths in the Caraballo Mountains and Northern Sierra Madre.

The Northern Sierra Madre Batholith (MMAJ, 1987) crops out along the axis of the Northern Sierra Madre range, merging at its southern end with the Coastal Batholith (Figure 2.2). The Northern Sierra Madre batholith consists of medium- to coarse-grained tonalites, quartz diorites and granodiorites (MMAJ, 1987; Billedo, 1994), which have intruded the Eocene volcanics of the Abuan River Formation, a correlate of the Caraballo Formation (MMAJ, 1987). The batholith has been dated by MMAJ (1987), using K-Ar methods, at  $31.1 \pm 1.5$  to  $22.3 \pm 1.1$  Ma (late Early Oligocene to early Early Miocene). Sajona *et al.* (1999) obtained a K/Ar age for a quartz-diorite of  $25.3 \pm 1.0$  Ma, Ar/Ar ages of 21 to 25 Ma on amphibole separates from the same sample, and K/Ar age determinations of  $28.8 \pm 0.8$  and  $28.6 \pm 1.0$  Ma (late Oligocene) for two dykes from opposing flanks of the Northern Sierra Madre range. Billedo (1994) reported a  $30.2 \pm 0.7$  K/Ar age for a diorite considered to be part of the Northern Sierra Madre Batholith.

## REGIONAL GEOLOGY

### ***Cordon Syenite Complex***

The Cordon Syenite Complex is located 30 km to the north of Didipio, along the faulted western margin of the Cagayan Valley Basin (Figure 2.2). The Cordon Syenite Complex consists of syenites and monzonites, with minor pseudoleucite-bearing syenite and cumulate pyroxenites that are preserved only as xenoliths within other phases (Knittel, 1987; Knittel & Cundari, 1990). The intrusive complex is hosted within co-magmatic analcite-bearing trachytic pyroclastics ('tephritic phonolites'). The typically equigranular medium- to coarse-grained syenites and commonly porphyritic monzonites consist of K-feldspar, plagioclase, clinopyroxene and biotite, with accessory apatite and magnetite (Knittel, 1987). Late stage medium- to coarse-grained alkali syenite pegmatites occur as dykes several tens of meters wide, and consist of perthitic tabular K-feldspar, clinopyroxene, biotite, apatite and rare muscovite, sphene and plagioclase (Knittel, 1987). The intrusions are hosted by a sequence of pre-Oligocene 'tuffs' (?Caraballo Formation; Knittel, 1987). These tuffs are overlain by analcite-bearing tephritic phonolite pyroclastic flows that are intercalated with subalkaline andesite to dacite conglomerates to the southwest (Knittel, 1987). The Cordon Syenite Complex hosts Au-Ag-Pb-Zn low sulphidation epithermal veins (Marian gold mine; Baquiran, 1975; Alapan, 1981; Knittel, 1982) and the Marian Porphyry, a small (8 Mt) Cu deposit associated with a syenite stock (Baquiran, 1975).

Knittel (1983) obtained a Rb-Sr age of  $25.1 \pm 0.7$  Ma on biotite, and a K/Ar age of  $23.1 \pm 3.0$  Ma for amphibole. These are in agreement with the  $23.3 \pm 0.5$  Ma K/Ar age for a syenite porphyry recorded by Billedo (1994). These ages are contemporaneous with the commencement of rifting along the Cagayan Valley Basin (Christian, 1964), and are also coeval with the Late Oligocene to early Miocene palaeontological ages for the Santa Fe and Columbus Limestones and with the youngest intrusions from the Dupax and Northern Sierra Madre batholiths. It is possible that there were two contemporaneous magmatic suites forming in northern Luzon during the Late Oligocene; one with tholeiitic affinities (the Dupax and Northern Sierra Madre Batholiths) and a second with high-K calc alkaline to shoshonitic affinities in the Palali-Cordon region.

### ***Palali Batholith***

The light pinkish grey, typically equigranular medium- to coarse-grained potassic syenites, nepheline syenite, and nepheline monzosyenites of the Palali Batholith intruded the subalkaline volcanics of the Mamparang Formation approximately 15 km to the northwest of Didipio (Figure 2.2; Albrecht & Knittel, 1990). Small syenite dykes have intruded diorites of the Dupax Batholith (MMAJ, 1977). K/Ar age dating of the Palali Batholith by MMAJ (1977) returned ages from 25 to 17 Ma. It is possible that the youngest age relates to argon loss due to thermal resetting (Albrecht & Knittel, 1990). If so, then the Palali Batholith has an age comparable both to the Cordon Syenite Complex and to the age of porphyry Cu-Au mineralisation at Dinkidi (Albrecht & Knittel, 1990; Knittel, 1983; Wolfe *et al.*, 1999).

The Palali Batholith consists of three main phases: a southern syenite body, a northern nepheline syenite body, and a small central mass of nepheline monzosyenite (Albrecht &

Knittel, 1990). The batholith has intruded what is interpreted to be a small caldera structure (Albrecht & Knittel, 1990). The nepheline syenites and monzosyenites consist predominantly of alkali feldspar and plagioclase, with 8 to 12 % modal nepheline and accessory clinopyroxene, amphibole, magnetite, biotite, apatite and sphene.

Alkaline trachyte lavas and pyroclastics of the Upper Mamparang Formation are associated with the intrusions. They are considered to be late stage caldera fill ignimbrites. Pseudoleucite-phyric trachyte dykes have intruded the Mamparang and Upper Mamparang Formations (Albrecht & Knittel, 1990).

The Palali Batholith hosts the Runruno high-sulphidation epithermal gold deposit, which is currently worked by a multitude of small- and no-claim owners.

### ***Alkaline Dykes***

Early Miocene alkaline magmatism in the Northern Sierra Madre and Caraballo Mountains produced numerous alkaline basaltic to andesitic dykes. Billedo (1994) reported a  $24.02 \pm 0.87$  Ma K/Ar age for a basaltic dyke located south of Baler, which has intruded the Coastal Batholith, and  $20.45 \pm 0.45$  Ma K/Ar whole rock and  $21.9 \pm 0.1$  Ma Ar/Ar amphibole ages for a shoshonitic hornblende andesite from north of Dinapigue, which has intruded the peridotites of the Isabella Ophiolite (Figure 2.2). The dykes are the last magmatic event known in the Northern Sierra Madre, post-dating the main alkaline intrusive centres in the Mamparang Mountains.

### ***Central Cordilleran Magmatism***

Magmatism in the Central Cordillera range occurred in two distinct periods. The Eocene island arc tholeiitic volcanic and related volcanoclastic rocks of the Pugo Formation (Sajona *et al.*, 1999), and Oligocene to Early Miocene dioritic batholiths, have similar geochemistry to the contemporaneous magmatism of the Caraballo Mountains and Northern Sierra Madre (Sajona *et al.*, 1999). A hiatus in magmatism in the cordillera is marked by the deposition of the Kennon Limestone, during the late Early Miocene to early Middle Miocene (Maleterre, 1989). The second phase of magmatism occurred along the Central Cordillera intermittently from the Middle Miocene to Quaternary. The two periods of magmatism in the Central Cordillera are geochemically distinct. The early Oligocene to Early Miocene magmas are characterised by a great chemical variety, with primitive island arc, tholeiitic and calc-alkaline trends, and high Pb isotope ratios suggestive of continental crust affinities (Maleterre, 1989). In contrast, the post-Kennon Middle Miocene to Quaternary magmatism is characterised by more homogeneous geochemistry with tholeiitic to calc alkaline trends, some  $K_2O$  and incompatible element enrichment, and Pb isotope ratios more consistent with a mantle source regime (Maleterre, 1989). Porphyry mineralisation in the Baguio district is associated with the second period of magmatism and the intrusion of the Black Mountain Porphyry (Balce *et al.*, 1980; Pena, 1994). Two diorite samples from this unit were radiometrically dated at 5.9 Ma and 3.8 Ma using the K/Ar method (Pena, 1994). Alteration within the Black Mountain Porphyry returned K/Ar ages of 5.6 Ma to 3.6 Ma (Wolfe, 1988). One of the worlds largest low sulphidation epithermal gold districts formed in the Baguio region during the Pleistocene (Wolfe, 1988).

## SUMMARY

The oldest rock units exposed in northern Luzon are tectonically juxtaposed metamorphics and Middle to Late Cretaceous ophiolites. They form the basement to the volcanics of the Caraballo Mountains and Northern Sierra Madre, and crop out in a belt that extends along the east coast of Luzon (Ringebach, 1992; Billedo, 1994). The schists and ultramafics were tectonically amalgamated and metamorphosed at some time between the Late Cretaceous and the Early Eocene (Karig, 1983; Ringebach, 1992).

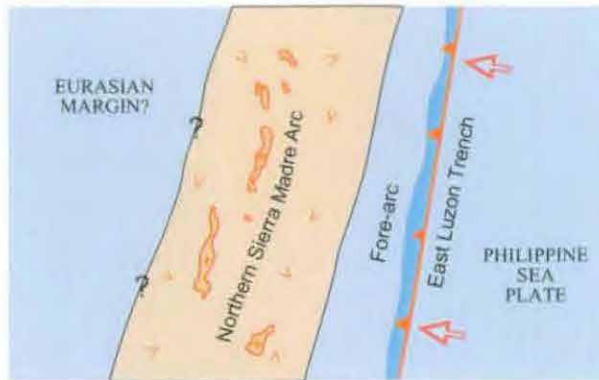
During the Eocene, a volcanic arc formed above the structurally complex basement in northern Luzon (Figure 2.4). Primitive island arc basaltic to andesitic submarine volcanics of the Eocene Caraballo Formation were deposited synchronously with pelagic sediments deposited in adjacent basins (MMAJ, 1977; Ringebach, 1992; Billedo, 1994). The Cretaceous (?) to Eocene volcanoclastics and lavas of the Pugo Formation in the Central Cordillera may be a distal facies of this arc (Sajona *et al.*, 1999). The Eocene volcanic pile, referred to as the 'Sierra Madre Arc' by Florendo (1994), was intruded by the Eocene (49-43 Ma) tonalite of the Coastal Batholith. The tonalite may be part of the batholith that sourced the Caraballo Formation (Lewis & Hayes, 1983). The termination of magmatic activity in the Late Eocene was marked by regional greenschist facies metamorphism and folding around NNW fold axes.

Oligocene batholiths intruded parallel to the axis of the 'Sierra Madre Arc', with magmatism propagating northwards with time (Sajona *et al.*, 1999). The diorites, tonalites and gabbros of the Dupax (33-23 Ma) and Northern Sierra Madre (32-22 Ma) batholiths and the northern dioritic mass of the Coastal Batholith (32-27 Ma) have island arc tholeiitic to calc-alkaline compositions, in contrast to the earlier (pre 30 Ma) primitive island arc magmatism (Sajona *et al.*, 1999), while the Oligocene to Early Miocene quartz diorites of the Central Cordillera (32-17 Ma) have primitive island arc, island arc tholeiite and calc alkaline compositions (Sajona *et al.*, 1999).

There is a similar magmatic history for pre-Miocene units in the Southern Sierra Madre, Northern Sierra Madre, Central Cordillera and Caraballo Mountains. It is possible that the volcanics and batholiths were components of an Eocene to Oligocene arc that was separated by rifting along the Cagayan Valley Basin in the Late Oligocene to Late Miocene (Florendo, 1994). The Eocene to Early Miocene magmatism is generally attributed to westward-subduction along the East Luzon Trough (Karig, 1983; Figures 2.1 & 2.4). Evidence for subduction off the east coast of Luzon at this time include the presence of a fossil subduction complex off the eastern coast of North Luzon (Lewis & Hayes, 1983), the presence of an ophiolite complex (the Isabella ophiolite) that was emplaced into the eastern flank of the North Luzon Terrain in the Late Oligocene or Early Miocene (Lewis & Hayes, 1983; MMAJ, 1990; Florendo, 1994; Sajona *et al.*, 1999), and the apparent lack of oceanic crust to the west of Luzon until the Late Oligocene (Wolfe, 1988; Rangin, 1991).

As tholeiitic and calc-alkaline magmatism waned in the Late Ordovician, the shallow marine to subaerial subalkaline and alkaline volcanics of the Mamparang Formation were deposited on

## Geological history of northern Luzon

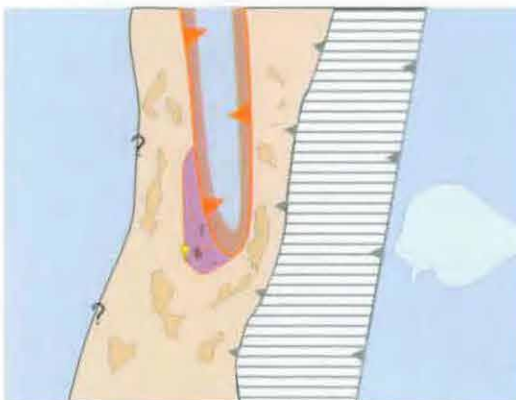
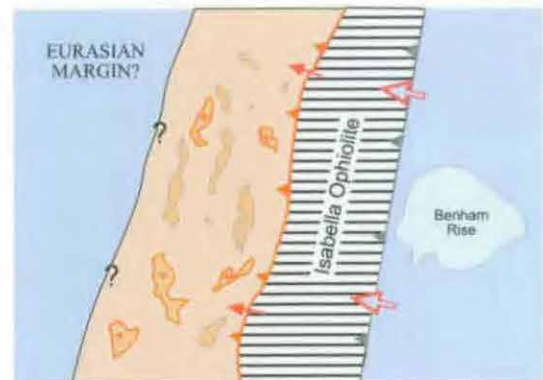


## 1) Eocene

- Westward-directed subduction along the East Luzon Trench
- Construction of the Sierra Madre Arc over a metamorphic basement
- Submarine extrusion of tholeiitic basalts and andesites (Caraballo Formation).
- Emplacement of tholeiitic diorite intrusions (Southern Coastal Batholith)

## 2) Late Oligocene

- Collision of the Benham Rise seamounts into the East Luzon Trench
- Termination of subduction along the East Luzon Trench.
- Compressional tectonics, with the emplacement of the Northern Sierra Madre fore-arc into the Caraballo Formation (forming the Isabella Ophiolite)
- Emplacement of calc-alkaline diorite intrusions (Dupax, Northern Sierra Madre and Northern Coastal Batholiths)



## 3) Late Oligocene to Early Miocene

- Period of extensional tectonism, with commencement of rifting along the Cagayan Valley Basin, coincident with rifting of the South China Sea
- Widespread limestone deposition
- Emplacement of alkaline volcanics (Mamparang Formation) and intrusions (Cordon Syenite Complex, Palali Batholith and Didipio Intrusive Complex) at the head of the Cagayan Valley
- Emplacement of alkaline dykes throughout the Caraballo Mountains and the Northern Sierra Madre
- Emplacement of late Early Miocene alkaline dacite lavas (Palali Formation)

## 4) Middle Miocene to Recent

- Commencement of eastward-directed subduction along the Manila Trench
- Continued subsidence of the Cagayan Valley Basin and uplift of the Central Cordillera and the Caraballo Mountains
- Intrusion of calc-alkaline diorite batholiths along the Central Cordillera
- Retreat of the sea from the Cagayan Valley Basin and deposition of clastic sediments
- Movement along the Philippine Fault juxtaposes the East Luzon Terrain with possibly Eurasian-derived terrains



Figure 2.4: Tectonic history of Northern Luzon. See Figures 2.1 & 2.2 for key to colours and symbols. Based on Ringenbach, 1992; Billedo, 1994; Florendo 1994 & Sajona *et al.*, 1999)

## REGIONAL GEOLOGY

the eroded surface of the folded, greenschist metamorphosed Caraballo Formation in the Caraballo and Northern Sierra Madre ranges. This marked the onset of alkaline magmatism in the location of the future Cagayan Valley Basin.

Undersaturated alkaline to potassic magmatism developed at the end of the Oligocene in association with the commencement of rifting along the Cagayan Valley Basin (Knittle, 1987). Extrusion of the potassic lavas of the Upper Mamparang Formation and the intrusion of alkaline intrusive centres occurred along the rifted western margin of the Cagayan Valley Basin. The alkaline intrusives were emplaced at 25-23 Ma, contemporaneous with the youngest diorites in the Caraballo Mountains and Northern Sierra Madre ranges. At this time, two contemporaneous magmatic suites were being emplaced into Northern Luzon: a waning arc-tholeiitic-calc alkaline suite (the Dupax and Northern Sierra Madre Batholiths) and the alkaline to potassic suite at the tip of the Cagayan Rift Valley (Figure 2.4). Despite the compositional differences, radiogenic isotope data suggests that both suites shared a similar mantle source (Knittel & Defant, 1988).

Unlike the coeval tholeiitic-calc alkaline magmatic suite, each of three main alkaline intrusive centres in northern Luzon hosts economic mineralisation. The Cordon Syenite Complex hosts the Marian Cu-Au porphyry and epithermal Au-Ag-Pb-Zn vein systems. The Palali Batholith hosts the Runruno epithermal gold system, and the Didipio Igneous Complex hosts the Dinkidi Cu-Au Porphyry deposit.

Gentle folding around NNW-trending fold axes occurred prior to the deposition of the Late Oligocene to Early Miocene Santa Fe and Columbus Limestones. The Late Oligocene sea level rise (the Binangoan Inundation, Vail *et al.*, 1977) resulted in widespread deposition of shallow water coralline limestones throughout the Northern Sierra Madre, the Central Cordillera, the Mamparang and Caraballo Mountains and the base of the Cagayan Valley Basin. On the basis of overlapping palaeontological and radiometric ages the limestones may have been partially coeval with the deposition of the Cordon Volcanics and the initial rifting of the Cagayan Valley Basin. This rifting is coeval with the rifting of the Eurasian margin (Figure 2.1), which is considered to have formed the South China and Sulu Seas in the Late Oligocene (Wolfe, 1988, Rangun, 1991).

The final period of magmatism in the Mamparang Mountains is marked by the extrusion of the alkaline Palali Formation volcanics at 17 Ma. The reported occurrence of welded 'tuffs' and primary pyroclastic material suggests at least partial subaerial emplacement of the Palali Formation. These units were subsequently overlain by ?Middle Miocene Limestone. In the Northern Sierra Madre Range the youngest magmatic unit known is a 20 Ma shoshonitic dyke that has intruded the Isabella Ophiolite. The waning of magmatism throughout northern Luzon in the Early Miocene is attributed to the termination of subduction along the East Luzon Trough (Knittle & Defant, 1988; Wolfe, 1988). Subduction may have been halted by the collision of the Benham Rise Seamounts into the East Luzon Trench in the late Oligocene to Early Miocene (Lewis & Hayes, 1983), contemporaneous with the emplacement of the Isabella Ophiolite (Figure 2.4). Since this time, the Northern Luzon Terrain has been coupled to the Philippine Sea

Plate. This collisional event may have been responsible for the weak folding of the Mamparang Formation that occurred prior to the deposition of the Santa Fe Limestone.

No Middle to Late Miocene sediments are preserved in the Caraballo or Northern Sierra Madre ranges, however sediment deposition continued in the Cagayan Valley Basin from the late Oligocene to the Quaternary. The Cagayan Valley Basin fill is at least 7 km deep (Caagusan, 1977), with the sediments progressing from marine in the Middle Miocene, through marine-brackish (Miocene-Pliocene) to alluvial facies in the Upper Pliocene-Pleistocene (Billedo, 1994). The sea is thought to have retreated from the Cagayan Valley Basin in the late Pleistocene (Ringebach, 1992). Slumping of sediments along the western flank of the valley and the eastward migration of the depocentre since the Middle Miocene are considered to relate to the rapid uplift of the Central Cordillera Range from Middle Miocene times (Christian, 1964; Caagusan, 1977).

Early Tertiary magmatism in the Central Cordillera is contemporaneous with magmatism in the Caraballo Mountains and Northern Sierra Madre, continuing throughout the Oligocene and terminating in the Early Miocene at ~17Ma (Maletterre, 1989). However, unlike the magmatism in the ranges to the east, magmatism in the Central Cordillera resumed in the Middle Miocene following a ~5 My hiatus. Magmatic activity was restricted to the axis of the Central Cordillera and was contemporaneous with the rapid uplift of the mountain range. Central Cordilleran magmatism continued intermittently until Quaternary times, ranging from tholeiitic to calc-alkaline compositions (Sajona *et al.*, 1999). This second period of Central Cordilleran magmatism is geochemically distinct from the Oligocene to Middle Miocene period, suggesting a different source to the magmas (Maletterre, 1989). It is associated with the formation of the Central Cordilleran metallogenic province, with emplacement of calc-alkaline porphyry Cu-Au and related high and low sulphidation epithermal and skarn deposits along the cordillera. This post Early-Miocene magmatism can be attributed to eastward-directed subduction along the Manila trench (Karig 1983, Lewis & Hayes 1983, Wolfe 1988, Maletterre 1989; Figure 2.1 & 2.4), with subduction considered to have commenced at ~25 Ma (Lewis & Hayes, 1983; Wolfe, 1988).

The rifting of the Eurasian margin in the Late Oligocene may have been a response to the oblique collision of the Philippine Mobile Belt along the margin of Eurasia, with continued northern movement of the western margin of northern Luzon against Eurasia leading to the development of rift basins in the thinned continental margin and the formation of rifting in the centre of the north Luzon block. Following the coupling of the Philippine Sea Plate and the North Luzon Terrain in the late Oligocene, continued movement of the Philippine Sea Plate set up a compression regime in northern Luzon. This westward-directed compression prevented further rifting of the Cagayan Valley Basin and may have initiated subduction along the Manila Trench, converting the shear zones that separated the rifting margin of Eurasia and the northward moving North Luzon Terrain into a subduction zone. Any further northward movement of the mobile belt was taken up by the Philippine Fault, which first developed in the Middle Miocene and continues to accommodate oblique convergence today (Fitch, 1972; Ringebach, 1992).

# LOCAL GEOLOGY

This chapter describes the geology of the Didipio region, with the aim of determining the volcanic and intrusive history that led to the development of the Dinkidi porphyry deposit. This study has provided the first detailed geological map of the Didipio region (Figure 3.1), which was derived from 10 weeks of mapping in 1995. The main geological feature of the Didipio region is the Didipio Igneous Complex. This igneous complex has intruded the andesitic volcanics of the Mamparang Formation and the trachytic volcanics of the Upper Mamparang Formation (Figure 3.1). The Didipio Igneous Complex consists of 4 main intrusions: an early diorite to monzodiorite pluton; a weakly mineralised monzonite pluton (the 'Surong Monzonite'); a strongly mineralised composite monzonite-syenite stock (the 'Dinkidi Stock'; located at the southern margin of the Surong Monzonite), and late-stage andesite dykes and sills. The Dinkidi Stock hosts the Dinkidi Cu-Au deposit and is described in detail in Chapter 5.

## VOLCANIC UNITS

The Mamparang Formation consists of an andesitic sequence that crops out in the southeastern corner of the map area (Figure 3.1). The overlying trachytic sequence (Upper Mamparang Formation) crops out on the eastern, northern and western edges of the map area (Figure 3.1). Both the andesitic and trachytic sequences have a similar stratigraphic thickness of at least 400 meters each. Figure 3.2 provides a simplified stratigraphic log through the volcanic package.

## Mamparang Formation

### *Andesite lavas*

The andesites of the Mamparang Formation occur as 5 to 30 meter thick flows that range in composition from dark grey clinopyroxene-phyric andesites to less common light grey trachyandesites (Plate 3.1A). They are separated by coarse volcaniclastic deposits. Individual andesite flows tend to be texturally inhomogeneous, with holocrystalline cores and glassy, porphyritic margins. The rubbly, commonly autobrecciated margins of the flows typically grade up into a monomict 'jigsaw fit' breccia and then into the overlying volcaniclastic breccias. The crystalline andesite and trachyandesite lavas in the Didipio region weather to pale green granular regolith whereas more glassy lavas invariably weather to a gritty reddish brown regolith that resembles a massive, fine-grained plagioclase-rich arkose, but with abundant small cream-coloured amygdales still distinguishable. Rare xenoliths include olivine-bearing gabbros, which are petrologically distinct from clinopyroxene-gabbros of the Didipio Igneous Complex, and small fragments of schist that are assumed to be sourced from a basement formation comparable to the Lubingan and Santa Fe Schists (Chapter 2).

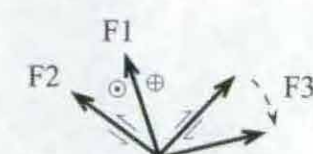


# Geology of the Didipio region

Simplified geological interpretation

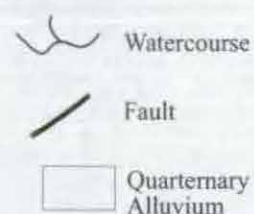


Scale 1: 20,000  
500 m

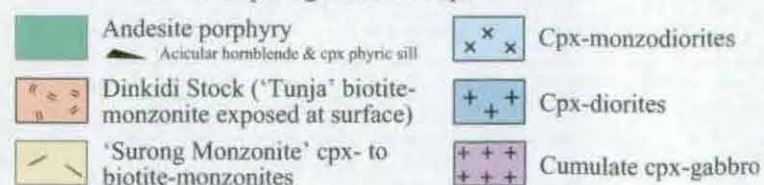


Fault generations

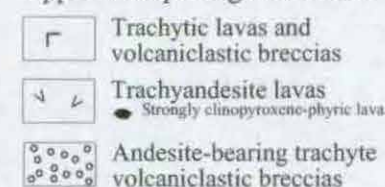
F1: Rare normal faults  
F2: Common sinistral strike-slip  
F3: Common dextral strike-slip



## Didipio Igneous Complex



## Upper Mamparang Formation



## Mamparang Formation

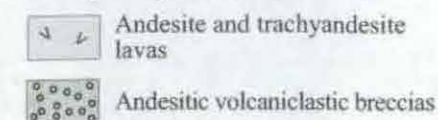


**Figure 3.1:** Geology of the Didipio region. Intrusive units of the Didipio Igneous Complex are shown in colour, volcanic units are in shades of grey. Both igneous and volcanic packages are highly simplified: monzonite, monzodiorite and diorite bodies are all comprised of multiple phases; 'lavas' are lava-dominated packages that contain multiple flows and interbedded volcaniclastic breccias. Position of streams and geological units on the map are approximately only ( $\pm 50$  to 100 m, based on hand-drawn basemap).





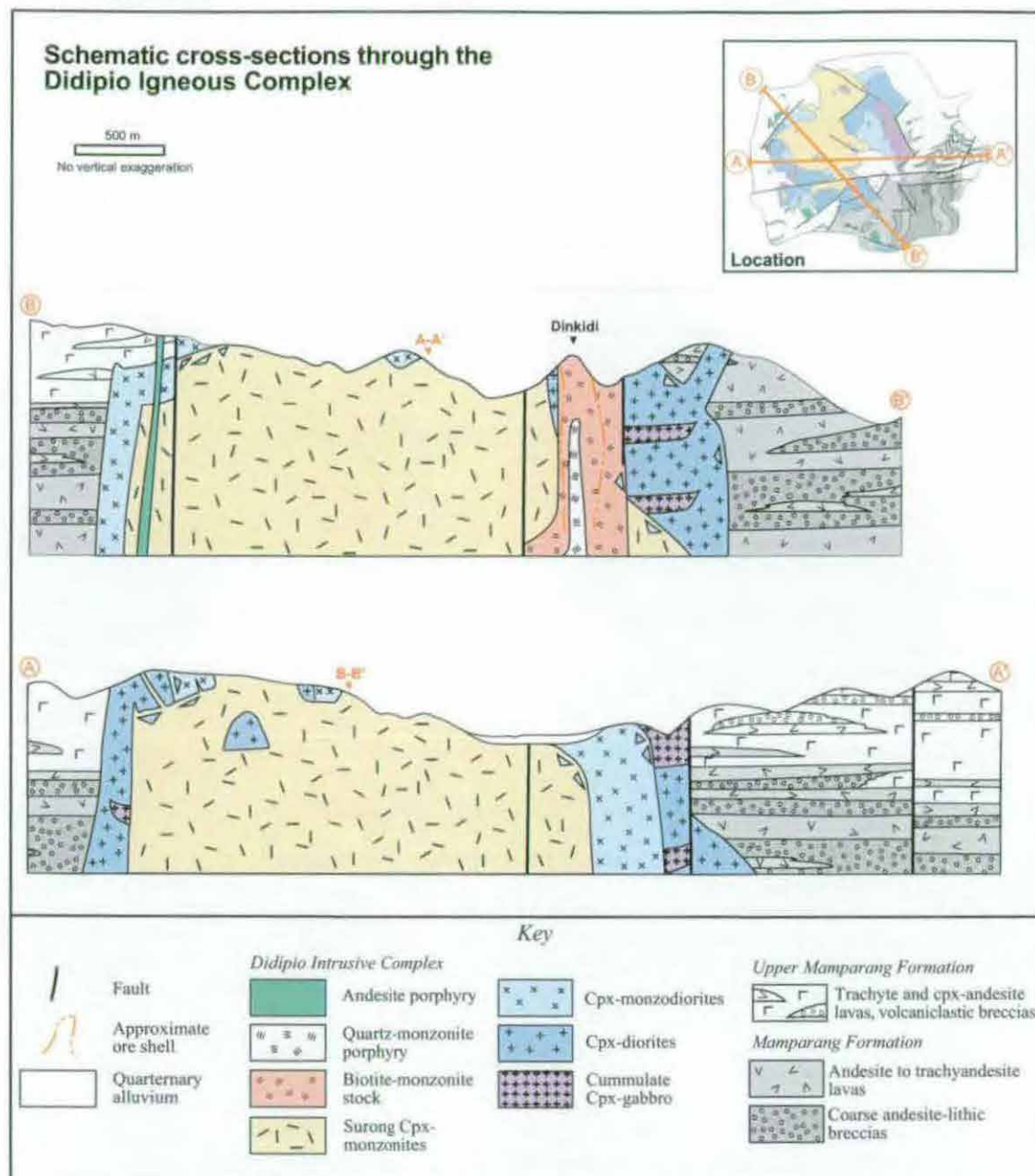


**Figure 3.3:** Simplified cross section through the Didipio Igneous Complex. See insert for location of sections on main map (Figure 3.1). Individual phases within the composite Surong Monzonite are not shown. The cumulate gabbros are assumed to form thick lenses or beds within the diorite intrusion. These cross-sections are based on surface mapping and regional drillcore logging.

The fine to medium-grained andesites are mostly weakly plagioclase-phyric, although uncommon coarsely crystal-crowded andesites are also present. The cores of individual andesite flows are dark blue-grey crystalline andesite, and range from fine-grained equigranular to weakly plagioclase-phyric, while the margins of the flows typically consist of dark grey to black glassy plagioclase-phyric to rarely crystal-crowded andesite. The phenocrysts include albite-twinning plagioclase (distinct from oscillatory-zoned plagioclase found in Didipio Igneous Complex phases) and unzoned clinopyroxene, both of which are typically fragmented (Plates 3.1B & F). There are also uncommon clinopyroxene glomerocrysts and rare, strongly iddingsite-altered olivine phenocrysts. In crystalline phases, these phenocrysts are set in a fine-



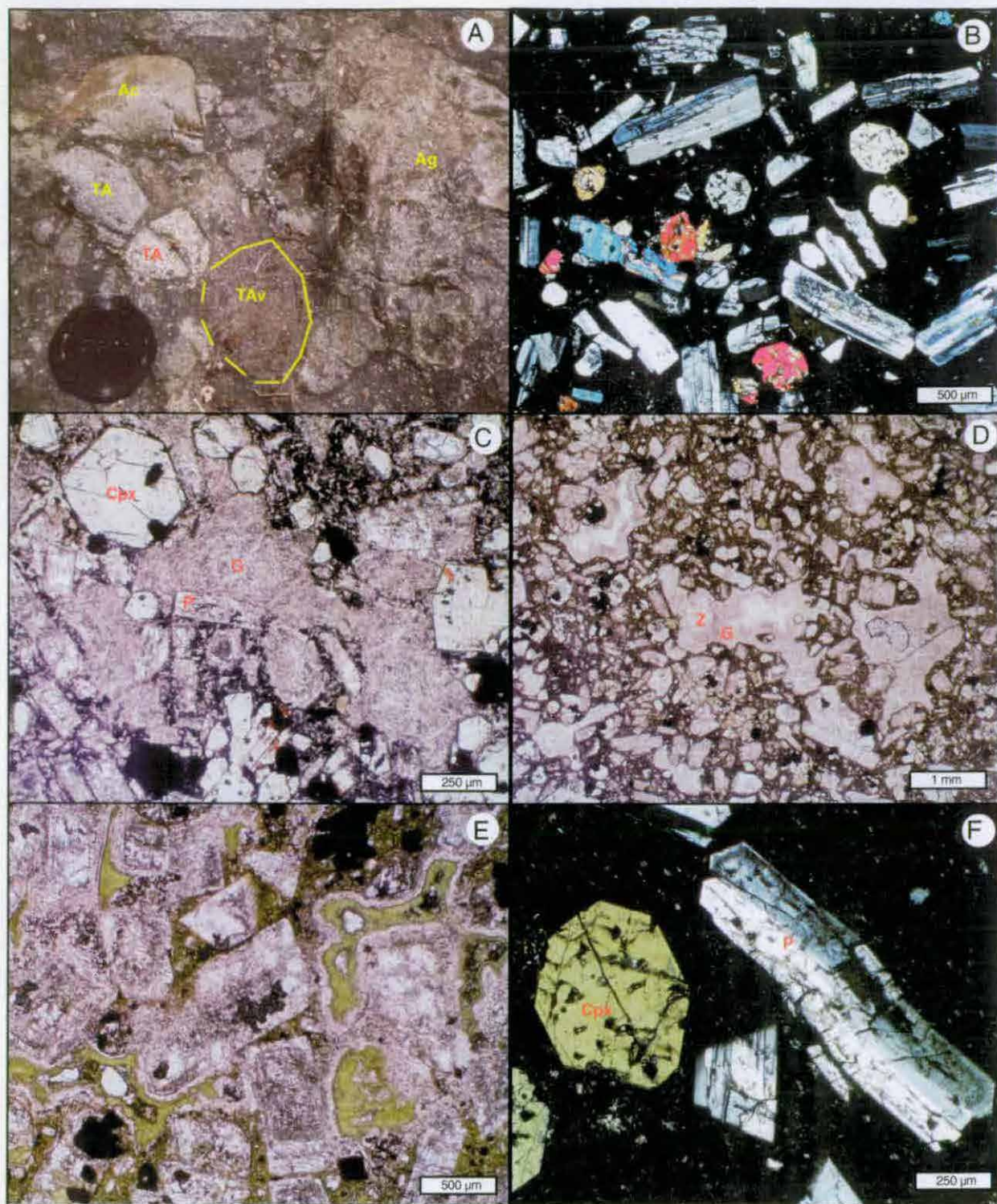


**Plate 3.1 A:** Coarse volcaniclastic breccia: poorly sorted subangular clasts of crystalline andesite (Ac), crystalline trachyandesite (TA), vesicular glassy trachyandesite (TAv) and glassy andesite (Ag) are hosted in a gritty arkose matrix.

**Plate 3.1 B:** Crystalline cpx-andesite: euhedral clinopyroxene and plagioclase phenocrysts are set in a fine-grained crystalline groundmass with abundant plagioclase microlites. XPL. Sample 14.20

**Plate 3.1 C:** Partially glassy cpx-andesite: clinopyroxene (Cpx) and plagioclase (P) phenocrysts are hosted in a microlite-rich crystalline groundmass surrounded by glass-filled amygdaloids (G). PPL. Sample 44.3

**Plate 3.1 D:** Glassy vesicular andesite: plagioclase and clinopyroxene phenocrysts are hosted within a glassy reddish brown groundmass with irregular amygdaloids that are rimmed by glass with the cores filled by zeolites (Z). PPL. Sample 9.2B

**Plate 3.1 E:** Highly vesicular glassy trachyandesite. Extremely clay-altered plagioclase phenocrysts are hosted in a glassy vesicular groundmass that has been extensively chlorite altered. Vesicles are filled by aggregates of chlorite and chlorite-altered glass. PPL. Sample 28.3

**Plate 3.1 F:** Crystalline andesite: clinopyroxene and plagioclase phenocrysts are hosted in a fine-grained groundmass with abundant plagioclase microlites. Many plagioclase crystals in the andesites are fragmented or broken. Closeup of sample in Plate B

## LOCAL GEOLOGY

grained crystalline to partially glassy groundmass. The groundmass contains abundant flow aligned plagioclase microlites, interstitial glass, accessory magnetite, rare apatite and common vesicles or calcite-zeolite-epidote filled amygdales (Plates 3.1B & C). In more glassy units, the phenocryst phases are set in a glassy vesicular groundmass with abundant flow aligned plagioclase microlites, vesicles and small glass, carbonate, epidote and chlorite (after glass) filled amygdales (Plate 3.1D). These amygdales and vesicles typically comprise ~10-20% of a glassy lava and are typically elongate, or, in crystal crowded units, blocky. Glassy fine-grained andesites are uncommonly flow banded.

Light-pinkish grey to dark grey trachyandesites are less common than the andesites, and are always more deeply weathered. They are typically crystal crowded with medium- to coarse-grained plagioclase phenocrysts set in a partially to fully glassy groundmass (Plate 3.1E).

Vesicles in the glassy units can comprise up to 60% of the rock volume and are typically filled by calcite, chlorite (after glass) or epidote.

The andesites and trachyandesites have been altered to a carbonate-clay-sericite assemblage. Typically, there has been strong calcite, illite or sericite replacement of plagioclase cores and clay-carbonate replacement of the groundmass. Clinopyroxene phenocrysts have undergone selectively pervasive biotite and epidote-chlorite alteration in many samples, especially where the unit is adjacent to the contact with the Didipio Igneous Complex. Glassy groundmasses have been altered to chlorite, calcite, zeolite, epidote or quartz, which have in turn been weathered to clay±hematite-rutile-spinel. Carbonate-glass filled vesicles have been replaced by zeolite, chlorite or epidote.

### *Volcaniclastic breccias*

3 to 20 meter thick beds or lenses of volcaniclastic breccia are interbedded with the andesite lavas. The breccias range from pale greenish-grey pebbly arkoses to boulder beds with clasts several meters wide. Individual units are typically between 2 and 8 meters thick. The thinner beds have lensoidal to lobate morphologies. Grading is weak to absent in the poorly-sorted matrix-supported breccias (Plate 3.2B). The top of the breccia lenses, which are rarely preserved, grade into a dark grey to pale green volcaniclastic arenite to arkose with common large fragments or pebbles (Plate 3.2E). The angular to subangular breccia clasts range in size from 0.5 to 150 cm (typically 3 to 15 cm). The breccias are polymictic, containing a range of coherent fragments, including:

- Uncommon cream-coloured coarsely porphyritic dacite
- Grey to reddish brown fine-grained to coarsely plagioclase-phyric or crystal-crowded andesite and trachyandesite (Plates 3.2C & D)



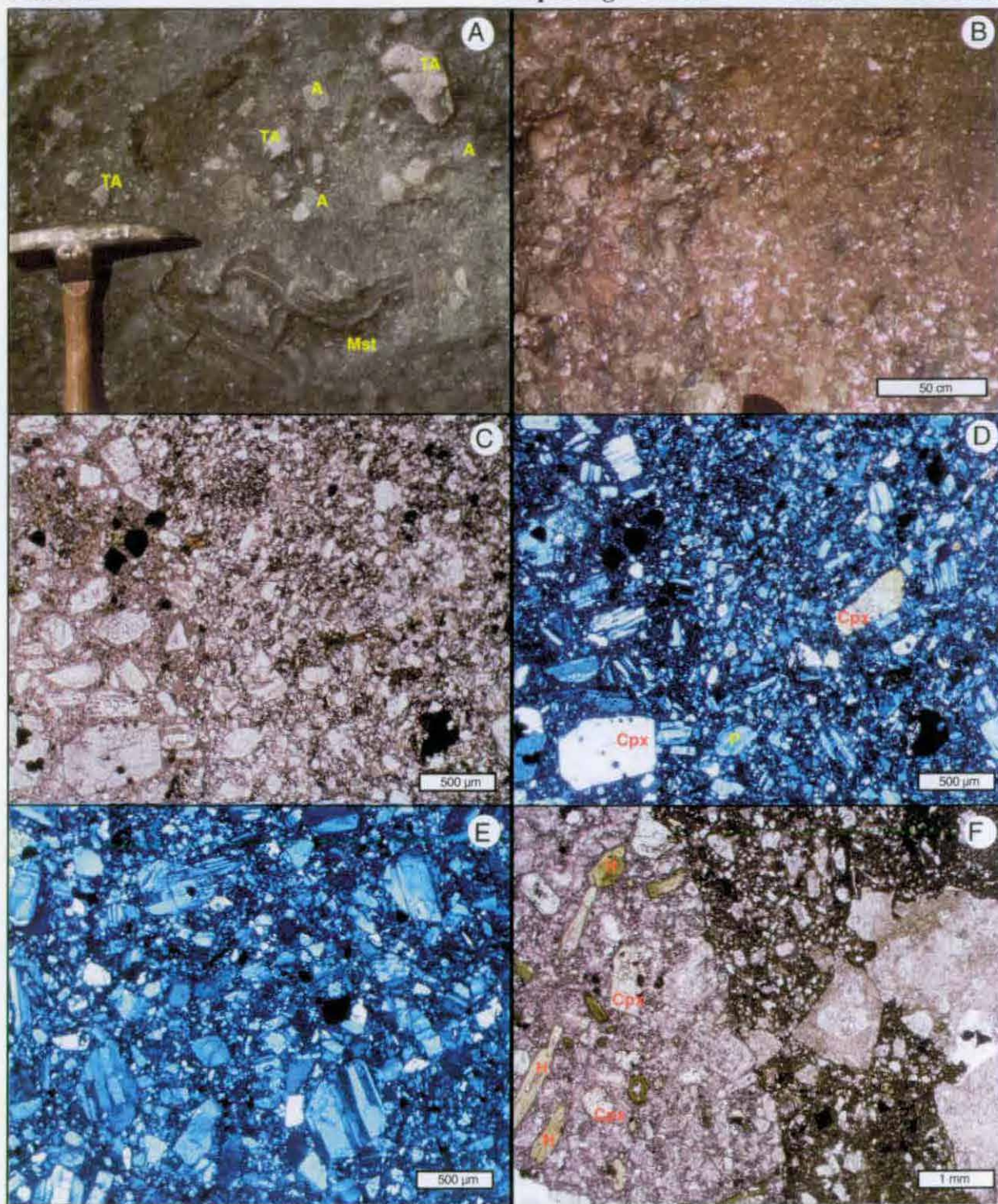


**Plate 3.2 A:** Matrix-supported volcaniclastic breccia within the Mamparang Formation: subangular andesite (A) and trachyandesite (TA) clasts are supported in a gritty arkose matrix. The folded mudstone in the lower half of the photo (Mst) was probably only partly indurated when incorporated into the breccia.

**Plate 3.2 B:** Weak grading within a Mamparang Formation volcaniclastic breccia. The unit ranges from a basal coarse breccia at left in this river bed exposure to overlying pebbly arkose on the right.

**Plate 3.2 C:** Photomicrograph of Mamparang Formation coarse volcaniclastic breccia: crystalline andesite clast (at left) is hosted within an immature arkose. PPL. Sample F23/91

**Plate 3.2 D:** XPL photomicrograph of the sample in Plate C. Fresh clinopyroxene fragments in the matrix and the compositional similarities between matrix and clast highlights the immaturity of the sediments.

**Plate 3.2 E:** Volcaniclastic arkose. Plagioclase fragments are supported within an aphanetic clay-altered cement. XPL. Sample F13/91

**Plate 3.2 F:** Hornblende-phyric andesite lava clast within a volcanic breccia that overlies, but is indistinguishable from, the trachyte-lithic breccias of the Upper Mamparang Formation. Clasts from the andesite porphyry suggest that at least some of the late stage andesite porphyry dykes vented and were incorporated into sediments. PPL. Sample 44.5

## LOCAL GEOLOGY

- Highly vesicular glassy andesite to trachyandesite
- Chilled, black, sparsely porphyritic glassy andesites,
- Rare dark grey olivine-bearing basaltic andesites,
- Rare siltstone and mudstone fragments (Plates 3.1A & 3.2A).

The andesite clasts are identical to the surrounding lavas. The presence of fresh angular clinopyroxene fragments in the matrix, and the textural similarity between the matrix and the andesite clasts that they support (eg Plate 3.2D), indicates that very little transport has occurred for these immature clastics. The clasts are supported within a dark grey to pale green gritty greywacke to volcanoclastic arkose, typically clay-altered, that contains abundant angular andesite, plagioclase and clinopyroxene fragments (Plate 3.2C & D).

### *Volcanoclastic sandstones*

Overlying and interbedded with the coarse volcanoclastic breccias are 10 cm to 2 meter thick beds of massive to diffusely bedded volcanoclastic arkose. These dark grey (fresh) to dull green (when weathered) arkoses are typically moderately sorted and fine- to medium-grained. They locally include well-sorted lenses of granule-sized gravels to coarse arkoses. The arkoses consist of broken plagioclase crystals, detrital magnetite and rare clinopyroxene set in a clay-altered silt or mud matrix (Plate 3.2E). The andesite clasts are monomictic, and are identical to the underlying coherent andesite. In many locations sedimentary rocks have been sericite-clay-carbonate altered, and close to the Didipio Igneous Complex they are typically recrystallised to a crystalline equigranular hornfels with patchy to strongly developed epidote alteration.

### **Upper Mamparang Formation**

The Mamparang Formation andesites are overlain by a sequence of pale-coloured, coarsely porphyritic trachytes and related trachytic volcanoclastic rocks (Plate 3.3A). The trachytes crop out on the eastern, northern and western flanks of the Didipio Igneous Complex and occupy the topographic highs of the Didipio region. All observed contacts between the trachytes and the main body of the Didipio Igneous Complex are faulted. Timing relationships can be determined from: 1) rare cross-cutting dykes of diorite in the trachytic volcanics; 2) widespread biotite alteration and 3) metamorphism of trachyte- and andesite-bearing volcanoclastic breccias close to the contact with the igneous complex and 4) the presence of trachyte clasts in a monzodiorite igneous breccia. All of these features indicate that the trachytes were emplaced prior to the intrusive complex. Although the contact with the underlying andesitic volcanics of the Mamparang Formation has not been observed directly, it appears to be conformable. The abundance of trachyte clasts increases upwards in the basal, andesite-dominated volcanoclastic units of the Upper Mamparang Formation, and both packages have similar



little displacement (Jones, 1985). Faults at E26, typically showing minor displacements, trend preferentially towards the northwest (Harris, 1997). At E48, the host sequence is structurally intact and late-stage faults show only minor displacements, with one exception. The post-mineralisation, low angle Altona Fault has truncated the top of the ore body at depths of ~100m below surface (Wolfe, 1994; this study).

An oriented core analysis conducted by Harris (1997) demonstrated that the stockwork and sheeted veins associated with the main stages of mineralisation at all four of the Endeavour deposits have a preferred orientation of ~140 – 170°, which was shown to indicate dilation in the direction of ~10 – 265°. The implication of similar preferred vein orientations for the four deposits was interpreted by Harris (1997) to indicate a regional structural control on vein emplacement (cf. Jones, 1985).

### 3.3 Intrusions of the Endeavour deposits

#### 3.3.1 *Intrusion classification*

Sillitoe (2000) listed a number of criteria that alone, or in combination, should be satisfied before different intrusions can be distinguished from one another in porphyry environments. They are 1) truncation of veins in older phases at contacts with younger phases; 2) narrow (<1cm) chilled margins in younger phases; 3) narrow (<2cm) zones of flow-aligned phenocrysts in younger phases along contacts with older phases; 4) xenoliths of older phases and/or quartz vein material in younger phases within a few 10's of centimetres of the contact with older phases; 5) better textural preservation and lower vein density in younger phases and 6) abrupt decrease in metal grade in younger intrusions.

Once different intrusions were established on the basis of these criteria at E22, E26, E27 and E48, they were described according to five textural characteristics as follows:

1. *phenocryst abundance (porphyritic rocks)* – uncrowded (20 - 50%) or crowded (50 - 70%);
2. *nature of the groundmass* – aphanitic, very fine-grained granular (microcrystalline with grains ranging in size from 20 – 50µm) or fine-grained granular (grains ranging in size from 50 – 100µm);
3. *mafic phenocrysts* – total proportion (<2 to ~15%) of biotite, magnetite, augite and/or hornblende phenocrysts population;



## LOCAL GEOLOGY

bedding orientations. The trachytes and volcaniclastics are overlain to the east of the map area by an interbedded sequence of finely-bedded feldspathic siltstones and coarsely bedded trachyte-volcaniclastic pebbly arkoses. The Upper Mamparang Formation is strongly weathered and intensely altered to argillic alteration (local) and intermediate argillic alteration assemblages (widespread). This strong weathering and alteration has obscured contacts between individual trachyte flows. Where observed, the trachyte lavas are overlain and onlapped by, a thick sequence of poorly-sorted light-coloured trachytic and andesitic matrix-supported volcaniclastic breccias (debris flows) and green-grey volcaniclastic arkoses. The trachytes are commonly interbedded with thinner 2 to 5 meter thick pale grey coarsely clinopyroxene-phyric trachyandesites.

### *Trachyte and trachyandesites*

Trachytes crop out as 5 to 20 meter thick, light grey to cream coloured units that range from coarsely porphyritic to medium-grained crystal-crowded trachyte. The flow margins are typically autobrecciated, with fine-grained angular porphyritic trachytic textured fragments supported in a coarse-grained porphyritic groundmass. The trachytes consist of approximately equal amounts of euhedral 5 to 15 mm long pinkish sanidine phenocrysts and subordinate 5 to 10 mm long cream coloured, typically carbonate altered, plagioclase phenocrysts, with uncommon clinopyroxene, biotite and amphibole phenocrysts that account for less than 10% of the phenocryst population (Plate 3.3A). The phenocrysts are set in a fine-grained groundmass that comprises up to 80% of individual flows. The groundmass consists of a mosaic of light grey to white euhedral secondary orthoclase and quartz with abundant sanidine microlites and rare domains of relic glass and accessory rutile, zircon and sphene (Plate 3.2B). Rare devitrified spherulitic patches have replaced primary glass and probably formed by high temperature devitrification of an originally glassy groundmass. The replacement of a glassy groundmass by orthoclase and quartz is also typical of high temperature devitrification. Rare glassy trachytes (Plate 3.3C) are typically flow banded, and microlite-rich bands alternating with glassy bands. The phenocrysts are aligned parallel to the flow bands. The lavas can be classified as trachyandesites based on phenocryst populations or as trachytes if the partially secondary glass-orthoclase-quartz groundmass is also taken into account. Whole-rock geochemical analyses are consistent with the classification as trachytes (Chapter 5).

Unlike the underlying Mamparang Formation andesites, many of the andesites and trachyandesites interbedded with the trachytes of the Upper Mamparang Formation are clinopyroxene-phyric (Plate 3.3E & F). Large oscillatory-zoned clinopyroxenes, together with plagioclase, sanidine, hornblende and biotite phenocrysts occur in an aphanitic

crystalline groundmass with abundant plagioclase microlites. The clinopyroxenes are texturally distinct from the unzoned clinopyroxenes that occur in the underlying Mamparang Formation andesites (Plate 3.1B). The plagioclase phenocrysts are characterised by fine oscillatory zoning, identical to that of phases in the Didipio Igneous Complex.

#### ***Trachytic volcanoclastic breccias***

Pale-coloured coarse volcanoclastic breccias are intercalated with the trachytes. The breccias consist of 5-10 meter thick beds that contain poorly-sorted angular trachyte, trachyandesite and andesite clasts (generally 1 to 20 cm diameter) supported in a fine-grained feldspathic, typically strongly clay-altered and weathered matrix. At the base of the Upper Mamparang Formation the breccias are dominated by andesite clasts sourced from the pre-existing Mamparang Formation. The base of the Upper Mamparang Formation is defined by the appearance of trachyte clasts.

The coarsely porphyritic trachyte clasts are texturally and compositionally identical to the surrounding trachyte lavas, consisting of large euhedral untwinned or simply twinned sanidine phenocrysts and albite-twinned plagioclase phenocrysts (locally rimmed by K-feldspar). No pumice or pyroclastic material has been observed within the volcanoclastic rocks. Within the clasts, feldspar phenocrysts are typically flow aligned and hosted in a granular mosaic of quartz-orthoclase with abundant flow aligned sanidine microlites. The quartz-orthoclase mosaic has replaced a glassy groundmass. The presence of strongly clay-sericite-carbonate altered clasts within an unaltered feldspathic groundmass suggests that advanced argillic alteration of the trachyte lavas has occurred, at least in part, during emplacement of the lavas and breccias, and hence predates the intrusion of the Didipio Intrusive Complex. Intense selectively pervasive biotite alteration of the trachytes is considered to be a contact metamorphic product associated with the emplacement of the Didipio Igneous Complex.

### **DIDIPIO IGNEOUS COMPLEX**

The Didipio Igneous Complex comprises an early dioritic series of clinopyroxenites, clinopyroxene-gabbros, clinopyroxene-diorites and clinopyroxene-monzonites that have been intruded regionally by a weakly-mineralised multiphase monzonite pluton (the Surong Monzonite), and by a series of strongly mineralised monzonite stocks at Dinkidi (Figures 3.1 & 3.3). All of these units, and the surrounding volcanics, are cut by thin, pyrite-bearing andesite dykes.

### Early dioritic units

#### *Clinopyroxenites and anorthosite*

Although no clinopyroxenites or anorthosites crop out in the Didipio region, or were intersected by drilling, all dioritic phases of the Didipio Igneous Complex contain common clinopyroxenite xenoliths, while diorite and monzodiorite phases contain rare anorthosite xenoliths. Also, the clinopyroxenites consist of a medium to coarse grained equigranular anhedral to subhedral mosaic of pale green, weakly pleochroic clinopyroxene with interstices filled by minor anorthite and magnetite. The alignment of subhedral clinopyroxene crystals is interpreted to indicate a cumulate origin for the clinopyroxenites, and it is likely that clinopyroxene fractionation was occurring within the diorites during their formation. The clinopyroxene is commonly biotite-magnetite and chlorite altered.

Large, angular, cream-coloured anorthosite xenoliths are rare, and only occur in the diorite and monzodiorite phases. The anorthosite xenoliths consist of single large anorthite fragments (up to 10 cm wide) or coarse-grained anhedral mosaics of albite-twinned anorthite with minor interstitial anhedral clinopyroxene and accessory magnetite. The anorthosite xenoliths have been albitised, sericitised and clay-carbonate altered, with the interstitial clinopyroxene altered to biotite and later chlorite.

#### *Clinopyroxene gabbro*

Black, fine- to medium-grained equigranular clinopyroxene-gabbro is exposed along the flanks of the Didipio Igneous Complex, apparently hosted within diorite units. All phases of the Didipio Igneous Complex contain xenoliths of medium- to coarse-grained clinopyroxene-gabbro (grainsizes of up to 1 cm; Plate 3.4A). The gabbros consist of a granular mosaic of anhedral to subhedral light green weakly pleochroic clinopyroxene and plagioclase with abundant magnetite (5-10%) and rare olivine (Plates 3.4B, C & D). Some gabbros have a strongly developed fabric defined by elongate subhedral clinopyroxene and anhedral to subhedral plagioclase crystals (Plates 3.4C, E & F). Others have diffuse compositional layering of clinopyroxene- and plagioclase-rich zones. The gabbros are strongly biotite-magnetite±orthoclase altered close to the contact with the neighbouring monzonites.

The preferred orientation of the plagioclase and clinopyroxene, partial alignment of clinopyroxene, high magnetite content (up to 10%) and rare weak compositional layering are interpreted to indicate that most, if not all, of the gabbros formed as plagioclase-clinopyroxene cumulates. The gabbros are interpreted, on the basis of a probable cumulate-origin, to have a bed-like morphology, occurring as pockets within the clinopyroxene-diorite host, as illustrated schematically in Figure 3.3.



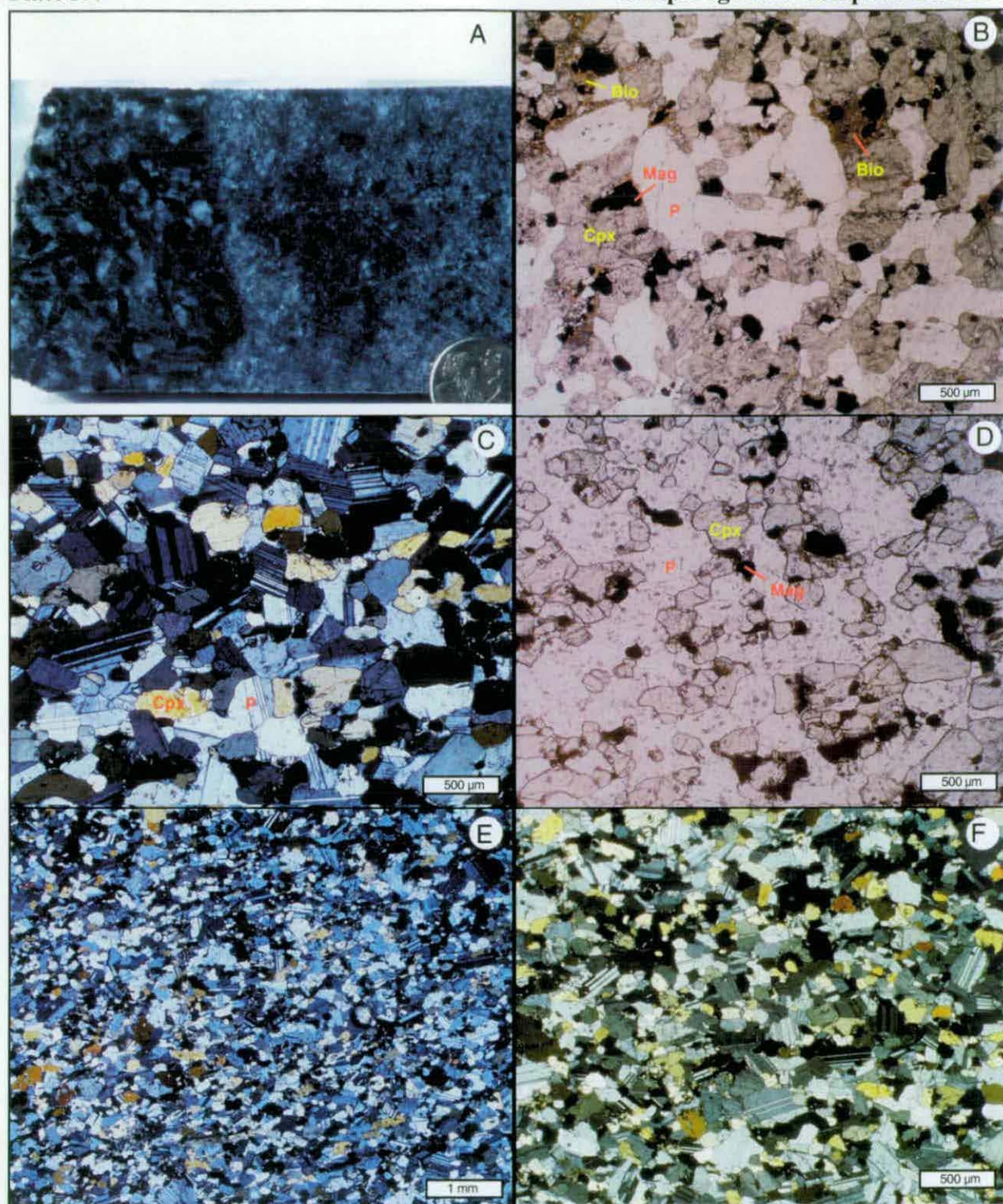


**Plate 3.4 A:** Part of a 20 cm wide coarse-grained cpx-gabbro xenolith hosted within a weakly plagioclase-phyric monzodiorite. Large elongate clinopyroxene phenocrysts within the gabbro reach up to 1 cm in length and are supported by an interstitial mosaic of anorthite and magnetite. DDH 34/455.

**Plate 3.4 B:** Clinopyroxene-dominated cpx-gabbro. Subhedral mosaic of clinopyroxene and anorthite with accessory magnetite (Mag). Clinopyroxene in top left of photograph has been biotite-altered, then subsequently chlorite-altered. PPL. Sample G1.

**Plate 3.4 C:** Anorthite-dominated cpx-gabbro. XPL. Sample 39/129.

**Plate 3.4 D:** PPL photomicrograph of gabbro in Plate C. Like all gabbros in the Didipio Igneous Complex, this unit contains abundant magnetite, which can comprise up to 10 vol%. Such enrichment suggests a cumulate origin for the gabbros.

**Plate 3.4 E:** Weak preferred orientation in a cpx-gabbro. Anorthite optical orientation and the elongation of both clinopyroxene and anorthite delineate a left to right originally horizontal fabric. XPL. Sample 39/129.

**Plate 3.4 F:** Close up of of gabbro in plate E. Anorthite optical alignment and clinopyroxene orientation display a subhorizontal alignment. XPL.

## LOCAL GEOLOGY

### *Clinopyroxene diorite*

The intrusion with the most primitive non-cumulate composition within the Didipio Igneous Complex is a fine- to medium-grained (rarely coarse-grained) dark grey clinopyroxene diorite (Plate 3.5A). This equigranular to weakly plagioclase-phyric diorite is the peripheral phase of the Didipio Igneous Complex (Figure 3.1). Dykes of medium-grained clinopyroxene and plagioclase-phyric diorite porphyry, and fine- to medium-grained equigranular diorite, have crosscut the andesites and trachytes of the surrounding Mamparang Formation. Adjacent to the diorite, there has been widespread recrystallisation, thermal metamorphism and epidote-chlorite alteration of the surrounding volcanic pile. The diorite contains abundant dark green-grey coloured medium- to coarse-grained gabbro xenoliths, and rare medium- to coarse-grained clinopyroxenite xenoliths. The fine-grained margins of the diorite are particularly xenolith-rich. The presence of uncommon diorite xenoliths indicates several phases of diorite intrusion or some degree of autobrecciation. The diorites weather from a dark blue-grey to a green-grey colour with small cream coloured plagioclase laths in a fine grained dull green groundmass.

The diorites consist of a random to weakly orientated framework of euhedral zoned plagioclase laths, rarely strongly aligned to crystal crowded. Interstices are filled by subhedral to euhedral pale green clinopyroxene crystals (which can occur as glomerocrysts), and accessory magnetite, orthoclase, apatite, biotite and rare olivine (Plates 3.5B, C, D, E & F). Individual diorite phases observed range in composition from clinopyroxene-gabbrodiorites (olivine- and clinopyroxene-rich) to borderline clinopyroxene-monzodiorite (biotite-, orthoclase- and apatite-rich). The Mamparang Formation adjacent to the diorites has been intruded by diorite porphyry dykes that range in width from 2 to 20 meters. These diorite porphyry dykes are plagioclase- and clinopyroxene-phyric. The phenocrysts are set in a fine-grained groundmass that contains small carbonate-filled miarolitic cavities. Carbonate, sericite, zeolites and clay minerals have selectively replaced plagioclase cores throughout the diorites. Mafic minerals in the diorites are typically replaced by epidote and chlorite.

### *Clinopyroxene-monzodiorite*

Fine- to medium-grained equigranular to plagioclase-phyric clinopyroxene-monzodiorite (Plates 3.4A, 3.5A & 3.6A) has the largest areal extent of any of the early dioritic intrusives in the Didipio Intrusive Complex (Figure 3.1). The monzodiorite has intruded the gabbros and diorites, and is in turn cut by clinopyroxene-monzonite and andesite porphyry dykes. The margins of the monzodiorite plutons is xenolith-rich, containing abundant clinopyroxene-diorite, clinopyroxene-gabbro and rare clinopyroxenite xenoliths. Compositional and textural variations and the presence of rare monzodiorite xenoliths provide evidence that the monzodiorite pluton consists of several discrete phases. The most mafic phase, a borderline



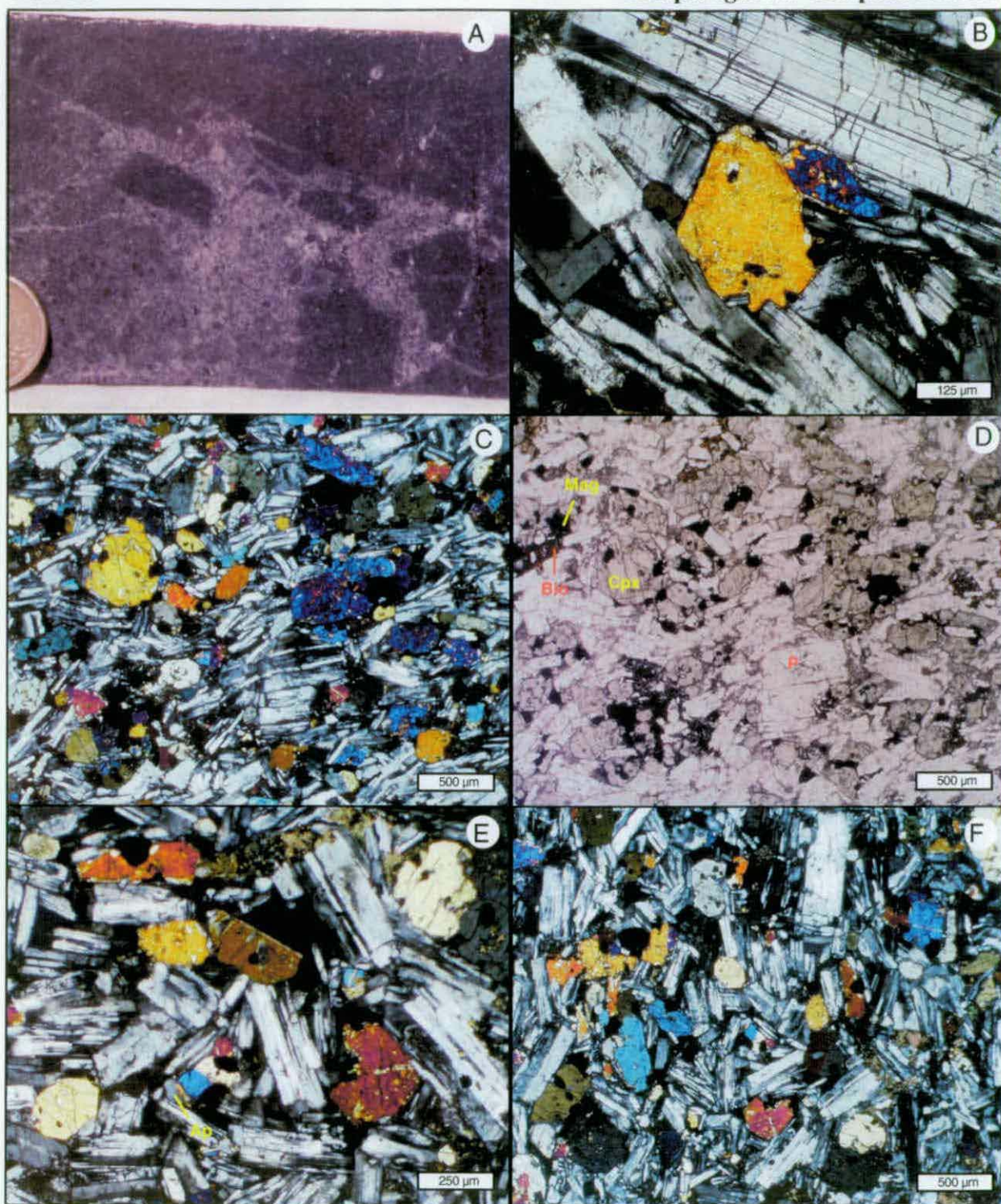


**Plate 3.5 A:** Magnetite-biotite altered diorite intruded by a light pinkish grey monzodiorite, Sample 37/302.

**Plate 3.5 B:** Interstitial subhedral clinopyroxene set within a framework of weakly albitised plagioclase laths. XPL. Sample D2.

**Plate 3.5 C:** Typical clinopyroxene-diorite with a weakly oriented framework of plagioclase laths that host subhedral to euhedral clinopyroxene phenocrysts. XPL. Sample DD1.

**Plate 3.5 D:** PPL photomicrograph of Plate C. Like most diorites within the Didipio Igneous Complex the mafic sites of this sample has been weakly biotite-magnetite altered due to the intrusion of the Surong Monzonite.

**Plate 3.5 E:** Clinopyroxene in a weakly oriented framework of plagioclase laths with minor apatite (Ap). XPL. Sample DD1.

**Plate 3.5 F:** Clinopyroxene diorite. The diorite phases of the Didipio Igneous Complex span the full compositional range from gabbrodiorites to cpx-monzodiorites. XPL. Sample D2.

## LOCAL GEOLOGY

dark grey diorite, consists of albite-twinned plagioclase crystals with thin rims of orthoclase, interstitial clinopyroxene and rare olivine phenocrysts (Plates 3.6C, D & F). The most felsic monzodiorite has thick atolls of orthoclase that contain oscillatory zoned plagioclase prisms with interstitial clinopyroxene and primary biotite (Plates 3.6B & E).

Petrographically, the main monzodiorite phase consists of euhedral plagioclase crystals, with albite twinning or oscillatory zones, typically enclosed by anhedral orthoclase grains (Plate 3.6E). The monzodiorites are generally crystal-crowded, the feldspar crystals have a preferred orientation and have wrapped around subhedral to euhedral green-yellow clinopyroxene crystals and rare glomerocrysts. Interstitial spaces have been filled by accessory primary biotite, magnetite, apatite and rare relic olivine, which has strong iddingsite reaction rims. Plagioclase is typically albitised and/or clay-sericite-carbonate altered whereas mafic minerals have been affected by patchy, intense epidote-carbonate alteration. The monzodiorites have undergone intense K-metasomatism adjacent to the Surong Monzonite, with selective replacement of mafic minerals by magnetite and biotite with accessory secondary orthoclase and fluid inclusion-rich apatite.

Porphyritic monzodiorites have intruded the diorites and the Mamparang Formation (Plate 3.6A). Monzodiorite porphyry dykes have a light grey colour and consist of strongly albitised flow-aligned twinned or zoned plagioclase phenocrysts, which typically have a thin rind of orthoclase. The groundmass consists of a fine-grained 'granular' mosaic of K-feldspar with abundant subhedral clinopyroxene, accessory magnetite and minor flow-aligned plagioclase microlites. The monzodiorite dykes have been strongly clay altered in most observed examples.

## Surong Monzonite

Diorites and monzodiorites of the Didipio Igneous Complex have been intruded by a weakly mineralised monzonite pluton, the Surong Monzonite. The monzonite occupies the core of the igneous complex (Figure 3.1). Erosion has exposed the monzonite roof zone. The diorite contact is characterised by a widespread jigsaw-fit igneous groundmass breccia (the most common breccia type in the Didipio region). Isolated rafts of diorite up to 200 meters long occur within the monzonite. The breccias are associated with a broad zone of intense biotite-magnetite alteration, with associated weak Cu-Au mineralisation that extends at least 200 meters into the surrounding diorites.

The Surong Monzonite is a composite pluton that contains several monzonite phases. Fine- to medium-grained equigranular clinopyroxene-monzonites are the most abundant. Individual clinopyroxene-monzonites can have fine-grained crystal-crowded margins, suggesting chilling, while others have gradational contacts, suggesting slow cooling. In the northern and southern



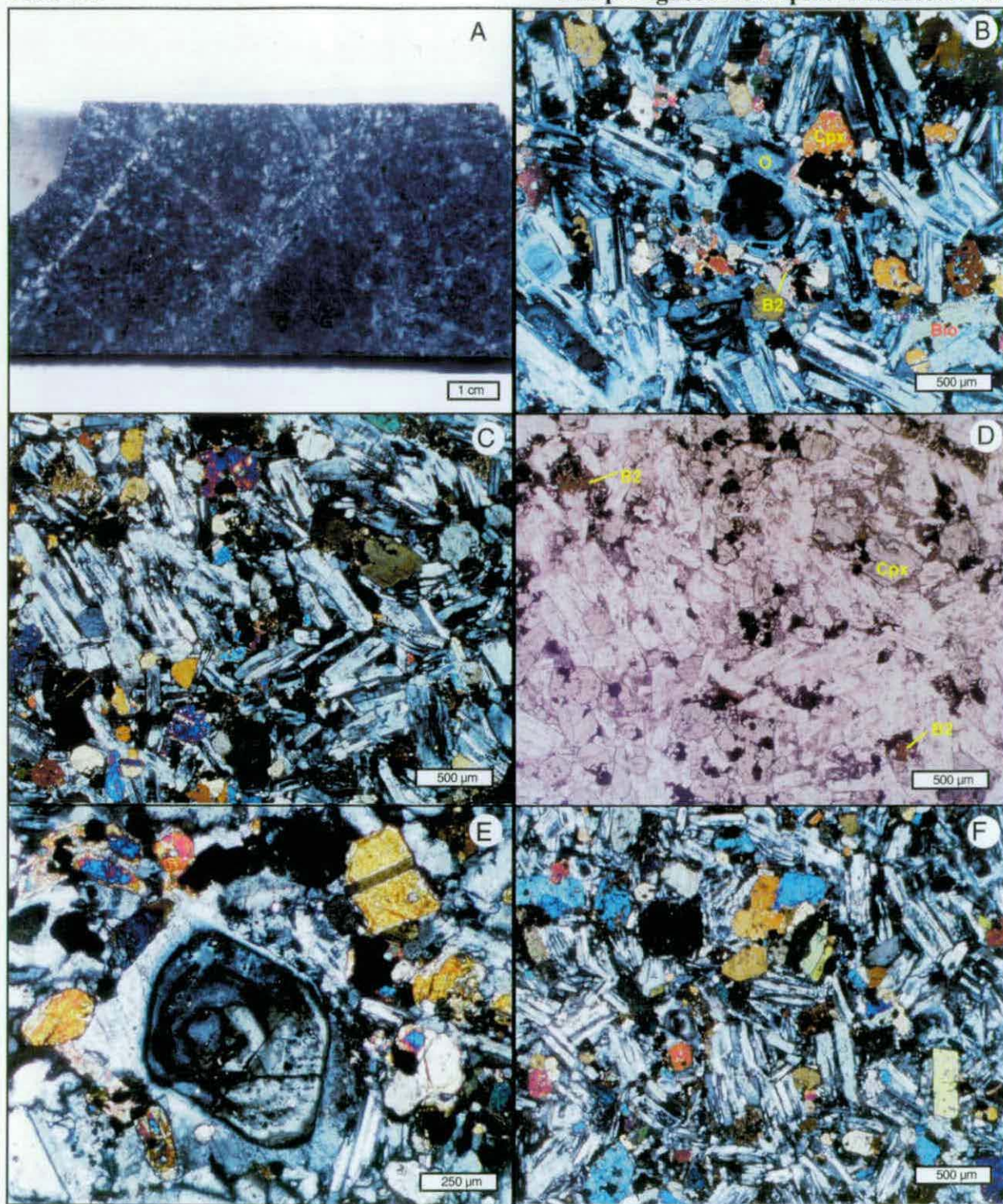


**Plate 3.6 A:** A black fine-grained gabbro xenolith (G) hosted within a plagioclase-phyric monzodiorite porphyry. The porphyritic monzodiorites are rich in xenoliths compared to the equigranular monzodiorites. DDDH49/393.

**Plate 3.6 B:** Typical monzodiorite with oscillatory zoned plagioclase, rimmed by orthoclase (O) with interstitial clinopyroxene and primary biotite (Bio). Clinopyroxenes are weakly biotite- (B2) and magnetite-altered. XPL. Sample MD 1.

**Plate 3.6 C:** Clinopyroxene-monzodiorite. This sample is less evolved than the sample illustrated in Plate B. There is no oscillatory plagioclase or primary biotite and only minor interstitial orthoclase. XPL. Sample MD 3.

**Plate 3.6 D:** PPL photomicrograph of sample in Plate C. Note deep red strongly pleochroic biotite (B2) and magnetite alteration of former mafic sites. Sample MD 3.

**Plate 3.6 E:** Oscillatory zoned plagioclase surrounded by a rim of orthoclase in a clinopyroxene-monzodiorite. Oscillatory zoning becomes more complex in later phases of the Didipio Igneous Complex (compare to Plate 3.7E or F). XPL. Sample D3.

**Plate 3.6 F:** Biotite-magnetite altered clinopyroxene-monzodiorite. XPL. Sample MD 3.



## LOCAL GEOLOGY

sections of the pluton, pale pinkish-red to orange red coloured crystal-crowded biotite-monzonites have intruded the clinopyroxene-monzonites. These are in turn cut by thin (30-500 cm wide) late-stage weakly-mineralised quartz-monzonite and equigranular micromonzonite dykes. All monzonite phases contain angular gabbro and diorite xenoliths which are typically biotite-magnetite altered (Plate 3.7A). Although the Surong Monzonite is a multiphase pluton, the small irregular surface expression of individual phases (due in part to only the roof of the pluton being exposed), deep weathering, lack of outcrop and structural complexity of the area has prevented individual phases being mapped in the field. Consequently, in both the map and cross-sections (Figures 3.1 & 3.2), the Surong Monzonite is treated as one composite pluton.

The monzonites are characterised by distinct oscillatory-zoning of euhedral plagioclase crystals. These occur together with subhedral to euhedral clinopyroxene in a coarse-grained mosaic of primary anhedral orthoclase, with accessory apatite and magnetite. Primary biotite, minor quartz and sphene occur in the more evolved phases. Monzonite textures include (1) a crystal-crowded framework of oscillatory-zoned plagioclase, which has produced a mutually impinging or trachytic texture, with only minor interstitial orthoclase (Plates 3.7C & D), and (2) plagioclase in a mosaic of K-feldspar and rare perthite (Plate 3.7B).

Diorites adjacent to the Surong Monzonite have been cut by fine- to medium-grained light grey to pinkish-orange plagioclase-phyric monzonite porphyry dykes that range in width from 1-2 cm to 10's of meters. The dykes contain euhedral to broken oscillatory and normal zoned plagioclase phenocrysts, and rare clinopyroxene phenocrysts. Both phenocryst phases typically occur as glomerocrysts, and in rare cases are rimmed by orthoclase (Plates 3.7E & F). The phenocrysts are set in fine-grained granular mosaic of anhedral orthoclase and euhedral clinopyroxene, with minor antiperthite replacement of plagioclase. In more evolved monzonites, such as the thin quartz monzonite dykes and the Dinkidi stock, plagioclase is partially to fully replaced by antiperthite. Equigranular micromonzonite dykes, and the chilled margins of more felsic phases of the Surong Monzonite, are leucocratic fine-grained and equigranular. These consist of a mesh of small plagioclase laths rimmed by K-feldspar with minor clinopyroxene and accessory magnetite, apatite and secondary biotite.

The margin of the composite Surong Monzonite pluton has undergone intense orthoclase-biotite alteration. Secondary magnetite and biotite have selectively replaced primary mafic minerals. Epidote, chlorite and actinolite have selectively replaced primary clinopyroxene and secondary biotite in some areas.



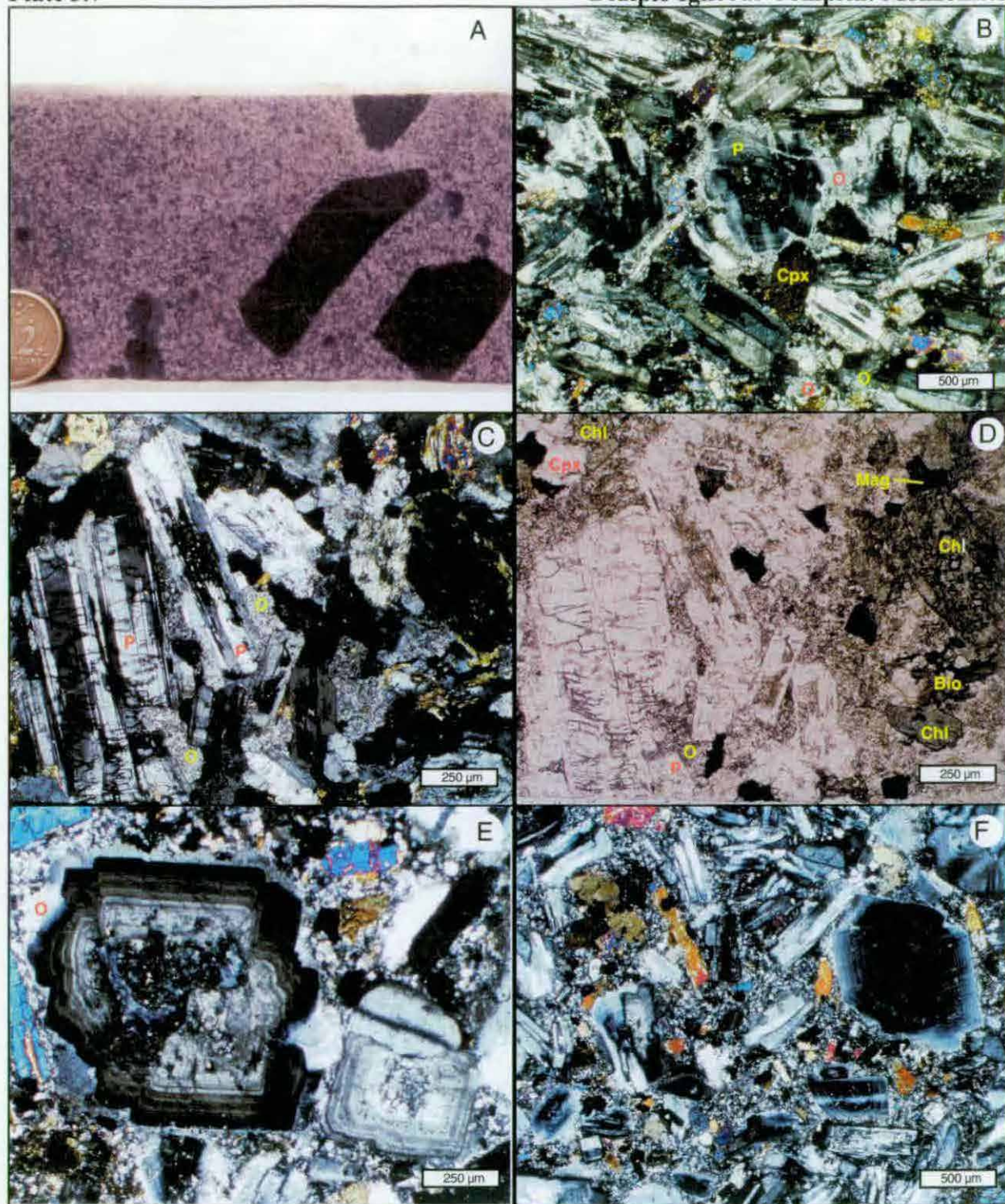


**Plate 3.7 A:** Biotite-altered diorite xenoliths (right) hosted within a typical pinkish-grey equigranular Surong clinopyroxene-monzonite. These igneous-matrix breccias form a 20 to 100 m wide zone along the margins of the Surong Monzonite. SDDH 46/~226.

**Plate 3.7 B:** Typical clinopyroxene-monzonite. Euhedral oscillatory- and normal-zoned plagioclase laths are hosted within a coarse-grained mosaic of orthoclase (O) with minor interstitial clinopyroxene. XPL. Sample M9.

**Plate 3.7 C:** Clinopyroxene-monzonite/monzodiorite. Plagioclase laths are surrounded by interstitial orthoclase and uncommon clinopyroxene. Oscillatory zoning of plagioclase is scarce in these less evolved samples. XPL. Sample M6.

**Plate 3.7 D:** PPL photomicrograph of sample in Plate C. Clinopyroxene at far right has been strongly biotite and chlorite altered.

**Plate 3.7 E:** Fine oscillatory zoning in plagioclase from an evolved cpx-monzonite porphyry. Oscillatory zoning in plagioclases increases with the evolution of magma composition in the Didipio Igneous Complex. Plagioclase in this sample is rimmed by optically continuous orthoclase (O), and is hosted within a granular mosaic of orthoclase. Albitised plagioclase, clinopyroxene, minor magnetite and secondary biotite are also present. XPL. Sample M10.

**Plate 3.7 F:** Monzonite porphyry: strongly oscillatory-zoned plagioclase phenocrysts are hosted within a granular orthoclase groundmass, with accessory clinopyroxene, biotite, apatite, and secondary biotite-chlorite. XPL. Sample M10.

## LOCAL GEOLOGY

### Dinkidi Stock

The Dinkidi Cu-Au porphyry deposit is associated with a multiphase intrusive stock located at the southern margin of the Surong Monzonite (Figure 3.1). This multiphase stock consists of four phases, each of which has a distinct hydrothermal assemblage described in Chapter 6. The oldest phase of the Dinkidi stock is an elongate equigranular biotite monzonite stock named the 'Tunja Monzonite' (Fig. 3.1 & 3.3). It has been intruded by a small thin clinopyroxene-syenite dyke (the 'Balut Dyke'), and late-stage monzosyenite porphyry (the 'Quan Porphyry') to crystal-crowded syenite (the 'Bufu Syenite'). These intrusives are petrologically distinct from the Surong Monzonite. These units are described in detail in Chapter 4.

### Andesite Dykes

The final stage of magmatic activity in the Didipio Region produced dark green-grey hornblende-bearing andesite porphyry dykes (Plate 3.8A), which have cross-cut the Didipio Igneous Complex and the surrounding volcanic pile. The fine- to medium-grained dykes are generally 1-5 meters wide. Locally extensive andesite sills and uncommon irregular intrusive bodies up to 200 meters wide have also been observed that appear to be related to the late stage dykes.

Petrographically, the dykes contain approximately equal amounts of euhedral, typically 0.1 to 10 mm long, weak to strongly oscillatory-zoned clinopyroxene, weakly-zoned hornblende, and albite-twinned plagioclase phenocrysts. These are hosted within an aphanitic holocrystalline groundmass that contains abundant flow-aligned plagioclase microlites, fragments of clinopyroxene and plagioclase, and rare miarolitic cavities (Plates 3.8B, C & D). Abundant magnetite (uncommonly pyrite) and minor apatite are ubiquitous accessory minerals. Hornblende crystals locally have an acicular morphology, up to 2 mm wide and 15 mm long (Plates 3.8E & F). Many hornblendes crystals have nucleated onto, or partially replaced, clinopyroxene (Plate 3.8B), and are enclosed by the microlite-rich groundmass. This replacement is interpreted to have occurred as a late-stage magmatic event prior to quenching of the groundmass. Clinopyroxene and hornblende glomerocrysts are common, and rare clinopyroxene-gabbro, clinopyroxenite, hornblendite, trachyte and monzodiorite xenoliths have been observed. The fine-grained groundmass contains rare miarolitic cavities and abundant microlites, and is identical to that of andesite lavas, suggesting shallow subsurface emplacement.

## STRUCTURE

The bedded volcanoclastic units that crop out in the Didipio region have shallow dips, with no preferred strike. These may be primary depositional dips, tilt blocks associated with the faults or



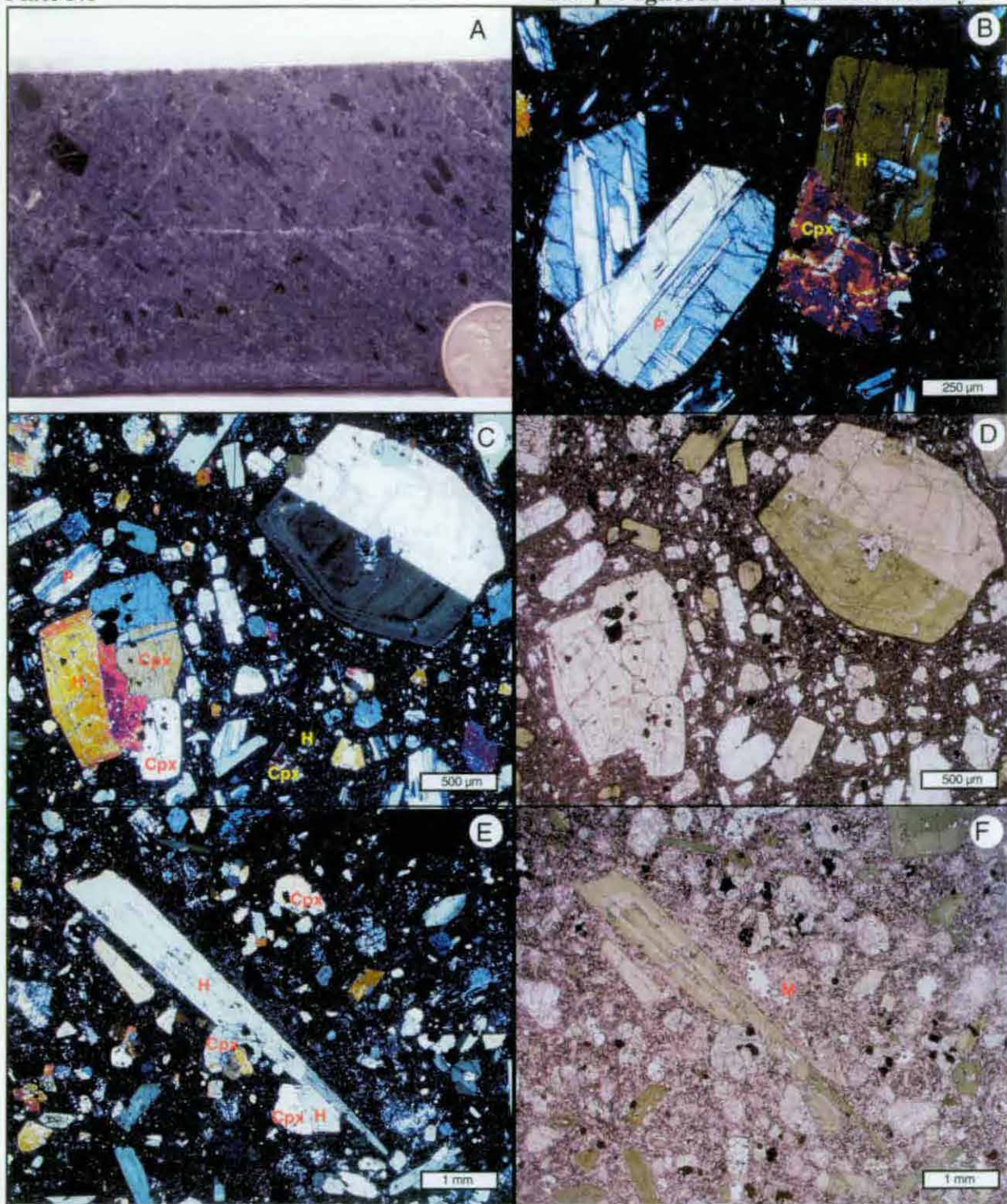


**Plate 3.8 A:** Typical andesite porphyry dyke: dark grey hornblende and clinopyroxene phenocrysts set in a dark grey fine-grained groundmass. These unaltered dykes cut argillic altered trachytes, indicating that the dykes, which are co-magmatic with the Didipio Igneous Complex, post-date argillic alteration.

**Plate 3.8 B:** Andesite dyke: Plagioclase, clinopyroxene and hornblende (H) phenocrysts hosted in an aphanitic, plagioclase microlite-rich groundmass. The hornblende has nucleated onto, and partially replaced, clinopyroxene. Plagioclase microlites are wrapped around each phenocryst. XPL. Close up of sample in Plate C.

**Plate 3.8 C:** Andesite porphyry dyke with hornblende (top right), clinopyroxene and plagioclase phenocrysts set in a fine-grained crystalline groundmass. XPL. Sample AP3.

**Plate 3.8 D:** PPL photomicrograph of sample in plate C.

**Plate 3.8 E:** Acicular hornblende laths in a porphyritic andesite sill. Hornblende crystals are up to 1 cm in length, and are hosted in a crystalline aphanitic groundmass with abundant clinopyroxene and plagioclase fragments. XPL. Sample 44.9.

**Plate 3.8 F:** PPL photomicrograph of sample in plate E. Note partially glassy miarolitic (M) cavity just to the right of the large hornblende phenocryst.

## LOCAL GEOLOGY

products of open folding. Shallow dips are characteristic of the Mamparang Formation andesites, whereas the underlying andesites of the Eocene Caraballo Formation have steep dips as a result of strong open folding (MMAJ, 1977; Billedo, 1994). No cleavage has been observed in any units of the map area.

The Didipio Igneous Complex and surrounding volcanics have been affected by at least three generations of faulting. Based on observed field relationships, an early period of NW-trending normal faulting, a second period of west-trending sinistral strike-slip faulting and a final period of dextral N to NE strike slip faulting affected the area (Figure 3.1).

Early NW-trending normal faults are parallel to the trend of the Cagayan Valley rift basin and appear to predate the Didipio Igneous Complex. The Palali-Didipio intrusions are elongated parallel to this trend (Figure 2.2). Syn-magmatic reactivation of these faults may have controlled the emplacement of the Surong Monzonite, because it displays a vague north-west orientation when the offsets of later faults has been removed. NW-trending faults should also appear to have controlled the emplacement of the NW-trending Dinkidi Stock. The crystallisation of the Surong Monzonite pluton may have 'plugged' this feeder structure, forcing the Dinkidi Stock to be emplaced on its margin.

All intrusive phases of the Didipio Igneous Complex have been disrupted by west-trending sinistral strike-slip faults. The F2 faults are cut by late stage north- to later northeast-trending dextral strike-slip faults at Didipio (F3 faults) that are found throughout the region. The Didipio Valley Fault is a late stage F3 northeast trending dextral fault with a displacement of at least 700 meters (Figure 3.1). It has displaced the northern section of the Dinkidi deposit 700 meters to the east. The northern section of Dinkidi is known as the True Blue prospect (Figure 3.1). The shear zone that connects the Dinkidi and True Blue mineralisation is a 50-100 wide zone of fault-bound blocks, with minor brecciation, weak clay alteration and abundant en-echelon zeolite-carbonate veins. Individual late stage strike-slip faults occur as 1-10 meter wide cataclastites infilled by rock flour (commonly clay altered) and abundant pyrite which locally has filled small 1-2 m wide fault zones. No major fault zone in the area is known to host significant mineralisation, although several of the 'high-sulphidation' (pyrite-quartz) epithermal prospects in the Didipio region have been controlled by west-trending F2 and north-east trending F3 structures.

All of the intrusives in the Didipio region are strongly jointed. Ignoring shallow angle exfoliation joints, most of the subvertical joint sets in the Didipio Igneous Complex are aligned parallel to, and are found only in the vicinity of, the major F2 and F3 fault sets. The steeply dipping quartz-stockwork vein sets exposed on Dinkidi Ridge display two weakly preferred orientations: (1) NNW, parallel to the Dinkidi stock and to the early normal faults, and (2) a less

well developed ENE-trending set. There is no obvious relationship between the joint sets in the neighbouring units and the orientation of the Dinkidi vein sets.

### ***Environment of Deposition***

The volcanic facies of the Mamparang formation in the Didipio region consists of alternating andesitic lavas and volcanoclastic breccias. Non-volcanic clastic or carbonate rocks have not been observed. Background sedimentation, rarely preserved on the top of the breccia beds, consists of volcanoclastic arkose. The immaturity of the breccias, indicated by the large, angular clasts and the close compositional and textural similarity between the breccia matrix and the andesite clasts that they support (eg Plate 3.2D), is interpreted to indicate local derivation. The matrix supported clasts, very rare grading and lack of stratification in these volcanoclastic breccias are characteristic of debris flows, such as the lahars found on the flanks of many stratovolcanoes (Cas & Wright 1988, McPhie *et al.*, 1993). A subaerial setting is suggested by the lack of background sedimentation and of any quenched textures on the lava surfaces (eg pillows, hydroclastite or peperite). The andesite lavas and volcanoclastic breccias of the Mamparang Formation, in the Didipio region, are identical to the proximal interbedded volcanoclastic breccia-lava flow facies found in most andesitic stratovolcanios (Cas & Wright, 1988). The abundance of lavas, relative to breccias, suggests that the Mamparang Formation in the Didipio Region was close to a volcanic vent. The proximal facies of most stratovolcanoes are typically intruded by abundant dykes, and are flanked by various types of pyroclastic and epiclastic rocks (Cas & Wright, 1988), suggesting that a similar distal assemblage may be preserved in the region. As individual stratovolcanoes rarely have basal diameters in excess of 50 km (Pike & Clow, 1981), the extent of the Mamparang Formation (at least 60 by 40 Km, with the northern border covered by Miocene sediments; Figure 2.2) suggests that the formation was sourced from a series of andesitic volcanic edifices, that ranged from Didipio in the south to at least Cordon in the north, along the western edge of the Cagayan Valley Basin.

Stratovolcanoes typically display major lithological and compositional changes in their vertical succession (Cas & Wright 1988), and many andesitic stratovolcanoes contain interbedded dacite to rhyodacite flows, commonly as late stage products (eg Santorini: Pichler & Kussmaul, 1980; Druitt & Sparks, 1982). However the trachytic magmatism of the Upper Mamparang Formation extends northward for over 60 km to Palali and Cordon, uniformly overlying the andesites of the Mamparang Formation. Due to its large regional extent, the Upper Mamparang Formation is interpreted to have formed from a separate volcanic event, above the andesitic volcanic pile, and erupted from multiple vents parallel to the Cagayan Valley Basin. Such felsic lavas are typically associated with pyroclastic eruptions (Cas & Wright, 1988), and the Upper Mamparang Formation in the Palali region (30km to the northwest; Figure 2.2) consists



## LOCAL GEOLOGY

predominantly of ignimbrite (Albrecht and Knittel, 1990). However, in the Didipio region the abundance of trachyte lavas and the lack of pyroclastic material (eg pumice) in the interbedded volcanoclastic breccias suggest a proximal setting at an effusive volcanic centre.

The estimated late Oligocene age of the Mamparang Formation (Billedo 1994), and the 25 to 23 Ma radiometric age determinations for the Cordon Syenite Complex and Palali Batholith (Knittel, 1983; Albrecht & Knittel, 1990) and  $23.2 \pm 0.6$  Ma for biotite alteration at Dinkidi (Climax-Arimco *pers comm.*, 1998), are coeval with the palaeontological ages of regionally extensive shallow water late Oligocene to early Miocene limestone sequences (eg the Santa Fe and Columbus Formations of the Caballo Mountains; MMAJ 1977; the Ibulao Formation of the Cagayan Valley Basin; Christian, 1964; Figure 2.3). This series of limestones were deposited both prior to, and after, formation of the Cagayan Valley Basin (MMAJ 1977; Billedo 1994). This suggests that the volcanic pile of the Mamparang and Upper Mamparang Formations were adjacent to, or emerged from, a shallow sea.

## Synthesis

The geological history of the Didipio region is shown schematically in Figure 3.4. The interbedded andesites lavas and debris flows of the Mamparang Formation (Figure 3.4: 1) in the Didipio region are interpreted to be the proximal facies of a terrestrial andesitic stratovolcano that formed in the Late Oligocene (MMAJ, 1977; Billedo, 1994), and that may have been adjacent to a shallow sea (the Late-Oligocene to Early Miocene limestones of Christian, 1964, MMAJ, 1977 and Billedo, 1994).

This andesitic volcanic pile provided the foundation for, and was covered by, the trachyte lavas and widespread trachytic volcanoclastics of the Upper Mamparang Formation (Figure 3.4: 2). Although only a stratigraphic thickness of only ~400 meters is preserved in the Didipio region, this volcanic pile must have attained sufficient thickness (1.5-2 km?) to confine and host the Didipio Igneous Complex. The 25-23 Ma alkaline intrusives of the region (Albrecht & Knittel 1990; Knittel 1987) are synchronous with the commencement of rifting along the Cagayan Valley Basin (Christian, 1964; Caagusan, 1977).

The emplacement of the initial dioritic phases of the Didipio Igneous Complex into the Mamparang and Upper Mamparang Formations was associated with weak thermal metamorphism of the surrounding volcanics (Figure 3.4: 3) and the emplacement of diorite dikes throughout the surrounding volcanic units. The initial clinopyroxene-diorite melt appears to have evolved, following a series of intermediate intrusives, into a series of monzodiorites, possibly by fractionation of clinopyroxene and plagioclase, as suggested by the presence of cumulate gabbros and clinopyroxenites within the diorite pluton.

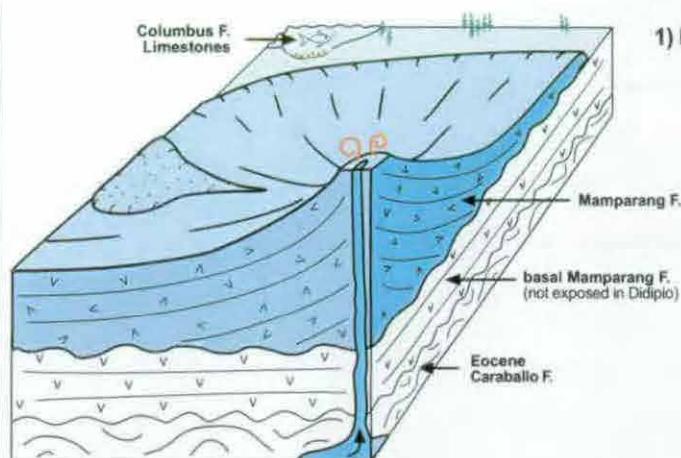
The diorites were intruded by the Surong Monzonite, a composite pluton composed of a series of clinopyroxene- to biotite-monzonites. Widespread igneous breccia and rafts of diorite and gabbro indicate that only the top of the pluton has been exposed, and that the pluton was emplaced, at least in part, by stoping of the diorites. The Surong Monzonite appears to have been emplaced at a greater relative depth than the diorites, because it has intruded the cumulate-rich base of the dioritic intrusives (Figure 3.4: 4). Economic porphyry Cu-Au mineralisation in the Didipio Region formed during the emplacement of the multiphase Dinkidi Stock (Figure 3.4: 5). The stock consists of late-stage highly evolved syenite intrusions and is described in the following chapter.

The common spatial and temporal association between a mineralised porphyry intrusion and a surrounding, or overlying, co-magmatic volcanic pile led Sillitoe (1973) to suggest that porphyry deposits were emplaced as apophyses of late-stage melt sourced from high-level magma chambers underneath andesitic-dacitic stratovolcanoes. The volcanic facies and intrusive history of the Didipio region supports a subvolcanic emplacement of the Didipio Igneous Complex, and a paleodepth for porphyry mineralisation of 1.5-3 km is inferred because this is the average height of andesitic stratovolcanoes (Pike & Clow, 1981). Despite being emplaced into a shallow volcanic setting, the width of the diorite and monzonite plutons within the Didipio Igneous Complex (estimated to be 1 – 1.5 km wide, after allowing for dilation by later intrusions) are considered to be too wide to be volcanic feeder dykes, and suggest emplacement at a relatively deep setting, possibly as a cupola above an underlying magma chamber. The proximal setting of the Mamparang and Upper Mamparang Formations in the Didipio region suggest that the intrusions of the Didipio Intrusive Complex may have utilised the same feeder structure as the surrounding volcanic units.

The final period of magmatism in the Didipio region resulted in the intrusion of abundant andesite dykes (Figure 3.4: 6). Late stage andesite porphyry dykes are a common feature of many Philippine porphyry systems (Sillitoe & Gappe, 1984). The emplacement of small quantities of mafic to intermediate melt, following a period of prolonged felsic magmatism, is typically attributed to the reinjection of residual mafic melt that underplates the felsic melt within a stratified magma chamber (Whitney et al 1988, Whitney, 1989).

## Geological history of the Didipio Region

(Not to scale)

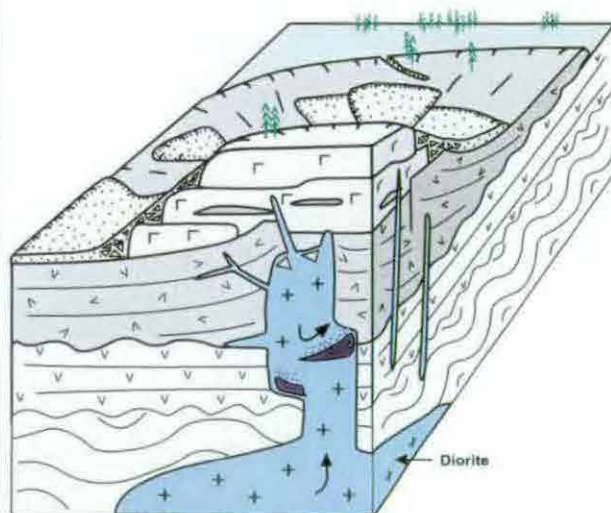
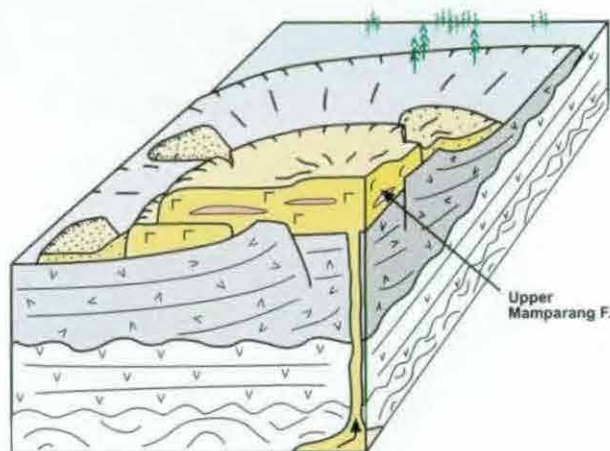


### 1) Late Oligocene: Mamparang Formation

- Construction of a Late Oligocene subaerial andesitic stratovolcano over basal Mamparang and Caraballo Formations
- Interbedded lahar debris flows and andesitic to trachyandesitic lavas
- Dominance of lavas and lack of pyroclastics indicates a proximal setting in the Didipio region
- Overlap with palaeontological ages for the Columbus Formation limestones suggests that the volcanic edifice was adjacent to shallow tropical seas.

### 2) Late Oligocene to Early Miocene: Upper Mamparang Formation

- Extrusion of extensive trachyte lavas and deposition of trachytic volcaniclastics
- Contemporaneous with extrusion of phonolites associated with the Palali Batholith and Cordon Syenite Complex
- Synchronous with the commencement of rifting along the adjacent Cagayan Rift Basin (Christan, 1964)



### 3) Late Oligocene to Early Miocene: Didipio Igneous Complex - diorites

- Emplacement of a series of clinopyroxene-diorites to clinopyroxene-monzodiorites into the Mamparang Formation and base of the Cordon Volcanics
- Extensive contact metamorphism and recrystallisation of surrounding volcanics
- Shallow level fractionation of clinopyroxene and plagioclase leads to the deposition of cumulate gabbros and clinpyroxenites

Figure 3.4: Geological history of the Didipio Region.

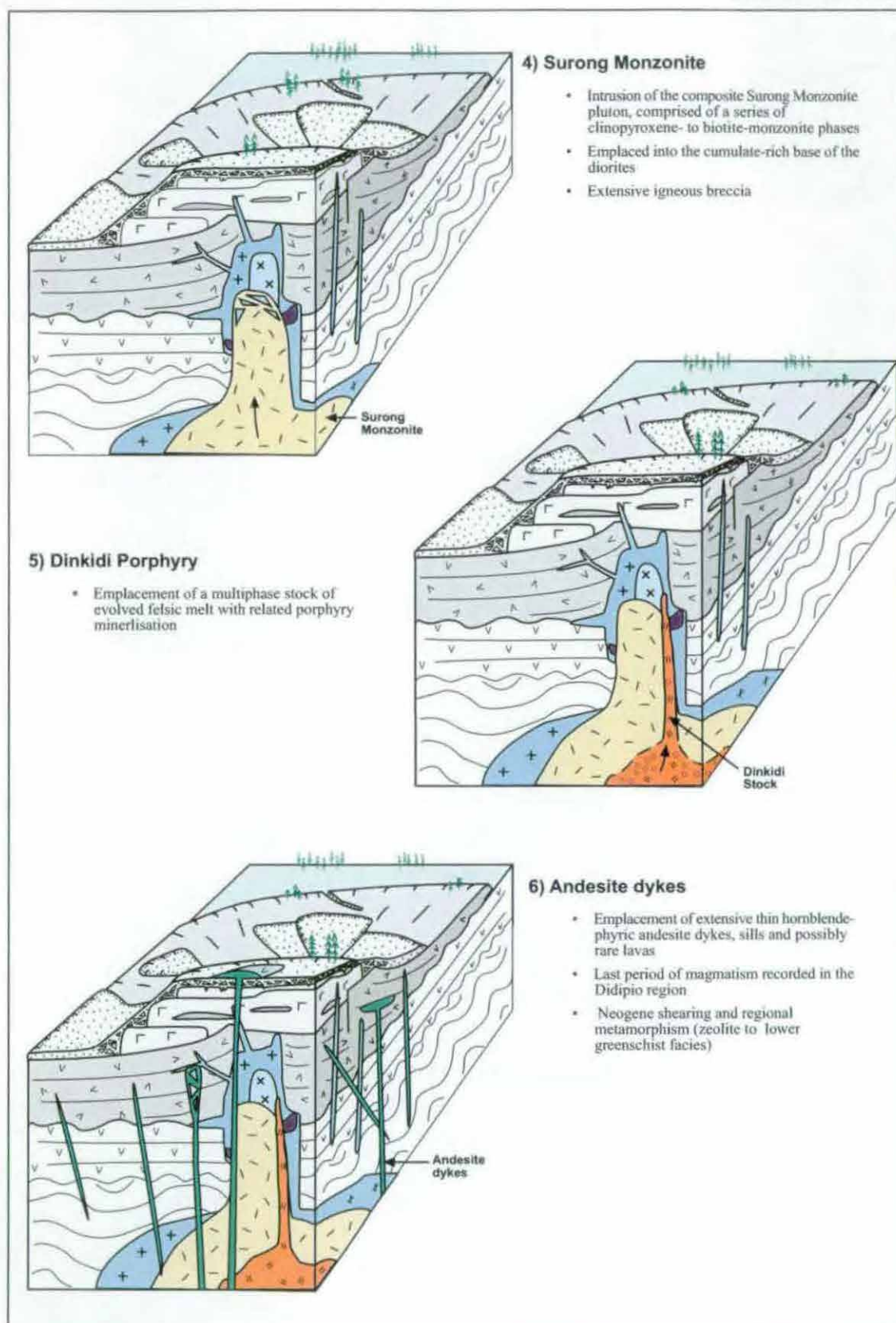


Figure 3.4 (Continued).

# DEPOSIT GEOLOGY

## INTRODUCTION

This chapter documents the geology of the Dinkidi deposit. The Dinkidi Cu-Au porphyry deposit is hosted within a composite monzonite stock. The intrusions of this stock are the last felsic intrusives of the Didipio Igneous Complex, and were emplaced at the southern margin of the Surong Monzonite (Figure 3.1). There are four main intrusions (Figure 4.1) that are, in order of emplacement:

- The Tunja Monzonite, an equigranular monzonite stock (Plate 4.1B)
- The Balut Dyke, a texturally variable clinopyroxene-syenite dyke (Plates 4.1C & D)
- The Quan Porphyry, a monzonite to syenite porphyry stock (Plate 4.1E)
- The Bufu Syenite, a leucocratic, crystal-crowded syenite body (Plate 4.1F)

The margins of the Bufu Syenite, which is typically gradational with the Quan Porphyry, hosts a zone of coarse-grained quartz and K-feldspar (the Bugoy 'pegmatite'; Plate 4.1F) that has been extensively brecciated, forming a quartz fragment breccia. Each of these intrusions has their own distinct hydrothermal assemblages, which are described in Chapter 6. The northern and southern ends of the Dinkidi stock have been truncated by shear zones (Figures 3.1 & 4.1) and the core of the stock has been brecciated extensively by late-stage faulting. The diorite and monzodiorite intrusions, which host the Dinkidi Stock (Figure 4.1; Plate 4.1A), were described in Chapter 3.

## METHOD

The geology of Dinkidi was determined by detailed geological logging of 29 drill holes, totalling 9900 meters, in March-June 1996 and August-September 1998. Logging was complemented by the detailed mapping of Dinkidi Ridge and the immediate surrounds at a scale of 1:1000 in March-May 1995 (Figure 3.1). Drillhole examined as part of this study are listed in Appendix A.

## INTRUSIVE UNITS

### Tunja Monzonite

The oldest and largest intrusion within the Dinkidi composite stock is the Tunja Monzonite. This monzonite hosts most of the mineralisation in the Dinkidi system. The Tunja Monzonite forms an elongated body 150 to 200 meters wide, 600 meters long and at least 800 meters deep. The stock cross-cuts, and contains xenoliths of, clinopyroxene-diorites and monzodiorites and a xenolith-rich monzodiorite breccia (Plate 4.1A; Figure 4.1). Small dykes of the Tunja Monzonite extend at least 100 metres laterally into the surrounding diorites and monzodiorites.



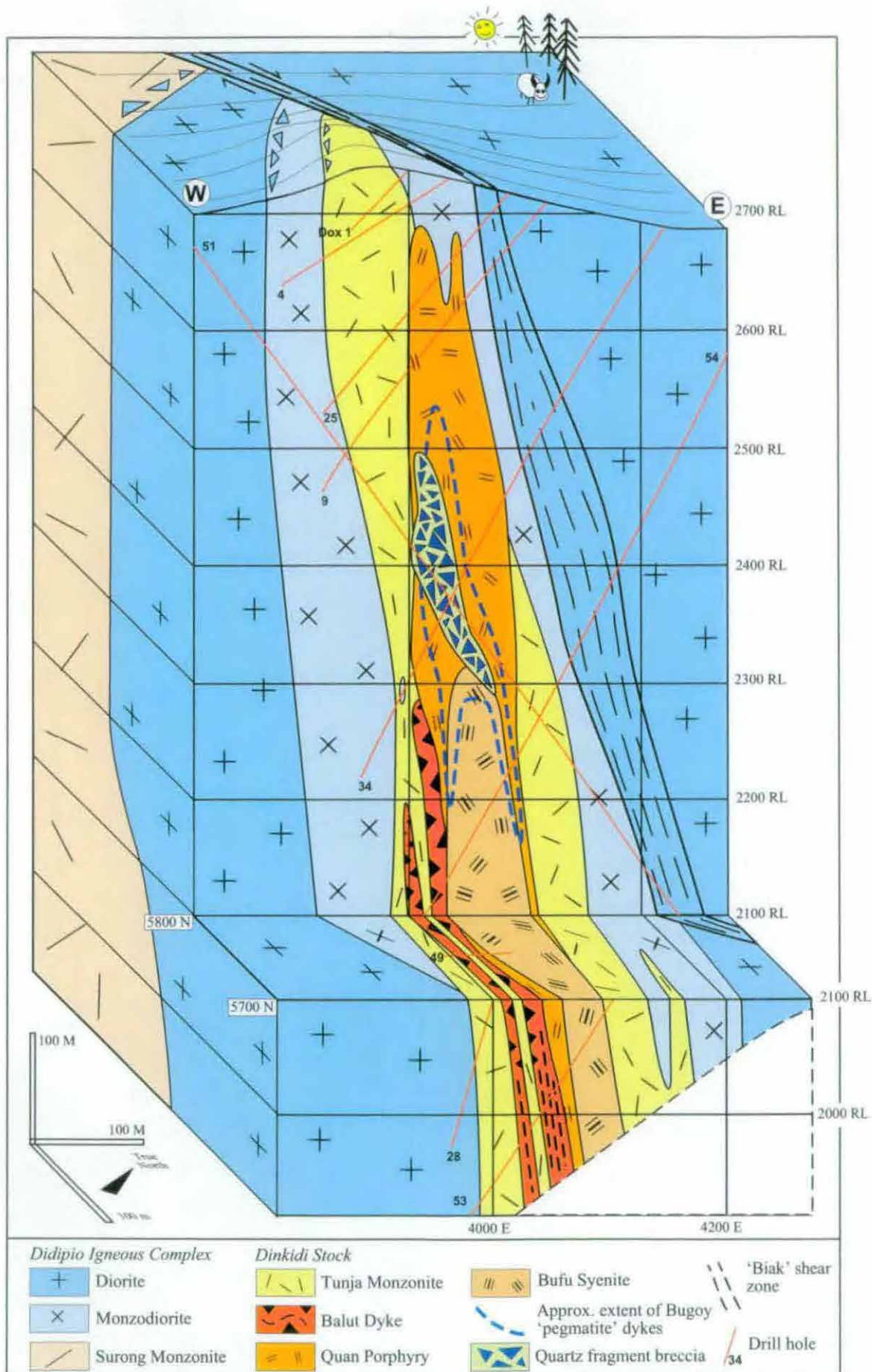


**Figure 4.1:** Geology of the Dinkidi Cu-Au porphyry deposit. The deposit is hosted within a multiphase stock. The oldest phase in the composite intrusion, the Tunja Monzonite (yellow) has cut a series of diorites and monzodiorites (blue). The Tunja Monzonite is in turn cut by a series of mineralised syenite intrusions: the clinopyroxene-phyrlic Balut Dyke (red), which was followed by the Quan Porphyry (orange) and the Bufo Syenite (light orange). Geology based on holes logged in Appendix B.



## DEPOSIT GEOLOGY

The northern and southern ends of the Tunja Monzonite have been truncated by east-trending faults (Figure 3.1).

The Tunja Monzonite is a medium-grained white to pale pink-grey biotite-amphibole monzonite that is typically equigranular to weakly plagioclase-phyric (Plate 4.1B). The monzonite has a crystal-crowded semi-orientated framework (Plate 4.2A & B) of subhedral strongly albitised plagioclase prisms (An 3-30), with relic oscillatory zoning. Plagioclase crystals are typically surrounded by a rind of K-feldspar (orthoclase or rarely perthite), and have in many cases been replaced by orthoclase, forming an irregular antiperthite rim. The plagioclase prisms are supported within a coarse mosaic of interstitial primary anhedral K-feldspar (orthoclase-perthite). Interstitial sites that once held primary biotite and amphibole (now typically chlorite or calcite-rutile) account for approximately 10% of the volume, with accessory apatite, magnetite and rare clinopyroxene.

### Balut Dyke

The Tunja Stock has been intruded by the Balut Dyke, a thin, texturally variable clinopyroxene-phyric syenite (Plate 4.1C & D). The Balut Dyke is approximately 10-30 meters wide and extends at least 600 meters vertically (Figure 4.1). Rare 10-20 cm wide dykes of the Balut Dyke cross-cut the Tunja Monzonite and the diorites on both flanks of the Dinkidi Stock. I first described the geology of the Balut Dyke in Kamenetsky *et al.* (1999), in combination with the melt inclusion study of Balut Dyke clinopyroxene conducted by D. Kamenetsky.

The Balut Dyke displays extreme textural variation over distances of only 1-2 meters. Three main textural styles are recognised: 1) fine-grained equigranular; 2) layered (Plates 4.1D) and coarsely porphyritic (Plate 4.1C). Drillcore intersections of the Balut Dyke display any or all of these textural styles, and/or associated hybrid textures. The Balut Dyke consists predominately of perthite and clinopyroxene (diopside) with accessory magnetite, sphene, apatite and plagioclase. The relative abundance of each mineral varies greatly between and within the three different textural domains.

The equigranular domains of the Balut Dyke typically consist of euhedral 0.5 to 5 mm long euhedral clinopyroxene phenocrysts (Plate 4.2C) that are hosted within a medium-grained mosaic of perthite, with accessory apatite, magnetite and sphene. The clinopyroxene is compositionally and optically identical to diopside found in hydrothermal veins associated with the Balut Dyke (described in Chapter 6). The euhedral nature of the clinopyroxene indicates that they crystallised before, rather than coeval with, the subhedral to anhedral perthite groundmass (Plate 4.2C). The equigranular Balut Dyke is locally a leucocratic clinopyroxene-poor syenite, consisting of a mosaic of perthite with accessory plagioclase, magnetite, apatite and sphene.

The coarsely porphyritic domains of the Balut Dyke consist of 1 to 30 cm long clinopyroxene phenocrysts (diopside; Plate 4.1C), or 0.2 to 1 cm long plagioclase phenocrysts (Plate 4.2D) that are set in a granular mosaic of perthite  $\pm$  albitised plagioclase-apatite-magnetite and, rarely,

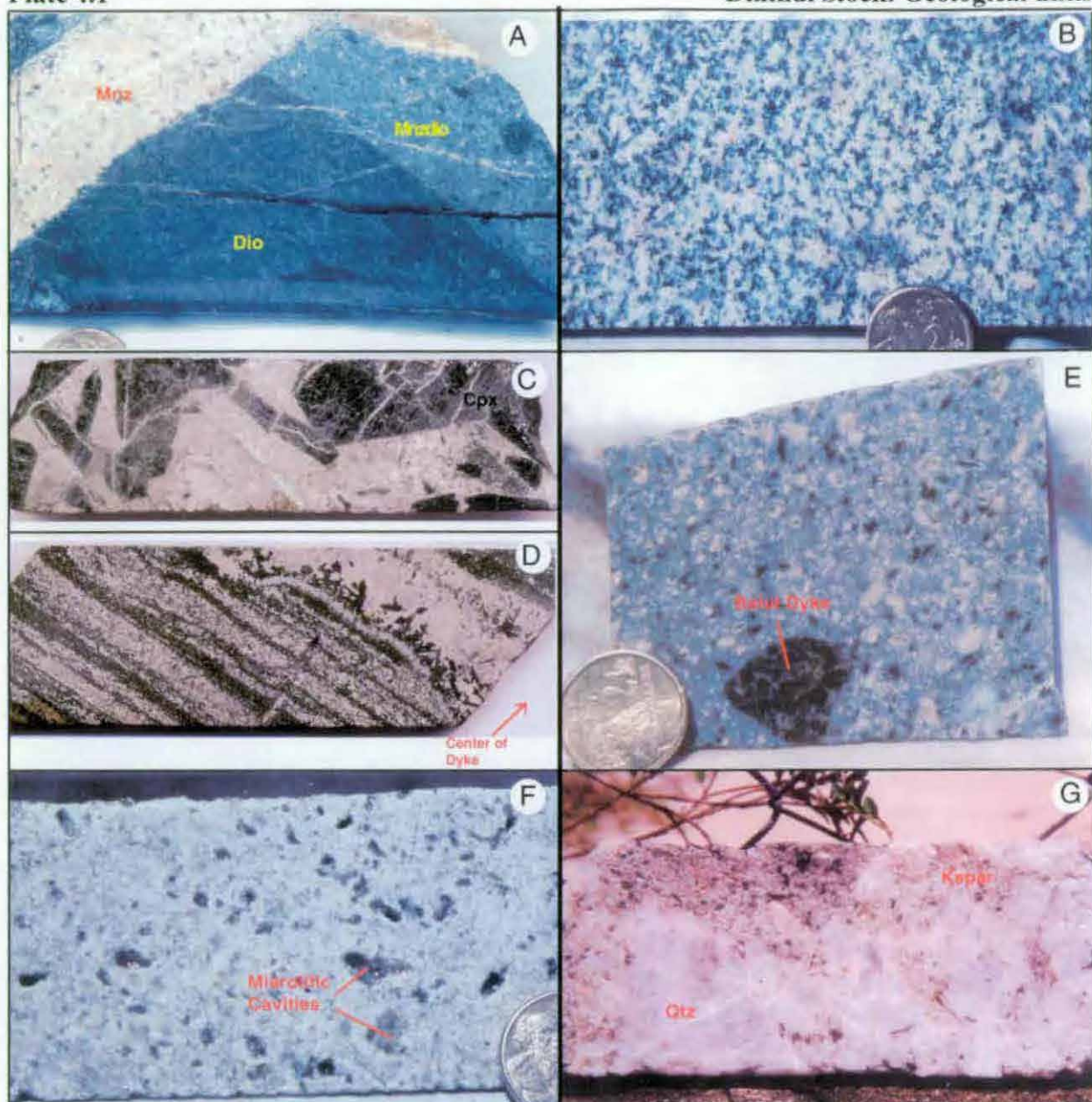


**Plate 4.1 A:** Dark equigranular diorite (bottom) and grey xenolith-rich monzodiorite porphyry (right), the two main country rocks that host the Dinkidi composite stock, are cross-cut by a small pale orange dyke of Tunja Monzonite (left). Monzonite dykes extend at least 200 m out from the main Dinkidi Stock. Sample 34/272.

**Plate 4.1 B:** Typical medium-grained equigranular Tunja Monzonite. Dark mafic sites are comprised of biotite and amphibole. This 150 wide and 600 long stock hosts most of the mineralisation at Dinkidi.

**Plate 4.1 C:** Coarsely-porphyritic Balut Dyke. Clinopyroxene phenocrysts are up to 30 cm in length and are hosted in a K-feldspar (perthite) matrix (see Plate 4.2E). Small porphyritic zones are found throughout the Balut Dyke. Sample 53/805. Sample 3.6 cm wide.

**Plate 4.1 D:** Finely laminated Balut Dyke. Oscillatory layers are comprised of alternating clinopyroxene-apatite-magnetite and perthite-dominated layers (see Plate 4.3E). These vertical layers run parallel to the walls of the dyke, range from 1 mm to 1-2 cm in thickness and can be traced for at least 10 meters along strike. Layered zones in the Balut Dyke can be up to 10 meters thick and occur on the flanks of the dyke at its deepest exposures (below 2100 RL). Sample 49/647. Drillcore 4.7 cm wide.

**Plate 4.1 E:** The Quan Porphyry, a plagioclase- and K-feldspar-phyric monzosyenite. The dark xenolith is a fragment of the Balut Dyke. Plagioclase cores have been altered to clay and chlorite (green centres) while the cream-colored perthite rims are unaltered. Phenocrysts are hosted in a perthite-quartz groundmass. Location DDH28/475m.

**Plate 4.1 F:** Typical leucocratic and vuggy Bufu Syenite. Although the unit resembles the product of extreme leaching and alteration, the perthite crystals in this sample are pristine (also see Plates 4.4 C & D). Miarolitic cavities comprise between 5 and 20% by volume, and in cases occur as partially interconnected trails. Sample 53/676.

**Plate 4.1 G:** Small coarse-grained quartz-perthite dyke of the Bugoy 'pegmatite', which has cross-cut the Quan Porphyry (top). The Bugoy 'pegmatite' is preserved as small dykes (as in this case and also in Plate 4.5A), and as small zones of massive quartz on the margins of the Bufu Syenite. Sample 69/247. Drillcore 6.2 cm wide.

## DEPOSIT GEOLOGY

sphene (Plate 4.2E). In many cases, coarse-grained clinopyroxene has nucleated on the margins of clasts in an igneous-matrix breccia, forming small pockets of coarse-grained clinopyroxene-phyric porphyry in otherwise fine-grained equigranular Balut Dyke. Plagioclase-phyric sections of the Balut Dyke are distinguished from the Quan Porphyry by their lighter cream colour, presence of abundant clinopyroxene phenocrysts and an intimate association with the layered or coarsely clinopyroxene-phyric domains (intimate in that they always occur within 1-10 meters of each other).

The layered domains of the Balut Dyke occur as 1 to 15 meter thick zones of alternating mafic and felsic layers that have a vertical orientation and occur parallel to the dyke walls (Plate 4.1D). These layered zones are found in the deepest exposures of the Balut Dyke, below 2100 RL. Individual layers are 0.1 to 5 cm thick and consist of alternating bands of fine-grained clinopyroxene-magnetite-apatite-perthite±sphene and perthite±clinopyroxene-magnetite-sphene (Plate 4.3E), both with rare plagioclase. Individual clinopyroxene phenocrysts are euhedral and are generally orientated parallel to individual layers (Plates 4.3E & F). Perthite crystals also display a preferred layer-parallel orientation (Plate 4.3F). Areas of layering range from mafic to felsic, with only rare mafic layers (eg Plates 4.3A & C). Individual layers display a range of textures, including erosion (Plate 4.1D), brecciation (Plate 4.3B), folding (Plate 4.3D) and draping over protuberances (Plate 4.3A). Crystal-crowded plagioclase layers are common in areas dominated by felsic layers (Plates 4.3G & H). Layers alternate locally from fine- to medium-grained, but within a single layer, individual crystals grain sizes are uniform.

### Quan Porphyry

Dykes of Quan Porphyry have intruded the Tunja Monzonite and the Balut Dyke. The Quan Porphyry grades, at depth, into a crystal-crowded syenite to quartz syenite core, the Bufu Syenite (Plate 4.1E; Figure 4.1). The Quan Porphyry is a light grey plagioclase-phyric monzonite- to syenite-porphyry that is distinguished by flow-aligned cream-coloured plagioclase phenocrysts up to 7 mm in length (Plate 4.1D). The Quan Porphyry consists of large albitised plagioclase laths (An 5-26) and uncommon biotite, amphibole and K-feldspar (orthoclase) phenocrysts that are hosted within a crystal-crowded groundmass of medium-grained euhedral plagioclase and medium to fine-grained subhedral perthite, quartz and euhedral apatite (Plates 4.4A & B). The sodic rims of the plagioclase phenocrysts have been typically replaced by orthoclase, forming antiperthite patches, and are generally enclosed within a 50-100 µm thick rim of euhedral orthoclase or perthite. Small miarolitic cavities (up to 1-2 mm) are common, and are filled by coarse-grained anhedral quartz (Plate 4.4B).

### Bufu Syenite

The leucocratic crystal-crowded Bufu Syenite occupies the core of the Dinkidi Stock (Figure 4.1), and is distinguished by its distinctive miarolitic cavities and bleached white colour (Plate 4.1E). Dykes of the Bufu Syenite have cross-cut the Quan Porphyry, Balut Dyke and Tunja Monzonite. The Bufu Syenite has both sharp and gradational contacts with the Quan Porphyry.



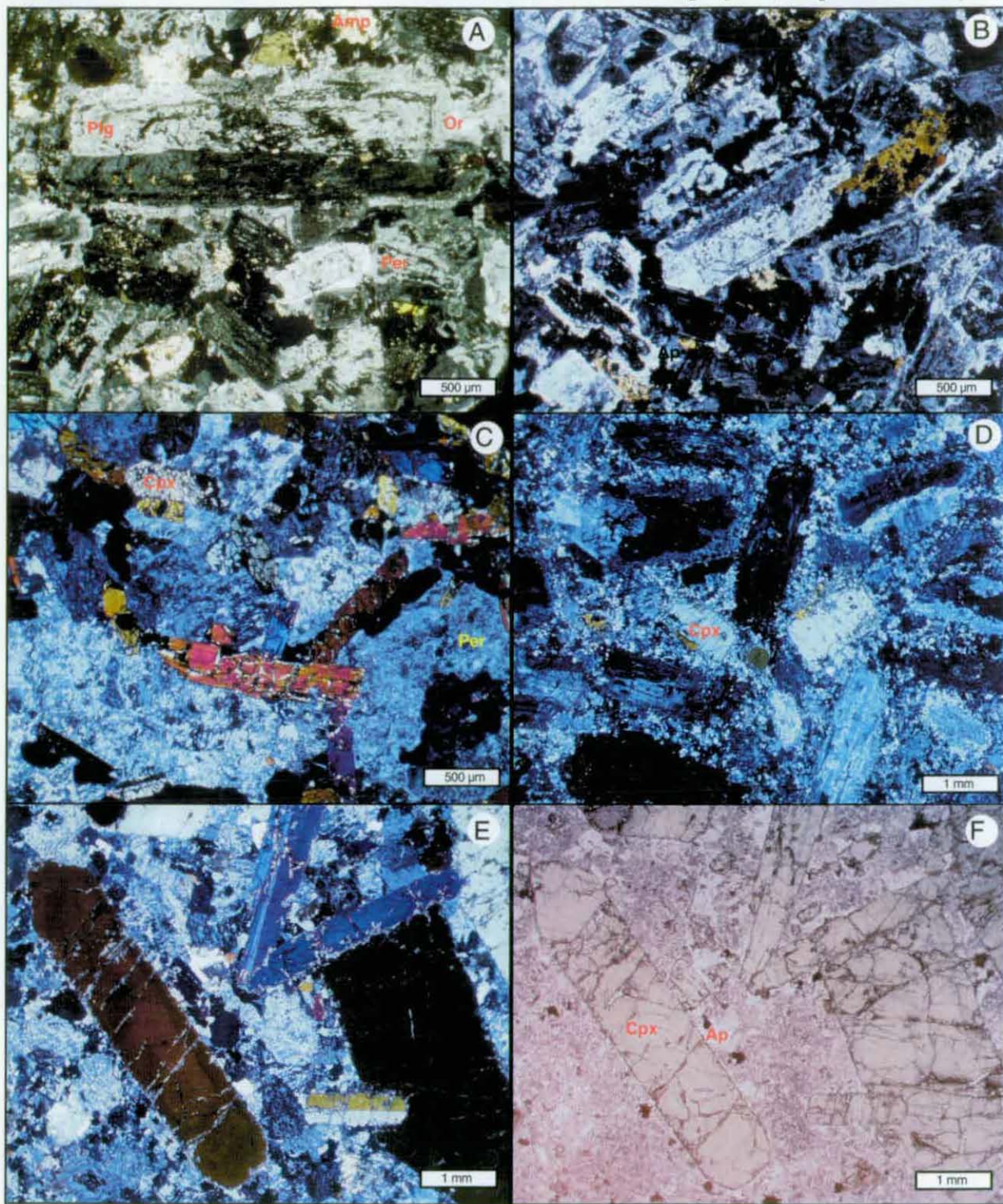


**Plate 4.2 A:** Tunja Monzonite. Albitised plagioclase laths (Plg) are rimmed by K-feldspar (orthoclase (Or)  $\pm$  perthite (Per)) with minor interstitial amphibole (Amp). XPL. Sample 41.3.

**Plate 4.2 B:** Tunja Monzonite. A semi-aligned framework of albitised plagioclase laths (with relict oscillatory zoning) hosted in interstitial orthoclase with accessory biotite (Bio) and apatite (Ap). XPL. Sample 41.3.

**Plate 4.2 C:** Equigranular Balut Dyke. Euhedral clinopyroxene (Cpx; diopside (salite)) crystals are hosted within a coarse-grained mosaic of perthite. XPL. Sample 49/644.

**Plate 4.2 D:** Plagioclase-phyric Balut Dyke. Albitised plagioclase laths are hosted in a granular perthite  $\pm$  orthoclase groundmass with accessory clinopyroxene. XPL. Sample 49/644.

**Plate 4.2 E:** Clinopyroxene-phyric Balut Dyke. Large euhedral clinopyroxene phenocrysts (diopside) are hosted in a K-feldspar groundmass (perthite  $\pm$  orthoclase) with accessory albitised plagioclase and apatite. XPL. Sample 31/334.

**Plate 4.2 F:** PPL photomicrograph of Balut Dyke in Plate E.



## DEPOSIT GEOLOGY

The gradational contacts are marked by an increase in the size and abundance of miarolitic cavities (from < 0.2 to up to 2 cm wide) and a gradual change from coarse-grained porphyritic syenite to medium-grained crystal-crowded syenite. The gradational contact is interpreted to indicate that the Bufu Syenite was emplaced at the same time as, and may have been sourced from the same melt that formed the Quan Porphyry. The cross-cutting relationships are interpreted to indicate that emplacement of the Bufu Syenite continued after final consolidation of the Quan Porphyry. Because of its vuggy and bleached appearance (Plate 4.1F), the texture of the Bufu Syenite superficially resembles a zone of intense leaching or vuggy silica, as observed in high sulphidation epithermal deposits. However, most of the Bufu Syenite is either only weakly sericite-carbonate altered or completely unaltered.

The Bufu Syenite ranges from syenite on the margins to quartz syenite ('Bufu quartz syenite') in the core. The abundance and size of miarolitic cavities increases towards the centre of the intrusion. The syenite consists of a medium- to fine-grained crystal-crowded mosaic of euhedral plagioclase, with 100-500  $\mu\text{m}$  thick subhedral K-feldspar rims (perthite $\pm$ orthoclase; Plate 4.4D), subhedral to euhedral perthite crystals, common subhedral quartz and rare relic biotite and amphibole sites (altered to chlorite). The perthite rims and plagioclase phenocrysts form an interlocking mosaic with common fine-grained interstitial perthite, orthoclase and quartz, with accessory apatite and magnetite (Plate 4.4D). In the quartz syenite, perthite and perthite-rimmed plagioclase phenocrysts display a cumulate fabric and are poikilitically enclosed in a coarse-grained mosaic of quartz (Plates 4.4C&D). The perthite and quartz-rich mineralogy of the Bufu Syenite is similar to the groundmass assemblage of the Quan Porphyry.

Miarolitic cavities in the Bufu Syenite are abundant, typically elongate, 0.2 to 10 mm wide, commonly occur as partially-interconnected trails with adjacent cavities and comprise between 5 and 20% of the rock by volume. In cases where otherwise anhedral interstitial quartz abuts a miarolitic cavity, the crystals have euhedral quartz faces that project into the cavity, indicating the primary nature of these voids. Many of the cavities have been subsequently infilled with secondary carbonates, sulphides and zeolites (Plate 4.4F).

### **The Bugoy 'pegmatite' and Bugoy breccia**

The margin of the Bufu Syenite, within the Quan Porphyry, is marked by a small, irregular zone of coarse-grained quartz and quartz-perthite dykes that crosscut the Quan Porphyry (the Bugoy 'pegmatite'; Plate 4.1F). The Bugoy 'pegmatite' occurs as an apophysis above the Bufu Syenite and also along its walls. The Bugoy 'pegmatite' is not a discrete geological unit, but a small irregular zone that ranges from medium-grained quartz phenocrysts hosted within the Bufu Syenite, to a coarse-grained quartz-perthite assemblage that has been emplaced along the margin of the Bufu Syenite ('massive quartz'; Plate 4.5 B & C) and neighbouring rare, small quartz-K-feldspar dykes ('pegmatites'; Plates 4.1F & 4.5A). Very little of the original massive quartz assemblage remains, as the unit has been almost completely brecciated (Plate 4.5D), forming the Bugoy quartz fragment breccia above the Bufu Syenite (Figure 4.1). The

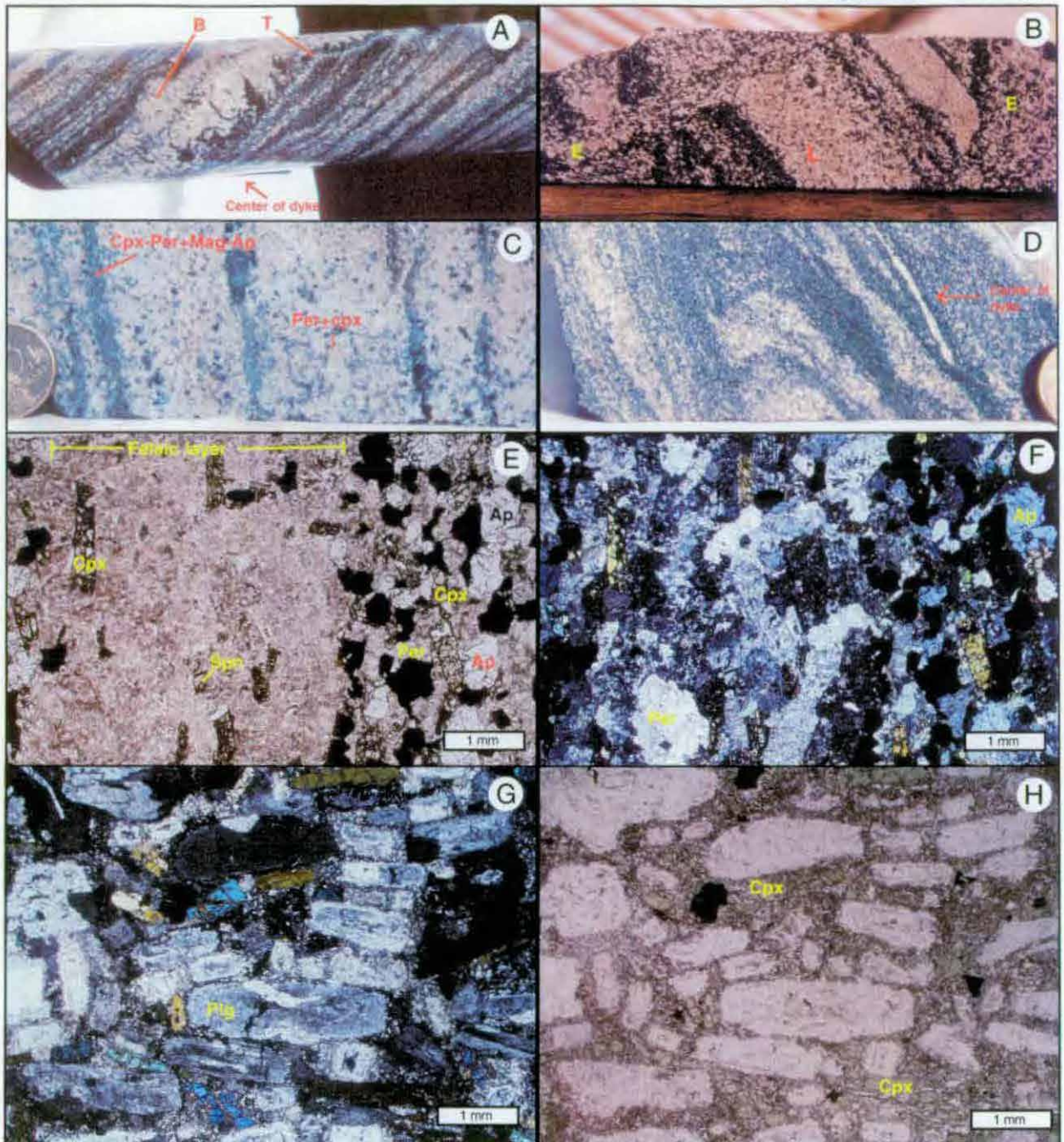


**Plate 4.3 A:** Thin, originally vertical oscillatory zoning of clinopyroxene- and perthite-dominated layers. Earlier layers on the right have been truncated (T) with clinopyroxene nucleating on the erosional surface. A 1 mm thin clinopyroxene-dominated layer has draped over a bump in the thick perthite layer (B) with the curvature smoothed out by successive layers. Sample DDH49/647. Drillcore 4.7 cm wide.

**Plate 4.3 B:** Autobrecciation in the Balut Dyke. A clast of layered Balut Dyke (L) is hosted within, and cross-cut by, equigranular Balut Dyke (E). Location DDH 68/575m. Drillcore 4.7 cm wide.

**Plate 4.3 C:** Thick perthite-plagioclase layers interbedded with thin clinopyroxene-dominated layers. Sample 54/635m.

**Plate 4.3 D:** Folding and truncation in the layered Balut Dyke. The folding is considered analogous to soft-sediment deformation. Truncated layers appear to have formed crossbed-like textures. Both textures are interpreted to indicate magma flow during crystallisation. Location DH49/648.

**Plate 4.3 E:** PPL photomicrograph of layered Balut Dyke. Mafic layer on the right is comprised of clinopyroxene-magnetite-apatite-perthite and minor sphene (Spn). Felsic layer on the left is comprised of perthite and albitised plagioclase with accessory clinopyroxene, sphene and apatite. The contact between the layers occurs over ~100  $\mu$ m. Sample 28/501.

**Plate 4.3 F:** XPL photomicrograph of Plate C. Euhedral clinopyroxene phenocrysts and subhedral perthite grains are aligned parallel to the layering.

**Plate 4.3 G:** XPL photomicrograph of plagioclase layering in the Balut Dyke. Plagioclase phenocrysts and small clinopyroxene phenocrysts are aligned parallel to a vertical crystal-crowded plagioclase layer. Sample 53/776.

**Plate 4.3 H:** PPL photomicrograph of Plate E. Large plagioclase phenocrysts and smaller, more dense clinopyroxene phenocrysts share similar size/density ratios.



## DEPOSIT GEOLOGY

emplacement of the coarse-grained quartz-perthite igneous mineral assemblage was associated with strong quartz-orthoclase flooding and quartz veining (Chapter 6). Widespread brecciation and intense hydrothermal alteration have prevented the author from mapping the Bugoy 'Pegmatite' as a discrete unit. The following description of the Bugoy 'Pegmatite' is based on fragments preserved within the Bugoy breccia, and from small dykes of Bugoy 'pegmatite' that are preserved along the margins of the Bufu Syenite.

The massive quartz assemblage is located along a 1 to 5 meter wide belt on the gradational contact between the Quan Porphyry and Bufu Syenite. This zone locally contains large euhedral quartz 'phenocrysts' (eg Plate 4.5B & 4.5C), zones of massive quartz-perthite (0.5 to 3-4 m wide) or intense zones of silicification. The silicified zones are rarely preserved, being strongly masked by later alteration or being incorporated into the Bugoy Breccia. The outer margin of the silicified zone is marked by intense quartz veining and rare 5cm to 50 cm wide dykes of the Bugoy 'Pegmatite' that have intruded the Tunja Monzonite, Balut Dyke and Quan Porphyry. The dykes consist of massive, coarse-grained grey to milky white quartz and cream-coloured perthite with accessory, typically euhedral, coarse-grained actinolite (typically intergrown with quartz), orthoclase and magnetite (Plates 4.1 F & 4.5 A). Although the dykes consist of a coarse-grained quartz-K-feldspar assemblage, they lack the megacrysts (>30 cm), muscovite alteration, REE-enrichment and genetic association with a granite to be called a pegmatite *sensu stricto*. In the case of the Bugoy body, the term 'pegmatite' is used in a textural sense to signify a coarse-grained dyke.

The Bugoy Breccia is a quartz-fragment breccia that overlies the Bufu Syenite and has cross-cut the Quan Porphyry and Tunja Monzonite (Figure 4.1). The clasts are predominately angular quartz fragments (with rare euhedral actinolite crystals and anhedral orthoclase), together with minor fragments of Tunja Monzonite, Quan Porphyry, Bufu Syenite and rare perthite. The clasts are up to 8 cm in diameter, angular and are hosted in a carbonate±sericite-chlorite altered matrix interpreted to have originally been rock flour. The breccia has sharp contacts with the Quan Porphyry, Bufu Syenite and Tunja Monzonite. Lithic clast abundances in the breccia increase close to the contact with the surrounding rock types. The Bufu Syenite is typically strongly silicified at its margin. The abundance of quartz fragments (typically 70 to 100% of all clasts) and paucity of wallrock fragments in the Bugoy Breccia is difficult to explain by brecciation of only the moderately quartz veined host rock. The Bugoy Breccia appears to have formed by the brecciation of a large zone of massive quartz at the apex of the Bufu Syenite. Mechanisms of formation for this breccia are discussed in Chapter 6.

## STRUCTURE

All intrusions of the composite Dinkidi Stock are elongated northwest, suggesting a structural control on their emplacement. There are a series of normal faults orientated northwest, parallel to the Cagayan Valley Basin (Figure 2.2), that predate the Didipio Igneous Complex, but may



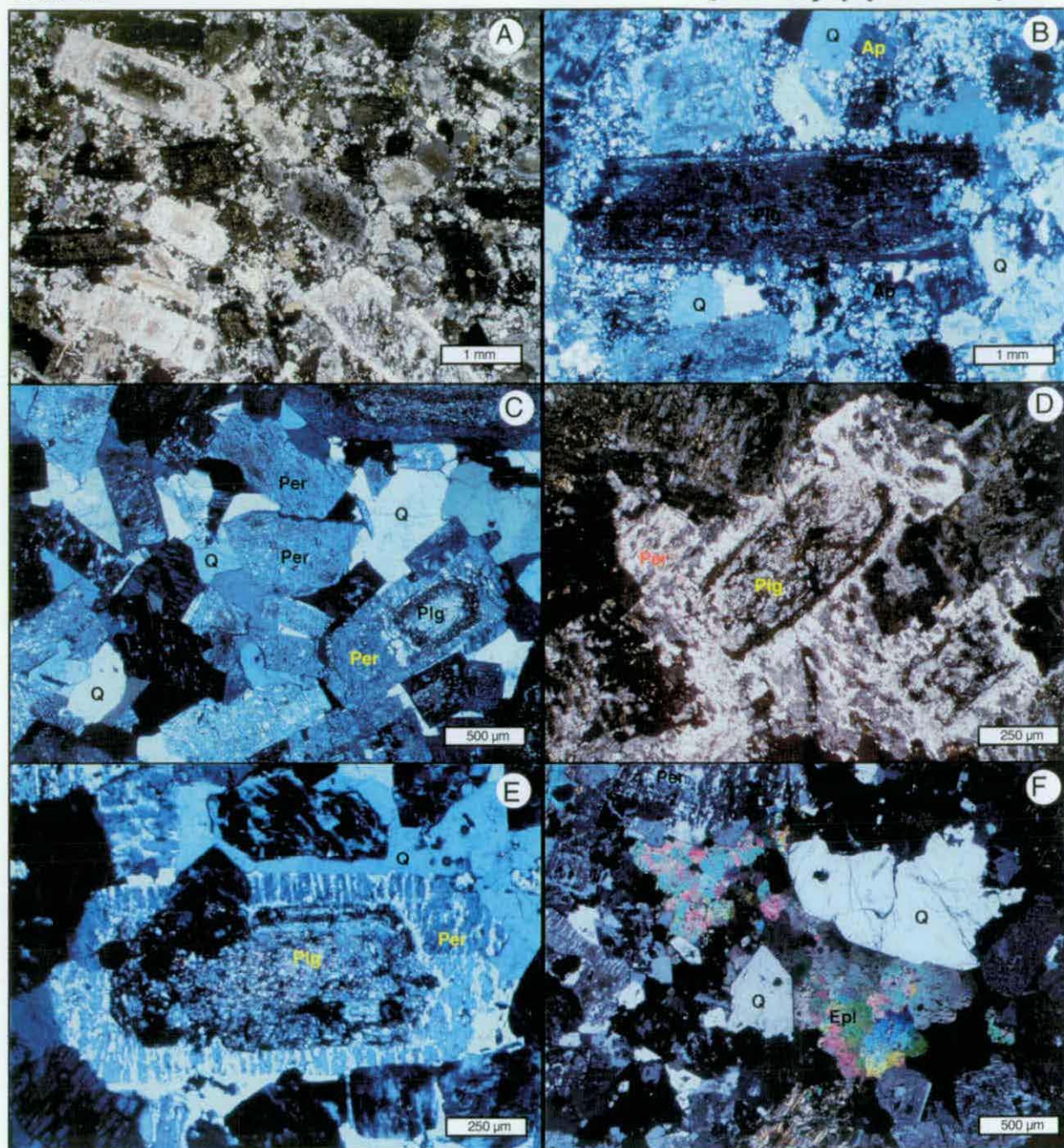


**Plate 4.4 A:** Quan Porphyry. Albitised plagioclase phenocrysts, rimmed by K-feldspar (perthite and orthoclase), and hosted in a granular mosaic of perthite and quartz. Note the chlorite-altered mafic minerals (primary biotite and amphibole). XPL. Sample 28/475.

**Plate 4.4 B:** Quan Porphyry. Interstitial spaces contain common quartz-filled voids in the granular K-feldspar groundmass. These mirolitic cavities are interpreted to be evidence for high volatile contents in the Quan Porphyry. XPL. Sample 3/66.

**Plate 4.4 C:** Cumulate texture in the Bufu quartz-syenite. Euhedral perthite crystals (most with plagioclase cores) are poikilitically enclosed within a coarse-grained mosaic of quartz  $\pm$  perthite. The unit is typical of the quartz-rich core of the Bufu Syenite. The presence of melt inclusions within the quartz indicates a magmatic, rather than hydrothermal, origin for the quartz. The texture suggests that the perthite crystals settled in a late stage, quartz- (and fluid- ?) rich melt. The quartz-rich core of the Bufu intrusion shares a similar composition to the Bugoy Pegmatite (Plate 4.5A) and early quartz veining (described in Chapter 6). XPL. Sample 49/587.

**Plate 4.4 D:** Bufu Syenite. Plagioclase prisms are rimmed by, and supported within, a coarse-grained perthite groundmass. Such units are generally located on the margins of the Bufu Syenite and are a transitional phase between the Quan Porphyry (eg Plate A) and the quartz-syenite core of the Bufu (eg Plate C). XPL.

**Plate 4.4 E:** Typical plagioclase phenocryst in the quartz syenite core of the Bufu Syenite. A carbonate-altered core is surrounded by a thick rim of perthite with interstitial quartz. The dominance of perthite, rather than orthoclase, as the main K-feldspar in the Dinkidi Stock, suggests prolonged cooling below the coherent one-feldspar solvus and high fluid contents. XPL. Sample 49/555.

**Plate 4.4 F:** Mirolitic cavity within the Bufu Syenite. Euhedral quartz crystals project into an epidote- and carbonate-filled cavity. XPL. Sample 49/555.



## DEPOSIT GEOLOGY

have been reactivated following crystallisation of the host diorite. It appears that northwest-trending faults controlled emplacement of monzodiorite porphyry (Figure 4.4) and the Surong Monzonite (Figure 3.1), based on the weak northwestern elongation, when offsets due to late-stage faulting have been removed (Figure 3.1).

The northern and southern margins of the Dinkidi Stock have been truncated by northeast-trending dextral strike-slip faults (F3). The northern fault, the sinistral Biak Shear Zone (Figure 3.1; also referred to as the Didipio Valley Fault), has sheared off the northern end of the Dinkidi Stock. The northern end of the Dinkidi deposit is interpreted to have been offset 700 meters to the east, forming the True Blue prospect. This fault is marked by a 30 to 80 meter wide zone containing 1 to 15 meter wide blocks of unmineralised but strongly carbonate-zeolite veined and brecciated diorite and Tunja Monzonite blocks (Plate 4.5F) that are separated by strongly clay-carbonate-chlorite altered fault zones.

F3, and possibly north to northwest-trending F2 faults, have also disrupted the core of Dinkidi, forming 2 to 15 meter wide cross-cutting fault zones that contain abundant fragments of clay-altered Tunja Monzonite and Quan Porphyry (Plate 4.5E), hosted in a zeolite- and clay-altered rock-flour matrix (see Plate 6.17B). These breccias cannot be correlated between sections.

Unlike the Bugoy Breccia, the fault-zone breccia is dominated by lithic clasts that reflect the composition of the surrounding host rock, and shares a gradational boundary with the surrounding units. The fault zone breccia merges with the Bugoy Breccia in the core of the system, forming a breccia with both abundant host rock clasts and quartz fragments. These breccias, and the hydrothermal mineral assemblages at Dinkidi, are described in more detail in Chapter 6.

## SUMMARY AND DISCUSSION

The Dinkidi Deposit is hosted within an elongate multiphase stock that was emplaced into a series of diorites and monzodiorites. The stock consists of four main intrusions, and represents the last period of felsic magmatism within the Didipio Igneous Complex. The oldest and largest intrusion, the Tunja Monzonite, is an equigranular monzonite that predates mineralisation and is compositionally similar to the biotite-monzonite phases of the Surong Monzonite. The Tunja Monzonite has been intruded by a series of mineralised syenite intrusives: the unusually textured clinopyroxene-syenite of the Balut Dyke, followed by a syenite porphyry (the Quan Porphyry) that grades, in its core, into a crystal-crowded leucocratic quartz-syenite (the Bufu Syenite). These three intrusions share a similar perthite-dominated composition. The Balut Dyke is distinguished by its clinopyroxene-phyric nature, whereas while the Quan Porphyry and Bufu Syenite are quartz-bearing.

The clinopyroxene-phyric nature of the Balut Dyke is unusual for a late-stage, highly evolved syenite melt. Nucleation textures within the porphyritic domains, within thin dykes and on uncommon truncated layers on the walls of the layered Balut Dyke indicate that some clinopyroxene grew *in situ* in these domains during crystallisation, rather than being

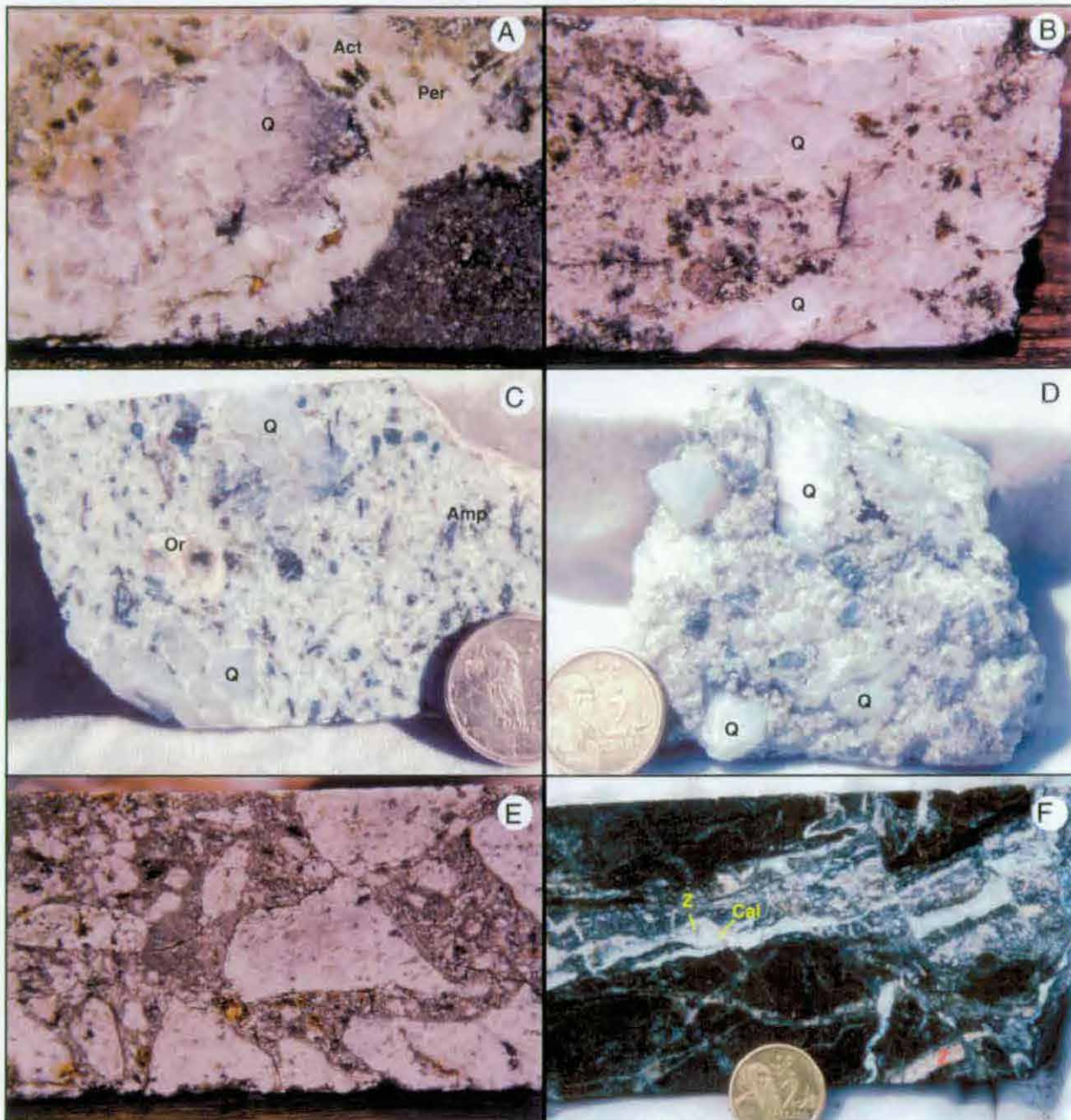


**Plate 4.5 A:** Dyke of the Bugoy 'Pegmatite' (left) cross-cutting magnetite-flooded equigranular Balut Dyke (bottom right). The Bugoy dyke consists of coarse-grained quartz and K-feldspar (perthite  $\pm$  orthoclase) with accessory actinolite. Location DDH53/825m. Drillcore 4.7 cm wide.

**Plate 4.5 B:** Coarse-grained massive quartz at the gradational boundary between the Quan Porphyry and Bufu Syenite. Patches of massive quartz up to 1-3 m wide have developed along this contact at the top of the Bufu Syenite. Location DDH49/628m. Drillcore 6.2 cm wide.

**Plate 4.5 C:** Large (1-10 cm) euhedral quartz crystals in the marginal phase of the Bufu Syenite. Sample 49/613.

**Plate 4.5 D:** The Bugoy 'breccia', a quartz-fragment breccia that overlies the Bufu Syenite. Angular quartz fragments are supported in a carbonate-, chlorite- and sericite-altered (originally rock flour?) matrix. Host rock lithic clasts are conspicuously rare to absent. The coarse-grained Bugoy 'pegmatite' quartz is interpreted to have been incorporated into the Bugoy breccia. Location DH34/394m.

**Plate 4.5 E:** Tectonic brecciation within the core of Dinkidi. A serate range of angular illite-altered fragments of the Tunja Monzonite are hosted within a rock flour matrix. The core of the Dinkidi Stock, especially most of the Quan-Tunja margin and the Bugoy breccia, have been extensively disrupted by 5 to 20 meter wide breccia zones. Sample 82/286.

**Plate 4.5 F:** Sample from the Biak Shear Zone (Figure 4.1). The northern end of the Dinkidi Stock has been truncated by a regional-scale fault zone (Figures 3.1 & 4.1). The shear zone is marked by abundant zeolite-calcite altered faults, with strong brecciation with calcite (Cal) and zeolite (Z) veining of the Tunja Monzonite and diorite blocks. Sample 34/239.

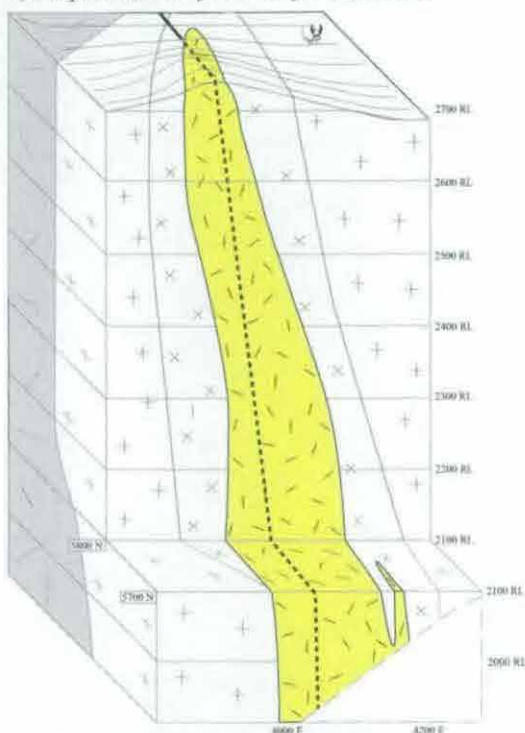
## DEPOSIT GEOLOGY

phenocrysts sourced from a deeper magma chamber. The euhedral clinopyroxene in the equigranular and layered domains probably grew in the melt prior to emplacement. The size of the phenocrysts and extreme textural variability suggests high volatile contents. This is supported by melt inclusion evidence (Kamenetsky *et al.*, 1999) that indicates that the Balut Dyke clinopyroxenes grew in an volatile- and salt-rich melt, probably in the presence of an immiscible phase, at magmatic temperatures of  $> 600^{\circ}\text{C}$ .

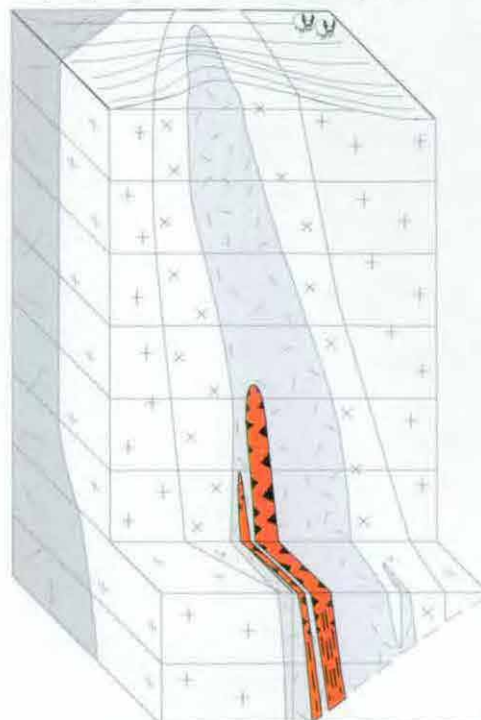
The unusual vertical layering in the Balut Dyke may have formed by flow segregation, where magmatic currents segregated crystals of different size and density, or by compositional variations in the magma during crystallisation, either by injection (or escape) of new magma/ volatiles in the magma body or by a diffusion-controlled processes at a stagnant crystallisation interface (Webber *et al.*, 1997). The alignment of phenocrysts parallel to the layers (eg Plates 4.3 D & E), combined with similar size-density ratios between different crystals in the same layer (eg Plate 4.3E), suggests that layering resulted from flow segregation. This is supported by evidence for current deposition in the Balut Dyke, including erosion of previous layers, cross bedding and autobrecciation (Plates 4.3A & B). Achieving strong, oscillating magma flow rates in a presumably viscous syenite melt, especially when confined to a dyke as thin as the Balut Dyke, probably required high volatile contents to lower the viscosity. Alternatively, oscillations in the volatile content of the Balut Dyke melt may have lead to cyclic changes in melt viscosity, leading to varying flow rates and development of the layering. Diffusion-controlled crystallization at a stagnant crystallisation interface (eg Webber *et al.*, 1997) can produce alternating layers of felsic and mafic minerals that grow towards the centre of the intrusion. Whereas such nucleation layers are not common in the Balut Dyke (eg the coarse band in 4.3A), their presence indicates periods of stagnation in the Balut Dyke and indicates that at least two processes were at work in forming the compositional layers.

Emplacement of the Quan and Bufu intrusions appears to have occurred along the same structure utilised by the Balut Dyke. The Balut Dyke is preserved on the western margin of the Quan Porphyry, but small, localised Balut dykes also occur on the eastern flank of the Quan Porphyry, 100 meters away, suggesting dilation during Quan Porphyry emplacement. It is interpreted that the Quan Porphyry is the early phase of the one Quan Porphyry-Bufu Syenite melt, which crystallised due to cooling when it came into contact with the surrounding country rock. The Bufu Syenite then crystallised from the residual K-feldspar-quartz dominated melt. Abundant miarolitic cavities (especially as interconnected trails), such as those observed in the Bufu Syenite, are one of the rare forms of textural evidence for volatile migration in a magma (Candela, 1997). This suggests that the Bufu Syenite was a major conduit for volatiles, connecting an underlying volatile-exsolving magma chamber to the site of ore deposition at Dinkidi. A high volatile content for the Bufu melt is supported by the accumulation of coarse-grained quartz and perthite in the Bugoy Pegmatite. This coarse-grained accumulation of quartz and perthite is located at the interface between the quartz-syenite core of the Bufu and the overlying quartz stockwork (see Chapter 6), a location similar to the position of quartz-K-

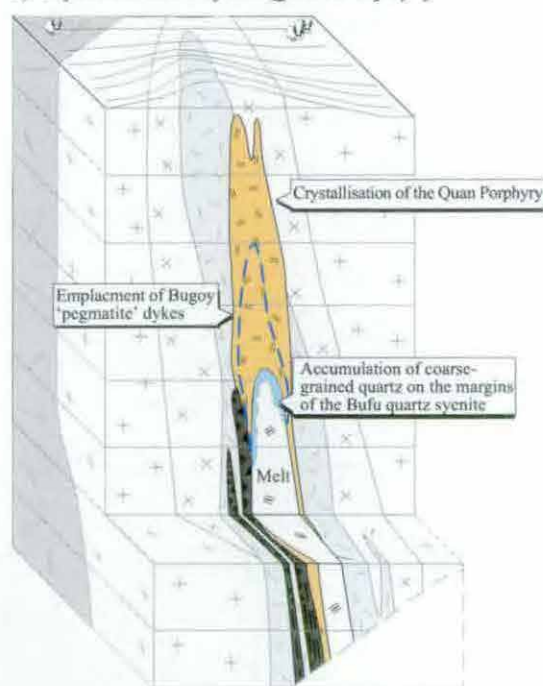


1) *Emplacement of the Tunja Monzonite*

Intrusion of the Tunja Monzonite along a north-west trending structure adjacent to the Surong Monzonite.

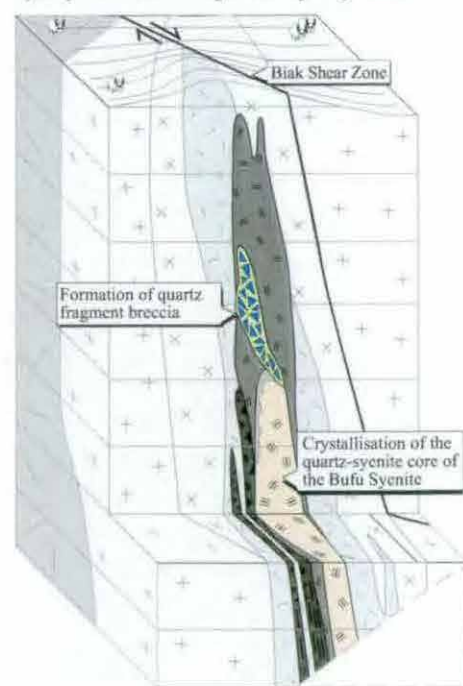
2) *Emplacement of the Balut Dyke*

Intrusion of the clinopyroxene-phyric Balut Dyke into the Tunja Monzonite stock.  
Development of porphyritic and layered textures.

3) *Crystallisation of the Quan Porphyry*

Intrusion of the Quan-Bufu stock up the same structure as the Balut Dyke. Crystallisation of the Quan Porphyry on the walls of the stock.

Crystallisation of the outer syenitic margin of the Bufu Syenite. Emplacement of the Bugoy 'pegmatite' dykes and accumulation of coarse-grained quartz on the margins of the Bufu quartz syenite.

4) *Crystallisation of the Bufu Syenite*

Crystallisation of the quartz-syenite core of the Bufu Syenite, and associated dykes in the Quan Porphyry Brecciation of the coarse-grained quartz body, forming the Bugoy Breccia.

Post-hydrothermal activity faulting shears off the northern section of Dinkidi.

**Figure 4.2:** Magmatic evolution of the Dinkidi composite stock. Legend for all symbols provided in Figure 4.1.



## DEPOSIT GEOLOGY

feldspar unidirectional solidification textures found in many other porphyry deposits (Kirkham & Sinclair, 1988; Barton *et al.*, 2000). Crystallisation of the quartz-syenite core of the Bufu Syenite may have been triggered by volatile loss, with the perthite phenocrysts of the Bufu melt settling into a cumulate-textured felsic 'mush' (eg Plate 4.4C), supported by interstitial quartz, and freezing into place the miarolitic cavities.

A northwest-trending feeder structure, which predates the monzodiorites of the Didipio Intrusive Complex, appears to have controlled emplacement of the Dinkidi Stock and possibly the Surong Monzonite. Emplacement of the Surong Monzonite may have 'plugged' this feeder structure, forcing the Dinkidi stock to be emplaced on the margin of the Surong pluton. Dilational emplacement for all intrusives of the Dinkidi composite stock is supported by a scarcity of xenoliths in any of the intrusions. This is in contrast to the xenolith-rich contacts of earlier Didipio Igneous Complex intrusions, such as the Surong Monzonite or the xenolith-rich diorites and monzodiorites. Emplacement up a structure could also have facilitated volatile transport to, and concentration at, the depositional area. The emplacement of the porphyry stocks would have been aided by the high volatile content of the melt that would be expected to lower viscosity, increase buoyancy and, at shallow crustal levels, increase the hydrostatic pressure via two-phase volatile exsolution. Repetitive 'crack-sealing' on the deposit scale could lead to the development of a multiphase porphyry stock such as Dinkidi.

Several compositional, textural and genetic features of the Dinkidi Stock are similar to features found in pegmatites from mid-crustal granitic intrusions. The Balut Dyke is similar to a pegmatite, is a mineralised, coarse-grained, texturally-variable dyke that has crystallised from a volatile-rich late-stage siliceous melt sourced originally from an evolved felsic magma chamber. The perthite-quartz assemblage of the Bufu Syenite is compositionally and texturally identical to a common intermediate zone assemblage found in many heterogeneous granitic pegmatites (Cameron *et al.*, 1949; Cerny, 1991), and the massive quartz-perthite of the Bugoy 'pegmatite' is similar to the inner quartz zone of most granitic pegmatites. It appears that high magmatic volatile contents in shallow (1-5 km) crustal melts at Didipio produced an intrusion with compositional, textural and possibly genetic similarities with pegmatites developed in the mid crust (Figure 4.3).

Based on the Balut Dyke, shallow crustal pegmatite-like bodies that are emplaced into a porphyry environment are predicted to display significant textural and mineralogical differences from granitic pegmatites, due in part to the lower pressures and greater undercooling in the shallow sub-volcanic environment, which causes an overall finer grain size. Differences also arise due to the more mafic dioritic-syenite melt composition, causing compositional differences in both the primary and secondary mineral assemblages relative to granitic pegmatites. For example, the Balut Dyke, and the associated vein system, have a 'mafic' K-feldspar-clinopyroxene-magnetite composition, with associated Cu-Au enrichment, while pegmatites, and related alteration, have a bulk composition close to that of granites with a K-feldspar-albite±quartz-muscovite mineralogy, with rare element mineralisation such as Li, Ta, Be, Li,

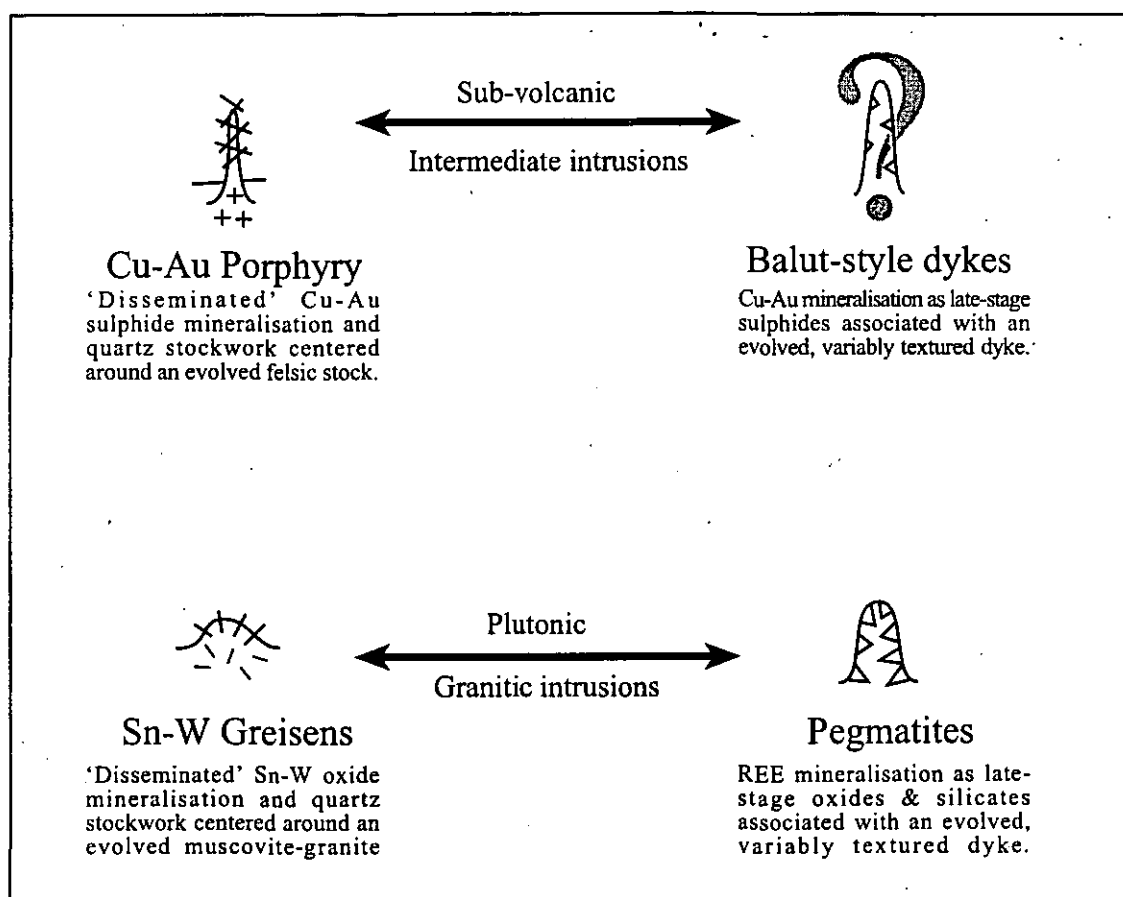


**Figure 4.3:** Comparison of mineralised intrusions in shallow and mid-crustal environments. Cu-Au porphyry quartz stockworks share similarities to W-Sn greisens in deeper granitic systems, in that both are zones of quartz veining, with disseminated mineralisation, that are sourced from, and centred around, late-stage evolved melts (although no genetic links between the two are implied). It therefore could be possible that the pegmatites found associated with granites in the mid-crustal environment will be represented by an analogous mineralisation style in the shallow crustal environment. It is proposed that the Balut Dyke can be considered such an analogy in that both are mineralised variably-textured dykes that are sourced from volatile-rich late-stage melt.

REE, Sn, Nb and Ga as late-stage silicates and oxides (Cerny, 1991).

Although the relationship between epithermal and porphyry environments has been extensively documented (eg Sillitoe 1973, 1995; Hedenquist *et al.*, 1998), a relationship between porphyry and pegmatite systems has only been rarely acknowledged in the literature, despite many textural, compositional and genetic similarities. Despite this, many descriptions of porphyry deposits refer, usually in passing, to 'pegmatite bodies', although this term is used to describe compositional and texturally different features at each deposit (eg the hydrothermal 'pegmatite-textured veins' at Copper Mountain, Stanley *et al.*, 1995; the igneous 'mineralised pegmatite dykes' at Aitik, Bergman *et al.*, 2001). It is likely that with recognition of the link between pegmatite and porphyry deposits, and the development of a consistent nomenclature for such bodies, that further pegmatite-like bodies will be recognised and described from porphyry Cu-Au deposits.

# GEOCHEMISTRY

## INTRODUCTION

In this chapter, whole-rock and mineral compositions are used to:

- 1) Geochemically classify the units present at Didipio;
- 2) Determine the relationships between individual intrusions of the Didipio Igneous Complex, and also the surrounding volcanic units;
- 3) Identify relationships between the units that crop out in the Didipio region and the regional formations and intrusions,
- 4) Determine the tectonic association of local and regional units, and the implications for magma sources.

The rock units of the Didipio region are classified here on the basis of alkali contents (Figure 5.1). Variation diagrams are used to determine the relationships between rock units (Figures 5.2 & 5.3) and determine fractionation processes. Rare-earth element compositions are used to determine the relationship between the Didipio units and the regional packages. The composition of mineral phases is used to provide insights into the relationships between local units, and has been used to model the fractionation history of the Didipio Intrusive Complex.

## METHOD

Fifty-two representative samples were collected from surface exposures and drill core. These samples include all major phases of the Didipio Igneous Complex and the lavas from the surrounding formations. Any oxidised rinds on these 0.5 to 2 kg samples were sawn off. The samples were then crushed in a hydraulic steel-plate crusher, and the ~0.5 cm<sup>3</sup> chips were sorted to remove any remaining weathered or altered fragments and any chips that had been in contact with a saw blade. The samples were then split and pulverised in a ceramic mill (potential weak Al<sub>2</sub>O<sub>3</sub> contamination), which was cleared with 1-2 passes of high purity quartz sand between each sample (potential weak SiO<sub>2</sub> contamination). A total of 30 to 40g of sample was milled in order to obtain a representative assay, with larger samples (60-80g) used for coarse-grained units. Major and trace elements were analysed on a Phillips PW1480 XRF spectrometer at the University of Tasmania, following the method of Norrish and Hutton (1969). Standard XRF samples and blanks were run once every 6-10 samples to ensure analytical precision. Loss on ignition was estimated by heating each sample to 1000°C for 16 hours and measuring the change in mass. A subset of 29 samples were analysed for rare earth elements (REE), following the ionic exchange-XRF analytical procedure of Robinson *et al.* (1986). Mineral compositions were determined with a Cameca SX50 electron microprobe at the University of Tasmania.



Unit No# of Samples	Didipio Igneous Complex					Dinkidi Stock				Mamparang F.	Upper M.F.
	Gabbro	Diorite	Monzodiorite	Monzonite	Andesite Dyke	Tunja	Balut	Quan	Bufu	Andesite	Trachyte
	2	5	8	13	2	5	1	3	2	4	6
SiO <sub>2</sub>	41.13	50.22	52.31	56.79	47.42	56.73	54.00	61.71	70.99	60.03	66.65
TiO <sub>2</sub>	0.99	0.71	0.63	0.48	0.73	0.44	0.24	0.29	0.13	0.36	0.27
Al <sub>2</sub> O <sub>3</sub>	15.97	18.45	18.38	18.13	17.96	18.79	8.96	17.90	15.16	17.95	16.89
Fe <sub>2</sub> O <sub>3</sub>	14.36	9.02	7.95	5.77	9.92	4.94	5.64	3.20	0.78	5.19	1.97
FeO	-	-	-	-	-	-	-	-	-	-	-
MnO	0.23	0.19	0.19	0.13	0.19	0.09	0.28	0.04	0.01	0.08	0.05
MgO	8.46	4.28	3.67	2.38	5.50	2.12	6.72	0.94	0.24	2.06	0.53
CaO	16.29	9.67	8.83	5.91	10.61	5.15	12.50	3.25	0.52	4.69	1.32
Na <sub>2</sub> O	0.96	3.41	3.91	4.43	2.69	5.49	2.92	6.35	3.25	4.50	4.37
K <sub>2</sub> O	0.51	2.86	3.00	4.21	2.25	3.47	3.40	3.82	8.04	2.52	6.45
P <sub>2</sub> O <sub>5</sub>	0.50	0.51	0.52	0.37	0.48	0.31	-	0.16	0.06	0.26	0.06
S	0.04	0.01	0.01	0.08	-	0.02	0.22	0.04	0.14	0.10	0.03
Loss	0.38	0.52	0.49	1.42	2.06	2.46	4.68	2.47	0.97	2.08	1.20
Total	99.76	99.85	99.88	100.02	99.77	99.99	99.40	100.13	100.11	99.71	99.76
<i>Trace elements (ppm)</i>											
Nb	1.3	1.4	1.5	1.9	1.4	1.7	-	1.8	0.1	1.9	4.7
Zr	20	59	70	94	51	52	-	87	116	84	223
Sr	992	1118	1160	972	1017	1033	-	884	172	928	364
Cr	34.1	8.5	10.5	5.1	17.8	2.2	-	1.8	2.0	6.2	2.2
Ba	135	528	539	597	361	1242	-	1181	862	581	390
Y	20	19	20	18	19	11	-	7	4	13	19
Rb	10	53	55	71	34	64	-	50	106	39	109
Th	0.1	1.4	0.4	1.6	0.1	-	-	-	-	-	7.6
Pb	3	9	10	9	10	6	-	6	3	7	11
Zn	86	69	71	48	78	27	-	22	7	37	30
Cu	139	122	157	183	166	100	-	442	320	278	22
Ni	22.3	7.7	7.6	4.1	15.7	1.3	-	0.8	0.8	4.6	1.0
Mg/Mg+Fe	37	32	32	29	36	30	33	23	23	28	21

Table 5.1. Representative analyses from the Didipio Igneous Complex and local volcanic units. Upper M.F.: Upper Mamparang Formation.

Representative analyses are provided in Table 5.1, with the full assay results provided in Appendix B. The Didipio data set was complemented by 120 whole-rock analyses of surrounding regional units compiled from the few analyses available in published work (Knittel, 1981, 1987; Knittel & Defant, 1988; Knittel and Cundari, 1990; Albrecht and Knittel, 1990) and the large number of analyses contained within unpublished works or theses (MMAJ, 1977; Knittel, 1982; Clooth, 1984; Oles, 1984; Albrecht, 1986; Ringenbach, 1992; Billedo, 1994). These regional whole-rock analyses are compiled in Appendix B. The assistance of Ulrich Knittel from the University RWTH-Aachen in Germany is gratefully acknowledged in providing the majority of these regional analyses from his own database ('Knittel, *pers com.* 1999' in Appendix B) and for providing many of the unpublished reports and theses.

Several acronyms are used throughout this chapter. 'HFSE' elements are the high field strength elements (eg Nb, Ti, Zr, Th, Hf & Ta). The HFSE includes the rare earth elements, 'REE', which can be subdivided into the light rare earths ('LREE'; eg La, Ce & Nd), the heavy rare earths ('HREE'; eg Lu, Yb, Tm & Er), and informally, the middle rare earths ('MREE'; eg Sm, Eu, Gd, Tb, Dy and Ho). 'LILE' elements are the large ion lithophile elements (eg: Ba, Sr, Rb, K). LOI refers to loss on ignition.

### Effect of alteration on analyses

All care has been taken to assure that the analyses used in this chapter represent primary whole rock values. Over 100 samples (from the least altered exposures of all units studied) were screened for alteration and weathering by both hand sample and thin section examination. Of

these samples, only 52 were selected for analysis.

Despite careful sample selection, samples collected from the Dinkidi Stock have been affected by weak sericite alteration and display high Cu and LOI values (eg 100-441 ppm Cu, 0.97-2.47 % LOI; Table 5.1). Thin sections of samples from other intrusions in the Didipio Igneous Complex indicate that they are not appreciably altered (eg 120 to 180 ppm Cu; Table 5.1) and have moderate LOI (0.3 to 2 % LOI; Table 5.1). Samples from the volcanic units display moderate LOI values (2 % LOI for the slightly weathered Mamparang Formation Samples; 1.2% LOI for the Upper Mamparang Formation; Table 5.1). Where necessary, the possible effects of hydrothermal alteration will be mentioned in the text, however, the discussion necessarily assumes, *caveat emptor*, that alteration has had a minimal effect on the whole rock composition.

The monzonite and syenite intrusions of the Didipio Igneous Complex are associated with extensively developed hydrothermal alteration assemblages (described in the following chapter). The high temperature secondary assemblages are interpreted to indicate that late-stage magmatic volatiles were present within the melt during crystallisation. The trends and discussions of this geochemical study are based on whole rock geochemistry and does not take into account the sequestering effects of any magmatic volatile phases that may have been present within the melt.

## TOTAL ALKALINE CLASSIFICATIONS

Analysis of whole-rock geochemical compositions allows a precise classification of both aphanitic and porphyritic rock units (Figure 5.1). Based on total alkali and silica (TAS) contents, the 'andesites' of the Mamparang Formation are classified as basaltic trachyandesites to trachyandesites and the 'latites' and 'dacites' of the Upper Mamparang Formation are classified chemically as trachytes (Figure 5.1B). Although TAS classifications were designed for volcanic units, the phases of the Didipio Intrusive Complex have also been plotted for reference, ranging in composition from gabbros to syenites (Figure 5.1C). The late stage Quan Porphyry is classified as a syenite (although the TAS scheme lacks a monzonite field) and the Bufu Syenite is classified as an alkali granite.

The trachytes of the Upper Mamparang Formation and all of the intrusive phases of the Didipio Intrusive Complex plot in the alkaline field of Irvine & Baragar (1971, Figure 5.1B & C) and plot in the shoshonite field of Peccerillo & Taylor (1976; Figure 5.1A). As  $\text{Na}_2\text{O} > \text{K}_2\text{O}$  for all phases of the Didipio Intrusive Complex, with the exception of the highly evolved Bufu Syenite, the Didipio Intrusive Complex is defined as an alkaline intrusive complex rather than potassic or shoshonitic. The Mamparang Formation in the Didipio region appears to become progressively more alkaline upward through the stratigraphy. For example, the three most silicious subalkaline trachyandesites were collected from adjacent flows considerably lower in the stratigraphy than the alkaline basaltic trachyandesite sample, which was collected at the top of stratigraphy. All these andesitic units plot within the high-K field of Peccerillo & Taylor

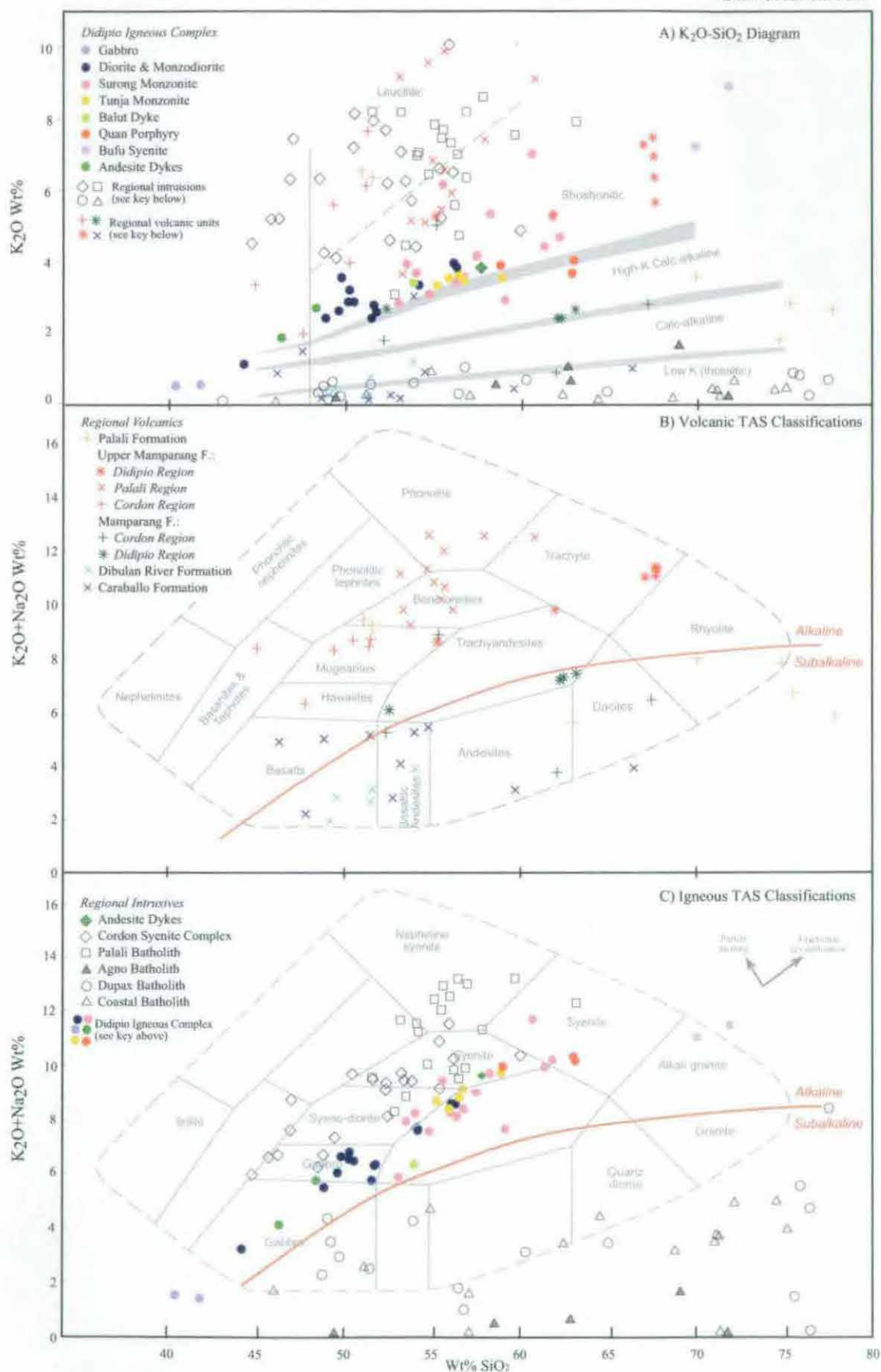


**Figure 5.1:** Classification diagrams for volcanic and igneous units from both the Didipio area and regional units. A)  $K_2O$ - $SiO_2$  diagram with the boundaries of Peccerillo & Taylor (1976). Boundary between leucitic and shoshonitic series (broken line; Wheller *et al.*, 1987) appears to chemically distinguish between sanidine and leucite-phyric units. B) TAS volcanic classification diagram (Cox *et al.*, 1979). C) Total alkali-silica (TAS) classification scheme of Cox *et al.* (1979) modified for igneous rocks by Wilson (1989). Alkaline-subalkaline curve in diagrams B & C from Irvine & Baragar (1971).



(1976; Figure 5.1A) and just inside the border of the sub-alkaline field of Irvine & Baragar (1971; Figure 5.1B). They are considerably less alkaline than the overlying Upper Mamparang Formation (Figure 5.1B).

The Late Oligocene intrusions of North Luzon displays a bimodal distribution with respect to their  $K_2O$  contents (Figure 5.1A). The Didipio Igneous Complex, Palali Batholith, Cordon Syenite Complex and the Upper Mamparang Formation are considerably more potassic than the tholeiitic Dupax or Northern Coastal Batholiths and the Dibulan River Formation (Figure 5.1 A & C). The Mamparang Formation appears to be intermediate between these two series. The Middle Miocene dacites of the Palali Formation are also intermediate between these two groups; plotting as calc-alkaline dacites and rhyolites, with the two ultrapotassic samples probably representing misidentified Upper Mamparang Formation lavas. The Upper Mamparang Formation in the Didipio Region is more siliceous, but less potassic than, the trachytes and phonolites of the Upper Mamparang Formation in the Cordon and Palali regions, reflecting a similar trend between the three intrusive centres.

## BIVARIATE VARIATION DIAGRAMS

Bivariate variation diagrams, where elemental abundances are plotted against an index of fractionation, such as  $SiO_2$ , can be used to interpret co-genetic relationships between rock units in the same area and allow the fractionation trends for one igneous suite to be determined. The smooth linear trend in the variation diagrams (Figures 5.2 & 5.3) suggests that all the phases of the Didipio Intrusive Complex are related by simple fractional crystallisation, with all major elements except  $Na_2O$  and  $K_2O$  decreasing in abundance with increasing  $SiO_2$ . These 'co-magmatic' trends are also developed when plotted with other indexes of fractionation, such as wt % MgO or Mg number. The depletion of MgO and CaO;  $TiO_2$  and  $Fe_{total}$ ; and  $P_2O_5$  with increasing  $SiO_2$  contents (Figure 5.2) indicates fractionation of clinopyroxene, Fe-Ti oxides (predominantly magnetite) and apatite, respectively. The depletion of  $Al_2O_3$  and Sr, (which substitutes for Ca in plagioclase) when of  $SiO_2$  is greater than 54% suggest the onset of plagioclase fractionation.  $K_2O$ ,  $Na_2O$ , Zr, Ba and Rb (which substitutes for K in K-silicates) behave incompatibly for most of the evolution of the Didipio Igneous Complex. The low Pb concentration shows no correlation with increasing silica, however, the Zn contents decrease steadily with increasing  $SiO_2$ , suggesting fractionation of a zinc-bearing mineral, possibly magnetite. The low Ni, Cr and MgO concentrations of the initial diorite melt (Ni < 25ppm; Cr < 50 ppm; MgO < 5%) and the low magnesium-iron ratios ( $100MgO/MgO+Fe_{total} < 38$ ) indicate that the diorites had already undergone extensive fractionation prior to emplacement. Ni and Cr concentrations decrease to sub-detectable levels in later phases of the Didipio Intrusive Complex. The late stage andesite porphyry dykes lie on the Didipio Igneous Complex fractionation trend, suggesting a co-magmatic relationship. The Surong Monzonite phases that have higher  $SiO_2$  contents than the later Tunja Monzonite are considered to represent *in situ* fractionation products within the Surong Monzonite pluton.

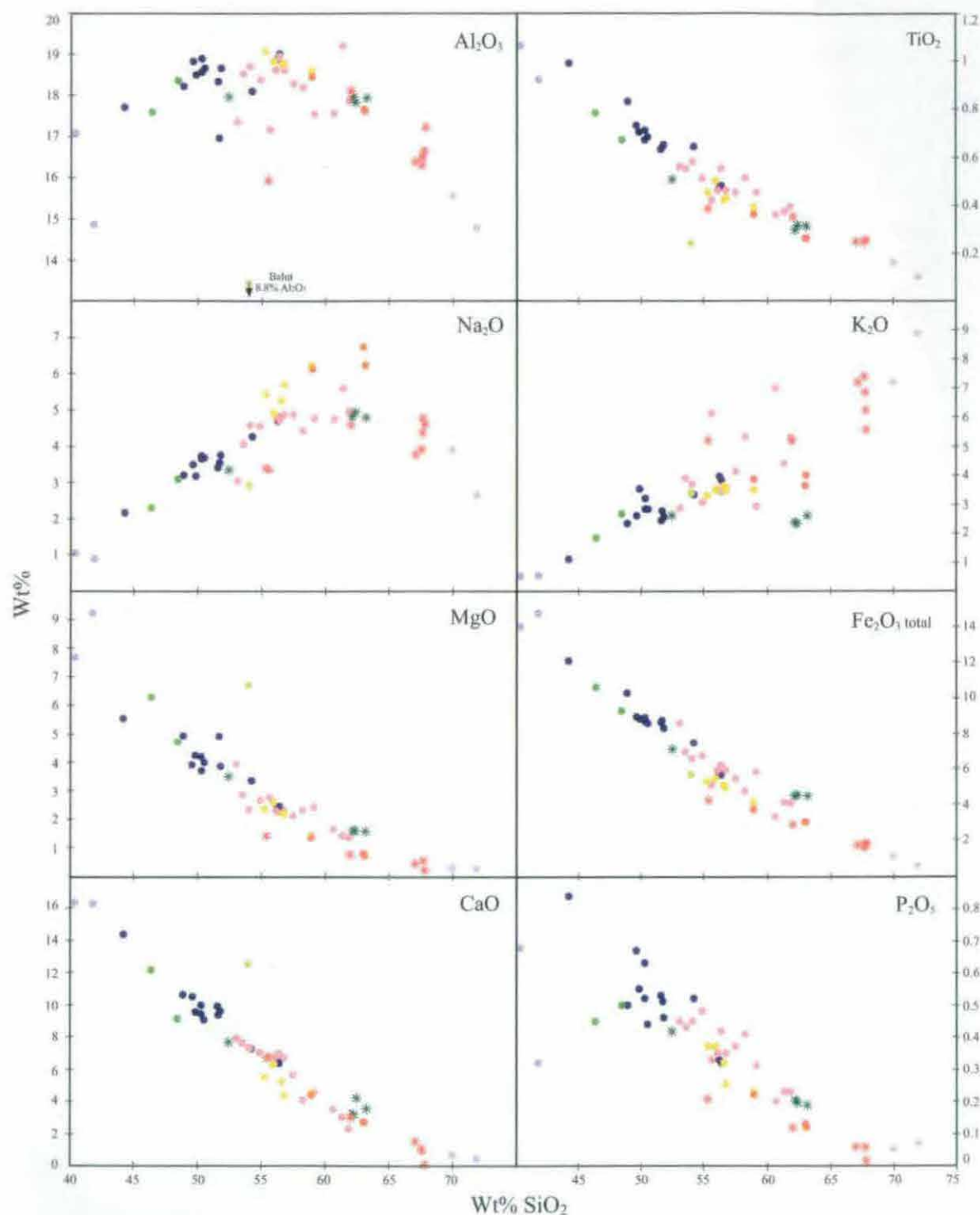


**Figure 5.2:** Major element harker diagram for the igneous phases of the Didipio Igneous Complex and the local volcanic units. Symbols used are the same as those used in Figure 5.1. All analyses were recalculated 100% volatile-free before plotting. When plotted against MgO or other indexes of fractionation, the major and trace element analyses display identical, or more tightly constrained, patterns.

## GEOCHEMISTRY

The Balut Dyke has anomalously high MgO and CaO and low  $Al_2O_3$  concentrations relative to all other igneous phases of the Didipio Igneous Complex (Figure 5.2), reflecting the unusual diopside-phyric nature of the dyke. The concentrations of Na, Mg and Ca in this dyke are similar to the concentrations within the late-stage andesite dykes, and suggests that the Balut Dyke was not derived from the same melt as the earlier Tunja Monzonite or later Quan Porphyry. The composition of the other intrusions of the Dinkidi Stock define two trends: a  $K_2O$  enrichment trend for the Bufu Syenite, and a  $Na_2O$  enrichment trend for the Tunja and Quan Porphyry (Figure 5.2). The potassic nature of the Bufu Syenite reflects its perthite-quartz composition, and is interpreted to be due to it being a late-stage 'exotic' residual melt fraction that followed crystallisation of the Quan Porphyry. Plagioclase fractionation is interpreted to have lead to increase in Na, and decrease in Ca and Sr, in the Tunja Monzonite and Quan Porphyry. The low  $K_2O$  and Rb concentrations of the Quan Porphyry is attributed to the *in situ* fractionation of K into the late-stage, residual Bufu Syenite. The Tunja Monzonite, and to a lesser extent the Quan Porphyry, are anomalously enriched in Ba (Figure 5.3). Electron microprobe analysis (Appendix B) has indicated that Ba is concentrated within the K-feldspar (0.1-0.3%) and biotite (0.2-0.32%) phases within the Tunja Monzonite. Mineral grains within earlier clinopyroxene-monzonites contain similar concentrations of Ba, with the exception of biotite, which is relatively depleted in Ba (0.08-0.15%). The elevated concentration of Ba in the Tunja Monzonite is interpreted to reflect the higher modal abundances of Ba-enriched biotite within this intrusion, relative to the earlier clinopyroxene monzonites and later syenites.

The andesites and trachyandesites of the Mamparang Formation share similar 'co-genetic' trends with the Didipio Igneous Complex on the variation diagrams (Figures 5.2 & 5.3), with the exception that the three most siliceous trachyandesites are considerably less potassic than the Didipio Igneous Complex or the overlying trachytes. The extremely low Ni and Cr contents and low magnesium-iron ratios of the Mamparang Formation andesites (Ni 4 ppm & Cr 6 ppm) and the Upper Mamparang Formation trachytes (1 ppm Ni & 2 ppm Cu) indicate that they were both sourced from melts that have undergone extensive fractionation. The trachytes of the Upper Mamparang Formation display similar elevated  $K_2O$  and low  $Na_2O$  concentrations as the Bufu Syenite, suggesting an origin from a similar highly evolved potassic melt.

### ***Tectonic Discrimination Diagrams***

The Didipio Intrusive Complex occupies an ambiguous tectonic setting, being apparently related to rifting but set in an oceanic island arc setting. The complex was emplaced after the cessation of westward-directed subduction along the East Luzon Trench (Figure 2.1).

Because alkaline magmas from different tectonic settings have distinct compositional characteristics, discrimination diagrams may be used to clarify the tectonic association of the



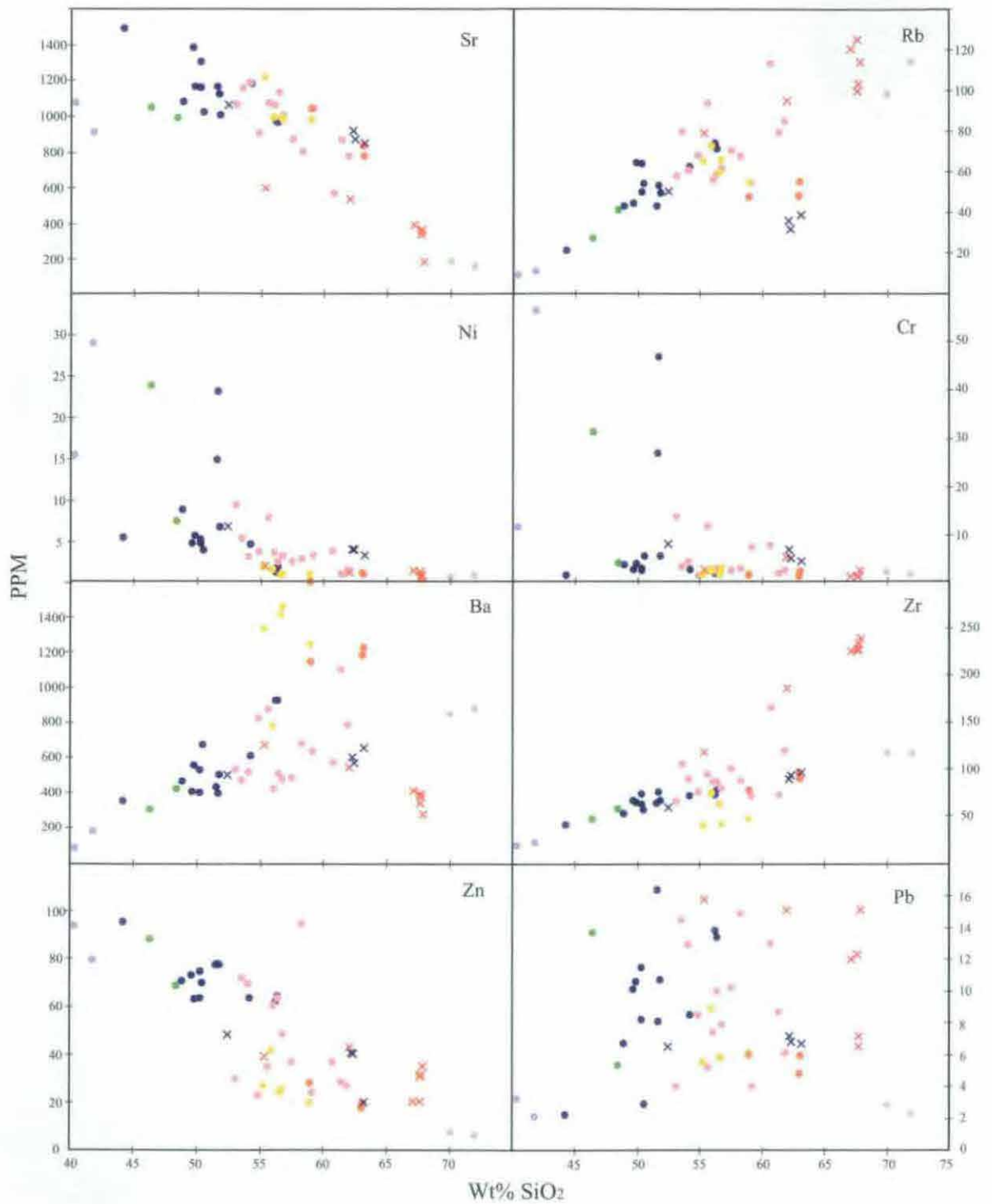


**Figure 5.3:** Trace element harker diagram for the igneous phases of the Didipio Igneous Complex and the local volcanic units. Symbols used are the same as those used in Figure 5.1.

Didipio magmas (Figure 5.4 & 5.5). Very few tectonic discrimination diagrams are available for alkaline or potassic rocks. The large number of discrimination diagrams developed for primary basaltic melts, and several developed for granitic rocks, are considered unsuitable for discriminating the tectonic setting of evolved alkaline intrusives. Muller *et al.* (1992) and Muller & Groves (2000) proposed a series of discrimination diagrams for potassic igneous rocks (Figure 5.4), based on melts from within-plate settings having higher  $\text{TiO}_2$  and Zr relative to  $\text{Al}_2\text{O}_3$  and initial oceanic arc melts having lower P, La and greater Ti concentrations than late oceanic arc units. The intrusions from the alkaline Didipio Igneous Complex and potassic Cordon Syenite Complex belong to the late oceanic arc series of this classification scheme (Figure 5.4). The intrusives of the Palali Batholith are enriched in Zr and plot within the continental arc or post-collisional series of the scheme. Pearce *et al.* (1984) proposed a discrimination diagram developed for granitic rocks, based on the high Rb concentration of syn-collisional and within-plate granitoids and the low HFSE (Y+Nb) concentrations of volcanic arc granitoids (Figure 5.5). The intrusives of the Didipio Igneous Complex, Cordon Syenite Complex and Palali Batholith plot in the 'volcanic arc' field of this scheme.

### Multi-element variation diagrams

Twenty-nine samples of the Didipio Igneous Complex and surrounding volcanics have been plotted on a MORB-normalised multi-element variation diagram ('spidergram'; Figure 5.6) using the normalisation values of Pearce (1983). The elements are plotted in order of decreasing compatibility with an aqueous fluid, with the most immobile elements (typically HFSE elements, including REE) plotted on the right side of the diagram, and mobile elements (generally LILE) plotted on the left. When normalised to MORB values, this diagram provides insights into the degree of enrichment of a subduction-zone magma compared to a source region, a source that was probably as depleted as a MORB, and that may have been metasomatically enriched by LILE-bearing aqueous fluids.

MORB-normalised spidergrams, such as Figure 5.6, were developed for primitive basaltic melts that have undergone little fractionation. Despite the highly fractionated alkaline Didipio Igneous Complex spanning a wide range of  $\text{SiO}_2$  values, spidergrams for the Didipio Igneous Complex, and other regional complexes, display well-defined patterns that allow insight into the magma sources and the relationships between intrusive complexes. Although the spidergram pattern for the most and least fractionated intrusives of the Didipio Igneous Complex (Figure 5.6) share a similar, well-constrained pattern (with the exception of Cr and Ni contents), fractionation is still expected to have contributed to the LILE enrichment for the alkaline intrusives and volcanic units.

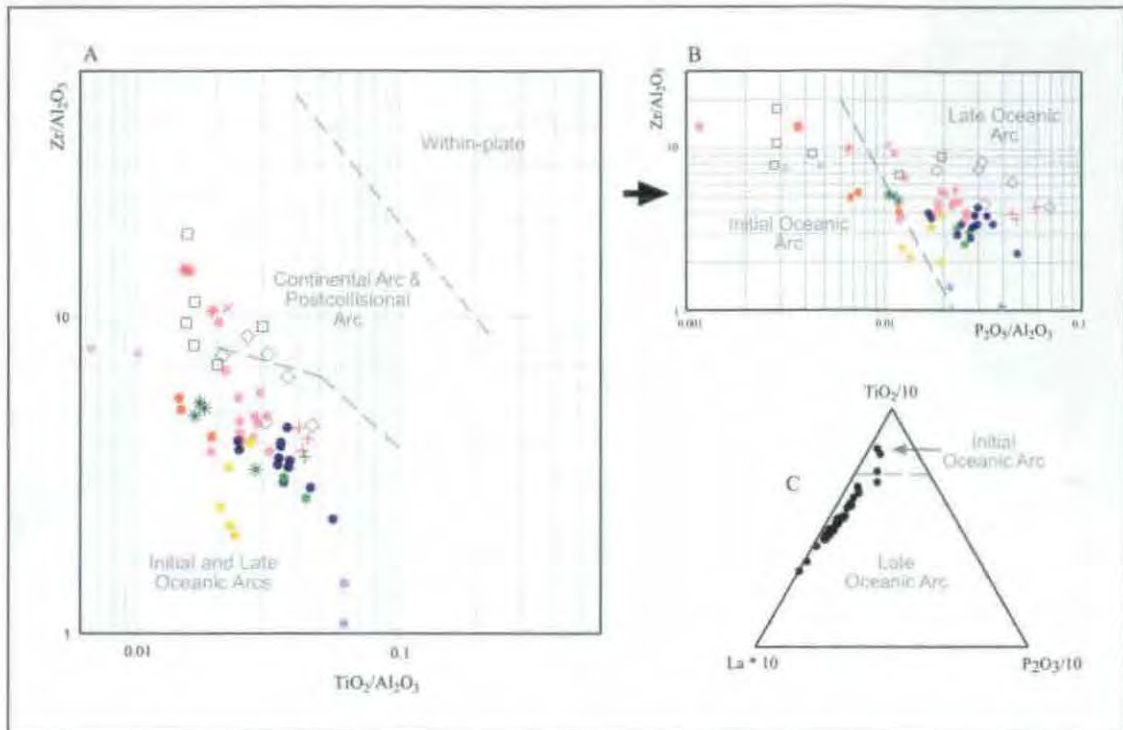


**Figure 5.4:** Discrimination diagrams derived for potassic rocks by Muller (2000). Figure A discriminates between within plate, continental arc and island arc potassic rocks. Figures B and C discriminate between initial oceanic arc and late oceanic arc. Symbols the same as in Figure 5.1. Individual symbols not available for the triangular plot.

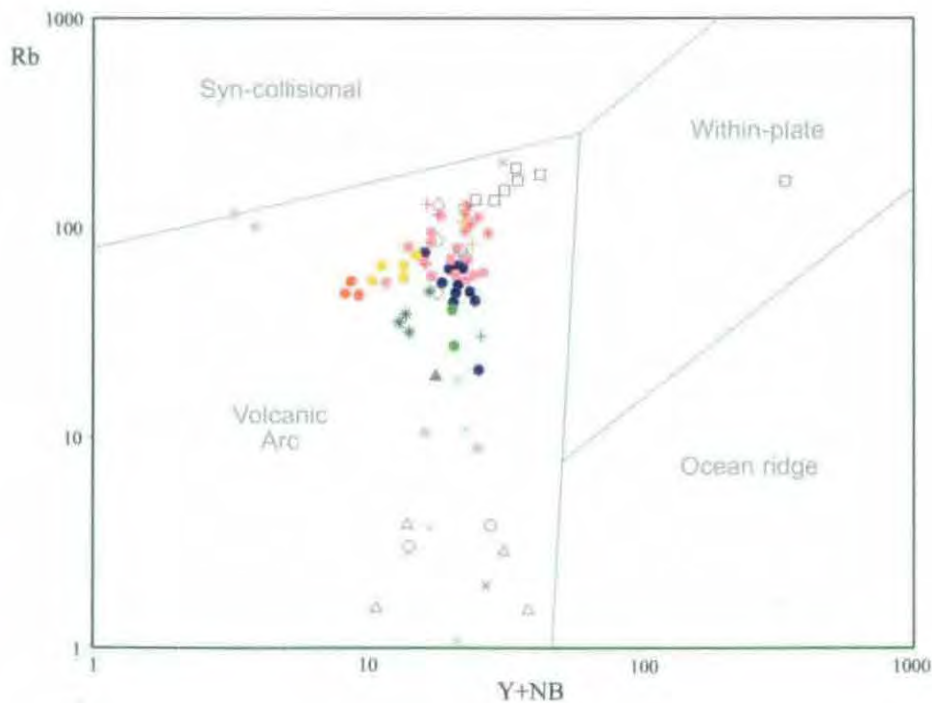


**Figure 5.5:** Discrimination diagram of Pierce (1984), derived for granitic rocks. Symbols the same as Figure 5.1. Tectonic discrimination is based on the high Rb for syn-collisional and within-plate granitoids and low HFSE for volcanic arc granitoids.

## GEOCHEMISTRY

Relative to MORB values, the units of the Didipio Intrusive Complex are strongly enriched in incompatible elements (the LILE Ba, Sr, Rb, K; the LREE La, Ce and in P), consistent with their alkaline nature. The intrusive rocks also display strong depletion in Cr and Ni, probably due to prior fractionation of olivine, clinopyroxene and/or magnetite. All units of the Didipio Igneous Complex are distinctly depleted in HFSE (eg: Th, Nb and Ti) relative to both the REE and the LILE. Depletion in HFSE is a typical feature of most oceanic arc rocks. The gabbros of the Didipio Igneous Complex are anomalously low in LILE, LREE and Zr, probably caused by their cumulate nature, with these elements partitioned into the remaining melt. Samples DD1, MD2, AP1, AP3 and M10 display anomalously low concentrations of Th (subdetectable <0.1 ppm) relative to other phases of the Didipio Igneous Complex.

The andesites of the Mamparang Formations display a similar LILE enrichment pattern to the Didipio Igneous Complex (Figure 5.6), but with depletion in K and Rb. The trachytes of the Upper Mamparang Formation are more strongly enriched in LILE and Zr and depleted in Ni relative to the Didipio Igneous Complex, and lack a negative Th and Nb anomaly, possibly reflecting a more enriched melt source (caused by a smaller degree of partial melting?) or a greater degree of fractionation. The andesites of the Eocene Caraballo Formation display a flat MORB-like pattern, indicating a depleted source. The basalts of the Oligocene Dibuluan River Formation range from unenriched to moderately LILE enriched, spanning the compositional gap between the underlying Caraballo Formation and the more enriched Mamparang Formation. This range of values suggests a progressive enrichment in the source region for the Dibuluan River Formation, and that the Dibuluan River Formation may be a precursor to the Mamparang Formation.

The Palali Batholith and the Cordon Igneous Complex have LILE-enriched spidergram patterns similar to the Didipio Igneous Complex (Figure 5.6). Higher Cr and Ni contents of the Cordon Syenite Complex indicates comparatively less fractionation. The Palali Batholith is more enriched in LILE and Zr and lacks a Nb-Th anomaly relative to the Didipio Igneous Complex. This is possibly due to stronger fractionation within the Palali Batholith (Albrecht & Knittel, 1990), crustal contamination, or a more enriched source, even though the two have similar low MgO, Cr and Ni contents. The Dupax and Coastal Batholiths define typical arc-tholeiitic trends on Figure 5.6, with no LILE enrichment and moderate Nb depletion, indicating a primitive source.

## REE Patterns

The REE patterns of both the Didipio units and regional formations are displayed in Figure 5.7. The REE values have been normalised to the MORB values of Pearce (1983). Despite the



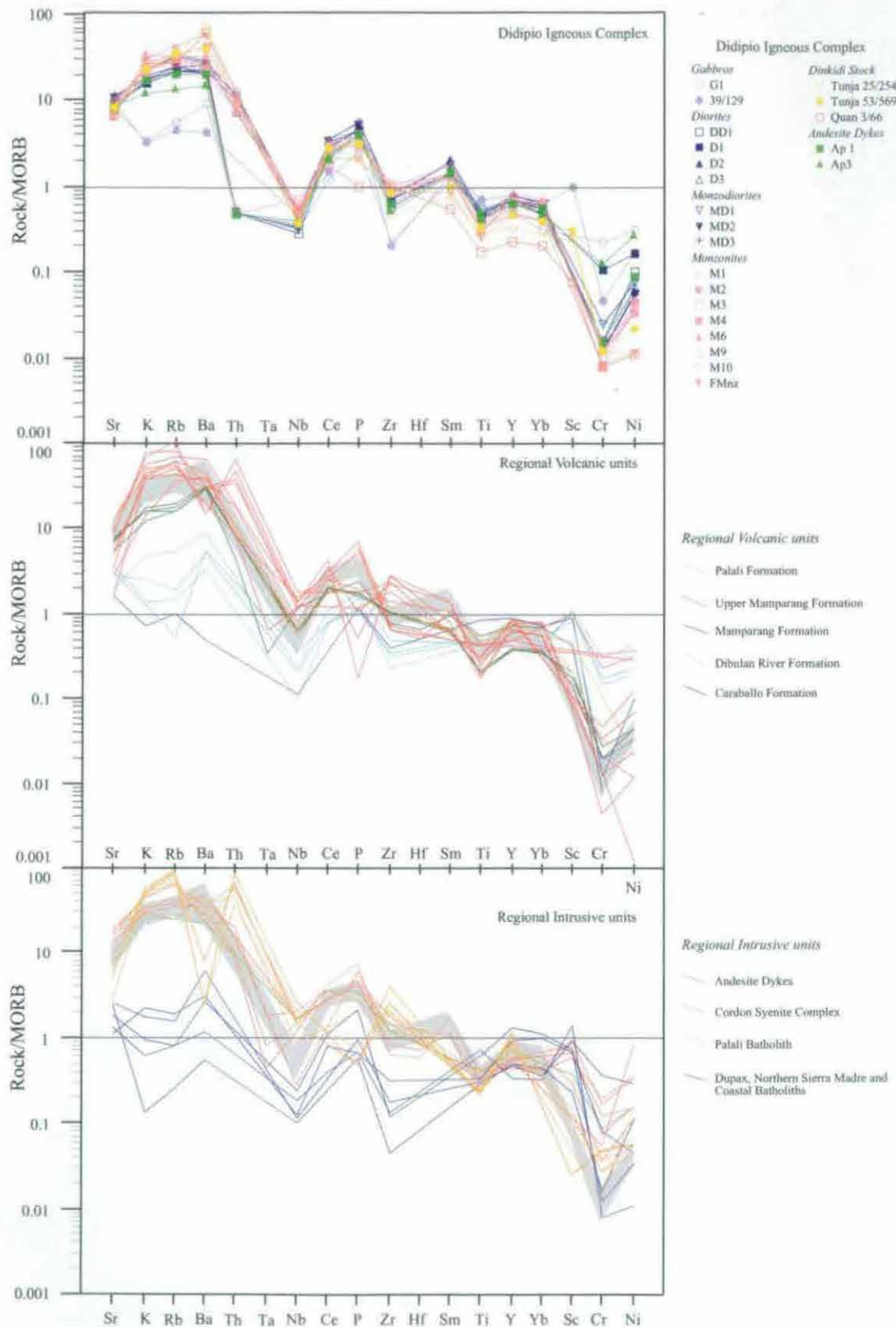
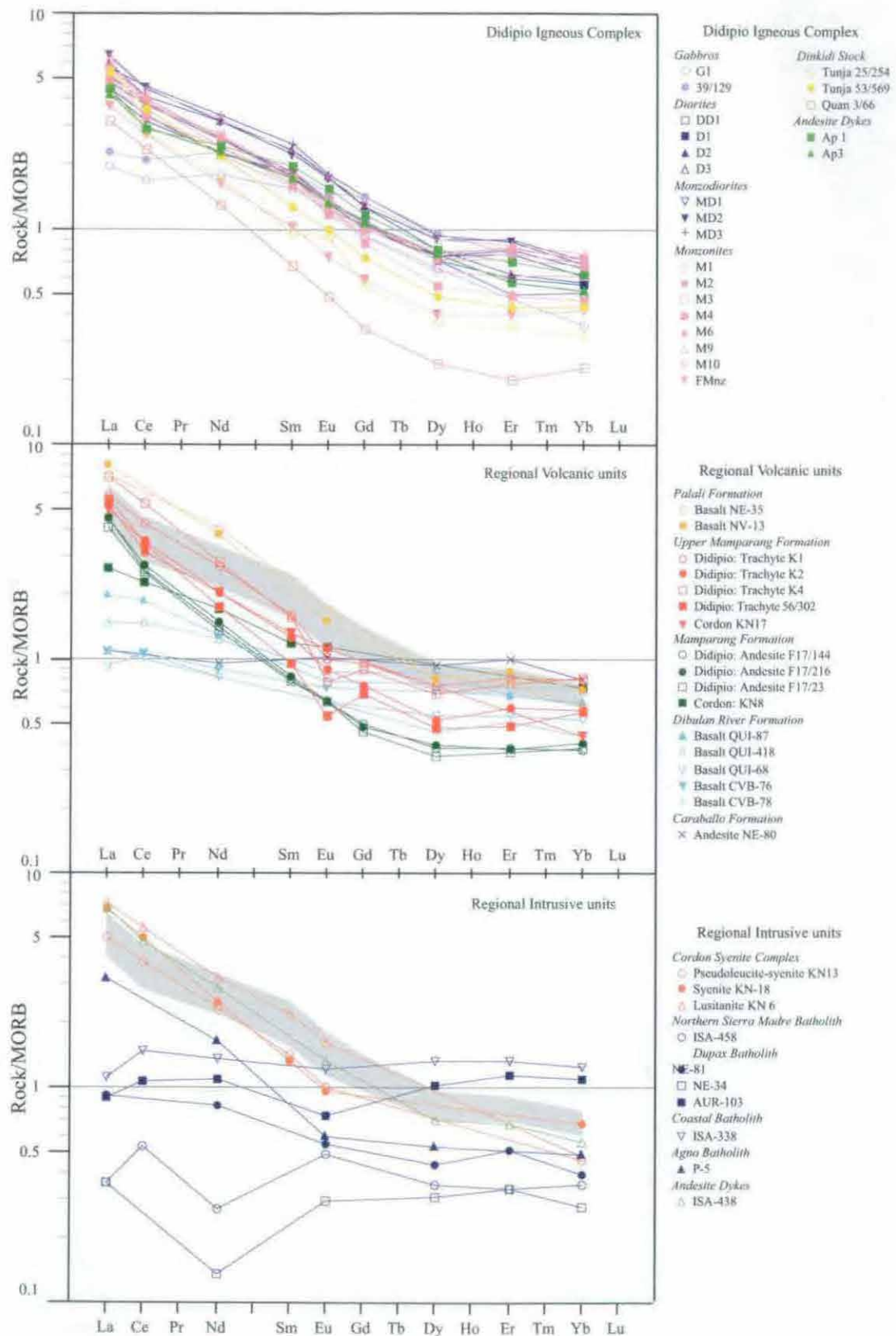


Figure 5.6: MORB-normalised spidergram, based on Pearce (1983). Grey field is the compositional range for intrusions from the Didipio Igneous Complex.

fractionated nature of the Didipio Igneous Complex, all the main diorite, monzodiorite and monzonite phases show a tightly constrained REE pattern, suggesting a common magmatic source. The intrusions of the Didipio Igneous Complex are strongly enriched in LREE (La, Ce, Pr, Nd) and moderately depleted in HREE (Yb, Tm, Lu, Er) relative to MORB values, with La/Yb ratios ranging from 6 to 8. Younger intrusions in the Didipio Igneous Complex typically have slightly lower concentrations of REE than earlier units, probably due to the partitioning of REE into crystallising apatite. The lack of an Eu anomaly in the REE pattern of the Didipio Igneous Complex phases indicates that either plagioclase was not an important fractionation phase or that Eu was present as  $\text{Eu}^{+3}$  rather than  $\text{Eu}^{+2}$ , due to oxidising conditions. This later conclusion is supported by both modal (anorthosite in cumulate gabbros) and compositional (Ca, Al & Sr depletion with increasing fractionation) evidence for plagioclase fractionation in the Didipio Igneous Complex.

Both the cumulate gabbros and late-stage intrusives of the Dinkidi Stock display atypical REE patterns when compared to the rest of the Didipio Igneous Complex (Figure 5.7). The gabbros have similar MREE and HREE abundances to the diorites and monzonites, but are strongly LREE (La, Ce & Nd) depleted relative to the other intrusions. As clinopyroxene has lower partition coefficients for LREE relative to MREE and HREE (Fujimaki *et al.*, 1984) this depletion may reflect the partitioning of LREE preferentially into the remaining melt rather than being incorporated into the cumulate gabbros. The intrusions of the Dinkidi Stock are depleted in all REE relative to the remainder of the Didipio Igneous Complex, but especially in the MREE and HREE. The overall depletion in REE may reflect the fractionation of REE-bearing phases, especially apatite and possibly sphene, both of which scavenge MREE preferentially (Fujimaki, 1986; Green & Pearson, 1986). The bowed, extremely-depleted middle HREE pattern of the Quan Porphyry is unlikely to have been caused by prior sphene fractionation in this sphene-bearing phase. The pattern is identical to that reported for strongly silicified rhyolites that have been altered by acidic fluids (Hoft, 1993), suggesting that the Quan Porphyry REE anomaly has been caused by leaching during alteration or, as the samples are not strongly altered, by volatiles present during crystallisation.

The trachytes and andesites of the Mamparang and Upper Mamparang Formations have a similar LREE-enriched and HREE-depleted pattern as the Didipio Intrusive Complex (Figure 5.7). The trachytes of the Upper Mamparang Formation have similar concentrations of REE as the Didipio Igneous Complex, consistent with a similar melt source. The trachytes also display a strong negative Eu anomaly, indicating the uptake of  $\text{Eu}^{+2}$  by fractionating plagioclase. The andesites of the underlying Mamparang Formation are more depleted in all REE relative to the Didipio Igneous Complex, especially in the MREE and HREE, suggesting a less enriched melt



**Figure 5.7:** MORB-normalised REE plots for the Didipio Igneous Complex and surrounding units. Grey field represents range of values for the diorite and monzonite plutons of the Didipio Igneous Complex. Normalisation values from Sun & McDonough (1989).

source. The andesites display no Eu anomaly, consistent with no plagioclase fractionation. The elevated LREE of the Mamparang Formation and the Upper Mamparang Formation contrasts with the primitive MORB-like values of the Caraballo Formation andesites (Figure 5.7) and the weak REE enrichment of the Dibuluan River Formation, which is intermediate between the Didipio Igneous Complex and the Caraballo Formation. The REE pattern of the Dibuluan River Formation is intermediate between the pattern for the Mamparang Formation and MORB values, with weak enrichment in LREE. This suggests that the Dibuluan Formation is not a distal correlate of the Mamparang Formation, as suggested by Billedo (1994).

The Cordon Syenite Complex has a similar LREE enriched pattern (La/Yb ratios of 8 to 12) as the Didipio Igneous Complex (Figure 5.7), highlighting the similarities in the melt source for the two intrusive centres. This contrasts with the flat (La/Yb=0.67-1.92) MORB-like pattern of the Dupax, Coastal and Northern Sierra Madre Batholiths, reflecting their tholeiitic to calc-alkaline nature (La/Yb = 0.67 to 1.92). The Cordon and Didipio REE patterns are also identical to the LREE-enriched patterns for middle Early Miocene shoshonitic andesite dykes (Billedo, 1994) that cross-cut the Isabella Ophiolite, on the eastern coastline of Luzon. This suggests that mantle enrichment in LREE spread trenchward throughout the Caraballo and Northern Sierra Madre Mountains (eg Ringenbach, 1992; Billedo, 1994), following the initial alkaline intrusive activity that was constrained to the margins of the Cagayan Valley Basin.

## Mineral Chemistry

Mineral phases for all units that crop out in the Didipio region were analysed using the Cameca electron microprobe at the University of Tasmania. These analyses were undertaken to confirm mineral identifications and to test possible genetic links between units exposed in the Didipio region, by characterising similarities in mineral chemistry.

### *Clinopyroxene*

There are two populations of clinopyroxene within the rock units of the Didipio region. Type 1 clinopyroxene phenocrysts occur in the dioritic to monzonitic phases of the Didipio Igneous Complex and in the andesites of the surrounding Mamparang Formation lavas. Type 1 clinopyroxenes are pale- to mid-green, weakly pleochroic and optically homogenous (eg Plate 3.5 C & D). Type 2 clinopyroxene phenocrysts are found in the Balut Dyke and the late-stage andesite dykes of the Didipio Igneous Complex and in the trachyandesites of the Upper Mamparang Formation. Type 2 clinopyroxenes are pale green, weakly pleochroic, and have weak to strong oscillatory zoning (eg Plate 3.3 E & F; Plate 3.8C).

The type 1 clinopyroxenes of the Didipio Igneous Complex plot as salites (Figure 5.8) and have magnesium-iron ratios of 60 to 70. The phases of the Didipio Igneous Complex share similar



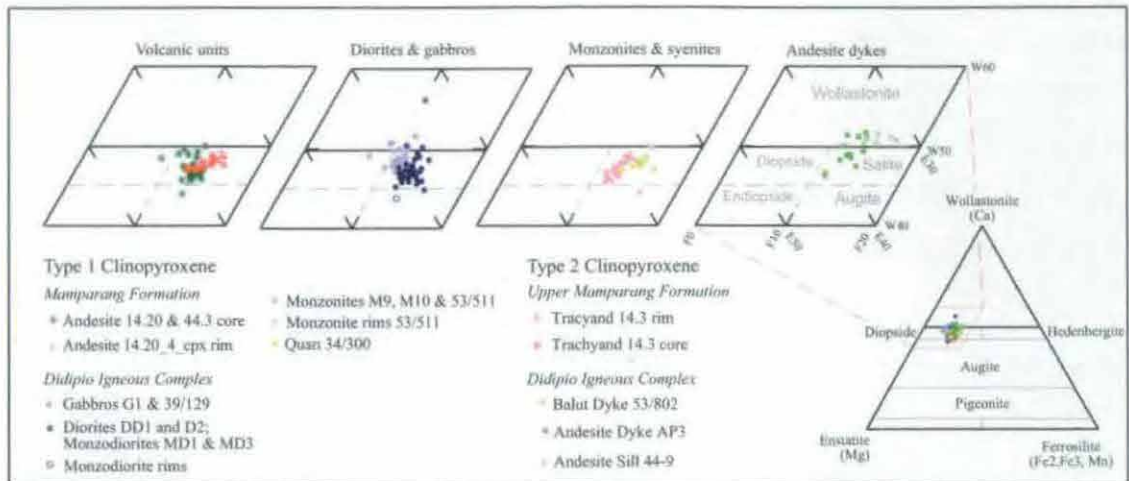


Figure 5.8: Composition of clinopyroxenes from the Didipio Igneous Complex and surrounding volcanic units.

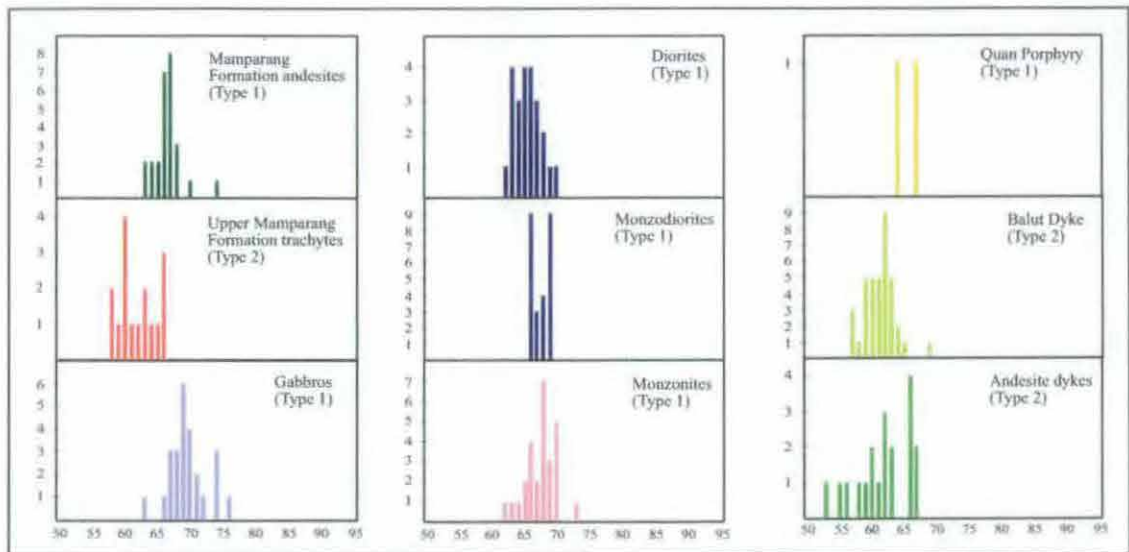


Figure 5.9: Histograms showing the range in the magnesium-iron ratio for clinopyroxenes from the Didipio Igneous Complex and the surrounding volcanic units.

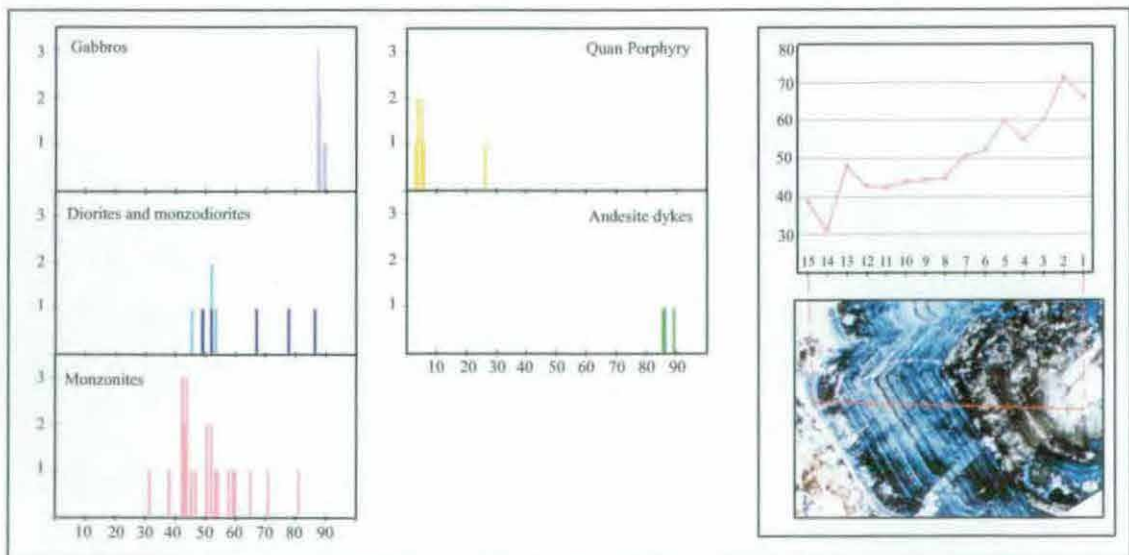


Figure 5.10: Left: Histograms showing the range in the anorthite content for units of the Didipio Igneous Complex; Right: range in anorthite content for an oscillatory zoned plagioclase phenocryst from monzonite 53/511.

magnesium-iron ratio for type 1 clinopyroxenes (Figure 5.9) from the slightly higher values of the early gabbros (76-63) to the diorites (70-62) and monzonites (70-62), suggesting a shared melt source that had not become strongly depleted in Mg or Fe by fractionation. The andesites of the Mamparang Formation have a similar clinopyroxene chemistry to the dioritic units of the Didipio Igneous Complex.

The type 2 clinopyroxenes also plot as salites (Figure 5.8), but are more calcic, and less Mg rich, than the type 1 clinopyroxene. The type 2 clinopyroxenes have lower Mg numbers (Balut Dyke 69-57; andesite Dykes 53-67; Upper Mamparang Formation, 66-58; Figure 5.9) than the Type 1 clinopyroxene. The Mg depletion in type two inclusions may reflect scavenging of Mg by early crystallizing intrusions. The low Mg of the andesite dykes suggests that the dykes were not sourced from a 'fresh' mafic melt source, but were rather sourced from residual melt from within the Didipio Igneous Complex, with the melt losing Mg by prior crystallisation of clinopyroxene in the dioritic phases. Both types of clinopyroxene have sufficient Si and Al to fill the tetrahedral sites to the stoichiometric value of  $T=2$ , unlike clinopyroxenes from the metaluminous Cordon Igneous Complex (Knittel & Cundari, 1990).

## Feldspars

Plagioclase in the early dioritic phases of the Didipio Igneous Complex and in the andesite dykes occur as a framework of euhedral normal-, to rarely oscillatory-zoned phenocrysts (eg Plate 3.5E). Oscillatory zoning in plagioclase becomes increasingly complex with continued fractionation during the evolution of the Didipio Igneous Complex (eg Plate 3.7E). Plagioclase within the evolved phases of the Dinkidi Stock are typically set in a broad mosaic of perthite, contain orthoclase laminae and are partially to completely albitised. In all of the volcanic units, plagioclase occurs as normally-twinned euhedral phenocrysts.

Plagioclase crystals within the Didipio Igneous Complex evolved to progressively more sodic compositions with continued fractionation. Plagioclase compositions within the early gabbros range from An 87-89, compared with An 86-54 in the diorites (with rims as low as An 48), and An 52-45 in the monzodiorites (Figure 5.10). The composition of plagioclases within the monzonites span a wide range (81-32) with individual crystals ranging from An 71 cores to An 38 rims (Figure 5.10). Plagioclase in the late stage intrusives of the Dinkidi stock are now predominantly albite (An 0-7) with rare relic phenocrysts reaching An 28 compositions. The shared An-depletion trend from the diorites to the late-stage monzonites is interpreted to relate to all phases of the Didipio Igneous Complex being sourced from the same melt, which underwent plagioclase fractionation.

Parent	Diorite (DD1)	Monzodiorite (MD1)	Monzonite (M9)	Tunja Monz. (25/254)	Quan Porph. (22/210)
Daughter	Monzodiorite (MD1)	Monzonite (M9)	Tunja Monz. (25/254)	Quan Porph. (22/210)	Bufu Felsite (54/565)
% of crystals removed	26.36%	51.77%	52.07%	39.69%	80.07%
% diorite melt crystallised	26.36%	64.48%	82.97%	89.73%	97.95%
<i>% of minerals removed:</i>					
Clinopyroxene	8.01%	13.86%	8.92%	0.90%	4.90%
Biotite	4.66%	3.45%	1.11%	10.29%	2.34%
Plagioclase	10.25% (An 78)	26.60% (An 52)	20.66% (An 52)	24.42% (An 52)	-
Orthoclase	-	4.23% (Or 61)	16.67% (Or 61)	1.28% (Or 87)	10.15% (Or 87)
Albite	-	-	-	-	59.25% (An 12)
Magnetite	3.29%	3.80%	3.49%	1.89%	2.37%
Apatite	0.13%	-0.19%	1.20%	0.90%	1.06%
Sum of least squares	0.08	0.22	0.16	0.23	0.51
Distance apart	0.29	0.47	0.4	0.48	0.71

**Table 5.2:** Major element modeling of fractionation using the least-squares model of Le Maitre (1981). Whole rock analyses and full calculations are provided in Appendix B.

## PETROGENETIC MODELLING

The petrographic characteristics of the Didipio Igneous Complex, trends in the variation diagrams (Figures 5.3 & 5.4), shared REE and spidergram patterns (Figure 5.5 & 5.7) and similar mineral compositions (Figures 5.9 and 5.10) are interpreted to indicate that all intrusive phases that crop out in the Didipio region are sourced from the same melt that has undergone crystal fractionation. To test this hypothesis, mass-balance calculations using the least-squares model of Le Maitre (1981) were applied to each phase of the Didipio Igneous Complex. Mass balance modelling of fractionation can be used to test hypothesised fractionation assemblages, and can calculate the 'best fit' fractionation assemblage for given whole rock and mineral compositions (Table 5.2). The degree of fractional crystallisation calculated by this method should only be used as an approximate estimate.

Representative mineral analyses for each whole-rock sample were acquired to allow calculation. The composition of plagioclase, which varies with fractionation, was estimated by testing the range of compositions in the parent melt, and the composition with the best fit used.

The modelling indicates that the monzodiorites could be produced from a clinopyroxene-diorite precursor by approximately 26% fractional crystallisation of plagioclase and clinopyroxene (Table 5.2). The Surong Monzonite could be produced from a clinopyroxene diorite precursor with approximately 64% fractional crystallisation, by removal of clinopyroxene and plagioclase phases (Table 5.2).

Calculations for the fractionation required to produce the intrusions of the Dinkidi Stock suggest that ~80% fractional crystallisation of the initial dioritic melt was required to produce the Tunja Monzonite, and at least 90% fractionation of a clinopyroxene-diorite was required to produce the highly mineralised Quan Porphyry (Table 5.2). Despite a close fit (0.16-0.23 sum of least squares), this modelling requires fractionation of plagioclase, orthoclase and minor clinopyroxene to produce the Tunja Monzonite, and fractionation of plagioclase, biotite and minor clinopyroxene for the production of the Quan Porphyry melt. Orthoclase and biotite

## GEOCHEMISTRY

within the Didipio Igneous Complex are not present as phenocryst phases, and are considered unlikely to have been easily fractionated. The requirement to fractionate orthoclase or biotite, and the large degree of fractionation involved, suggest that a process other than simple fractional crystallisation of observed mineral phases was required to produce the late stage intrusions of the Dinkidi Stock. This may suggest that the Dinkidi Stock intrusions were sourced from differentiates within a larger fractionating magma body. In such a case the degrees of fractionation that have been calculated can only be considered as a measurement of the enrichment of the late stage melt ('equivalent fractionation'). The high degree of fractionation required to produce the Bufu Syenite (over 97% of a diorite melt), and the need for albite removal, reflects the quartz-perthite composition of the Bufu Syenite and suggests that the Bufu Syenite formed from a late-stage quartz-K-feldspar differentiate, probably as a residual melt after crystallisation of the Quan Porphyry.

These mass balance calculations indicate that fractionation of plagioclase and clinopyroxene can produce the observed igneous compositions within the Didipio Igneous Complex, up to the composition of the Surong Monzonite. The production of the late stage melts of the Dinkidi Stock appears to require a process other than, or in conjunction with, crystal fractionation.

## CONCLUSIONS

Because of the alkaline nature of the Didipio Igneous Complex, the Dinkidi porphyry Cu-Au deposit classified as alkaline porphyry system, similar to the Marian alkaline Cu-Au porphyry deposit located in Cordon (Baquiran, 1975; Alapan, 1981; Knittel, 1982).

Coherent trends in whole rock major, trace and REE element chemistry and similarities in mineral chemistry are interpreted to indicate that the Didipio Igneous Complex intrusions were sourced from a single melt that underwent fractional crystallisation. The initial dioritic melt was already depleted in Mg, Cr, and Ni, indicating that substantial fractionation had already occurred prior to the emplacement of the diorite body in the shallow sub-volcanic environment. *In situ* clinopyroxene-plagioclase±biotite-magnetite fractionation of the emplaced dioritic melt is interpreted to have formed the monzodiorite phases (as a residual 73% fraction of the diorite melt), with the gabbros considered to be clinopyroxene- and plagioclase-cumulates formed from the fractionated phases. Further fractionation of clinopyroxene and plagioclase within the magma chamber formed a residual monzonite melt, which is equivalent to a 35% fraction of the original diorite melt, and which was emplaced into the diorites, forming the Surong Monzonite pluton. Continued fractional crystallisation within the magma chamber may have produced the late stage Quan Porphyry, which represents a residual 10% of the initial diorite melt or a 28% fraction of the Surong Monzonite, following clinopyroxene-plagioclase-biotite fractionation.



Alternatively, the Quan Porphyry may represent a late-stage differentiate within a larger magma body. The extreme  $\text{SiO}_2$  and  $\text{K}_2\text{O}$  enrichment of the Bufu Syenite suggests that it is an 'exotic' residual late-stage melt, which, as the strong REE depletion suggests, has been metasomatised by late stage magmatic-hydrothermal fluids. In total, modelling suggests that the equivalent to 89% fractional crystallisation would have to be required to produce the highly mineralised Quan melt from the unmineralised diorites. Fractional crystallisation is considered to have been the main process in volatile build up (2<sup>nd</sup> boiling), as indicated by the development of stronger alteration halos with successive intrusions (Chapter 6).

The calcic Balut Dyke does not fit on the whole-rock or mineral chemistry fractionation trends for the other intrusives of the Dinkidi Stock. This suggests the dyke was sourced from a different but genetically related melt. The late stage andesite dykes show similar whole rock trends to the Didipio Igneous Complex, indicating a co-genetic origin. The emplacement of small quantities of mafic melt following this felsic magmatism, may represent the escape of residual mafic magma from the base of a stratified magma reservoir (eg the underplating model of Whitney *et al.*, 1988, Whitney, 1989). Clinopyroxene phenocrysts in the andesite dykes are depleted in Mg, suggesting that this magma reservoir had already been depleted in Mg, possibly by prior emplacement of the Didipio Igneous Complex intrusions. The origin of the Balut Dyke and andesite dykes is discussed in Chapter 8.

The Mamparang Formation andesites in the Didipio region have a similar LILE and LREE enriched composition to the Didipio Igneous Complex, but are less enriched overall in REE and are significantly less potassic. In contrast, the Mamparang Formation is significantly more LREE enriched than the neighbouring Dupax Batholith or Dibuluan River Formation (Figure 5.7). Consequently, the Mamparang Formation is concluded to be a subalkaline precursor to the alkaline intrusive centres and the Upper Mamparang Formation. Late Oligocene regional units become gradually LREE- and LILE-enriched over time, from the flat MORB-like values of the Dupax Batholith, through the weak LREE & LILE enriched values of the Dibuluan River Formation to the strong LREE & LILE enrichment of the Mamparang Formation (Figures 5.6 & 5.7). This indicates a source region that became progressively more LILE & LREE enriched over time.

The trachytes of the Upper Mamparang Formation have similar LILE and LREE enrichment trends to the Didipio Igneous Complex, and are significantly more REE- and LILE-enriched than the Mamparang Formation. This suggests that the Upper Mamparang Formation trachytes shared the same HFSE-depleted and LILE-enriched source as the Didipio Igneous Complex, and are not related to the Mamparang Formation by fractionation. The trachytes that crop out in the Didipio region are best correlated with the feldspathoid-bearing trachytes that host, and are co-

genetic with, the Cordon and Palali intrusive centres.

Similarities in major, trace and REE element abundances (Figures 5.1, 5.6 & 5.7) indicate that the Didipio Igneous Complex was sourced from a similar LILE enriched source to the potassic Palali Batholith and Cordon Syenite Complex, rather than being a more evolved member of the nearby calc-alkaline Dupax Batholith. The close spatial and temporal association with rifting for these intrusive centres suggests that some of the processes that form potassic melts in continental rift settings (eg Bailey, 1974; Lloyd & Bailey 1975; the Group II potassic rocks of Foley *et al.*, 1987; the African Rift province of Barton, 1979) may have been active in northern Luzon (Knittel, 1983). However, the alkaline intrusive centres have island arc geochemical characteristics (low  $\text{TiO}_2$  (<1%), high  $\text{Al}_2\text{O}_3$  (17-18%) and very low HFSE) and Sr/Nd isotope values (Knittel & Defant, 1988) indicate that the Cordon Syenite Complex shared the same mantle source to that for the Oligocene calc-alkaline batholiths, such as the Dupax and Northern Sierra Madre Batholiths (Knittel & Defant, 1988). Rift-related melts from continental settings, or those with a crustal component would be expected to have higher  $\text{TiO}_2$ , Zr, Nb, and Ta, and lower  $\text{Al}_2\text{O}_3$  (Foley *et al.*, 1987; Muller & Groves, 2000).

The North Luzon alkaline-potassic suite is considered here to represent the potassic end members of island arc magmatism. They have geological and geochemical similarities with the Roman Province Melts of Barton (1979) and the Group III island arc potassic rocks of Foley *et al.* (1987; Knittel & Cundari, 1990), although the sodic Didipio Igneous Complex, and to a much smaller extent the potassic Palali and Cordon suites, have a lower K/Na ratio than Group III ultrapotassic rocks (Albrecht & Knittel, 1990). Small volumes of these island arc potassic rocks are emplaced late in arc formation, commonly during the mature back-arc formation stage (Foley *et al.*, 1987). Similar potassic magmatism, associated with the initial stages of back arc basin formation, have been documented in the Izu-Bonin-Mariana arc (Stern *et al.*, 1984, 1993; Bloomer *et al.*, 1989), New Hebrides arc (Monjaret *et al.*, 1991) and Fiji island group (Gill & Whelan, 1989). Rather than causing decompression and melting, the rifting that formed the Cagayan Valley Basin appears to have tapped arc-related LILE-enriched mantle, with extension ceasing before maturation of the Cagayan Valley into a back arc basin.

Several models exist to explain the LILE-enrichment and HFSE-depletion of island arc potassic melts. The shared melt source for the Oligocene calc-alkaline and potassic intrusives (Knittel & Defant, 1988) indicates that models for potassic magmatism that rely on an exotic component for the LILE-enrichment, such as subducted marine sediment (Rogers *et al.*, 1985), crustal melting or old enriched mantle (Varne, 1985) are not applicable to Northern Luzon. The melt source, which becomes progressively more LILE and LREE enriched during the Late Oligocene, is likely to have been related to the westward-directed subduction along the

Philippine Sea Plate, the only subduction zone considered to have been active in Northern Luzon at this time (Karig, 1983). This subduction is considered to have stalled in the late Oligocene (Lewis & Hayes, 1983; Wolfe, 1988; Florendo 1994). The enrichment in LILE and LREE in island arc potassic melts is generally attributed to low degrees of partial melting in areas of the mantle wedge that have been previously enriched in LILE by slab-derived fluids or melt. Studies of mantle xenoliths (Bailey, 1982; Menzies & Hawkesworth, 1987) indicate that the LILE and LREE are preferentially sited in veins and disseminations of hydrous minerals such as phlogopite, amphibole and apatite that crosscut and replace mantle peridotite. This metasomatic enrichment may be achieved by overprinting the mantle wedge by either LILE enriched fluids or LILE-enriched partial melts, both-derived during dehydration of the subducted oceanic slab (Menzies & Hawkesworth, 1987; Peccerillo, 1992). Partial melting of these enriched areas, under hydrous conditions, would yield potassic melts, with partial melting of normal mantle peridotite considered unable to produce extensive LILE-enrichment (eg Kay and Gast, 1973). Retention of the HFSE in titanite phases residual after the partial melting event is considered to have caused the depletion of HFSE in arc rocks (Foley & Wheller, 1991). In the case of North Luzon, the period of LILE enrichment is concurrent with cessation of subduction and trenchward migration in alkaline magmatism during the Late Oligocene to middle Early Miocene, with alkaline dykes cross-cutting the collisional ophiolite at ~20 Ma (Billedo, 1994). The migration of alkaline magmatism trenchward could be explained by rising thermal gradients in the stalled slab, leading to enrichment and melting of progressively shallower areas of the mantle wedge.

# ALTERATION AND MINERALISATION

## INTRODUCTION

This chapter describes the hydrothermal alteration and mineralisation assemblages present in the Didipio region, in particular the porphyry-style mineralisation hosted within the Dinkidi Stock.

Detailed mapping of the Didipio region and logging of both Dinkidi and regional drill holes has revealed four main regional alteration events that are, in order of formation:

- A unmineralised contact metamorphic aureole that is located around the margins of the early diorites
- A weakly Cu-Au mineralised halo of K-silicate alteration that surrounds the Surong Monzonite
- Well developed porphyry Cu-Au mineralisation, and associated hydrothermal assemblages, hosted within the Dinkidi Stock
- A blanket of late-stage argillic alteration that has overprinted the Didipio Igneous Complex, with associated weak silica-pyrite Au mineralisation.

The hydrothermal alteration and mineralisation assemblages at the Dinkidi porphyry deposit have been divided into five main stages:

- 1) Early, weakly mineralised K-silicate alteration associated with the intrusion of the Tunja Monzonite.
- 2) Calc-potassic alteration and Au-Cu mineralisation associated with the intrusion of the Balut Dyke.
- 3) Emplacement of a quartz-stockwork associated with the intrusion of the Quan Porphyry and Bufu Syenite with associated sericite-carbonate-sulphide Cu-Au mineralisation
- 4) Unmineralised selectively pervasive argillic alteration (synchronous with the regional argillic alteration assemblage).
- 5) Unmineralised zeolite veins associated with extensive brecciation, (related to regional faulting).

The Stage 2 calc-potassic assemblage contains minor high-grade gold mineralisation (2-15 g/t Au). Widespread lower grade Cu-Au mineralisation (0.5-3 g/t Au; 0.5-1% Cu) is associated with the Stage 3 quartz stockwork. Figure 6.1 outlines the spatial and temporal distribution of veining and alteration at Dinkidi, based predominately on drillcore logging, and Figure 6.2 outlines the mineral paragenesis of Dinkidi based on thin section descriptions.

## METHOD

Regional alteration assemblages were documented initially described during 10 weeks of mapping in May 1995 in conjunction with logging of regional drill holes. The alteration assemblages at the Dinkidi deposit were examined by the detailed graphical logging of 29 drill holes (totalling 9600 meters) in March-July 1996 and August-September 1998. Logging focused initially on the 5800N, 5750N and 5700N cross-sections (Figure 4.1), the core of the Dinkidi system, with follow up reconnaissance logging of other sections. Drill holes logged as part of this study are listed in Appendix A. The paragenesis of Dinkidi was refined by examination of over



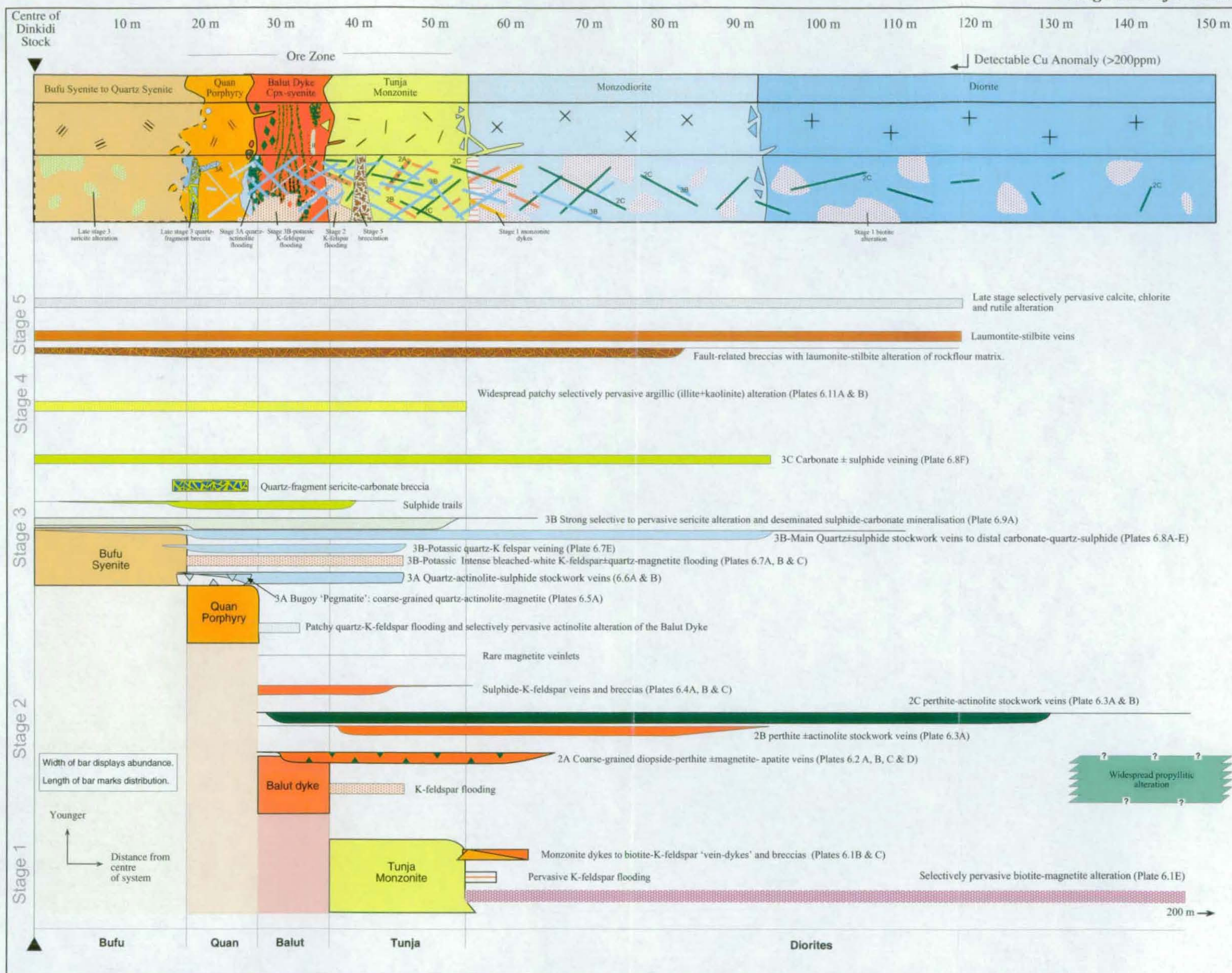


**Figure 6.1:** Schematic time-space diagram and paragenesis for the Dinkidi Cu-Au porphyry deposit. Earliest events are at the base of the diagram, with the length of the bars representing how far distally a feature extends from the centre of the Dinkidi Stock. Vertical grey lines represent the current position of igneous phases within the Dinkidi Stock. Diagram based on cross-cutting alteration relationships in logged drill core.

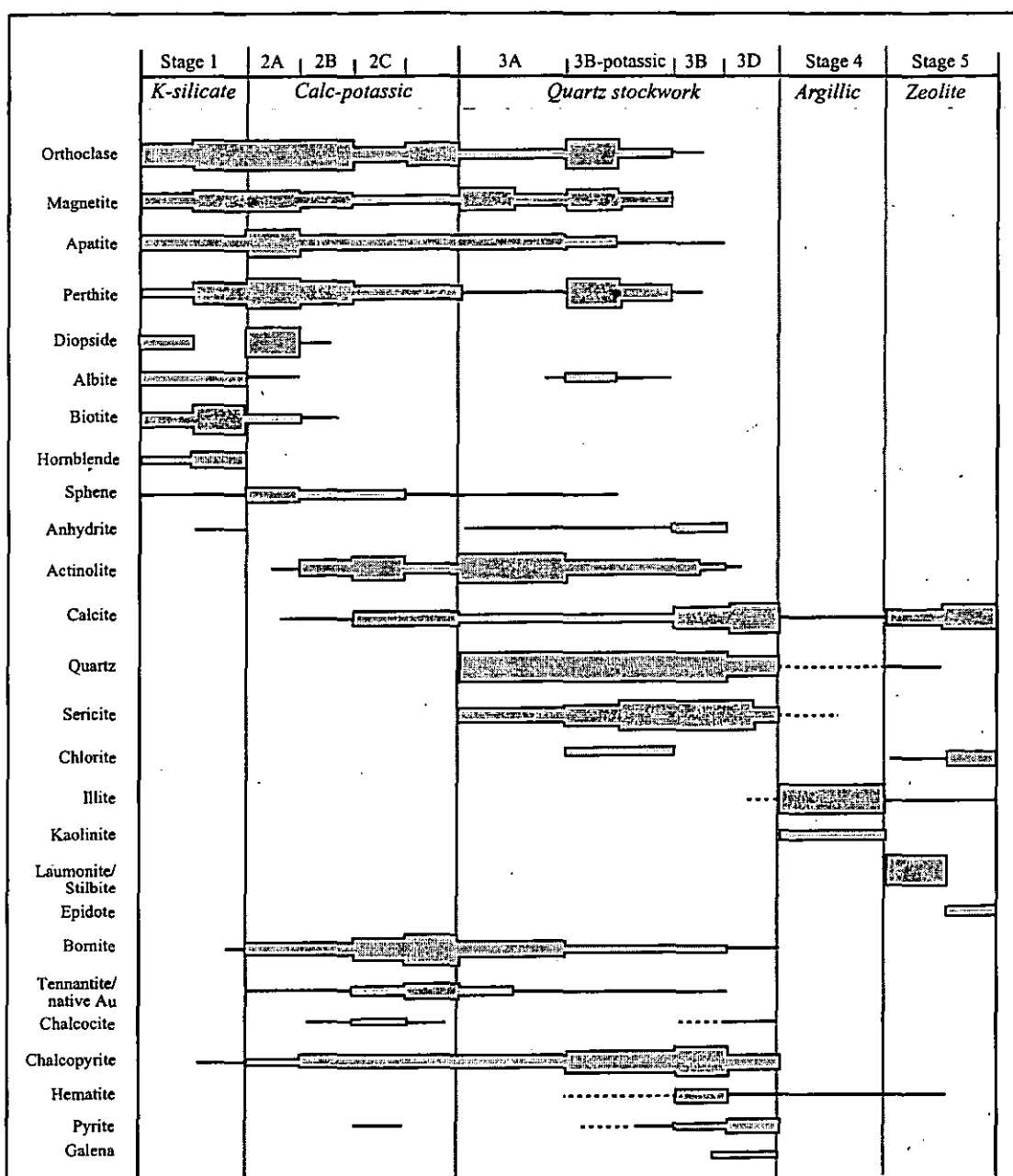


Figure 6.2: Mineral paragenesis in the core of the Dinkidi deposit, based on thin-section petrology.

200 thin sections, with mineral identification assisted by microprobe and Portable Infra-red Mineral Analyser (PIMA) analysis at the University of Tasmania and X-ray diffraction (XRD) analysis Mineral Resources Tasmania in Hobart. All named clay minerals described within this chapter were identified using PIMA and whole rock XRD. All named zeolite minerals described within this chapter were identified XRD analysis of powdered whole rock samples and mineral separates.

## ALTERATION AND MINERALISATION AT DINKIDI

Figures 6.1 and 6.2 describe the five main stages of hydrothermal activity recognized at Dinkidi. Figures 6.4, 6.5, 6.6 and 6.7 display the interpreted distribution of the main alteration assemblages for each stage, based on logged drill holes. The distribution of mineralisation at Dinkidi is shown in Figure 6.3. Mineralisation at Dinkidi is focused around the barren Bufu Syenite intrusion, with strong Cu-Au mineralisation spatially associated with the Balut Dyke and the now-brecciated Bugoy Pegmatite (Figure 6.3). Unpublished metal zonation studies by



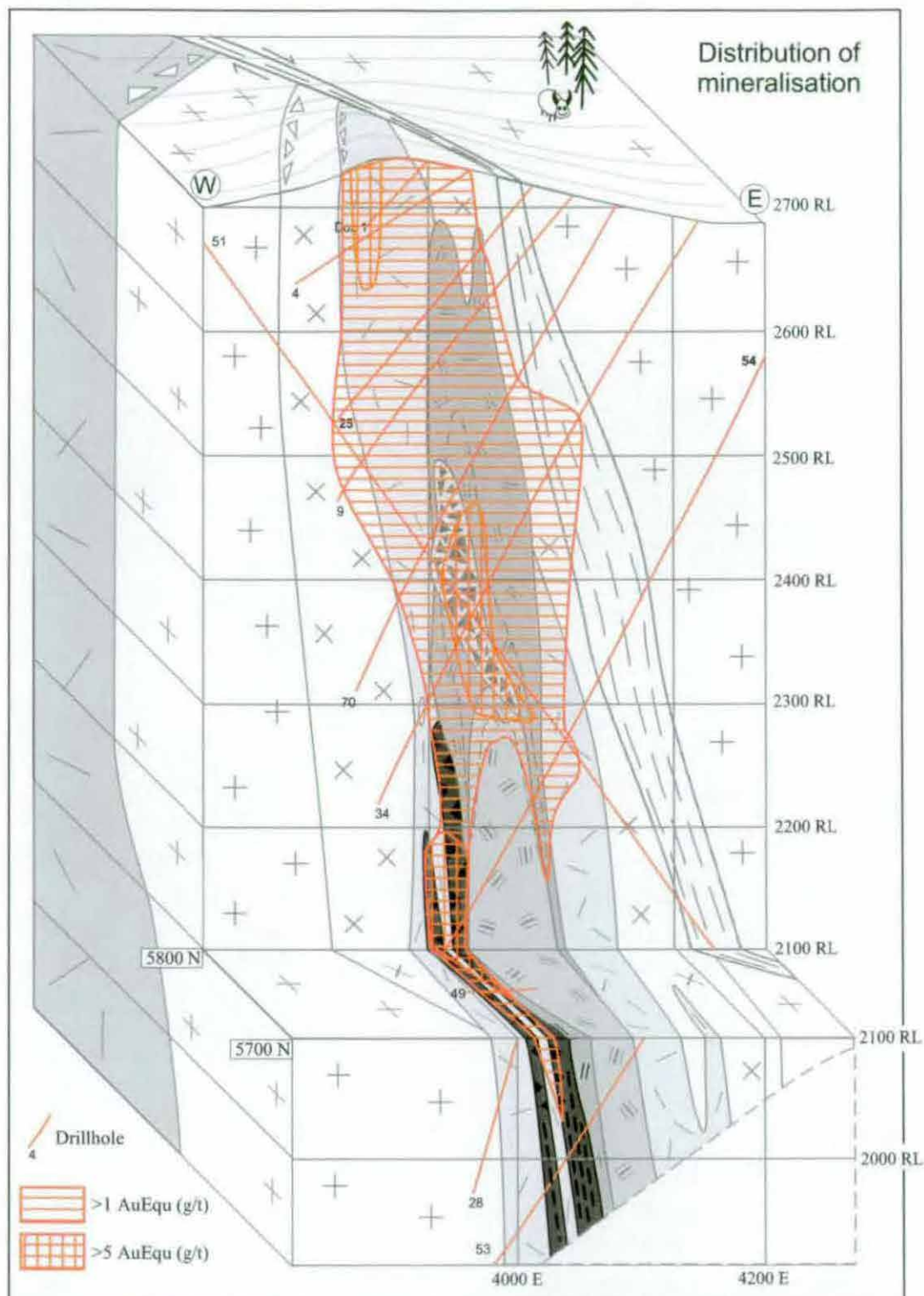


**Figure 6.3:** Distribution of mineralisation at the Dinkidi porphyry deposit. Cu and Au assays are calculated as equivalent gold (AuEq). The high grade zones at the top and bottom of the deposit are associated with Stage 2D sulphide-K-feldspar veining and breccias (eg Plate 6.6A -F). The high grade zone at the center of the deposit is associated with intensely developed Stage 3 quartz veins, brecciated Bugoy Pegmatite and sericite-carbonate-sulphide mineralisation (eg Plate 6.11E). Key for all rock symbols in Figure 4.1.

Climax-Arimco indicate that Au is focused in the core of the orebody and Pb, Zn, Ag and Mo are focussed on the margins of the Cu halo, a distribution typical of zonation observed at other porphyry deposits (eg Jones, 1992). Restrictions on access to the assay database, combined with the limited number of assays for Mo and other non-ore grade elements has prevented any detailed study of metal zonation at Didipio.

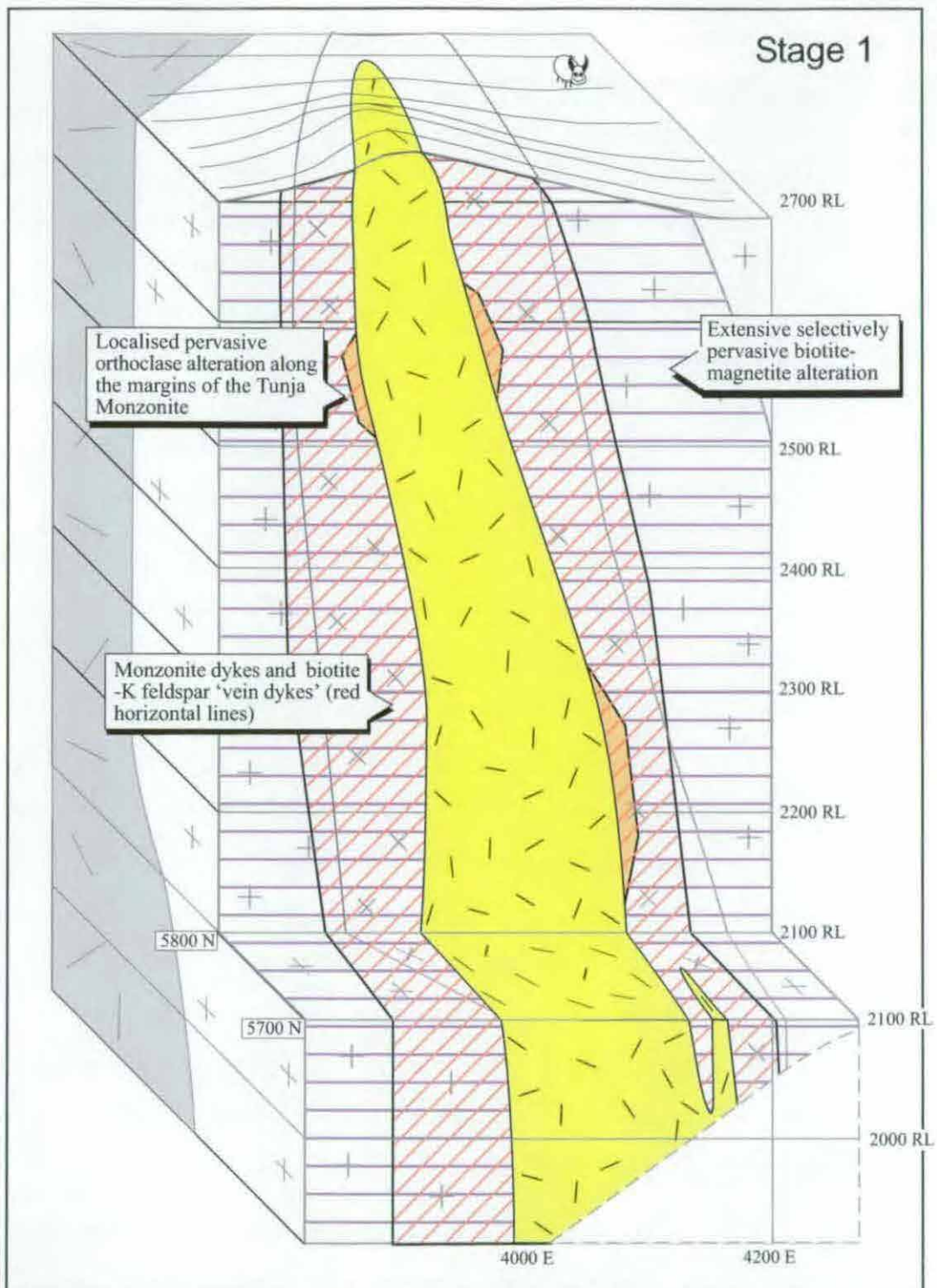


**Figure 6.4:** Schematic distribution of Stage 1 hydrothermal assemblages based on logged drill holes. The intrusion of the Tunja Monzonite is associated with strong selectively pervasive biotite-magnetite alteration and patchy orthoclase flooding close to the igneous contact. Stage 1 biotite alteration (blue lines) is the most extensive hydrothermal assemblage present at Dinkidi, extending at least 200 meters out from margin of the Tunja Monzonite.

### Stage 1 K-silicate alteration

The Tunja Monzonite is spatially associated with a biotite-magnetite-K-feldspar (orthoclase and perthite) alteration assemblage that has been intensely developed within the adjacent diorites (Figure 6.4). Strong selectively pervasive biotite-magnetite±orthoclase alteration extends at least 200 to 500 meters into the diorites adjacent to the Dinkidi Stock (Figure 6.4 & Plate 6.1C



## ALTERATION

& E), forming an alteration halo that is far more extensive than later vein sets or alteration assemblages. The biotite-magnetite alteration assemblage grades distally (~500 meters from the Dinkidi stockwork) into a broad zone of well developed secondary epidote-pyrite (propylitic) alteration, except for along the western margin, where the biotite alteration halo associated with the Tunja Monzonite merges with the biotite alteration halo surrounding the neighbouring Surong Monzonite (Figure 6.8). The selectively pervasive biotite-magnetite alteration assemblage has replaced clinopyroxene within the diorites (Plate 6.1E), and contains apatite, anhydrite, chalcopyrite and pyrite as accessory alteration minerals. This alteration is commonly domainal, forming dark clots of biotite and magnetite within xenolith-rich monzodiorites. Within 20 meters of the Tunja Monzonite, local pervasive orthoclase alteration of the diorite has occurred, with fine- to coarse-grained orthoclase replacing the matrix of the diorites (Plate 6.1F).

Although no vein stockwork is associated with the Stage 1 alteration assemblage, diorites close to the margins of the Tunja Monzonite contain monzonite dykes and regions of igneous breccia. These igneous dykes and breccias commonly grade, over a distance of a few centimetres, into coarse-grained biotite-K feldspar 'vein-dykes' (eg Plates 6.1A, B & C). These hybrid vein-dykes consist of medium- to coarse-grained biotite, plagioclase and magnetite (and rare diopside or amphibole) that are enclosed in a mosaic of K-feldspar (Plate 6.1 D). Small interstitial cavities are filled by apatite, anhydrite, gypsum, rare sphene and secondary (Stage 25) chlorite, calcite, stilbite and chabazite. The vein-dykes are an illustration of the difficulty that can be encountered when attempting to classify early, high temperature porphyry assemblages as purely magmatic or hydrothermal. The Stage 1 biotite-magnetite alteration halo also contains common, irregular biotite and magnetite veinlets.

The Tunja Monzonite is spatially associated with, and contains, an extensively developed sodic alteration assemblage. This has resulted in the ubiquitous albitisation of plagioclase laths within the Tunja Monzonite. Albitisation is widespread, occurring throughout the unaltered and altered sections of the stock, regardless of distance to the core of the hydrothermal system, and is apparently unrelated to any veins or later intrusives. It is therefore interpreted to be a late-stage magmatic alteration assemblage.

### *Stage 1 Propylitic alteration*

The Stage-1-biotite-magnetite alteration assemblage has been overprinted by, and grades distally into, a selectively pervasive chlorite-epidote-pyrite propylitic alteration

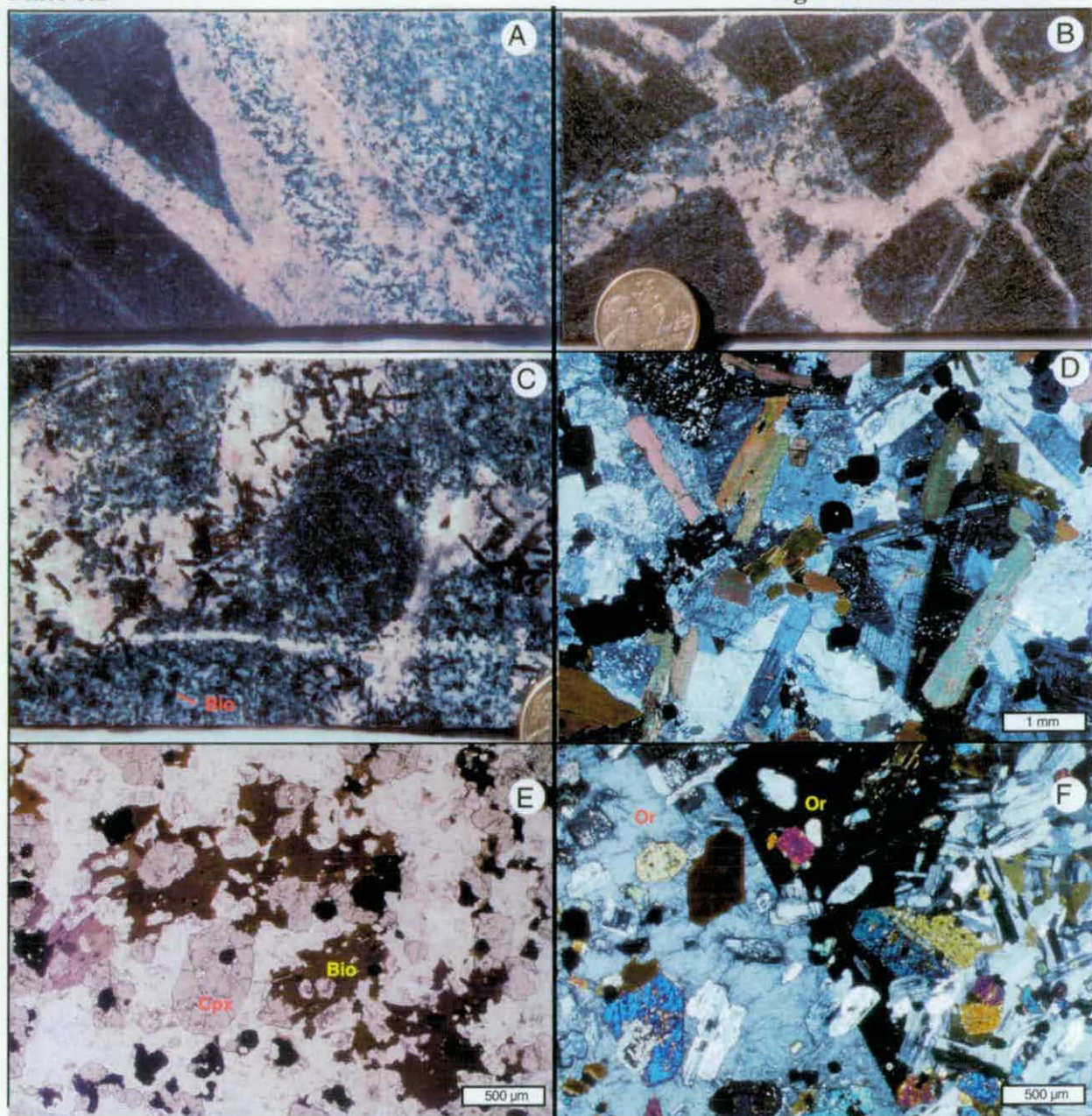


**Plate 6.1 A:** Pink K-feldspar rind concentrated along the contact between the Tunja Monzonite and a biotite-altered diorite. The small dyke on the left is a transitional magmatic-hydrothermal feature, consisting of a K-feldspar-biotite vein and a K-feldspar-flooded monzonite dyke. Location DDH60/309m. Drillcore 4.7 cm wide.

**Plate 6.1 B:** Tunja Monzonite-diorite igneous breccia. The mid-grey coloured 'magmatic' monzonite groundmass grades into a 'late-stage' medium- to coarse-grained light orange K-feldspar+biotite 'hydrothermal' groundmass. Sample 33/394.

**Plate 6.1 C:** Igneous breccia on the margin of the Tunja Monzonite. This hybrid 'magmatic-hydrothermal' breccia grades from 'magmatic' Tunja Monzonite on the far left of the picture to 'hydrothermal' coarse-grained biotite-K-feldspar-magnetite to the right. The assemblage represents the high-temperature hydrothermal deposition of a monzonite-composition assemblage. Note the typically spotty biotite alteration. Biotite has nucleated from primary clinopyroxene sites, in an orthoclase-altered diorite. Sample 25/273.

**Plate 6.1 D:** XPL photomicrograph of a coarse-grained 'magmatic-hydrothermal' breccia matrix similar to that in Plate 6.1C. The hybrid hydrothermal-magmatic assemblage consists of coarse-grained biotite, plagioclase and magnetite, with rare diopside and amphibole, that are enclosed in a subhedral mosaic of K-feldspar (weakly to strongly perthitic orthoclase and/or strongly twinned albite). Sample 53/894

**Plate 6.1 E:** PPL photomicrograph of Stage 1 selectively pervasive biotite alteration within a clinopyroxene-diorite. Within the biotite alteration halo, fine- to coarse-grained orange-red strongly pleochroic biotite has nucleated from, and replaced, clinopyroxene and has poikilitically enclosed plagioclase and clinopyroxene. Fine-grained magnetite grains are disseminated within the clinopyroxene phenocrysts, and commonly have biotite rims. Sample 60/571.

**Plate 6.1 F:** Clinopyroxene-diorite (right) partially assimilated by Stage 1 secondary coarse-grained orthoclase (Or) flooding (left). Orthoclase textures in the alteration zone range from fine-grained granular to, as shown, coarse-grained mosaics. In this example a coarse-grained subhedral mosaic of orthoclase poikilitically encloses plagioclase and clinopyroxene (which is corroded and biotite-altered).



## ALTERATION

assemblage. This propylitic alteration is intensely-developed within the diorites on the margins of the Dinkidi System. Within this propylitic alteration halo, clinopyroxene is selectively replaced by chlorite-calcite-rutile-epidote-pyrite and patches of diorite are commonly pervasively replaced by epidote-pyrite domains. The propylitic hydrothermal alteration zone also contains rare epidote-chlorite-pyrite veinlets. Within the monzonites of the Dinkidi Stock, propylitic alteration consists of the selectively pervasive alteration of primary and secondary biotite, actinolite and diopside by chlorite-calcite (and rare epidote). Intrusion-related propylitic alteration can be distinguished from weak background regional greenschist metamorphism by the presence of abundant epidote-pyrite, which is absent in the greenschist assemblage.

The propylitic assemblage had a protracted history of formation, given that it overprinted potassic alteration in the core of the system, but also appears to have formed synchronous with potassic alteration on the fringes of the system. This distribution in time and space is consistent with (but does not prove) that the propylitic assemblage formed at lower temperatures than the biotite assemblage, and the collapse of the thermal anomaly over time allowed for the formation of propylitic alteration minerals in the core of the system.

### **Stage 2 Calc-potassic assemblage**

The first episode of high-grade Cu-Au mineralisation at Dinkidi was associated with the intrusion of the Balut Dyke and the emplacement of the Stage 2 K-feldspar-actinolite±sulphide-apatite-diopside hydrothermal assemblage (Figure 6.5). The first Stage 2 veins are coarse-grained diopside-perthite veins (Stage 2A; Plates 6.2A to E), which are cross-cut by pink-coloured perthite±actinolite veins (Stage 2B; Plates 6.3A & C) that grade into an extensive stockwork of green-coloured actinolite dominated actinolite±perthite-bornite-apatite veins (Stage 2C; Plates 6.3A, B, C & D). High-grade Stage 2 mineralisation is associated with irregular 'dykes' of massive bornite-orthoclase (Plate 6.4A to F). All of these Stage 2 vein and dyke assemblages have crosscut the Tunja Monzonite, but not the Quan Porphyry, and are in turn overprinted by Stage 3 quartz veins.

#### ***Stage 2A 'Pegmatitic' veins***

Constrained spatially to within the Balut Dyke and or within 30 meters of its margins, are 'pegmatitic' Stage 2A veins (Figure 6.5; Plates 6.2A to E). These distinctively coarse-grained veins range in thickness from 2 to 10 cm and consist of medium- to coarse-grained

## Stage 2

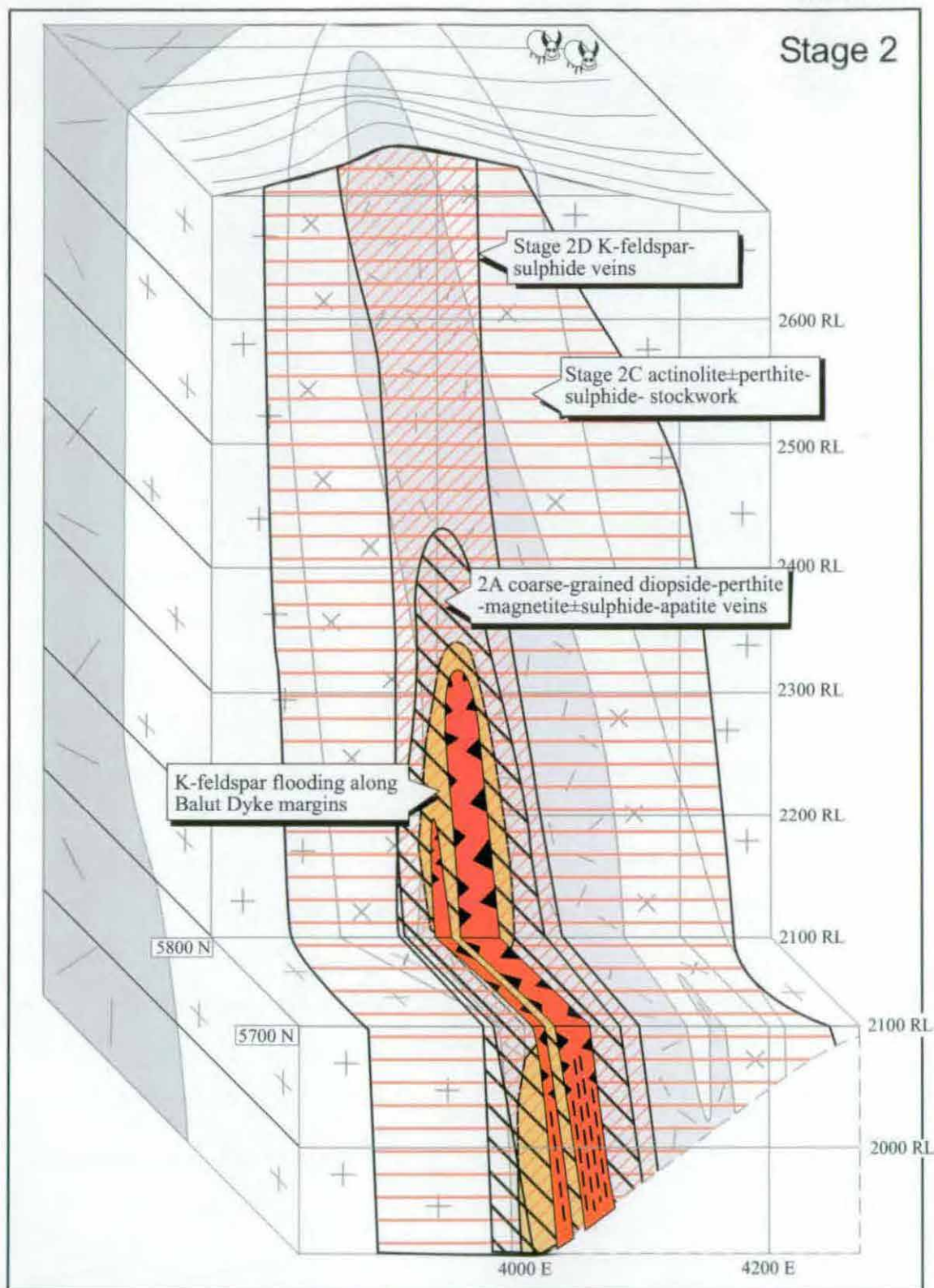


**Figure 6.5:** Approximate distribution of Stage 2 hydrothermal assemblages. The intrusion of the Balut Dyke was associated with the formation of patchy pervasive K-feldspar alteration along its margins, which has obscured the contact with the Tunja Monzonite. This event was associated with the emplacement of a gold-rich K-feldspar-actinolite-magnetite-sulphide stockwork vein assemblage. Stage 2A 'vein-dykes' of diopside-K-feldspar-magnetite extend 10 to 30 metres into the surrounding Tunja Monzonite. Stage 2C actinolite-perthite-sulphide veins are the most extensive vein set at Dinkidi, extending at least 200 metres into the host rocks. Most high-grade gold mineralisation at Dinkidi (5-20 g/t eqAu) is associated with sulphide-K-feldspar breccias and veins that have overprinted, and were emplaced along a structure above the Balut Dyke. This quartz-free stockwork assemblage is typical of many alkaline porphyry systems (eg Lang *et al.* 1995). Distribution partially reconstructed by removal of the Stage 3 Quan Porphyry and Bufu Syenite units.



## ALTERATION

perthite and diopside. Coarse-grained apatite, bornite (Plate 6.2F), and magnetite occur interstitial to the perthite. The bornite-rich Stage 2A veins are commonly associated with high-grade gold mineralisation, with vein intersections reaching up to 2-15 g/t Au.

Surrounding the 2A veins are halos of diopside alteration (Figure 6.2D & E) or, within the Tunja Monzonite, K-feldspar alteration. Associated with this stage are irregular, 5 cm to 30 cm wide Balut Dyke 'igneous breccia' zones. These zones comprise Tunja Monzonite and diorite clasts hosted within a matrix of unmineralised coarse-grained diopside and perthite (Plate 6.2B). The euhedral clinopyroxene has typically nucleated from the walls of the breccia, and locally crystals are up to 10 centimetres long, closely resembling the porphyritic phases of the Balut Dyke (compare plates 6.2B and Plate 4.1C).

### *Stage 2B & 2C actinolite-perthite veins*

Based on cross-cutting relationships, the Stage 2 vein stockwork can be subdivided into early perthite±actinolite 2B veins (Plate 6.3A) and late actinolite±perthite 2C veins (Plates 6.3A to D). Although the Stage 2B veins are typically cross-cut by the more extensively developed 2C veins they are both characterised by perthite-actinolite and an absence of quartz, and are interpreted to have formed during the same period of stockwork formation. Both vein sets occur within the Tunja Monzonite, terminate within the Balut Dyke and do not cross-cut the Quan Monzonite or Bufu Syenite. Stage 2C veins extend at least 200 meters out from the centre of the Dinkidi Stock and are the most extensive vein set at the Dinkidi deposit (compared to approximately 150 meters for the Stage 3 quartz veining). 2B veins are typically barren or weakly mineralised, whereas 2C veins are typically weakly to moderately mineralised. Local Stage 2C stockwork zones are associated with elevated, but commonly subeconomic, Cu-Au mineralisation.

Stage 2B veins consist of subhedral to euhedral perthite-actinolite with interstitial apatite, magnetite, bornite, chalcopryrite, pyrite and rare sphene (Plate 6.3G). The bornite commonly contains native Au. Voids in the centre of Stage 2 veins are filled by calcite and Stage 5 chabazite-laumontite-stilbite (Plate 6.3G). The Stage 2B veins are surrounded by a halo of orthoclase or actinolite, and rarely, biotite-magnetite alteration.

Stage 2C veins consist of euhedral to subhedral actinolite±perthite, with the perthite occurring commonly as an outer euhedral rind. Also present are interstitial apatite, sphene, calcite, bornite, chalcopryrite and pyrite (Plates 6.3B, D & F). Rare native Au and tennantite inclusions occur in the chalcopryrite and bornite (Plate 6.3E). A few interstitial

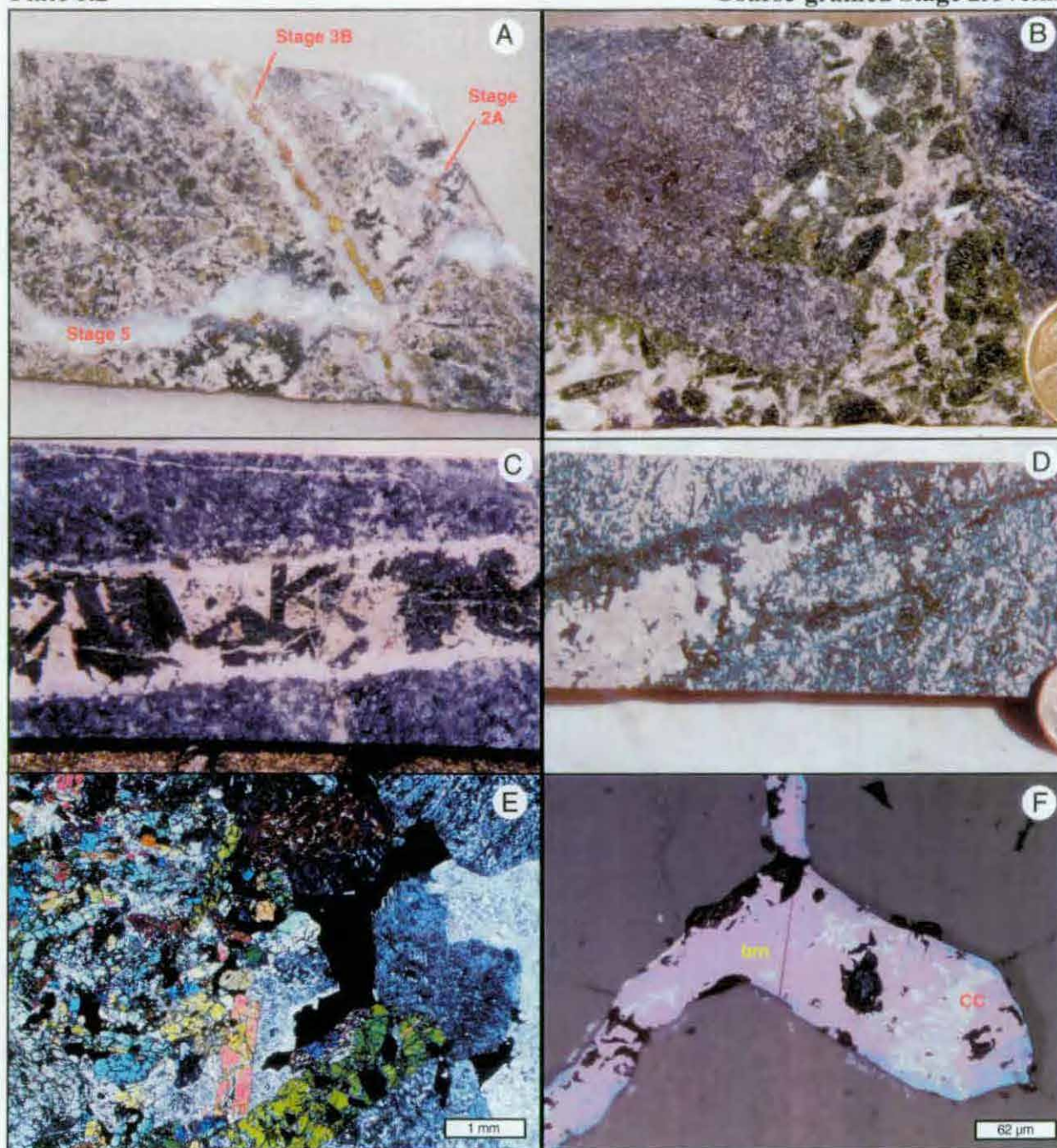


**Plate 6.2 A:** Representative veins from the three main stockwork stages at Dinkidi that have cross-cut the Tunja Monzonite. A coarse-grained Stage 2A perthite-actinolite vein (Stage 2A) is cross-cut by a stage 3B quartz-chalcopyrite vein (Stage 3C) which, in turn, has been cross-cut by a Stage 5 stilbite  $\pm$  laumontite vein. Sample 28/83.

**Plate 6.2 B:** Stage 2A diopside-perthite-magnetite breccia with cavities infilled by anhydrite and Stage 3B chalcopyrite-calcite. Diorite clasts are weakly biotite-K-feldspar altered. Sample 37/15.

**Plate 6.2 C:** Coarse-grained 2A diopside-K-feldspar vein that has cross-cut a weakly biotite-orthoclase altered monzodiorite-porphyry. Diopside in Stage 2A veins is commonly altered to actinolite, either by an overprint of Stage 3 assemblage, or possibly by retrograde Stage 2 fluids. Location DDH 47/704m.

**Plate 6.2 D:** Coarse-grained diopside-perthite-magnetite-apatite-bornite 2A vein cross-cutting equigranular Balut Dyke. The margin of the vein is marked by a dense 'alteration' halo of diopside. The 2A veins (or 'vein-dykes') share a similar bulk composition to the Balut Dyke, and the secondary diopside on the margin of the 2A vein is compositionally identical to the primary diopside within the Balut Dyke. Sample 49/644.

**Plate 6.2 E:** XPL photomicrograph of the diopside margin of the vein in Plate 6.3D. Coarse-grained perthite core of the vein (right) hosts abundant interstitial magnetite. Sample 49/644.

**Plate 6.2 F:** Stage 2 bornite (bm) with late-stage chalcocite (CC). Stage 2 bornite (and uncommon chalcopyrite) contain uncommon pyrite grains, rare chalcocite and tetrahedrite blebs and small native Au inclusions. Sample 28/508.

## ALTERATION

cavities have been filled by Stage 5 laumontite, calcite or aggregates of ferroan chlorite. Stage 2C veins are typically surrounded by a pink halo of orthoclase or perthite (Plates 6.3B). Stage 2B and 2C veins do not display strong changes in composition with distance from the centre of the system. Stage 2C veins appear to contain more actinolite, sulphide and apatite in the core of the vein stockwork. The intensity of the orthoclase alteration generally decreases outwards from the core of the system.

### *Stage 2D*

High-grade Au mineralisation at Dinkidi (Figure 6.3) is associated with emplacement of an orthoclase-bornite assemblage along a 1 to 20 metre wide zone that extends from within the Balut Dyke to the near surface (Figure 6.6; Plates 6.6 A to F). No cross-cutting relationships with other Stage 2 veins were observed for this assemblage, however the mineralisation crosscuts the Tunja Monzonite, terminates at the contact with the Quan Porphyry and is cross-cut by the Stage 3 quartz stockwork. It is classified here as Stage 2D because it is interpreted to be associated with the Balut Dyke. However, its timing with respect to Stages 2A, B & C remain unknown.

The Stage 2D assemblage forms irregular breccias and dykes (Plates 6.4A & B) that consist of an equigranular mosaic of orthoclase and bornite±chalcopyrite (Plates 6.4D). Interstitial to the sulphides and orthoclase are minor sphene, apatite, magnetite, and either actinolite or rare diopside. In rare cases, the assemblage forms 'blebs' of orthoclase and sulphide (Plate 6.4C). The blebs are zoned and have radial infilling textures (Plates 6.4E & F). These 'blebs' may have filled voids within the Tunja Monzonite, however, no equivalent zeolite- or calcite-filled miarolitic cavities have been recognised elsewhere in the Tunja Monzonite. The blebs are interpreted to be the shaved edge of a Stage 2D breccia zone or a cross-cut 'bump' in a nearby Stage 2D orthoclase-sulphide dyke. Alternatively, they may represent a Stage 1 feature, forming from immiscible sulphide droplets that were contained within silicate melt of the Tunja Monzonite. However, the close compositional and textural similarities between the blebs and the Stage 2D assemblage suggests a Stage 2 origin for the 'blebs'. Intergrowths of sulphide (chalcopyrite-pyrite) and silicates (clinopyroxene and biotite) have also been reported from the Lorraine Cu-Au Porphyry Deposit in British Columbia (Bishop *et al.*, 1995) and were attributed to the crystallisation of magmatic sulphides.



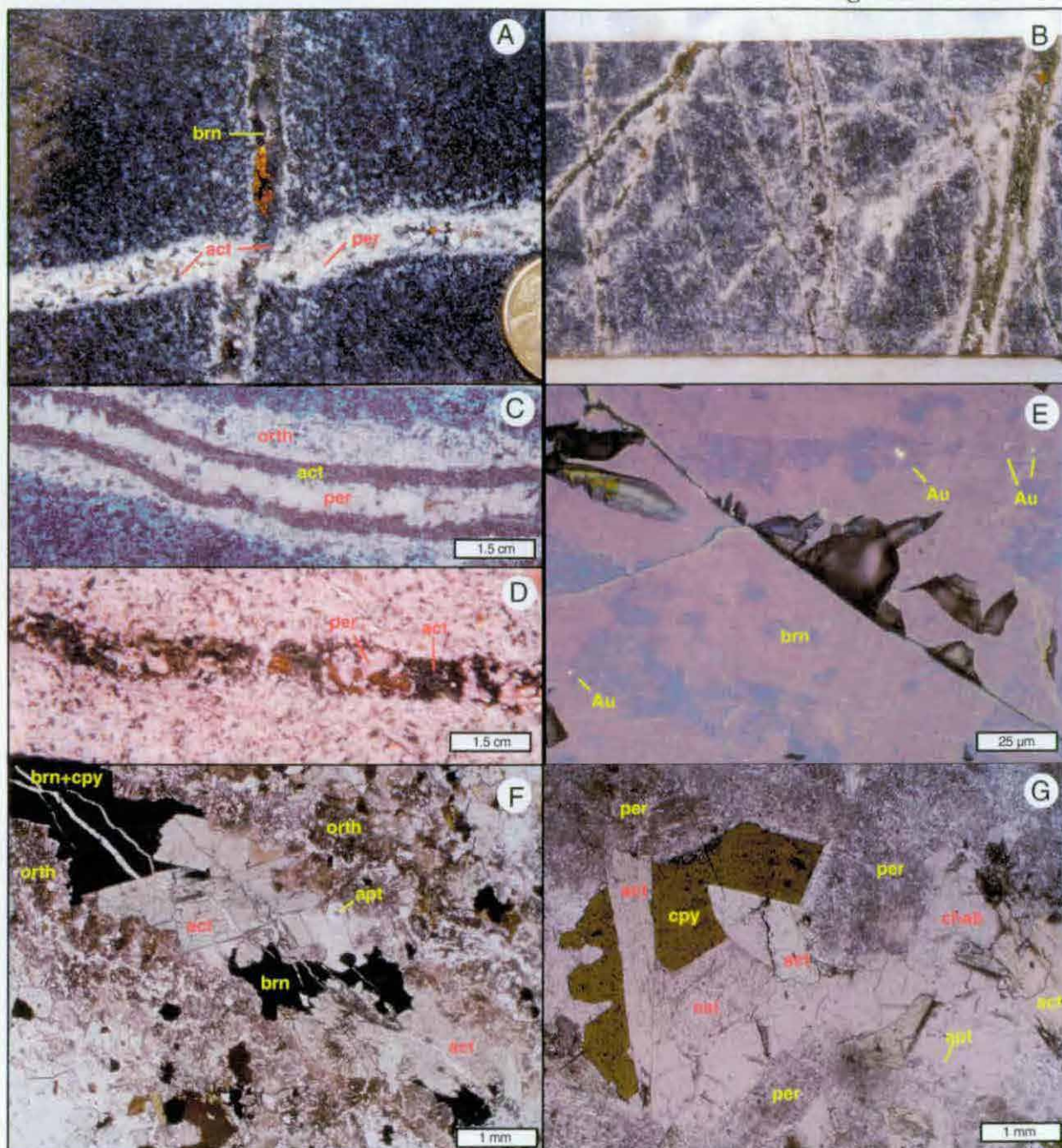


**Plate 6.3 A:** Light-orange coloured Stage 2B perthite+actinolite vein cross-cut by a Stage 2C actinolite-perthite-chalcopyrite-bornite vein. Stage 2B veins consist of subhedral to euhedral perthite and actinolite, with interstitial apatite, magnetite, bornite chalcopyrite and sphene. 2B veins are typically surrounded by an alteration halo of fine-grained granular orthoclase. Sample 37/176.

**Plate 6.3 B:** Stage 2C vein stockwork. Actinolite veins, with a characteristic halo of orange orthoclase alteration, cross-cut a weakly K-feldspar-altered diorite. 2C veins are typically surrounded by a halo of orthoclase and perthite, with the typically granular orthoclase emplaced along the host rock grain boundary. Drillcore 4.7 cm wide.

**Plate 6.3 C:** Hybrid Stage 2B-2C vein. The Stage 2B and 2C veins are classified by their dominate core component: perthite for 2B and actinolite for 2C (Plate 6.4B). Stage 2C veins tend to have formed later than 2B veins, however, both are interpreted to be components of the same calc-potassic vein set. This example is a hybrid between the idealized 2B and 2C vein endmembers.

**Plate 6.3 D:** Stage 2B vein within the Tunja Monzonite. The alteration halos of Stage 2B veins are strongly lithology-dependant. Stage 2B veins hosted within the Tunja Monzonite lack the distinctive orthoclase halo that is characteristic of Stage 2B veins hosted within diorite (compare with Plates 6.4A, B & C). Drillcore 4.7 cm wide. Location DDH 69/338m.

**Plate 6.3 E:** Native gold inclusions (Au) within Stage 2 bornite. Stage 2 sulphides consist of bornite and minor chalcopyrite, with inclusions of native Au and tennantite and are commonly replaced by chalcocite or digenite. Sample 28/508

**Plate 6.3 F:** XPL photomicrograph of a Stage 2C vein. Euhedral actinolite and apatite are hosted within interstitial calcite, chalcopyrite and bornite. The vein has been reopened by a network of thin Stage 5 stilbite-chabazite veinlets. Sample 53/882.

**Plate 6.3 G:** PPL and reflected light photomicrograph of the core of a Stage 2B vein. The interstitial cavity inbetween the coarse-grained subhedral perthite rind is filled by chalcopyrite, actinolite, calcite and minor Stage 5 chabazite (Chab), the later possibly a replacement of anhydrite. Sample 37/146.



### Stage 3 Quartz-stockwork assemblage

Most of the ore grade Cu-Au mineralisation at Dinkidi is associated with the intrusion and crystallisation of the Bufu Syenite during Stage 3, and the synchronous formation of an extensive quartz vein stockwork. A quartz-actinolite-K-feldspar-magnetite-carbonate-sulphide mineral assemblage was emplaced as both a quartz vein stockwork and as a coarse-grained accumulation above the Bufu Syenite (the Bugoy 'Pegmatite'; Figure 6.6; Plates 4.1F, 4.5A & B, 6.5A). Although many individual vein assemblages are observable, the Stage 3 quartz stockwork has been grouped into 3 vein subsets to aid description (Figure 6.1). They are:

**Stage 3A** Quartz-actinolite $\pm$ K-feldspar-magnetite-sulphide veins (Plates 6.5A; 6.6 A, B & C) & the Bugoy 'Pegmatite' (pre-Bufu Syenite crystallisation).

**Stage 3B** quartz veins that formed synchronous with the crystallisation of the Bufu quartz-syenite. They have been further subdivided into:

**3B-potassic** quartz-perthite veins (Plates 6.7A, D & E), which occur along the margin of the Bufu Syenite

**3B-main** quartz-sericite-carbonate-sulphide veins (Plates 6.8A to D; Plate 6.9A), which are found throughout the Quan Porphyry and Tunja Monzonite

**Stage 3C** calcite-sulphide $\pm$ quartz-sericite veins (Plate 6.8F), with associated calcite-sericite sulphide mineralisation and late stage brecciation of the Bugoy pegmatite. Stage 3C is interpreted to have formed after the formation of the Bufu quartz-syenite, based on cross-cutting relationships.

Although Stage 3 quartz veins have been subdivided into three subsets for the purpose of description, the quartz stockwork is interpreted to have been a continuum of events that evolved, temporally and spatially from the early quartz-actinolite-magnetite assemblage (3A) through the main quartz $\pm$ K-feldspar-sulphide-carbonate-sericite assemblage (3B) to late stage carbonate-sulphide assemblages (3C). The subdivisions described above are idealised 'end members', with hybrid veins the norm, rather than the exception. The Stage 3 quartz veins have reactivated Stage 2 veins in many samples and have cross-cut rare pre-Quan Porphyry magnetite veins and quartz veins.

#### *Pre-Quan Porphyry magnetite-sulphide trails and quartz veins*

Rare, thin magnetite-chalcopyrite $\pm$ pyrite-quartz veinlets and very rare quartz veins formed prior to the intrusion of the Quan Porphyry. These veins have crosscut the Tunja Monzonite and the Balut Dyke, and are preserved in Tunja Monzonite xenoliths within the

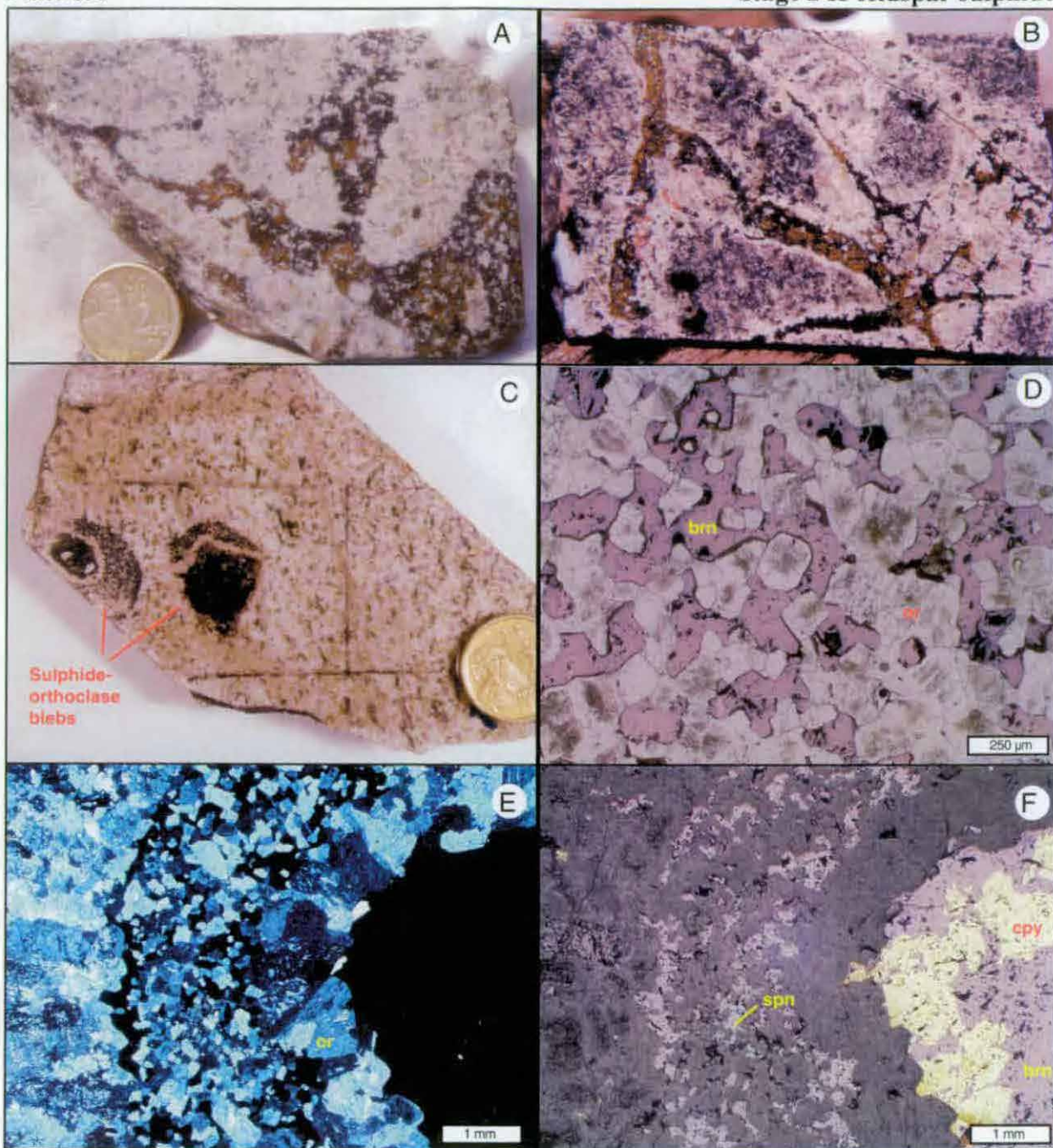


**Plate 6.4 A:** Stage 2 sulphide breccia. Medium-grained chalcopyrite, bornite and K-feldspar have cemented and replaced K-feldspar-altered clasts of Tunja Monzonite. This sulphide-K-feldspar assemblage forms a narrow but vertically extensive zone of high-grade copper-gold mineralisation above the Balut Dyke (Figure 6.6).

**Plate 6.4 B:** Stage 2 sulphide-cement breccia. Stage 2 bornite-chalcopyrite, with associated K-feldspar alteration halos, have brecciated the Tunja Monzonite. Sample 16/543. Drillcore 4.7 cm wide.

**Plate 6.4 C:** Sulphide-orthoclase 'blebs'. These tube-shaped features are comprised of a fine-grained mosaic of bornite and orthoclase, with the central core of bornite+chalcopyrite-calcite surrounded by a rim of euhedral orthoclase. Cavities in the core of the bleb are filled by calcite and locally the bornite has been partially replaced by chalcocite and chalcopyrite. The bleb is hosted in weakly sericite-altered Tunja Monzonite. Sample 4/96.

**Plate 6.4 D:** Reflected light and PPL photomicrograph of sulphides from bleb in Plate 6.6C. Fresh perthitic orthoclase and bornite form an equigranular mosaic with 3-way grain boundaries, with a conspicuous lack of calcite, sericite or any hydrothermal minerals typically associated with sulphide deposition. Such a mosaic of orthoclase and bornite is unlikely to have formed from descending meteoric water, such as Leach (1998) proposed in his mineralisation model for Dinkidi.

**Plate 6.4 E:** XPL photomicrograph of the left hand bleb in Plate 6.6C. An outer zone of equigranular sulphide-K-feldspar has a sharp contact with the surrounding Tunja Monzonite and grades into a relatively coarse-grained orthoclase rind that projects euhedral faces into a sulphide-filled core.

**Plate 6.4 F:** Reflected light photomicrograph of Plate 6.6E. Orthoclase is intergrown with bornite, chalcopyrite and uncommon sphene (spn). The copper sulphides contain inclusions of magnetite, native Au and tennantite.

## ALTERATION

Quan Porphyry. These <2 mm wide veinlets consist of magnetite-chalcopyrite±pyrite with accessory quartz and perthite. This Pre-Quan Porphyry vein assemblage has only been recognised on the basis of its incorporation into Tunja Monzonite xenoliths hosted within the Quan Porphyry. The scarcity of these veins is indicated by the lack of any appreciable increase in quartz or magnetite vein density on either side of the Tunja Monzonite-Quan Porphyry contact. The margins of the Quan Porphyry is typically unaltered, or, below the 2300 RL (Figure 6.7), overprinted by intense Stage 3A quartz-actinolite alteration and Stage 3B quartz-perthite flooding.

### *Stage 3A*

Stage 3A resulted in the deposition of a quartz-actinolite-magnetite-sulphide mineral assemblage, as quartz-actinolite veins, magnetite-sulphide veinlets and as the Bugoy Pegmatite. Intense quartz±sulphide flooding of the Balut Dyke and associated actinolite alteration is associated with this stage. The Stage 3A assemblage cross-cuts the Tunja Monzonite, Balut Dyke and Quan Porphyry, but is crosscut by dykes of the Bufu Syenite and Stage 3B veins (Plate 6.5B). The Stage 3A vein assemblage is distinguished from Stage 2C by the presence of quartz in the Stage 3 assemblage.

### *Stage 3A quartz-actinolite veins*

Stage 3A quartz-actinolite veins (Plates 6.6A & B) cross-cut the Quan Porphyry, Tunja Monzonite and surrounding diorites, extend at least 100 metres from the core of the Dinkidi stock, and are found from the margin of the Bufu Syenite to the near-surface environment (Figure 6.6). Stage 3A veins range in width from 0.2 to 8 cm, and many individual veins have reactivated earlier-formed Stage 2 calc-potassic veins. The veins consist of clear to milky quartz-actinolite, with interstitial cavities filled by calcite, apatite, sphene, bornite, chalcopyrite and pyrite (Plates 6.8E & F). Bornite contains small (<1 mm) inclusions of native gold and tennantite and has been partially replaced by chalcopyrite (Plate 6.6F). Associated with the Stage 3A veins is the selectively pervasive actinolite alteration of biotite and clinopyroxene in the Tunja Monzonite and quartz-actinolite flooding of the Balut Dyke and Quan Porphyry. The abundance of actinolite and sulphide in Stage 3A veins decreases with increasing distance from the centre of the system, with a proximal grey quartz-bornite-chalcopyrite assemblage within the veins grading out to a calcite-milky quartz-pyrite-chalcopyrite assemblage in distal settings (>80 meters from the stock).



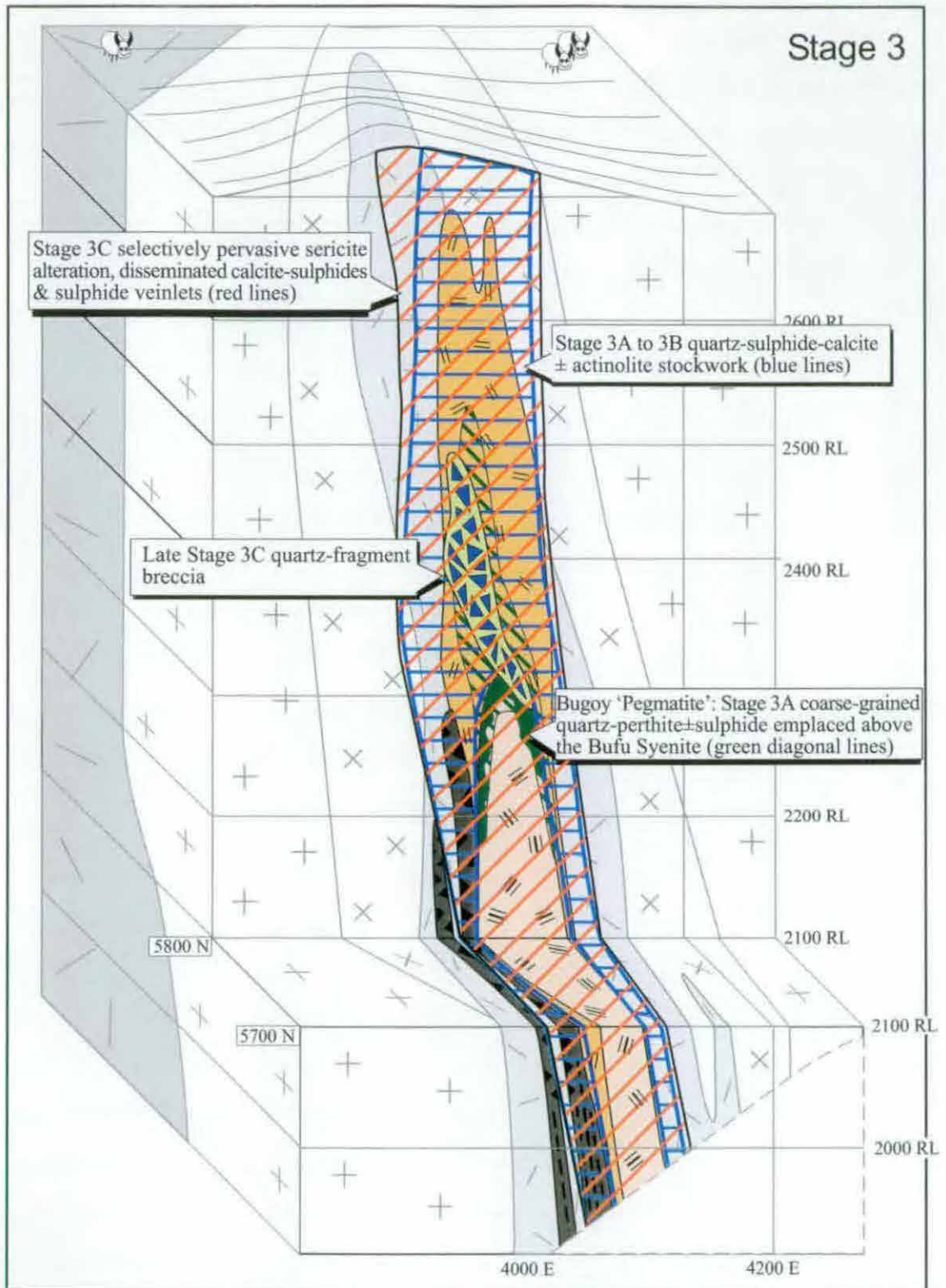


**Figure 6.6:** Approximate distribution of Stage 3 hydrothermal assemblages. The crystallization of the Bufu Syenite is interpreted to have been associated with the emplacement of a quartz stockwork throughout the Tunja Monzonite and Quan Porphyry. The Stage 3 quartz stockwork grades out along the outer margin of the Bufu Syenite, with the core of the Bufu hosting only rare late Stage 3B quartz veinlets. The distribution of the Stage 3B to 3C sericite-carbonate alteration and associated disseminated sulphide mineralisation overlaps the distribution of the quartz stockwork. In contrast to the quartz veins sericite alteration (and minor Stage 3C sulphides) has also overprinted the core of the Bufu Syenite.



## ALTERATION

### *Stage 3A Bugoy Pegmatite*

The core of the Dinkidi quartz stockwork, above the Bufu Syenite, is a coarse-grained quartz-actinolite-magnetite-perthite rock, informally named the Bugoy 'Pegmatite' (Plates 4.1F, 4.5A & B, 6.5A). The term pegmatite is used here in a textural sense, denoting a coarse-grained rock consisting of 'hydrothermal' minerals, rather than in the genetic sense of a REE-bearing granitoid intrusive body. The petrology of the Bugoy Pegmatite has been described in Chapter 4. The main body of massive quartz has undergone two periods of brecciation (late Stage 3C and Stage 5, both described below; Plate 6.6D), with only peripheral coarse-grained dykes preserved as coherent bodies. Coarse-grained Stage 3A quartz-actinolite-magnetite veins and Stage 3B-Potassic quartz-perthite veins are compositionally and texturally identical to vein clasts of the Bugoy Pegmatite (eg Plates 4.1F; 6.6C & D), suggesting that most of the Bugoy Pegmatite formed synchronously with hydrothermal Stages 3A to 3B-Potassic. A close spatial and temporal relationship between the Bugoy Pegmatite and the early Stage 3 quartz vein assemblage is implied by the observation that Stage 3A and 3B-Potassic veins merge with the coarse-grained pegmatite veins (eg Stage 6.7D), via an intermediate quartz-matrix breccia. This is interpreted to indicate that the Bugoy pegmatite formed as an open space filling of the early Stage 3 quartz stockwork in the central, and presumably most fractured, section of the hydrothermal system.

### *Stage 3A pervasive and selectively pervasive alteration assemblages*

The margins of the Bufu Syenite and the Bugoy Pegmatite hosts a zone of intense, unmineralised to strongly mineralised quartz $\pm$ sulphide flooding (Plates 6.5B, C & F), with associated disseminated chalcopyrite, bornite, actinolite, magnetite and rare sphene. Within the Balut Dyke this hydrothermal assemblage is characterised by intense quartz-actinolite alteration. Similar quartz flooding is associated with the Stage 3B-Potassic vein assemblage, although intense K-feldspar alteration and an absence of actinolite distinguishes the Stage 3B event from Stage 3A (eg Plate 6.7B).

### *Stage 3B-Potassic*

The main period of quartz veining at Dinkidi consists of two assemblages: A) quartz-perthite veins and related K-feldspar alteration (Stage 3B-Potassic veins), which occur in a proximal setting along the Quan Porphyry-Bufu Syenite contact; and B) the widespread

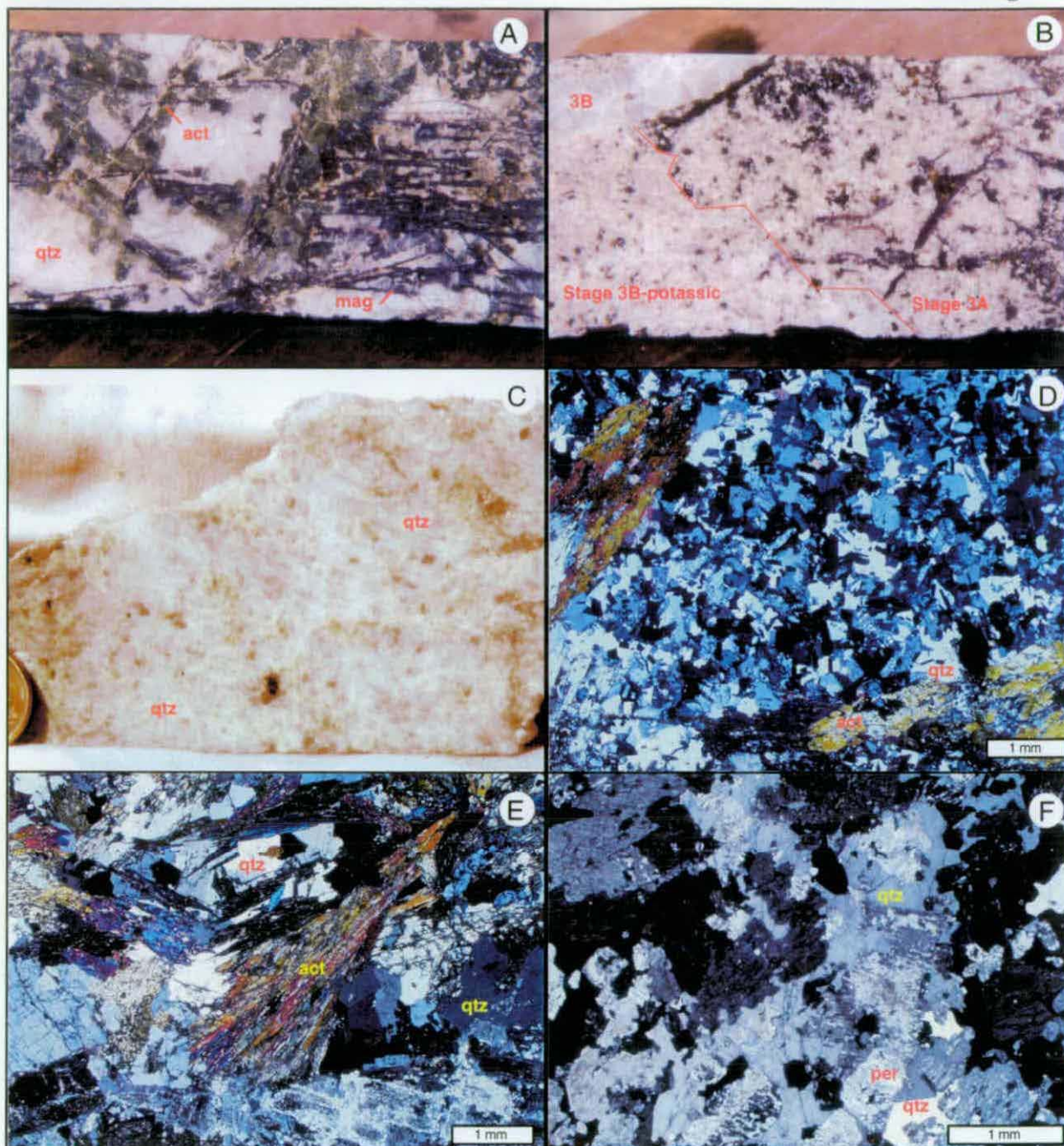


**Plate 6.5 A:** Stage 3A: massive quartz-actinolite-magnetite+K-feldspar assemblage that has cross-cut the Quan Porphyry. Magnetite typically occurs as acicular needles. This assemblage, where forming dykes or massive accumulations, is referred to as the Bugoy 'Pegmatite'. Sample 47/726. Drillcore 4.7 cm wide.

**Plate 6.5 B:** Stage 3A pervasive magnetite-actinolite-quartz replacement of the Quan Porphyry (right) cross-cut by a Stage 3B-proximal perthite-quartz dyke and a stage 3B quartz vein (left). Location 47/725. Drillcore 4.7cm wide.

**Plate 6.5 C:** Stage 3A to Stage 3B-potassic massive quartz flooding of the Quan Porphyry. The margins of the Bufu Syenite have been flooded by quartz during Stages 3A (with associated actinolite) and 3B (with associated perthite).

**Plate 6.5 D:** XPL photomicrograph of the core of a Stage 3A K-feldspar-quartz-actinolite vein with an intergrown mosaic of subhedral quartz and euhedral orthoclase and large actinolite phenocrysts. Sample 261170.

**Plate 6.5 E:** XPL photomicrograph of typical massive quartz-actinolite textures in Stage 3A veins. Radial fans of actinolite are typically poikilitically enclosed within, or interstitial to, a granular mosaic of quartz, with interstitial spaces filled by sulphides (chalcopyrite+pyrite or bornite) and calcite. Sample 34/427.

**Plate 6.5 F:** Stage 3A-3B quartz flooding of the margin of the Bufu Syenite. Perthite has been partially replaced by quartz. The core, and upper margins, of the Bufu consist of a quartz syenite that is interpreted to be associated with the formation of the Stage 3 stockwork. There is no clear transition from the quartz-flooded syenite margin to the 'magmatic' quartz-syenite core (which contains melt inclusions within the interstitial quartz). Sample 28/510.

## ALTERATION

main quartz stockwork (3B-main veins) with related quartz-sericite-carbonate alteration. Both vein sets have overprinted the Stage 3A assemblage (Plate 6.5B). The 3B-Potassic assemblage is intimately associated with the Bufu quartz syenite, with which it shares a similar quartz-perthite composition. Below the Bugoy pegmatite, at the contact between the Quan Porphyry and the Bufu Syenite, Stage 3B quartz vein density decreases gradually, with the inner quartz-syenite core of the Bufu containing only rare, irregular unmineralised quartz trails of presumed Stage 3B timing.

### *Stage 3B-Potassic quartz-perthite veins*

Closely associated with the crystallisation of the Bufu quartz syenite are uncommon unmineralised Stage 3B grey quartz veins with perthite rinds and rare interstitial magnetite, chalcopyrite and apatite (Plates 6.7D, E & G). The Stage 3B-potassic assemblage has cross-cut the Quan Porphyry and is restricted to within 30 meters of the Bufu Syenite margin. The 0.5 to 1.5 cm wide Stage 3B potassic veins are typically surrounded by a 2 to 5 cm wide bone-white K-feldspar alteration halo, with associated selectively pervasive chlorite along the margins of the halo (Plate 6.9F). Interstitial cavities have been infilled by Stage 3C chalcopyrite-calcite. High densities of Stage 3B-Potassic veins are associated with patchy K-feldspar-quartz flooding of the host rock.

Uncommon 5 to 30 cm thick perthite-rich 3B-potassic 'vein-dykes' (Plate 6.7A) resemble Bufu quartz-syenite dykes and consist of a quartz-orthoclase-perthite groundmass (with uncommon quartz-filled miarolitic cavities), commonly centred around an irregular central trail of quartz (Plate 6.7A). These aplite vein-dykes are associated with strong magnetite-K-feldspar-quartz-chlorite alteration of the Balut Dyke (Plate 6.7A).

### *Stage 3B-Potassic pervasive and selectively pervasive alteration assemblages*

In many drill core intercepts the margin of the Bufu Syenite is characterised by intense, pervasive bone-white to pale green K-feldspar flooding (perthite±orthoclase) with accessory quartz, magnetite, sericite and rare chalcopyrite, surrounded by an alteration halo of selectively pervasive chlorite alteration (Plate 6.7C & F). The Balut Dyke has been extensively affected by Stage 3B-Potassic K-feldspar flooding (Plate 6.7B). The high degree of replacement of the Balut Dyke (relative to the neighbouring Tunja Monzonite) suggests that the fluid responsible for the K-feldspar flooding were focused in the Balut Dyke.



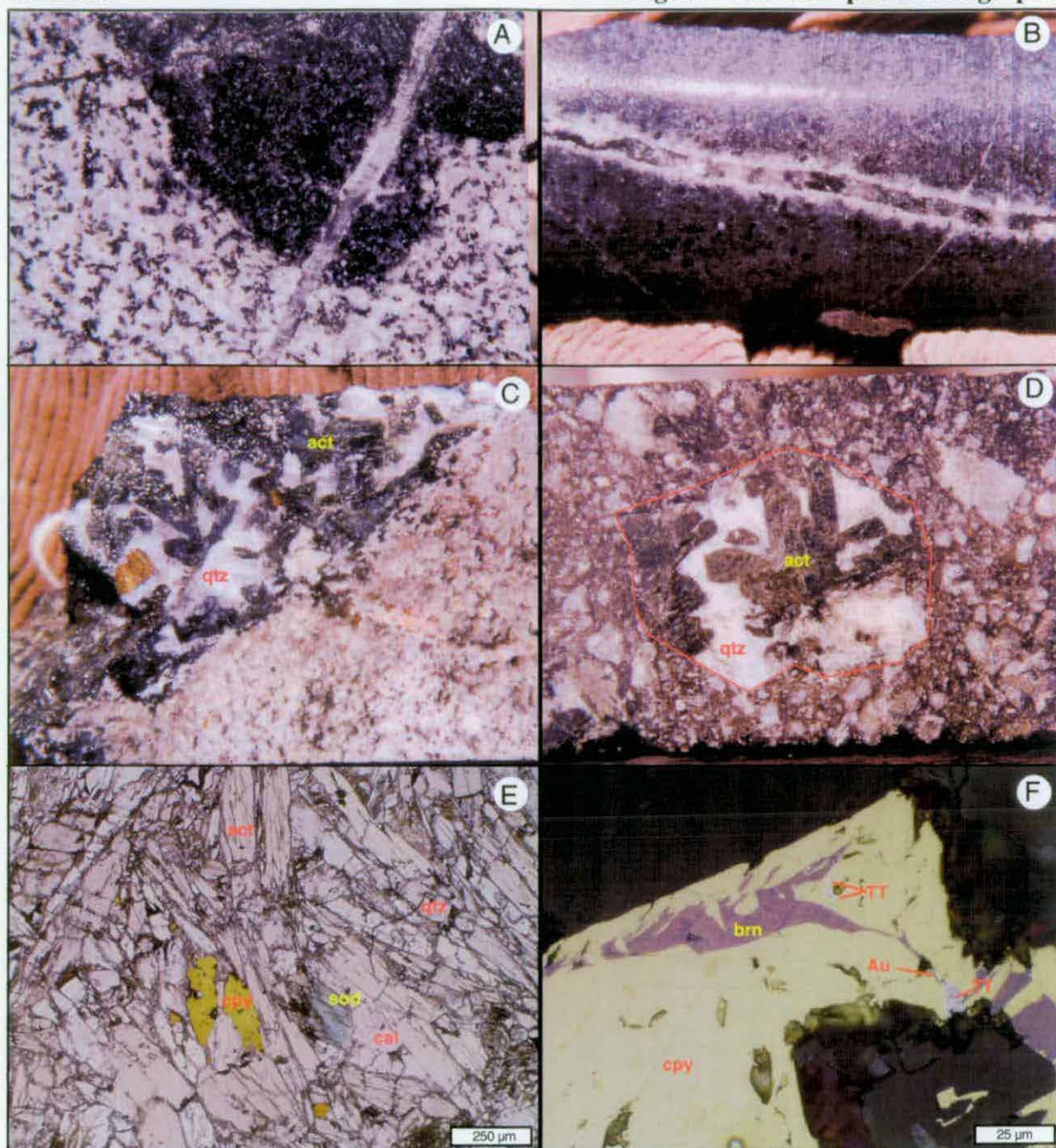


**Plate 6.6 A:** Stage 3A quartz-actinolite vein crosscutting the Tunja Monzonite and a diorite xenolith, with weak K-feldspar alteration developed adjacent to the vein within the xenolith. Location DDH 14/487m. Drillcore 4.7 cm wide.

**Plate 6.6 B:** Stage 3A quartz-actinolite vein, with minor interstitial calcite and a thin, intense orthoclase alteration halo, cross-cutting monzodiorite. Location DDH 37/205m. Drillcore 6.2 cm wide.

**Plate 6.6 C:** Coarse-grained Stage 3A quartz-apatite-actinolite-K-feldspar-magnetite-chalcopyrite vein, which has cut the Tunja Monzonite. Drillcore 4.7 wide. Location 37/139.

**Plate 6.6 D:** Fragment of the Bugoy 'pegmatite' in the Bugoy Breccia. The fragment is identical in composition and texture to the vein in Plate 6.8C. The abundance of quartz fragments in the quartz-fragment breccia, and presence of these coarse-grained quartz-actinolite-magnetite clasts, suggests that the Bugoy 'pegmatite' was brecciated to form the quartz fragment breccia. Location 83/387. Drillcore 4.7 cm wide.

**Plate 6.6 E:** Typical Stage 3A vein containing intergrown actinolite and quartz, with interstitial spaces infilled by chalcopyrite and Stage 5 calcite. Stage 3A actinolite is commonly replaced by Stage 3C calcite and, in this example, has been partially replaced by blue sodic amphibole (sod). Reflected light & PPL. Sample 34/427.

**Plate 6.6 F:** Partially re-assimilated bornite rind on Stage 3A chalcopyrite. The re-assimilation is interpreted to be a Stage 3B event. Bornite is associated with small grains of tennantite (TT) and native gold (Au). Stage 3A copper sulphides are commonly partially replaced by chalcocite. Sample 33/285.



## ALTERATION

### *Stage 3B-main quartz stockwork*

The bulk of low-grade mineralisation at Dinkidi is associated with a quartz-sericite-calcite stockwork and disseminated sulphide mineralisation (eg Plate 6.9A). The Stage 3B quartz stockwork extends from the margin of the Bufu quartz syenite to the surface and individual quartz veins extend up to 150 meters into the surrounding diorites (Figure 6.6). Strong stockwork veining is localised within 70 meters of the centre of the Dinkidi stock.

Stage 3B quartz stockwork veins are typically 0.5 to 15 cm wide and consist of grey to milky quartz. Interstitial spaces within, and fractures through the quartz, are filled by calcite, anhydrite, chalcopryrite and pyrite (Plate 6.8C). Accessory actinolite, orthoclase and bornite are present locally in early, proximal veins (Plates 6.8B). Stage 3B veins that were emplaced late in the history of the stockwork, or in a distal setting, typically contain higher relative abundances of calcite and pyrite (Plate 6.8D). Quartz veining on the periphery of the Dinkidi system (>150 meters) consist of barren, typically banded quartz-chalcedony veinlets (Plate 6.8E). Rare unmineralised Stage 3B veins in the core of the Dinkidi Stock (within 20 meters of the Bufu Syenite) consist of grey quartz with a wispy or irregular morphology and were associated with K-feldspar alteration (Plate 6.8A). These wispy quartz veins resemble the 'A veins' of Gustafson & Hunt (1975).

### *Stage 3B sericite-sulphide-carbonate alteration*

The Stage 3B quartz stockwork is spatially and temporally associated with an intensely-developed sericite-calcite alteration assemblage and disseminated sulphide mineralisation (Plate 6.9A). The bulk of this mineralisation is hosted within the Tunja Monzonite and Quan Porphyry. Within this alteration zone, sericite has replaced plagioclase cores (Plate 6.9B) and hematite has replaced magnetite (Plates 6.9C & D). Stage 2 and 3A actinolite is also commonly replaced by Stage 3B calcite-sericite. Chalcopryrite is the main sulphide mineral, and occurs with accessory pyrite, bornite, sphalerite and galena (Plate 6.9C & D). The sulphides occur within quartz veins or as disseminated grains and sulphide-calcite veinlets within the host rock (Plate 6.9E). Stage 3B chalcopryrite has typically replaced Stage 2 and Stage 3A bornite. Distal Stage 3B quartz veins are associated with weak chlorite-calcite alteration of the diorites (Plate 6.8D).

### *Stage 3C*

Stage 3C is characterised by calcite veins (Plate 6.8F) and widespread selectively pervasive calcite±sericite alteration of actinolite and plagioclase. Stage 3C veins have

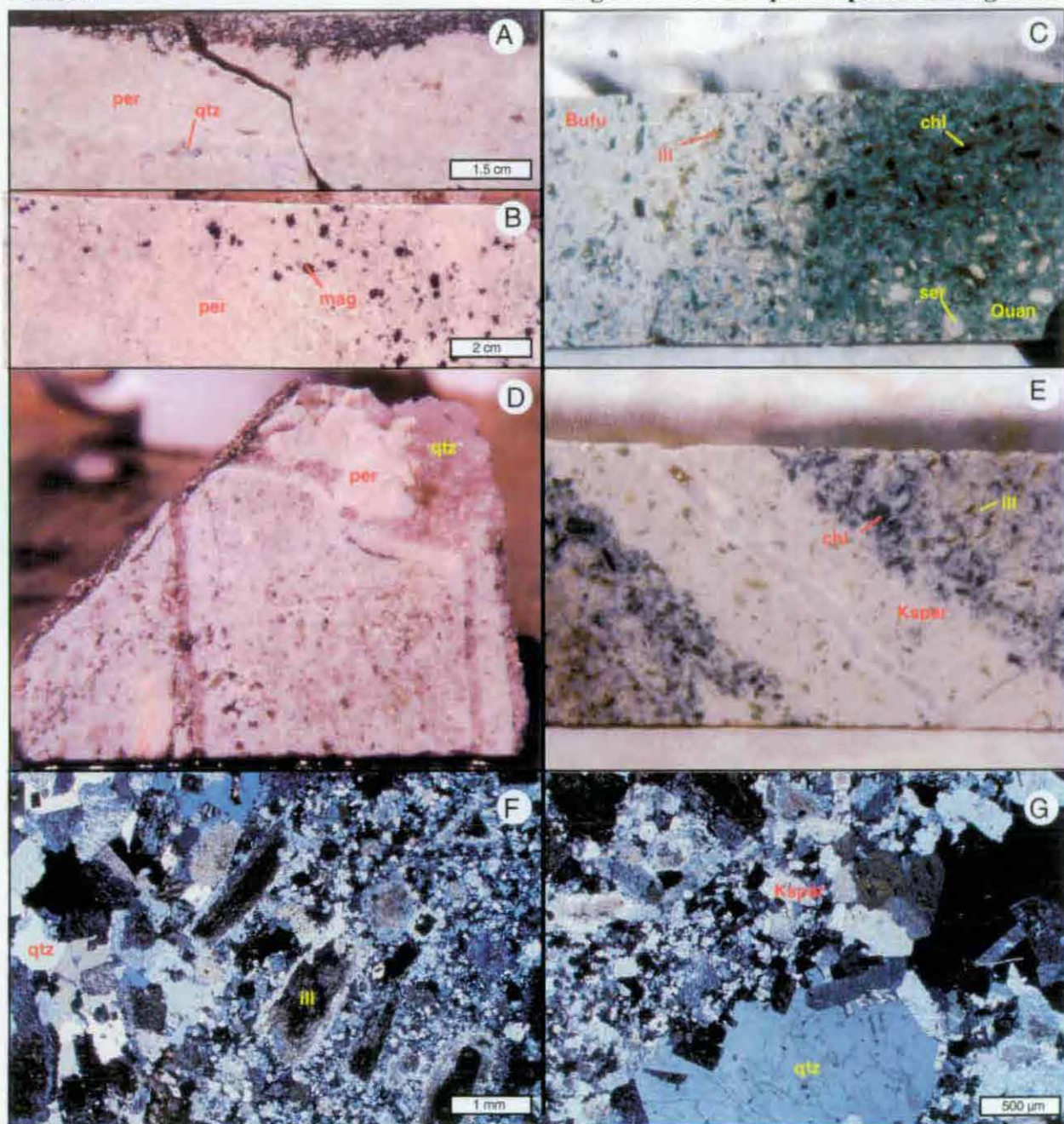


**Plate 6.7 A:** 3B-Potassic 'vein-dyke' cross-cutting the Balut Dyke. These 5 to 200 cm thick pale-coloured vein-dykes, consists of a subhedral mosaic of perthite, commonly with a vuggy quartz core (qtz). Diffuse to cuspatate boundaries indicates partial replacement of the Balut Dyke by pervasive K-feldspar alteration. The vein-dykes are surrounded by a broad halo of well developed magnetite-quartz-orthoclase-chlorite alteration. Location DDH47/701m. Drillcore 4.7 cm wide.

**Plate 6.7 B:** Pervasive perthite-magnetite flooding of the Balut Dyke. Near-total replacement of the Balut Dyke typically results in 'spongy' fine-grained perthite intergrowths and 'spotty' magnetite alteration. Sample 49/675. Drillcore 4.7 cm wide.

**Plate 6.7 C:** Contact between the Bufu Syenite (left) and the Quan Porphyry (right). Note olive green selectively pervasive ferroan chlorite alteration of plagioclase laths.

**Plate 6.7 D:** Contact between a small Bugoy 'pegmatite' dyke and Stage 3 quartz veins: the quartz veins connect into the Bugoy 'pegmatite', indicating that they represent different morphologies of the same event. Sample 33/407. Drillcore 4.7 cm wide.

**Plate 6.7 E:** Typical Stage 3B-Potassic vein cutting the Quan Porphyry, consisting of grey quartz with late-stage chalcopyrite-calcite infill and a characteristically broad K-feldspar alteration halo, with marginal chlorite-illite alteration. The alteration halo is either granular orthoclase replacement of the groundmass, or uncommonly, a medium-grained mosaic of perthite. The Stage 3B K-feldspar alteration is commonly overprinted and obscured by late-stage 3B to 3C sericite alteration. Drillcore 4.7 cm wide.

**Plate 6.7 F:** XPL photomicrograph of a sharp contact between the Quan Porphyry (left) and a dyke of the Bufu quartz syenite (right). The groundmass of the Quan Porphyry has been replaced by a granular mosaic of Stage 3B-Potassic orthoclase and plagioclase cores have been strongly chlorite-illite altered. Sample 28/385.

**Plate 6.7 G:** XPL photomicrograph of a Stage 3B-potassic vein that has cross-cut the Quan Porphyry. A broad subhedral perthite rind projects euhedral faces into an unmineralised quartz core. Plagioclase cores in the Quan Porphyry have been altered to Stage 3C sericite and Stage 4 clay (both after chlorite?). Sample 28/448.

## ALTERATION

overprinted the Stage 3B quartz stockwork. During Stage 3C, miarolitic cavities within the Bufu Syenite were filled by calcite, chalcopryrite and pyrite (Plates 6.10A & B). Stage 3C sphalerite-galena-pyrite trails crosscut the Tunja Monzonite, Quan Porphyry and Bufu Syenite. Stage 3C sulphides and calcite also locally occur within the Bufu Syenite, infilling miarolitic cavities (Plate 6.10A). This period of hydrothermal activity was disrupted by at least one period of brittle faulting (described below).

### *Late Stage 3C sericite-quartz brecciation*

Late during the development of the Stage 3C carbonate-sericite alteration system, brecciation resulted in the disruption of most of the Bugoy Pegmatite, forming a distinctive quartz-fragment breccia in the core of Dinkidi (Figure 6.6; Plates 4.5D & 6.10C). This clast-supported breccia consists of >95% angular quartz fragments (Plate 6.10D). There is minor rock flour matrix (1-5%), which has been replaced by Stage 3C calcite  $\pm$ sericite, Stage 4 illite and Stage 5 laumontite-stilbite (Plate 6.10E). The quartz clasts are up to 12 cm in diameter, which is wider than most Stage 3 quartz veins, and locally contain intergrowths of large, euhedral crystals of actinolite (Plate 6.6D), K-feldspar, apatite, and magnetite. These clasts have textures identical to the Bugoy Pegmatite (eg Plates 6.5A and 6.6C), which is interpreted to be their source. Abundant angular fragments of sericite, chalcopryrite and pyrite are also present (Plate 6.15F), with the chalcopryrite resulting in local high Cu-Au grades in the breccia.

Although the breccia was originally considered to be hydrothermal in origin (eg Wolfe *et al.*, 1999) its angular, clast-supported nature, presence of rock flour, uncommon weak tectonic fabric (Plate 6.10D), abundance of fine-grained angular fragments in the matrix (eg Plate 6.10F), *in situ* jigsaw-fit brecciation and the scarcity of hydrothermal cement all suggests a tectonic origin. The coarse-grained nature of the quartz fragments, and the scarcity of host rock clasts, indicate that the protolith for the quartz-fragment breccia was not the Stage 3 quartz vein stockwork. Instead, it is interpreted to have been a body of massive, coarse-grained quartz $\pm$ actinolite, which contained high-grade sulphide mineralisation and which was weakly sericite-altered (i.e. Bugoy Pegmatite). The presence of abundant secondary calcite and sericite in the matrix, which have been overprinted by Stage 4 argillic alteration, indicates a late Stage 3C timing for the quartz fragment breccia.



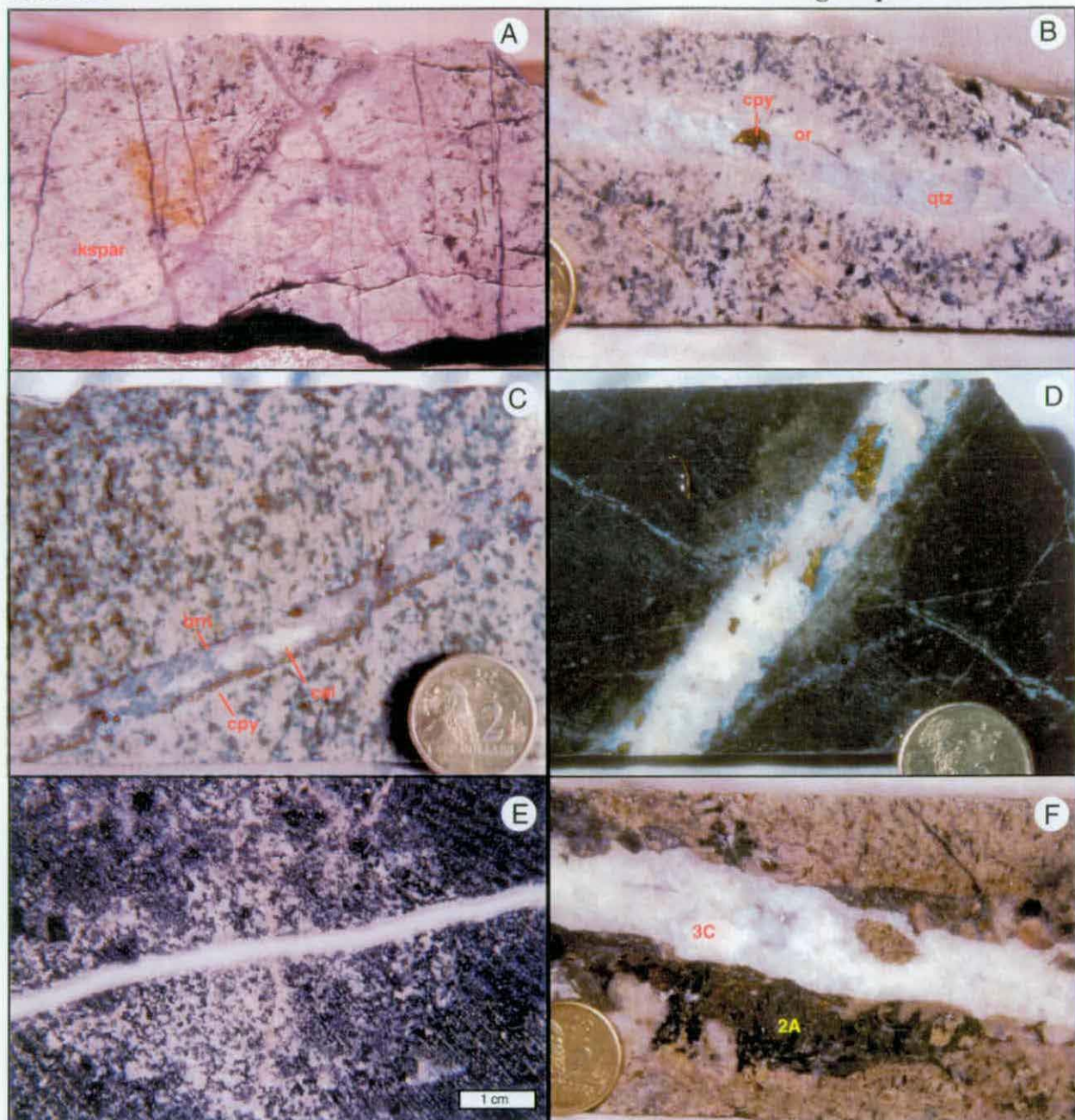


**Plate 6.8 A:** Early unmineralised 'wispy' Stage 3 grey quartz veins associated with orthoclase flooding of the Tunja Monzonite. The veins lack the distinctive perthite rind of Stage 3B-Potassic veins. Location DDH 50/564m. Drillcore 4.7 cm wide.

**Plate 6.8 B:** Early Stage 3B quartz vein with a well-developed orthoclase alteration halo and minor chalcopyrite that has cross-cut the Tunja Monzonite.

**Plate 6.8 C:** Typical Stage 3B quartz-calcite-chalcopyrite vein cross-cutting the Tunja Monzonite. 3B veins consist of subhedral to anhedral clear to milky quartz, with minor apatite and sphene. Interstitial spaces within, and fractures through the quartz are filled by calcite, chalcopyrite, pyrite or rare bornite. The chalcopyrite and bornite contain rare sphalerite and native Au inclusions and have commonly been partially replaced by chalcocite. Sample 25/223.

**Plate 6.8 D:** Stage 3B milky quartz-calcite-chalcopyrite vein, with a weak sericite alteration halo that has overprinted a biotite- and magnetite-altered diorite. This vein is typical of the Stage 3B veins that are distal to the quartz stockwork

**Plate 6.8 E:** Distal, unmineralised quartz veinlet, with a chalcedony core, cross-cutting a monzodiorite. These veinlets are the most distal expression of the quartz stockwork, extending up to 250 metres from the core of the system and merging with a distal propylitic halo of strong pyrite-epidote veining and patchy strong epidote alteration. Location DDH 43/537m

**Plate 6.8 F:** Unmineralised Stage 3C calcite vein, which has cross-cut an earlier formed diopside-orthoclase 2A vein (which has been partially replaced by a Stage 3 chalcopyrite-actinolite-quartz assemblage).

## ALTERATION

### Stage 4 argillic alteration

The Tunja Monzonite, Quan Porphyry and Bufu Syenite have undergone widespread, selectively pervasive intermediate argillic alteration (Plates 6.11B, C & D). The mineralogy of the argillic alteration assemblage was determined using PIMA and whole rock XRD analysis. Illite and kaolinite have replaced Stage 3 sericite and calcite (Plates 6.10C & D), with illite alteration developed only in samples that contained Stage 3B sericite as a precursor.

Although clay dusting of plagioclase cores is common throughout the Dinkidi Stock, argillic and advanced argillic alteration is restricted to the near surface environment, along Dinkidi Ridge (Plate 6.11A). Patchy advanced argillic alteration (kaolinite±pyrophyllite), and minor silicification, were observed in samples collected from Dinkidi ridge, but these assemblages do not extend below the 2700 RL or extend into the surrounding diorites (Figure 6.7). Illite and kaolinite within this shallow, near-surface assemblage have typically been weathered to montmorillonite.

### Stage 5 Zeolite assemblage

Zeolite veins, rock flour-filled fractures and a zeolite-cemented breccia characterise the final stage of hydrothermal activity at Dinkidi (Plates 4.5E, 6.11F, 6.12A & B). Zeolite minerals were identified using electron microprobe and XRD analyses of mineral separates from individual veins. The laumontite-stilbite-chabazite-clinoptilolite veins have cut argillic alteration (Plate 6.12E), and are associated with a widespread chlorite-calcite alteration assemblage (Plate 6.12F). The Stage 5 mineral assemblages are unmineralised, only containing minor pyrite. The zeolite-cemented tensional gashes and breccias are interpreted to have formed during faulting along the Biak Shear Zone, located at the northern end of Dinkidi (Figure 6.8). The Biak Shear is an offshoot of the F3 Didipio Valley Fault (Figure 3.1). The shear zone is characterised by the intense development of zeolite-calcite veins and moderate carbonate-chlorite alteration (Plates 4.5F & 6.17A).

#### *Zeolite veins*

Unmineralised clear, cream, grey to pale orange Stage 5 zeolite veins typically have a sigmoidal or en-echelon geometry (eg Plate 6.12A), consistent with a tectonic origin. The veins consist of stilbite ± laumontite or, rarely, chabazite. The vein margins are typically unaltered (minor weak calcite alteration has been noted locally). The zeolite veins are



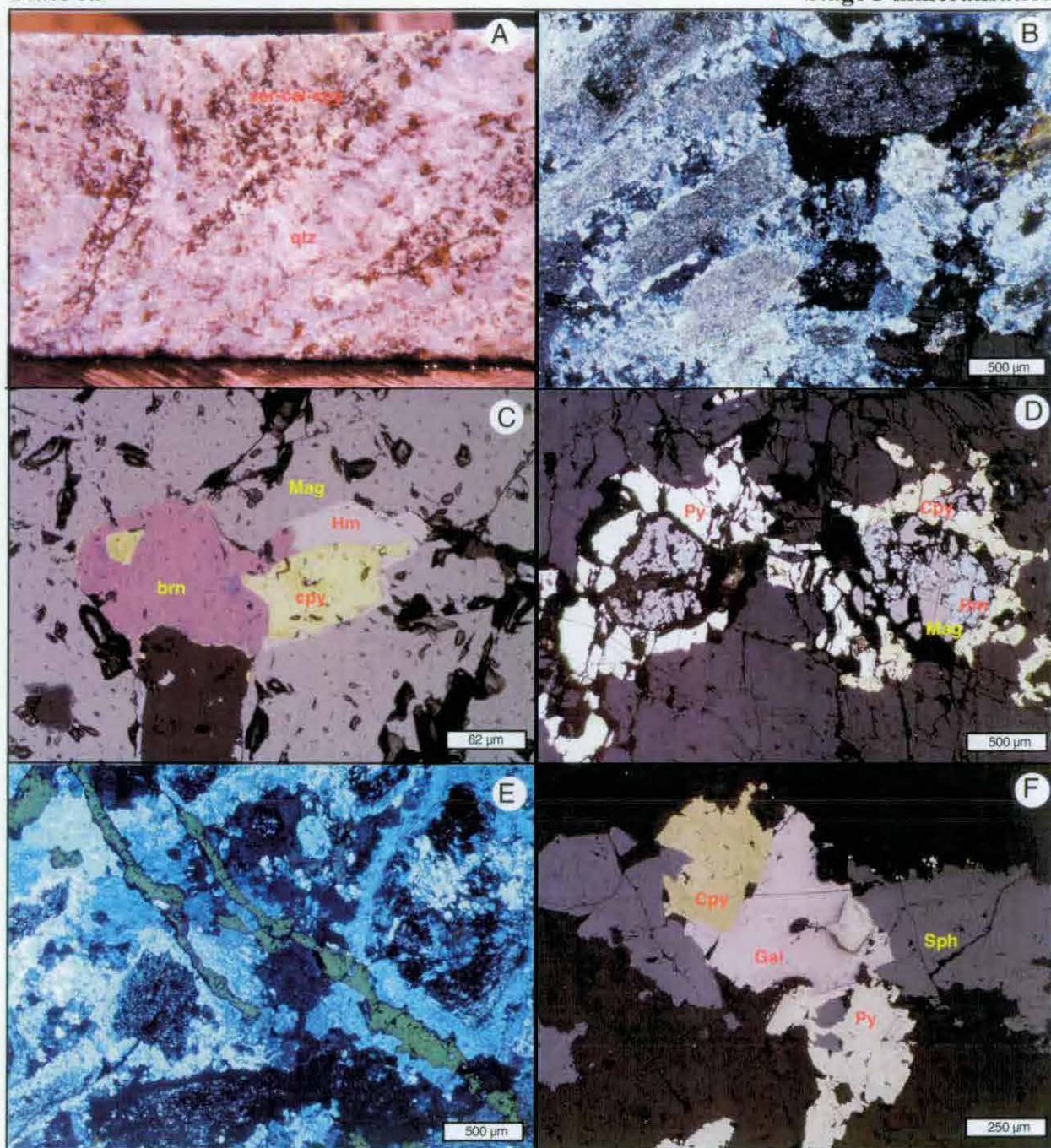


**Plate 6.9 A:** Stage 3B quartz stockwork associated with intense associated sericite-carbonate alteration and disseminated sulphide mineralisation. This sample is representative of the main quartz stockwork in the core of Dinkidi. (Figure 6.6) and is associated with most of the low-grade Cu-Au mineralisation at Dinkidi. Despite the late timing of the sulphides and carbonate, they only occur in the vicinity of the Stage 3B quartz veins, which is interpreted to indicate a genetic relationship. Location 69/297m

**Plate 6.9 B:** Sericite-altered plagioclase crystals. Early-formed K-feldspar rinds have not been altered during the sericite alteration event. Sericite-calcite alteration also overprints Stage 3A and 3B-potassic actinolite to K-feldspar alteration assemblages. Sample 60/447.

**Plate 6.9 C:** Stage 3B chalcopyrite-bornite-hematite hosted within a Stage 2 magnetite grain. Alteration of magnetite to hematite by the chalcopyrite-hematite stable Stage 3B fluid is interpreted to have reduced the fluid, leading to deposition of bornite. Stage 3B hematite has commonly replaced Stage 1, 2 and 3A magnetite.

**Plate 6.9 D:** Late Stage 3B pyrite-chalcopyrite surrounding Stage 2 magnetite. The deposition of Stage 3B sulphides is associated with hematite alteration of magnetite. Reduction of the chalcopyrite-stable fluid by alteration of magnetite may have promoted the deposition of pyrite. Sample 34/370.

**Plate 6.9 E:** Stage 3B chalcopyrite trail in sericite- and carbonate-altered Quen Porphyry. The sulphides cross-cut and replace sericite-altered plagioclase cores. Stage 3B copper sulphides contain common sphalerite inclusions and rare native Au and tennantite inclusions. Sample 54/489

**Plate 6.9 F:** Late Stage 3B sphalerite-chalcopyrite-galena trail. Galena and chalcopyrite have nucleated on pyrite grains in the wallrock. Pyrite, sphalerite, galena and rare enargite are typically found in late-stage sulphide trails. Sample 28/131.



## ALTERATION

overprinted locally by late calcite and chlorite alteration. Chabazite and clinoptilolite are also present in the interstitial spaces of shallow Stage 1 and 2 hydrothermal assemblages, possibly as a replacement of anhydrite (or analcite?).

Zeolite veins at Dinkidi are identical to veins within the Biak Shear Zone (Figure 6.7). The shear zone is typically 30 to 80 meters in width and contains 1 to 15 wide blocks of unmineralised but strongly zeolite±calcite veined and brecciated diorite and Tunja Monzonite. These blocks are typically separated by strongly clay-carbonate-chlorite altered fault zones.

### *'Mud veins'*

The laumontite-stilbite veins locally contain abundant laminated to massive aggregates of rock flour. These earthy green-grey fine-grained 'mud veins' have infilled tensional gashes throughout the Dinkidi Stock (Plate 6.11F). The mud veins consist of rock, feldspar and quartz fragments hosted in a fine-grained altered rock flour matrix, together with stilbite±laumontite needles, which have filled cavities. The rock flour matrix has been commonly calcite-altered. The 'mud' veins are commonly surrounded by a halo of weak selectively pervasive carbonate alteration. The layered mud is interpreted to have formed via gravitational settling of fine-grained clastic particles abraded from the fracture walls either during or after tectonism.

### *Zeolite-matrix lithic breccias*

The core of the Dinkidi deposit has been strongly disrupted by zeolite-cemented lithic breccias (Plates 4.5F & 6.12B, C & D). The breccia zones have apparent thicknesses of 10 to 80 meters, but locally occur as 1-2 meter wide fault zones. The breccias are dominated by lithic clasts of the surrounding host rock (i.e. minimal clast transport). The zeolite-cemented breccia has a gradational boundary with the Bugoy quartz-fragment breccia, and with other wall rocks. Angular clasts of clay- and sericite-altered Tunja Monzonite, Quan Porphyry, Bufu Syenite and quartz vein fragments are cemented by stilbite ± laumontite (Plate 6.12C & D). Zeolite grains have nucleated on the clast margins and project into abundant calcite-filled cavities (eg Plate 6.17D). Angular fragments of chalcopyrite, pyrite and mineralised Stage 3 quartz veins occur locally.

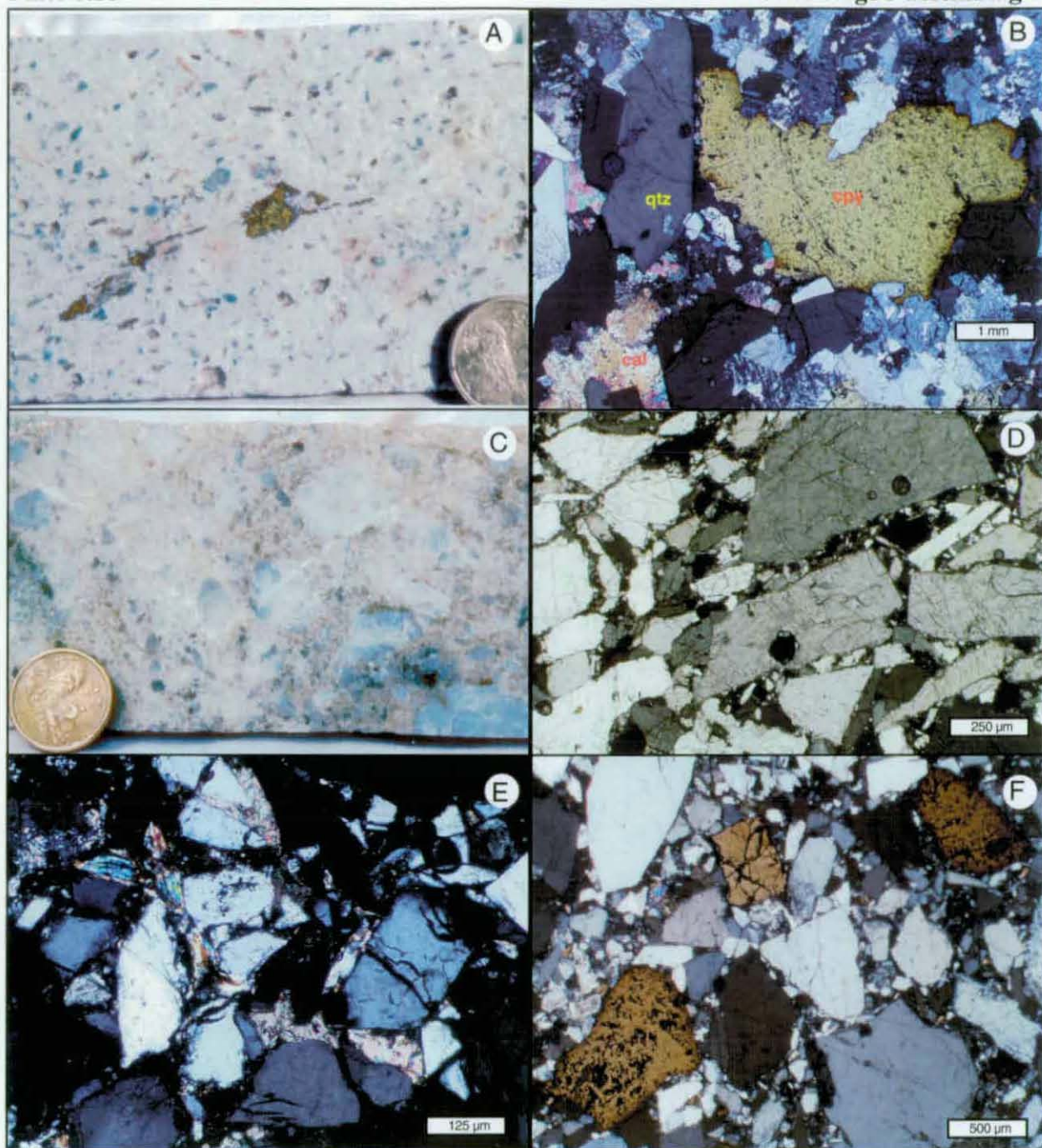


**Plate 6.10 A:** Chalcopyrite and calcite within a miarolitic cavity in the Bufu Syenite. The Bufu Syenite also contains unmineralised grey quartz veins and irregular quartz trails. Sample 49/555.

**Plate 6.10 B:** Stage 3C chalcopyrite-calcite infilling a quartz-lined miarolitic cavity within the Bufu Syenite (see plate 6.10A). Sample 49/555.

**Plate 6.10 C:** Typical Bugoy quartz fragment breccia. Quartz clasts are hosted within a cream-coloured sericite-and calcite-altered rockflour matrix. In addition to quartz+actinolite-feldspar clasts, single mineral clasts of perthite, sericite and sulphide, and clasts of quartz-flooded Bufu Syenite (with euhedral perthite 'grains' enclosed in a coarse-grained quartz groundmass) have also been observed. See also Plates 4.5D and 6.6D.

**Plate 6.10 D:** XPL photomicrograph of the Bugoy quartz fragment breccia. The sample consists of angular clasts that are weakly aligned. The crowded fragment-supported framework contains only 1-5% calcite-sericite matrix (as replacement of rockflour). The jigsaw fit of optically continuous clasts indicates in situ fracturing of massive quartz, with little, or no transport of fragments. Sample 34/393

**Plate 6.10 E:** Fine-grained sericite-calcite cement in the Bugoy breccia. Sericite and calcite are interpreted to have replaced a rock-flour matrix. Sample 34/393.

**Plate 6.10 F:** Angular chalcopyrite fragments in the quartz-fragment breccia. Sample 34/393

## ALTERATION

### ***Retrograde calcite-chlorite alteration***

A widespread, unmineralised calcite-chlorite alteration assemblage has overprinted all earlier formed hydrothermal assemblages at Dinkidi. The matrix of the Stage 3C quartz-fragment breccias, Stage 5 lithic-fragment breccias and the Stage 5 zeolite veins have been replaced by calcite and chlorite. Primary mafic sites throughout the Dinkidi Stock and surrounding diorites are commonly replaced by calcite-rutile or by dull green ferroan chlorite (Plate 6.12E). This alteration may reflect weak regional chlorite-zeolite facies alteration or a late stage component of the Dinkidi System.

## REGIONAL ALTERATION ASSEMBLAGES

This section describes the hydrothermal assemblages observed in the region surrounding the Dinkidi deposit, and is based on mapping and the logging of regional drill holes. Figure 6.8 outlines the distribution of the four main alteration assemblages that occur in the Didipio region. These assemblages have all been overprinted by low-grade regional chlorite-zeolite to phrenite-pumpellite metamorphism.

### **Contact metamorphism**

The intrusion of the initial dioritic phases of the Didipio Igneous Complex is associated with a narrow contact metamorphic aureole within the surrounding Mamparang and Upper Mamparang Formations. Volcaniclastic units in the Mamparang Formation have been recrystallised to a cordierite±biotite spotted hornfels, which extends up to 150 meters from the contact with the Didipio Igneous Complex (Figure 6.2). The hornfels assemblage is typically overprinted by intense selectively pervasive to patchy pervasive epidote-chlorite alteration, which forms a zone that extends at least 300 meters from the intrusive contact. Contact metamorphism within the trachytes of the Upper Mamparang Formation is less distinct, comprising a diffuse zone of selectively pervasive biotite alteration that extends at least 100 meters from the contact with the diorites. No sulphide mineralisation or veins appear to be associated with this metamorphic event.

### **Surong Monzonite K-silicate alteration**

The Surong Monzonite pluton is surrounded by a broad halo of K-silicate alteration (Figure 6.8), subeconomic Cu-Au mineralisation and small, weakly mineralised quartz-monzonite dykes. The gabbros, diorites and monzodiorites within this ~200 metres wide halo, and the marginal phases of the Surong Monzonite, have been altered to a selectively



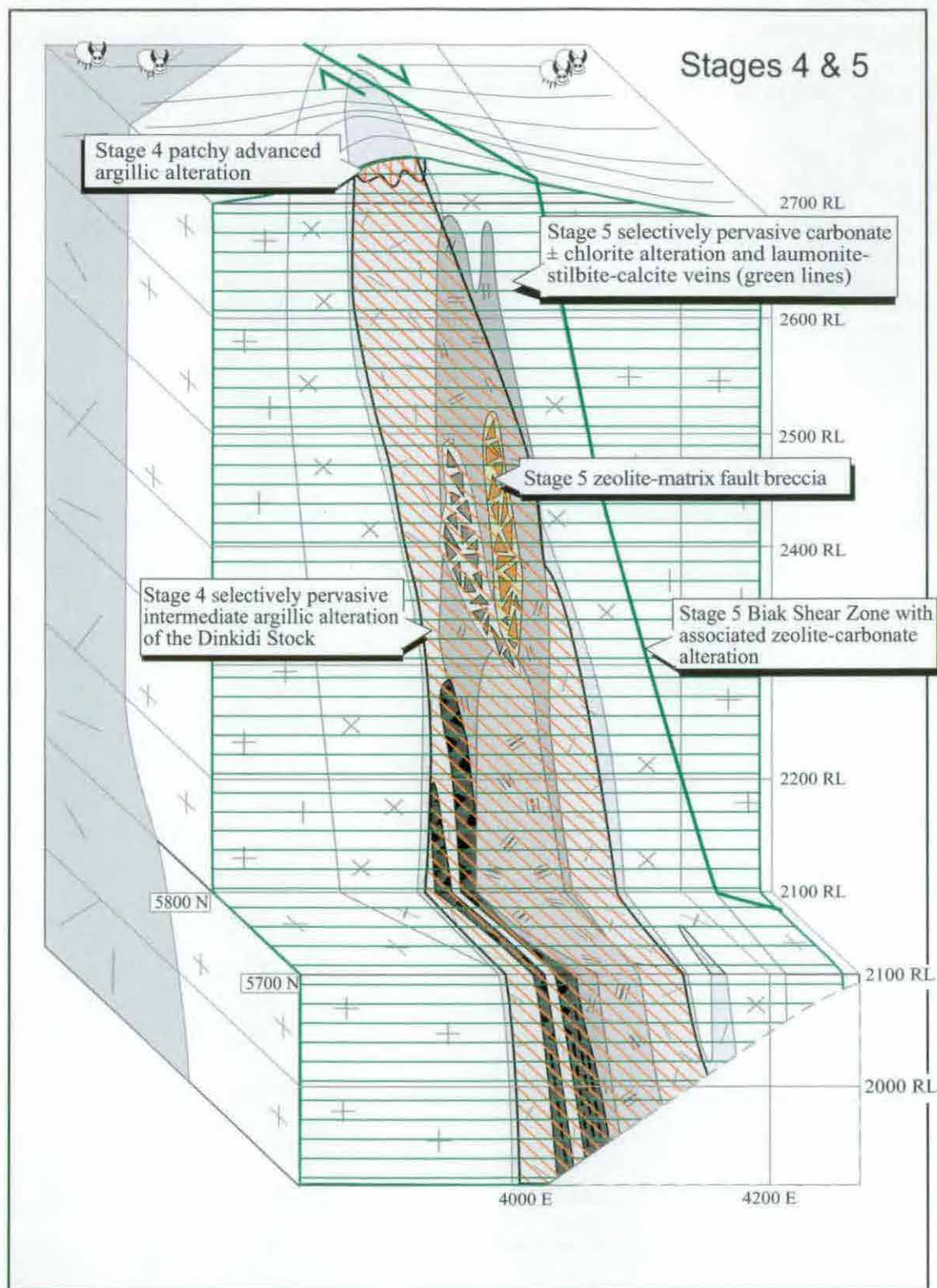


**Figure 6.7:** Approximate distribution of Stage 4 and 5 hydrothermal assemblages. Stage 3 sericite-altered plagioclase cores are selectively replaced by Stage 4 intermediate argillic clays (predominately illite) throughout the Dinkidi Stock. Advanced argillic alteration, although responsible for the formation of the Dinkidi Ridge, is constrained to the surface, above the 2700 RL. Widespread zeolite (laumontite-stilbite) and calcite veins and breccias and calcite, chlorite and zeolite (stilbite-chabazite) alteration of Stage 5, the final hydrothermal stage recorded at Dinkidi, is associated with the emplacement of the Biak Shear and other faults, through the Dinkidi Stock.

## ALTERATION

pervasive biotite±magnetite-K-feldspar assemblage. Spotty biotite alteration, consisting of coarse-grained, strongly red-brown pleochroic biotite, has replaced and embayed primary clinopyroxene in the diorites (Plates 3.5D & 3.6D). The diorites and gabbros within this zone have also undergone patchy K-feldspar flooding, contain K-feldspar±anhydrite or biotite veinlets and have elevated 'background' copper concentrations (200-400 ppm). Subeconomic disseminated chalcopyrite-pyrite mineralisation in and around the margins of the Surong pluton is associated with K-silicate veining, commonly centred on 1-20 meter wide, biotite- to quartz-monzonite dykes (e.g. the San Pedro, Century Eggs and Midnight J prospects; Figure 6.8). Outside, and overprinting the K-silicate alteration halo, patchy epidote-chlorite-pyrite alteration of mafic minerals has occurred within the mafic intrusions. This propylitic assemblage is considered to be a retrograde or distal component of the weakly mineralised Surong Monzonite hydrothermal system, and may have formed from heated groundwater.

### **Porphyry-style mineralisation**

Apart from Dinkidi, porphyry-style Au-Cu mineralisation in the Didipio Igneous Complex also occurs at the True Blue prospect, which is interpreted to be the displaced northern segment of the Dinkidi Stock, and is located 700 meters to the east of Dinkidi Ridge (Figure 6.8). The True Blue prospect contains the same hydrothermal assemblages as the Dinkidi Deposit. Sub-economic porphyry mineralisation is also located 1 km to the south of the map area (Figure 6.8) at the D'Fox prospect. Allowing for offsets by F2 and F3 faults, all three prospects, appear to have been emplaced along the same NW-trending structure (Figure 6.8).

### **Argillic alteration**

The youngest major regional alteration assemblage preserved in the Didipio region is the extensive intermediate- to advanced-argillic alteration 'blanket'. This assemblage has been preserved on the topographic heights of the northwestern to eastern border of the map area (Figure 6.8). It also occurs as an overprint within the core of the Didipio Igneous Complex, along small structurally controlled argillic alteration zones. Clay minerals in this alteration assemblage have been identified by whole rock XRD and PIMA analyses.

Small zones of subeconomic Cu-Au mineralisation are associated with pyrite-silica altered fault zones and low-sulphidation epithermal quartz-carbonate veins (eg the Chinni-Chinga



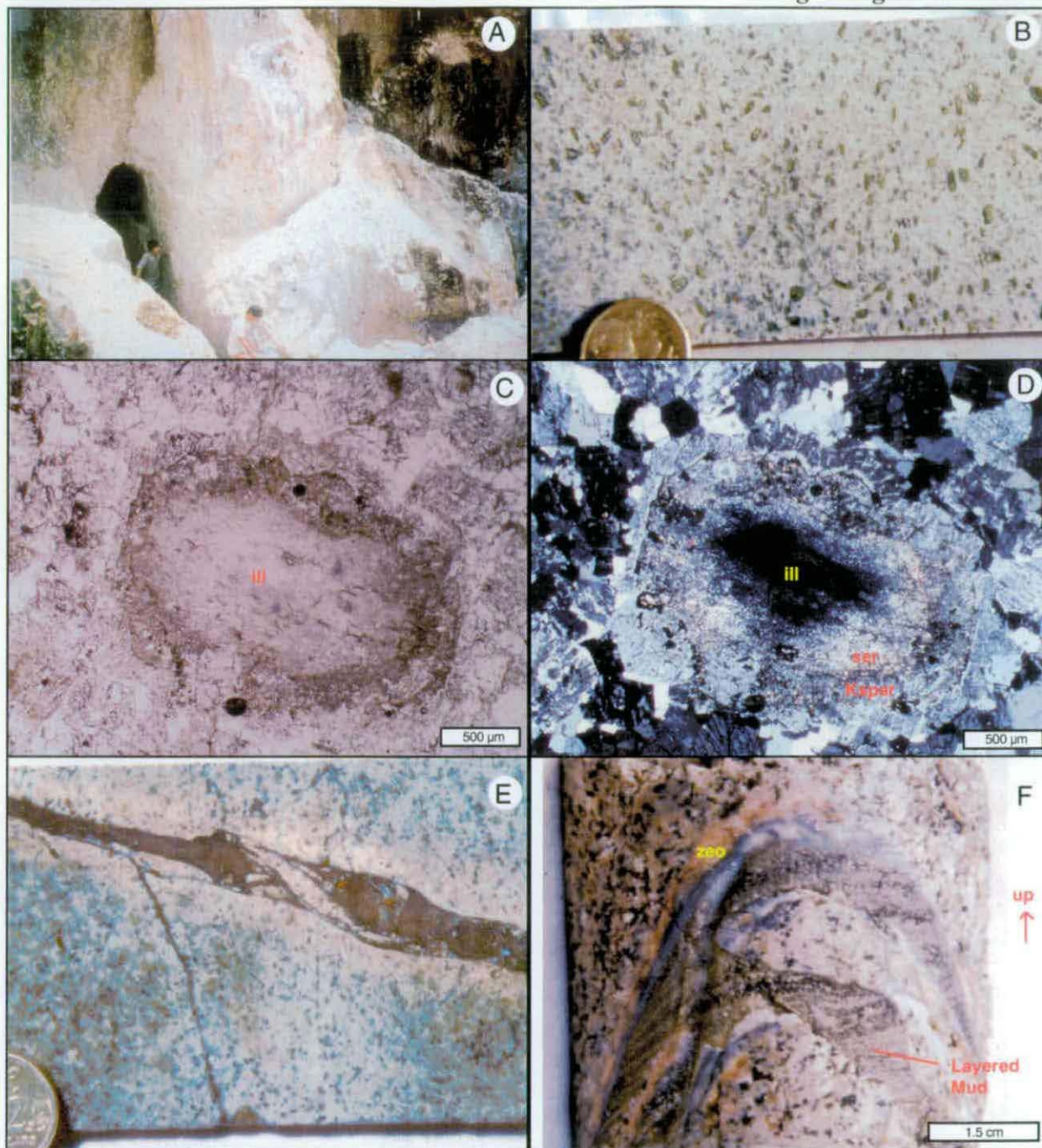


**Plate 6.11 A:** Advanced argillic alteration at the surface of Dinkidi Ridge. Strong advanced argillic alteration at Dinkidi is only patchily developed at the surface. A network of tunnels within the advanced argillic alteration follow the relic Stage 3B quartz stockwork, with rock chip samples containing native gold and assays of up to 1g/t Au are recorded. Photo courtesy Climax-Arimco.

**Plate 6.11 B:** Typical selectively pervasive pale-green illite alteration of plagioclase cores within the Quan Porphyry.

**Plate 6.11 C:** Illite-altered plagioclase phenocryst. Illite has only altered the sericitised core of this crystal. PPL. Sample 49/555.

**Plate 6.11 D:** XPL photomicrograph of Plate 6.16C. Illite has replaced the Stage 3B sericite-altered plagioclase core, leaving the primary K-feldspar rind intact.

**Plate 6.11 E:** Weakly laminated Stage 5 'mud vein'.

**Plate 6.11 F:** Typical Stage 5 orange and blue-grey zeolite fracture fill (zeo), reopened by a finely-laminated Stage 5 'mud vein' (mud). The laminations are perpendicular to the drillcore axis, and are interpreted to have formed by hydrothermally altered mud settling downwards through the fracture ("neptunian dyke"). Sample 53/375.



## ALTERATION

prospect; Figure 6.8). The hydrothermal alteration associated with this stage consists of early-formed intermediate argillic alteration (selectively pervasive illite±chlorite-quartz-sericite) to bleached white pockets of advanced argillic alteration (pervasive illite-kaolinite-silica and kaolinite-pyrophyllite ± rare dickite). These hydrothermal assemblages have then been partially to completely weathered to smectite (montmorillonite) in near surface exposures. The intermediate argillic and argillic alteration zones host abundant pyrite veinlets, which have been typically altered and weathered to limonite±jarosite-magnesium oxides, and host small areas of silicification. Zones of advanced argillic alteration contain local pockets of pockets of vuggy silica and rare quartz-alunite. All of the regional argillic alteration assemblages have a strong lithological control, being well developed in the felsic Surong Monzonite, Tunja Monzonite and Upper Mamparang Formation, while the more mafic diorites and andesites tend to have preserved earlier K-silicate and propylitic alteration. The advanced argillic alteration preserved on the surface of Dinkidi Ridge is interpreted to be part of this regional argillic alteration assemblage.

Most of the late-stage andesite dykes of the Didipio Igneous Complex have not been affected by the argillic alteration event. This is interpreted to indicate that most argillic alteration occurred after the emplacement of the Dinkidi Stock, but prior to the cessation of magmatic activity in the region. However, there are illite-carbonate-kaolinite (?) altered andesite, trachyandesite and trachyte clasts that occur in otherwise unaltered volcanoclastic units of both the Mamparang Formation and Upper Mamparang Formation. This suggests that an argillic alteration event occurred before the emplacement of the Didipio Igneous Complex. The extent and significance of this early event is unknown.

Mineralisation associated with the regional argillic alteration assemblage consists of a 'high sulphidation' quartz-pyrite assemblage and a 'low sulphidation' quartz-calcite assemblage. 'Low sulphidation' veins are typically 10-70 cm thick, and have crustiform textures. The veins are dominated by quartz and chalcedony veins and contain local patches of silicified bladed calcite and sub-economic Au-Ag grades. Some fault-zones within the Didipio Igneous Complex contain rare 'high sulphidation' style quartz-pyrite Cu-Au mineralisation. Both styles of epithermal mineralisation are preserved beneath the main argillic alteration 'blanket' in the topographic lows of the map area, and are hosted within the Surong Monzonite. At Dinkidi, the exposure of the Tunja Monzonite along the Dinkidi ridge is strongly argillically altered, and contains pockets of advanced argillic

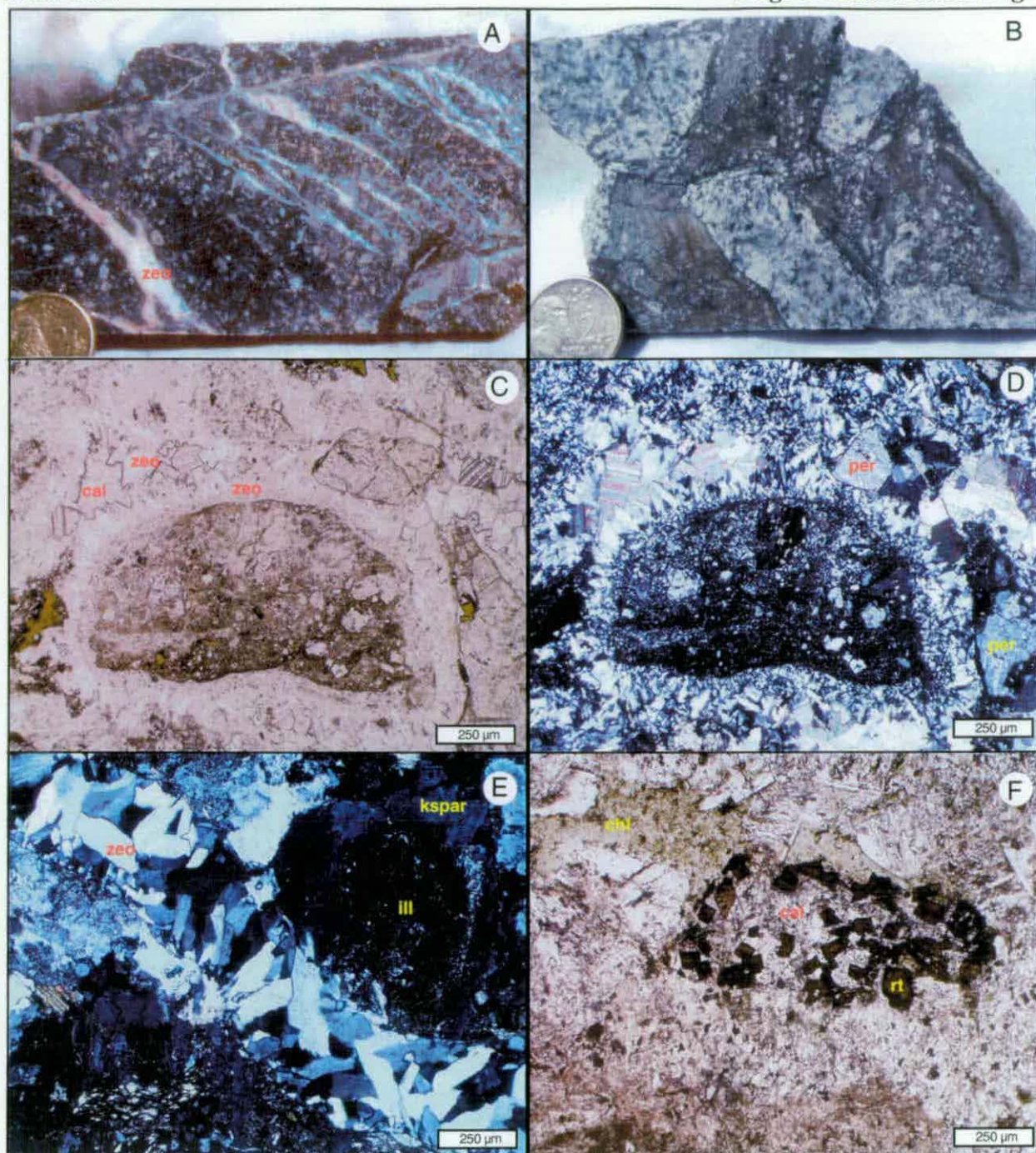


**Plate 6.12 A:** Zeolite (zeo) and calcite-filled Stage 5 veins, with a typical sigmoidal geometry, hosted in a monzodiorite block within the Biak Shear zone.

**Plate 6.12 B:** Stage 5 zeolite-cemented lithic breccia. Angular clay-altered Tunja Clasts are hosted within a fine-grained zeolite-rock flour cement and matrix, which displays a weak fabric.

**Plate 6.12 C:** PPL photomicrograph of a stage 5 zeolite-cemented lithic breccia. Clasts include perthite fragments (containing Stage 3 chalcopryite) and re-brecciated zeolite breccia. Sample 33/216.

**Plate 6.12 D:** XPL photomicrograph of plate 6.17C. The zeolite groundmass hosts abundant calcite-filled cavities, with zeolites projecting euhedral faces off clasts and into cavities.

**Plate 6.12 E:** Typical laumontite-stilbite vein (zeo) cross-cutting Stage 4 clay-altered plagioclase. XPL. Sample 49/470.

**Plate 6.12 F:** Late Stage 5 chlorite-calcite-rutile alteration of biotite within the Tunja Monzonite. Sample 53/768.

## ALTERATION

alteration. Here, the advanced argillic alteration assemblage has overprinted the porphyry quartz stockwork and contains relic fine grained native gold with grades of up to 1 g/t. This shallow-level gold mineralisation, hosted in soft easily minable clays, initially attracted prospectors to Dinkidi in the mid-1970's (Plate 6.11A). More detailed mapping is required to discriminate clay alteration zones potentially associated with high sulphidation and low sulphidation mineralisation styles, and those associated with barren steam-heated blankets in the Didipio region.

## DISCUSSION

Based on the results of this study four main hydrothermal events are concluded to have affected the Didipio Igneous Complex:

- Early diorite-related contact metamorphism
- K-silicate alteration and weak Cu-Au mineralisation associated with the Surong Monzonite
- Ore-grade porphyry Cu-Au mineralisation related to intrusions within the Dinkidi Stock
- Late-stage argillic, carbonate and zeolite alteration with weak associated epithermal mineralisation

At the Dinkidi deposit, repeated intrusive and hydrothermal activity were localised along a northwest-trending structural corridor adjacent to the Surong Monzonite, forming a multiphase and mineralised monzonite to syenite stock (Figure 4.1). Each of the four main intrusions that comprise the Dinkidi Stock is associated with a discrete hydrothermal event:

- Stage 1 K-silicate alteration surrounds the Tunja Monzonite,
- A strongly Au-Cu mineralised Stage 2 calc-potassic alteration assemblage occurs within & around the Balut Dyke
- The Stage 3 quartz stockwork is spatially and temporally associated with the Bufu Syenite.

These porphyry-style hydrothermal assemblages have been overprinted by two late-stage district-scale hydrothermal assemblages:

- Stage 4 argillic alteration
- Stage 5 zeolite veining and brecciation

The Dinkidi hydrothermal system is interpreted to have been disrupted by two periods of tectonic brecciation. Late during Stage 3, faulting disrupted the Bugoy Pegmatite, forming the quartz-fragment breccia with a sericite-bearing cement. Stage 5 brecciation was triggered by 700m of strike-slip dextral movement of the Biak Shear Zone, forming a



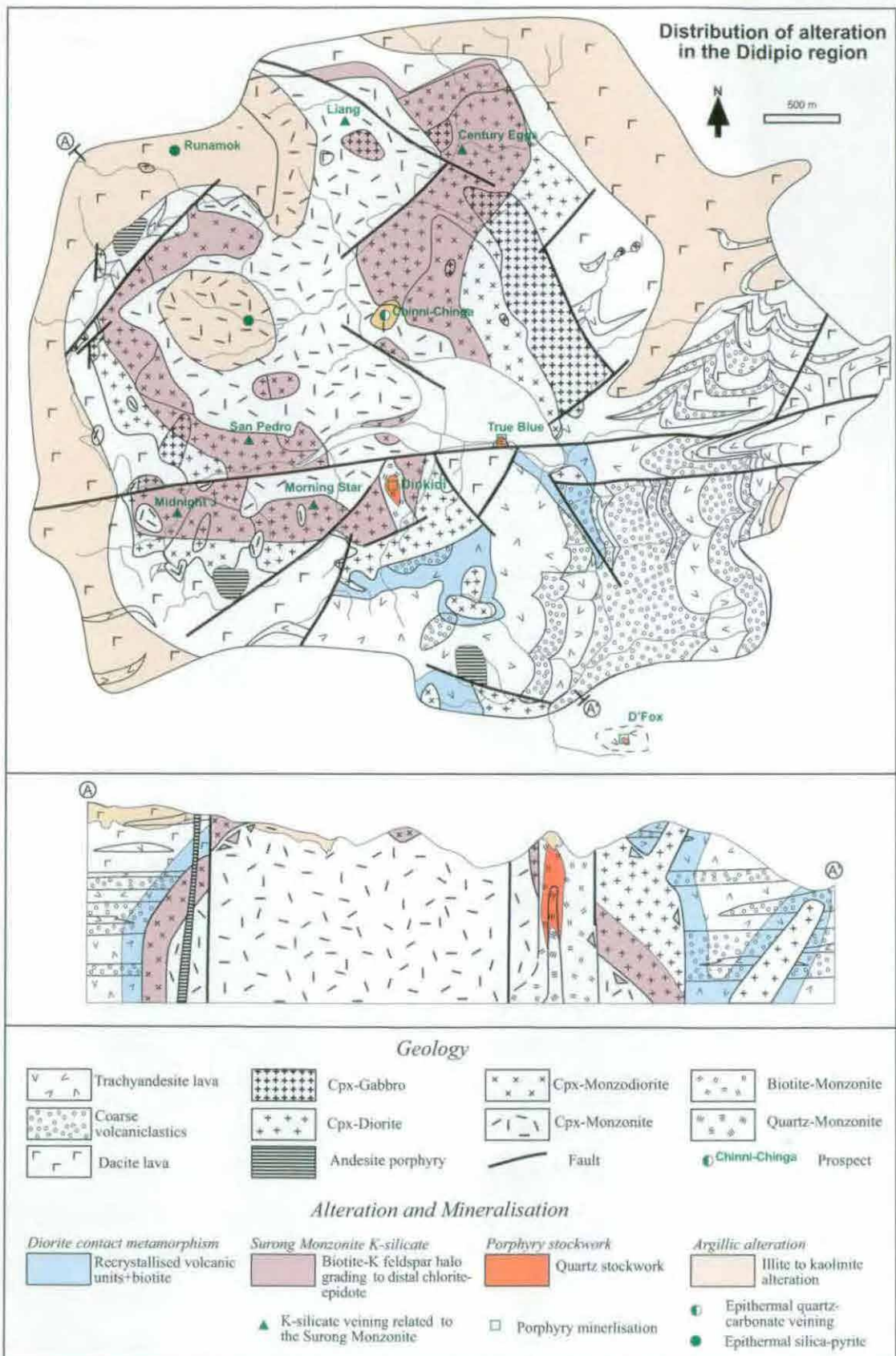


**Figure 6.8:** Schematic distribution of alteration in the Didipio region. Erosion has exposed the deeper diorite contact metamorphism in the southwestern section of the map area and has preserved argillic alteration in the topographic highs of the western and northern sections.

## ALTERATION

lithic-fragment breccia, with a zeolite groundmass, and displacing the True Blue prospect east of Dinkidi.

Repeated cycles of volatile build up and melt-volatile release appear to have occurred within the fractionating Didipio Igneous Complex. The early hydrothermal assemblages that are developed in the Didipio region reflect the igneous rock composition and therefore, the degree of fractionation of the parent melt:

- The emplacement of the 'anhydrous' clinopyroxene-diorites is associated with biotite-cordierite contact metamorphism and 'dry' recrystallisation.
- Volumes of magmatic hydrothermal fluid are believed to have been released during the development of the biotite-magnetite±orthoclase K-silicate alteration halo and weak Cu-Au mineralisation around the Surong and Tunja Monzonites. This hydrothermal assemblage reflects the biotite- and orthoclase-bearing composition of the monzonites.
- The emplacement of late-stage syenite melts in the Dinkidi Stock was associated with the most intense hydrothermal activity. The diopside-phyric Balut Dyke is surrounded by a calc-potassic hydrothermal assemblage.
- The highly fractionated quartz-bearing melt of the Bufu Syenite produced a quartz-rich vein assemblage.

The first stage of ore deposition at Dinkidi is associated with the intrusion of the variably-textured Balut Dyke clinopyroxene-syenite and the deposition of quartz-free calc-potassic hydrothermal assemblage. The diopside-perthite-magnetite composition of the early Stage 2A vein-dykes mimic the primary igneous composition of the Balut Dyke. This assemblage was overprinted by the Stage 2B and 2C actinolite-perthite-bornite vein stockwork. High-grade Stage 2 Au-Cu mineralisation is associated with a narrow zone of bornite-orthoclase intergrowths that appear to have been emplaced along the same structure utilised by the Balut Dyke. The high Au grades and lack of quartz in the Stage 2 hydrothermal assemblage is typical of most silica-undersaturated, and many silica-saturated, alkaline porphyry systems (Lang *et al.*, 1995a). Similar actinolite-orthoclase bearing, quartz-deficient assemblages have been recorded at Galore Creek (bornite ± chalcopyrite in albite-diopside-epidote and K-feldspar-biotite-magnetite assemblages; Ennes *et al.*, 1995; Staney *et al.*, 1995) and Mt Polley (chalcopyrite-bornite in actinolite, biotite, albite and magnetite breccias; Frazer *et al.*, 1995). The Dinkidi deposit however, lacks the abundant epidote, garnet, scapolite and other common calc-alkaline 'skarn minerals' that typify British Columbian alkaline porphyry systems (eg Lang *et al.*, 1995a).

Stage 3A to 3B quartz stockwork and the massive quartz-actinolite body (the Bugoy 'Pegmatite') are interpreted to have formed during the emplacement of the Bufu Syenite. The Stage 3A vein assemblage has been overprinted by unmineralised Stage 3B-Potassic quartz-perthite veins (along the syenite margin of the Bufu), and by the main Stage 3B quartz-calcite-sulphide stockwork, with strong associated sericite-carbonate alteration and disseminated sulphide mineralisation. The abundance of Stage 3B veins gradually decreases away from the Bufu Syenite. The syenite itself only contains rare, irregular unmineralised quartz trails. This vein distribution, and the abundant trails of miarolitic cavities in the core of the intrusion (which provides textural evidence for volatile migration; Candela, 1997) is interpreted to indicate that the Bufu quartz syenite was the main conduit for the mineralising fluids during Stage 3B quartz stockwork formation. The Stage 3B assemblage then evolved into the calcite  $\pm$  quartz-sericite assemblage of Stage 3C. The Stage 3B quartz stockwork, with associated sericite-calcite-sulphide mineralisation, is typical of the mineralisation at many high-K to calc-alkaline Cu-Au porphyry systems, such as those at North Parkes, NSW (Heithersay & Walshe, 1995) and El Salvador (Gustafson & Hunt, 1975).

Selectively pervasive illite-kaolinite alteration formed throughout the Didipio region during Stage 4. Advanced argillic alteration also formed at this time, but was confined to the present day surface area of Dinkidi, and the topographic heights of the Didipio region, forming an overlying 'lithocap' (eg Sillitoe, 1995). Argillic alteration overprinting of porphyry mineralisation is common in many Philippine porphyry systems (eg Lepanto-Far Southeast; Arribas *et al.*, 1995; Hedenquest *et al.*, 1987; and numerous other examples described by Sillitoe & Gappe, 1984) but is rare in other alkaline porphyry systems (Lang *et al.*, 1995a). The development of advanced argillic alteration indicates the formation and influx of acidic fluids, which are commonly assumed to be the acidic condensates of magmatic vapour, possibly sourced from the degassing porphyry system (eg., Meyer & Hemley, 1967; Brimhall & Ghiorso, 1983; Sillitoe, 1995). The overprint of the Didipio Igneous Complex by strong argillic alteration and epithermal veins with shallow near-surface, open-space filling textures (eg bladed calcite) suggests that there was significant erosion and telescoping of alteration assemblage in the Didipio region (eg., Sillitoe, 1994). This erosion occurred between the cessation of Stage 3B porphyry mineralisation and the commencement of Stage 4 argillic alteration.



## ALTERATION

Stage 5 tectonism was associated with widespread zeolite (stilbite-laumontite-clinoptilolite-chabazite) veins, tensional gashes and breccias. These calcium zeolites are common hydrothermal zeolites in volcanic environments (eg the 'zeolite tuffs' found in Oregon, Gude & Sheppard, 1973; and the Roman Region of Italy, Gottardi & Obradovic, 1978), and a distal, retrograde zeolite assemblage (laumontite-apophyllite-calcite-chlorite) has been described from the Gaspé Porphyry Cu deposit in Canada (Allcock, 1977). Late-stage chabazite has also been described from the Panguna and Aitik (Eastoe, 1979; Bergman *et al.*, 2001) porphyry deposits. Within these systems the zeolite may display thermal zonation from high temperature laumontite (<280°C) to stilbite (<180°C) and low temperature chabazite (<150-200°C; Gottardi & Galli, 1985). The presence of zeolites in the Dinkidi system indicate that F3 faulting disrupted a low temperature hydrothermal system (280 to 80°C) that contained alkaline, bicarbonate fluids (Gottardi & Galli, 1985). These waters may have been drawn down into the Dinkidi Stock, precipitating zeolites as they were heated and/or mixed with Ca-bearing groundwater. Similar zeolites, with associated propylitic alteration, are common in the distal, shallow-level convection zones of geothermal systems (eg the Wairakei geothermal region, NZ; Steiner, 1977), at a distal setting to any argillic alteration. The zeolite assemblage indicates that the fluids responsible for Stage 4 argillic alteration had been diluted, cooled and neutralised by an influx of bicarbonate water. The late stage hydrothermal assemblages indicate there was a range of fluid compositions in the late-stage Didipio hydrothermal system, from acidic fluids responsible for argillic alteration and quartz-pyrite mineralisation, to low acidity high temperature fluids responsible for 'low sulphidation' quartz-carbonate veining, to neutral, low temperature fluids responsible for the zeolite assemblage. Warm groundwaters are still present at Didipio, as shown by the presence of hot springs (~60-80°C) 700 metres to the east of Dinkidi.

## SUMMARY

The hydrothermal history of Dinkidi records a distinctive switch from a quartz-free and gold-rich Stage 2 calc-potassic assemblage typical of alkaline porphyry systems, to a quartz-bearing Stage 3 stockwork assemblage that is typical of calc-alkaline to high-K porphyry systems. These compositional differences mimic the composition of the intrusions, with the clinopyroxene-bearing Balut Dyke being quartz-free, and the late-stage Bufu Syenite containing abundant primary quartz. This change in the hydrothermal mineral

assemblages therefore relates to the evolution of the fractionating parent melt, from a calcic silica-undersaturated diopside-stable melt, to a late-stage, clinopyroxene-free quartz-saturated melt, which was initially Ca and Fe-rich (Stage 3A actinolite-magnetite-quartz) then final Ca-Fe deficient (quartz-sericite). The physio-chemical conditions of the hydrothermal assemblages present at Dinkidi are investigated further in Chapter 7, fluid inclusions, and are discussed in Chapter 8, synthesis and genetic model.

# FLUID INCLUSIONS & SULPHUR ISOTOPES

## INTRODUCTION

This chapter presents the results of a fluid inclusion and sulphur isotope study on the Dinkidi deposit. The fluid inclusion study was used to characterise the fluids responsible for stockwork formation and mineralisation, using both microthermometric techniques and Proton-Induced X-Ray Emission (PIXE) analysis of inclusion compositions. Workable fluid inclusions were found only in Stage 2 apatite and Stage 3 quartz veins, the two mineralised vein stages at the deposit.

The sulphur isotope study of sulphides from the Dinkidi deposit was undertaken to characterise temporal variations in sulphide values, from Stage 2 to 3, in order to identify any changes in fluid compositions and/or sulphur sources. The sulphur isotope study has also been undertaken to examine the spatial variations in sulphide isotopic compositions in order to constrain possible depositional mechanisms.

## FLUID INCLUSIONS

### Methods

Petrographic observations and microthermometric measurements were made on doubly polished thick sections. A total of 20 plates were made, consisting of 4 samples of Stage 2C apatite and 16 samples of Stage 3 quartz, the later incorporating Stage 3A and 3B stockwork veins from both proximal & distal settings, and also the Bugoy Pegmatite. No workable fluid inclusions were observed in Stage 3 calcite or in Stage 5 zeolites. Microthermometric analyses were conducted on a Linkam MDS 600 Stage. The precision of the stage was calibrated against the melting point of water (0°C) and the critical point of water (374.1°C), using synthetic fluid inclusions manufactured by Syn-FliC. The precision of measured temperatures are  $\pm 1.0^\circ\text{C}$  for heating and  $\pm 0.3^\circ\text{C}$  for freezing.

Microthermometric analyses for liquid-rich fluid inclusions (Type LV; Figure 7.1) consisted of  $T_{h\text{vl}}$  (homogenisation of the fluid phase by vapour bubble disappearance),  $T_{m\text{H}_2\text{O}}$  (ice melting) and the temperature of first ice melting,  $T_e$  (eutectic temperature). Salinities were calculated using the equations of Bodnar *et al.* (1989a) from  $T_{m\text{H}_2\text{O}}$  and assume a simple NaCl-water system (equivalent NaCl wt%: 'wt% eq.NaCl').

Microthermometric analyses for hypersaline fluid inclusions (Type B; Figure 7.1) consisted of  $T_{m\text{NaCl}}$  (halite dissolution temperature;  $T_{h\text{hl}}$  where this resulted in inclusion homogenisation) and  $T_{h\text{vl}}$  (temperature of vapour phase disappearance). The melting temperature of clathrate ( $T_c$ ) was measured for rare CO<sub>2</sub>-hydrate bearing inclusions. Salinities were calculated using the equations of Bodnar *et al.* (1989a) from  $T_{m\text{NaCl}}$  and assume a simple NaCl-water system (equivalent NaCl wt%). All fluid inclusion data is provided in Appendix C.

PIXE analysis were conducted on 5 multiphase, hypersaline fluid inclusions from one Stage 3B



vein (Sample 25/223; Plate 6.11D). Analysis were carried out using the CSIRO-GEMOC Nuclear Microprobe housed at CSIRO, North Ryde, Sydney. Element concentrations within the fluid inclusions were determined using the methodology of Heinrich *et al.* (1992). PIXE spectra are provided in Figure 7.3 and elemental abundances are detailed in Table 7.1 and Plate 7.2.

The values reported in this chapter are uncorrected for pressure, and will be lower than the trapping temperature. In addition to this fluid inclusion study, a melt inclusion study focused on silicate inclusions hosted within clinopyroxene phenocrysts within the Balut Dyke. The results were described by Kamenetsky *et al.* (1999).

## Classification of Inclusions










Four major types of fluid inclusions were recognised during this study (Figure 7.1):

**L (liquid).** Liquid-filled fluid inclusions without a vapour bubble (Plate 7.1B). Present as late-stage secondary inclusions that are typically elongated along partially annealed fracture plains. The lack of a vapour bubble suggests that these fluid inclusions were formed at near-surface pressures and temperatures, possibly during Stage 5.

**LV (liquid-vapour).** Liquid-vapour fluid inclusions (Plates 7.1A, B & C) that homogenise by vapour bubble disappearance. At room temperature the vapour bubble may occupy from 5 to 60% of the inclusion volume. Some LV fluid inclusions contain an opaque daughter mineral, but none contain daughter salts. LV inclusions typically occur as secondary inclusions in Stage 3 quartz (rarely as a primary inclusion) and as primary fluid inclusions in Stage 2 apatite.

**V (vapour).** Vapour-rich fluid inclusions, which homogenise by vapour bubble disappearance. V inclusions may contain minor fluid along the walls of the inclusion (Plates 7.1B, F & J). V-type fluid inclusions occur as uncommon primary and secondary inclusions in both Stage 3 quartz and Stage 2 apatite. V-type fluid inclusions typically occur with B-type inclusions (Plates 7.1 F, J & L). In addition, Stage 3 quartz commonly contains solid inclusions (of a lath-shaped mineral; probably actinolite) that are surrounded by a vapour-filled pocket ('V<sub>A</sub>' inclusions; Plate 7.1 F). V<sub>A</sub> inclusions are an abundant primary inclusion type, but do not homogenise upon heating.

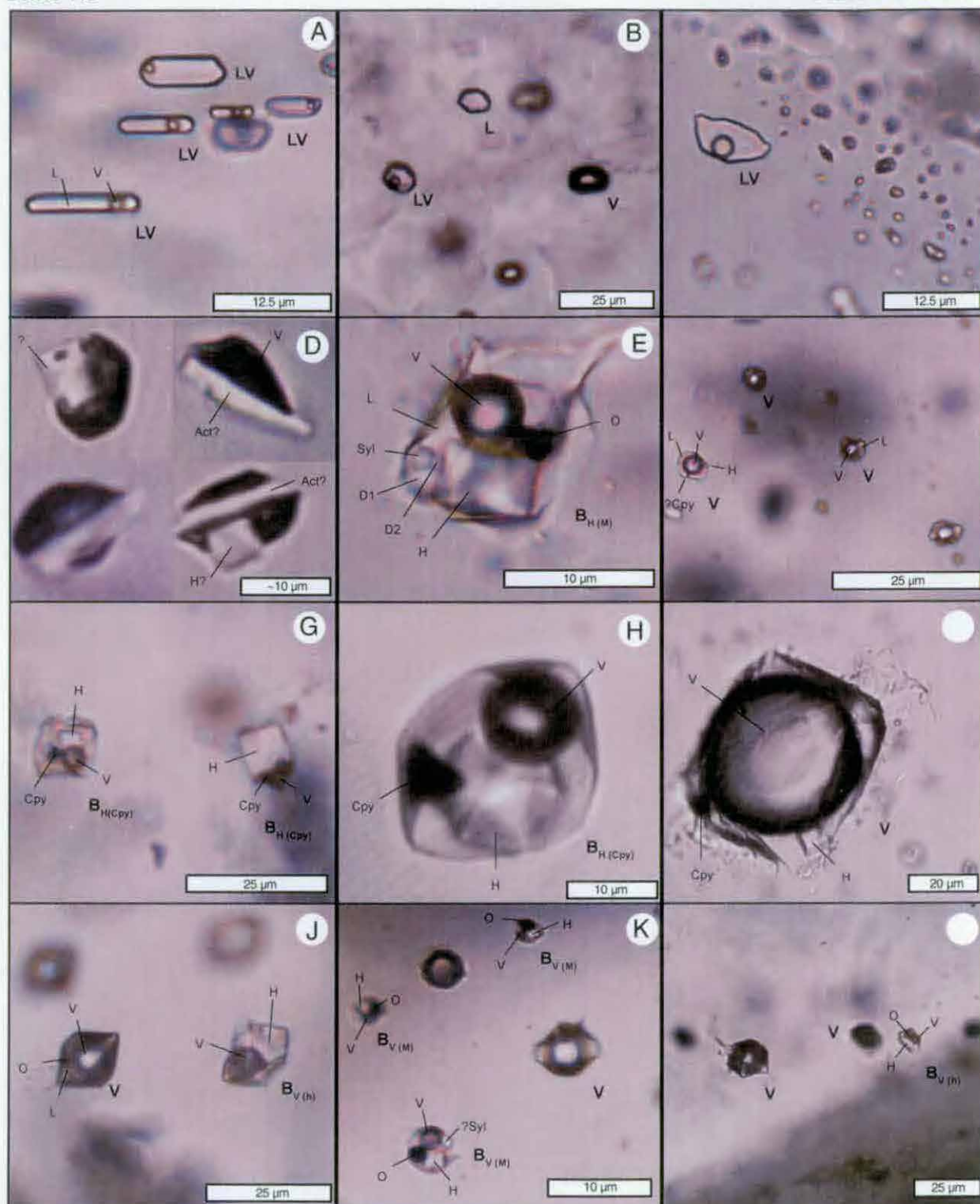
**B (brine).** Halite-bearing fluid inclusions. B type fluid inclusions are subdivided into inclusions that homogenise by salt melting following vapour bubble disappearance (B<sub>H</sub>) and inclusions which homogenise by vapour bubble disappearance, following halite melting (B<sub>V</sub>). B<sub>H</sub> and B<sub>V</sub> inclusions have been further subdivided based on their composition. B<sub>H(b)</sub> and B<sub>V(b)</sub> contain liquid, vapour and halite. B<sub>H(o)</sub> and B<sub>V(o)</sub> inclusions contain an opaque phase in addition to liquid, vapour and halite (Plate 7.1K). Where the opaque phase is identified as chalcopyrite based on a triangular habit and/or PIXE analysis, B<sub>H(o)</sub> and B<sub>V(o)</sub> inclusions are labelled B<sub>H(Cpy)</sub> and B<sub>V(Cpy)</sub> (Plate 7.1G, H & I). Multiphase B-type fluid inclusions are labelled B<sub>H(M)</sub> or B<sub>V(M)</sub>. B<sub>H</sub> inclusions are the most

	Type	Phases present at 25 C	Homogenization behavior
<b>L-Type</b>			
Liquid only	 L	L	NA
<b>LV-Type</b>			
Undersaturated liquid-rich	 LV	L+V+O	Vapour bubble disappearance
<b>V-Type</b>			
Undersaturated vapour-rich	 V	V+L+O	Disappearance of liquid
<b>B-Type</b>			
<b>B<sub>V</sub></b>			
Saturated	 B <sub>V(h)</sub>	L+V+H	Vapour bubble disappearance
	 B <sub>V(cpy)</sub>	L+V+H+Cpy	
	 B <sub>V(M)</sub>	L+V+H, O-D <sub>2-6</sub>	
<b>B<sub>H</sub></b>			
Saturated	 B <sub>H(h)</sub>	H+L+V	Salt dissolution
	 B <sub>H(O)</sub>	H <sub>2</sub> +L+V+O (*B <sub>H(cpy)</sub> if opaque phase has triangular habit)	
	 B <sub>H(M)</sub>	H, D <sub>2-6</sub> , L, V (+ O)	

**Figure 7.1:** Classification of fluid inclusions types observed at the Dinkidi Cu-Au porphyry deposit. B-Type inclusions (brine-type) are defined as any halite-bearing inclusion, and are subdivided into halite bearing inclusions which homogenise by vapour bubble disappearance (B<sub>V</sub>), and halite-bearing inclusions which homogenises by halite dissolution (B<sub>H</sub>). B-type inclusions are further subdivided on the basis of their composition at room temperature. B<sub>H(O)</sub> inclusions contain an opaque phase (B<sub>H(cpy)</sub> if the opaque mineral is triangular). B<sub>m</sub> inclusions are multiphase and may contain between 2 and 6 phases, including 1-3 opaque phases, 1-3 unidentified translucent solids (commonly laths of ?anhydrite, which do not dissolve on heating), sylvite and halite; Plate 7.1E & K). The same nomenclature is applied to B<sub>V</sub> inclusions, although no B<sub>V(O)</sub> inclusions were measured in this study. Phase proportions within B-type inclusions are extremely variable; with halite, vapor and opaque phases each account for between 5 to 90% of the inclusions volume. Halite crystal+opaque mineral typically exceeds 70% of B<sub>H</sub> inclusion volume. Opaque phases are potentially present in all inclusion types. L-type inclusions are found as late-stage secondary inclusions in Stage 3 quartz, typically along partially healed fracture plains, but are the most common primary and secondary inclusion type in Stage 2 apatite. Liquid-vapor inclusions (LV-type) are typically secondary. Vapor- (V-type) and B-type inclusions are the most common primary inclusion in Stage 3 quartz. Stage 3 quartz also commonly contains common solid inclusions (incorporated mineral grains, typically actinolite, apatite or biotite) and, within the Bufu quartz syenite, rare melt inclusions. Phases present: L: liquid; V: vapor; H: halite; O: opaque phase; D: daughter minerals.

common primary inclusions in Stage 3 quartz (accounting for over 90% of all primary inclusions) and are an abundant early secondary inclusion in Stage 3 quartz. Because of the apparent association between chalcopyrite-bearing inclusions and sulphide mineralisation, secondary B<sub>H(cpy)</sub> and B<sub>V(cpy)</sub> inclusions were also analysed.

Most of the primary B-type fluid inclusions did not homogenise below the maximum temperature of the Linkham MDS 600 Stage (600°C). Opaque daughter minerals do not dissolve upon heating. Few homogenisation temperatures were recorded for V-type inclusions, because of the difficulty in determining accurately the final disappearance of liquid (Roedder, 1984). Primary and secondary fluid inclusions have been identified using the criteria of Roedder (1984). No pseudosecondary inclusions were observed.



Mineral abbreviations: L: liquid; V: vapour; H: halite; O: opaque daughter mineral; Cpy: chalcopyrite. D<sub>2-4</sub>: daughter minerals.

**A:** Primary liquid-vapor (LV) fluid inclusions in Stage 2 apatite. Sample 53/828.

**B:** Secondary liquid-vapor (LV), vapour (V) and liquid (L) fluid inclusions in Stage 2 apatite. Sample 42.1

**C:** Secondary liquid-vapour (LV) fluid inclusion trail in Stage 3 quartz. Sample 33/256.

**D:** Primary 'V<sub>A</sub>' solid inclusions. A lath-shaped mineral, tentatively identified as actinolite, is partially incorporated into surrounding quartz. 'V<sub>A</sub>' inclusions are the most common primary inclusion within Stage 3 quartz.

**E:** Primary multiphase fluid inclusion from within a Stage 3 quartz vein (Sample 54/468).

**F:** Primary vapor-rich (V) fluid inclusions in a Stage 3 quartz vein. Sample 28/486.

**G:** Primary B<sub>H(Cpy)</sub> fluid inclusions in a Stage 3 quartz vein. The co-existing inclusions have variable halite-vapour-opaque phase abundances. Each of these phases may occupy from 5 to 90% of the B-type inclusions volume. Sample 61/103.

**H:** Typical B<sub>H(Cpy)</sub> fluid inclusion in Stage 3 Bugoy Pegmatite quartz. Sample 33/393.

**I:** V-type fluid inclusion, with halite and chalcopyrite daughter minerals, in the Bugoy Pegmatite. Sample 34/393.

**J:** Co-existing primary vapour- and brine-type fluid inclusions within a Stage 3 quartz vein. Sample 37/322

**K:** Co-existing secondary V and B-type fluid inclusions within a Stage 3 quartz vein. Sample 37/322

**L:** Co-existing secondary V and B-type fluid inclusions in Stage 3 quartz. Sample 34/393



## Microthermometry Results

### Stage 2

The abundant Stage 2 vein minerals (eg K-feldspar, diopside or actinolite) do not contain any workable fluid inclusions, although a high temperature of formation for diopside ( $>500^{\circ}\text{C}$ ) is inferred on the basis of melt inclusions (Kamenetsky *et al.*, 1999). Late-stage apatite from Stage 2C veins contain abundant LV fluid inclusions with negative crystal shapes and uncommon V and L-type inclusions (Plate 7.1A). These fluid inclusions locally comprise up to 10% of the apatite crystals volume.  $T_c$  for primary LV Stage 2 inclusions range from  $-23$  to  $-43^{\circ}\text{C}$  (average  $-32^{\circ}\text{C}$ ),  $T_{m\text{H}_2\text{O}}$  ranges from  $-10$  to  $-19$  (average  $-15$ ) and  $T_{h\text{vl}}$  ranges from  $201$  to  $321^{\circ}\text{C}$  (average  $274^{\circ}\text{C}$ ; Figure 7.2). The measured  $T_e$  temperatures are lower than that for the pure  $\text{H}_2\text{O}$ - $\text{NaCl}$  ( $-21.1^{\circ}\text{C}$ ) and  $\text{H}_2\text{O}$ - $\text{NaCl}$ - $\text{KCl}$  ( $-22.9^{\circ}$ ) systems (Hall *et al.*, 1988), suggesting components in addition to  $\text{NaCl}$  and  $\text{KCl}$  are present (eg  $\text{Ca}$ ,  $\text{PO}_4$  or  $\text{Mg}$ ). Calculated salinities for these LV inclusions range from 13 to 24 wt% eq.  $\text{NaCl}$  (Figure 7.2; average 18 wt% eq.  $\text{NaCl}$ ). Despite the moderate salinities and the association between sulphide mineralisation and Stage 2C stockwork veins, no opaque daughter minerals have been observed in these inclusions, and halite-bearing  $B_H$  inclusions are rare.

### Stage 3

Both Stage 3 vein quartz and quartz from the Bugoy Pegmatite contain abundant primary B-type inclusions. The primary and early secondary B-type fluid inclusions typically consist of a halite crystal, an opaque phase, a fluid and a vapour bubble (abundant  $B_{H(O)}$  inclusions and uncommon  $B_{V(O)}$  inclusions; Plate 7.1H). The proportion of individual phases in co-existing  $B_{H(O)}$  fluid inclusions highlights a surprising variability (eg Plates 7.1G, H & I). Early B-type fluid inclusions within individual veins (located within euhedral quartz on the walls of the vein) commonly contain sylvite, and possibly one or two other daughter minerals (eg  $B_{H(M)}$  in Plate 7.1E). The opaque phases are iron oxide (identified using PIXE; probable magnetite because it is opaque) and chalcopyrite (triangular habit; composition confirmed by PIXE analysis). Late stage primary B-type fluid inclusions (assumed to be those found in the centre of veins in anhedral quartz, commonly adjacent to interstitial sulphides) and secondary B-type inclusions trails typically lack the additional daughter minerals characteristic of the earlier-forming primary inclusions, and have chalcopyrite as the opaque phase (eg  $B_{H(Cpy)}$  and  $B_{V(Cpy)}$ -type inclusions; Plates 7.1G, H & I). Populations of vapour-rich inclusions (Plate 7.1F) are spatially associated with populations of both primary and secondary B-type fluid inclusions. Where B-type inclusions are found to co-exist on the same trail or growth band as V-type inclusions (eg Plates 7.1J, K & L), the B-type inclusions consist of  $B_V$ -type fluid inclusions. LV-type inclusions are a rare primary, but abundant secondary, fluid inclusion type.

### Stage 3A: Bugoy Pegmatite

Primary fluid inclusions in quartz from the Bugoy Pegmatite consist of abundant  $B_{H(O)}$ ,  $B_{H(Cpy)}$  and  $B_{H(M)}$ -type inclusions, uncommon primary  $V_A$ ,  $B_{H(h)}$ ,  $B_{V(Cpy)}$  and V inclusions and abundant

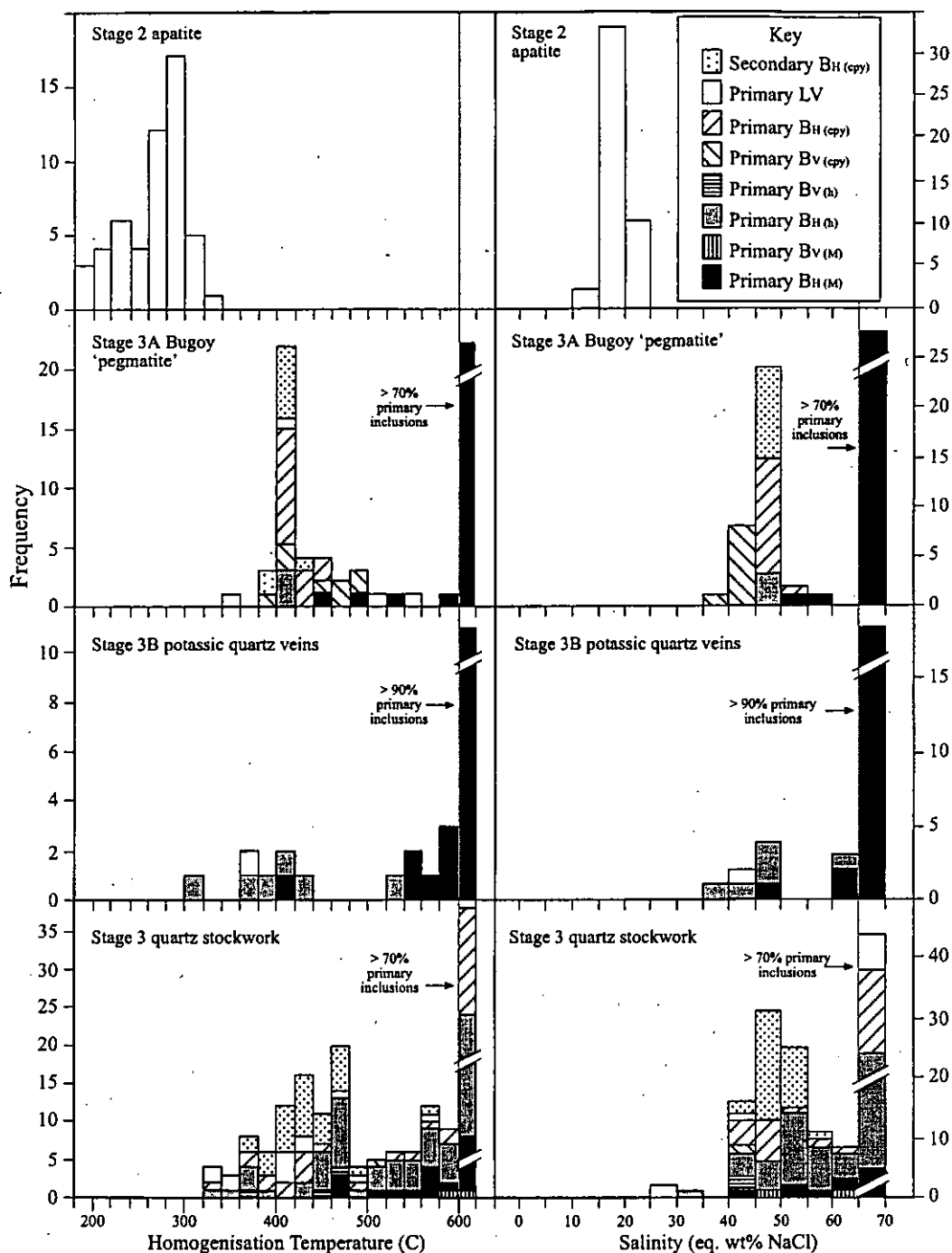


**Figure 7.2:** Homogenisation temperature and apparent salinities for fluid inclusions from hydrothermal Stages 2 and 3 at the Dinkidi Cu-Au porphyry. The majority of primary inclusions have homogenisation temperatures above 600°C (the limit of the Linkham 600 stage; unhomogenised inclusions are recorded as 600-620°C).

secondary  $B_{H(cpy)}$  inclusions. The Bugoy Pegmatite also contains abundant actinolite (?), apatite, opaque mineral and biotite-solid inclusions. Typically, none of the fluid inclusions homogenised before 600°C (Figure 7.2), indicating a salinity of at least 68 wt% eq. NaCl for the majority of  $B_H$  inclusions. Measured  $T_{hvl}$  for primary  $B_{H(M)}$  inclusions ranges from 320 to >600°C and  $T_{hhl}$  ranged from 450 to >600°C, corresponding to a calculated salinity from 51 to >68 wt % eq. NaCl. Measured  $T_{hvl}$  for primary chalcopyrite-bearing fluid inclusions (including both  $B_{H(cpy)}$  and  $B_{V(cpy)}$ ; Figure 7.2) ranged from 225 to 390°C and  $T_{hhl}$  ranged between 383 and 488°C (average 430°C; Figure 7.2), corresponding to a calculated salinity range of 39 to 51 wt % eq. NaCl (Figure 7.2). Secondary  $B_{H(cpy)}$  inclusions are the most abundant fluid inclusion type

## FLUID INCLUSIONS & SULPHUR ISOTOPES

hosted within the Bugoy Pegmatite, and have a measured  $T_{h\text{vi}}$  from 253 to 345°C, and a  $T_{h\text{hl}}$  range from 393 and 428 °C (average 409 °C; Figure 7.2), corresponding to a calculated salinity range of 45 to 50 wt % eq. NaCl (Figure 7.2).

### Stage 3B-Potassic

Primary inclusions within Stage 3B-Potassic veins are typically small (<5mm)  $B_H$  inclusions ( $B_{H(M)}$ ,  $B_{H(O)}$ ,  $B_{H(Cpy)}$  and  $B_{H(h)}$ ) with uncommon  $B_V$ , V and rare LV types. Typically, none of the fluid inclusions homogenised before 600°C (indicating a salinity of at least 68 wt% eq. NaCl, Figure 7.2) and many B-type inclusions decrepitated at temperatures greater than 500°C.  $T_{h\text{vi}}$  was not recorded for the analysed  $B_H$  inclusions. Measured  $T_{h\text{hl}}$  for primary  $B_{H(M)}$  inclusions ranges from 420 to >600°C, corresponding to a calculated salinity from 47 to >68 wt % eq. NaCl. Measured  $T_{h\text{hl}}$  for primary  $B_{H(h)}$  inclusions ranges from 320 to 540°C, corresponding to a calculated salinity from 39 to >68 wt % eq. NaCl. The presence of triangular chalcopyrite crystals in  $B_{H(M)}$  and  $B_{H(Cpy)}$  primary fluid inclusions indicate that the fluids that formed these apparently barren quartz veins (eg Plates 6.9A, E & F; Plate 6.10E) were high-temperature copper-bearing saline brines.

### Stage 3A & 3B quartz stockwork

Primary fluid inclusions within the main Stage 3 quartz stockwork consist common of  $B_H$  ( $B_{H(O)}$ ,  $B_{H(Cpy)}$  and  $B_{H(h)}$ ), V and  $V_A$  type inclusions and rare LV and  $B_{H(M)}$  (typically halite, sylvite and an opaque phase, with 1-2 other unidentified phases) type inclusions. No differences in composition, or microthermometric behaviour, was observed between Stage 3A and 3B veins, and the two vein sets are treated here together. Measured  $T_{h\text{vi}}$  for primary  $B_{H(M)}$  and  $B_{H(O)}$  inclusions ranges from 174 to >600°C and  $T_{h\text{hl}}$  ranged from 480°C to in most cases, temperatures greater than 600°C (Figure 7.2). This range in  $T_{h\text{hl}}$  corresponds to a calculated salinity of 40 to >68 wt % eq. NaCl. Measured  $T_{h\text{vi}}$  for primary chalcopyrite-bearing  $B_{H(Cpy)}$  inclusions range from 230 to >600°C and  $T_{h\text{hl}}$  ranged from 330 to greater than 600°C (with a small peak at 430°C; Figure 7.2). The measured range in  $T_{h\text{hl}}$  corresponds to salinities of 40 to >68 wt% eq. NaCl (Figure 7.2).

Secondary fluid inclusions are abundant within the Stage 3 quartz veins and comprise  $B_H$  ( $B_{H(M)}$ ,  $B_{H(h)}$ ,  $B_{H(O)}$  &  $B_{H(Cpy)}$ ),  $B_V$  ( $B_{V(h)}$  &  $B_{V(Cpy)}$ ), V, LV and L-type inclusions. Measured  $T_{h\text{vi}}$  for secondary  $B_{H(Cpy)}$  inclusions range from 240 to 315°C and  $T_{h\text{hl}}$  ranged from 376 to 570°C (average 437°C; Figure 7.2), corresponding to salinities of 43 to 55 wt% eq. NaCl (average 49 wt% eq. NaCl; Figure 7.2).

The fluid inclusions in distal Stage 3 quartz stockwork veins are similar to those in the proximal veins. Distal quartz veins (~150 meters lateral extent from the apex of the Bufu Syenite) contain primary  $B_{H(M)}$ ,  $B_{H(O)}$ , V and LV fluid inclusions. V-type inclusions are typically spatially associated with the B-type inclusions. Homogenisation temperatures for the distal primary B-type fluid inclusions are typically >600°C, and there is no discernable difference in the temperature or composition of the Stage-3 stockwork with distance from the Bufu Syenite.



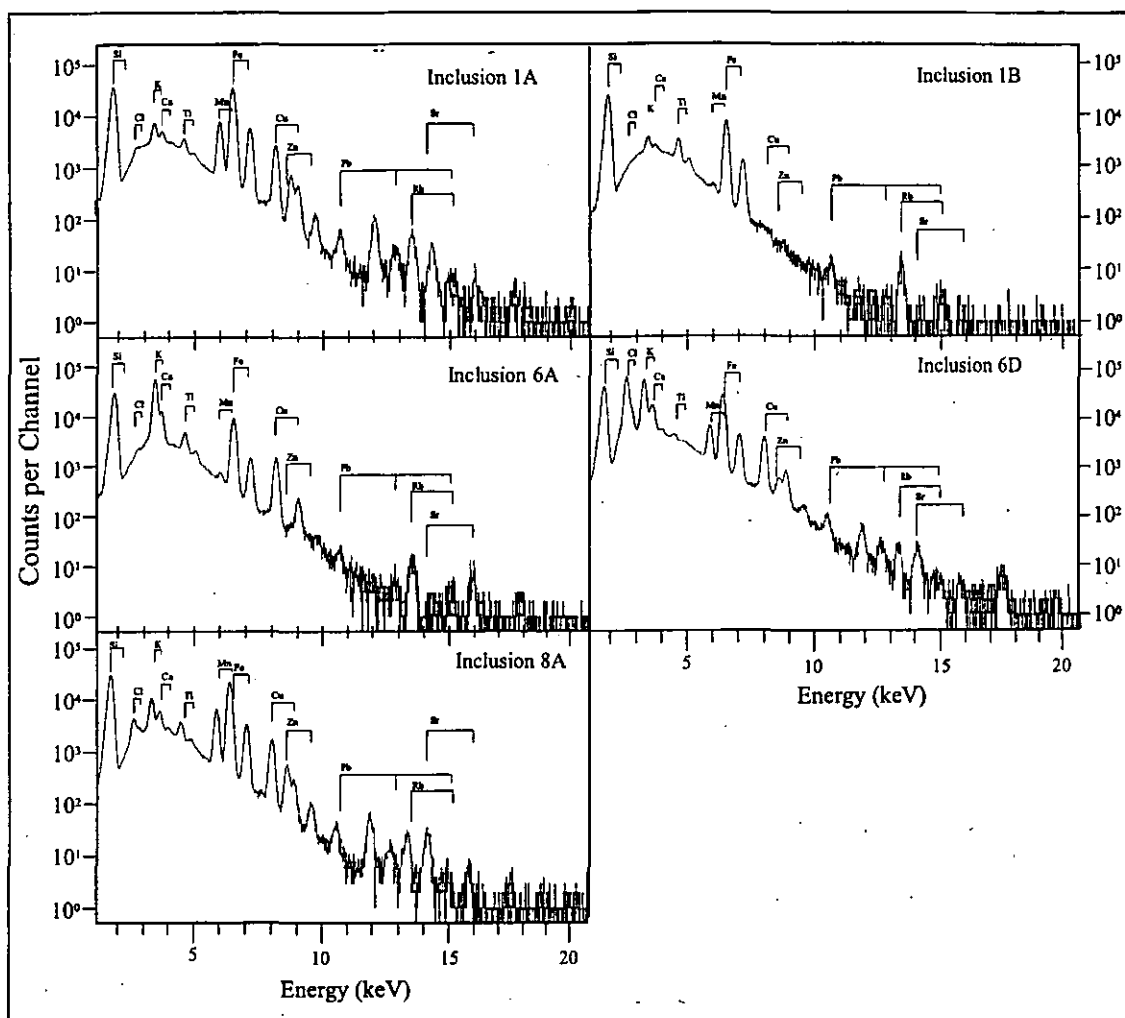


**Figure 7.3:** PIXE spectra for fluid inclusions within a Stage 3B quartz vein (Sample 25/223; Plate 6.11D). Inclusions 1A & 1B are primary  $B_{H(M)}$ -type fluid inclusions located from subhedral quartz on the margin of the quartz vein ( $T_h > 600^\circ\text{C}$ ). Inclusions 6A, 6D are primary  $B_{H(O)}$  fluid inclusions located in the middle of the vein ( $T_h > 550$ ) and inclusion 8A is a late-stage primary  $B_{H(O)}$  fluid inclusion ( $T_h > 550$ ) located in anhedral quartz with interstitial sulphide in the centre of the vein.

## PIXE Results

Five fluid inclusions from one proximal Stage 3B quartz vein (Sample 25/223; Plate 6.11D) were analysed by proton induced X-ray emission (PIXE). PIXE analysis can provide non-destructive compositional information on the contents of fluid inclusions. Inclusion compositions are presented in Table 7.1, element distributions within individual inclusions are displayed in Plate 7.2, and the PIXE spectra are shown in Figure 7.3. The X-ray signals from S, Cl and K are attenuated during passage through quartz. This has prevented accurate measurement of K and Cl concentrations in fluid inclusions located at depths greater than 10mm below the surface of the thin section. Sodium cannot be detected by PIXE analysis, but was detected in some inclusions by gamma ray spectroscopy, although signal attenuation was also a problem for this element.

The fluid inclusions selected for analysis consisted of two 'early' primary  $B_{H(M)}$  inclusions (Inclusions 1A & 1B;  $T_h > 550$ -600; Plates 7.2A & B), hosted in subhedral quartz grains on the vein margin, two primary  $B_{H(O)}$  inclusions (Inclusions 6A, 6B  $T_h > 550$ ; Plates 7.2C & D) from the central seam of the vein, and one late-stage primary  $B_{H(O)}$  inclusion (Inclusion 8A; Plate 7.2E), hosted in anhedral quartz with interstitial sulphide in the core of the vein.

ppm or wt%	Inclusion 1A	Inclusion 1B	Inclusion 6B	Inclusion 6D	Inclusion 8A	Average
Cl	0.95% (too deep)	too deep	too deep	46.35%	too deep	46.35%
K	26.68%	4.54%	4.07%	5.50%	7.19%	9.59%
Fe	3.16%	3.49%	5.21%	2.63%	8.26%	4.55%
Mn	657	440	1.01%	0.46%	2.12%	0.74%
Cu	0.86%	149	0.62%	0.65%	1.08%	0.64%
Ti	0.76%	1.17%	0.28%	392	0.58%	0.56%
Ca	0.17%	0.21%	0.41%	0.36%	1.13%	0.45%
Zn	197	87	0.19%	938	0.43%	0.15%
Br	41		0.12%	397	0.19%	717
Rb	770	1021	510	145	745	639
Sr	233	82	684	367	0.19%	650
Pb	498	207	844	585	0.14%	699
As	21	142	32	130	112	88
Th	> 600 C	Td: 550 C	Td: 550 C	-	-	
eqNaCl%	> 68 %	> 62 %	> 49.7%	-	-	

**Table 7.1:** PIXE analyses for inclusions within a 1 cm thick Stage 3 quartz vein sample 25/223 (Plate 6.11D).

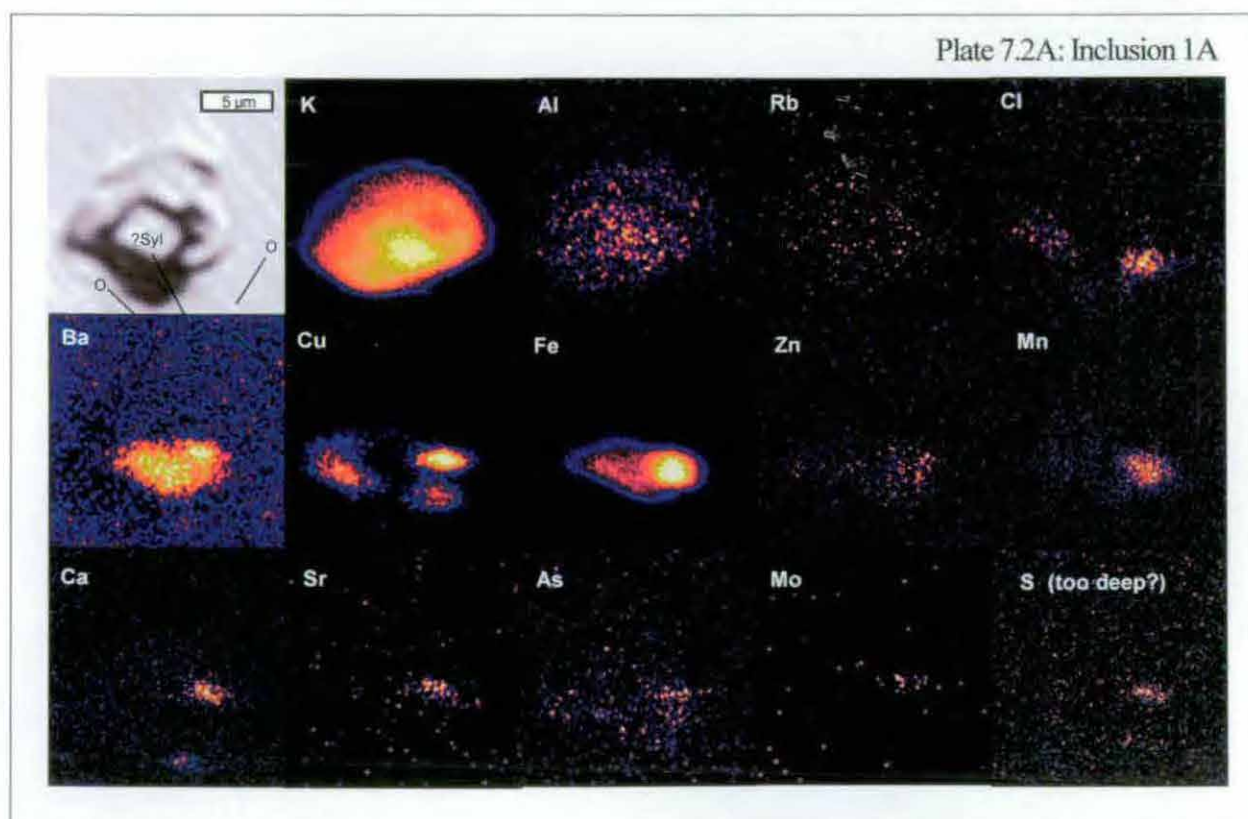


**Plate 7.2A:** PIXE element distribution for inclusion 1A. Liquid phase contains elevated concentrations of K, Al & Rb. K, Al and Ba are also hosted in the main solid phase (probable sylvite). Cu, Fe, Mn, Zn, Ca, Sr, Mo & S are concentrated in 3 opaque phases (probable chalcopyrite & Fe-oxide) adjacent to the sylvite grain.

Plate 7.2B: Inclusion 1B

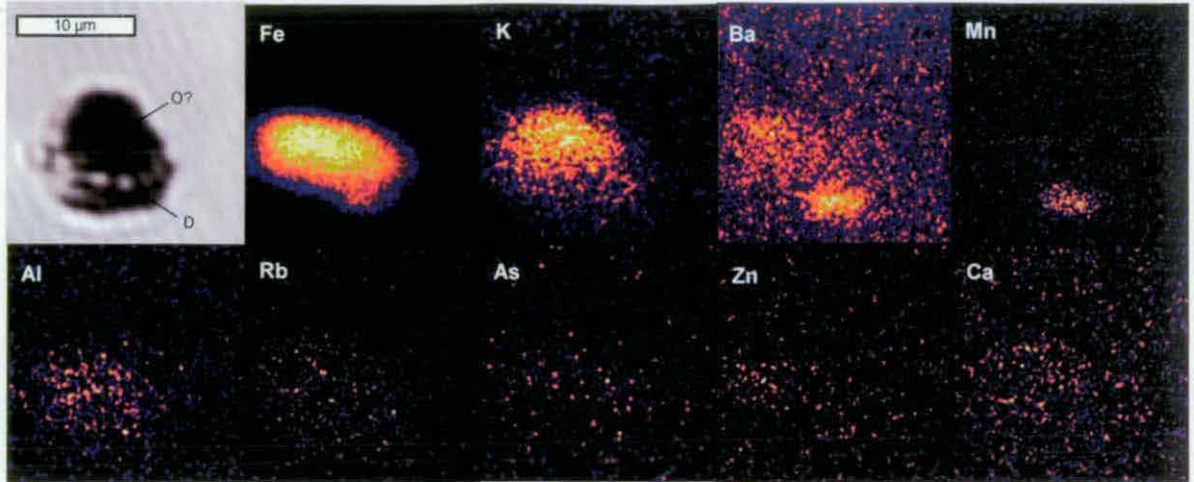
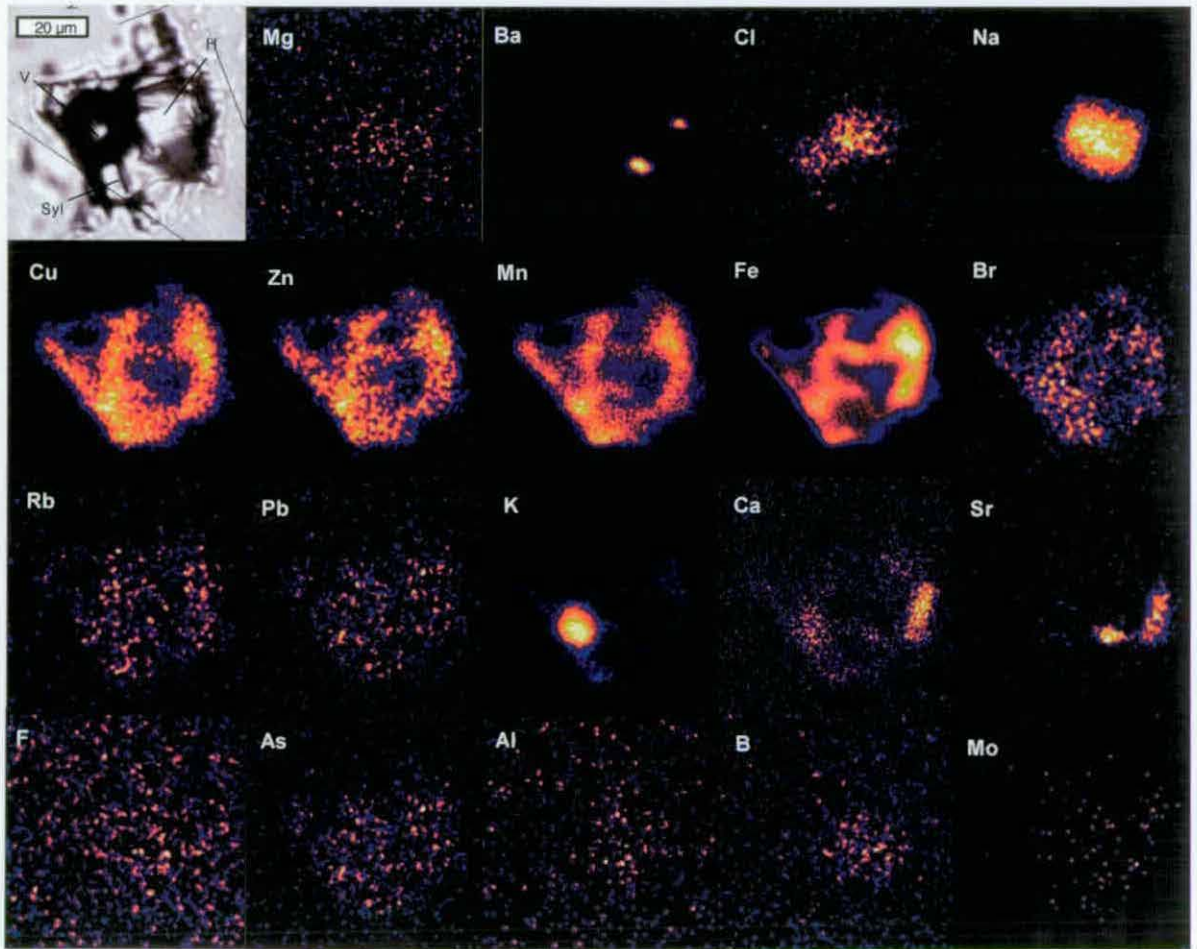


Plate 7.2C: Inclusion 6B



**Plates 7.2B:** PIXE element distribution for inclusion 1B. Fe, K & Ba  $\pm$  Al, Rb, As, Zn & Cl appear to be distributed evenly throughout both the fluid and opaque phase. Ba & Mn are concentrated in a separate translucent crystal.

**Plates 7.2C:** PIXE element distribution for inclusion 6B. Cu, Zn, Mn, Fe, Br  $\pm$  Rb appear to be concentrated in the liquid phase. Na and Cl appear to be concentrated in the halite crystal. Sr-Ca, Ba & K are concentrated in several smaller daughter phases.



## FLUID INCLUSIONS & SULPHUR ISOTOPES

PIXE analyses has revealed that in addition to H<sub>2</sub>O, the fluid inclusions analysed are dominated by Na, Cl (both inferred from the presence of large halite daughter crystals), K and Fe, which are present at concentrations of several weight percent (Table 7.1). In addition, the fluid inclusions contain 100's to 1000's of ppm Cu, Ti, Mn, Ca, and Zn. Also detected were Sr, Rb, Ba, As, Mo, Br and Pb. No definite temporal variation in fluid inclusion compositions was detected, although Ca, Sr, Mn, Fe, Cu, Pb, and Zn appear to have higher concentrations in the 'late' inclusions. Assuming that chlorine was the main ligand at high temperatures then PIXE analysis indicates that the hydrothermal fluid that formed the Stage 3 stockwork was a Na-K-Fe-Cl brine, with significant concentrations of Cu, Ca, Mn, Ti, and Zn. Elevated concentrations of Br in some inclusions (eg Plates 7.2C & E) suggest that some cations may have been transported at least in part as Br complexes, although no data on other possible ligands (eg S, F, I, P) was obtained by PIXE analysis. Based on the available PIXE data, it is likely that Cu, and by inference Au, were transported as Cl complexes in the Dinkidi magmatic-hydrothermal brines.

### Melt Inclusion Results

Kamenetsky *et al.* (1999) reported the results of a melt inclusion study on clinopyroxene hosted within the Balut Dyke. Complex multiphase inclusions coexist with rare silicate melt and hypersaline melt inclusions, contain from 5 to 14 phases (including chlorides, sulphates (anhydrite), sulphides (chalcopyrite), silicates (biotite), oxides (magnetite, hematite), hydroxides, carbonates, vapour bubbles and water) and homogenise from 700° to over 900°C. The melt inclusions contain elevated quantities of S, Cl, As and metals (Cu, Mo, Pb, Zn, W & Ag). Water soluble components of the inclusions contain Cl, S, N, F, Na and K. Variable phase proportions between coeval inclusions suggest the presence of several immiscible phases within the melt during diopside crystallisation, namely silicate melt, salt-rich melt or fluid (brines), and aqueous saline fluid (Kamenetsky *et al.* 1999).

### Discussion

Fluid and melt inclusion studies on the Dinkidi system have highlighted the presence of several fluid phases and the metal-carrying capacity of the high temperature magmatic-hydrothermal brines. This is consistent with results of fluid inclusions studies from other porphyry deposits (eg Eastoe, 1979; Reynolds & Beane, 1985; Cline & Bodnar 1994; Rowlands & Wilkinson, 1999).

#### *Fluid compositions*

No high temperature Stage 2 minerals contained workable fluid inclusions. Melt inclusions within Balut Dyke diopside homogenises at temperatures of 700 to >900°C (Kamenetsky *et al.*, 1999), and appear to have trapped an immiscible mixture of silicate melt, aqueous fluid and a hydrosaline melt (or brine). The melt contained elevated concentrations of all the typical porphyry-deposit metals (Mo, Cu and probably Au; Kamenetsky *et al.*, 1999). The presence of elevated Mo concentrations in the 'parent' melt for a Au-Cu porphyry deposit (with only trace

Plate 7.2D: Inclusion 6D

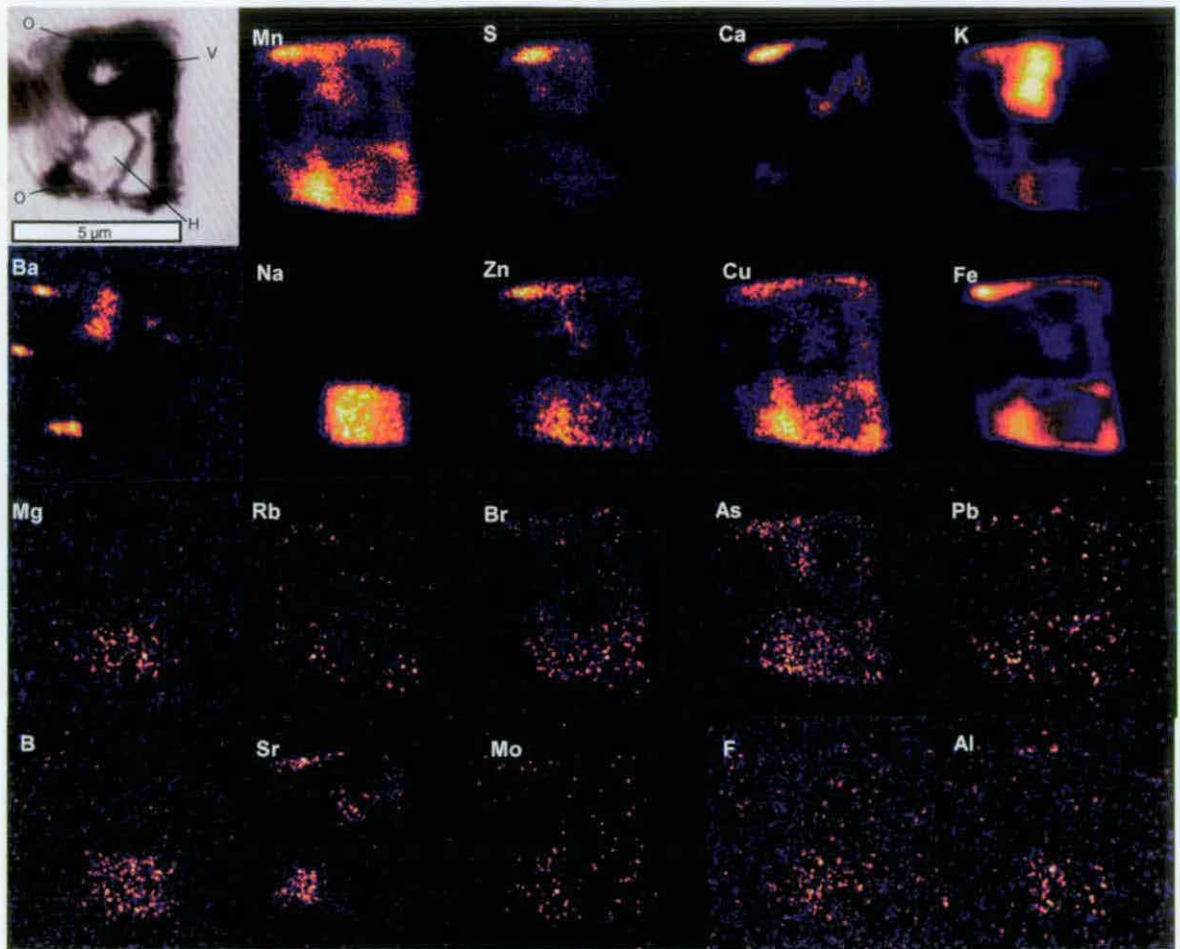
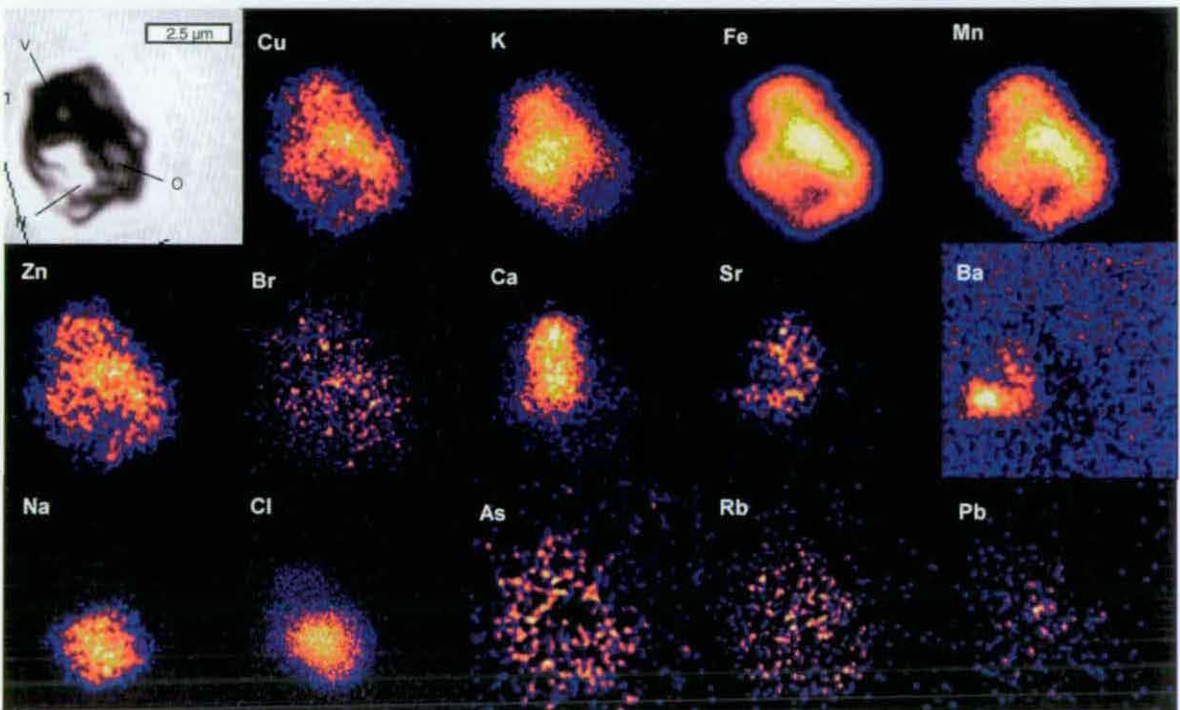


Plate 7.2E: Inclusion 8A



**Plates 7.2D:** PIXE element distribution for inclusions 6D. K is concentrated in a single daughter mineral. Liquid phase contains Mn, Fe, Cu, Zn, Br, Pb & As. Mn, S, Cu, Zn, Fe and As are concentrated within two opaque phases. Ba is incorporated into both the K-bearing daughter mineral and several small daughter crystals (possibly as barite inclusions within other solid phases).

**Plates 7.2E:** PIXE element distribution for inclusion 8A. Opaque phase contains Cu, Fe, Mn & Zn (chalcopyrite?). Calcium, Ba and Sr appear to be concentrated within underlying phases.

concentrations of Mo recorded at the deposit, typically in distal settings) suggests that the style of porphyry deposit that is developed around an intrusive stock (Mo, Cu-Mo, Cu-Au or Au) may be controlled by late-stage geochemical processes at the site of deposition, rather than by the relative degree of metal enrichment of the source region.

Microthermometric measurements indicate that apatite, which is typically found in, but is not confined to, Stage 2 hydrothermal assemblages, formed at relatively low temperatures and salinities ( $T_h = 201$  to  $321^\circ\text{C}$ ; average  $274^\circ\text{C}$ ; Salinity 13 to 24 wt% eq. NaCl; average 18 wt% eq. NaCl). Eutectic temperatures ( $-23$  to  $-43^\circ\text{C}$ ; average  $-32^\circ\text{C}$ ) are lower than that for the pure  $\text{H}_2\text{O}$ -NaCl ( $-21.1^\circ\text{C}$ ) and  $\text{H}_2\text{O}$ -NaCl-KCl ( $-22.9^\circ\text{C}$ ) systems (Hall *et al.*, 1988), suggesting components in addition to NaCl and KCl are present (such as  $\text{Ca PO}_4$  and Mg). The relatively low  $T_h$  suggests that the apatite was precipitated later, and at lower temperatures than the associated orthoclase-actinolite hydrothermal mineral assemblage.

Microthermometric and PIXE analyses indicates that the Stage 3 quartz assemblage, including both proximal and distal veins from hydrothermal stages 3A and 3B, and the Bugoy Pegmatite, formed from a high salinity ( $>68$  wt% eq. NaCl) NaCl-KCl-FeCl brine at sub-magmatic temperatures ( $T_h > 600^\circ\text{C}$ ). Large variations in halite, vapour and opaque mineral volumes in Stage 3 B-type inclusions that share the same primary growth band (eg Plate 7.1G) suggest deposition from a heterogeneous, possibly immiscible (eg Roedder, 1992), hydrothermal fluid. Mineralisation is associated with late primary to secondary chalcopyrite-bearing  $B_{H(Cpy)}$  inclusions (40 to  $>68$  wt% eq. NaCl), which homogenise at temperatures typically  $>600^\circ\text{C}$ , but with a second peak at  $360$ - $500^\circ\text{C}$  (the later especially with secondary  $B_{H(Cpy)}$ ; Figure 7.2). Uncommon vapour-rich inclusions are spatially associated with populations of both primary and secondary B-type inclusions.

The bimodal distribution of  $T_h$  in Stage 3 quartz stockwork, from early  $B_{H(M)}$  with  $T_h > 600^\circ\text{C}$ , to later  $B_{H(Cpy)}$  with  $T_h \sim 360$ - $480^\circ\text{C}$ , suggests at least  $120$  to  $240^\circ\text{C}$  of cooling occurred between emplacement of the quartz stockwork and the main period of sulphide deposition. The lower salinities of this second group of  $B_{H(Cpy)}$  inclusions ( $\sim 40$ - $55$  wt% eq. NaCl) still lie on the halite saturation curve for their temperature range, suggesting that the lower salinities reflect cooling of a salt-saturated hydrothermal brine, rather than dilution by external groundwaters. A 1-2 Kbar increase in pressure would also produce a similar shift to lower  $T_h$  (Bodnar, 1982), but would not lead to the observed salinity decrease. A limited number of PIXE analyses suggest that the fluid composition remained relatively homogeneous during vein crystallisation, with small increases in the concentration of Ca, Sr, Mn, Fe, Pb and Zn in late fluid inclusions (Table 7.1). The elevated Zn contents (Table 7.1) in Stage 3 fluid inclusions suggest that base metals within the deposit, which are found as both sphalerite inclusions within Stage 3 copper sulphides and as uncommon late Stage 3 sphalerite-galena-pyrite sulphide trails, have precipitated due to the cooling of the Stage 3 hydrothermal fluid, rather than by mixing with meteoric water.



*Evidence for phase separation*

Fluid inclusion studies of most porphyry deposits (including Cu-Au, Cu-Mo, Sn-W and Au porphyry deposits) have described overlapping populations of hypersaline and vapour-rich fluid inclusions (Roedder, 1984). The close spatial association between the two inclusions styles has lead most workers to interpret this feature as evidence for phase separation ('2<sup>nd</sup> boiling' of Bowen, 1933; Burnham, 1979). This process is applicable for vapour-rich inclusions that coexist with LV or B<sub>v</sub>-type inclusions. If phase separation has occurred, trapping of the immiscible mixture must occur along the liquid-vapour stability curve ('L-V' in Figure 7.4 A & B) at pressures less than 1500 bars (Figure 7.4B). However, phase equilibria constraints indicate that hypersaline inclusions that homogenise by salt dissolution (B<sub>H</sub> inclusions) cannot co-exist with a vapour phase under any pressure or temperature conditions (see Figure 7.4A; Bodnar 1994; Cline & Bodnar 1994). At Dinkidi, although co-existing B<sub>v</sub> and V-type inclusions were observed (eg Plate 7.1J) no unambiguous examples of coexisting B<sub>H</sub>-type fluid inclusions and V-type inclusions were found, although the two populations were observed in parallel trails. Two processes can be invoked to explain the formation of the B<sub>H</sub> inclusions, and their apparent spatial and temporal association with vapour-rich inclusions:

- The vapour formed during phase separation that may have formed the hypersaline brines. This model requires that the hypersaline brines were formed from an initially halite-undersaturated brine by phase separation along the L-V path at temperatures significantly higher than trapping (at least 740°C to in excess of 900°C; Figure 7.4B, red dashed line). Cooling of this brine (in the case of Dinkidi by a minimum of ~ 160°C) under conditions of constant, or increasing, pressure would produce B<sub>H</sub> inclusions (Path A on Figure 7.4B). This model would however require the low density vapour phase to remain *in situ* at the site of exsolution, during the cooling process.
- The vapour formed after generation of the brine by depressurisation at the site of trapping. In this model the hypersaline brine formed (either by high temperature phase separation and cooling, or by direct exsolution of a saline brine from the melt) and was emplaced at the site of the stockwork at >600°C and under at least lithostatic pressure. Pressure loss, possibly due to a switch from lithostatic to hydrostatic pressures during hydraulic fracturing, resulted in the production of V and B<sub>v</sub>-type inclusions (Path B on Figure 7.4B). Repeated 'crack-sealing' as the quartz stockwork formed would lead to cyclic high (lithostatic?) pressure (with B<sub>H</sub> inclusions) and low (hydrostatic?) pressure (vapour inclusions).

The degree of cooling required to produce the observed salinities that are found in B<sub>H</sub> inclusions from a 'boiling' magmatic fluid (salinities of >68 wt% eq. NaCl would require 160° to 250°C of cooling), appear to be geologically plausible, as a similar degree of cooling (120° to 240°C) has been recorded in the fluid inclusion population during quartz growth (from >600°C to later B<sub>H</sub> (Cpy) with T<sub>h</sub> ~ 360-480°C). Depressurisation during quartz crystallisation is supported by the

## FLUID INCLUSIONS & SULPHUR ISOTOPES

apparently episodic nature of vapour formation, with vapour-rich inclusions in Stage 3 quartz found within early primary, late primary and secondary inclusion trails, a distribution that is unlikely to be produced where the vapour was only exsolved during a period prior to stockwork formation. The scarcity of co-existing B & V-type inclusions, and of inclusions with intermediate compositions (eg Plate 7.1F & I) in regional of intermixed B- and V-type populations, also suggests that brine and vapour were not trapped strictly simultaneously at the time of quartz precipitation.

It is interpreted that both high-temperature vapour-brine exsolution (producing the hypersaline brine), and episodic depressurisation (producing the vapour at the site of the quartz stockwork) were required to produce the observed fluid inclusion populations in Stage 3 quartz. Although production of a high salinity brine (~57 wt% eq. NaCl) direct from a magma has been suggested by Bodnar *et al.*, (1989b) and Cline & Bodnar (1994), the elevated metal concentrations in the Stage 3 brine at Dinkidi (eg Cu 0.64%; Zn 0.14%; Table 7.1) could be explained by extensive volatile loss, resulting in the concentration of both metals and salts in the residual brine. In this case, the precursor magmatic fluid may have had a considerably lower salinity (eg 5-10 wt % eq. NaCl; Bodnar *et al.*, 1989b). However, without knowing precisely the degree of vapour loss, an accurate salinity for the primary magmatic fluid can not be calculated.

### *Pressure Estimates*

For  $B_H$  inclusions, the temperature of vapour bubble disappearance can be used to estimate pressure (eg Roedder & Bodnar, 1980). Pressure estimates using this method, using the isochores of Bodnar (1994), for  $B_H$  fluid inclusions with 40% NaCl, and Cline & Bodnar (1994), for inclusions with 43 & 47% NaCl, indicate pressures of 820 to 1260 bar, with a minimum pressure of 720 bar (Figure 7.4B). These pressures are equivalent to a lithostatic depth from 2.9 to 4.5 km, with a minimum depth of 2.6 km (Figure 7.4B). A significant degree of overpressurisation (or decompression?) within the stockwork during quartz growth could explain the wide range of vapour-bubble disappearance temperatures for similar homogenisation temperatures (Figure 7.4A & B), giving pressures that range from 720 bar (2.6 lithostatic depth) to >1500 bar (>5 km lithostatic depth). This wide range of pressure/depth estimates may also reflect the inaccuracies in isochore slope, caused by the lack of adequate phase equilibrium data for high salinity fluids (see Roedder & Bodnar, 1980; Bodnar, 1994), and the small number of suitable samples that could be plotted.

The depths estimated from fluid inclusion studies (2.6 to 4.5 km) are equal to greater than the depth estimate based on geological relationships. The Didipio Igneous Complex is interpreted to have been emplaced into a comagmatic volcanic pile (the Upper Mamparang Formation), with an inferred depth of between 1.5 to 3 km (based on the average height of trachyte to trachyandesite volcanoes; Pike & Clow, 1981; Cas & Wright, 1988). If the higher pressures estimated from microthermometric analyses of  $B_H$ -type fluid inclusions are considered to relate to overpressurisation, and taking into account the 'subvolcanic' geological setting, then Stage 3 mineralisation at Dinkidi is interpreted to have formed at 2.6 to ~3.5 km depth. A depth of 2.6

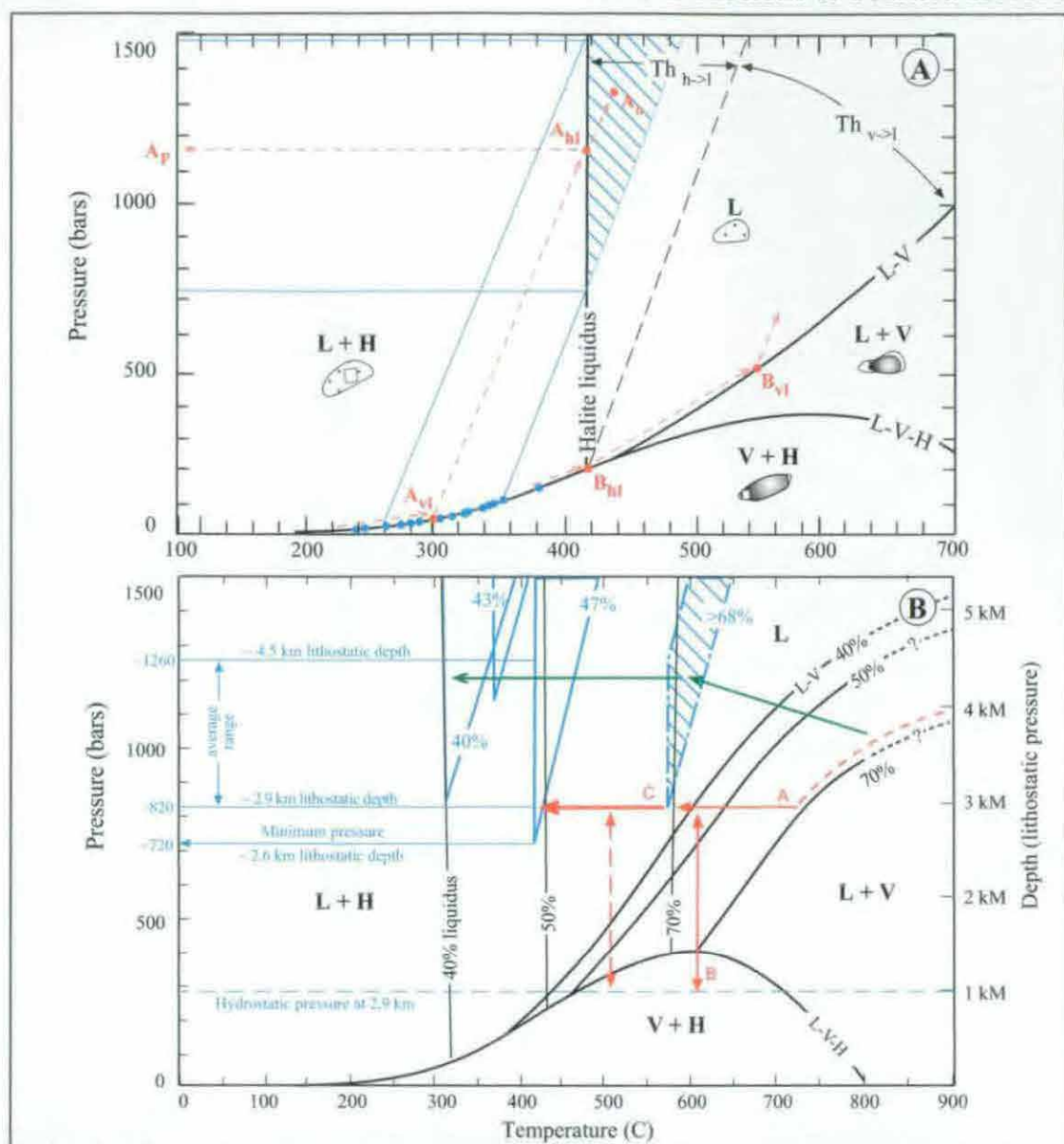


**Figure 7.4A:** Temperature-pressure diagram for a 47 wt% NaCl-H<sub>2</sub>O solution, based on Bodnar (1994) and Cline & Bodnar (1994). The 'L-V' curve separates the stability fields for liquid+vapour (L+V) and liquid (L). The 'L-V-H' curve separates the stability fields for liquid+vapour and vapour+halite (V+H). The 'halite liquidus' separates the stability field for liquid+halite (L+H) and liquid. B<sub>H</sub> inclusions follow the L-V-H curve upon heating until vapour disappearance at A<sub>vl</sub>. At this point the path enters the L+H stability field, following an isochore until homogenisation at the halite liquidus (A<sub>hl</sub>). The true trapping temperature will lie at some higher temperature (A<sub>tr</sub>), depending on pressure. The intersection of the isochore and halite solidus provides a rough estimate of minimum pressure (A<sub>p</sub>). The shaded region is the range covered by Stage 3 B<sub>H</sub> fluid inclusions with ~47 wt% eq. NaCl. Halite within B<sub>V</sub> inclusions will melt at the halite liquidus (B<sub>hl</sub>), the B<sub>V</sub> inclusion will then follow the L-V curve until vapour disappearance (B<sub>vl</sub>). The liquid field (L) is therefore subdivided into two regions: inclusions which homogenise by salt melting (Th<sub>h>l</sub>), and inclusions which homogenise by vapour bubble disappearance (Th<sub>v>l</sub>). The Th<sub>h>l</sub> field does not adjoin any vapour-stable field (V+H, L+V), therefore B<sub>H</sub> inclusions that homogenise by salt dissolution cannot have been trapped with a co-existing vapour phase.

**Figure 7.4B:** Temperature-pressure diagram showing, in black, the stability fields for the NaCl-H<sub>2</sub>O system, from 0 to 800 C and for salinities of 40, 50 and 70 wt% NaCl (Bodnar & Vityk, 1994). The thick blue lines enclose the trapping conditions for primary and early secondary Stage 3 B<sub>H</sub> inclusions that have salinities of approximately 40, 43 and 47 wt% eq. NaCl. Isochores to plot these fields were derived from Bodnar (1994, 40% NaCl) and Cline & Bodnar (1994; 43 & 47% NaCl). Infilled area encloses the estimated trapping conditions for primary Stage 3 B<sub>H</sub> inclusions with salinities of ~68 wt% eq. NaCl and Th of 600 C. As no isochores exist for this later field, the inclusions are assumed to have been trapped at the same pressures as the 40 to 47% salinity inclusions. Pressure estimate for B<sub>H</sub> inclusions with 40 to 47 wt% eq. NaCl range from a minimum to 720 bars to an average range of 820 to 1260 bars, corresponding to lithostatic depths of 2.6, 2.9 and 4.5 km respectively. At 820 bars, obtaining a 68 wt% brine by phase separation would require phase separation along the L-V curve at temperatures >750 C (dashed red line), assuming isobaric cooling along path A (red arrow). Average high temperature B<sub>H</sub> inclusions require phase separation at higher temperatures (probably >850 C), and/or a pressure increase during cooling (thin green arrow). Vapour-rich inclusions can be formed from the brine by depressurisation (Paths B; red arrow) to hydrostatic pressures, which, for the estimated depths, lies in a vapour-stable field (V+H). The lower salinity B<sub>H</sub>(C<sub>py</sub>) brines are considered to have been produced by cooling of this high temperature brine (Path C).



km would produce a hydrostatic pressure of 260 bars, indicating a pressure drop of ~460 bars during stockwork brecciation. Such a pressure drop would be enough cause vapour saturation (Figure 7.4B; Path B), and produce the observed vapour-rich inclusions.

## Trapping Temperatures

Accurate pressure determinations can allow an estimate of the trapping temperature ( $T_t$ ) from the measured homogenisation temperature ( $T_h$ ). Unfortunately, the wide-range of pressure estimates described above, and the lack of accurate isochores for high salinity fluids, combine to hinder the determination of accurate trapping temperatures. An approximate trapping temperature can be estimated using data for the NaCl-H<sub>2</sub>O system at 40% salinity (Bodnar, 1994). For inclusions with  $T_h = 400^\circ\text{C}$ ,  $T_t$  is estimated to be 450 to 475°C (at 2.6 and 3.5Km lithostatic pressure respectively), and for inclusions that homogenise at 600°C,  $T_t$  is estimated to be 600 to 635°C (at 2.6 and 3.5Km lithostatic pressure respectively). As the salinity increases from 0 to 40 wt% eq. NaCl causes the slopes of the isochores in the NaCl-H<sub>2</sub>O system to increase (Bodnar & Vityk, 1994), the corrections for higher salinities (eg 50-70 wt% eq. NaCl) may require larger temperature corrections, however the magnitude of this correction cannot currently be estimated (Bodnar & Vityk, 1994). The main Stage 3 stockwork at Dinkidi is therefore concluded to have been emplaced at temperatures >600°C, while the late-stage  $B_{H(Cpy)}$  inclusions were trapped at temperatures of approximately 405 to 520°C (at 2.6 km depth) or 415 to 545°C (at 3.5 km depth). Fluid inclusion in apatite from Stage 2 (average  $T_h$  274°C; average salinity 18wt% eq. NaCl) are estimated to have trapping temperatures of 235 to 365°C (at 2.6 km depth) or 255 to 385°C at 3.5 km depth.

## Conclusions

The high trapping temperatures, and high salinities, of primary fluid inclusions within the Stage 3 quartz stockwork are indicative of a magmatic-hydrothermal origin, with the fluids interpreted to be sourced from the Bufu Syenite. Water-saturated granite pegmatites and Cl, F, and B-rich granitic melts have a similar bulk composition to the Bufu Syenite, and have solidus temperatures as low as 500°C, while water-saturated granodiorites have a solidus temperature of ~600°C (Kosukhin *et al.*, 1984, Manning, 1981; Webster *et al.*, 1987; London, 1989). The homogenisation temperatures of the Stage 3 stockwork (>600°C) are equal to, or higher than, these solidus temperatures, suggesting that the Bufu Syenite would have remained molten during emplacement of the brine under lithostatic loads. Based on textural, compositional, spatial and temporal relationships, the Bufu Syenite is considered to have been the feeder or conduit for the fluids that formed the Stage 3 quartz stockwork. Influx of high temperature volatiles into the Bufu Syenite melt, believed to be sourced from an underlying magma chamber, may have assisted in keeping this 'conduit' molten during emplacement of the stockwork. The low solidus temperatures for similar melts suggest that final crystallisation of the Bufu Syenite is likely to have occurred at ~500°C, possibly after depressurisation-driven volatiles loss (pressure quenching). This is approximately the same temperature as the  $B_{H(Cpy)}$  inclusions were being trapped throughout the overlying stockwork, presumably with associated

sulphide deposition.

The fluid inclusion results, combined with geological constants have been combined to develop a model for the formation of Stage 3 stockwork mineralisation. Co-existing melt and volatiles are interpreted to have risen up a magmatic conduit, in this case the Bufu Syenite. At depths of between ~4-5km under lithostatic pressures, the volatile phase entered the two-phase field of stability (Figure 7.4B; Bodnar & Vityk, 1994), and separated into vapour and brine. At the site of deposition (at a minimum of 2.6 km depth, and probably 2.9 to 3.5 km depth, based on isochores of Bodnar, 1994; and Cline & Bodnar, 1994) this brine would appear to be exsolving directly from the magmatic stock. Expansion of the vapour phase during ascent led to high vapour pressures, which is interpreted to have caused the extensive fracturing located around, and within, the porphyry stock (Burnham, 1979). The pressure loss during fracturing would lead to further vapour expansion, possibly with disruption and vesiculation of the magma (Shinohara & Kazahaya, 1995). Cooling of the brine, possibly combined with a build up of pressure, produced a hypersaline NaCl-KCl-FeCl brine (eq. NaCl > 68 wt%; with elevated concentrations of Cu, Ca, Mn, Ti, and Zn). This brine precipitated quartz throughout the network of stockwork fractures, and also produced a massive accumulation of coarse-grained quartz and perthite in the core of the system (the Bugoy Pegmatite). Prevailing depositional temperatures were over 600°C. Periods of quartz growth and fracture sealing appear to have been interrupted by episodic depressurisation, with trapping of V and B<sub>v</sub>-type inclusions. These vapour-rich inclusions cannot co-exist with the hypersaline brines (Bodnar, 1994), indicating that a significant pressure drop occurred between the formation of the two fluid inclusion types. This pressure loss is assumed to have been caused by periods of hydraulic fracturing, with depressurisation to hydrostatic pressures (~260 bar). Loss of the vapour phase is interpreted to have helped produced the high metal concentrations measured within the residual magmatic-hydrothermal brine. Ore mineralisation appears to have formed after cooling of this residual brine, from >600°C to at least 405 to 545°C, forming a cupriferous 39 to 50 wt% eq. NaCl brine that is preserved as chalcopyrite-bearing primary and secondary hypersaline fluid inclusions that are spatially associated with sulphide grains.

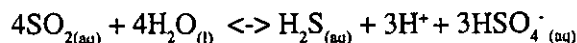
## SULPHUR ISOTOPES

### Introduction

Measured variations in the ratio of <sup>34</sup>S to <sup>32</sup>S in sulphide minerals can be used to gain insights into the physiochemical conditions and mechanisms of sulphide deposition within an ore body, and can help to determine the source(s) of sulphur in the hydrothermal fluid. <sup>34</sup>S partitions preferentially into oxidised sulphur (as SO<sub>2</sub> at >400°C and SO<sub>4</sub> <400°C; Ohmoto & Rye, 1979), so that any fluids that is undergoing enrichment in oxidised sulphur (by reduction and precipitation of isotopically light sulphides, or by addition of sulphate-rich fluids such as seawater) become isotopically heavy, while fluids that have gained reduced sulphur (as H<sub>2</sub>S, the main ligand required for sulphide formation) through oxidation of sulphides and the

## FLUID INCLUSIONS & SULPHUR ISOTOPES

precipitation of sulphates or degassing of  $\text{SO}_2$ , will become isotopically lighter. The isotopic composition of sulphur in an oxidised magmatic fluid is a function of the original source composition and the isotopic fractionation factor between  $\text{H}_2\text{S}$  and  $\text{SO}_2$  (or  $\text{SO}_4$ ), which is temperature dependent, and the  $\text{H}_2\text{S}/\text{SO}_4$  ratio of the fluid, which is dependent on  $f\text{O}_2$ , pressure, temperature and pH, according to the reaction:



The relationship between the  $\delta^{34}\text{S}_{\text{total sulphur}}$  of the hydrothermal fluid and the  $\delta^{34}\text{S}_{\text{H}_2\text{S}}$  of the precipitated sulphide can be summarised as:

$$\delta^{34}\text{S}_{\text{Asulphur fluid}} = \delta^{34}\text{S}_{\text{H}_2\text{S}} X_{\text{H}_2\text{S}} + \delta^{34}\text{S}_{\text{SO}_2} X_{\text{SO}_2}$$

Where  $X_{\text{H}_2\text{S}}$  and  $X_{\text{SO}_2}$  are the mole fractions of  $\text{H}_2\text{S}$  and  $\text{SO}_2$  relative to total sulphur in the fluid (Ohmoto & Rye, 1979). Increased fractionation between sulphide and sulphate, caused by increased oxidation and cooling (Ohmoto & Rye, 1979) will result in lighter  $\delta^{34}\text{S}$  sulphide values. Therefore, with large amounts of sulphate, the  $\delta^{34}\text{S}_{\text{Asulphur}}$  of the fluid can be far heavier than the sulphide value, while in reduced,  $\text{H}_2\text{S}$ -rich systems  $\delta^{34}\text{S}_{\text{sulphide}}$  is approximately equal to  $\delta^{34}\text{S}_{\text{Asulphur fluid}}$  (Ohmoto & Rye, 1979).

## Method

A total of 57 sulphide samples were analysed for their sulphur isotopic compositions at the University of Tasmania. The samples consist of all major sulphide minerals found within Stage 2, 3 and 5 hydrothermal assemblages. Only trace amounts of anhydrite have been observed in the Stage 2 and Stage 3 mineral assemblages. This may reflect the replacement of anhydrite by Stage 5 zeolite minerals, which infill the interstitial cavities of most Stage 2 and Stage 3 veins. No co-existing sulphide-sulphate pairs were observed or analysed during this study. Sulphide samples were hand drilled and analysed using the analytical techniques of Robinson & Kusakabe (1975). Isotopic measurements were made on a VG Micromass 602D mass spectrometer. Internal standards were run with a  $\text{SO}_2$  reference gas and analytical uncertainty is estimated as  $\pm 0.2\text{‰}$ . The results (Appendix D) are presented as  $\delta^{34}\text{S}\text{‰}$  values, the ratio of  $^{34}\text{S}$  to  $^{32}\text{S}$  in the sample relative to triolite from the Canyon Diablo iron meteorite (CDT).

## Sulphur Isotope results

Sulphide minerals from Dinkidi display a narrow range of  $\delta^{34}\text{S}$  values, from  $-0.2\text{‰}$  to  $-4.2\text{‰}$  (average  $-2.4\text{‰}$ ; Figure 7.5A and Appendix D). All hydrothermal stages display a similar range in isotopic compositions, although sulphides from hydrothermal Stages 3B, 3C and 5 appear to be isotopically lighter than Stage 2 sulphides (Figure 7.5A). Bornite, pyrite and chalcopyrite within individual sub-stages share a similar range of isotopic compositions (Figure 7.5A). Progressive substages within hydrothermal stages 2 and 3 appear to become isotopically lighter over time (Figure 7.5A).

The  $\delta^{34}\text{S}$  sulphide range at Dinkidi is similar to that of sulphides from south-west USA and Chilean porphyry deposits, and to  $\delta^{34}\text{S}$  values for the alkaline Valley Copper deposit in British



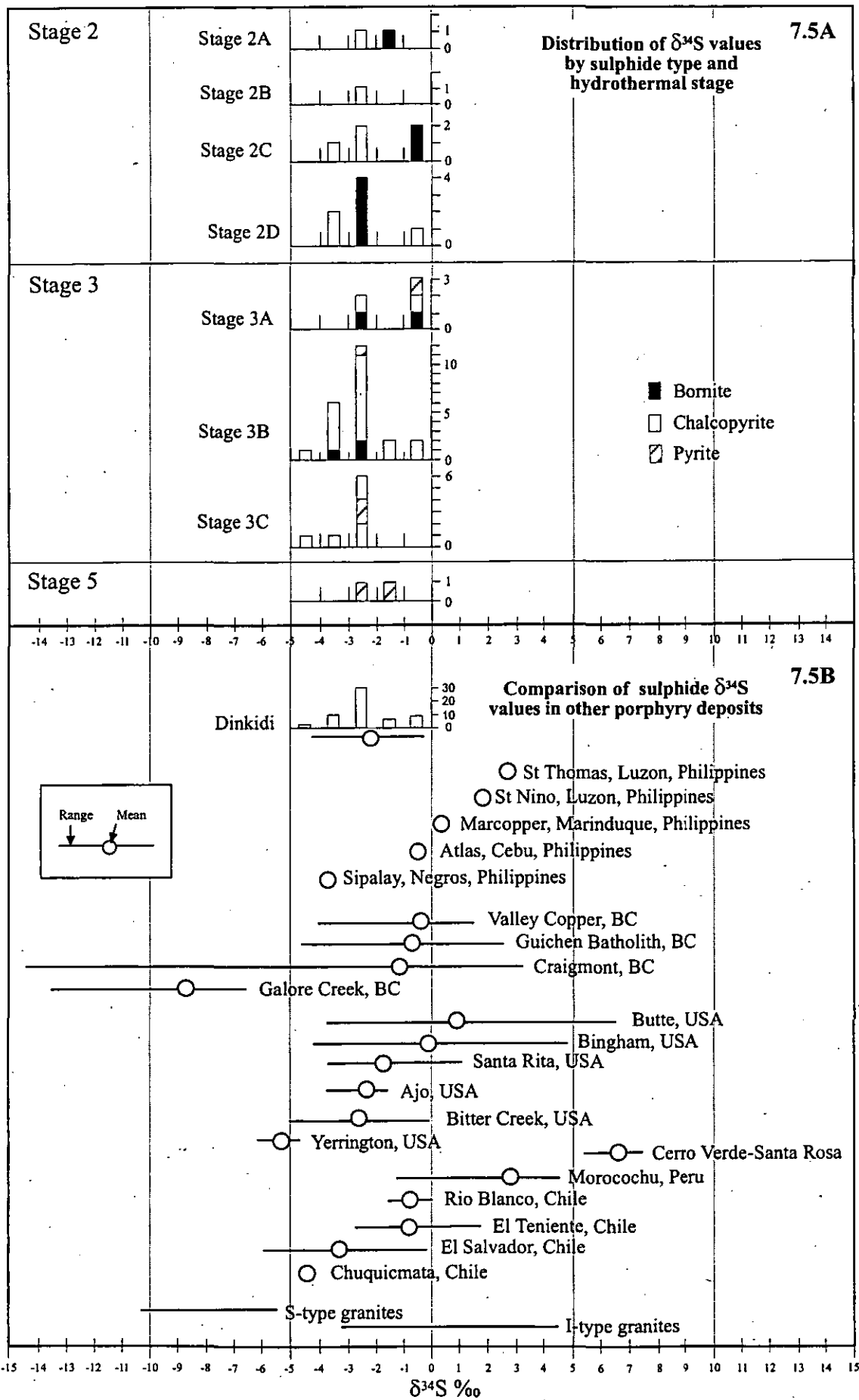


Figure 7.5: Range of  $\delta^{34}\text{S}$  isotope values for sulphides at the Dinkidi porphyry deposit (A), and comparison to sulphide values from other porphyry deposits (B). Philippine porphyry values consist of one analysis from each deposit (from Sasaki *et al.*, 1984). Data for all other porphyry deposits from Ohmoto & Rye (1979), Sasaki *et al.* (1984) and Taylor (1987).

## FLUID INCLUSIONS & SULPHUR ISOTOPES

Columbia (Figure 7.5B; Ohmoto & Rye, 1979; Sasaki *et al.*, 1984; Talyor, 1987). The  $\delta^{34}\text{S}\text{‰}$  sulphide values are also within the  $\delta^{34}\text{S}$  range for magmatic sulphides from I-type granites (Figure 7.5B; Talyor, 1987). Sulphides at Dinkidi do not display the distinctly light  $\delta^{34}\text{S}$  values found in three alkaline porphyry systems (Galore Creek & Craigmont, BC; Yerrington, USA; Figure 7.5B), a trend considered to have been caused by extensive sulphate fractionation within highly oxidised fluids or by the assimilation of sedimentary sulphides (Ohmoto & Rye, 1979; Dilles & Field, 1996). Sulphides at Dinkidi are isotopically lighter than most of the  $\delta^{34}\text{S}$  values reported for other Philippine deposits (Figure 7.5B; Sasaki *et al.*, 1984). These heavier values are interpreted to represent a seawater sulphur contribution to the hydrothermal fluids (Sasaki *et al.*, 1984). The significantly heavier  $\delta^{34}\text{S}$  values at Morococha (and probably Cerro Verde; Figure 7.5B) have been attributed to incorporation of sulphates from evaporites in the host rock sequences (Ohmoto & Rye 1979).

The isotopic composition of sulphides from Dinkidi are characterised by well-developed spatial zonation (Figure 7.6). An isotopically heavy zone ( $\delta^{34}\text{S} = -0.2$  to  $-0.9\text{‰}$ ; Figure 7.6) is located above the Balut Dyke, to the west of the Quan Porphyry and the main Stage 3 quartz stockwork (Figure 6.7). This anomaly is spatially associated with high-grade Stage 2D bornite-orthoclase mineralisation and moderate Stage 3 quartz stockwork veining. Within this zone both Stage 2 and Stage 3 sulphides have similar isotopically heavy values. Sulphides in the main Stage 3 quartz stockwork zone, centred above the apex of the Bufu Syenite, have  $\delta^{34}\text{S}$  values of approximately  $-2\text{‰}$  (Figure 7.6). Stage 2 and 3 sulphides located on the margins of the Dinkidi Stock have lighter  $\delta^{34}\text{S}$  values, with a sharp transition to distal  $\delta^{34}\text{S}$  values of  $-3$  to  $-4\text{‰}$  at shallow levels and a more gradual transition at depth (Figure 7.6). The  $\delta^{34}\text{S}$  values for Stage 5 fault-zone pyrite are typically slightly lighter than the surrounding Stage 3 sulphides (Figure 7.6).

## Sulphur Isotope Discussion

### Sources of sulphur

The narrow range of sulphide  $\delta^{34}\text{S}$  values, and similarity to MORB magmatic values ( $\delta^{34}\text{S} = 0 \pm 5\text{‰}$ ; Ohmoto & Rye, 1979; Talyor, 1987), is typical of sulphides from most porphyry deposits (Figure 7.5B). The  $\delta^{34}\text{S}$  values for sulphides at Dinkidi are also similar to values for mantle-derived sulphides ( $0 \pm 3\text{‰}$ ; Chaussidon & Lorand, 1990), and suggest that there is no 'exotic' source of sulphur within the hydrothermal fluids, such as isotopically heavy marine sulphate ( $+20\text{‰}$ ; Rees *et al.*, 1978; i.e. the marine sulphate signature found in several other Philippine porphyry deposits; Sasaki *et al.*, 1984; Figure 7.5B), isotopically light 'organic' sulphide ( $-20.7$  to  $-40\text{‰}$ ; Ohmoto & Rye, 1979) and possibly by the basement island arc volcanic rocks ( $\delta^{34}\text{S} = -0.2$  to  $+20.7\text{‰}$ ; Rollinson, 1993). However, the adherence to this  $\delta^{34}\text{S}$  range is misleading in that the relatively oxidised character of most porphyry magmas means that the sulphide values are likely significantly below the actual value of total  $\delta^{34}\text{S}$ .

The narrow range of sulphide  $\delta^{34}\text{S}$  values present at Dinkidi (Figure 7.5A) suggest that the Stage 2 and Stage 3A hydrothermal fluids shared similar physiochemical conditions during

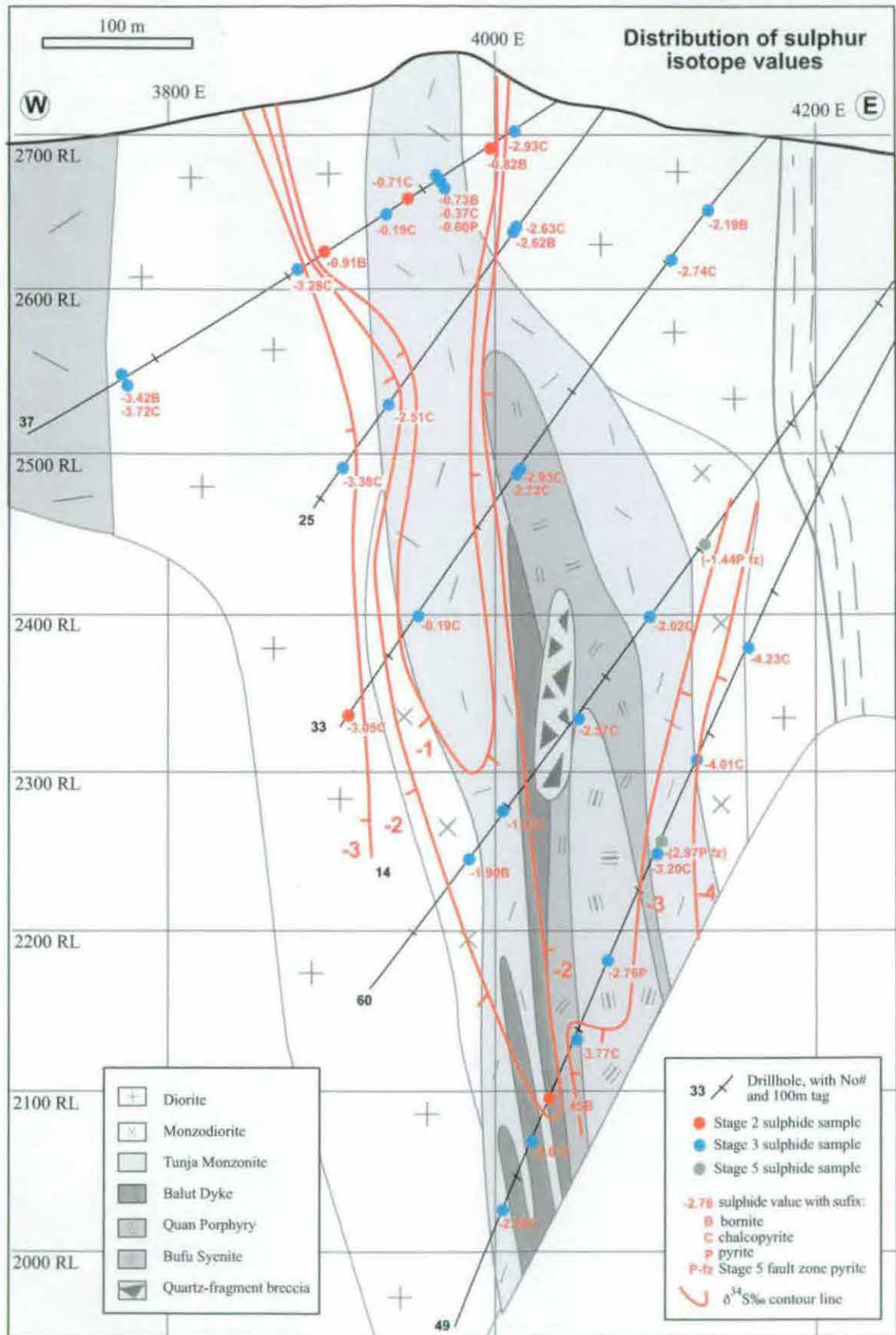


**Figure 7.6:** Distribution of sulphur isotope values on the 5750 cross-section of the Dinkidi Cu-Au deposit. The zone of isotopically heavy values ( $\delta^{34}\text{S}\text{‰} = 0$  to 1) is characterised by abundant Stage 2 mineralisation (particular Stage 2D orthoclase-bornite), moderate potassic alteration of the Tunja Monzonite, and abundant Stage 3 quartz veins. Key for all rock symbols in Figure 4.1. Geology based on logged drill holes (Appendix A).



sulphide precipitation. This could reflect stable sulphide-sulphate ratios, temperatures, pressures,  $fO_2$  and melt to fluid ratios (Ohmoto & Rye, 1979).

#### *Development of light $\delta^{34}S$ values*

Late-stage sulphides at Dinkidi (Stages 3B and 3C; Figure 7.5A) are isotopically lighter (Figure 7.5A) than earlier stages, and  $\delta^{34}S$  decreases along the margins of the Dinkidi Stock (Figure 7.6). This is consistent with increased isotopic fractionation, which can occur in magmatic systems from cooling or oxidation, in this case of the Stage 3 fluid (producing the hematite-stable Stage 3B and 3C mineral assemblage). Similar isotopic zonation to lighter distal values has been described at a small number of other porphyry deposits (eg Bingham: Field, 1966; North Parkes: Heithersay & Walshe, 1995), and have been attributed to cooling and/or oxidation (Field, 1966; Heithersay & Walshe, 1995). Although oxidation may have produced the lighter late-stage and distal  $\delta^{34}S$  compositions, the simplest explanation for the isotopically lighter values is cooling under conditions of constant  $SO_2/H_2S$  (ie. no oxidation). Modelling of the chalcopyrite sulphur isotope systematics (G. Davidson *pers. com.*, 2001) indicates that cooling an oxidised fluid from ~600 to 350°C (temperatures estimated from fluid inclusion results, with an estimated  $H_2S/SO_2=1$  for an oxidised melt and total sulphur estimated at = 2‰; Omoto & Rye, 1976; Taylor, 1987) will result in a decrease in sulphide  $\delta^{34}S$  from -1‰ to -6‰, with a drop from -2.5 to -5‰ at approximately 400°C (G. Davidson *pers. com.*, 2001). This drop at ~400°C occurs in response to the change in oxidised sulphur speciation to  $SO_4$ , and the re-equilibrium of  $H_2S$  with  $SO_4$ , rather than  $SO_2$ . The sharp transition in  $\delta^{34}S$  values over the first 50 meters into the diorites suggests that there was only limited lateral fluid movement into the surrounding, largely impermeable, diorites, with most fluids focussed up along the Dinkidi Stock. The lack of a similar shift over time to lighter values in the Stage 2 assemblage may indicate that the Stage 2 fluids were relatively reduced and  $H_2S$  rich. Alternatively, the Stage 2 fluids may not have undergone a significant degree of cooling prior to the emplacement of the Quan Porphyry.

#### *Formation of the heavy $\delta^{34}S$ zone*

Stage 2 and 3 sulphides have isotopically heavy compositions above the Balut Dyke. This zone overprints the Stage 2D sulphide-orthoclase mineralisation, and isotopically heavy values are not found within the adjacent Stage 3 intrusions. This increase in  $\delta^{34}S$  values suggests a decrease in the degree of isotopic fractionation (Ohmoto & Rye, 1979). This can be caused by either heating or reducing the hydrothermal fluids (Ohmoto, 1972). Heating of the Stage 3 fluid is not consistent with fluid inclusion evidence, which records cooling of a hypersaline brine from temperatures >600 to ~400°C during emplacement of the stockwork, at locations throughout the deposit. For a fluid with  $H_2S/SO_2=1$  (and total sulphur estimated at 2‰), producing chalcopyrite with a  $\delta^{34}S$  composition of -0.2 from a fluid which was depositing chalcopyrite initially with compositions of -2.5‰ would require heating of the fluid from ~400 to 600°C, prior to cooling and deposition of the sulphides. Heating of a relatively cool fluid is not consistent with fluid inclusion results, which suggest the hypersaline brine formed from

phase separation of at least 750°C. A heating mechanism also cannot explain the restriction of isotopically heavy  $\delta^{34}\text{S}$  sulphide values to outside the Quan Porphyry.

The isotopically heavy sulphide values may reflect the reduction of an oxidised Stage 3 fluid by interaction with a relatively reduced wall rock. The close spatial association between the isotopically heavy values and Stage 2D mineralisation (see Figures 6.5 and 7.7 for Stage 2D distribution) suggests that the Stage 2D sulphides may have reduced the Stage 3 fluids. Control by a pre-Stage 3 feature is supported by the lack of isotopically heavy values within the Quan Porphyry (Figure 7.6 & 7.7). This model is consistent with petrological evidence, with Stage 2 magnetite within the isotopically heavy zone commonly rimmed by Stage 3B hematite; Plates 6.9C & D).

Other models do not adequately address the distribution of the isotopically heavy sulphide values. Down-welling of reduced fluids may have reduced the oxidised Stage 3 brines and produced the observed isotopic zonation. However down-welling fluids would be expected to have been emplaced throughout the permeable Stage 3 quartz stockwork (see Figures 6.5, 6.6 and 7.6 for stockwork distribution) rather than focused over only the Stage 2D mineralisation. Furthermore, the zone above the Balut Dyke is not highly permeable, with Stage 2D mineralisation focused along a diffuse zone of orthoclase alteration within weakly altered Tunja Monzonite. Down-drawn Stage 3C to Stage 5 fluids would also be expected to have been focused within the late Stage 3C Bugoy quartz-fragment breccia and Stage 5 fault zones. Sulphides in these highly permeable zones do not have isotopically heavy  $\delta^{34}\text{S}$  values.

The distribution of the isotopically heavy zone is best explained by the wall rock interaction model, with reduction of Stage 3 fluids by Stage 2 sulphides (Figure 7.7). As even at elevated temperatures there is little or no re-equilibration between solid sulphides (Ohmoto & Goldhaber, 1997), the isotopically heavy values of Stage 2 sulphides within this zone are considered to reflect primary Stage 2 isotopic compositions. This supports the presence of two isotopically distinct sulphur populations: heavy, relatively reduced Stage 2 sulphides ( $\delta^{34}\text{S} = 0$  to  $-1$  ‰) and lighter oxidised Stage 3 sulphides ( $\delta^{34}\text{S} = -2$  to  $-3$  ‰).

The sulphur isotope composition of Stage 5 pyrite is similar to the values of adjacent samples of Stage 2 and 3 sulphides (Figure 7.6). The source of sulphur for the late-stage pyrite is interpreted to have been the remobilisation of earlier-formed copper-sulphides that were incorporated into the fault zone after ore formation.

Calculation of the  $\delta^{34}\text{S}_{\text{sulphur fluid}}$  for a hydrothermal fluid from the measured sulphide  $\delta^{34}\text{S}$  requires, in an oxidised system, a precise knowledge of the temperature,  $\delta^{34}\text{S}_{\text{SO}_4}$  and  $f\text{O}_2$  during precipitation of the sulphide. Without measured in equilibrium  $\delta^{34}\text{S}_{\text{H}_2\text{S}}$  and  $\delta^{34}\text{S}_{\text{SO}_4}$  values the total  $\delta^{34}\text{S}$  of the fluid cannot be accurately determined. An estimation of  $\delta^{34}\text{S}_{\text{sulphur fluid}}$  may be made from measured  $\delta^{34}\text{S}_{\text{H}_2\text{S}}$  based on an estimated oxidation state of the fluid derived from the associated mineral assemblage (Omoto & Rye, 1979). Using the fractionation factors of Ohmoto & Rye (1979), a temperature of 400°C, an average proximal Stage 3 sulphide  $\delta^{34}\text{S}$  value of -

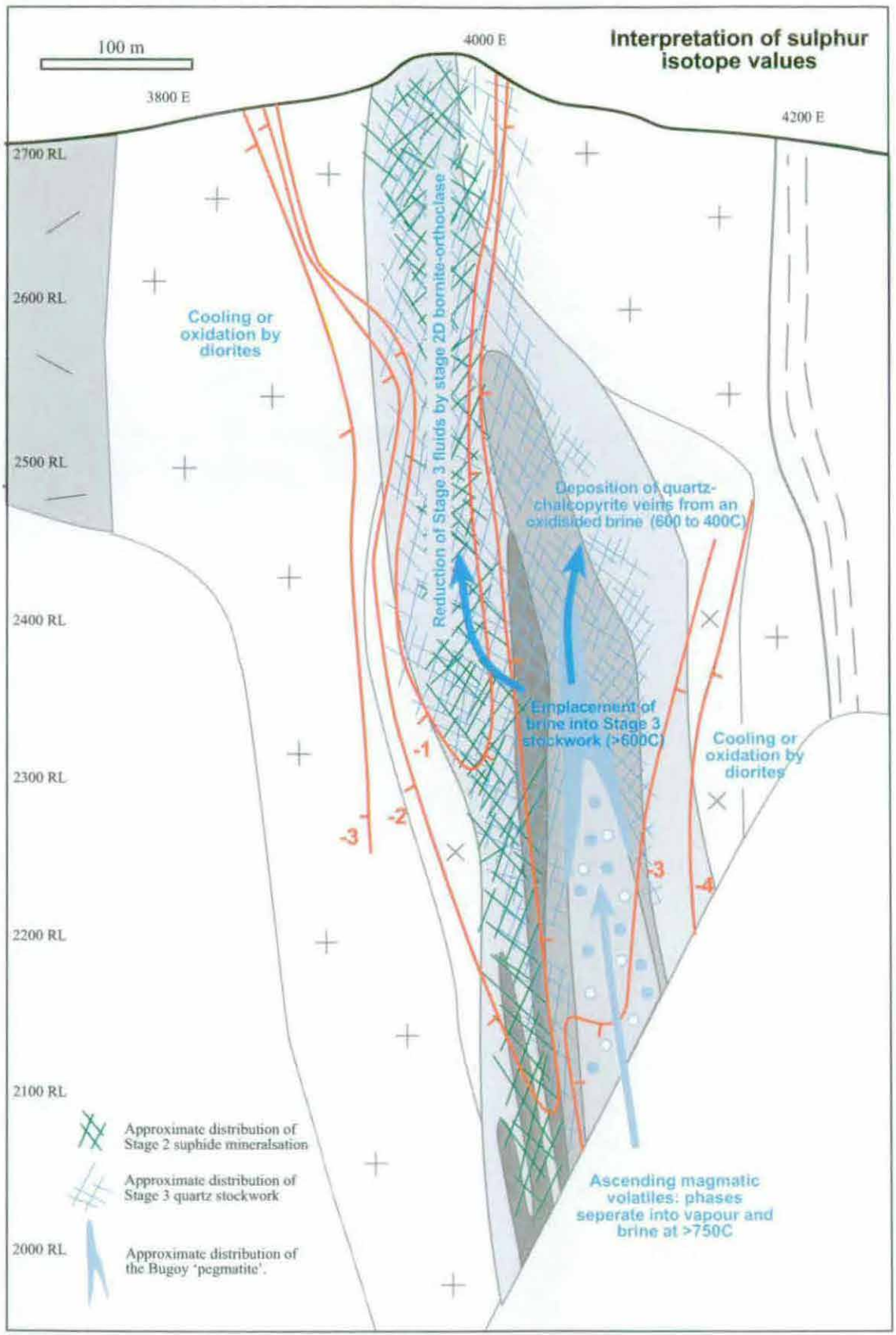


**Figure 7.7:** Interpretation of sulphur isotope values, plotted on the 5750 cross-section. The isotopically heavy core is interpreted to have formed by wall-rock interaction between the oxidised Stage 3 fluids and the relatively reduced Stage 2D sulphide mineralisation hosted within the Tunja Monzonite. Key for rock symbols in Figures 4.1 and 7.6.



2.7‰, and assuming a magnetite-hematite stable fluid, the total sulphur in the Stage 3B hydrothermal fluid can be estimated as  $\delta^{34}\text{S}_{\text{fluid}} = -1.2\text{‰}$  (and at 500°C  $\delta^{34}\text{S}_{\text{fluid}} = +1.3\text{‰}$ ). More reduced conditions, such as interpreted for the Stage 2 fluids, would lower the degree of fractionation. For a magnetite stable fluid, at both 400 and 500°C, assuming an average proximal Stage 2 sulphide  $\delta^{34}\text{S}$  value of 1.5 ‰, the total sulphur in the Stage 3B hydrothermal fluid can be estimated as approximately  $\delta^{34}\text{S}_{\text{fluid}} = -0.5\text{‰}$ . The similar  $\delta^{34}\text{S}$  values estimated for Stage 2 and Stage 3 fluids suggests a shared sulphur source.

The well-developed zonation of sulphide  $\delta^{34}\text{S}$  values observed at Dinkidi is in contrast to the majority of S isotope studies on porphyry deposits (eg, Panguna, Eastoe, 1983; El Salvador, Field & Gustafson, 1976), which do not display strong spatial zonation. The lack of zoning in other deposits may reflect a wide range of causes, such as overprinting of multiple sulphide-bearing fluids, complex fluid paths and numerous other geological, paragenetic and physiochemical processes. In the case of Dinkidi, the isotopic zonation is interpreted to reflect the degree of cooling and wall-rock interaction with the zoning pattern indicating that fluids were focussed upwards, along the stock, rather than dispersing laterally.

# SYNTHESIS AND GENETIC MODEL

The Dinkidi Au-Cu Porphyry deposit is one of only a few alkaline porphyry deposits that have been described from outside British Columbia (Jensen & Barton, 2000). The principle aims of this thesis were to produce the first detailed geological description of both the Dinkidi deposit and the regional geology and to interpret the evolution of the magmatic-hydrothermal system within that geological context. This chapter summarises these findings, and uses these descriptions to construct a genetic model for the Dinkidi porphyry deposit. The holistic approach of this study, placing the geology and mineralisation of the ore deposit into the context of the intrusive history of the region, has allowed insights into the processes that must occur prior to, and during, the formation of a mineralised porphyry melt.

## OVERVIEW: GEOLOGY AND MINERALISATION OF THE DIDIPIO REGION

The main geological feature of the Didipio Region is the Didipio Igneous Complex (Figure 3.1). This alkaline intrusive complex is hosted within the subalkaline andesite lavas of the Mamparang Formation and the potassic trachytic lavas of the Upper Mamparang Formation. The Didipio Igneous Complex was emplaced during four main stages of intrusive activity: emplacement of an early diorite phase, intrusion of the weakly mineralised Surong biotite monzonite, structurally-controlled emplacement of the strongly mineralised monzonites and syenites of the Dinkidi Stock, and the intrusion of late-stage andesite dykes (Figure 3.4; Figures 8.1, 8.2, 8.3 & 8.4). The geochemical affinities of the intrusive rocks are interpreted to indicate that all the Didipio Igneous Complex intrusions have been sourced from the same body of LREE and LILE-enriched melt, and are related to each other by low-pressure fractional crystallisation. The trachytes of the Upper Mamparang Formation are interpreted to have also shared a similar LILE-enriched melt source. The diorite to monzonite melt composition, and strong fractionation, are typical features of intrusions associated with quartz-saturated alkaline porphyry deposits (eg: Lang *et al.*, 1995a).

Each intrusive phase of the Didipio Igneous Complex has a distinct hydrothermal assemblage associated with its emplacement, with the degree and style of alteration reflecting the degree of fractionation of the intrusion. The diorites are associated with thermal metamorphism of the surrounding Mamparang Formation. The Surong Monzonite is surrounded by a broad halo of K-silicate alteration and weak Cu-Au mineralisation. Within the Dinkidi Stock, the Tunja biotite monzonite is associated with K-silicate alteration, the Balut Dyke clinopyroxene-syenite is associated with calc-potassic veining and high Au-grade K-feldspar-bornite mineralisation, and the Quan Porphyry and Bufu Syenite quartz syenites are associated with the emplacement of a Cu-Au mineralised quartz stockwork. This change in alteration style with different intrusive compositions highlights the importance of crystallisation, shallow level fractionation and volatile build up (the 'second boiling' of Bowen, 1933 and Burham, 1979) in producing the late-

stage melts that formed the Dinkidi porphyry deposit. Following porphyry-style alteration, the Didipio Igneous Complex and surrounding volcanics were overprinted by district-scale argillic alteration, minor high- and low-sulphidation epithermal mineralisation formed, and late stage zeolite veins were developed in association with faulting.

### TECTONIC SETTING AND THE GENESIS OF THE ALKALINE MELTS

The start of alkaline magmatism in northern Luzon is marked by the extrusion of the potassic, quartz-undersaturated trachytes and phonolites of the Upper Mamparang Formation at the end of the Oligocene (25-23Ma; Knittel, 1981, 1987). This alkaline to potassic magmatism has island arc radiogenic (Knittel & Defant, 1988) and geochemical (low  $\text{TiO}_2$  and HFSE; high  $\text{Al}_2\text{O}_3$ ) signatures, suggesting that it represents the final LILE-enriched end product of island arc magmatism, sourced from partial melting of the mantle wedge above the stalled, and dehydrating, East Luzon Trench. The Upper Mamparang Formation overlies an arc sequence that ranges from early tholeiitic submarine basalts (the Eocene Caraballo Formation) to later subalkaline subaerial andesites (the Oligocene Mamparang Formation).

The Upper Mamparang Formation hosts the three main alkaline to potassic intrusive centres of northern Luzon: the Cordon Syenite Complex (Knittel, 1987), the Palali Batholith (Albrecht & Knittel, 1990) and the Didipio Igneous Complex. The volcanics occur as an elongate belt located along the western margin of the Cagayan Valley Basin, and apparently formed coeval with the commencement of rifting along this basin in the Late Oligocene to Early Miocene (Christian, 1964; Knittel, 1987). This rifting must have tapped the LILE-enriched source of the alkaline magmas. Extensional tectonism (which formed a rift basin with an estimated depth of 7 km; Caagusan, 1977) also allowed the emplacement of a large body of melt into the shallow crustal environment, where plagioclase fractionation and volatile exsolution could occur. The radiogenic (Knittel & Defant, 1988) and geochemical composition of these alkaline melts indicates a mantle-derived source, with negligible contamination from crustal sources.

### VOLCANIC ENVIRONMENT: MAMPARANG & UPPER MAMPARANG FORMATIONS

The oldest rocks exposed in the Didipio region are the interbedded andesites lavas and debris flows of the late Oligocene Mamparang Formation (MMAJ, 1977; Billedo, 1994), which are interpreted to be the proximal facies of a terrestrial andesitic stratovolcano that formed in the Late Oligocene. Overlapping palaeontological ages suggest that these volcanics may have been deposited adjacent to a shallow sea (the Late-Oligocene to Early Miocene limestones of Christian, 1964; MMAJ, 1977 and Billedo, 1994). The magmatism that formed the Mamparang Formation is interpreted to be a subalkaline precursor to late-stage alkaline magmatism. Furthermore, the Mamparang Formation becomes progressively more alkaline up-stratigraphy. In the Didipio region, the Mamparang Formation is overlain by the trachyte lavas and apparently terrestrial volcanoclastic rocks of the Upper Mamparang Formation, which are correlated here to the feldspathoid-bearing trachytes (phonolites) that host the Cordon Syenite

## GENETIC MODEL

Complex and the Palali Batholith. The predominance of coherent extrusive units (rather than pyroclastic or volcanoclastic units) suggests proximal settings for the intrusive complexes within trachytic volcanic piles, most probably comprised of irregular domes with extensive volcanoclastic and pyroclastic aprons. Such a setting contrasts with the typical model of calc-alkaline porphyry formation, in which porphyry deposits are considered to form beneath andesitic stratovolcanos (eg Ransome, 1919; Emmons 1927; Sillitoe 1973). In many cases, the first geologically recognisable stage in the development of a porphyry deposit is the extrusion of a 'co-magmatic' volcanic pile. The volcanic cover may provide a heat source and insulation for the porphyry system, allowing emplacement of porphyry stocks along shallow sub-volcanic feeder structures, where phase separation can occur. Although only a stratigraphic thickness of about 400 meters is preserved in the Didipio region, the Upper Mamparang Formation is interpreted to have been thick enough (~1.5-3 km) to confine and host the Didipio Igneous Complex.

## EMPLACEMENT OF THE DIDIPIO IGNEOUS COMPLEX

The Didipio Igneous Complex is interpreted to have intruded one of the main vents for the Upper Mamparang Formation volcanic pile, with successive intrusives rising up the same feeder structure utilised by the trachyte lavas. Intrusion close to the volcanic source is supported by the proximal nature of the volcanic facies exposed in the Didipio region. The feeder structure is interpreted to have had a NNW orientation, parallel to the trend of the Dinkidi Stock, the rough elongation of the Surong Monzonite (after the offset of faulting is removed), the elongation and trend of the Palali-Didipio intrusive belt, and the elongation of the Upper Mamparang Formation volcanic belt. This structure is also parallel to F1 faults and to the margins of the Cagayan Valley basin. It is speculated to have originally been a normal fault zone associated with the rifting of the Cagayan Valley Basin.

The intrusions that comprise the Didipio Igneous Complex changed from early, comparatively large equigranular plutons, that were emplaced with some degree of stoping, to later narrow, structurally-controlled porphyritic intrusions, followed by thin late-stage andesite dykes and sills. This change in intrusion morphology suggests that the overlying volcanic edifice was being actively eroded during the lifetime of magmatism.

### **The first intrusion: diorites and monzodiorites**

The first Late Oligocene intrusive event within the Didipio region was the emplacement of a clinopyroxene-diorite pluton. The equigranular nature of this intrusion indicates emplacement at either moderate depths, or at shallower levels within an elevated geothermal gradient (possibly caused by extensional tectonism and the magmatism that sourced the overlying volcanic pile). The low Mg, Cr, and Ni concentrations suggest that the diorites had undergone substantial fractionation (most probably of olivine  $\pm$  clinopyroxene) prior to the emplacement into the subvolcanic environment. *In situ* fractionation of clinopyroxene, anorthite and magnetite lead to the emplacement of a series of diorite to clinopyroxene-monzodiorite phases (the latter.



representing a residual 73% of the initial dioritic fraction), with deposition of cumulate gabbros, anorthites and clinopyroxenites from the fractionated phases. The emplacement of the clinopyroxene-diorite was associated with the contact metamorphism of the surrounding Mamparang Formation (Figure 8.1), with weak development of biotite and cordierite, and an overprint of patchy propylitic alteration, which is tentatively interpreted to represent the ingress effects of heated meteoric water.

### **Emplacement of the Surong Monzonite and the start of volatile exsolution**

The diorites and monzodiorites of the Didipio Intrusive Complex were intruded by a multiphase monzonite pluton, the Surong Monzonite. Widespread igneous breccia and rafts of diorite and gabbro indicate that only the top of the pluton has been exposed.

The monzonite shares the same geochemical trends at the early diorite to monzodiorite rocks, suggesting that both intrusions were sourced from the same underlying magma chamber (Figure 8.1). The monzonite is considered to represent a 35% melt fraction of the initial clinopyroxene-diorite melt, following fractionation of plagioclase, clinopyroxene and magnetite. Fractionation of plagioclase and clinopyroxene following emplacement of the clinopyroxene-monzonite intrusion is interpreted to have formed the series of clinopyroxene-, biotite-, and late-stage quartz-monzonite phase that comprise the pluton, and which typically have diffuse gradational contacts with each other. The crystallisation of anhydrous phases, both during fractionation from a dioritic melt within the underlying magma chamber, and during the crystallisation of the pluton after emplacement, is interpreted to have enriched the residual melt in water, leading to volatile build up (the 'second boiling' of Bowen, 1933), and which triggered the crystallisation of hydrous phases such as biotite (at ~3.3 wt% H<sub>2</sub>O for a dioritic melt; Burnham, 1997).

Exsolution of a volatile phase would cause strong partitioning of metals and ligands into the fluid from the silicate melt (Candela, 1989a & 1989b). Release of a high temperature, K-Fe-Cl enriched brine from the crystallising Surong Monzonite is interpreted to have formed the broad halo of K-silicate biotite-magnetite alteration and anomalous, sub-ore grade Cu-Au mineralisation that surrounds the pluton (Figure 8.1):

### **Model for the emplacement of the Dinkidi Stock**

The Dinkidi deposit is hosted within an elongate multiphase stock that was emplaced into a series of diorites and monzodiorites (Figure 4.1). The stock consists of four main intrusions, which are the last and most evolved felsic intrusions emplaced within the Didipio Igneous Complex. The oldest and largest intrusion of this stock, the Tunja Monzonite, is an equigranular biotite monzonite that predates the formation of high-grade Cu-Au mineralisation and is petrologically similar to the main phase of the Surong Monzonite. The Tunja Monzonite has been intruded by a series of mineralised syenites: the variably-textured clinopyroxene-syenite of the Balut Dyke, and a monzosyenite porphyry (the Quan Porphyry) that grades, in its core, into a crystal-crowded leucocratic quartz-syenite (the Bufu Syenite). All three syenitic phases, the Balut Dyke, the Quan Porphyry and the Bufu Syenite, have a similar perthite-dominated composition. However, the Balut Dyke is clinopyroxene-phyric while the Quan Porphyry and

## GENETIC MODEL

Bufu Syenite are quartz-bearing. Alteration assemblages within the Dinkidi Stock reflect the igneous rock compositions. The Tunja Monzonite is surrounded by biotite-magnetite-orthoclase alteration. The Balut Dyke is associated with a high Au-grade but quartz-undersaturated diopside-actinolite-K-feldspar-bornite assemblage. The highly fractionated quartz-bearing melt of the Bufu Syenite is associated with a quartz-rich pegmatite and associated quartz-vein stockwork.

The large tonnages of porphyry deposits suggests that extensive fractionation is required to form an economic porphyry melt, assuming an orthomagmatic model for deposit formation (eg Hutton, 1795; Playfair, 1802; Lingren, 1905; Burnham 1979; Sillitoe 2000). In the case of the Yerrington Batholith, the modelling of Cline & Bodnar (1991) suggested that fractional crystallisation of 48 to 58 km<sup>3</sup> of monzodiorite magma was required to produce the 1280 Mt of ore (with 5.3 Mt contained Cu) hosted within three Cu porphyry deposits and within several skarn and carbonate replacement deposits (Cline & Bodnar, 1991; Dilles et al. 1995). At Dinkidi, the 0.417 Mt of Cu that is contained within the orebody would require extraction from 1.47 Km<sup>3</sup> of clinopyroxene-dioritic melt, assuming a initial Cu concentration in the melt of 65 ppm (using the concentration of Cu in the least evolved diorite, DD1; Appendix B), a density of 2.7 g/cm<sup>3</sup> for diorite and 1.0 for water, and assuming 100% efficiency in extraction of all copper from the silicate melt into a volatile phase and transport to the depositional site.

The amount of copper present within the Dinkidi orebody could be transported into the trap site in a one-off influx of 0.065 km<sup>3</sup> of hypersaline brine, at the relatively high PIXE-measured concentration of 0.64 wt% Cu (Table 7.1; assuming no concentration by phase separation). In Didipio, the early-formed clinopyroxene-phyric diorite is anhydrous, and the melt must have had a water content below 2.7% (the minimum required to nucleate amphibole in a dioritic melt; Burnham, 1997). If we assume that the nucleation of biotite within the Surong Monzonite represents the build up of volatiles to 3.3 wt% H<sub>2</sub>O (Burnham, 1997), and modelling indicates that the Surong Monzonite is a 35% residue of a clinopyroxene-diorite parent melt (Table 5.2), then the initial water content of the clinopyroxene-diorite is calculated to have been ~1.2 wt% H<sub>2</sub>O. Using the estimated initial water concentration, a density of 2.7 g/cm<sup>3</sup> for the diorite and 1.0 g/cm<sup>3</sup> for the fluid, then the generation of this volume of volatiles would require crystallisation of 1.6 km<sup>3</sup> of diorite, or, in the case of a 2.7 wt% H<sub>2</sub>O-bearing 'Burnham melt', 1.1 km<sup>3</sup> of diorite. These models suggest that crystallisation of a minimum 1.4 to 1.7 km<sup>3</sup> of diorite was required to exsolve a magmatic-hydrothermal fluid into which the copper fully partitioned, and then this fluid deposited its entire copper into the Dinkidi ore body. The actual amount of diorite that crystallised is likely to be significantly higher, as these estimates require 100% efficiency throughout all stages of magmatic volatile release and ore deposition. Consequently, the volume of melt displayed in Figures 8.1, 8.2, 8.3 and 8.4 are 10 times greater than the minimum required melt volumes, although even this may be an underestimate.

Given that considerable volume of melt was required to generate the mineralising fluids that formed the Dinkidi ore body, this in turn would have required an efficient aqueous transport

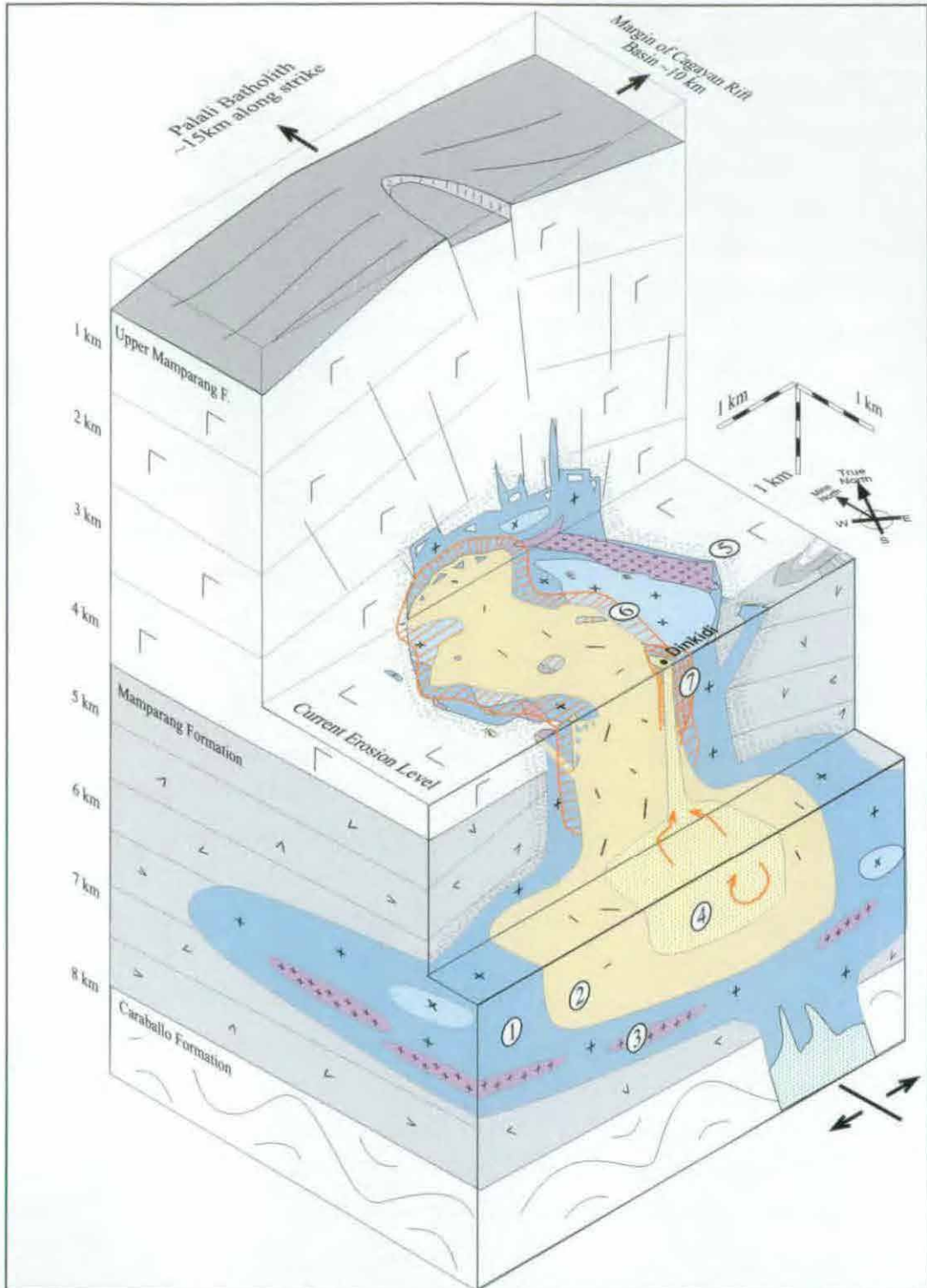


**Figure 8.1:** Highly schematic model for the emplacement of the Didipio Igneous Complex. The early equigranular diorite and monzonite intrusives are considered to be structurally focused apophyses or cupolas above a larger melt reservoir and may have been emplaced coeval with continued rifting along the margin of the Cagayan Valley Basin. This reservoir is shown with a sill like morphology, although there are no constraints on actual morphology. Emplacement of a clinopyroxene diorite (1) led, via fractionation of clinopyroxene and plagioclase, to the production of a clinopyroxene to biotite monzonite, the Surong Monzonite (2) as a residual 35% of the diorite melt. Fractionation also lead to the deposition of cumulate gabbros and clinopyroxenites (3) from the fractionated phases. Emplacement of the diorite phases was associated with the thermal metamorphism of the surrounding volcanic units (5), while the emplacement of the Surong Monzonite is associated with strong biotite-magnetite alteration and weak Cu-Au mineralisation (6). Further fractionation of clinopyroxene and plagioclase lead to the formation of the Tunja biotite monzonite (4), as a 48% fraction of the Surong Monzonite. This biotite monzonite was focused along a NW trending structure, forming the Dinkidi Stock (7), and is associated with intense Stage I K-silicate alteration. Volumes of melt displayed are ~10 times greater than the amount required to produce the copper content of the Dinkidi deposit. The paleosurface is estimated to be ~1 Km higher than the estimated depth for Stage 3 stockwork emplacement (2.5-3 km). Rock symbols are as used in Figure 3.1. Stippled colours denote melt, solid colour denote crystallised rock.

## GENETIC MODEL

mechanism from the site of crystallisation ( $> 1\text{--}2\text{ km}^3$  of melt) to the site of deposition within the Dinkidi stockwork zone (less than  $0.035\text{ km}^3$  of fractured rock). Initial concentration of volatiles within the melt may have occurred by transport of buoyant melt-volatile plumes along the walls of the crystallisation interface up into the upper portions of the magma body (eg Shinohara & Kazahaya, 1995). Evidence for this style of enrichment is indicated in the difficulty in modelling the evolved compositions of intrusions from the Dinkidi Stock by simple fractional crystallisation of observed phenocryst phases. This crystallisation-driven volatile build up (the 'second boiling' of Bowen, 1933) may have been assisted by pressure-driven exsolution of the entire melt body during convection. This build up of volatiles within the magma chamber would have been disrupted by the escape and emplacement of the Surong and Tunja Monzonite phases, which may have 'drained' the volatile reservoir (Figure 8.1). It is interpreted that the volatiles that were responsible for mineralisation at the Dinkidi deposit were exsolved from the crystallisation of the residual biotite-monzonite melt, following emplacement of the Surong and Tunja Monzonites. Assuming that the Tunja Monzonite represents the equivalent of a 17% melt fraction of the clinopyroxene diorite, then  $0.27$  to  $0.37\text{ km}^3$  of residual, volatile-saturated biotite-monzonite melt would have contained the volume of metals and volatiles required to form the Dinkidi orebody, allowing for 100% efficiency in transport and no loss of Cu to other environments.

Following the accumulation of a late-stage volatile reservoir, a northwest-trending feeder structure is interpreted to have tapped the magma chamber. Structurally controlled emplacement of the Balut Dyke and Quan Porphyry is indicated by the lack of xenoliths within the intrusives of the Dinkidi Stock, suggesting dilational emplacement, and the elongated NNW trends for all intrusives of the Dinkidi Stock. This structure is parallel to the F1 faults, which appear to have also controlled emplacement of the Upper Mamparang Formation, the emplacement of the regional alkaline intrusives, and the emplacement of the Surong Monzonite. The structure is interpreted to be a reactivated F1 fault, related to rifting along the margins of the Cagayan Valley Basin. Emplacement of the Surong Monzonite may have 'plugged' this feeder structure, forcing the Dinkidi stock to be emplaced on the margin of the Surong Pluton. Structurally-controlled emplacement of the porphyry melt is considered to have facilitated volatile transport to, and concentration at, the depositional area, and allowed emplacement of narrow, vertically extensive stocks of relatively viscous felsic melt into the surrounding sub-volcanic environment. The most extreme example of this is Balut Dyke, which is only 5 to 30 meters wide, but has an observed vertical extent of over 800 meters.

The high aspect ratio of the mineralising stocks would have allowed a significant pressure gradient to exist through the melt. At lithostatic confining pressures the supercritical volatile phase would enter the two-phase field of stability at depths of 4 to 5km (Bodnar & Vityk, 1994), triggering separation into vapour and brine phases. In the case of the Stage 3 assemblage this phase separation is estimated to have occurred at a temperatures of at least  $>750^\circ\text{C}$  (Figure 7.4B), and probably  $>850^\circ\text{C}$ , allowing for the pressure decrease (Figure 7.4B). Expansion of the



vapour phase as it ascended through the melt would lead to vesiculation of the magma and increasing vapour pressures within the conduit (Lowenstren, 1994; Shinohara & Kazahaya, 1995; Shinohara *et al.*, 1995), eventually leading to the lithostatic failure of the host rocks, with repeated periods of hydrostatic fracturing forming the extensive fracture network located around, and within, the porphyry stock (Gilluly, 1946; Burnham 1979). These fractures were then infilled and sealed by hydrothermal minerals, forming the porphyry deposit stockwork veins, and allowing further pressure build up within the melt (Burnham 1979). Structurally-controlled emplacement of the porphyry melt would also facilitate the rapid ascent of magma, which would be required to prevent the depressurisation-driven crystallisation of the water-saturated melt prior to emplacement at the shallow subvolcanic levels (Cashman & Blundy, 2000). Repetitive 'crack-sealing' along the structure, at deposit scale, would lead to the development of a multiphase porphyry stock such as Dinkidi. In this way, a porphyry stock could be considered analogous to a 1 km long sub-volcanic igneous crustiform vein, connecting a mid- to upper-crustal crystallising magma chamber to the shallow sub-volcanic upper crustal environment.

### **The Tunja Monzonite and Stage 1 K-silicate alteration**

The oldest and largest intrusion of the Dinkidi Stock, the Tunja Monzonite, is an equigranular biotite monzonite stock ~800 m long and 200 m wide. Texturally and compositionally, the Tunja Monzonite is more evolved than the Surong clinopyroxene monzonite. The Tunja Monzonite is a pre-mineralisation intrusion, hosted most of the Stage 2 and Stage 3 veins distal to the syn-mineralisation intrusions. The Tunja Monzonite is surrounded by a broad biotite-magnetite  $\pm$  orthoclase K-silicate alteration halo, which is the most extensive alteration halo present in the Dinkidi system. The K-silicate alteration grades distally into, or is overprinted by, an intensely developed epidote-chlorite-pyrite propylitic alteration assemblage. Although no microthermometric measurements were conducted on the Stage 1 hydrothermal assemblage, the biotite-magnetite-orthoclase assemblage is comparable to similar early alteration and vein assemblages in other Philippine porphyry deposits which formed at temperatures greater than 400°C (eg Takenouchi, 1980; Cooke & Bloom, 1990; Trudu, 1992). The hydrothermal fluids responsible for the K-silicate alteration were relatively magnetite-stable,  $\text{SiO}_2$ -undersaturated and were K- and Fe-saturated, a composition close to equilibrium with the orthoclase-biotite-plagioclase-bearing Tunja Monzonite.

The similarities in composition and hydrothermal assemblages between the Tunja and Surong Monzonites suggests that the Tunja Monzonite was emplaced soon after the Surong Monzonite, whereas a significant period of fractionation separated the Tunja biotite monzonite melt from the late-stage, highly-mineralised syenite intrusives. This is supported by the lack of strong stockwork veining associated with this stage, which is consistent with a lower volatile content and/or higher pressures than for the later intrusives.

## The Balut Dyke and Stage 2 calc-potassic alteration

The first stage of high-grade ore deposition at Dinkidi was associated with the intrusion of a variably-textured clinopyroxene-syenite, the Balut Dyke (Figure 8.2). The Balut Dyke consists of diopside phenocrysts hosted within a perthite groundmass, with accessory sphene and magnetite. Nucleation textures (eg Plate 4.3A) suggest that many of the calcic diopside phenocrysts grew *in situ*, at the site of deposition, rather than being sourced as phenocrysts from the underlying magma chamber. Textures within the dyke range from equigranular to coarsely porphyritic, with uncommon zones of rhythmic banding. This banding is interpreted to have formed by both flow segregation and diffusion-controlled nucleation at a stagnant crystallisation interface (eg Webber *et al.*, 1997). The presence of flow banding, and common truncation and cross-bedding within the bands, suggest that periods of flow were interspersed with periods of stagnation and inward crystallisation. Given that the dyke is 5 to 15 meters wide, high water contents must have been present to lower the melt viscosity and allow continued flow during crystallisation. A high volatile content for the melt is supported by the coarse grain size, extreme textural variability, melt inclusion evidence (Kamenetsky *et al.*, 1999) and the close spatial and temporal association between the dyke and the extensive Stage 2 hydrothermal alteration assemblage. Fluctuations in the water content during hydrostatic fracturing and formation of the Stage 3 stockwork may have caused variations in the melt viscosity, leading to varying flow rates and development of the layering in the Balut Dyke. These periods may have then been followed by periods of stagnation and volatile build up, leading to crystallisation of the inward nucleating layers. Repeated episodes of magma upwelling, hydrostatic fracturing and magmatic quiescence may have then produced the observed rhythmic layering. Megaporphyritic textures, similar to those in the Balut Dyke, have been reported from a number of intrusions associated with silica-undersaturated porphyry deposits (Lang *et al.*, 1995a).

The alteration assemblage associated with the emplacement of the Balut Dyke reflects the SiO<sub>2</sub>-undersaturated nature of the melt. The diopside-perthite-magnetite composition of the early pegmatitic Stage 2A veins is the same composition as the Balut Dyke, but contains strong bornite mineralisation. The 2A hydrothermal assemblage was overprinted by the Stage 2B perthite-actinolite±bornite veins, and the Stage 2C actinolite-perthite-bornite stockwork, the later being the most spatially extensive vein set at Dinkidi (Figure 6.6). High Cu and Au grades are associated with a narrow zone of fine-grained bornite-orthoclase mineralisation that is focused above the Balut Dyke and that appears to have been emplaced along the same feeder structure as that utilised by the melt. The high Au grades (1 to >10g/t Au) and lack of quartz in the Stage 2 assemblage is typical of most silica-undersaturated, and many silica-saturated, alkaline porphyry systems (Lang *et al.*, 1995a). Similar calcic diopside has been reported from the early hydrothermal assemblages at several British Columbian porphyry deposits (eg Galore Creek, Ennes *et al.*, 1995; Copper Mountain, Staney *et al.*, 1995), and from the prograde assemblages of skarns (Einaudi *et al.*, 1981). Despite deposition from a fluid-rich melt, the Balut Dyke diopsides have similar compositions, but a lower Mg number, than the magmatic clinopyroxene found throughout the rest of the Didipio Igneous Complex (Figure 5.10).

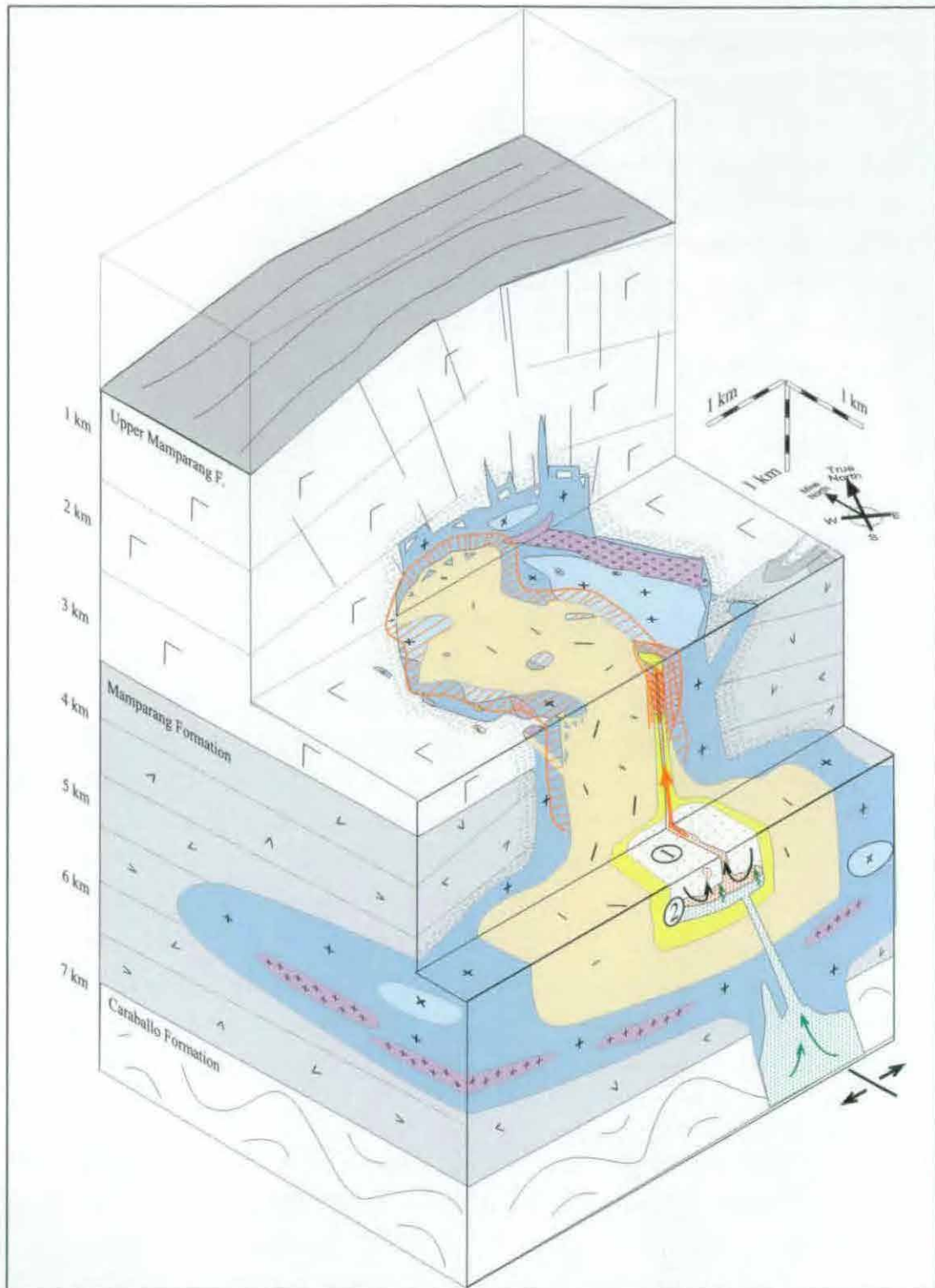


**Figure 8.2:** Model for the generation and emplacement of the Balut Dyke melt. Following emplacement of the Tunja Monzonite, the cessation of biotite fractionation led to the production of a volatile-rich syenite melt (1). The high temperature, low Mg and highly calcic nature of the Balut Dyke, and the inhibition of quartz-saturation, is attributed to the interaction between the perthitic melt and a body of hotter,  $\text{SiO}_2$ -undersaturated mafic melt, which underplated the mafic magma chamber (2). This mafic melt is interpreted to have been sourced from the feeder structure to the Didipio Igneous Complex, and may have been emplaced in response to the evacuation of the magma chamber during emplacement of the Surong or Tunja Monzonites. The Balut Dyke melt is interpreted to have been sourced from the boundary layer between the two melts, gaining Ca and heat from the mafic layer, and losing  $\text{SiO}_2$  (eg Dorasis, 1987; Whitney, 1989). Heating of the silicic melt may have formed buoyant plumes of hybrid magma within the chamber and triggered an increase in convection rates, leading to increased rates of volatile exsolution by pressure loss. The resultant hot, volatile-rich but  $\text{SiO}_2$ -undersaturated melt was emplaced along a narrow NW-trending structure into the Dinkidi Stock, with associated strong Au-Cu mineralisation and a calc-potassic alteration assemblage. The depth estimate of 3 km is based on fluid inclusion pressure estimates for the Stage 3 assemblage and geological considerations.

## GENETIC MODEL

Melt inclusion evidence suggests that the Balut Dyke, and the Stage 2A pegmatitic veins, were emplaced at temperatures in excess of 500-600°C from a complex and immiscible mixture of silicate melt, salt melt (or brine) and aqueous saline fluid, rather than from a single homogeneous silicate melt (Kamenetsky *et al.*, 1999). Compositional data from melt inclusions suggests that the melt-volatile mix contained elevated concentrations of Cl, S, N, F, As, Na, K, Mo, Pb, Cu, Ag and Zn (Kamenetsky *et al.*, 1999). The diopside-magnetite-K-feldspar hydrothermal assemblage is interpreted to have precipitated from a hot, saline, H<sub>2</sub>O-, Ca-, Fe- and K-saturated, but silica-undersaturated fluid. The lack of adequate phase equilibria data at high temperatures and salinities, and the complex multiphase nature of the Dinkidi system, prevents the construction of meaningful phase equilibria diagrams for the Stage 2 and 3 hydrothermal assemblages.

The transition from diopside- to actinolite-stable fluids in the hydrothermal Stage 2B & 2C assemblages is interpreted to represent the cooling of the hydrothermal fluids to temperatures < 450°C (assuming 1 Kbar pressure; Ernst, 1966). Microthermometric analysis of late-stage apatite in Stage 2B and 2C veins indicates trapping conditions of 235 to 365°C (at an estimated 2.6 Km lithostatic depth) and salinities of 13 to 24 wt% eq. NaCl. The deposition of the Stage 2D bornite-orthoclase assemblage, which lacks quartz, sericite or carbonate, indicates deposition from a fluid that was saturated with K<sup>+</sup>, H<sub>2</sub>S, Cu<sup>+</sup>, and Fe<sup>2+</sup>, with a high  $aK^+/aH^+$  ratio and that was undersaturated with respect to quartz. The elevated H<sub>2</sub>S of this stage, and the reduction of later Stage 3 fluids by this assemblage (as indicated by the sulphur isotope anomaly), suggests reduced, magnetite-stable conditions and the lack of sericite alteration suggests relatively neutral pH fluids. Reduced, alkaline fluids have a high silica solubility (Fleming & Crerar, 1982), therefore the reduced nature of the fluids may have inhibited the precipitation of quartz, not only during the high temperature crystallisation of diopside (which would also inhibit quartz precipitation for small concentrations of SiO<sub>2</sub>), but also during the cooling of the hydrothermal fluids, which would normally trigger quartz precipitation.

The production of a high-temperature, Ca-rich, Mg-depleted diopside-bearing syenitic melt, emplaced late in the fractionation history of the Didipio Intrusive Complex, cannot be explained by simple crystal fractionation. Crystallisation of a biotite-monzonite melt would be expected to lead to increased concentration of SiO<sub>2</sub>, Na and possibly K in the residual melt, leading to the production of a late-stage quartz-orthoclase-albite assemblage, such as the Stage 3 hydrothermal assemblage. Any calcium present in the melt would be scavenged by crystallising plagioclase. Production of diopside, a common mineral in prograde heating assemblages (eg Einaudi *et al.*, 1981) would also require heating of a biotite-stable assemblage (Yardley, 1989). Relatively high temperature emplacement of the Balut Dyke is supported by melt inclusion evidence that indicates temperatures of 600 to 900°C during clinopyroxene crystallisation (Kamenetsky *et al.*, 1999). Several models can be proposed to explain the unusual calcic, silica-undersaturated composition (Table 5.1) and apparent higher temperatures of the Balut Dyke assemblage:



- The commencement of strong volatile exsolution, triggered by the cessation of biotite crystallisation, may have 'purged' the magma chamber of components such as Fe & Ca. However, this model does not explain why Ca was not incorporated into crystallising plagioclase, or how the fluid and melt remained  $\text{SiO}_2$ -undersaturated. This mechanism also cannot explain the higher temperatures required to produce the Stage 2 assemblage.
- The Balut Dyke was fully, or partially, sourced from the injection of a fresh calcic melt into the magma chamber, or was sourced separately from a totally new melt unrelated to the Didipio Igneous Complex. Whereas this model can explain the higher temperatures and calcium enrichment of the Balut Dyke, it is expected that such a process would also produce increased Mg concentrations within the melt, and should have triggered the crystallisation of plagioclase rather than perthite. The clinopyroxenes of the Balut Dyke share a similar, but Mg depleted, chemistry to the remainder of the Didipio Igneous Complex (Figure 5.8), suggesting that they were sourced from a late-stage Mg-depleted melt from the same source as the remainder of the Didipio Igneous Complex, instead of being sourced from a fresh batch of melt. Magma mixing would also be expected to have affected the chemistry of the later Quan Porphyry, producing a more 'mafic' assemblage.
- Closed-system heating of a biotite-stable melt, without contribution of elements from a separate source, may lead to the precipitation of diopside (Yardley, 1989). Such heating may have been caused by proximal emplacement of an unobserved intrusion. However, heating alone would not lead to an increase in calcium, and depletion in  $\text{SiO}_2$ , K or Na characteristic of the Balut Dyke (Table 7.1) and would not inhibit quartz formation on cooling.
- The calcic nature of the Balut Dyke is consistent with the hydration and assimilation of earlier dioritic phases, such as gabbros, clinopyroxenites and anorthites (Table 7.1). Assimilation of these earlier phases, either within the magma chamber, or, more likely, during ascent, may have produced the observed high Ca and low Mg and  $\text{SiO}_2$  concentrations, with alteration leaching the calcic cores of plagioclase and buffering the low  $\text{SiO}_2$  concentration by clinopyroxene and biotite alteration. However this model does not explain the heating of the fluids required to produce the diopside (Yardley 1989; Kamenetsky *et al.*, 1989).
- Heating of meteoric water by the intrusion produced the Dinkidi calc-potassic assemblage (eg as proposed for deep, marginal, unmineralised calc-sodic alteration at Yerrington, USA, by Dilles *et al.*, 1992). Although external fluids may have produced marginal propylitic alteration of the margin of Dinkidi, and the diorites may have enriched the local groundwaters in calcium, melt inclusions indicate that the Balut Dyke was deposited from a mixture of silicate melt and mineralised hypersaline brine at magmatic temperatures (Kamenetsky *et al.*, 1999). Although some of this essentially

## GENETIC MODEL

'magmatic' fluid may have been derived from external sources, it is considered unlikely that the associated Stage 2D orthoclase-bornite assemblage (Plates 6.4A to F) was deposited from heated meteoric water. The model cannot be tested with the current data, and requires O, D and Sr isotopic studies.

- The preferred explanation is that the Balut Dyke was sourced from a compositionally stratified magma chamber. In this model, the highly-evolved, volatile-rich felsic melt that formed the Balut Dyke was 'underplated' by a layer of denser, hotter mafic melt. Such layers can form where mafic melt has been injected into a silicic magma chamber (eg Dorasis, 1987; Whitney *et al.*, 1988; Whitney, 1989; the mafic melt either being residual melt from the feeder structure, or a fresh batch of magma). The mafic melt is typically partially quenched against the cooler felsic melt, and a boundary layer forms along the contact in the silicic magma (Dorasis, 1987; Whitney, 1989; Figure 8.2). Felsic melt in this contact zone gains heat and assorted elements from the mafic layer through mechanical and chemical diffusive methods. In the case of the Carpenter Ridge Tuff, Colorado, USA, the felsic melt gained Ca, Ba, Na and hydrogen, and lost K, Rb and oxygen (Whitney *et al.*, 1988; Whitney, 1989). The calcic melt of the Balut Dyke is interpreted to have been sourced from this contact zone, gaining Ca and heat from the magma, but retaining the high volatile content and perthite composition of the felsic melt. The lack of quartz in the Stage 2 calc-potassic assemblage may be attributed to the buffering of quartz by clinopyroxene or biotite within by the mafic silica-undersaturated magma.

The mafic underplating model is the only model that adequately explains Ca-enrichment (Table 5.1 & Figure 5.8), Mg and SiO<sub>2</sub>-depletion and the high temperatures (600-900°C; Kamenetsky *et al.*, 1999) of the Balut Dyke melt. Although no mafic enclaves were observed in any felsic units, the presence of a body of mafic melt underlying, but in contact with, the silicic melt is supported by the presence of abundant late-stage andesite dykes. The late-stage andesite dykes show similar whole rock and mineral chemistry trends (in major, trace and REE elements) to the Didipio Igneous Complex, indicating a co-genetic origin. The intrusion of more mafic, but still co-magmatic, dykes, following a period of felsic magmatism is interpreted to have resulted from late-stage reinjection of residual mafic melt from the feeder structure of the magma chamber. Clinopyroxene phenocrysts in the andesite dykes are similar to those within the Balut Dyke, in that they are highly calcic and are depleted in Mg (Figure 5.8). The andesite melt must have either undergone strong fractionation (which would have produced a more felsic melt) or had been in contact with the late-stage silicic melt, such as the Balut Dyke melt reservoir, to have become depleted in Mg.

### **The Quan Porphyry, the Bufu Syenite and the Stage 3 quartz stockwork**

The emplacement of the Balut Dyke into the Dinkidi Stock was followed by the emplacement of a monzosyenite to quartz-syenite melt. This intrusion grades from a chilled porphyritic margin

(the Quan Porphyry) to a vuggy crystal-crowded syenite to quartz syenite core (the Bufu Syenite). The Quan Porphyry and Bufu Syenite are not Ca enriched, in contrast to the Balut Dyke (Table 5.1). A narrow but vertically extensive quartz vein stockwork is localised above the apex of the Bufu Syenite (Figure 6.6). The Stage 3 quartz stockwork formed in the Quan Porphyry, Balut Dyke and Tunja Monzonite, adjacent to and above the Bufu Syenite. The Stage 3 quartz stockwork grades to wispy 'A-type' veins (Gustafson & Hunt, 1975) and irregular quartz trails within the Bufu Syenite. This spatial association and compositional similarities with the Bufu Syenite, and the presence of abundant miarolitic cavities and strong REE depletion within the Bufu Syenite are interpreted to indicate that the intrusion was the main conduit for volatile migration during Stage 3 quartz stockwork formation. This is supported by an estimated solidus temperature (500-600°C; Chapter 7) that is lower than the temperature of stockwork formation (>600°C; Figure 7.2), and by the gradational interface between the quartz syenite and the quartz stockwork that is occupied by the coarse-grained quartz-perthite±actinolite-magnetite Bugoy Pegmatite (Figure 8.3). It is possible that the influx of high temperature volatiles through the Bufu Syenite melt (at least 0.065 km<sup>3</sup> of hypersaline brine), sourced from the underlying magma chamber, may have assisted keeping this 'conduit' molten during emplacement of the stockwork.

The least squares modelling of fractionation presented in Chapter 5 (Table 5.2) suggest that if the Quan Porphyry and Bufu Syenite had formed from simple fractionation of a clinopyroxene diorite melt, then they would be equivalent to a residual 10 and 3% melt fraction respectively. As it is considered unlikely that a residual 10% melt fraction could escape from a 90% crystallised magma chamber, this apparent small degree of residual melt highlights the large degree of fractionation required to produce a mineralised porphyry melt, the importance of structural tapping of a nearly-crystallised magma reservoir in the formation of the Dinkidi deposit, and the requirement for a focusing and enrichment mechanism within the main magma body, such as the formation of a flotation differentiate.

At the apex of the Bufu Syenite, the intrusion consists of perthite enclosed in a coarse-grained quartz groundmass. This rock grades, via a transitional zone of coarse-grained quartz-perthite±magnetite-actinolite (the Bugoy Pegmatite), upwards into the initial quartz±perthite-actinolite quartz Stage 3A stockwork (Figure 8.3). The Stage 3A assemblage was overprinted by both the unmineralised Stage 3B-potassic quartz-perthite veins (located along the margin of the Bufu Syenite) and the main Stage 3B quartz-calcite-chalcopryrite sulphide quartz stockwork, the later associated with strong sericite-carbonate alteration and disseminated sulphide mineralisation. The Stage 3B & 3C stockwork is typical of the veins present at most high-K to calc-alkaline Cu-Au porphyry systems, such as at El Salvador (Gustafson & Hunt, 1975) and in deposits throughout the southwest USA (Titley, 1993) and the Philippines (Sillitoe & Gappe, 1984). The narrow, but vertically extensive distribution of the Stage 3 quartz stockwork (Figure 6.6), and the sharp transition in  $d^{34}\text{S}$  values at the contact between the Dinkidi Stock and the surrounding diorites (Figure 7.6), suggest that there was only limited lateral fluid movement

## GENETIC MODEL

into the surrounding, largely impermeable, host rock, with most fluids focused up along the main feeder structure. Following the emplacement of the quartz stockwork, the quartz veins were overprinted by Stage 3C carbonate veins and were disrupted by faulting that disrupted the core of the Dinkidi Deposit, and which formed the Bugoy quartz fragment breccia.

Microthermometric and PIXE analysis indicates that the Stage 3 hydrothermal assemblage formed from a high salinity (>68 wt% eqNaCl) NaCl-KCl-FeCl<sub>2</sub> brine that was emplaced at magmatic to near-magmatic temperatures ( $T_f$  >600°C). This brine contained elevated concentrations of Cu, Ca, Mn, Ti, and Zn and precipitated quartz ( $\pm$ actinolite-magnetite-perthite-sericite-calcite-sulphide) throughout the network of stockwork fractures and as a massive accumulation of coarse-grained quartz and perthite in the core of the system (the Bugoy Pegmatite). Based on fluid inclusion evidence (Figure 7.4) the generation of this hypersaline brine is interpreted to have required phase separation at temperatures greater than 750°C, followed by cooling of the brine either isobarically or with a pressure increase of up to ~500 bars (Figure 7.4). Mineralisation is associated with late primary to secondary chalcopyrite-bearing saturated fluid inclusions (40 to >68 wt% NaCl), which homogenise at temperatures typically >600°C, but with a second peak at 360–480°C (the later peak is associated with the secondary chalcopyrite-bearing saturated fluid inclusions). This second peak suggests that there was at least 120 to 240°C of cooling between emplacement of the quartz stockwork and the main period of sulphide deposition. Pressure estimates of 820 to 1200 bars indicate an emplacement depth of 2.9 to 4.5 km, with a minimum depth of 2.6 km (assuming lithostatic pressures; Figure 7.4). The pressure estimates also indicate that there was a significant degree of overpressurisation within the stockwork during quartz growth (ranging from 720 bar to >1500 bar). Co-existing vapour-rich fluid inclusions suggest episodic depressurisation of the brine during quartz growth, probably during fracturing, with depressurisation to hydrostatic pressures (at least 260 bar). This loss of the vapour phase, both during initial brine exsolution and during periods of fracturing, is interpreted to have produced the observed high metal concentrations measured within the hydrothermal fluid (eg Table 7.1). Abundant late-stage secondary trails of LV-type inclusions indicate there was significant circulation of low salinity (?meteoric) fluids following sulphide deposition.

The lack of phase equilibria data for high temperature brines (>600°C and >68 wt% NaCl) prevented the construction of meaningful phase equilibria diagrams for this stage. The quartz-actinolite-magnetite-chalcopyrite-bornite hydrothermal assemblage of Stage 3A suggests deposition from a hot, magnetite-stable fluid that contained elevated concentrations of K, Ca, Fe and Cu. The presence of sericite and hematite within the Stage 3B assemblage indicates that the Stage 3B fluids were acidic and were oxidised. This increase in oxidation state may reflect the oxidation of the fluids by loss of hydrogen to the vapour phase or condensation of SO<sub>2</sub> back into the brine (Eastoe, 1979; Czamanske & Wones, 1973). Phase equilibrium constraints indicate that high temperature porphyry deposits contain bornite and magnetite (Simon *et al.*, 2000). The transition from Stage 2 and Stage 3A bornite- and magnetite-stable assemblages to Stage 3



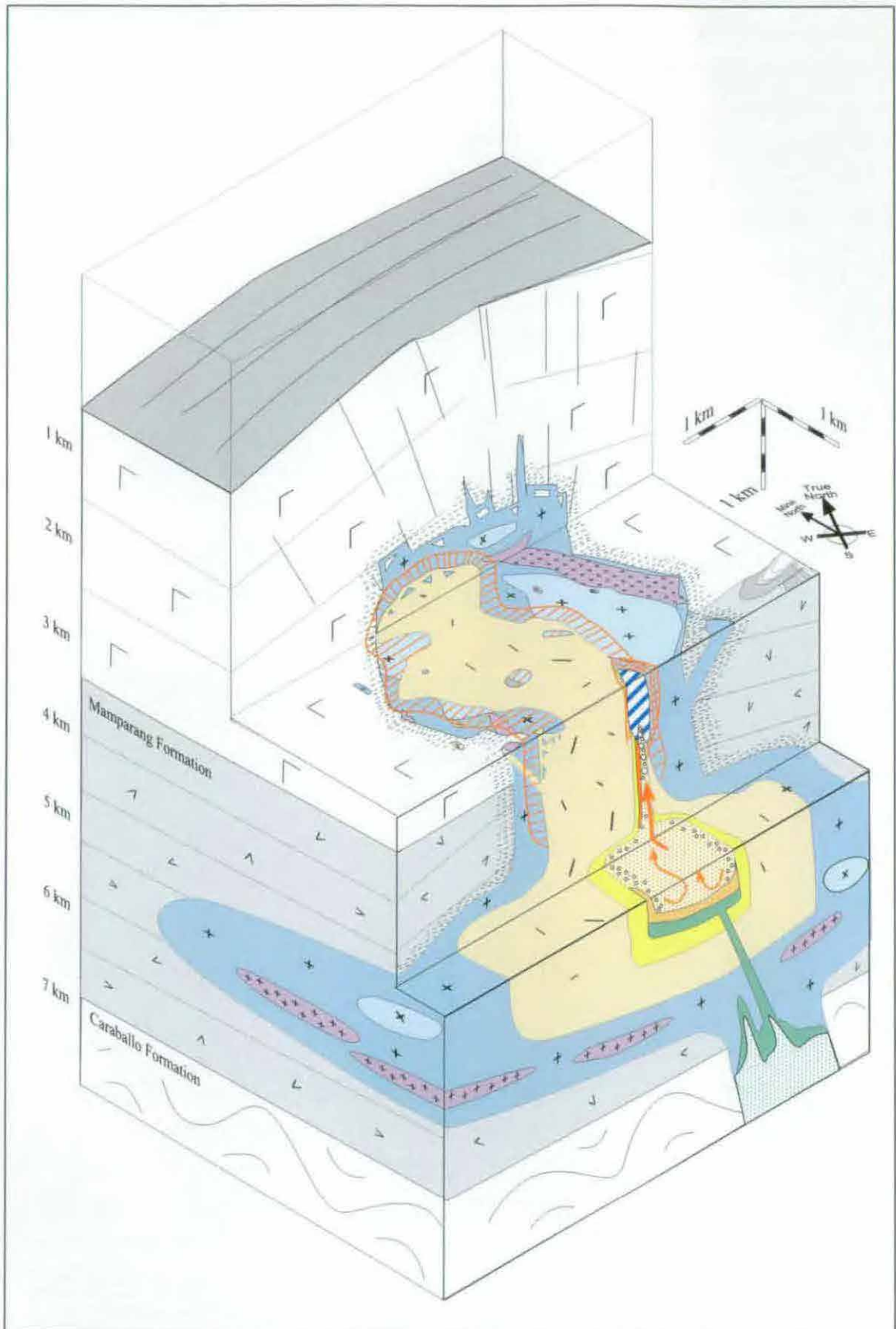


**Figure 8.3:** Model for the emplacement of the Quan Porphyry and Bufu Syenite. Following emplacement of the Balut Dyke melt further crystallisation is interpreted to have isolated the remaining felsic melt from the underlying mafic melt, with associated crystallisation-driven volatile build up and the attainment of  $\text{SiO}_2$ -saturation. This late-stage melt was emplaced along the same structure as the Tunja Monzonite and Balut Dyke, producing a quartz-K-feldspar-sericite stockwork and Cu-Au mineralisation.

## GENETIC MODEL

chalcopyrite-bearing assemblages may therefore also reflect cooling, in addition to any changes in oxidation state or sulphur activity (Simon *et al.*, 2000). These Stage 3B fluids were subsequently neutralised and cooled after emplacement from >600°C (orthoclase stable) to 400°C (sericite stable). Late Stage 3C fluids were relatively neutral (calcite-stable) and were most likely reduced (pyrite stable).

Mechanisms that have been proposed for sulphide precipitation in porphyry deposits include cooling, dilution, water-rock interaction and boiling, and in most cases more than one mechanism was probably active. For the Stage 3 hydrothermal assemblage at Dinkidi, there were at least four potential depositional mechanisms:

- Cooling from >600 to ~400°C within Stage 3 quartz veins, with the later, cooler fluids becoming copper-saturated (as indicated by the abundance of chalcopyrite daughter crystals);
- Neutralisation of an originally acidic fluid by wall rock interaction, as indicated by the close association between sericite alteration (a hydrolysis reaction which drops the pH of the fluid), calcite and the sulphide mineralisation.
- Phase separation, as indicated by the abundant vapour-rich inclusions within Stage 3 veins. However at the elevated temperatures and pressures involved, phase separation may have concentrated metals in the residual brine, rather than causing direct precipitation of sulphides.
- Reduction of the oxidised Stage 3 fluids by pre-existing Stage 2 sulphides, as indicated by the development of hematite rims on Stage 2 (and early Stage 3) magnetite grains (with coeval chalcopyrite-bornite precipitation), and by the heavy  $\delta^{34}\text{S}$  values for sulphides in Stage 3 quartz veins where they have overprinted the Stage 2 mineralisation.

Based on the above observations a combination of cooling and neutralisation of the fluid by wall rock interaction are considered most likely to have lead to sulphide precipitation at Dinkidi, forming late stage sulphide-calcite infill within the veins and disseminated sulphide-calcite mineralisation throughout regions of sericite alteration. Reduction of the oxidised Stage 3B fluids by pre-existing sulphides may have been a contributing process in the region around, and above, the Balut Dyke. No evidence of fluid mixing (eg systematic salinity variations in fluid inclusions) was observed in this study, although late-stage secondary liquid-vapour inclusions are interpreted to record the influx of meteoric water during the thermal collapse of the system. The lower salinity of secondary  $B_{H(Cpy)}$  inclusions in Stage 3 quartz veins are still halite-saturated, suggesting that these fluids formed by cooling of the brine, rather than by mixing with an external dilute water.

There is a distinctive switch in composition from the quartz-undersaturated Stage 2 vein assemblage to a quartz bearing Stage 3 vein stockwork. If magmatic processes controlled this switchover then it may be that the syenitic melt in the magma chamber had become compositionally isolated from the mafic boundary layer, by cooling and inward crystallisation of either the syenite and/or mafic melt. Continued crystallisation without the silica-buffering effects of either the boundary layer or of biotite crystallisation would have lead eventually to quartz saturation. An alternative explanation for the formation of the quartz-syenite melt, that the Quan Porphyry and Bufu Syenite represent the injection of a totally new melt into the magma chamber, is not supported by the close petrological similarities between the Balut Dyke and the Quan Porphyry.

### **Andesite dykes and retrograde assemblages**

Following the emplacement of the Dinkidi stock, the regional volcanic units and the more felsic intrusions of the Didipio Igneous Complex were overprinted by widespread intermediate argillic (illite-chlorite-quartz-sericite) to advanced argillic (illite-kaolinite-silica±pyrophyllite-dickite) alteration assemblages. The development of advanced argillic alteration indicates the formation and influx of fluids with low pH (<2; Stoffregen, 1987) and moderate temperatures (100-350°C; Giggenbach, 1997). The source of these fluids is commonly assumed to be the acidic condensates of magmatic vapour, possibly from a degassing porphyry system (eg Meyer & Hemley, 1967; Brimhall & Ghiorso, 1983). At Lepanto-Far Southeast this model is supported by the contemporaneous formation of both advanced argillic alteration and porphyry mineralisation (Arribas *et al.*, 1995; Hedenquist *et al.*, 1998). In the case of Didipio, the source of the fluids responsible for argillic alteration can not be unambiguously determined, however, based on the formation of advanced argillic alteration in other hydrothermal and geothermal systems (eg Brimhall & Ghiorso, 1983), the acidic fluids are assumed to be a mixture of steam-heated groundwater (eg Hedenquist, 1991) and condensed magmatic vapours. The overprint of the Didipio Igneous Complex by strong argillic alteration and epithermal veins with shallow near-surface, open-space filling textures (eg bladed calcite) suggests that there was significant erosion (~2.5 to 3 km) during the lifetime of the hydrothermal system in the Didipio region, assuming that the argillic alteration assemblage and epithermal vein textures formed within 1 km of the paleowatertable (eg the telescoping model of Sillitoe, 1989, 1994). The juxtaposition of porphyry mineralisation and argillic alteration may have resulted from rapid erosion following the rift-related tectonic uplift along the margins of the Cagayan Valley Basin. Weak Cu-Au mineralisation formed during argillic alteration, in association with pyrite-silica flooded fault zones and minor calcite-quartz veins of low sulphidation epithermal character..

Abundant andesite dykes and sills were emplaced during the final period of magmatism in the Didipio region. These dykes are only weakly affected by argillic alteration, suggesting that they may post-date development of most of this alteration. Whole rock geochemical trends are interpreted to indicate that these dykes are comagmatic with the other intrusions of the Didipio Igneous Complex (Figures 5.2 & 5.3). However, unlike the earlier intrusions, these andesites are

## GENETIC MODEL

pyrite-bearing, and contain amphibole, typically as reaction rims around clinopyroxene (eg Plate 3.8B). It is possible that the melt was saturated with  $H_2S$  and that the melt switched from anhydrous to hydrous relatively late in the crystallisation history. The presence of amphibole, rather than biotite, as the primary hydrous phase may reflect crystallisation at greater depths than the biotite-bearing melts. Clinopyroxene phenocrysts in the andesite dykes are highly calcic and, like the diopside within the Balut Dyke, are depleted in Mg (both with Mg numbers of 53 to 67; Figure 5.10). This geochemical similarity suggests that the andesite melts are not 'fresh' primary mafic melt, but have been depleted in Mg, either by strong fractional crystallisation (which would be expected to have produced a more evolved melt) or by interaction with the late stage felsic melts. The andesite dykes are assumed to have formed from the injection of residual mafic melt that had underplated the Didipio Igneous Complex (eg Whitney *et al.*, 1988) into the overlying igneous and volcanic complex (Figure 8.4), possibly in response to the collapse and subsidence of the evacuated magma chamber. This melt may have been originally andesitic, or may have been more mafic but evolved to andesitic compositions by fractionation or by interaction with the felsic melt. The hydration of the melt may have occurred by contact with the late-stage felsic melts.

The last period of hydrothermal activity observed in the Didipio region is the emplacement of a zeolite (stilbite-laumontite-chabazite) mineral assemblage, during widespread dextral strike-slip faulting. During this stage, the True Blue prospect was faulted off the northern end of Dinkidi, and displaced 700 meters to the east. The zeolite assemblage present in the Dinkidi deposit indicates relatively cold (80 to 280°C; Aoki, 1978; Aiello & Franco, 1968; Tomita *et al.*, 1969; Holler *et al.*, 1974) and alkaline (bicarbonate) waters may have been drawn down into the Dinkidi Stock, precipitating zeolites as they were heated and/or mixed with Ca-bearing groundwater. This assemblage formed both zeolite veins (typically as infill within tensional gashes) and a lithic-fragment breccia in the core of Dinkidi with a zeolite groundmass. Zeolites, with associated propylitic alteration, are common in the distal, shallow-level sections of convection zones associated with active geothermal systems that have low  $O_2$  contents (Wairaki, NZ; Browne 1978). Warm groundwaters are still present at Didipio, as shown by the presence of hot springs (~60-80°C) 700 metres to the east of Dinkidi.

### **Possible sources of gold enrichment in the alkaline melts at Dinkidi**

The gold-rich nature of the Dinkidi deposit may be attributed to a range of factors, including enrichment of the melt source, conditions within the magma chamber allowing enrichment of gold into the volatile phase during fractionation, and favourable physiochemical conditions at the site of deposition. No one factor is likely to have been the sole control on gold enrichment at the deposit. Many alkaline melts are enriched in LILE, metals, ligands and volatiles (Muller & Groves, 2000), making belts of alkaline to potassic rocks highly prospective for porphyry and epithermal mineralisation. Such enrichment is characteristic of the Late Oligocene to Early Miocene alkaline intrusions of northern Luzon, where each of the three main alkaline intrusive



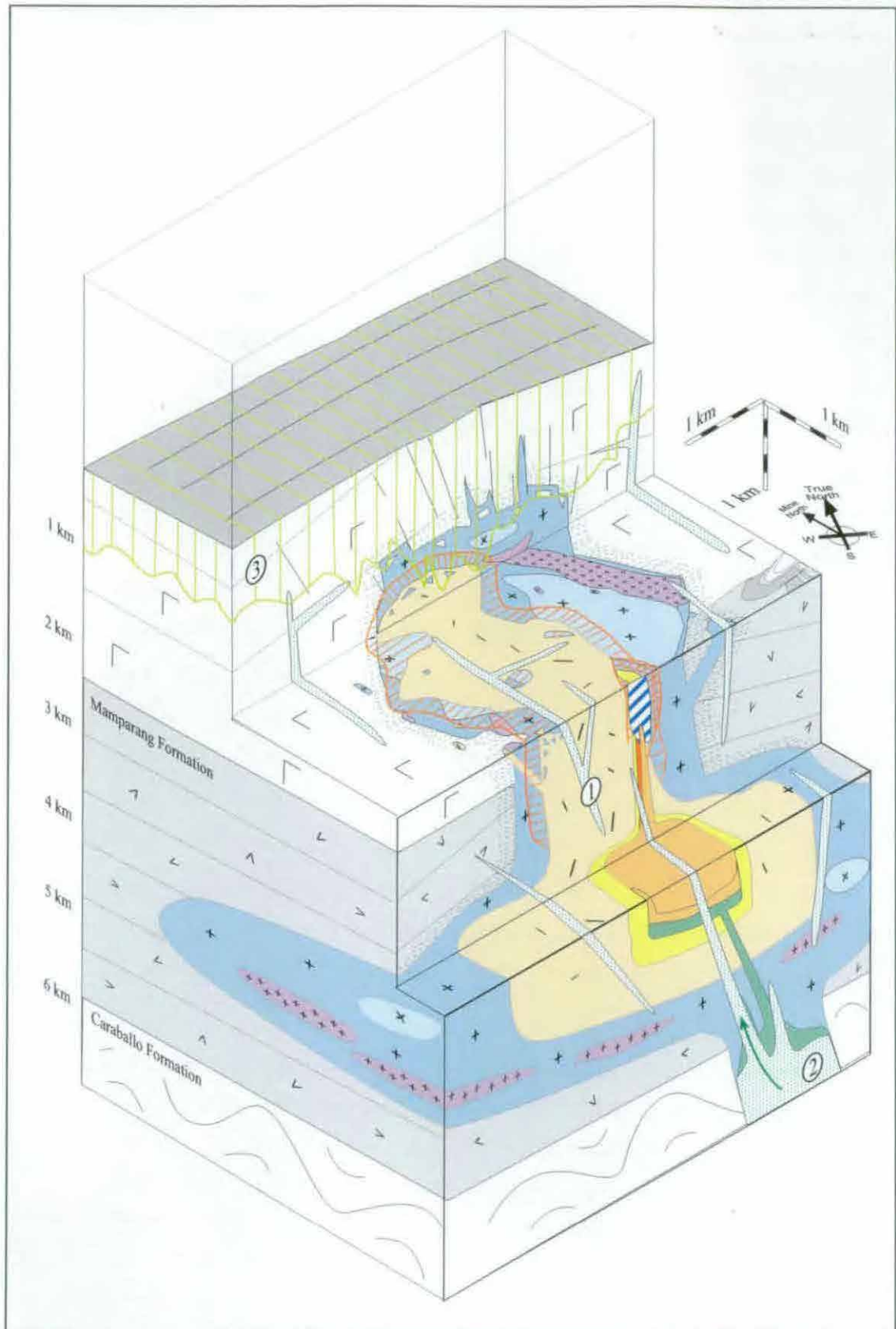


**Figure 8.4:** Model for post-mineralisation stages in the Didipio region. The emplacement of widespread andesite dykes is the final magmatic event within the Didipio region (1). The emplacement of this 'co-magmatic' mafic melt, following a prolonged period of felsic magmatism, is attributed to the emplacement of deeper residual melt from the feeder zone of the Didipio Igneous Complex (2), possibly in response to the evacuation and collapse of the overlying magma chamber. The Didipio Igneous Complex, and the Upper Mamparang Formation, have been overprinted by strong argillic alteration (3), indicating a significant degree of erosion during the lifetime of the Didipio hydrothermal system.

## GENETIC MODEL

centres hosts economic Au-Cu mineralisation, compared to the barren Oligocene calc-alkaline batholiths found in the same region.

Based on radiogenic (Knittel & Defant, 1988) and whole rock compositions the source of the Didipio melt appears to be melting of the mantle wedge above the stalled east Luzon trench, with no 'exotic' melt components detected (eg the assimilation of sedimentary basement at Grasberg as proposed by Ryan *et al.*, 2000). It appears that the small degree of partial melting of an enriched mantle source that produce a LILE-enriched melt also enriched the melt in metals and volatiles. The typically oxidised ( $\text{SO}_2$ -predominant) nature of the high-K melts may have assisted the accumulation of metals during both partial melting of the mantle source and shallow crustal fractionation, preventing scavenging of copper and gold by  $\text{H}_2\text{S}$ , which would sequester metals into magmatic sulphides in the mantle and in early crystallised intrusions (Hamlyn & Keays, 1987). Solomon (1990) proposed that gold enrichment in island arc high-K rocks is the result of two-stage melting of the mantle wedge, during 'subduction reversal', such as the change in subduction zone that occurred in Luzon during the Tertiary. The estimated 23-25 Ma age of emplacement of the Didipio Igneous Complex is approximately the same age as that estimated for the commencement of eastward-directed subduction along the Manila Trench (at ~25 ma; Lewis & Hayes, 1983; Wolfe, 1988). If Solomon's (1990) model is applicable, then the second period of melting would have had to have occurred within 1-2 Ma of subduction beginning, at a location currently 200 km inwards from the Manila Trench. This makes a 'subduction-reversal' mechanism difficult to test in the case of Didipio. Whatever the source of gold enrichment, it appears, in the case of northern Luzon, that late-stage shallow-level fractionation had invariably produced economic porphyry or epithermal mineralisation, as long as the source melt has been enriched in LILE (and ore constituents) at the mantle source.

The importance of hydrothermal controls on the style of mineralisation is highlighted by the differences between the metal content of the melts and that of the deposit. Melt inclusion evidence indicates that the Balut Dyke melt-volatile mix contained Mo and Cu (and presumably Au; Kamenetsky *et al.*, 1999). However the Dinkidi deposit is Mo-deficient, with only trace amounts of Mo detected in the distal setting. This suggests that late stage physiochemical conditions of ore deposition (pH, temperature, pressure and  $f\text{O}_2$ ) were fundamental for the saturation and subsequent deposition of Cu and Au, whereas Mo remained undersaturated in the fluids and was dispersed out of the system. So although the source region determines the metal budget of a particular melt it is the conditions at the site of deposition that determine the style of porphyry mineralisation: oxidised conditions may favour the transport of Mo out of the system (eg forming porphyry Cu-Au deposits in alkaline systems; porphyry Cu in non-calc alkaline deposits), while reduced conditions may favour the dispersion of gold and deposition of Mo (forming Cu-Mo deposits). The highest gold-grades at Dinkidi are associated with the

hydrothermal Stage 2D bornite-orthoclase assemblage. This may reflect the ability of bornite to contain one order of magnitude more gold than chalcopyrite (Grigore *et al.*, 2000). As phase equilibrium constraints indicate that high temperature porphyry deposits will contain bornite and magnetite (Simon *et al.*, 2000), the high gold grades may reflect the higher temperature of the Stage 2 assemblage.

# CONCLUSIONS

- Drilling by Australian Company Climax Mining has delineated a 110 Mt resource with unusually high gold grades of 1.2 g/t Au and 0.5% Cu, including a high-grade core of 2 to 9 g/t Au.
- Detailed geological mapping of the region, and logging of regional and Dinkidi drill core, has revealed that the Dinkidi deposit is situated in a composite intrusion, the Dinkidi Stock, which is, in turn, part of a larger intrusive body, the Didipio Igneous Complex.
- The Didipio Igneous Complex has intruded a sequence of andesite lavas and volcanoclastic breccias (the Mamparang Formation) and also a package of trachyte lavas and volcanoclastic units, which this study has informally named the Upper Mamparang Formation.
- The Mamparang Formation that crops out in the Didipio region is interpreted to be the proximal, lava-dominated facies of a terrestrial andesitic stratovolcano that formed in the Late Oligocene. Late-Oligocene to Early Miocene shallow water limestones (MMAJ 1977) suggest that this andesite volcanic pile, and the overlying trachytes, may have been surrounded by a shallow sea.
- This andesitic volcanic pile provided the foundation for, and was covered by, the trachyte lavas and widespread trachytic volcanoclastic units of the Upper Mamparang Formation. The Upper Mamparang Formation is interpreted to be the proximal lava-dominated facies of a terrestrial trachytic volcanic pile. The formation, as defined, also incorporates the trachyte lavas and pyroclastic units that host the Palali Batholith and the analcite-bearing trachytic pyroclastic rocks that host the Cordon Syenite Complex.
- The Mamparang and Upper Mamparang Formations are interpreted to have been emplaced along, and are considered to be synchronous with displacement along basin-boundary faults of the Cagayan Rift Valley. They formed a belt of andesitic and trachytic volcanic edifices that was at least 60 km long.
- The proximal nature of the volcanic facies exposed in the Didipio region is interpreted to indicate that the Didipio Igneous Complex is the intrusive core of one of the Upper Mamparang Formation feeders, with successive intrusions being emplaced along the same feeder structure that was utilised by the trachyte lavas.
- The volcanic setting of the Dinkidi deposit contrasts with the model for volcanic-hosted calc-alkaline porphyry deposits (eg Sillitoe, 1973), in which the intrusions are hosted within an andesitic volcanic pile. The association between the trachyte lavas and the mineralised intrusive centres makes these potassic lavas an important exploration target in northern Luzon and other convergent margin settings.



- The intrusions of the Didipio Igneous Complex were emplaced into the Mamparang and Upper Mamparang Formations during four main intrusive events:
  - Intrusion of an early clinopyroxene-diorite phase with *in situ* fractionation of clinopyroxene and plagioclase producing a residual monzodiorite melt and cumulate gabbros to clinopyroxenites
  - Emplacement of the Surong clinopyroxenite monzonite, possibly controlled by a NW-trending feeder structure, with *in situ* fractionation of clinopyroxene and plagioclase producing biotite and quartz monzonite phases.
  - Emplacement of three monzonite to quartz syenite intrusions within the Dinkidi Stock by dilation of a NW-trending structure. Three main intrusive events, producing four distinct intrusions, are recognised:
    - Emplacement of the Tunja Monzonite, an equigranular biotite monzonite stock.
    - Emplacement of the Balut Dyke, a texturally variable clinopyroxene syenite.
    - Emplacement of the Quan Porphyry, a monzonite to syenite porphyry that grades, in its core, into the vuggy, leucocratic Bufu Syenite to quartz syenite
  - Emplacement of post-mineralisation andesite dykes and sills.
- Significant erosion of the host volcanic edifice is suggested by the change in intrusion morphology from large equigranular diorite and monzonite plutons to late-stage porphyritic stocks and dykes. The width and equigranular nature of the early diorite and monzonite intrusions suggest that they were emplaced as cupolas above a magma chamber.
- The Tunja Monzonite is compositionally similar to the Surong Monzonite, suggesting that the two were emplaced at similar times, whereas a significant period of fractionation is interpreted to have occurred after the emplacement of the Tunja biotite monzonite melt, prior to intrusion of the late-stage highly mineralised syenites.
- The textural variability and coarse-grained size of the Balut Dyke is interpreted to indicate high volatile contents, as does the emplacement of an orthoclase-actinolite Cu-Au mineralised stockwork around the intrusion dyke. Rhythmic layering within the dyke is interpreted to have formed by flow segregation and diffusion-controlled nucleation, during alternating periods of strong magma flow and stagnation. This may have been caused by alternating periods of hydrofracturing, and subsequent hydrothermal sealing and volatile build up. The textures within the dyke are analogous to UST textures in quartz-saturated porphyry systems, and to pegmatite dykes found in mid-crustal granitic systems.

## CONCLUSIONS

- Geochemically, the highly calcic Balut Dyke is distinct from the rest of the Didipio Igneous Complex (Figure 5.3). The dyke is interpreted to have been sourced from a hybrid melt that formed by interaction between an evolved syenitic melt and a mafic melt that underplated the chamber (eg Whitney *et al.*, 1988). The mafic layer is interpreted to have contributed heat and Ca to the syenitic melt and buffered the  $\text{SiO}_2$  content.
- The Quan Porphyry is interpreted to have been sourced from a late-stage silica-saturated syenite melt, and represents the chilled outer margin of the Quan-Bufu intrusion. The Bufu Syenite is considered to have crystallised from the residual quartz-perthite melt, following emplacement of a quartz stockwork into the surrounding country rocks. Abundant miarolitic cavities within the Bufu Syenite suggest high volatile concentrations within the melt during crystallisation.
- The emplacement of andesite dykes and sills represents the final period of magmatism in the Didipio region. The andesite dykes share 'co-magmatic' geochemical trends with the rest of the Didipio Igneous Complex and are assumed to have formed from the injection of residual mafic melt that had underplated the magma chamber (eg: Whitney *et al.*, 1988) into the overlying igneous and volcanic complex (Figure 8.4). This may have occurred in response to the collapse and subsidence of the evacuated magma chamber.
- The Didipio Igneous Complex has been disrupted by at least three stages of faulting: northwest-trending F1 normal faults, west-trending F2 sinistral strike-slip faults and northeast-trending F3 dextral strike slip faults. The northern end of Dinkidi has been displaced by a F3 fault, forming the True Blue prospect 700m to the east of Dinkidi (Figure 6.8).
- F1 structures appear to have facilitated the emplacement of narrow, vertically extensive stocks of viscous melt into the subvolcanic environment. Uprise of melt and volatiles along these structures, which drained an evolved volatile-rich magma chamber, is considered to have triggered phase separation and stockwork fracturing. This feeder zone may have been 'plugged' by the Surong Monzonite, forcing the Dinkidi Stock to be emplaced on the margin of the Surong Pluton.
- Whole rock and mineral geochemical analyses have revealed that the intrusions of the Didipio Igneous Complex are alkaline, and are related to each other by fractional crystallisation. The Didipio Igneous Complex shares a similar LILE-enriched source to the Cordon Syenite Complex, the Palali Batholith and the Upper Mamparang Formation. These alkaline to ultrapotassic rocks are interpreted, on the basis of their geochemical (low HFSE and  $\text{TiO}_2$ , high  $\text{Al}_2\text{O}_3$ ) and radiogenic (Knittel & Defant, 1988) compositions to be the LILE-enriched end-product of subduction, sourced from the stalled East Luzon Trench, with negligible crustal contamination.

- Enrichment of LILE within the 'Sierra Madre Arc' is indicated by increasing LILE and LREE concentrations in volcanic units and intrusions during the Oligocene from the flat MORB-like values of the Dupax Batholith to the strong LREE and LILE enrichment of the Upper Mamparang Formation. The subalkaline Mamparang Formation is interpreted to be the subalkaline precursor to the Upper Mamparang Formation, sourced from a weakly LILE-enriched mantle source.
- The increase in LILE and LREE-enrichment and silica-undersaturation northward from the alkaline Didipio Igneous Complex to the feldspathoid-bearing ultrapotassic Cordon Syenite Complex is interpreted to reflect smaller degrees of partial melting of an enriched mantle source or an increase in the degree of enrichment of the mantle source.
- Five main hydrothermal periods occurred in the Didipio Region:
  - Contact metamorphism and weak overprinting K-Fe metasomatism associated with emplacement of the clinopyroxene diorites.
  - K-silicate alteration and weak Cu-Au mineralisation associated with emplacement of the Surong Monzonite.
  - Well developed porphyry-style mineralisation associated with emplacement of the Dinkidi Stock. Within the stock, three main hydrothermal assemblages are recognised, each associated with an intrusive event:
    - Stage 1 K-silicate alteration associated with emplacement of the Tunja Monzonite
    - Stage 2 high-grade calc-silicate mineralisation associated with the emplacement of Balut Dyke.
    - Stage 3 quartz-stockwork mineralisation associated with emplacement of the Quan Porphyry and crystallisation of the Bufu Syenite.
  - Widespread argillic alteration (Stage 4 within the Dinkidi Stock),
  - Zeolite veining associated with widespread faulting (Stage 5 within the Dinkidi Stock)
- The main control on the composition of all early hydrothermal assemblages present at Didipio has been the composition and degree of fractionation of the parent melt. The early 'anhydrous' diorites are associated with thermal metamorphism, and minor K-Fe metasomatism. The Tunja and Surong monzonite intrusions, which contain primary hydrous phases (biotite, indicating an increase in volatile content), are surrounded by a biotite-orthoclase alteration halo with associated weak Cu-Au mineralisation. Associated with emplacement of the calcic, silica-undersaturated Balut Dyke is a quartz-free calc-potassic hydrothermal assemblage. The quartz syenites of the Quan Porphyry and Bufu Syenite, is associated with a quartz stockwork hydrothermal assemblage.

## CONCLUSIONS

- The Stage 1 biotite-magnetite assemblage is interpreted to have formed from high temperature K-Fe-Cl enriched brines. This alteration halo is the most extensive hydrothermal alteration halo present at Dinkidi, and grades distally into patchy epidote-chlorite propylitic alteration.
- The first stage of ore deposition is associated with the emplacement of the Balut Dyke and emplacement of a calc-potassic hydrothermal assemblage characteristic of silica-undersaturated alkaline porphyry deposits. The components were:
  - Stage 2A diopside-perthite-K-feldspar 'vein dykes'.
  - Stage 2B & 2C actinolite-K-feldspar-bornite stockwork veins.
  - Stage 2D massive orthoclase-bornite. This assemblage, focused above the Balut Dyke, formed the high-grade (2-9 g/t Au) core at Dinkidi.
- The Stage 2 assemblage is interpreted to have formed from a hot ( $>600^{\circ}\text{C}$ ), saline, Ca-Fe-Fe-K-Cu-H S enriched fluid, which was undersaturated with respect to  $\text{SiO}_2$ . Deposition is interpreted to have occurred under reduced conditions (magnetite-stable), and at near neutral pH (as suggested by the lack of sericite).
- Crystallisation of the Bufu Syenite is associated with the emplacement of a narrow, but vertically extensive quartz stockwork, that was focused above, and grades into, the apex of the Bufu Syenite. The Bufu Syenite is interpreted to have been the conduit during Stage 3 mineralisation, linking an underlying volatile-saturated magma chamber to the stockwork site.
- The Stage 3 hydrothermal assemblage consists of:
  - Stage 3A quartz-actinolite-K-feldspar-magnetite-bornite-chalcopryrite veins
  - Stage 3B-Potassic quartz-perthite veins, with the same composition as the quartz-syenite core of the Bufu Syenite
  - Stage 3B quartz-sericite-calcite-chalcopryrite-hematite assemblage, typical of the stockwork at many calc-alkaline porphyry deposits.
  - A Stage 3C carbonate-sulphide assemblage.
- The Bugoy Pegmatite is interpreted to be a coarse-grained massive accumulation of the Stage 3A vein assemblage, which filled open spaces in the core of the stockwork. The 'pegmatite' forms an 'interface' zone between the smaller stockwork veins and the underlying Bufu quartz syenite 'conduit'.
- Microthermometric and PIXE analysis indicates that the Stage 3 hydrothermal assemblage formed from a high salinity ( $>68$  wt% eqNaCl) NaCl-KCl-FeCl<sub>2</sub> enriched brine that was emplaced at magmatic to near-magmatic temperatures ( $T > 600^{\circ}\text{C}$ ). This brine contained elevated concentrations of Cu, Ca, Mn, Ti, and Zn.



- Pressure estimates indicate an emplacement depth for the Stage 3 assemblage of 2.9 to 4.5 km, with a minimum depth of 2.6 km (Figure 7.4), and also indicate that there was a significant degree of overpressurisation within the Stage 3 stockwork during quartz growth (ranging from 720 bar to >1500 bar).
- Co-existing vapour rich and hypersaline inclusions suggest episodic depressurisation of the brine during quartz growth, probably as a result of fracturing, with depressurisation to hydrostatic pressures (at least 260 bar).
- The generation of this hypersaline brine is interpreted to have required phase separation at temperatures greater than 750°C (and probably greater than 850°C), followed by cooling of the brine either isobarically or with a pressure increase of up to ~500 bars (Figure 7.4).
- Both cooling and neutralisation of the fluid by wall rock interaction is considered to have led to sulphide precipitation, forming late stage sulphide-calcite infill within the veins and disseminated sulphide-calcite mineralisation throughout regions of sericite alteration. Stage 3 sulphide mineralisation is associated with late primary to secondary chalcopyrite-bearing fluid inclusions (40 to >68 wt% NaCl), which homogenise at temperatures typically >600°C, but with a second peak at 360–480°C (the later peak associated with secondary chalcopyrite-bearing inclusions). This suggests that there may have been at least 120 to 240°C of cooling between emplacement of the quartz stockwork and the main period of sulphide deposition.
- Sulphur isotopes indicate a magmatic source for sulphur in the Stage 2 and 3 sulphides, with no 'exotic' sources, and indicate that Stage 3 fluids may have been reduced by pre-existing Stage 2 sulphides. The sharp transition in sulphur isotope values suggests that there was only limited lateral fluid movement into the surrounding diorites, with most fluids focused up along the main feeder structure.
- The lack of strong sulphide-sulphate fractionation at Dinkidi suggests that the fluids which formed the Stage 2 and possibly the Stage 3 assemblages were relatively reduced compared to other porphyry deposits.
- Late Stage 3C brecciation formed the 'Bugoy Breccia', a quartz fragment breccia sourced from the Bugoy Pegmatite.
- Following the emplacement of the Dinkidi Stock, the regional volcanic units and the more felsic intrusives of the Didipio Igneous Complex were overprinted by widespread intermediate (illite-chlorite-quartz-sericite) to advanced argillic (illite-kaolinite-silica±pyrophyllite-dickite) alteration (possibly a steam heated blanket associated with late-stage geothermal activities). The argillic alteration assemblage is associated with subeconomic silica-pyrite 'high-sulphidation' and quartz-chalcedony-calcite 'low-sulphidation' mineralisation.

## CONCLUSIONS

- The source of the acidic fluids responsible for argillic alteration is assumed to be a mixture of steam heated groundwater (with the Didipio Igneous Complex providing a heat pump for fluids in the volcanic pile) and condensed magmatic vapours (eg Brimhall & Ghiorso, 1983; Hedenquist, 1991).
- The overprint of the Didipio Igneous Complex by strong argillic alteration and by epithermal veins with near-surface, open-space filling textures (eg bladed calcite and crustiform to botryoidal banding in chalcedony) suggests that there was significant erosion (~2.5 to 3 km) during the lifetime of the hydrothermal system in the Didipio region, possibly in response to the increase in relief during rifting of the Cagayan Valley Basin.
- The last period of hydrothermal activity observed in the Didipio region is the emplacement of a zeolite (stilbite-laumontite-chabazite) assemblage, during widespread dextral strike-slip faulting. During this stage the True Blue prospect was faulted off the northern end of Dinkidi, and displaced 700 meters to the east. The zeolite assemblage present in the Dinkidi deposit indicates that relatively cold (80 to 280°C) and alkaline (bi-carbonate) waters may have been drawn down into the Dinkidi Stock.
- Overall, the formation of the Dinkidi deposit is inferred to be the result of:
  - Metal enrichment at the mantle source (interpreted to be caused by partial melting of a metasomatically enriched mantle), forming a favourable incompatible element-enriched alkaline melt,
  - Rifting that allowed the emplacement of the melt into the shallow crustal environment, where shallow level fractionation could 'refine' the melt.
  - Extensive fractionation of anhydrous phases, leading to the exsolution and concentration of a volatile phase
  - The tapping of the late-stage, volatile-rich melt from the magma chamber along syn-magmatic faults
  - Emplacement and focusing of melt and volatiles along vertically extensive structures, allowing phase separation and stockwork formation
  - Uplift and erosion leading to exposure of the deposit.
- Despite the requirement for extensive fractionation, the inferred shallow-crustal magma chamber is interpreted to have been tapped repeatedly (by the Surong, Tunja and Balut melts). This suggests that the magma chamber acted as a relatively open system, yet still formed a mineralised porphyry deposit. This contrasts with the opinion that magma chambers need to act as a sealed volatile container in order to form economic porphyry mineralisation.

- The high gold grades at Dinkidi can be attributed to a range of factors, none of them conclusive. The parent melt was alkaline, a composition typically associated with gold-rich deposits (eg Muller & Groves, 2000) although the source of gold enrichment in alkaline melts remains unclear. The melt was oxidised enough to prevent sequestering of gold by magmatic sulphides during fractionation (but not by magnetite). The deposit is bornite-rich (due in part to high temperature?), which can contain more gold than other copper sulphides.
- Late-stage silicic magma chambers, produced after long periods of fractionation, are unlikely to be simple, homogeneous bodies when emplaced in the shallow to mid-crustal environment. At Didipio, the late-stage syenitic magma chamber responsible for porphyry mineralisation is interpreted to have become compositionally stratified. A late-stage syenitic melt, sourced from fractionation of a silica-saturated alkaline melt, is interpreted to have interacted with reinjected mafic melt, promoting the formation of a hydrothermal assemblage typical of silica-undersaturated alkaline porphyry systems. Further crystallisation is interpreted to have compositionally isolated the siliceous melt from the mafic layer, leading to development of a quartz-saturated 'calc-alkaline' porphyry assemblage, following the cessation of biotite and diopside crystallisation.
- The presence of abundant quartz, in both the Dinkidi and the nearby Marian Porphyry deposits, indicates that silica-saturated alkaline porphyry deposits (such as Dinkidi) and silica-undersaturated ultrapotassic porphyry deposits (such as Marian) may still contain quartz-dominated hydrothermal assemblages. This is in contrast to the silica-saturated and undersaturated alkaline porphyry deposits described from British Columbia, in which quartz is either absent, or a minor, late-stage component (eg uncommon late-stage quartz veins in the alkaline silica-saturated DM deposit, BC; Lang & Stanley, 1995). The formation of quartz in the Philippine alkaline porphyry deposits difference may reflect, in the case of Dinkidi, prolonged fractionation of a silica-saturated melt, and in the case of Cordon, fractionation of feldspathoids leading to the development of a residual monzonite melt (Knittel & Cundari, 1990) and late-stage quartz saturation.
- It is unusual that more quartz-bearing systems did not develop in the alkaline porphyry systems of British Columbia, even among the feldspathoid-bearing melts. The difference between the Canadian and Philippine alkaline porphyry systems may reflect different degrees of enrichment at the mantle source and different histories of magmatic emplacement, both of which would cause differences in the subsequent fractionation history between the Philippine and Canadian alkaline porphyry suites. However, answers for this question awaits a comparison of the intrusive chemistry and magmatic evolution between the two provinces.

## REFERENCES

- Aoki, M, 1978: Hydrothermal alteration of chabazite. *Journal Japanese Association Mineralogists, Petrologists & Economic Geologists*, 73: 155-166.
- Albrecht, A, 1986: Geologisch-petrologische Untersuchung der Kali-Intrusion von Palali (Nord-Luzon, Philippinen). *Unpublished Masters Thesis RW Technische Hochschule, Aachen* (in German). 109pp.
- Albrecht, A and Knittel, U, 1990: The petrology of the K-rich alkaline rocks in the Palali Mountains (northern Luzon, Philippine island arc). *Neues Jahrbuch fuer Mineralogie Abhandlungen*, 161(3): 255-286.
- Alapan, GA, 1981: The Marian gold mine projects in Cordon, Isabela, Philippines. *Proceedings 4<sup>th</sup> Regional Conf. Geology of SE Asia*, pp601-613.
- Allcock, JB, 1977: Zeolites as a final stage in porphyry copper mineralisation. *Economic Geology*, 72(4): 724p.
- Aiello, R & Franco, E, 1968: Formazione di zeoliti per trasformazione di halloysite e montmorillonite a bassa temperatura ed in ambiente alcalino. *Rend. Acad. Sci. Fis. Mat. Soc. Naz. Sci. Lett. Arti. Napoli Ser 4*, 35: 1-29.
- Arribas, A Jnr, Hedenquist, JW, Itaya, T, Okada, T, Concepcion, RA & Garcia, JS Jnr, 1995: Contemporaneous formation of adjacent porphyry and epithermal Cu-Au deposits over 300 ka in northern Luzon, Philippines. *Geology*, 23: 337-340.
- Aurelio, MA & Billedo, EB, 1987: Tectonic implications of the geology and mineral resources of northern Sierra Madre. *Mines and Geosciences Bureau (Philippines) unpublished report*.
- Bailey, DK, 1974: Continental rifting and alkaline magmatism. *In. The Alkaline Rocks, Regional Distribution and Tectonic Relations. Ed. Sorensen, H. John Wiley & Sons, London.* pp148-159.
- Bailey, DK, 1982: Mantle metasomatism – continuing chemical change within the earth. *Nature*, 296: 525-530.
- Balce, GR, Encina, RY, Momongan, A & Lara, L, 1980: Geology of the Baguio District and its implications on the tectonic development of the Luzon Central Cordillera. *Geology & Paleontology of Southeast Asia*, 21: 265-287.
- Baquiran, GB, 1975: Notes on the geology and exploration of the Marian copper deposit, Cordon, Isabela. *Journal Geological Society Philippines*, 24(1): 1-12.
- Barr, DA, Fox, PE, Northcote, KE & Preto VA, 1976: The alkaline suite porphyry deposits - a summary. *In Porphyry deposits of the Canadian Cordillera. Ed. A. Sutherland Brown. Canadian Institute of Mining and Metallurgy, Special Volume*, 15: 359-367.



- Barrie, CT, 1993: Petrochemistry of shoshonitic rocks associated with porphyry copper-gold deposits of central Quesnellia, British Columbia, Canada. *Journal of Geochemical Exploration*, 48: 225-258.
- Barton, M, 1979: A comparative study of some minerals occurring in the potassium-rich alkaline rocks of the Leucite Hills, Wyoming, the Vico Volcano, western Italy, and the Toro-Ankole region, Uganda. *Neues Jahrbuch fuer Mineralogie Abhandlungen*, 137(2): 113-134.
- Bergman, S., Kubler, L & Martinsson O, 2001: Description of regional geological and geophysical maps of northern Norrbotten county (east of the Caledonian Orogen). *Sveriges Geologiska Undersokning (SGA, Sweden)*. Ba 56. 110p.
- Billedo, EB, 1994: Geologie de la Sierra Madre Septentrionale et de l'archipel de Polillo (ceinture mobile est Philippine) - Implications geodynamiques. Documents et travaux 20. *Translated title*, Geology of the northern Sierra Madre and the Pollilo Islands (east Philippine mobile belt) - Geodynamic Implications, Documents and Work 20. *Unpublished Thesis Institut de Geodynamique, Universite Nice Sophia Antipolis* (in English). 244 p.
- Bishop, ST, Heah, TS, Stanley, ST & Lang, JR, 1995: Alkaline intrusion hosted copper-gold mineralisation at the Lorraine deposit, north-central British Colombia. *In* Porphyry deposits of the northwestern cordillera of North America. Ed. TG Schroeter. *Canadian Institute of Mining and Metallurgy, Special Volume*, 46: 623-629.
- Bloomer, SH, Stern, RJ, Fisk, E & Geschwind, CH, 1989: Shoshonitic volcanism in the northern Mariana Arc, 1. Mineralogic and major and trace element characteristics. *Journal of Geophysical Research, B, Solid Earth and Planets*, 94: 4469-4496.
- Bodnar, RJ, 1982: Fluid inclusions in porphyry type deposits. *In* Mineral deposits. Research review for industry, course notes. *Pennsylvania State University*.
- Bodnar, RJ, 1994: Synthetic fluid inclusions XII, the system H<sub>2</sub>O-NaCl; experimental determination of the halite liquidus and isochores for a 40 wt% NaCl solution. *Geochimica et Cosmochimica Acta*, 58(3): 1053-1063.
- Bodnar, RJ, Sterner, SM & Hall, DL, 1989a: SALTY: a Fortran program to calculate compositions of fluid inclusions in the system NaCl-KCl-H<sub>2</sub>O. *Computers and Geosciences*, 15: 19-41.
- Bodnar, RJ, Binns, PR, & Hall, DL, 1989b: Synthetic fluid inclusions VI, Quantitative evaluation of the decrepitation behaviour of fluid inclusions in quartz at one atmosphere confining pressure. *Journal of Metamorphic Geology*, 7(2): 229-242.
- Bodnar, RJ & Vityk, MO, 1994: Interpretation of microthermometric data for H<sub>2</sub>O-NaCl fluid inclusions. *In* Fluid Inclusions in Minerals: Methods and Applications<sup>2</sup>. Eds De Vivo, B & Frezzotti, ML. Virginia Polytechnic Instit. & State Univ. Blacksburg, Virginia. pp117-130.

## REFERENCES

- Bottomer, LR & Leary, GM, 1995: Copper Canyon porphyry copper-gold deposit, Galore Creek area, northwestern British Columbia. *In* Porphyry deposits of the northwestern cordillera of North America. Ed. TG Schroeter. *Canadian Institute of Mining and Metallurgy, Special Volume*, 46: 645-649.
- Bowen, NL, 1933: The broader story of magmatic differentiation, briefly told. *In* Ore deposits of the Western States. *American Inst. Mining & Metallurgical Engineers, Lindgren vol.*: 106-128.
- Brimhall, GH & Ghiorso, MS, 1983: Origin and ore forming consequences of the advanced argillic alteration process in hypogene environments by magmatic gas contamination of meteoric fluids. *Economic Geology*, 78: 73-90.
- Browne PRL, 1978: Hydrothermal alteration in active geothermal fields. *Annual Review of Earth and Planetary Sciences*, 6. p229-250
- Bureau of Mines and Geosciences (Philippines), 1981: *Geology and mineral resources of the Philippines*, 1: 406p.
- Burnham, CW, 1979: Magmas and hydrothermal fluids. *In* Geochemistry of hydrothermal ore deposits (2<sup>nd</sup> ed.). Ed. Barnes HL. Wiley-Interscience Publication, New York. pp34-76.
- Burnham, CW, 1997: Magmas and hydrothermal fluids. *In* Geochemistry of hydrothermal ore deposits (3<sup>rd</sup> ed.). Ed. Barnes HL. John Wiley & Sons. New York, NY, United States. pp63-125.
- Burnham, CW & Jahns RH, 1962. A method for determining the solubility of water in silicate melts. *American Journal of Science*, 260. 721-745.
- Caagusan, NL, 1977: Source material, compaction history and hydrocarbon occurrence in the Cagayan Valley Basin, Luzon, Philippines. *Offshore South East Asia Conference, Singapore 1977*. Southeast Asia Petroleum Exploration Society Session.
- Caagusan, NL, 1980: Stratigraphy and evolution of the Cagayan Valley Basin, Luzon, Philippines. *Geology & Paleontology Southeast Asia*, 21: 163-182.
- Caagusan NL, 1981 Late Tertiary stratigraphy, paleogeography and paleostrucutures of the Cagayan Basin, Philippines – Geology and tectonics of the Luzon-Marianas region. *Phil. SEATAR Committee Spec. Publ.* p119-131.
- Cameron, EN, Jahns, RH, McNair, A & Page, LR, 1949: Internal structure of granitic pegmatites. *Economic Geology Monograph* 2.
- Candela, PA, 1989a: Magmatic ore-forming fluids; thermodynamic and mass transfer calculations of metal concentrations. *In* Ore deposition associated with magmas. Eds Whitney JA & Naldrett AJ. *Reviews in Economic Geology*, 4: 203-221.
- Candela, PA, 1989b: Felsic magmas, volatiles, and metallogenesis. *In* Ore deposition associated with magmas. Eds Whitney JA & Naldrett AJ. *Reviews in Economic Geology*, 4: 223-233.

- Candela, PA, 1997: A review of shallow, ore-related granites: textures, volatiles, and ore metals. *Journal of Petrology* 38(12): 1619-1633.
- Cardwell, RK, Isacks, BL & Karig, DE, 1980: The spatial distribution of earthquakes, focal mechanism solutions and subducted lithosphere in the Philippine and northeastern Indonesian Islands. In The tectonic and geologic evolution of the Southeast Asian seas and islands, part 2. Ed. Hayes, DE. *American Geophysical Union Monograph*, 23: 1-36.
- Cas, RAF & Wright, JV, 1988: Volcanic successions: Modern & ancient: a geological approach to processes, products and successions. Unwin Hyman. London. 487p.
- Cashman, K & Blundy, J 2000: Degassing and crystallization of ascending andesite and dacite. In The causes and consequences of eruptions of andesite volcanoes; papers of a discussion meeting. Eds Francis, P, Neuberg, J, Sparks, RSJ, *Philosophical Transactions Royal Society. Mathematical, Physical and Engineering Sciences*, 358: 1487-1513. Royal Society of London.
- Cerny, P, 1991: Rare element granitic pegmatites, Part I, anatomy and internal evolution of pegmatite deposits. *Geoscience Canada*, 18(2): 49-67.
- Chaussidon, M & Lorand, JP, 1990: Sulphur isotope composition of orogenic spinel ilmenite massifs from Ariège (NE Pyrenees, France): an ion microprobe study. *Geochemica et Cosmochimica Acta*, 54: 2835-2846.
- Christian, LB, 1964: Post-Oligocene tectonic history of the Cagayan Valley Basin, Philippines. *Philippine Geologist*, 18: 114-147.
- Cline, JS & Bodnar, RJ, 1991: Can economic porphyry mineralisation be generated by a typical calc-alkaline melt. *Journal of Geophysical Research, B, Solid Earth and Planets*, 96(5): 8113-8126.
- Cline, JS & Bodnar, RJ, 1994: Direct evolution of brine from a crystallizing silicic melt at the Questa New Mexico, molybdenum deposit. *Economic Geology*, 89: 1780-1802.
- Clooth, G, 1984: Mikroskopische und geochemische untersuchungen an gesteinen des Coastal Batholiths (Philippinen). *Unpublished non-diploma thesis, Institut für mineralogie und Lagerstättenlehre an der Rheinisch-Westfälischen Technischen Hochschule Aachen* (in German).
- Cooke, DR & Bloom, MS, 1990: Epithermal and subjacent porphyry mineralisation, Acupan, Baguio District, Philippines: a fluid inclusion and paragenetic study. *Journal of Geochemical Exploration*, 35: 297-340.
- Crawford, AJ, Kamenetsky, VS, Wolfe, RC & Danyushevsky, LV, 1998: Melt inclusions: a new tool for monitoring volatiles and chalcophile metals in evolving magma suites. *Geological Society of Australia Abstracts*, 49: p131. (14<sup>th</sup> Australian Geological Convention, Townsville, July 1998).
- Corby, GW, 1951: Geology and oil possibilities of the Philippines. *Department of Agriculture and Natural Resources Technical Bulletin*, 21: 363p.

## REFERENCES

- Czamanske, GK, & Wones, DR, 1973: Oxidation during magmatic differentiation, Finnmarka Complex, Oslo area, Norway. Part 2: the mafic silicates. *Journal of Petrology*, 14: 349-380.
- De Boer, J, Odom, LA, Ragland, PG, Snider, FG & Tilford, NR, 1980: The Bataan orogene: Eastward subduction, tectonic rotations and volcanism in the western Pacific (Philippines). *Tectonophysics*, 67: 251-282.
- Dilles, JH & Field, CW, 1996: Sulfur geochemistry of porphyry copper deposits as a record of magma degassing: data from the Yerington district, Nevada. *Abstracts with Programs - Geological Society of America*, 28(7): p93.
- Dilles, JH, Solomon, GC, Taylor, HP & Einaudi, MT, 1992: Oxygen and hydrogen isotope characteristics of hydrothermal alteration at the Ann-Mason porphyry copper deposit, Yerington, Nevada. *Economic Geology*, 87: 44-63.
- Dilles, JH, Farmer, GL & Field, CW, 1995: Sodium-calcium alteration by non-magmatic saline fluids in porphyry copper deposits: results from Yerington, Nevada. In, *Magmas, Fluids and Ore Deposits. Ed., Thompson, JFH. Mineralogical Association of Canada Short Course Notes*, 23.
- Dorais, MJ, 1987: The mafic enclaves of the Dinkey Creek granodiorite and the Carpenter Ridge Tuff: a mineralogical, textural and geochemical study of their origins with implications for the generation of Silicic batholiths. *Unpublished PhD thesis, University of Georgia, Athens*, 185p.
- Druitt, TH & Sparks, RSJ, 1982: A proximal ignimbrite breccia facies on Satorini volcano, Greece. *Journal Volcanol. Geotherm. Research*, 13: 147-171.
- Durkee, EF & Pederson, SL, 1961: Geology of northern Luzon, Philippines. *American Association Petroleum Geologists, Bulletin*, 45: 137-168.
- Eastoe, CJ, 1979: The formation of the Panguna Porphyry Copper Deposit, Bougainville, Papua New Guinea. *Unpublished PhD Thesis, University of Tasmania*, 255p.
- Eastoe, CJ, 1983: Sulfur isotope data and the nature of the hydrothermal systems at the Panguna and Frieda porphyry copper deposits, Papua New Guinea. *Economic Geology and the Bulletin of the Society of Economic Geologists*, 78(2): 201-213.
- Einaudi, MT, Meinert, LD, Newberry, RJ, 1981: Skarn Deposits. In *Economic Geology 75<sup>th</sup> anniversary volume, 1905-1980, Ed. Skinner, BJ*. pp317-391.
- Emmons, 1927: Relations of disseminated copper ores in porphyry to igneous intrusions. *American Institute of Mining & Metallurgical Engineers, Transactions*, 75: 797-809.
- Ennes, SG, Thompson, JFH, Stanley, CR & Yarrow, EW, 1995: The Galore Creek porphyry copper-gold deposits, northwestern British Columbia. In *Porphyry deposits of the northwestern cordillera of North America. Ed. TG Schroeter. Canadian Institute of Mining and Metallurgy, Special Volume*, 46: 630-644.



- Ernst, WG, 1966: Synthesis and stability relations of ferrotremolite. *American Journal of Science*, 264(1): 37-65.
- Field, CW, 1966: Sulphur isotope abundance data, Bingham District, Utah. *Economic Geology*, 61: 850-871.
- Field, CW, Gustafson, LB, 1976: Sulfur isotopes in the porphyry copper deposit at El Salvador, Chile. *Economic Geology and the Bulletin of the Society of Economic Geologists*, 71(8): 1533-1548.
- Fitch, TJ, 1972: Late convergence, transcurrent faulting and internal deformation adjacent to Southeast Asia and Western Pacific. *Journal Geophysical Research*, 77: 4432-4460.
- Fleming, BA & Crerar, DA, 1982: Silicic acid ionization and calculations of silica solubility at elevated temperature and pH. *Geothermics*, 11: 15-29.
- Florendo, FF, 1994: Tertiary arc rifting in northern Luzon, Philippines. *Tectonics*, 13(2): 623-640.
- Foley, SF, Venturelli, G, Green, DH & Toscani, L, 1987: The ultrapotassic rocks: characteristics, classification, and constraints for petrogenetic models. *Earth Science Reviews*, 24: 81-134.
- Foley, SF & Wheller, GE, 1991: Parallels in the origin of the geochemical signatures of island arc volcanics and continental potassic igneous rocks: the role of residual titanates. *Chemical Geology*, 85: 1-18.
- Fournier, RO, 1999: Hydrothermal processes related to movement of fluid from plastic to brittle rock in the magmatic-epithermal environment. *Economic Geology*, 94(8): 1193-1211.
- Fraser, TM, Stanley, CR, Nikic, ZT, Pesalj, R & Gore, D, 1995: The Mount Polley alkalic porphyry copper-gold deposit, south-central British Columbia. In Porphyry deposits of the northwestern cordillera of North America. Ed. TG Schroeter. *Canadian Institute of Mining and Metallurgy, Special Volume*, 46: 609-623.
- Frie, R, 1995: Evolution of mineralizing fluid in the porphyry copper system of the Skouries deposit, Northeast Chalkidiki (Greece): evidence from combined Pb-Sr and stable isotope data. *Economic Geology*, 90: 746-762.
- Fujimaki, H, Tatsumoto, M & Aoki, K, 1984: Partition coefficients of Hf, Zr and REE between phenocrysts and groundmasses. In Proceedings of the fourteenth lunar and planetary science conference, Part 2. *Journal Geophysical Research*, B, 89: Suppl. 662-672.
- Fujimaki, H, 1986: Partition coefficients of Hf, Zr and REE between zircon, apatite and liquid. *Contributions to Mineralogy & Petrology*, 94: 42-45.
- Garrett, S, 1996: The geology and mineralisation of the Dinkidi porphyry related Au-Cu deposit. In Porphyry related copper and gold deposits of the Asia Pacific region. (Australian Mineral Foundation, Cairns, 12-13 August 1996). pp6.0-6.15.

## REFERENCES

- Gervasio, FC, 1971: Geotectonic development of the Philippines. *Journal Geol. Soc. Philippines*, 25(1): 122-126.
- Giggenbach, WF, 1997: Origin and evolution of fluids in magmatic-hydrothermal systems. In *Geochemistry of hydrothermal ore deposits* (3<sup>rd</sup> ed). Ed. Barnes HL. John Wiley & Sons. New York, NY, United States. p737-796.
- Gill, J & Whelan, P, 1989: Early rifting of an oceanic island arc (Fiji) produced shoshonitic to tholeiitic magmatism. *Journal Geophysical Research*, 94: 4561-4578.
- Gilluly, J, 1946: The Ajo mining district. *US Geological Survey Paper* 209: 112p.
- Green, TH & Pearson, NJ 1986: Rare-earth partitioning between sphene and coexisting silicate liquid at high pressure and temperature. *Chemical Geology*, 55: 105-119.
- Grigore, S, Kesler, SE, Essene, EJ & Chryssoulis, SL, 2000: Gold in porphyry copper deposits; experimental determination of the distribution of gold in the Cu-Fe-S system at 400 to 700 degrees C. *Economic Geology*, 95(2): 259-270.
- Gottardi, G & Galli, E, 1985: Natural Zeolites. *Springer-Verlag*, 409p.
- Gustafson, LB, Hunt, JP, 1975: The porphyry copper deposit at El Salvador, Chile. *Economic Geology and the Bulletin of the Society of Economic Geologists*, 70(5): 857-912.
- Haggman, JA, 1997: The discovery, exploration and future development of the Didipio project. In *World Gold 1997 Conference* (Singapore 1-3 September 1997). pp183-189.
- Hall, DL, Strener, SM, Lipman, PW, 1988: Freezing point depression of NaCl-KCl-H<sub>2</sub>O solutions. *Economic Geology*, 83: 197-202.
- Hamilton, W, 1979: Tectonics of the Indonesian region. *U.S. Geological Survey Professional Paper*, 1078: 345p.
- Hashimoto, WE, Aoki, N, David, PP, Balce, GG & Alcantara, PM, 1978: Discovery of *Nummulites* from the Lubingan crystalline schist exposed east of Bongabon, Nueva Ecija, Philippines and its significance on the geologic development of the Philippines. *Geology and Paleontology of Southeast Asia*, 19: 57-63.
- Hashimoto, W, 1980: Geologic development of the Philippines. *Geology and Paleontology of Southeast Asia*, 21: 83-170.
- Hashimoto, W, Matsumaru, K & Fuchimoto, H, 1980: Consideration of the stratigraphy of the Caraballo Range, Northern Luzon: Larger Foraminiferal ranges of the Cenozoic of the Philippines. *Geology and Paleontology of Southeast Asia*, 21: 119-134.
- Haskin, LA, Haskin, MA, Frey, FA & Wildman, TR, 1968: Relative and absolute terrestrial abundances of the rare earths. In *Origin and distribution of the elements*, 1. Ed. Ahrens LH. Pergamon, Oxford. pp889-911.

- Hedenquest, JW, Arribas, A Jnr & Reynolds, TJ, 1998: Evolution of an intrusion-centered hydrothermal system: Far Southeast-Lepanto porphyry and epithermal Cu-Au deposits, Philippines. *Economic Geology*, 93: 373-404.
- Hedenquist, JW, 1991: Boiling and dilution in the shallow portion of the Waiotapu geothermal system, New Zealand. *Geochimica et Cosmochimica Acta*, 55: 2753-2765.
- Heinrich, CA, Ryan, GG, Mernagh, TP & Eadington, PJ, 1992: Segregation of ore metals between magmatic brine and vapour – a fluid inclusion study using PIXE microanalysis. *Economic Geology*, 87: 23-43.
- Heithersay, PS & Walshe, JL, 1995: Endeavour 26 North; a porphyry copper-gold deposit in the Late Ordovician, shoshonitic Goonumbra volcanic complex, New South Wales, Australia. *Economic Geology and the Bulletin of the Society of Economic Geologists*, 90(6): 1506-1532.
- Holland, HD, 1972: Granites, solutions and base metal deposits. *Economic Geology*, 67: 281-301.
- Holland, HD & Malinin, SD, 1979: The solubility and occurrence of non-ore minerals. In *Geochemistry of hydrothermal ore deposits* (2<sup>nd</sup> ed). Ed. Barnes HL. Wiley-Interscience. New York. pp461-508.
- Höller, H, Wirsching, U & Fakhuri, M, 1974: Experimente zur Zeolithbildung durch hydrothermale Umwandlung. *Contributions to Mineralogy & Petrology*, 46: 49-60.
- Hollister, VF, 1975: An appraisal of the nature and source of porphyry copper deposits. *Minerals Science & Engineering*, 7: 225-233.
- Hollister, VF, 1978: Geology of the porphyry copper deposits of the Western Hemisphere. *Society of Mining Engineers, New York*, 219p.
- Hopf, S, 1993: Behaviour of rare earth elements in geothermal systems of New Zealand. *Journal of Geochemical Exploration*, 47: 333-357.
- Hutton, J, 1795: Theory of the earth. *Edinburgh*.
- Irvine, TN & Baragar, WRA, 1971: A guide to the chemical classification of the common volcanic rocks. *Canadian Journal Earth Sciences*, 8: 523-548.
- Jensen, EP & Barton, MD, 2000: Gold deposits related to alkaline magmatism. *Reviews in Economic Geology*, 13: 279-314.
- Jones, BK, 1992: Application of metal zoning to gold exploration in porphyry copper systems. *Journal of Geochemical Exploration*, 43(2): 127-155.
- Kamenetsky, V, Wolfe, R C, Eggins, S M, Mernagh, T and Bastrakov, E, (in press). Volatile exsolution at the Dinkidi Cu-Au porphyry deposit, Philippines: a melt inclusion record of the initial ore forming processes. *Geology*.

## REFERENCES

- Karig, DE, 1983: Accreted terranes in the northern part of the Philippine archipelago. *Tectonics*, 2(2): 211-223.
- Kay, SM & Gast, PW, 1973: The rare earth content and origin of alkali-rich basalts. *Journal of Geology*, 81: 653-582.
- Kirkham, RV & Dunne, KPE, 2000: World distribution of porphyry, porphyry-associated skarn, and bulk-tonnage epithermal deposits and occurrences. *Geological Survey of Canada*. Open File 3792a.
- Kirkham, RV & Sinclair WD, 1988: Comb quartz layers in felsic intrusions and their relationship to porphyry deposits. In: Recent advances in the geology of granite-related mineral deposits. Eds. Taylor, RP & Strong DF. *Canadian Institute of Mining and Metallurgy*. Special Volume 39: p50-71.
- Knittel, U, 1981: Alkaline magmatism in the Cordon area, Isabella, Philippines. *Proc. 4<sup>th</sup> Regional Conf. Geology of SE Asia*. pp309-312.
- Knittel, U, 1982: Genese und Vererzungen des Syenitkomplexes von Cordon (Philippinen). *Unpublished Ph.D. thesis, University RWTH Aachen*.
- Knittel, U, 1983: Age of the Cordon Syenite Complex and its implication on the Mid-Tertiary history of North Luzon. *The Philippine Geologist* 37(2): 22-31.
- Knittel, U, 1987: The Cordon Syenite Complex: an undersaturated potassic igneous center in the Philippine island arc. *Neues Jahrbuch fuer Mineralogie Abhandlungen*, 157(1): 57-80.
- Knittel, U, 1989: composition and association of arsenian goldfieldite from the Marian Gold deposit, Northern Luzon, Philippines. *Mineralogy and Petrology* 40: 145-154.
- Knittel, U & Cundari, A, 1990: Mineralogical evidence for the derivation of metaluminous, potassic rocks from peralkaline precursors: the Cordon Syenite Complex (Philippines). *Mineralogy and Petrology*, 41: 163-183.
- Knittel, U & Defant, MJ, 1988: Sr isotopic and trace element variations in Oligocene to Recent igneous rocks from the Philippine island arc: evidence for recent enrichment in the sub-Philippine mantle. *Earth and Planetary Science Letters*, 87: 87-99.
- Kosukhin, ON, Bakumenko, IT & Chupin, VP, 1994: Magmatic stage of formation of the granite pegmatites. *Trudy Inst. Geol. Geophys.* 476: 17-173. (In Russian).
- Lang, JR & Stanley, CR, 1995: Contrasting styles of alkalic porphyry copper-gold deposits in the northern part of the Iron Mask batholith, Kamloops, British Columbia. In: Porphyry deposits of the northwestern cordillera of North America. Ed. TG Schroeter. *Canadian Institute of Mining and Metallurgy, Special Volume*, 46: 581-592.



- Lang, JR, Stanley, CR & Thompson, JF, 1995a: Porphyry copper-gold deposits related to alkalic igneous rocks in the Triassic-Jurassic arc terranes of British Columbia. *Arizona Geological Society Digest*, 20: 219-236.
- Lang, JR, Stanley, CR, Thompson, JF & Dunne KPE, 1995b: Na-K-Ca magmatic-hydrothermal alteration in alkalic porphyry Cu-Au deposits, British Columbia, *In* Magma, fluids and ore deposits. Ed. JF Thompson. *Mineralogical Association of Canada Short Course Volume*, 23: 339-367.
- Lang, JR & Titley, SR, 1998: Isotopic and geochemical characteristics of Laramide magmatic systems in Arizona and implications for the genesis of porphyry copper deposits. *Economic Geology*, 93: 138-170.
- Le Maitre, RW, 1981: GENMIX; a generalized petrological mixing model program. *Computers and Geosciences*, 7(3): 229-247.
- Leveille, RA, Newberry, RJ & Bull, KF, 1988: An oxidation state-alkalinity diagram for discriminating some gold-favourable plutons: an empirical and phenomenological approach. *Abstracts with Programs - Geological Society America*, 20: p142.
- Lewis, SD & Hayes, DE, 1983: The tectonics of northward propagating subduction along eastern Luzon, Philippine Islands. *In* The Tectonic and Geological Evolution of the Southeast Asian Seas and Islands. Ed. Hayes DE. *American Geophysical Union Monograph*, 27: 57-78.
- Lindgren, W, 1905: The copper deposits of the Clifton-Morenci district, Arizona. *U.S. Geological Survey Professional Paper*, 43: 375p.
- Lloyd, FE & Bailey, DK, 1975: Light element metasomatism of the continental Mantle: the evidence and consequences. *Physics & Chemistry of the Earth* 9: 127-147.
- London, D, 1989: Lithophile rare element concentration in peraluminous silicate systems: summary of experimental results with Macusani glass. *Mineralogical Association Canada, Program with Abstracts*, 14: A32.
- Lowenstern, JB, 1994: Dissolved volatile concentrations in an ore-forming magma. *Geology*, 22: 893-896.
- Meyer, C & Hemley JJ, 1967: Wall rock alteration. *In* Geochemistry of hydrothermal ore deposits. Ed. Barnes, HL. Holt, Rinehart and Winston. New York, Toronto, and London, International. pp166-235.
- Maletierre, P, 1989: Histoire sedimentaire, magmatique, tectonique et metallogenique d'un arc cenozoique deforme en regime de transpression: Cordillere centrale de Luzon. *Unpublished Ph.D. Thesis, Universite de Bretagne Occidentale*.
- Manning, DAC, 1981: The effect of fluorine on liquidus phase relationships in the system Qz-Ab-Or with excess water at 1 kb. *Contributions to Mineralogy and Petrology*, 76(2): 206-215.

## REFERENCES

- Manning, CE & Bird, DK, 1986: Hydrothermal clinopyroxenes of the Skaergaard intrusion. *Contributions to Mineralogy and Petrology*, 92: 437-447.
- McPhie, J, Doyle, M & Allen, R, 1993: Volcanic textures. *CODES Key Centre, University of Tasmania*. 198p.
- Menzies, MA & Hawkesworth, CJ, 1987: Mantle Metasomatism. Academic Press, London, 472p
- MMAJ (Metal Mining Agency of Japan) 1976: Report on geological survey of northeastern Luzon, Part 1. International cooperation agency. *Government of Japan, Unpublished*.
- MMAJ (Metal Mining Agency of Japan) 1977: Report on geological survey of northeastern Luzon, Part 2 (consolidated report). International cooperation agency. *Government of Japan, Unpublished*.
- MMAJ (Metal Mining Agency of Japan) 1981: Report on geological survey of the northeastern Luzon, part 3. International cooperation agency. *Government of Japan, Unpublished*.
- MMAJ (Metal Mining Agency of Japan) 1987: Report on the mineral exploration, mineral deposits and tectonics of two contrasting geological environments in the Philippines, Phase 3 (part1), northern Sierra Madre Area. International cooperation agency. *Government of Japan, Unpublished*.
- MMAJ (Metal Mining Agency of Japan) 1990: Mineral deposits and tectonics of two contrasting geologic environments in the Republic of the Philippines, terminal report. 121pp.
- Monjaret, MC, Bellon, H & Maillet, P, 1991: Magmatism of the troughs behind the New Hebrides island arc (RV Jean Charcot SEAPSO 2 cruise): K-Ar geochronology and petrology. *Journal of Volcanology & Geothermal Research*, 46: 265-280.
- Muller, D, Rock, NMS, Groves, DI, 1992: Geochemical discrimination between shoshonitic and potassic volcanic rocks from different tectonic settings: a pilot study. *Mineralogy and Petrology*, 46: 259-289.
- Muller, D & Groves, DI, 2000: Potassic igneous rocks and associated gold-copper mineralisation, third edition. Springer-Verlag
- Nakamura, N, 1974: Determination of REE, Ba, Fe, Mg, Na and K in carbonaceous and ordinary chondrites. *Geochimica et Cosmochimica Acta*, 38: 757-775
- Ney, CS & Hollister, VF, 1976: Geological setting of porphyry deposits of the Canadian Cordillera. In *Porphyry deposits of the Canadian Cordillera*. Ed. Sutherland Brown, A. *Canadian Institute of Mining Metallurgy, Special Volume*, 15: 21-29.
- Norrish, K & Hutton, JT, 1969: An accurate X-ray spectrographic method for the analysis of a wide range of geological samples. *Geochimica et Cosmochimica Acta*, 33: 431-453

- Oles, D, 1984: Geologische untersuchung der westlichen randzone des Dupax-Batholithen (Nordluzon/Philippinen). *Unpublished Diploma Thesis, Institut fur Mineralogie und Lagerstättenlehre an der RWTH Aachen*. (in German).
- Ohmoto, H, 1972: Systematics of sulphur and carbon isotopes in hydrothermal ore deposits. *Economic Geology*, 67: 551-574.
- Ohmoto, H & Rye, RO, 1979: Isotopes of sulfur and carbon. In *Geochemistry of hydrothermal ore deposits* (2<sup>nd</sup> ed). Ed. Barnes HL. Wiley-Interscience. New York. pp 509-567.
- Ohmoto, H & Goldhaber, MB, 1997: Sulfur and carbon isotopes. In *Geochemistry of hydrothermal ore deposits* (3<sup>rd</sup> ed). Ed. Barnes HL. John Wiley & Sons. New York, NY, United States. pp517-612.
- Pearce, JA, 1983: Role of sub-continental lithosphere in magma genesis at active continental margins. In *Continental basalts and mantle xenoliths*. Eds Hawkesworth, CJ & Norry, MJ. Shiva. Nantwich. pp230-249.
- Pearce, JA, Harris, NBW & Tindle, AG, 1984: Trace element discrimination diagrams for the tectonic interpretation of granitic rocks. *Journal of Petrology* 25: 956-989.
- Peccerillo, A, 1992: Potassic and ultrapotassic rocks: compositional characteristics, petrogenesis, and geologic significance. *IUGS Episodes*, 15: 243-251
- Peccerillo, A & Taylor, SR, 1976: Geochemistry of Eocene calc-alkaline volcanic rocks from the Kastamonu area, northern Turkey. *Contributions to Mineralogy & Petrology*, 58: 63-81.
- Pena, RE, 1994: Stratigraphy of the Baguio District. *Unpublished Report, Mines and Geosciences Bureau (Philippines)*.
- Pichler, H & Kussmaul, S 1980: Comments on the geological map of the Santori Islands. In *Thera and the Aegean World Vol. II*. Ed. Doumas, C. London. pp15-30.
- Pike, RJ & Clow, GD, 1981: Revised classification of terrestrial volcanoes and a catalog of topographic dimensions with new results on edifice volume. *US Geological Survey Open File Report*, OF 81: 1038p.
- Playfair, J, 1802: Illustrations of the Hutton theory of the earth. Edinburgh.
- Radclyffe, D, 1995: Regional scale propylitic alteration in the Goonumbla Mineral Field, Parkes, NSW. *Unpublished B.Sc (Honours) Thesis, University of Tasmania*. 118p.
- Rangin, C, 1991: The Philippine mobile belt: a complex plate boundary. *Journal of Southeast Asian Earth Sciences*, 6(3/4): 209-220.
- Ransome, FL, 1919: The copper deposits of Ray and Miami. *US Geological Survey Professional Paper*, 115: 152p.

## REFERENCES

- Rees, CE, Jenkins WJ & Monster J, 1978: The sulphur isotopic composition of ocean water sulphate. *Geochimica et Cosmochimica Acta*, 42(4): 377-382.
- Reynolds, TJ & Beane, RE, 1985: Evolution of hydrothermal fluid characteristics at the Santa Rita, New Mexico, porphyry copper deposit. *Economic Geology*, 80: 1328-1347.
- Ringenbach, JC, 1992: La Faille Philippine et les chaines en decrochement associees (centre et nord de Luzon): evolution cenozoique et cinématique des deformations quaternaires. *Translated title* The Philippine Fault and the associated strike-slip mountain belt (center and north Luzon): Cenozoic evolution and tectonics of Quaternary deformation. *Unpublished Ph.D. Thesis, Institut de Géodynamique, Université Nice Sophia Antipolis* (in English and French). 316p.
- Robinson, P, Higgins, NC & Jenner, JG, 1986: Determination of rare earth elements, yttrium and scandium in rocks by ion exchange X-ray fluorescence technique. *Chemical Geology*, 55: 121-137.
- Robinson, BW & Kusakabe, M 1975: Quantitative preparation of sulphur dioxide for  $^{34}\text{S}/^{32}\text{S}$  analyses, from sulphides by combustion with cuprous oxide. *Analytical Chemistry*, 47: 1179-1181.
- Rogers, NW & Setterfield, TN, 1994: Potassium and incompatible-element enrichment in shoshonitic lavas from the Tavua Volcano, Fiji. *Chemical Geology* 118 pp 43-62.
- Rogers, NW, Hawkesworth, CJ, Parker, RJ & Marsh, JS, 1985: The geochemistry of potassic lavas from Vulcini, central Italy, and implications for mantle enrichment processes beneath the Roman Region. *Contributions to Mineralogy & Petrology*, 90: 244-257.
- Roedder, E, 1984: Fluid Inclusions. *Reviews in Mineralogy*, 12: 644p. Mineralogical Society of America, Washington, DC.
- Roedder, E, 1992: Fluid inclusion evidence for immiscibility in magmatic differentiation. *Geochimica et Cosmochimica Acta*, 56: 5-20.
- Roedder, E & Bodnar, RJ, 1980: Geologic pressure determinations from fluid inclusion studies. *Annual Review of Earth and Planetary Sciences*, 8: 263-301.
- Rollinson, H, 1993: Using geochemical data: evaluation, presentation, interpretation. Longman Scientific & Technical, England. 352p.
- Ross, KV, Godwin, CI, Bond, L & Dawson, KM, 1995: Geology, alteration and mineralisation of the Ajax East and Ajax West copper-gold alkalic porphyry deposits, southern Iron Mask batholith, Kamloops, British Columbia. In Porphyry deposits of the northwestern cordillera of North America. Ed. TG Schroeter. *Canadian Institute of Mining and Metallurgy, Special Volume*, 46: 609-623.
- Rowins, SM, 2000: Reduced porphyry copper-gold deposits; a new variation on an old



- theme. *Geology*, 28(6): 491-494.
- Rowlands, & Wilkinson, 1999: Significance of intermediate stage veins at Quebrada Blanca, Chile. Mineral deposits, processes to processing. P99-102.
- Rutland, RWR, 1968: A tectonic study of part of the Philippine Fault zone. *Quarterly Journal of the Geological Society of London*, 123: 295-325.
- Ryan, M, Ruiz, J, Titley, S, Gibbins, S & Margotomo, W, 2000: Different crustal sources for Au-rich and Au-poor ores of the Grasberg Cu-Au porphyry deposit. *Earth and Planetary Sciences Letters*, 183(1-2): 7-14.
- Rye, RO, 1993: The evolution of magmatic fluids in the epithermal environment; the stable isotope perspective. *Economic Geology*. 88(3): p733-752.
- Sajona, FG, Bellon, H, Maletterre, P, Ringenbach, JC, Billedo, EB, David, SD, Stephan, JF, Delteil, J, Feraud, G, Winter, W & Cotton, J, 1999: Time and space geochemical evolution of magmatism in Luzon (Philippines) and its geodynamic implications. *Unpublished manuscript*.
- Sasaki, A, Ulriksen, CE, Sato, K & Ishihara, S, 1984: Sulphur isotope reconnaissance of porphyry copper and manto-type deposits in Chile and the Philippines. *Bulletin of the Geological Survey of Japan*, 35(11): 615-622.
- Shinohara, H & Hedenquist, JW, 1997: Constraints on magma degassing beneath the Far Southeast Porphyry Cu-Au Deposit, Philippines. *Journal of Petrology*, 38(12): 1741-1752.
- Shinohara, H, Kazahaya, K & Lowenstern, JB, 1995: Volatile transport in a convecting magma column: implications for porphyry Mo mineralisation. *Geology*, 23(12): 1091-1094.
- Shinohara, H & Kazahaya, K, 1995: Degassing processes related to magma chamber crystallisation. In *Magmas, fluids and ore deposits*. Ed. JF Thompson. *Mineralogical Association of Canada Short Course Notes*, 23: 47-70.
- Sillitoe, RH, 1973: The tops and bottoms of porphyry copper deposits. *Economic Geology*, 68: 799-815.
- Sillitoe, RH, 1987: Copper, gold and subduction: a trans-pacific perspective. In *Proceedings Pacific Rim Congress 1987*: 399-403. Australian Institute of Mining and Metallurgy.
- Sillitoe, RH, 1989: Gold deposits in western Pacific island arcs; the magmatic connection. In *The geology of gold deposits; the perspective in 1988*. eds Keays, RR, Ramsay, WRH & Groves, DI. *Ichnos*, 6: 274-291.
- Sillitoe, RH, 1994: Erosion and collapse of volcanoes: causes of telescoping in intrusion-centered ore deposits. *Geology*, 22: 945-948.
- Sillitoe, RH, 1995: Exploration of porphyry copper lithocaps. In *Proceedings of the 1995*

## REFERENCES

- PACRIM congress; Exploring the rim. Australasian Institute of Mining and Metallurgy 9/95. pp527-532.
- Sillitoe, RH, 2000: Gold-rich porphyry deposits; descriptive and genetic models and their role in exploration and discovery. *In* Gold in 2000, eds Hagemann, SG & Brown, PE. *Reviews in Economic Geology*, 13: 315-345.
- Sillitoe, RH & Gappe, IM Jnr, 1984: Philippine porphyry copper deposits: geologic setting and characteristics. *CCOP Project Office RAS*, 81/120: 1-88.
- Simon, G, Kesler, SE, Essene, EJ & Chryssoulis, SL, 2000: Gold in porphyry copper deposits; experimental determination of the distribution of gold in the Cu-Fe-S system at 400 degrees to 700 degrees C. *Economic Geology*, 95(2): 259-270.
- Solomon, M, 1990: Subduction, arc reversal, and the origin of porphyry copper-gold deposits in island arcs. *Geology*, 18(7): 630-633.
- Stanley, CR, Holbek, PM, Huyck, HLO, Lang, JR, Preto, VAG, Blower, SJ & Bottaro, JC, 1995: Geology of the Copper Mountain alkalic porphyry copper-gold deposits, Princeton, British Columbia. *In* Porphyry deposits of the northwestern cordillera of North America. Ed. TG Schroeter. *Canadian Institute of Mining and Metallurgy, Special Volume*, 46: 537-564.
- Steiner, A, 1977: The Wairakei geothermal area, North Island, New Zealand. *NZ Geological Survey Bulletin*, 90: 136p.
- Stern, RJ, Yamazaki, T, Martinez, P, Fryer, P & Bloomer, SH, 1983: The northward-propagating rift axis of the Mariana Trough (abs). *Eos Trans. AGU*, 74(43) *Fall Meeting Suppl.* p594.
- Stern, RJ, Smoot, NC & Rubin, M, 1984: Unzipping of the volcano arc, Japan. *Tectonophysics*, 102: 153-174.
- Stoffregen, RE, 1987: Genesis of acid-sulfate alteration and Au-Cu-Ag mineralization at Summitville, Colorado. *Economic Geology*, 82(6): 1575-1591.
- Snyder, LD & Russell, JK, 1995: Petrogenetic relationships and assimilation processes in the alkalic Iron Mask batholith., south-central British Columbia. *In* Porphyry deposits of the northwestern cordillera of North America. Ed. TG Schroeter. *Canadian Institute of Mining and Metallurgy, Special Volume*, 46: 593-608.
- Takenouchi, S, 1980: Preliminary studies on fluid inclusions of the Santo Tomas II (Philex) and Tapian (Marcopper) porphyry copper depositions in the Philippines. *In* Granitic magmatism and related mineralisation, eds Ishihara, S & Takenouchi, S. *Mining Geology, Special Issue*, 8: 141-150.
- Taylor, HP, 1987: Isotopes of ore forming Fluids. *In* Short course in Stable Isotope Geochemistry of low temperature fluids, ed. Kyser, TK. *Mineralogical Association of Canada: Short Course Notes Volume* 13.

- Tamesis, EV, 1976: The Cagayan Valley Basin: a second exploration cycle is warranted. *SEAPEX program, offshore South East Asia Conf. Paper*, 14: 21p.
- Titley, SR, 1982: The style and progress of mineralisation and alteration in porphyry copper systems. *In* advances in geology of the porphyry Copper deposits, southwestern North America, *ed.* Titley, SR. University of Arizona Press. pp93-116.
- Titley, SR, 1993: Characteristics of porphyry copper occurrence in the American southwest. *In*, Mineral deposit modeling, *eds* Kirkham, RV, Sinclair, WD, Thrope, RI & Duke, JM. *Geological Association of Canada, Special Paper*, 40: 433-464.
- Titley, SR, & Beane 1981: Porphyry copper deposits, Part 1; Geologic settings, petrology, and tectogenesis, *In* Seventy-fifth anniversary volume. *ed.* Skinner, BJ. *Society of Economic Geologists*. p214-234.
- Tomita, K, Yamashita, H & Oba, N, 1969: Artificial crystallization of volcanic glass to sodium and potassium form of chabazite at room pressure. *Journal of the Japanese Association of Mineralogists, Petrologists and Economic Geologists*, 62(2): 80-89.
- Trudu, AG, 1992: The Tirad porphyry copper-gold prospect (Guinaoang, NW Luzon, Philippines), with a special study on tellurian sulphides. *Unpublished PhD Thesis, Department of Earth Sciences, Monash University, Australia*.
- Vail, PR, Mithcum, RM, Todd, RG, Widmier, JM, Thompson, S, Sangree, JB, Bubb, JN & Hatlelid, WG, 1977: Seismic stratigraphy and global changes of sea level, part 1-11. *In* Seismic stratigraphy – applications to hydrocarbon exploration, *ed.* Payton, CE. *American Association Petroleum Geologists Memoir*, 26: 49-212.
- Varne, R, 1985: Ancient subcontinental mantle: a source for K-rich orogenic volcanics. *Geology*, 13: 405-408.
- Webber, KL, Falster, AU, Simmons, WB & Foord, EE, 1997: The role of diffusion-controlled oscillatory nucleation in the formation of line rock in pegmatite-aplite dikes. *Journal of Petrology* 38(12): 1777-1791.
- Webster, JD, Holloway, JR & Hervig, RL, 1987: Phase equilibria of a Be, U and F-enriched vitrophyre from Spor Mountain, Utah. *Geochemica et Cosmochimica Acta*, 52: 2091-2107.
- Whitney, JA, Dorais, MJ, Stormer, JCJnr, Kline, SW & Matty, DJ, 1988: Magmatic conditions and development of chemical zonation in the Carpenter Ridge Tuff, central San Juan volcanic field, Colorado. *American Journal of Science*, 288-A: 16-44.
- Whitney, JA, 1989: Origin and evolution of silicic magmas. *In* Ore deposition associated with magmas, *eds* Whitney, JA & Naldrett, AJ. *Reviews in Economic Geology*, 4: 183-201.

#### REFERENCES

- Wilkinson, JJ, 2001: Fluid inclusions in hydrothermal ore deposits. *Lithos*, 55(1-4): 229-272.
- Wolfe, J, 1981: Philippine Geochronology. *Journal Geological Society Philippines*, 35 (1): 1-30.
- Wolfe, J, 1988: Arc magmatism and mineralisation in North Luzon and its relationship to subduction at the East Luzon and North Manila Trenches. *Journal South East Asian Earth Sciences*, 2(2): 79-93.
- Wolfe, RC, Cooke, DC & Joyce, P, 1998: The Dinkidi Au-Cu Porphyry – an alkaline porphyry deposit from North Luzon, Philippines. *Geological Society of Australia Abstracts*, 49: p131. (14<sup>th</sup> Australian Geological Convention, Townsville, July 1998).
- Wolfe, RC, Cooke, DR & Joyce, P, 1999: Geology, mineralisation and genesis of the alkaline Dinkidi Cu-Au porphyry, North Luzon, Philippines. *In PACRIM '99 Congress Proceedings*, pp509-516. Australasian Institute of Mining and Metallurgy.
- Yardley, BWD 1999: An introduction to metamorphic petrology. Longman Group Limited, Essex, England. 248p.



# LIST OF APPENDICES

Appendix A: List of all drill holes

Appendix B: Geochemical data

- B1-1: Whole rock major, trace and REE data (this study)
- B1-2: Whole rock data for regional intrusions (various sources)
- B1-3: Whole rock data for regional batholiths (various sources)
- B1-4: Whole rock data for regional volcanic units (various sources)
- B2-1: Electron microprobe analyses of primary igneous minerals (this study)
- B2-2: Electron microprobe analyses of alteration minerals (this study)
- B3: Results of least-squares fractionation modelling

Appendix C: Fluid inclusion microthermometric data

Appendix D: Sulphur isotope results

*List of all holes graphically logged:*

Detailed graphical drill logs (1:200 scale) can be obtained by contacting the author (rohanwolfe@yahoo.com.au).

Dinkidi Drillholes: DDH 3; 4; 14; 16; 28; 33; 34; 36; 37; 43; 49; 50; 51; 52; 53; 54; 60; 67; 77; 81; 82; 83.

Regional Drillholes: Morning Star MS 7; 39; 40; 84; 85.

Century Eggs KPTD 2; 3.

San Pedro 15.

Kamgut 46.

Midnight J 93; 94; 101

Chinni Chinga 104.

True Blue 111

Liang 102; 106; 108

Zone-9 96; 97; 100.

D'Beau 86, 87, 88, 89

D'Fox 91, 105.

Major and Trace element data from this study

Sample	Rock type	SiO2 (wt%)	TiO2	Al2O3	Fe2O3	MnO	MgO	CaO	Na2O	K2O	P2O5	S	Loss	Total	Nb (ppm)	Zr	Sr	Cr	Ba	Y	U	Rb	Th	Pb	As	Zn	Cu	Ni	Se	Sc	
Didipio Igneous Complex																															
G1	Cpx-Gabbro	41.84	0.92	14.85	14.74	0.23	9.25	16.25	0.88	0.52	0.32		0.21	100.01	1.1	21	910	57	183	15	0.1	11	0.1	2	<3	79	134	29			
39/129	Cpx-Gabbro	40.41	1.06	17.08	13.98	0.22	7.67	16.33	1.03	0.5	0.68	0.04	0.54	99.5	1.6	18	1073	12	87	24		9		3	<3	94	144	16		40	
DD1	Cpx-diorite	48.89	0.83	18.22	10.24	0.19	4.91	10.6	3.18	2.34	0.5		0.24	100.14	1	52	1079	4	463	20	2.6	43	0.1	7	<3	71	93	9			
D1	Cpx-diorite	51.57	0.63	18.33	8.6	0.16	4.13	9.88	3.39	2.42	0.53		0.07	99.71	1.3	63	1165	27	432	19	1.5	43	2	16	<3	77	168	15			
D2	Cpx-diorite	50.29	0.71	18.56	8.9	0.19	4.15	9.36	3.64	3.19	0.52	0.4	0.991		1.8	62	1160	3	529	20	0.1	64	2.1	8	3	63	131	5			
D3	Cpx-diorite	49.84	0.7	18.5	8.84	0.2	4.22	9.49	3.17	3.51	0.55		0.45	99.47	1.7	64	1163	4	550	21	1.5	64	1.5	11	<3	63	65	6			
33/155	Cpx-diorite	50.51	0.68	18.64	8.54	0.22	4	9.01	3.67	2.83	0.44	0.01	1.46	100	1.1	56	1023	6	668	18		54	3	<3	70	155	4		20		
MD1	Cpx-Monzodior	51.81	0.65	18.66	8.29	0.19	3.86	9.54	3.75	2.57	0.46		0.23	100.01	1.5	66	1005	6	502	20	0.1	49	2.3	11	3.6	77	160	7			
MD2	Cpx-Monzodior	50.29	0.67	18.88	8.65	0.22	3.68	9.93	3.72	2.83	0.63		0.43	99.93	1.1	73	1305	3	401	23	2.5	50	0.1	12	<3	75	169	5			
MD3	Cpx-Monzodior	49.63	0.73	18.82	8.93	0.21	3.89	10.44	3.49	2.58	0.67		0.41	99.8	1.2	65	1382	3	405	24	1.5	44	0.1	10	<3	73	168	5			
60/623	Cpx-Monzodior	44.25	0.99	17.7	12.06	0.24	5.53	14.36	2.15	1.09	0.84	0.02	0.66	99.87	1.7	40	1487	2	349	24		21	2	<3	95	169	6		24		
39/57	Cpx-Monzodior	51.68	0.64	16.95	8.71	0.18	4.88	9.34	3.54	2.76	0.51	0.01	0.7	99.89	1.8	75	1120	47	395	20		53	8	<3	78	139	23		24		
34/496	Cpx-Monzodior	56.25	0.47	18.89	5.66	0.16	2.37	6.47	4.67	3.94	0.33	0.01	0.61	99.82	1.4	71	970	2	923	15		74	14	<3	62	164	1		10		
53/558	Cpx-Monzodior	56.39	0.48	19	5.65	0.16	2.43	6.36	4.79	3.83	0.32	0.01	0.41	99.82	1.6	77	968	2	924	15		71	13	10	64	130	2		10		
Kpid2/43	Cpx-Monzodior	54.22	0.64	18.09	7.44	0.16	3.32	7.26	4.26	3.33	0.52	0.01	0.56	99.8	2.2	71	1181	3	606	18		62	9	4	63	143	5		17		
M1	Surong Monz	57.55	0.45	18.29	5.44	0.13	2.09	5.65	4.87	4.13	0.37		0.76	99.73	1.9	100	872	3	484	18	2.2	70	2.5	10	<3	37	105	3			
M2	Surong Monz	56.79	0.46	18.61	5.89	0.16	2.28	6.68	4.86	3.55	0.35		0.5	100.13	1.4	79	1005	3	471	20	1.7	62	1.8	8	<3	48	207	3			
M3	Surong Monz	56.11	0.46	18.6	5.9	0.16	2.26	6.74	4.82	3.49	0.35		1.38	100.27	1.8	86	1063	3	422	22	2.4	56	1.6	7	<3	60	163	4			
M4	Surong Monz	54.87	0.51	18.38	6.72	0.18	2.67	7	4.54	3.04	0.48		1.04	99.43	1.6	75	901	2	820	15	1.5	68	2.1	9	3.3	23	812	4			
M6	Surong Monz	58.32	0.51	18.19	4.73	0.07	2.28	4.06	4.4	5.32	0.41		2.77	101.06	2.1	86	800	3	676	21	1.5	67	1.6	15	<3	95	131	3			
M9	Surong Monz	54.11	0.58	18.69	6.56	0.18	2.33	7.28	4.58	3.68	0.45		2.13	100.57	1.6	89	1184	4	517	25	2.4	60	1.6	13	<3	69	159	3			
M10	Surong Monz	56.43	0.55	18.93	6.16	0.16	2.22	6.95	4.71	3.43	0.42		0.32	100.28	2.5	86	1133	3	504	22	1.8	59	0.1	10	<3	64	114	3			
15/110	Surong Monz	61.88	0.39	17.86	4.05	0.05	1.33	2.3	4.94	5.29	0.23	0.24	1.39	99.71	1.6	119	777	3	780	16		85	6	4	27	95	2		1.1	6	
15/212	Surong Monz	59.17	0.45	17.54	5.77	0.08	2.38	4.52	4.75	2.91	0.31	0.2	2.06	99.94	1.5	71	1040	7	635	10		55	4	3	24	116	3		15		
15/351	Surong Monz	53.11	0.56	17.34	8.58	0.11	3.93	7.87	3.03	2.85	0.45	0.01	1.83	99.66	1	64	1061	14	534	16		58	4	4	30	34	9		0.6	25	
48/212	Surong Monz	60.72	0.36	17.56	3.27	0.09	1.62	3.45	4.72	6.99	0.2	0.02	1.07	100.05	2.7	165	570	8	571	16		113	13	<3	37	145	4		8		
R46/65	Surong Monz	55.66	0.42	17.17	5.06	0.11	2.73	6.75	3.32	6.11	0.33	0.01	1.8	99.46	2.5	94	1075	12	874	15		94	5	<3	35	131	8		12		
S48/85	Surong Monz	53.57	0.55	18.51	6.89	0.16	2.81	7.62	4.03	3.9	0.43	0.01	1.44	99.91	2.5	105	1153	3	470	19		80	15	4	72	172	5		11		
FMnz	Surong Monz	61.4	0.37	19.19	4.11	0.07	1.4	2.97	5.58	4.38	0.23		0.99	100.69	1.7	72	864	2	1100	13	1.5	79	1.7	9	<3	28	256	1			
AP1	Andesite dykes	48.45	0.67	18.35	9.25	0.19	4.71	9.08	3.09	2.66	0.5		2.61	99.56	1.3	57	986	4	420	19	0.1	41	0.1	5	<3	68	188	8			
AP3	Andesite dykes	46.38	0.78	17.57	10.58	0.19	6.28	12.13	2.28	1.83	0.45		1.5	99.97	1.4	46	1047	31	302	19	2.3	27	0.1	14	<3	88	144	24			
Dinkidi Stock																															
25/236	Tunja bi monz	58.98	0.39	18.59	4.09	0.06	1.41	4.5	6.22	3.49	0.23	0.03	1.92	99.88	2.5	46	979	2	1243	8		55	6	<3	19	112	1		6		
25/254	Tunja bi monz	56.81	0.43	18.77	4.88	0.09	2.16	4.38	5.68	3.45	0.26	0.02	3.17	100.045	1.3	41	980	3	1458	10		66	6	<3	25	129	1		0.3	9	
33/376	Tunja bi monz	56.6	0.42	18.74	5.04	0.08	2.15	5.18	5.23	3.62	0.32	0.01	2.94	100.32	2.1	62	995	2	1408	12		59	6	<3	24	45	1		10		
53/569	Tunja bi monz	55.97	0.5	18.81	5.43	0.13	2.55	6.26	4.89	3.5	0.37	0.02	1.56	99.97	1.3	74	996	3	774	14		73	9	<3	41	168	2		0.1	12	
60/600	Tunja bi monz	55.31	0.45	19.05	5.26	0.08	2.34	5.45	5.43	3.29	0.37	0.01	2.69	99.72	1.5	39	1216	2	1328	12		65	6	<3	27	47	2		7		
14/407	Bahut Cpx syen	54	0.24	8.96	5.64	0.28	6.72	12.5	2.92	3.4		0.22	4.68	99.4																	
3/66	Quan Porphyry	63.1	0.26	17.6	2.96	0.04	0.7	2.71	6.23	3.98	0.12	0.05	2.27	99.97	1.8	89	777	2	1220	7		55	6	<3	20	676	1		1.6	3	
25/110	Quan Porphyry	63.02	0.26	17.65	2.98	0.04	0.77	2.67	6.72	3.63	0.13	0.05	2.24	100.11	1.7	96	834	1	1178	7		48	5	3	18	448	1		0.1		
34/300	Quan Porphyry	59	0.36	18.45	3.67	0.05	1.34	4.37	6.1	3.85	0.22	0.03	2.89	100.3	2.1	76	1040	2	1145	7		48	6	4	28	201	0		4		
49/539	Bufu Syenite	70.03	0.16	15.55	1.07	0.01	0.25	0.63	3.87	7.19	0.05	0.26	1.13	99.93	0.1	117	184	2	847	4		98	3	5	7	595	1		1.9	0.1	
54/565	Bufu Syenite	71.95	0.1	14.76	0.48	0.01	0.22	0.4	2.62	8.88	0.07	0.02	0.81	100.29	0.1	116	160	2	878	3		114	2	<3	6	45	1		1.2	0.1	
Didiplo 'Maparang Formation'																															
F17/144	Cpx-And lava	62.35	0.32	17.87	4.57	0.07	1.58	4.27	4.97	2.37	0.2	0.05	1.01	99.58	2.2	93	874	5	568	12		32	7	<3	40	395	4		8		
F17/216	Cpx-And lava	63.15	0.31	17.95	4.54	0.04	1.55	3.57	4.82	2.65	0.19	0.1	1.47	100.24	1.9	95	852	5	655	12		39	7	<3							

*REE data from this study*

Sample	Rock type	La (ppm)	Ce	Pr	Nd	Pm	Sm	Eu	Gd	Tb	Dy	Ho	Er	Tm	Yb	Lu
<b>Didipio Igneous Complex</b>																
G1	Cpx-Gabbro	4.85	12.57	2.43	13.13		4.07	1.27	3.48	0.58	3.02		1.43		1.1	
39/129	Gabbro	5.7	15.59	2.76	16.52		4.79	1.5	5.23	0.73	4.35	0.87	2.3		2.17	0.28
DD1	Cpx-diorite	11.31	25.14	4.06	16.29		4.84	1.37	4.01	0.66	3.45		2.27		1.85	
D1	Cpx-diorite	11.92	28.2	4.37	18.83		4.78	1.34	3.89	0.56	3.32		1.75		1.68	
D2	Cpx-diorite	14.44	30.62	4.76	23.24		6.12	1.78	4.71	0.73	3.64		1.86		1.75	
D3	Cpx-diorite	12.74	28.55	4.29	19.58		4.62	1.26	3.84	0.61	3.25		1.48		1.57	
MD1	Cpx-Monzodior	10.76	23.81	3.95	16.73		4.62	1.34	3.72	0.66	3.45		2.38		2.02	
MD2	Cpx-Monzodior	15.95	33.58	5.4	22.97		5.88	1.75	4.65	0.75	4.07		2.67		2.2	
MD3	Cpx-Monzodior	13.89	34.01	5.51	24.52		6.49	1.85	5.23	0.83	4.26		2.62		2.11	
M1	Surong Monz	14.85	29.01	4.21	17.55		4.22	1.2	3.4	0.5	2.89		1.82		1.85	
M2	Surong Monz	13.82	29.95	4.46	18.82		4.49	1.28	3.77	0.63	3.49		2.46		2.19	
M3	Surong Monz	13.7	29.05	4.44	19.4		4.78	1.41	3.84	0.59	3.3		2.29		2.13	
M4	Surong Monz	11.57	24.62	3.52	15.95		4.17	1.36	3.19	0.5	2.47		1.45		1.42	
M6	Surong Monz	12.62	24.8	4.06	17.44		4.52	1.19	3.71	0.56	3.25		2.15		2.06	
M9	Surong Monz	15.67	33.12	5.22	23.62		6.02	1.75	4.87	0.72	4.07		2.51		2.37	
M10	Surong Monz	13.09	28.2	4.51	19.94		4.77	1.36	3.95	0.67	3.59		2.39		2.23	
FMnZ	Surong Monz	9.17	20.28	2.88	11.83		2.68	0.75	2.13	0.32	1.82		1.2		1.28	
AP1	Andesite dykes	11.22	21.74	3.81	17.69		5.14	1.57	4.24	0.68	3.64		2.12		1.91	
AP3	Andesite dykes	10.5	22.33	3.36	16.78		4.54	1.34	3.97	0.58	3.49		1.7		1.59	
<b>Dinkidi Stock</b>																
25/254	Tunja bt monz	10.8	20.73	2.85	12.65		2.53	0.93	2	0.29	1.68	0.35	1.04		0.98	0.15
53/569	Tunja bt monz	13.31	27.2	3.7	16.03		3.35	1.03	2.69	0.37	2.21	0.49	1.31		1.35	0.23
3/66	Quan Porphyry	7.94	17.56	2.3	9.56		1.77	0.5	1.27	0.19	1.09	0.22	0.59		0.69	0.12
<b>Didipio Upper Mamparang F.</b>																
K1	Trachyte	14.66	32.38	4.5	19.8		4.28	1.03	3.52	0.54	3.45		2.45		2.48	
K4	Trachyte	17.57	39.88	4.95	20.76		4.18	0.81	3.33	0.54	3.13		2.29		2.52	
<b>Didipio 'Maparang Formation'</b>																
F17/144	Cpx-And lava	11.52	19.64	2.53	10.44		2.12	0.65	1.82	0.27	1.74	0.39	1.13		1.15	0.21
F17/216	Cpx-And lava	11.33	20.73	2.68	10.97		2.21	0.66	1.81	0.31	1.84	0.39	1.15		1.26	0.22
F17/53	Cpx-And lava	10.25	19.18	2.48	9.83		2.05	0.64	1.69	0.27	1.62	0.33	1.09		1.17	0.21



Major and Trace element data for regional intrusives (Knittel pers com.)

Sample	Rock type	Source	SiO2	TiO2	Al2O3	Fe2O3	FeO	MnO	MgO	CaO	Na2O	K2O	P2O5	Loss	Total	Nb	Zr	Sr	Cr	Ba	Y	Rb	Th	Ni	Sc	V	Co	Ga	
Palali Batholith																													
J 11 (B214 in MMAJ)	foiid-syenite	MMAJ, 1977	54.27	0.41	20.29	1.71	2.30	0.33	1.47	3.11	4.26	7.00	0.19	3.62	98.96														
J 14 (B335 in MMAJ)	foiid-syenite	MMAJ, 1977	54.17	0.49	20.06	1.87	2.52	0.26	1.38	3.94	4.62	6.94	0.23	3.10	99.58														
J 15 (B337 in MMAJ)	foiid-syenite	MMAJ, 1977	56.59	0.53	19.58	3.08	1.19	0.12	1.73	3.14	4.82	4.70	0.13	3.89	99.50														
J 16 (B339 in MMAJ)	foiid-syenite	MMAJ, 1977	57.95	0.42	19.95	2.86	0.79	0.06	2.55	1.17	2.78	8.55	0.05	2.27	99.40														
J 22 (C102 in MMAJ)	foiid-syenite	MMAJ, 1977	55.20	0.51	20.24	1.83	2.05	0.23	1.38	1.84	4.64	7.82	0.15	3.09	98.98														
J 23 (C109 in MMAJ)	foiid-syenite	MMAJ, 1977	56.31	0.52	19.88	2.87	2.55	0.27	2.19	2.22	4.30	5.55	0.30	2.38	99.34														
PR44	neph-syenite	Albrecht	55.67	0.32	20.52	2.92		0.20	0.64	2.46	5.30	7.66	0.09	4.36	100.14	7	192	864	9	442	25	148	11	5	3	128	5	21	
PR42	neph-syenite	Albrecht	56.50	0.33	20.94	2.29		0.21	0.48	1.65	6.19	6.99	0.06	4.36	100.00	9	371	334	7	49	34	174	17	4	5	95	2	26	
PR128	neph-syenite	Albrecht	56.11	0.36	21.69	2.76		0.26	0.44	2.72	5.27	7.30	0.06	3.33	100.30	5	172	642	11	50	30	192	7	6	4	116	2	23	
ISOT1	neph syenite	Knittel	57.02	0.35	20.98	2.40		0.20	0.87	1.51	4.86	8.16	0.06	3.40	99.81	5	228	620	12	160	31	170	13	5	1	110	4	21	
PR45	syenite	Knittel	55.57	0.41	19.95	3.91		0.22	1.24	3.46	4.63	7.44	0.24	2.98	100.05	3	137	1642	7	758	22	133	9	5	6	192	10	19	
PR99a	neph monzosy	Albrecht	51.62	0.69	18.83	9.08		0.36	2.03	5.37	1.39	8.16	0.36		97.89			1467	13	1062	343	165		35					
PR11	syenite	Albrecht	53.53	0.68	19.79	6.53		0.22	2.68	7.34	4.44	4.42	0.51		100.14														
PR 1	syenite	Albrecht	54.82	0.60	19.81	5.52		0.24	1.60	5.37	3.67	6.39	0.39		98.41	5.5	178	2010	3	637	24	133		14			19		
J 12 (B225 in MMAJ)	monzonite	MMAJ, 1977	52.88	0.63	16.75	5.49	1.78	0.13	4.16	5.71	5.27	3.03	3.61		97.66														
PR 86	alk.syen.	Albrecht	59.75	0.30	20.20	2.24		0.16	0.33	2.02	5.73	7.49	0.02		98.24														
PR 11G	alk.syen.	Albrecht	63.26	0.49	19.71	2.95		0.14	0.21	1.65	4.43	7.86	0.07		100.77														
J 17 (B342 in MMAJ)	Syenite	MMAJ, 1977	56.98	0.32	19.98	2.33	1.28	0.07	1.81	3.11	3.61	6.32	3.94		98.47														
J 24 (C125 in MMAJ)	Syenite	MMAJ, 1977	53.24	0.43	20.83	1.55	1.72	0.31	1.16	3.84	3.54	8.14	4.75		97.79														

Cordon Syenite Complex

KN 1	pslc syenite	Knittel	52.35	0.52	16.68	6.26	0.13	3.08	7.74	1.47	7.66	0.50	3.85	100.24			2231	31	869	169	14	238						
KN 1	pslc syenite	Knittel	50.55	0.49	16.21	6.52	0.14	2.79	8.05	1.60	8.12	0.46	3.38	98.31			2335	49		157	16	185	18					
KN 7	pslc syenite	Knittel	50.51	0.54	16.07	6.63	0.15	3.71	8.48	2.01	7.19	0.59	4.62	100.50			1777	32	726	174		250	11					
KN13	pslc syenite	Knittel	52.55	0.49	15.87	8.38	0.12	4.58	7.42	3.60	4.59	0.51	1.91	100.02	5	74	1091	48	568	13	88	2.05	31	23.3	24	13		
KN 15	Syenite	Knittel	51.64	0.48	16.41	6.29	0.13	2.97	7.16	1.63	7.93	0.49	3.79	98.92			2272	53	963	146	17	188	18					
KN 18	Syenite	Knittel	55.40	0.37	17.45	5.16	0.13	1.86	6.40	4.30	6.61	0.32	1.87		7	131	1996	9	723	16	125	4	10	11.7	23	15		
Q 36III	Syenite	Knittel	49.47	0.69	18.12	8.01	0.17	4.26	9.37	3.30	4.09	0.73	1.97	100.18			1669	15	846	73	21	325	28					
Q 43	Syenite	Knittel	53.85	0.49	17.18	6.49	0.16	3.43	7.25	3.71	5.72	0.63	1.34	100.25			1508	27	716	100		219	19					
Q 72	Syenite	Knittel	52.45	0.60	16.91	7.56	0.14	3.59	6.52	3.19	6.20	0.69	1.78	99.63			1740	19	1057	143								
'18	Syenite	Knittel	48.84	0.62	16.41	9.60	0.20	4.14	9.14	2.51	4.26	0.73	3.25	99.70	1	106	1939	18	956	17	49	3	14	32	370	27	17	
KN20	Pegmatit	Knittel	55.98	0.17	18.04	3.80	0.13	0.95	5.85	1.54	10.06	0.09	2.32	98.93			2978		1088	135		111	19					
KN 2		Knittel	56.27	0.39	17.98	5.11	0.14	1.84	5.29	3.86	6.48	0.28	2.20	99.84			1938	31	747	115		149	14					
KN 16	Monzonite	Knittel	53.28	0.51	17.59	5.89	0.15	2.25	5.78	2.68	7.05	0.40	3.49	99.07			2272	2	963	146	17							
Q 51	Monzonite	Knittel	55.50	0.48	18.36	5.83	0.13	2.08	5.76	4.02	5.19	0.57	2.12	100.04	6	158	2155	14	959	16	77	76	228	87				
Q56	Monzonite	Knittel	54.16	0.54	17.40	7.38	0.14	2.53	6.04	3.30	4.41	0.52	3.51	99.93	6	132	1596	32	698	17	72	12	14	27	291	18	17	
A6.6	Monzonite	Knittel	60.06	0.33	17.40	5.32	0.13	2.13	1.48	5.56	4.86	0.47	1.43	99.17			848	10	734	72		157	10					
M 20	Monzonite	Knittel	53.48	0.51	17.60	6.37	0.18	2.89	5.69	3.23	6.26	0.62	2.83	99.66			1686	17	821	143		220						
KN3	Lusitanite	Knittel	46.28	0.63	11.35	11.93	0.27	7.06	11.97	1.56	5.20	1.19	2.19	99.63														
KN4	Lusitanite	Knittel	44.79	0.81	8.84	13.71	0.35	8.50	13.84	1.49	4.52	1.44	1.49	99.78			1137.0		1023.0	85								
KN5	Lusitanite	Knittel	47.05	0.65	12.83	11.44	0.47	5.43	9.30	1.36	7.42	1.08	2.44	99.47														
KN6	Lusitanite	Knittel	46.93	0.65	12.75	10.60	0.22	6.54	10.36	1.33	6.33	0.83	3.25	99.79			2137	59	1414	162	25	352	23					
KN6 (Av 2)	Lusitanite	Knittel	48.55	0.60	12.89	10.71	0.24	6.06	10.14		6.33	0.89	3.06		4	58	2243	42		14	130	1.76	30	37.9	30	12		
X5	Lusitanite	Knittel	45.81	0.61	12.00	12.23	0.31	7.13	12.12	1.48	5.18	1.11	2.27	100.25			1569	63	904	123	36	348	25					

REE data for regional intrusives (Knittel pers com.)

Sample	Rock type	Source	Hf	La	Ce	Pr	Nd	Pm	Sm	Eu	Gd	Tb	Dy	Ho	Er	Tm	Yb	Lu	(Ta)
<b>Cordon Syenite Complex</b>																			
KN13	pslc syenite	Knittel	1.67	12.6	29.1		17.1		3.71	1.02		0.43					1.41	0.24	0.14
KN 18	Syenite	Knittel	3.02	17	37.2		18.2		3.48	0.98		0.49					2.05	0.33	0.32
KN6 (Av 2)	Lusitanite	Knittel	1.38	18.2	41.4		23.4		5.705	1.63		0.54					1.45	0.25	0.08

Major and trace element data for regional batholiths

Major and trace element data for regional batholiths																												
Analysis Name	Rock type	Source	SiO2	TiO2	Al2O3	Fe2O3	FeO	MnO	MgO	CaO	Na2O	K2O	P2O5	H2O	Loss	Total	Nb	Zr	Sr	Cr	Ba	Y	Rb	Ni	Sc	V	Co	
Coastal Batholith																												
330 (D80 in Knittel 87)	Qtz-dio	Clooth 84	71.35	0.38	13.13	4.58		0.07	1.20	4.23	3.48	0.26	0.04	1.19		99.98		51	78		36	32	3					
329	<?> Qtz-dio	Clooth 84	71.03	0.38	12.74	4.92		0.09	1.15	4.78	3.09	0.46	0.03	0.7		99.44												
328	<?> Qtz-dio	Clooth 84	68.78	0.38	13.37	5.47		0.11	1.32	4.82	3.00	0.21	0.04	1.28		98.93												
324 (D1G in Knittel 87)	diorite	Clooth 84	57.15	0.25	14.76	7.71		0.15	6.56	9.56	1.44	0.25	0.02	1.09		98.99		28	35		42	14	4					
A-200	Granite	MMAJ *	75.15	0.58	11.72	1.68	1.12	0.02	1.00	4.30	3.51	0.50	0.02	0.87		100.47												
PA-14	Qtz-diorite	MMAJ *	54.98	0.71	16.89	5.07	2.06	0.01	5.26	9.23	3.86	0.94	0.05	0.89		100.55												
A-20	Qtz-diorite	MMAJ *	72.16	0.34	13.67	1.08	2.66	0.12	0.77	3.21	4.34	0.70	0.06	0.76		99.87												
A-44	Qtz-gabbro	MMAJ *	71.19	0.33	14.23	1.20	2.59	0.08	0.88	4.50	3.41	0.40	0.06	0.97		99.81												
L-22	Qtz-gabbro	MMAJ *	74.59	0.28	13.07	0.79	2.08	0.07	0.54	2.21	4.62	0.43	0.05	0.87		99.6												
L-33	Qtz-diorite	MMAJ *	62.49	0.56	15.74	2.10	5.21	0.14	2.67	6.45	3.23	0.30	0.06	0.81		99.76												
L-38	Amp-gabbro	MMAJ *	51.22	0.79	17.02	3.82	7.40	0.27	4.88	9.89	2.32	0.32	0.05	1.32		99.3												
D1G	Dio	Knittel pers. com	57.20						6.60																			
D80	Qdio	Knittel pers. com	71.40						1.20																			
ISA-338	Qtz-diorite	Billedo 94	64.50	0.90	16.30	5.43		0.11	1.57	6.02	4.38	0.14	0.25		0.40	100	0.85	11	217	3	52	38	1.6	3	28	60	6	
ISA-458	Qtz-diorite	Billedo 94	46.10	1.08	17.20	15.60		0.23	5.53	10.85	1.70	0.09	0.08		1.21	99.73	0.65	12	160	2	23	10.2	1.6	1	56	510	37	
* MMAJ data is contained in Clooth, 1984																												
Dupax Batholith																												
AUR-103	Qtz-diorite,	Billedo 94	65.00	0.49	15.30	5.77		0.14	2.49	6.00	3.12	0.33	0.08		1.39	100.11	0.45	28	133	20	62	28	3.8	4	27	155	11	
S9	Dio	Knittel	56.90						3.60			1.00							519		371		10					
C7	Tonalite	MMAJ *	60.38	1.04	15.80	4.23	3.63	0.23	5.08	3.91	2.45	0.65	0.19	1.86		99.45												
C21	Q-diorite	MMAJ *	54.01	0.85	17.96	3.15	5.78	0.19	3.10	8.29	3.66	0.58	0.15	1.64		99.36												
C26	Q-diorite	MMAJ *	49.09	0.97	18.85	3.56	7.47	0.23	3.16	10.16	4.28	0.08	0.33	1.19		99.37												
B34	Gabbro	MMAJ *	51.46	0.85	18.72	3.87	5.83	0.18	5.67	11.11	1.98	0.53	0.07	0.34		100.6												
H20	Granophyre	MMAJ *	75.60	0.35	12.49	0.43	2.34	0.05	4.56	1.13	0.64	0.84	0.06	1.21		99.7												
NE-81	Gabbro	Ringenbach 92	48.50	0.44	19.18	9.25		0.18	6.46	12.86	1.35	0.25	0.11		1.99	100.57	0.40	16	304	87	120	14	3	25	35	253	31	
NE-34	Gabbro	Ringenbach 92	43.10	0.72	20.52	14.08		0.20	6.25	15.00	0.83	0.02	0.07		0.03	100.82	0.35	4	280	4	11	9	0.5	10	51	545	45	
326	Idio	Clooth 84	56.56	0.23	15.70	7.98		0.16	6.60	9.74	1.55	0.27		1.38		100.18												
33	Hrn-gabbro	Oles 84	48.83	1.02	18.77	12.96		0.24	5.35	10.86	1.80	0.47	0.13			100.4												
34	Hrn-gabbro	Oles 84	49.30	0.89	18.50	12.06		0.23	4.93	10.29	2.94	0.59	0.17			100.1												
35	q-dio	Oles 84	76.46	0.42	12.43	1.31		0.05	0.90	2.08	4.50	0.22	0.08			98.45												
36	q-dio	Oles 84	77.57	0.37	13.07	2.49		0.08	0.73	1.17	7.76	0.66	0.07			103.97												
37	q-dio	Oles 84	75.92	0.31	12.87	2.48		0.13	0.51	1.22	4.78	0.78	0.07			99.07												
41	Hrn-dio dyke	Oles 84	49.77	0.77	20.80	6.66		0.10	6.77	12.94	2.77	0.18	0.07			100.91												
72	Trondhj	Knittel	76.50						0.90			0.22							132		33		3					
* MMAJ data is contained in Oles, 1984.																												
Agno Batholith																												
P-5	Calc-alk granod	Ringenbach 92	62.75	0.42	16.00	4.68		0.15	1.97	5.55	3.60	1.10	0.13		0.54	99.89	2.70	4	425	4	380	15	20	3	9	85	11	
BAJ 37	Trondhj	Knittel	71.80						0.90			0.25							210				15					
BAL 24	Qz dior	Knittel	62.90						1.90			0.70							380				26					
PI-170	Qz dior	Knittel	58.70						3.10			0.57							387		166		6					
PI-135	Qz dior	Knittel	69.10						1.00			1.70							418		211		24					
KRL 18	Basalt	Knittel	49.50						5.30			0.23							805				8					

REE data for regional batholiths

Analysis Name	Rock type	Source	La	Ce	Pr	Nd	Pm	Sm	Eu	Gd	Tb	Dy	Ho	Er	Tm	Yb	Lu
<b>Coastal Batholith</b>																	
ISA-338	Qtz-diorite	Billedo 94	2.8	11		10			1.25			6		3.9			3.75
ISA-458	Qtz-diorite	Billedo 94	0.9	4		2			0.5			1.6		1			1.08
<b>Dupax Batholith</b>																	
AUR-103	Qtz-diorite	Billedo 94	2.25	8		8			0.75			4.6		3.4			3.35
NE-81	Gabbro	Ringenbach 92	2.3			6			0.55			2		1.5			1.2
NE-34	Gabbro	Ringenbach 92	0.9			1			0.3			1.4		1			0.85
<b>Agno Batholith</b>																	
P-5	Calc-alk granod	Ringenbach 92	8			12			0.6			2.4					1.5

*REE data from Regional Volcanic units (Kntstl Pers. Com.)*

Appendix B1-4, Geochemical data for regional volcanic units

# Mineral Chemistry - Primary igneous mineral compositions

## Sphene

		F	Na2O	Al2O3	SiO2	CaO	TiO2	FeO	H2O	Sum Ox%
34/300	Quan Porph <sup>1</sup>	0.21	0.03	0.56	29.63	28.43	37.31	1.25	1.01	98.34
41.3	Tunja Monzonite	0.06	0.02	0.44	29.7	28.9	37.55	1.41	1.09	99.15
41.3	Tunja Monzonite	0.09	0	0.37	29.94	28.68	38.3	1.06	1.08	99.49

## Amphibole

sample	rock type	SiO2	TiO2	Al2O3	Cr2O3	Fe2O3	FeO	MnO	MgO	CaO	Na2O	K2O	ZrO2	NiO	F	Cl	H2O(c)	Sum Ox%	Sum Cat#	XMg
14.2	MP andesite anph?	42.69	2.38	11.17	0.01	4.1	7.7	0.34	14.39	12.21	2.25	0.84	0.12	0.03	0.19	0.03	1.96	100.29	17.703	0.769
ap3	andesite dyke	38.8	1.33	15.64	0	5.01	6.98	0.12	13.1	12.6	1.83	1.74	0	0	0.1	0.02	1.96	99.2	17.864	0.77
ap3	andesite dyke	39.32	1.64	15.43	0	4.82	7.45	0.12	12.93	12.35	2.06	1.55	0	0.01	0.14	0.03	1.96	99.74	17.837	0.756
ap3	andesite dyke (core)	39.72	1.21	15.17	0.04	4.73	6.27	0.1	14.04	12.7	1.86	1.94	0.04	0.08	0.09	0.02	1.99	99.96	17.894	0.8
ap3	andesite dyke (middle)	38.62	1.37	16.13	0	6.02	6.23	0.09	13.24	12.57	1.91	1.74	0.01	0	0.13	0.01	1.97	99.98	17.859	0.791
ap3	andesite dyke (rim)	39.72	1.71	14.39	0	6.17	5.73	0.15	13.97	12.26	2.15	1.49	0.02	0.03	0.18	0.02	1.95	99.87	17.824	0.813
34/300	Quan Porph (amph/cpx?)	51.96	0.36	1.53	0.01	0	7.03	0.49	13.88	23.25	0.68	0	0.01	0	0.03	0	2.07	101.3	17.444	0.779
41.3	Tunja Monz (amph?)	51.27	1.02	3.89	0.02	4.65	5.25	0.67	17.45	11.62	1.38	0.31	0.03	0	0.2	0.1	1.98	99.73	17.216	0.856
41.3	Tunja Monz (amph?)	51.29	0.98	3.83	0	4.75	4.84	0.78	17.5	11.41	1.5	0.32	0.05	0.05	0.23	0.08	1.97	99.46	17.221	0.866
41.3	Tunja Monz (cpx?)	54.74	0.07	0.33	0	16.41	6.8	0.11	10.54	0.85	6.46	0.21	0	0	0.19	0.01	1.96	98.59	17.003	0.734
41.3	Tunja Monzonite	53.5	0.51	2.44	0.02	5.47	3.28	0.78	18.85	11.67	1.09	0.2	0	0.02	0.22	0.05	2.01	100.01	17.093	0.911
41.3	Tunja Monzonite	51.55	0.88	3.69	0	3	6.5	0.77	17.33	11.79	1.49	0.33	0.02	0	0.2	0.08	1.98	99.31	17.283	0.826

## Apatite

sample	rock type	SiO2	Fe2O3	MnO	MgO	CaO	Na2O	P2O5	SO3	La2O3	Ce2O3	Y2O3	SrO	BaO	K2O	F	Cl	H2O	O=F	O=Cl	Sum Ox%
14.2	Mamparung F and	0.28	0.34	0.15	0.13	55.3	0.16	41.22	0.55	0.04	0.11	0.06	0.14	0.12	0.02	1.29	0.86	0.96	0.54	0.19	101
dd1	Diorite	0.23	0.27	0.11	0.11	55.43	0.07	41.89	0.12	0	0.14	0	0.11	0.02	0	1.92	0.96	0.64	0.81	0.22	101
dd1	Diorite	0.17	0.26	0.09	0.13	55.56	0.06	41.08	0.07	0.08	0.16	0	0.02	0.16	0.02	1.81	1.07	0.64	0.76	0.24	100.38
dd1	Diorite	0.16	0.17	0.1	0.13	54.92	0.09	41.08	0.04	0.02	0.19	0	0.13	0.14	0.06	1.8	1.03	0.65	0.76	0.23	99.73
dd1	Diorite	0.18	0.19	0.05	0.1	55.37	0.06	41.43	0.03	0.09	0.28	0.02	0.06	0.16	0.04	1.82	1.06	0.65	0.77	0.24	100.58
dd1	Diorite	0.16	0.29	0.09	0.12	54.47	0.06	40.75	0.06	0.12	0.2	0	0.12	0.3	0.01	1.65	1.15	0.68	0.7	0.26	99.27
dd1	Diorite	0.19	0.5	0.05	0.1	54.63	0.05	40.92	1.07	0.01	0.09	0.05	0.18	0.21	0.01	1.85	0.97	0.67	0.78	0.22	100.55
nd1	Monzodiorite	0.23	0.26	0.17	0.08	54.01	0.15	41.05	0.38	0.11	0.23	0.12	0.06	0.18	0	1.12	2.88	0.5	0.47	0.65	100.42
dd1	Monzonite	0.31	0	0.12	0	54.69	0.16	40.94	0.4	0.04	0.05	0.04	0.02	0.37	0	1.8	1.27	0.59	0.76	0.29	99.76
dd1	Monzonite	0.31	0.11	0.21	0	54.63	0.19	40.23	0.49	0.08	0.04	0.08	0.02	0.3	0	1.76	1.31	0.59	0.74	0.3	99.3
dd1	Monzonite	0.24	0.08	0.21	0.01	54.96	0.19	40.65	0.47	0	0.01	0.09	0.04	0.18	0	1.98	1.09	0.55	0.83	0.25	99.68
dd1	Monzonite	0.27	0.05	0.14	0	54.6	0.2	40.34	0.49	0.01	0.06	0.08	0.07	0.24	0	1.97	1.05	0.55	0.83	0.24	99.05
dd1	Monzonite	0.52	0.05	0.18	0	54.23	0.29	39.82	0.87	0.02	0.05	0.16	0.04	0.44	0	1.95	1.3	0.5	0.82	0.29	99.32
53/511	Monzonite	0.24	0.14	0.25	0.01	55.02	0.18	40.86	0.38	0.12	0.24	0.05	0.06	0.34	0.01	1.54	1.39	0.69	0.65	0.31	100.56
53/511	Monzonite	0.33	0.14	0.31	0.05	54.21	0.31	40.19	0.84	0.08	0.22	0.19	0.06	0.33	0	1.34	1.53	0.74	0.56	0.35	99.95
53/511	Monzonite	0.49	0.01	0.22	0.02	53.59	0.28	39.07	0.81	0.2	0.36	0	0.12	0.49	0.01	1.26	1.64	0.71	0.53	0.37	98.38
53/511	Monzonite	0.25	0.07	0.31	0.03	54.66	0.25	40.54	0.65	0.09	0.22	0.08	0	0.27	0	1.39	1.52	0.72	0.58	0.34	100.13
41.3	Tunja Monzonite	0.19	0.05	0.1	0.03	54.56	0.11	41.49	0.22	0.05	0.27	0.03	0.11	0.27	0	1.66	0.73	0.8	0.7	0.16	99.8

## Mica (biotite)

sample	rock type	SiO2	TiO2	Al2O3	FeO	MnO	MgO	CaO	Na2O	K2O	BaO	F	Cl	H2O(c)	O=F	O=Cl	Sum Ox%
14.20	Mamparung F and	36.43	4.32	14.36	15.19	0.37	14.75	0.03	0.5	8.88	0.1	0.39	0.06	3.78	0.17	0.01	99.03
53/511	Surong Monzonite	37.36	4.44	13.64	12.72	0.36	16.39	0	0.17	9.61	0.15	0.43	0.15	3.77	0.18	0.03	99.06
53/511	Surong Monzonite	37.28	4.68	13.9	12.89	0.4	15.84	0.02	0.22	9.68	0.08	0.43	0.16	3.77	0.18	0.04	99.3
nd1	Monzodiorite	37.59	5.37	13.47	12.05	0.18	16.13	0.01	0.22	9.69	0	0.54	0.29	3.7	0.23	0.06	98.98
m9	Surong Monzonite	35.91	5.29	14.71	15.46	0.39	13.78	0.04	0.26	9.71	0.32	0.25	0.15	3.83	0.11	0.03	100.24
m9	Surong Monzonite	36.06	5.14	14.25	14.77	0.43	14.28	0.02	0.23	9.67	0.32	0.29	0.14	3.8	0.12	0.03	99.39

(Rb and Cs also analysed and were below detection)

## Spinel (magnetite)

sample	rock type	SiO2	TiO2	Al2O3	Cr2O3	Fe2O3(c)	FeO	Y2O3	MnO	MgO	Sum Ox%	XCr	XF2+	YFe3+
39/129	Gabbro	0.04	0.55	0.77	0.01	65.4	30.35	0.48	0.23	0.31	98.26	0.519	98.194	98.187
39/129	Gabbro	0.03	0.24	0.54	0	65.71	30.15	0.41	0.1	0.16	97.43	0.015	99.085	98.738
dd1	diorite	0.09	6.1	4.05	0.02	52.15	32.76	0.06	0.61	2.29	98.23	0.314	88.942	89.114
nd1	Monzodiorite	0.03	4.33	0.82	0.02	58.72	33.13	0	0.75	0.37	98.51	1.331	98.048	97.841
nd1	Monzodiorite	0.03	0.23	0.46	0	66.83	30.88	0.52	0.03	0.12	99.11	0.567	99.324	98.936
m9	Surong Monzonite	0	0.25	0.42	0.06	66.33	30.25	0.52	0.25	0.05	98.4	8.287	99.678	98.938
53/511	Surong Monzonite	0.03	0.34	0.43	0.01	66.97	30.74	0.37	0.34	0.17	99.6	1.35	99.014	98.99
41.3	Tunja Monzonite	0.03	0.17	0.08	0	67.48	30.78	0.55	0.11	0.02	99.39	0.099	99.893	99.808
34/300	Quan Porphyry	0.03	0.2	0.08	0.03	67.25	30.91	0.68	0.15	0	99.32	18.811	99.998	99.77
AP3	Andesite Dyke	3.63	4.12	0.4	0.05	47.5	37.6	0	0.1	0	93.47	7.156	99.998	98.597



## Feldspar

sample	rock type	Label	SiO2	TiO2	Al2O3	Fe2O3	MnO	MgO	CaO	SrO	BaO	Na2O	K2O	Rb2O	P2O5	Sum Ox%	Sum Cat#	Ab	An	Or	Celsin	Sr-Feld
14.20	Mamparang Fand.	Andesite 14.20_1_plag rim	54.79	0.02	28.7	0.55	0.02	0.03	10.76	0.17	0.07	5.04	0.67	-	0.04	100.87	5.006	43.877	51.731	3.83	0.122	0.439
14.20	Mamparang Fand.	Andesite 14.20_1_plag core	53.54	0.06	29.2	0.49	0.03	0.02	11.48	0.27	0.15	4.67	0.71	-	0.04	100.66	5.014	40.257	54.738	4.045	0.253	0.707
14.20	Mamparang Fand.	Andesite 14.20_5_plag core	54.52	0.05	28.88	0.44	0.02	0.02	10.89	0.13	0.02	5.25	0.49	-	0	100.72	5.017	45.126	51.716	2.787	0.03	0.341
44.3	Mamparang Fand.	MF andesite 44.3_3_lrg plag	54.74	0	23.47	0	0.03	0	12.9	0	0	0.21	0	-	0.05	91.41	4.685	2.875	97.124	0.001	0	0
44.3	Mamparang Fand.	MF andesite 44.3_3_lrg plag2	55.41	0	23.47	0.02	0.01	0	11.09	0	0	1.92	0.03	-	0	91.95	4.755	23.795	75.946	0.259	0	0
39/129	Gabbro	gab39_2_plag core	45.15	0.04	35.15	0.51	0	0.02	18.35	0	0	1.12	0.04	-	0	100.37	5.01	9.889	89.88	0.231	0	0
39/129	Gabbro	gab39_2_plag rim	44.97	0.03	35.37	0.7	0.02	0.02	18.32	0	0	1.13	0.05	-	0.04	100.66	5.014	10.045	89.645	0.309	0.002	0
39/129	Gabbro	gab39_4_plag	45.06	0.02	35.17	0.48	0.03	0.02	18.28	0	0.03	1.22	0.06	-	0.04	100.4	5.017	10.72	88.911	0.322	0.047	0
39/129	Gabbro	gab39_5_plag	45.54	0.02	34.84	0.54	0.01	0.03	18.17	0	0	1.25	0.04	-	0.05	100.48	5.009	11.072	88.723	0.204	0	0
39/129	Gabbro	gab39_7_plag	45.72	0.02	34.8	0.51	0.04	0.03	18.21	0	0	1.25	0.04	-	0.04	100.66	5.009	11.041	88.718	0.241	0	0
39/129	Gabbro	gab39_8_plag	44.92	0	35.07	0.55	0.03	0.02	18.42	0	0	1.09	0.06	-	0.03	100.2	5.014	9.661	90.012	0.327	0	0
ddl	diorite	ddl_1_plag	54.02	0.02	28.82	0.28	0.03	0.01	11.01	0.24	0.08	5.22	0.41	-	0	100.14	5.02	44.762	52.184	2.292	0.141	0.622
ddl	diorite	ddl_1_lsp	63.49	0.01	19.9	0.25	0	0.01	0.74	0.12	0.39	2.8	12.38	-	0.04	100.14	5.026	24.386	3.564	71.035	0.695	0.319
ddl	diorite	ddl_4_plag	44.95	0.05	35.23	0.31	0	0.01	18.36	0.25	0.01	1.35	0.08	-	0	100.58	5.031	11.644	87.268	0.442	0.012	0.633
ddl	diorite	ddl_7_plag	50.35	0.02	31.18	0.4	0	0.02	13.94	0.25	0.1	3.49	0.28	-	0.05	100.08	5.012	30.401	67.156	1.6	0.184	0.66
ddl	diorite	ddl_8_plag core	47.6	0.04	33.73	0.24	0.03	0.03	16.12	0.11	0	2.31	0.15	-	0.06	100.43	5.014	20.392	78.463	0.852	0	0.293
ddl	diorite	ddl_8_plag rim	54.57	0.04	28.8	0.21	0	0	10.49	0.14	0.08	5.55	0.49	-	0.01	100.38	5.025	47.327	49.425	2.762	0.135	0.35
mdl	Monzodiorite	mdl1_1_feld	64.44	0.03	19.76	0.25	0	0	0.79	0	0.21	3.88	10.78	-	0.05	100.19	5.014	33.86	3.821	61.944	0.375	0
mdl	Monzodiorite	mdl1_1_plag	54.39	0.03	29.2	0.33	0.02	0	11.01	0.26	0.1	5.14	0.26	-	0	100.73	5.006	44.719	52.943	1.496	0.173	0.669
mdl	Monzodiorite	mdl1_3_plag	54.02	0.02	29.32	0.41	0.02	0.02	11.26	0.29	0.06	5.04	0.25	-	0.01	100.71	5.01	43.734	53.976	1.44	0.1	0.75
mdl	Monzodiorite	mdl1_3_feld	64.28	0.01	19.77	0.22	0.02	0.01	0.76	0	0.18	3.44	11.39	-	0.01	100.11	5.014	30.209	3.695	65.776	0.319	0
mdl	Monzodiorite	mdl1_6_plag	55.98	0.04	27.61	0.35	0	0.01	9.39	0.19	0.05	5.89	0.51	-	0.03	100.06	5.007	51.329	45.193	2.894	0.095	0.488
M9	Surong Monzonite	m9_2_plag core	53.38	0.08	29.73	0.39	0.01	0.01	11.94	0	0.06	4.56	0.23	-	0.02	100.41	4.997	40.25	58.302	1.333	0.116	0
M9	Surong Monzonite	m9_2_plag rim	57.13	0.02	27.08	0.33	0	0.01	8.69	0	0.06	6.46	0.18	-	0.05	100.01	4.999	56.72	42.15	1.017	0.113	0
M9	Surong Monzonite	m9_2_orthocl ne plag rim	64.56	0.03	18.94	0.07	0	0	0.03	0	0.17	1.7	14.91	-	0	100.43	5.029	14.667	0.162	84.87	0.301	0
M9	Surong Monzonite	m9_3_plag core	55.14	0.01	28.64	0.23	0	0	10.45	0	0.03	5.53	0.22	-	0.01	100.26	5.004	48.273	50.422	1.246	0.059	0
M9	Surong Monzonite	m9_3_plag rim	56.65	0.06	27.54	0.31	0	0	9.26	0	0.08	6.21	0.22	-	0	100.33	5.003	54.046	44.544	1.263	0.147	0
M9	Surong Monzonite	m9_3_matrix ?	64.11	0.03	22.45	0.34	0.01	0	3.18	0	0.01	9.52	0.24	-	0.06	99.95	4.991	83.222	15.352	1.402	0.024	0
M9	Surong Monzonite	m9_6_matrix orthocl	65.72	0	21.62	0.15	0	0	2.14	0	0	10.13	0.24	-	0	100.01	4.989	88.319	10.308	1.373	0	0
53/511	Surong Monzonite	Monz 53/511_1_plag_trav_1	50.4	0.03	31.85	0.38	0.02	0.01	13.76	0.21	0	3.78	0.13	-	0.03	100.59	5.022	32.762	65.964	0.723	0	0.551
53/511	Surong Monzonite	Monz 53/511_1_plag_trav_2	49.43	0.01	32.39	0.4	0	0.02	14.63	0.25	0.01	3.14	0.07	-	0.04	100.4	5.01	27.66	71.233	0.418	0.02	0.669
53/511	Surong Monzonite	Monz 53/511_1_plag_trav_3	52.33	0.02	30.38	0.36	0	0.01	12.42	0.23	0.07	4.34	0.2	-	0.04	100.4	5.007	38.004	60.114	1.149	0.119	0.614
53/511	Surong Monzonite	Monz 53/511_1_plag_trav_4	53.91	0.01	29.53	0.39	0.06	0.01	11.51	0.3	0.05	5.02	0.21	-	0.05	101.03	5.013	43.203	54.767	1.183	0.079	0.768
53/511	Surong Monzonite	Monz 53/511_1_plag_trav_5	52.36	0.06	30.43	0.32	0.06	0	12.46	0.27	0	4.4	0.21	-	0.08	100.67	5.011	38.25	59.847	1.195	0.003	0.705
53/511	Surong Monzonite	Monz 53/511_1_plag_trav_6	54.49	0	29.13	0.24	0.02	0	10.97	0.22	0.05	5.37	0.21	-	0.02	100.71	5.015	46.118	52.055	1.178	0.084	0.565
53/511	Surong Monzonite	Monz 53/511_1_plag_trav_7	54.77	0.02	28.89	0.29	0	0.01	10.57	0.22	0.03	5.45	0.28	-	0	100.51	5.011	47.197	50.606	1.589	0.05	0.558
53/511	Surong Monzonite	Monz 53/511_1_plag_trav_8	56.35	0.02	27.69	0.38	0.01	0.02	9.31	0.21	0.08	6.05	0.38	-	0.05	100.54	5.007	52.541	44.649	2.141	0.135	0.534
53/511	Surong Monzonite	Monz 53/511_1_plag_trav_9	56.12	0	27.11	0.43	0.05	0.02	9.25	0.16	0.14	6.13	0.4	-	0.04	99.85	5.013	52.947	44.113	2.278	0.239	0.424
53/511	Surong Monzonite	Monz 53/511_1_plag_trav_10	56.5	0.01	27.55	0.48	0	0	9.12	0.23	0.04	6.16	0.43	-	0.04	100.56	5.01	53.289	43.596	2.448	0.065	0.603
53/511	Surong Monzonite	Monz 53/511_1_plag_trav_11	56.83	0.01	26.96	0.48	0	0.01	8.75	0.23	0.06	6.26	0.41	-	0.02	100.04	5.004	54.673	42.238	2.382	0.111	0.596
53/511	Surong Monzonite	Monz 53/511_1_plag_trav_12	56.58	0.03	27.02	0.39	0	0.03	8.93	0.21	0.08	6.28	0.42	-	0.05	99.99	5.011	54.269	42.647	2.416	0.137	0.531
53/511	Surong Monzonite	Monz 53/511_1_plag_trav_13	55.47	0.01	28.14	0.36	0	0	9.99	0.23	0.19	5.73	0.29	-	0.05	100.46	5.008	49.627	47.805	1.632	0.332	0.604
53/511	Surong Monzonite	Monz 53/511_1_plag_trav_14	59.62	0	25.07	0.27	0	0	6.5	0.12	0.01	7.61	0.49	-	0.13	99.83	5.005	65.799	31.077	2.79	0.017	0.317
53/511	Surong Monzonite	Monz 53/511_1_plag_trav_15	58.15	0.02	26.63	0.21	0	0	8.05	0.07	0.03	6.97	0.21	-	0	100.35	5.007	60.172	38.394	1.212	0.045	0.177
53/511	Surong Monzonite	Monz 53/511_3_feld gm	64.41	0	19.15	0.09	0.01	0	0.09	0	0.28	2.28	14.08	-	0	100.4	5.036	19.587	0.413	79.514	0.485	0
53/511	Surong Monzonite	Monz 53/511_4_feld gm	64.73	0.03	19.44	0.19	0.01	0	0.23	0	0.33	3.68	11.77	-	0	100.4	5.028	31.658	1.086	66.68	0.576	0
53/511	Surong Monzonite	Monz 53/511_5_plag core	46.56	0	34.03	0.48	0.03	0	16.86	0.25	0.04	1.87	0.07	-	0.03	100.24	5.013	16.545	82.296	0.409	0.076	0.673
53/511	Surong Monzonite	Monz 53/511_5_plag int	56.42	0.03	27.41	0.46	0.04	0.01	9.1	0.16	0.03	6.11	0.43	-	0	100.2	5.007	53.24	43.801	2.471	0.06	0.429
41.3	Tunja Monzonite	Tunja 41.3_3_feld	67.47	0.01	20.51	0.19	0.01	0.01	0.7	0.01	0	11.21	0.24	-	0.02	100.37	5.004	95.331	3.281	1.365	0	0.023
41.3	Tunja Monzonite	Tunja 41.3_3_perthite	65.89	0.05	21.25	0.32	0	0	1.78	0.08	0	10.45	0.43	-	0.02	100.28	5.006	88.994	8.379	2.42	0	0.207
41.3	Tunja Monzonite	Tunja 41.3_3_perthite	64.1	0.02	18.92	0.13	0	0.01	0.01	0	0.31	1.35	15.44	-	0	100.28	5.035	11.651	0.034	87.777	0.537	0
41.3	Tunja Monzonite	Tunja 41.3_6_feld	59.96	0.05	25.56	0.28	0.01	0.01	6.42	0	0.13	7.79	0.31	-	0.03	100.56	5.007	67.353	30.653	1.77	0.224	0
34/300	Quan Porphyry	Quan 34/300_1_feld1	63.94	0	18.87	0.27	0.02	0.01	0.04	0	0.25	1.09	15.76	-	0.02	100.29	5.034	9.444	0.189	89.923	0.444	0
34/300	Quan Porphyry	Quan 34/300_1_feld2	64.44	0	18.8	0.28	0.02	0.01	0.01	0	0.22	1.54	15.05	-	0	100.38	5.027	13.384	0.057	86.17	0.388	0
34/300	Quan Porphyry	Quan 34/300_2	66.65	0	20.81	0.18	0	0.02	1.16	0.01	0	10.7	0.47	-	0.02	100.04	5.001	91.765	5.522	2.679	0	0.035
34/300	Quan Porphyry	Quan 34/300_5_feld1	67.11	0.01	20.59	0.15																

Pyroxene

sample	rock type	SiO2	TiO2	Al2O3	Cr2O3	Fe2O3	FeO	MnO	MgO	CaO	Na2O	K2O	Sum Ox%	Wt(Ca)	En(Mg)	Fs(Fe2+,3+,Mn)	X <sub>Mg</sub>	Mg/Mg+Fe
14.20	Mamparang F And. (core)	50.58	0.49	2.78	0	4.17	3.68	0.45	13.89	23.31	0.46	0.01	99.81	47.79	39.62	12.59	0.87	65.16
14.20	Mamparang F And. (rim)	51.4	0.37	2.17	0	3.37	4.47	0.57	14.04	23.08	0.45	0.02	99.95	47.18	39.94	12.89	0.85	65.18
14.20	Mamparang F And.	52.21	0.27	1.25	0.04	3.66	4.33	0.84	14.44	23.1	0.45	0.02	100.61	46.38	40.34	13.28	0.86	65.43
14.20	Mamparang F And.	51.73	0.29	1.72	0	4.36	4.25	0.81	14.23	23.04	0.46	-	100.9	46.25	39.71	14.05	0.86	64.56
14.20	Mamparang F And.	51.46	0.27	1.85	0	4.14	3.93	0.73	15.23	21.79	0.44	-	99.85	43.99	42.77	13.24	0.87	66.31
14.20	Mamparang F And.	51.21	0.33	2.17	0	4.67	3.4	0.56	14.42	23.33	0.43	-	100.52	46.86	40.31	12.83	0.88	67.26
14.20	Mamparang F And.	50.93	0.28	1.96	0	4.61	3.46	0.66	14.5	22.73	0.44	-	99.57	46.05	40.83	13.12	0.88	65.15
14.20	Mamparang F And.	50.5	0.4	2.54	0.01	4.28	3.75	0.47	14.28	22.62	0.45	-	99.32	46.37	40.74	12.90	0.87	64.28
14.20	Mamparang F And.	51.34	0.28	1.6	0	4.32	4.26	0.72	13.8	23.46	0.43	-	100.22	47.30	38.71	14.00	0.85	66.19
14.20	Mamparang F And.	51.76	0.26	1.62	0	4.24	4.37	0.71	14.03	23.35	0.46	-	100.8	46.86	39.21	13.93	0.85	66.45
14.20	Mamparang F And.	50.42	0.39	2.43	0	4.35	4.3	0.71	13.87	22.38	0.48	-	99.34	45.96	39.67	14.37	0.85	63.23
14.20	Mamparang F And.	51.1	0.32	1.99	0.02	4.37	3.85	0.62	14.41	22.68	0.47	-	99.83	45.99	40.65	13.36	0.87	65.04
14.20	Mamparang F And.	50.79	0.26	1.63	0	4.63	3.74	0.67	13.96	23.23	0.41	-	99.34	47.05	39.35	13.60	0.87	66.82
44.3	Mamparang F And.	49.46	0.79	4.51	0.03	4.61	3.09	0.24	14.01	23.14	0.41	0.01	100.29	47.71	40.22	12.07	0.89	65.93
44.3	Mamparang F And.	50.23	0.49	4.45	0.1	4.43	1.46	0.1	15.24	24.15	0.18	0	100.85	48.59	42.67	8.74	0.95	73.67
44.3	Mamparang F And.	48.86	0.61	5.39	0.07	4.94	2.53	0.18	13.71	23.79	0.29	0	100.36	49.09	39.40	11.52	0.91	66.28
44.3	Mamparang F And.	48.46	0.57	4.97	0	5.53	1.48	0.18	13.91	24.25	0.2	-	99.56	49.72	39.65	10.63	0.94	67.71
44.3	Mamparang F And.	51.72	0.31	1.26	0.01	4.15	3.29	0.76	14.93	22.83	0.47	-	99.75	45.96	41.81	12.23	0.89	66.45
44.3	Mamparang F And.	48.45	0.58	3.78	0	5.8	1.75	0.24	14.25	23.16	0.3	-	98.31	47.63	40.76	11.60	0.94	66.42
44.3	Mamparang F And.	46.1	0.68	6.24	0.02	7.97	0.25	0.13	13.31	23.9	0.22	-	98.82	49.46	38.34	12.20	0.99	67.07
44.3	Mamparang F And.	47.56	0.82	4.86	0	6.75	2	0.37	13.51	22.71	0.44	-	99.03	47.19	39.09	13.72	0.92	62.40
44.3	Mamparang F And.	47.94	0.66	4.43	0.01	5.95	2.28	0.22	13.84	22.76	0.34	-	98.43	47.28	39.99	12.73	0.92	65.96
44.3	Mamparang F And.	46.67	0.64	5.72	0.01	7.19	1.15	0.15	13.43	23.36	0.26	-	98.58	48.56	38.85	12.59	0.95	66.81
44.3	Mamparang F And.	45.97	0.75	7.16	0	7.5	0.86	0.15	12.84	24.06	0.2	-	99.49	50.16	37.23	12.62	0.96	63.39
44.3	Mamparang F And.	48.4	0.52	4.67	0.04	5.54	1.34	0.14	14.18	23.93	0.2	-	98.97	49.13	40.52	10.35	0.95	69.54
44.3	Mamparang F And.	48.73	0.64	3.94	0	5.72	2.06	0.28	14.25	23.02	0.35	-	99	47.29	40.70	12.01	0.93	62.74
14.3	U. Mamp. F. trach (core)	50.09	0.46	3.65	0	4.61	3.4	0.2	14.33	23.33	0.26	0.02	100.36	47.34	40.43	12.23	0.88	65.49
14.3	U. Mamp. F. trach (rim)	46.8	0.78	7.25	0	6.6	2.99	0.17	12.27	23.43	0.35	0	100.64	49.21	35.86	14.93	0.88	57.88
14.3	U. Mamp. F. trach	48.07	0.76	5.54	0	5.48	3.12	0.25	13.26	23.17	0.3	0.02	99.99	48.15	38.37	13.48	0.88	62.22
14.3	U. Mamp. F. trach (core)	47.22	0.85	6.65	0	6.67	2.6	0.08	12.89	23.61	0.27	0.02	100.88	48.85	37.07	14.08	0.90	59.96
14.3	U. Mamp. F. trach (rim)	47.83	0.7	6.45	0.01	5.88	3.21	0.26	12.97	23.19	0.32	0.01	100.84	48.24	37.53	14.23	0.88	60.42
14.3	U. Mamp. F. trach	50.13	0.4	3.4	0	4.21	3.62	0.34	14.35	23.08	0.25	0.01	99.78	47.01	40.67	12.31	0.88	65.97
14.3	U. Mamp. F. trach	45.64	0.93	6.66	0	7.82	2.44	0.28	12.53	22.75	0.26	-	99.31	47.62	36.45	15.93	0.90	57.31
14.3	U. Mamp. F. trach	47.15	0.79	6.01	0.04	5.66	3.5	0.2	12.68	22.9	0.31	-	99.23	48.33	37.24	14.44	0.87	58.53
14.3	U. Mamp. F. trach	45.96	0.82	6.69	0.03	6.66	3.14	0.24	12.09	22.79	0.34	-	98.77	48.53	35.85	15.62	0.87	61.39
14.3	U. Mamp. F. trach	48.19	0.5	4.81	0.01	5.86	3.14	0.25	13.43	22.88	0.31	-	99.38	47.32	38.67	14.01	0.88	65.35
14.3	U. Mamp. F. trach	48.68	0.53	4.28	0.02	5.25	3.37	0.3	13.56	22.93	0.32	-	99.24	47.43	39.04	13.53	0.88	63.95
14.3	U. Mamp. F. trach	48.34	0.53	3.87	0	5.94	2.76	0.34	13.82	23.02	0.23	-	98.85	47.11	39.36	13.53	0.90	64.26
14.3	U. Mamp. F. trach	48.44	0.5	3.6	0.01	6.04	2.34	0.31	14.06	23.11	0.23	-	98.63	47.17	39.91	12.92	0.92	62.51
14.3	U. Mamp. F. trach	45.53	0.91	6.42	0.03	7.07	2.49	0.27	12.4	22.75	0.27	-	98.13	48.24	36.62	15.15	0.90	59.60
14.3	U. Mamp. F. trach	47.14	0.67	4.57	0.05	7.08	2.25	0.33	13.15	23.07	0.3	-	98.61	47.71	37.83	14.46	0.91	59.34
14.3	U. Mamp. F. trach	46.71	0.69	5.56	0.01	6.79	2.6	0.3	12.94	22.81	0.28	-	98.69	47.66	37.62	14.72	0.90	59.04
G1	Didipio Gabbro	50.2	0.34	2.13	0.01	5.07	1.34	0.33	15.02	23.47	0.39	-	98.3	47.70	42.45	9.84	0.95	73.61
G1	Didipio Gabbro	47.91	0.64	4.2	0.02	5.78	1.74	0.26	13.58	23.13	0.44	-	97.69	48.58	39.66	11.76	0.93	68.44
G1	Didipio Gabbro	46.47	0.61	5.76	0.24	7.17	0.12	0.16	13.44	23.71	0.33	-	98.01	49.74	39.25	11.01	1.00	67.49
G1	Didipio Gabbro	47.65	0.63	4.72	0	6.77	0.67	0.25	13.63	23.51	0.48	-	98.3	49.05	39.56	11.40	0.97	66.53
G1	Didipio Gabbro	47.8	0.47	5.05	0.05	6.38	0.14	0.13	14.17	24.29	0.2	-	98.69	49.87	40.47	9.66	0.99	71.23
G1	Didipio Gabbro	48.66	0.44	3.52	0	6.03	1.05	0.4	14.14	23.22	0.47	-	97.94	48.11	40.75	11.15	0.96	68.46
G1	Didipio Gabbro	48.35	0.5	3.64	0.01	6.41	0.61	0.23	14.2	23.78	0.35	-	98.08	48.86	40.59	10.55	0.98	73.55
G1	Didipio Gabbro	49.86	0.34	3.37	0.03	5.49	1.76	0.3	14.63	23.14	0.46	-	99.38	47.26	41.53	11.21	0.94	68.59
G1	Didipio Gabbro	47.73	0.6	5.89	0.36	5.92	0.91	0.13	13.75	24.03	0.27	-	99.6	49.92	39.76	10.32	0.96	68.09
G1	Didipio Gabbro	50.1	0.3	3.86	0.57	4.51	0.55	0.03	15.46	24.38	0.17	-	99.94	49.23	43.44	7.33	0.98	75.70
39/129	Didipio Gabbro	49.63	0.67	4.83	0.03	4.8	2.24	0.2	13.97	23.67	0.49	0.01	100.54	48.93	40.18	10.90	0.92	68.03
39/129	Didipio Gabbro	49.89	0.23	4.22	0	4.69	2.16	0.1	14.26	23.52	0.44	0.01	99.53	48.57	40.99	10.44	0.92	69.08
39/129	Didipio Gabbro	49.7	0.64	4.29	0	5.05	1.85	0.22	14.46	23.63	0.4	0.01	100.25	48.32	41.13	10.55	0.93	69.36
39/129	Didipio Gabbro	50.44	0.54	3.85	0.01	4.06	2.58	0.3	14.5	23.26	0.48	0.01	100.05	47.89	41.54	10.57	0.91	69.93
39/129	Didipio Gabbro	50.39	0.58	3.92	0.01	4.37	2.29	0.25	14.56	23.69	0.4	0.02	100.49	48.32	41.33	10.36	0.92	70.05
39/129	Didipio Gabbro	46.52	0.43	4.03	0	5.1	1.63	0.27	13.31	22.06	0.45	-	93.81	48.32	40.55	11.13	0.94	62.47
39/129	Didipio Gabbro	0.19	0	0.01	0	0.29	0	0.04	0	51.99	0.11	-	52.63	99.55	0.00	0.45	1.00	67.08
39/129	Didipio Gabbro	45.52	0.54	3.83	0.03	7.06	0	0.4	13.08	23.66	0.44	-	94.57	50.23	38.61	11.16	1.00	65.24
39/129	Didipio Gabbro	47.16	0.47	4.82	0.02	4.85	1.7	0.2	13.41	22.59	0.45	-	95.66	48.95	40.47	10.58	0.93	67.28
39/129	Didipio Gabbro	48.19	0.6	3.61	0.01	4.55	2.23	0.38	13.87	22.32	0.48	-	96.25	47.62	41.19	11.19	0.92	69.21
39/129	Didipio Gabbro	46.31	0.45	4.6	0.09	6.03	0	0.1	13.7	24.1	0.15	-	95.54	50.79	40.13	9.08	1.00	70.06
39/129	Didipio Gabbro	47.11	0.65	4.1	0	5.39	1.69	0.29	13.46	22.51	0.45	-	95.66	48.32	40.21	11.47	0.93	66.20
39/129	Didipio Gabbro	48.72	0.33	2.52	0.01	5.3	2.15	0.44	13.98	22.58	0.46	-	96.49	47.28	40.72	12.00	0.92	73.03
39/129	Didipio Gabbro	47.11	0.43	4.76	0.21	5.82	0.09	0.08	13.9	24.25	0.15	-	96.8	50.72	40.44	8.84	1.00	68.33
39/129	Didipio Gabbro	44.8	0.69	6.66	0.07	7.34	0	0.09	12.44	24.11	0.25	-	96.45	51.68	37.12	11.20	1.00	66.09

## Pyroxene

sample	rock type	SiO2	TiO2	Al2O3	Cr2O3	Fe2O3	FeO	MnO	MgO	CaO	Na2O	K2O	Sum Ox %	Wt(Ca)	En(Mg)	Fe(Fe+2+3+Mn)	X <sub>Mg</sub>	Mg/Mg+Fe
dd1	Diorite diorite	51.35	0.23	2.03	0	3.36	5.56	0.46	13.97	22.26	0.46	0.02	99.99	45.67	39.88	14.45	0.82	61.93
dd1	Diorite diorite	50.64	0.6	3.11	0	4.13	3.89	0.35	14.33	22.7	0.47	0.02	100.24	46.44	40.82	12.75	0.87	65.32
dd1	Diorite diorite	50.6	0.59	2.86	0	3.59	4.57	0.45	13.81	22.4	0.57	0.01	99.45	46.62	39.97	13.41	0.84	63.90
dd1	Diorite diorite	50.69	0.39	2.16	0	4.12	4.47	0.44	13.42	22.88	0.61	-	99.18	47.38	38.68	13.94	0.84	62.69
dd1	Diorite diorite	49.88	0.5	2.89	0.03	4.49	3.69	0.35	14.06	22.6	0.44	-	98.54	46.64	40.34	13.02	0.87	62.43
dd1	Diorite diorite	48.49	0.51	3.56	0.01	6.38	1.76	0.26	14.04	23.25	0.35	-	98.61	47.62	40.01	12.37	0.93	67.17
dd1	Diorite diorite	48.91	0.56	3.67	0	5.45	2.53	0.3	14.09	22.96	0.35	-	98.82	47.29	40.34	12.37	0.91	66.12
dd1	Diorite diorite	49.4	0.53	3.72	0	4.84	3.29	0.39	13.69	23.08	0.41	-	99.35	47.71	39.36	12.93	0.88	63.15
dd1	Diorite diorite	50.58	0.3	2.24	0.01	3.8	4.96	0.47	13.85	22.33	0.44	-	99	46.01	39.72	14.26	0.83	64.25
dd1	Diorite diorite	50.37	0.29	2.14	0	4.31	4.7	0.6	13.8	22.33	0.43	-	98.96	45.88	39.42	14.70	0.84	68.01
dd1	Diorite diorite	49.22	0.49	2.75	0	5.44	3	0.42	13.85	22.65	0.47	-	98.28	46.79	39.82	13.39	0.89	65.60
dd1	Diorite diorite	49.19	0.43	2.8	0.02	5.74	1.89	0.37	14.28	23.27	0.36	-	98.36	47.55	40.58	11.87	0.93	65.86
dd1	Diorite diorite	48.75	0.61	3.24	0.01	5.41	3.12	0.29	13.65	22.52	0.48	-	98.09	46.97	39.59	13.44	0.89	62.73
d2	Diorite diorite	46.74	0.75	6.51	0	6.22	2.17	0.11	13.07	23.38	0.22	-	99.17	49.01	38.07	12.92	0.92	62.09
d2	Diorite diorite	49.07	0.6	3.45	0.02	5.65	3.12	0.39	13.78	22.51	0.5	-	99.08	46.51	39.63	13.86	0.89	64.73
d2	Diorite diorite	48.92	0.65	3.62	0.02	6.92	1.99	0.42	13.92	22.68	0.6	-	99.75	46.49	39.72	13.79	0.93	66.48
d2	Diorite diorite	47.24	0.68	5.39	0.05	6.94	1.19	0.29	13.05	23.5	0.48	-	98.83	49.30	38.08	12.62	0.95	65.40
d2	Diorite diorite	48.07	0.59	3.31	0	8.73	1.76	0.31	14.12	22.22	0.5	-	99.61	44.79	39.58	15.63	0.94	66.81
d2	Diorite diorite	49.47	0.58	3.39	0	5.29	2.65	0.45	14.38	22.65	0.42	-	99.28	46.42	40.99	12.59	0.91	64.20
d2	Diorite diorite	48.3	0.4	4.19	0.01	5.85	2.32	0.22	13.27	23.32	0.44	-	98.33	48.71	38.57	12.72	0.91	63.06
d2	Diorite diorite	45.52	0.78	6.78	0	8.14	0.27	0.17	12.63	23.74	0.38	-	98.41	50.16	37.10	12.75	0.99	69.35
d2	Diorite diorite	46.38	0.74	5.22	0	7.29	1.69	0.34	12.56	22.87	0.52	-	97.6	48.60	37.15	14.25	0.93	67.16
d2	Diorite diorite	49.43	0.55	3.01	0	4.78	2.64	0.44	14.31	22.69	0.42	-	98.26	46.91	41.18	11.92	0.91	64.62
md1	Didipto Monzodio. (core)	52.24	0.27	1.19	0	2.64	4.72	0.59	15.09	22.25	0.43	0	99.4	45.19	42.60	12.21	0.85	68.03
md1	Didipto Monzodio. (rim)	52.8	0.24	1	0.05	2.46	5.14	0.88	15.4	21.64	0.45	0.02	100.09	43.71	43.25	13.04	0.84	67.66
md1	Didipto Monzodio.	51.37	0.3	2.02	0	3.73	3.91	0.58	14.54	22.73	0.47	0	99.65	46.27	41.22	12.51	0.87	66.68
md1	Didipto Monzodio.	51.49	0.31	2.12	0	3.18	4.59	0.53	14.23	22.86	0.45	0	99.75	46.75	40.49	12.76	0.85	65.65
md1	Didipto Monzodio.	50.82	0.34	2.96	0	3.39	3.67	0.36	14.14	22.96	0.52	0.01	99.16	47.66	40.86	11.47	0.87	67.78
md1	Didipto Monzodio.	47.35	0.44	2.98	0	8.38	0	0.49	13.61	24.04	0.47	-	97.76	48.81	38.44	12.75	1.00	67.42
md1	Didipto Monzodio.	49.72	0.29	1.92	0	4.75	2.72	0.56	14.35	22.44	0.45	-	97.2	46.48	41.32	12.20	0.90	68.22
md1	Didipto Monzodio.	49.56	0.35	2.1	0	4.9	2.65	0.46	14.17	22.73	0.45	-	97.38	47.03	40.80	12.16	0.91	65.46
md1	Didipto Monzodio.	49.47	0.35	2.33	0	5.71	2.02	0.68	14.64	22.47	0.41	-	98.08	45.87	41.59	12.54	0.93	68.18
md1	Didipto Monzodio.	49.17	0.43	2.68	0	5.62	2.69	0.61	13.76	22.75	0.47	-	98.18	47.00	39.53	13.47	0.90	68.86
md1	Didipto Monzodio.	49.74	0.26	1.91	0.01	5.16	2.1	0.54	14.49	22.99	0.38	-	97.59	47.06	41.28	11.66	0.93	68.50
md1	Didipto Monzodio.	47.5	0.64	4.27	0	5.8	2.6	0.57	13.13	22.13	0.53	-	97.16	47.17	38.92	13.91	0.90	65.42
md1	Didipto Monzodio.	48.36	0.44	3.97	0.01	6.14	1.71	0.22	13.97	23.41	0.3	-	98.53	48.09	39.95	11.96	0.94	66.46
md1	Didipto Monzodio.	48.8	0.49	3.99	0	3.63	4.09	0.55	13.74	21.61	0.42	-	97.33	46.03	40.76	13.20	0.86	65.33
md1	Didipto Monzodio.	49.14	0.41	2.62	0.07	4.85	2.93	0.52	13.76	22.7	0.44	-	97.45	47.32	39.93	12.75	0.89	65.52
MD3	Didipto Monzodio.	41.78	0.4	2.43	0.02	6.72	0	0.41	12.06	27.89	0.53	-	92.23	56.12	33.77	10.11	1.00	67.42
MD3	Didipto Monzodio.	48.32	0.44	3.57	0	6.29	1.46	0.35	13.99	22.96	0.43	-	97.81	47.58	40.35	12.07	0.95	68.22
MD3	Didipto Monzodio.	49.23	0.47	2.96	0	5.75	1.98	0.39	14.53	22.65	0.43	-	98.39	46.47	41.44	12.09	0.93	65.46
MD3	Didipto Monzodio.	49.4	0.45	2.87	0	5.88	1.77	0.54	14.17	23.09	0.5	-	98.68	47.38	40.41	12.21	0.94	68.18
MD3	Didipto Monzodio.	48.43	0.47	3	0	6.25	1.83	0.45	13.51	22.99	0.53	-	97.48	47.94	39.23	12.84	0.93	68.86
MD3	Didipto Monzodio.	48.05	0.59	3.42	0.01	7.01	1.15	0.57	13.53	22.71	0.66	-	97.69	47.51	39.36	13.12	0.95	68.50
MD3	Didipto Monzodio.	48.58	0.43	3	0	5.45	1.96	0.42	14.27	22.47	0.41	-	96.99	46.77	41.33	11.90	0.93	65.42
MD3	Didipto Monzodio.	48.7	0.43	2.96	0	6.97	1.11	0.45	13.41	23.39	0.69	-	98.11	48.59	38.73	12.67	0.96	66.46
MD3	Didipto Monzodio.	57.87	0.22	14.77	0	0	2.28	0.17	4.82	8.75	1.96	-	90.84	50.44	38.63	10.93	0.79	65.33
MD3	Didipto Monzodio.	50.24	0.28	1.98	0.01	5.5	2.83	0.61	13.93	22.64	0.66	-	98.67	46.61	39.93	13.46	0.90	65.52
M9	Surong Monzonite	49.56	0.78	4.11	0	4.91	2.8	0.3	13.71	23.52	0.49	0.01	100.2	48.52	39.38	12.10	0.90	65.50
M9	Surong Monzonite	51.73	0.45	2.25	0	3.47	3.93	0.4	14.56	23.32	0.45	0.01	100.57	47.21	41.00	11.79	0.87	67.36
M9	Surong Monzonite	51.55	0.45	2.16	0	3.15	4.05	0.61	14.43	22.96	0.48	0	99.86	46.94	41.08	11.98	0.86	67.68
md10	Surong Monzonite	47.72	0.57	3.04	0	5.73	1.9	0.44	13.4	22.59	0.52	-	95.92	47.96	39.57	12.47	0.93	64.41
md10	Surong Monzonite	49.82	0.12	0.42	0	3.1	5.55	1.27	13.57	20.87	0.42	-	95.15	44.16	39.94	15.90	0.81	65.42
md10	Surong Monzonite	46.73	0.88	4.15	0	5.45	2.68	0.58	12.66	22.02	0.57	-	95.72	47.88	38.28	13.85	0.89	61.18
md10	Surong Monzonite	47.43	0.42	3.6	0	4.35	2.88	0.25	13.75	21.73	0.35	-	94.76	46.88	41.27	11.85	0.90	67.19
md10	Surong Monzonite	48.16	0.54	2.85	0.01	4.99	2.38	0.43	13.64	22.53	0.45	-	95.99	47.75	40.18	12.07	0.91	65.29
md10	Surong Monzonite	46.24	0.76	4	0.01	6.17	1.47	0.42	12.95	22.51	0.47	-	95	48.59	38.87	12.54	0.94	66.78
md10	Surong Monzonite	48.04	0.56	2.75	0.02	5.49	1.81	0.52	13.87	22.3	0.5	-	95.86	47.17	40.80	12.03	0.93	65.79
md10	Surong Monzonite	44.74	1.13	5.79	0	6.67	1.97	0.42	11.7	22.62	0.5	-	95.53	49.76	35.78	14.46	0.91	62.72
md10	Surong Monzonite	47.44	0.55	3.68	0.01	5.43	2.25	0.39	13.09	23.02	0.38	-	96.24	48.85	38.66	12.49	0.91	63.44
md10	Surong Monzonite	48.17	0.45	3.37	0	5.54	2.75	0.39	13.13	22.89	0.46	-	97.16	48.18	38.45	13.36	0.90	64.40
53/511	Surong Monzonite	51.92	0.23	1.63	0	3.39	3.5	0.76	14.53	23.28	0.49	0.01	99.74	47.29	41.06	11.64	0.88	68.93
53/511	Surong Monz. (core)	52.15	0.26	1.82	0	3.21	3.78	0.59	15.06	22.98	0.41	0.01	100.27	46.30	42.22	11.47	0.88	69.29
53/511	Surong Monz. (rim)	51.6	0.29	1.98	0	4.12	3.33	0.71	14.55	23.03	0.53	0.01	100.15	46.68	41.05	12.27	0.89	67.39
53/511	Surong Monz. (core)	52.05	0.26	1.91	0.04	2.43	4.22	0.63	14.92	22.91	0.36	0	99.73	46.57	42.22	11.21	0.86	69.95
53/511	Surong Monz. (rim)	51.98	0.27	1.84	0	3.48	3.5	0.74	14.45	23.28	0.55	0	100.1	47.38	40.91	11.70	0.88	68.54
53/511	Surong Monz.	52.22	0.25	1.87	0.01	3.98	3.31	0.78	15.3	22.95	0.41	-	101.07	45.69	42.39	11.93	0.89	69.02
53/511	Surong Monz.	51.75	0.23	1.7	0	4.42	3.17	0.82	14.74	22.92	0.53	-	100.28	46.16	41.28	12.56	0.89	68.16
53/511	Surong Monz.	51.41	0.3	1.99	0	4.72	2.73	0.64	15.17	22.87	0.44	-	10					

# Pyroxene

sample	rock type	SiO2	TiO2	Al2O3	Cr2O3	Fe2O3	FeO	MnO	MgO	CaO	Na2O	K2O	Sum Ox %	Wt(Ca)	En(Mg)	Fs(Fe2+3+Mn)	X <sub>Mg</sub>	Mg/Mg+Fe
34/300	Quan Porphyry	52.22	0.4	1.18	0.03	3.28	4.09	0.64	14.05	22.56	0.89	0	99.35	46.91	40.61	12.48	0.86	66.60
34/300	Quan Porphyry	51.07	0.48	2.11	0	3.9	4.08	0.68	13.44	22.75	0.78	0	99.31	47.45	39.03	13.51	0.86	63.91
AP3	Didipio And. Dyke	47.69	0.69	6.49	0.04	6.13	2.09	0.17	13.44	23.68	0.23	0	100.65	48.93	38.60	12.47	0.92	63.88
AP3	Didipio And. Dyke	49.45	0.57	4.74	0	4.42	3.27	0.23	13.94	23.51	0.25	0.01	100.39	48.24	39.79	11.97	0.88	65.78
AP3	Didipio And. Dyke	48.68	0.6	5.47	0	5.23	3.05	0.27	13.35	23.49	0.33	0	100.47	48.57	38.41	13.03	0.89	63.26
AP3	Didipio And. Dyke	44.74	0.63	6.99	0	7.24	1.53	0.14	11.77	23.65	0.24	-	96.94	50.96	35.28	13.76	0.93	65.08
AP3	Didipio And. Dyke	46.43	0.53	4.86	0	5.93	2.76	0.45	12.93	22.18	0.29	-	96.36	47.35	38.39	14.26	0.89	61.19
AP3	Didipio And. Dyke	44.52	0.75	7.75	0.01	7.3	0.78	0.13	12.12	23.71	0.22	-	97.3	51.10	36.31	12.59	0.97	58.78
AP3	Didipio And. Dyke	45.51	0.68	6.42	0.02	8.4	0.78	0.26	12.57	23.58	0.3	-	98.5	49.36	36.59	14.05	0.97	62.81
AP3	Didipio And. Dyke	48.62	0.37	2.86	0	5.96	1.31	0.31	14.86	22.73	0.27	-	97.28	46.51	42.30	11.19	0.95	66.34
AP3	Didipio And. Dyke	44.47	0.7	6.85	0	7.35	0	0.11	12.54	23.93	0.17	-	96.13	51.32	37.42	11.27	1.00	65.03
AP3	Didipio And. Dyke	46.26	0.6	5.19	0	7.74	0.71	0.23	13.26	23.42	0.28	-	97.7	48.75	38.41	12.84	0.97	62.56
AP3	Didipio And. Dyke	47.94	0.43	2.89	0	6.02	1.29	0.29	14.66	22.31	0.3	-	96.13	46.35	42.38	11.27	0.95	61.14
AP3	Didipio And. Dyke	44.09	0.66	7.28	0	8.3	0.21	0.15	11.84	24.15	0.2	-	96.87	51.68	35.23	13.09	0.99	61.47
44.9	Didipio And. Dyke	44.34	1.13	7.84	0	8.1	2.54	0.31	10.77	23.53	0.4	-	98.96	50.69	32.28	17.04	0.88	55.16
44.9	Didipio And. Dyke	46	0.8	6.56	0	6.77	2.69	0.25	11.66	23.68	0.36	-	98.77	50.42	34.55	15.03	0.89	59.03
44.9	Didipio And. Dyke	44.67	1.13	7.84	0.04	8.01	2.2	0.29	10.94	23.82	0.41	-	99.36	51.08	32.65	16.27	0.90	52.37
44.9	Didipio And. Dyke	48.08	0.49	5.15	0	6.13	1.5	0.16	13.5	24.32	0.23	-	99.57	49.95	38.55	11.50	0.94	65.39
44.9	Didipio And. Dyke	45.32	0.8	7.93	0.04	7.7	1.19	0.12	11.99	24.3	0.24	-	99.62	51.26	35.20	13.54	0.95	59.53
44.9	Didipio And. Dyke	45.97	0.65	6.61	0.01	7.59	1.41	0.08	12.37	24.12	0.24	-	99.05	50.44	35.97	13.59	0.94	66.58
44.9	Didipio And. Dyke	22.4	0.4	2.81	0.03	5.06	0	0.19	5.79	39.04	0.31	-	76.03	76.86	15.86	7.28	1.00	54.16
44.9	Didipio And. Dyke	44.92	0.76	7.61	0	7.93	1.09	0.09	11.96	24.06	0.23	-	98.66	50.99	35.25	13.76	0.95	61.00
44.9	Didipio And. Dyke	44.93	0.64	7.31	0	8.25	1.25	0.14	11.4	24.19	0.34	-	98.46	51.51	33.82	14.67	0.94	57.63
44.9	Didipio And. Dyke	47.99	0.5	4.87	0.03	6.14	1.58	0.14	13.38	24.36	0.23	-	99.22	50.08	38.26	11.66	0.94	65.32
53/802	Bahut Dyke	51.96	0.32	1.09	0	3.74	4.83	0.55	13.09	23.25	0.84	0	99.68	48.17	37.73	14.11	0.83	61.49
53/802	Bahut Dyke (core)	51.24	0.44	1.43	0	4.43	4.43	0.5	12.72	23.31	0.9	0	99.4	48.60	36.90	14.49	0.84	60.19
53/802	Bahut Dyke (rim)	51.64	0.3	1.15	0.01	4.73	4	0.59	13.25	22.98	0.92	0.03	99.6	47.57	38.13	14.29	0.86	61.61
53/802	Bahut Dyke	51.1	0.51	1.68	0	5.04	4.68	0.67	12.75	22.71	0.95	0	100.09	47.15	36.84	16.01	0.83	58.05
53/802	Bahut Dyke	52.15	0.33	0.76	0.02	3.17	5.3	0.69	13.33	23.63	0.56	0	99.94	48.14	37.77	14.08	0.82	62.05
53/802	Bahut Dyke	52.11	0.28	0.96	0	3.86	4.98	0.5	12.96	23.21	0.91	0	99.77	48.09	37.38	14.53	0.82	60.55
31/334	Bahut Dyke	52.51	0.14	0.47	0.00	8.32	0.62	0.62	13.60	22.85	0.71	-	99.22					
31/334	Bahut Dyke	52.36	0.16	0.79	0.02	7.96	0.85	0.85	13.77	22.53	0.84	-	99.29					
31/334	Bahut Dyke	52.71	0.13	0.39	0.00	8.88	1.01	1.01	13.67	22.52	0.72	-	100.04					
31/334	Bahut Dyke	53.02	0.21	0.75	0.00	8.67	0.68	0.68	13.73	22.21	0.86	-	100.12					
31/334	Bahut Dyke	52.71	0.19	0.60	0.00	8.05	0.77	0.77	13.85	22.23	0.81	-	99.22					
31/334	Bahut Dyke	52.99	0.24	0.74	0.00	8.99	0.91	0.91	13.42	22.17	0.90	-	100.35					
31/334	Bahut Dyke	53.11	0.21	0.74	0.02	8.98	0.82	0.82	13.43	22.45	0.82	-	100.58					
31/334	Bahut Dyke	52.34	0.29	0.96	0.00	9.86	0.83	0.83	12.72	22.29	0.98	-	100.28					
31/334	Bahut Dyke	53.35	0.11	0.47	0.00	8.57	0.62	0.62	13.66	22.68	0.79	-	100.26					
31/334	Bahut Dyke	52.79	0.24	0.80	0.00	8.77	0.69	0.69	13.79	22.50	0.87	-	100.45					
31/334	Bahut Dyke	52.08	0.23	0.79	0.00	9.89	0.88	0.88	12.66	22.40	0.84	-	99.77					
31/334	Bahut Dyke	51.41	0.18	1.13	0.00	7.98	0.73	0.73	13.44	21.97	0.76	-	97.60					
31/334	Bahut Dyke	52.87	0.20	0.58	0.02	8.06	0.72	0.72	13.52	22.48	0.80	-	99.24					
31/334	Bahut Dyke	52.19	0.35	1.02	0.01	9.94	0.90	0.90	12.84	21.60	0.97	-	99.83					
31/334	Bahut Dyke	52.51	0.30	0.92	0.00	9.15	0.91	0.91	13.14	21.79	0.98	-	99.70					
31/334	Bahut Dyke	53.20	0.12	0.36	0.00	9.27	0.74	0.74	13.25	22.61	0.78	-	100.34					
31/334	Bahut Dyke	52.57	0.20	0.65	0.01	8.55	0.72	0.72	13.63	22.61	0.80	-	99.74					
31/334	Bahut Dyke	52.52	0.18	0.63	0.00	8.58	0.75	0.75	13.59	22.41	0.90	-	99.55					
31/334	Bahut Dyke	52.46	0.19	0.71	0.00	9.05	0.70	0.70	13.29	22.38	0.85	-	99.62					
31/334	Bahut Dyke	52.53	0.21	0.80	0.00	8.63	0.77	0.77	13.35	22.29	0.96	-	99.55					
31/334	Bahut Dyke	52.30	0.33	0.99	0.00	9.58	0.79	0.79	12.97	21.86	0.93	-	99.75					
31/334	Bahut Dyke	53.08	0.19	0.55	0.00	8.48	0.69	0.69	13.62	22.79	0.83	-	100.23					
31/334	Bahut Dyke	52.86	0.19	0.61	0.00	9.17	0.93	0.93	13.51	22.14	0.83	-	100.25					
31/334	Bahut Dyke	52.52	0.26	0.84	0.00	9.45	0.77	0.77	13.26	22.08	0.89	-	100.08					
31/334	Bahut Dyke	52.24	0.23	0.96	0.00	9.11	0.76	0.76	13.11	22.28	0.95	-	99.64					
31/334	Bahut Dyke	53.14	0.14	0.30	0.01	8.57	0.86	0.86	13.41	22.69	0.64	-	99.77					
31/334	Bahut Dyke	53.06	0.14	0.29	0.03	8.16	0.95	0.95	13.62	22.83	0.52	-	99.60					
31/334	Bahut Dyke	53.48	0.07	0.27	0.00	7.66	0.73	0.73	13.91	22.69	0.95	-	99.77					
31/334	Bahut Dyke	52.42	0.20	0.82	0.03	8.73	0.79	0.79	13.35	22.59	0.93	-	99.87					
31/334	Bahut Dyke	52.17	0.22	0.86	0.00	8.80	0.82	0.82	13.16	22.30	0.98	-	99.30					
31/334	Bahut Dyke	54.70	0.59	1.38	0.01	8.76	0.51	0.51	18.80	10.30	1.68	-	96.75					
31/334	Bahut Dyke	50.95	0.44	1.61	0.00	9.78	0.72	0.72	12.45	22.94	0.95	-	99.85					
31/334	Bahut Dyke	52.89	0.25	0.41	0.00	8.00	0.55	0.55	13.69	22.58	1.08	-	99.46					
31/334	Bahut Dyke	52.47	0.21	1.08	0.02	8.46	0.70	0.70	13.33	22.75	1.06	-	100.08					



## Mineral Chemistry - alteration mineral compositions

### Amphibole

Sample	mineral	Label	SiO2	TiO2	Al2O3	Cr2O3	Fe2O3(c)	FeO(c)	MnO	MgO	CaO	Na2O	K2O	BaO	SrO	ZrO2	F	Cl	H2O(c)	O=F	O=Cl	Sum Ox%	Sum Cat#	XMg
37/176	Stage 2 actinolite	37/176_4_amph1	55.52	0.26	1.11	0.02	2.48	6.23	0.36	18.73	12	0.77	0.15	0	0	0.1	0.28	0.04	1.99	0.12	0.01	99.92	17.047	0.843
37/176	Stage 2 actinolite	37/176_4_amph2	54.32	0.16	1.67	0	1.52	10	0.46	16.64	12.32	0.82	0.14	0	0	0.05	0.17	0.04	2.01	0.07	0.01	100.23	17.135	0.748
37/176	Stage 2B actinolite	37/122_1_amph1	55.07	0.46	1.51	0.04	3.62	5.05	0.37	18.94	11.12	1.54	0.35	0.03	0	0.07	0.64	0.02	1.83	0.27	0.01	100.39	17.152	0.87
37/122	Stage 2B actinolite	37/122_1_amph2	55.39	0.52	1.4	0.01	5.25	3.92	0.46	18.94	10.59	1.64	0.39	0.07	0	0.09	0.57	0.03	1.88	0.24	0.01	100.91	17.092	0.896
37/122	Stage 2B actinolite	37/122_2_blue amph	56.73	0.09	0.45	0	5.69	4.07	0.7	18.34	8.5	2.93	0.53	0	0	0.01	0.23	0.01	2.03	0.1	0	100.22	17.164	0.889

### Apatite

Sample	mineral	Label	SiO2	Fe2O3	MnO	MgO	CaO	Na2O	P2O5	SO3	La2O3	Ce2O3	Y2O3	SrO	BaO	F	Cl	H2O(c)	O=F	O=Cl	Sum Ox%
49/644	Stage 2 apatite	49/644_4_apat1	0.13	0.07	0.14	0.01	54.85	0.34	40.91	0.89	0	0.03	0.01	0.08	0.27	2.41	0.71	0.46	1.02	0.16	100.14
37/176	Stage 2 apatite	37/176_2_apat1	0.2	0	0.07	0	54.95	0.1	41.93	0.18	0.06	0.16	0.05	0.11	0.23	2.48	0.68	0.44	1.04	0.15	100.43

### Pyroxene

Sample	mineral	Label	SiO2	TiO2	Al2O3	Cr2O3	Fe2O3(c)	FeO(c)	MnO	MgO	CaO	Na2O	K2O	Sum Ox%	Sum Cat#	Wt(Ca)	En(Mg)	Fs(Fe2+)	XMg
49/644	Stage 2A diopside	49/644_1_cpx1	52.2	0.31	1.49	0	3.87	5.49	0.52	12.9	23.03	0.89	0.02	100.72	4	50.868	39.657	9.475	0.807
49/644	Stage 2A diopside	49/644_2_cpx2	51.69	0.52	1.9	0.02	4.03	6.4	0.53	12.15	22.7	0.99	0	100.93	4	50.906	37.887	11.208	0.772
49/644	Stage 2A diopside	49/644_3_cpx3	51.67	0.36	1.27	0.03	3.84	5.98	0.55	12.39	22.99	0.85	0.04	99.97	4	51.211	38.386	10.404	0.787
37/122	Stage 2A diopside	37/122_3_cpx	54.14	0.05	0.2	0	2.72	5.09	0.64	14.13	23.47	0.81	0	101.26	4	49.825	41.737	8.438	0.832
37/122	Stage 2A diopside	37/122_3_amph3	54.9	0.6	1.76	0	8.75	0.41	18.8	10.6	1.71	0.42	97.96	3.993	24.318	60.016	15.666	0.793	

### Feldspar

Sample	mineral	Label	SiO2	TiO2	Al2O3	Fe2O3	MnO	MgO	CaO	SrO	BaO	Na2O	K2O	Rb2O	P2O5	Sum Ox%	Sum Cat#	Ab	An	Or	Celsian	Rb-Feld	Sr-Feld
37/176	Pvt. Bahut Dyke Kspar	37/176_1_kfs	65.95	0.02	19.65	0.17	0.01	0	0.24	0	0.27	4.05	11.28	-	0.03	101.68	5.017	34.768	1.155	63.618	0.459	0	0
54/625	Primary Bufu perthite	54/625_5_perthite trav1	65.06	0.01	18.65	0.33	0.01	0.01	0	0	0	0.97	15.73	-	0	100.77	5.01	8.608	0.001	91.391	0	0	0
54/625	Primary Bufu perthite	54/625_5_perthite trav2	65.53	0	18.89	0.2	0	0.02	0.06	0	0.14	2.69	13.64	-	0	101.18	5.028	22.911	0.276	76.563	0.249	0	0
54/625	Primary Bufu perthite	54/625_5_perthite trav3	67.67	0.03	19.59	0.33	0	0.01	0.12	0	0.25	8.51	4.31	-	0.01	100.82	4.988	74.257	0.573	24.736	0.435	0	0
4/52	Stage 2D Kfeldspar	4/52_3_kspar	65.05	0.04	18.9	0.56	0.01	0	0.04	0	0.06	3.27	12.21	-	0	100.14	5.011	28.845	0.188	70.861	0.106	0	0
4/52	Stage 2D Kfeldspar	4/52_4_kspar2	65.09	0.01	18.79	0.5	0.02	0	0.04	0	0.1	1.81	14.64	-	0.04	101.04	5.018	15.726	0.192	83.904	0.178	0	0

### Illite

Sample	mineral	Label	SiO2	TiO2	Al2O3	Fe2O3	MnO	MgO	CaO	Na2O	K2O	H2O(c)	Sum Ox%	Sum Cat#
54/468	Stage 5 Clay (Ill?)	54/468_3_clay?	65.92	0.02	22.08	0.04	0	0.04	1.99	10.06	0.24	4.99	105.38	17.7
54/468	Stage 5 Clay (Ill?)	54/468_3_clay72	43.23	0.05	15.09	1.01	0.01	2.04	0.37	1.33	0.49	3.25	66.88	16.615
28/328	Stage 5 Clay (Kaol?)	28/328_1_clay71	58.22	0.01	23.33	1.98	0.05	3.28	0.58	0.16	1.38	4.54	93.53	16.529
28/328	Stage 5 Clay (Kaol?)	28/328_2_clay72	57.93	0.03	23.33	2.43	0.07	3.72	0.56	0.27	1.61	4.56	94.53	16.625

### Mica

Sample	mineral	Label	SiO2	TiO2	Al2O3	Cr2O3	FeO	V2O5	ZnO	MnO	MgO	CaO	Na2O	K2O	BaO	SrO	NiO	F	Cl	H2O(c)	O=F	O=Cl	Sum Ox%
54/625	Stage 5 Clay?	54/625_1_clay1	32.76	0.01	17.75	0.06	16.45	0	0	0.07	7.12	0.23	0.04	0.7	0.01	0	0.03	0.08	0.24	3.23	0.03	0.05	78.71
54/625	Stage 5 Clay?	54/625_1_clay2	15.06	0.01	10.52	0.01	0.7	0.01	0.07	0	0.24	0.08	0.07	4.42	0	0	0.07	0.09	0.67	1.22	0.04	0.15	33.06
54/625	Stage 3 sericite	54/625_2_wh mica	50.03	0.01	31.98	0	1.68	0.05	0.04	0	1.71	0.01	0.07	10.86	0.1	0	0	0.37	0.02	4.39	0.15	0	101.15
54/625	Stage 4 clay/chl	54/625_3_chl?	30.54	0	18.26	0	20.27	0.05	0.11	0.04	7.99	0.25	0.03	0.37	0.04	0	0	0.06	0.09	3.3	0.02	0.02	81.37
54/665	Stage 5 chlorite	54/665_1_chl?	29.72	0	12.98	0.01	40.52	0.08	0.03	0.16	3.14	0.52	0.18	0.87	0	0	0	0.09	0.04	3.29	0.04	0.01	91.59
54/665	Stage 5 chlorite	54/665_2_chl72	21.24	0	10.01	0	31.42	0.19	0.07	0.12	3.14	0.59	0.08	0.35	0	0	0	0.06	0.05	2.48	0.02	0.01	69.75

### Zeolites (Sodalite label)

Sample	mineral	Label	SiO2	Al2O3	Fe2O3	MgO	CaO	Na2O	K2O	SO3	Cl	O=Cl	Sum Ox%
54/468	Stage 5 Zeolite	54/468_2_zeolite1	60.8	19.02	0	0	8.24	0.64	0.12	0	0.01	0	88.82
54/468	Stage 5 Zeolite	54/468_2_zeolite2	60.92	18.58	0	0	8.41	0.87	0.08	0	0	0	88.87
37/176	Stage 5 Zeolite	37/176_3_zeol1	53.82	21.02	0.01	0.01	8.54	2.25	1.46	0	0.01	0	87.12
37/176	Stage 5 Zeolite	37/176_3_zeol2	53.1	20.77	0.03	0	8.34	2.21	1.21	0	0.01	0	85.67
28/129	Stage 5 Zeolite	28/129_1_zeol1	62.19	17.78	0.01	0	8.5	0.48	0.07	0.02	0	0	89.05
28/129	Stage 5 Zeolite	28/129_2_zeol2	52.78	22	0.02	0	11.73	0.03	0.39	0.03	0	0	86.97
28/328	Stage 5 Zeolite	28/328_3_zeol1	63.15	15.84	0.04	0	8.44	0.1	0.09	0	0.01	0	87.66
28/328	Stage 5 Zeolite	28/328_4_clay73	57.43	22.81	2.48	2.93	0.92	0.65	1.65	0.07	0.05	0.01	88.96
25/136	Stage 5 Zeolite	25/136_1_zeol1	54.65	15.66	0.04	0.06	5.03	0.19	0.47	0.05	0.01	0	76.16
25/136	Stage 5 Zeolite	25/136_2_zeol2	55.59	16.66	0	0.06	4.89	0.26	0.35	0	0.01	0	77.82

## Least-squares modelling of fractionation

Major element modelling of fractionation, using the least-squares model of Le Maitre (1981) and the Genmix mixing program.

### Modelling of fractionation from diorite (DD1) to monzodiorite (MD1)

	% amount:	SiO <sub>2</sub>	TiO <sub>2</sub>	Al <sub>2</sub> O <sub>3</sub>	Fe <sub>2</sub> O <sub>3</sub>	FeO	MgO	CaO	Na <sub>2</sub> O	K <sub>2</sub> O	P <sub>2</sub> O <sub>5</sub>	MnO	Total
<i>Reactants Used</i>													
Diorite (DD1)	100.00%	48.89	0.83	18.22	10.24	0	4.91	10.6	3.18	2.34	0.5	0.19	99.9
<i>Products Used</i>													
Monzodiorite (MD1)	73.64%	51.81	0.65	18.66	8.29	0	3.86	9.54	3.75	2.57	0.46	0.19	99.78
Clinopyroxene (DD-1)	8.01%	50.69	0.39	2.16	8.59	0	13.42	22.88	0.61	0.01	0	0.44	99.19
Biotite (mdl_2_bio)	4.67%	37.59	5.37	13.47	12.05	0	16.13	0.01	0.22	9.69	0	0.18	94.71
Plagioclase An 78 (ddl_8_core)	10.26%	47.6	0.04	33.73	0.24	0	0.03	16.12	2.31	0.15	0.04	0	100.26
Magnetite (ddl_2_mag)	3.30%	0.09	6.1	4.05	84.91	0	2.29	0	0	0	0	0.61	98.05
Apatite (ddl_9d_apat)	0.13%	0.16	0	0	0.29	0	0.12	54.47	0.06	0.01	40.75	0.09	95.95
<i>Estimated Compositions (normalised)</i>													
Reactants		48.89	0.83	18.22	10.24	0	4.91	10.60	3.18	2.34	0.50	0.19	
Products		48.85	0.97	18.14	10.18	0	4.75	10.58	3.06	2.36	0.40	0.20	
Differences		0.04	-0.14	0.08	0.06	0	0.16	0.02	0.12	-0.02	0.10	-0.01	

Residual sum of squares = 0.08; Distance apart = 0.29; Degree of fractionation (crystals removed) = 26.36%.

### Modelling of fractionation from monzodiorite (MD1) to monzonite (M9)

	% amounts	SiO <sub>2</sub>	TiO <sub>2</sub>	Al <sub>2</sub> O <sub>3</sub>	Fe <sub>2</sub> O <sub>3</sub>	FeO	MgO	CaO	Na <sub>2</sub> O	K <sub>2</sub> O	P <sub>2</sub> O <sub>5</sub>	MnO	Total
<i>Reactants Used</i>													
Monzodiorite (MD1)	100.00%	51.81	0.65	18.66	8.29	0	3.86	9.54	3.75	2.57	0.46	0.19	99.78
<i>Products Used</i>													
Monzonite (M9)	48.23%	54.11	0.58	18.69	6.56	0	2.33	7.28	4.58	3.68	0.45	0.18	98.44
Clinopyroxene (mdl_5_cpx)	13.86%	50.82	0.34	2.96	7.06	0	14.14	22.96	0.52	0.01	0	0.36	99.17
Biotite (mdl_2_bio)	3.46%	37.59	5.37	13.47	12.05	0	16.13	0.01	0.22	9.69	0	0.18	94.71
Plagioclase An 52 (mdl_1_plag)	26.60%	54.39	0.03	29.2	0.33	0	0	11.01	5.14	0.26	0	0.02	100.38
Orthoclase Or 61 (mdl_1Or)	4.24%	64.44	0.03	19.76	0.25	0	0	0.79	3.88	10.78	0.05	0	99.98
Magnetite (mdl_1_TiMag)	3.81%	0.03	4.33	0.82	91.85	0	0.37	0	0	0	0	0.75	98.15
Apatite (ddl_9d)	-0.19%	0.16	0	0	0.29	0	0.12	54.47	0.06	0.01	40.75	0.09	95.95
<i>Estimated Compositions (normalised)</i>													
Reactants		51.81	0.65	18.66	8.29	0	3.86	9.54	3.75	2.57	0.46	0.19	
Products		51.64	0.69	18.53	8.15	0	3.65	9.55	3.82	2.64	0.14	0.18	
Differences		0.17	-0.04	0.13	0.14	0	0.21	-0.01	-0.07	-0.07	0.32	0.01	

Residual sum of squares = 0.22; Distance apart = 0.47; Degree of fractionation (crystals removed) = 51.77%.

### Modelling of fractionation from monzonite (M9) to Tunja Monzonite (25/254)

	% amounts	SiO <sub>2</sub>	TiO <sub>2</sub>	Al <sub>2</sub> O <sub>3</sub>	Fe <sub>2</sub> O <sub>3</sub>	FeO	MgO	CaO	Na <sub>2</sub> O	K <sub>2</sub> O	P <sub>2</sub> O <sub>5</sub>	MnO	Total
<i>Reactants Used</i>													
Monzonite M9	100.00%	54.11	0.58	18.69	6.56	0	2.33	7.28	4.58	3.68	0.45	0.18	98.44
<i>Products Used</i>													
25/254 Tunja	47.93%	56.805	0.425	18.77	4.88	0	2.155	4.38	5.675	3.445	0.255	0.085	96.875
Clinopyroxene (mdl_5_cpx)	8.92%	50.82	0.34	2.96	7.06	0	14.14	22.96	0.52	0.01	0	0.36	99.17
mdl_2_biotite (high mg)	1.11%	37.59	5.37	13.47	12.05	0	16.13	0.01	0.22	9.69	0	0.18	94.71
Plagioclase An 52 (mdl_1_plag)	20.67%	54.39	0.03	29.2	0.33	0	0	11.01	5.14	0.26	0	0.02	100.38
Orthoclase Or 61 (mdl_1Or)	16.67%	64.44	0.03	19.76	0.25	0	0	0.79	3.88	10.78	0.05	0	99.98
Magnetite (m9_1)	3.50%	0	0.25	0.42	96.58	0	0.05	0	0	0	0	0.25	97.55
Apatite (ddl_9d)	1.21%	0.16	0	0	0.29	0	0.12	54.47	0.06	0.01	40.75	0.09	95.95
<i>Estimated Compositions (normalised)</i>													
Reactants		54.11	0.58	18.69	6.56	0	2.33	7.28	4.58	3.68	0.45	0.18	
Products		54.16	0.31	18.75	6.60	0	2.48	7.21	4.48	3.61	0.62	0.09	
Differences		-0.05	0.27	-0.06	-0.04	0	-0.15	0.07	0.10	0.07	-0.17	0.09	

Residual sum of squares = 0.16; Distance apart = 0.40; Degree of fractionation (crystals removed) = 52.07%.

Modelling of fractionation from Tunja Monzonite (25/254) to Quan Porphyry (22/110)

	% amounts	SiO2	TiO2	Al2O3	Fe2O3	FeO	MgO	CaO	Na2O	K2O	P2O5	MnO	Total
<i>Reactants Used</i>													
Tunja Monzonite (25/254)	100.00%	56.805	0.425	18.77	4.88	0	2.155	4.38	5.675	3.445	0.255	0.085	96.875
<i>Products Used</i>													
Quan Porphyry (25/110)	60.31%	63.02	0.26	17.65	2.98	0	0.77	2.67	6.72	3.63	0.13	0.04	97.87
Clinopyroxene (md1_5_cpx)	0.90%	50.82	0.34	2.96	7.06	0	14.14	22.96	0.52	0.01	0	0.36	99.17
Biotite (md1_2_bio)	10.29%	37.59	5.37	13.47	12.05	0	16.13	0.01	0.22	9.69	0	0.18	94.71
Plagioclase An 52 (Mnz53_trav_12)	24.43%	56.58	0.03	27.02	0.39	0	0.03	8.93	6.28	0.42	0.04	0	99.72
Orthoclase Or 87 (Tunj41.3_3_or)	1.29%	64.1	0.02	18.92	0.13	0	0.01	0.01	1.35	15.44	0	0	99.98
Magnetite (m9_1)	1.89%	0	0.25	0.42	96.58	0	0.05	0	0	0	0	0.25	97.55
Apatite (ddl_9d)	0.90%	0.16	0	0	0.29	0	0.12	54.47	0.06	0.01	40.75	0.09	95.95
<i>Estimated Compositions (normalised)</i>													
Reactants		56.81	0.43	18.77	4.88	0	2.16	4.38	5.68	3.45	0.26	0.09	
Products		56.98	0.72	18.91	5.03	0	2.26	4.49	5.63	3.49	0.45	0.05	
Differences		-0.17	-0.30	-0.14	-0.15	0	-0.11	-0.11	0.04	-0.04	-0.20	0.03	

Residual sum of squares = 0.23; Distance apart = 0.48; Degree of fractionation (crystals removed) = 39.69%.

Modelling of fractionation from Quan Porphyry (22/110) to Bufu Felsite (54/565)

	% amounts	SiO2	TiO2	Al2O3	Fe2O3	FeO	MgO	CaO	Na2O	K2O	P2O5	MnO	Total
<i>Reactants Used</i>													
Quan Porphyry (25/110)	100.00%	63.02	0.26	17.65	2.98	0	0.77	2.67	6.72	3.63	0.13	0.04	97.87
<i>Products Used</i>													
Bufu Felsite (54/565)	19.93%	71.95	0.1	14.76	0.48	0	0.22	0.4	2.62	8.88	0.07	0.01	99.49
Clinopyroxene (md1_5_cpx)	4.90%	50.82	0.34	2.96	7.06	0	14.14	22.96	0.52	0.01	0	0.36	99.17
Biotite (md1_2_bio)	2.34%	37.59	5.37	13.47	12.05	0	16.13	0.01	0.22	9.69	0	0.18	94.71
Orthoclase Or 87 (Tunj 41.3_3_or)	10.15%	64.1	0.02	18.92	0.13	0	0.01	0.01	1.35	15.44	0	0	99.98
Albite An 12 (Tunj41.3_3_pertha)	59.25%	65.89	0.05	21.25	0.32	0	0	1.78	10.45	0.43	0.02	0	100.19
Magnetite (m9_1_magn)	2.37%	0	0.25	0.42	96.58	0	0.05	0	0	0	0	0.25	97.55
Apatite (ddl_9d_apat)	1.06%	0.16	0	0	0.29	0	0.12	54.47	0.06	0.01	40.75	0.09	95.95
<i>Estimated Compositions</i>													
Reactants		63.02	0.26	17.65	2.98	0	0.77	2.67	6.72	3.63	0.13	0.04	
Products		63.26	0.20	17.92	3.22	0	1.12	2.84	6.88	3.82	0.46	0.03	
Differences		-0.24	0.06	-0.27	-0.24	0	-0.35	-0.17	-0.16	-0.19	-0.33	0.01	

Residual sum of squares = 0.51; Distance apart = 0.71; Degree of fractionation (crystals removed) = 80.07%.

## Fluid inclusion data

### Stage 2 Apatite

Inclusion No#	Type	Phases	Tm first ice	Tm ice	Tm Halite	Th vapor	Th	NaCl (wt % equiv)
<i>Primary inclusions:</i>								
(used rough textures as start of first melting; maybe too high)								
28_602_(frag1) 1	LVI	LV	-25	-14		305	305	34.53
28_602_2	LVI	LV	-25	-14		321	321	34.53
28_602_3	LVI	LV	-26			314	314	
28_602_4	LVI	LV	-25	-14		302	302	34.53
28_602_5	LVI	LV	-23	-14		320	320	34.53
28_602_6	LVI	LV	-30	-13		300	300	31.33
28_602_7	LVI	LV	-28	-13		302	302	31.33
28_602_(frag2) 8	LVI	LV	-30	-16		262	262	41.33
28_602_9	LVI	LV	-43	-16		290	290	41.33
28_602_10	LVI	LV	-39	-15		207	207	37.86
28_602_11	LVI	LV	-35	-15		279	279	37.86
28_602_12	LVI	LV	-35	-15		285	285	37.86
28_602_13	LVI	LV	-34	-16		290	290	41.32
28_602_(frag3) 14	LVI	LV	-34	-16		277	277	41.32
28_602_15	LVI	LV	-25	-16		244	244	41.32
28_602_16	LVI	LV	-48	-16		217	217	41.32
28_602_17	LVI	LV	-33	-17		233	233	44.92
28_602_18	LVI	LV	-36	-19		263	263	52.54
28_602_19	LVI	LV	-38	-16		282	282	41.33
28_602_20	LVI	LV	-36	-16		201	201	41.33
28_602_21	LVI	LV	-38	-16		212	212	41.33
28_602_22	LVI	LV	-41	-17		275	275	44.92
28_602_23	LVI	LV	-41	-17		229	229	44.92
28_602_24	LVI	LV	-40	-17		276	276	44.92
28_602_25	LVI	LV	-42	-17		264	264	44.92
28_602_(frag4) 26	LVI	LV	-29	-16		291	291	41.33
28_602_27	LVI	LV	-29	-13		286	286	31.33
28_602_28	LVI	LV	-24	-13		294	294	31.33
28_602_29	LVI	LV	-38	-16		285	285	41.33
28_602_30	LVI	LV	-31	-13		280	280	31.33
28_602_31	LVI	LV	-32	-15		293	293	37.86
28_602_32	LVI	LV	-33	-14		297	297	34.53
28_602_33	LVI	LV	-40	-15		285	285	37.86
28_602_34	LVI	LV	-28	-18		277	277	48.66
28_602_(book frag) 35	LVI	LV	-30	-16		285	285	41.33
28_602_36	LVI	LV	-31	-16		285	285	41.33
28_602_37	LVI	LV	-27	-15		275	275	37.86
28_602_38	Blh	LV (H)			230	291	291	33.48
28_602_39	LVI	LV	-30	-13		268	268	31.32
28_602_40	LVI	LV	-30	-12		295	295	28.52
28_602_41	LVI	LV	-30	-15		293	293	37.86
28_602_42	LVI	LV	-35	-11		248	248	25.30
28_602_43	LVI	LV	-31	-10		230	230	22.46
28_602_44	LVI	LV		-10		260	260	22.46
(Main Th is 270-290, main first melt is -31, main ice melt is -14 to -16, any salts in uncommon LVH melt before 240.)								
53_821_1	LVI	LV				250	250	
53_821_2	LVI	LV				240	240	
53_821_3	LVI	LV				280	280	
53_821_4	LVI	LV				185	185	
53_821_5	LVI	LV				175	175	
53_828_1	LVI	LV	-50	-23		223	223	69.54
53_828_2	LVI	LV	-34	-23		227	227	69.54
53_828_3	LVI	LV	-25	-23		149	149	69.54



Stage 3- Quartz from the Bugoy Pegmatite

Inclusion No#	Type	Phases	Tm first ice	Tm ice	Tm Halite	Th vapor	Th	NaCl (wt % equiv)	Comments
<b>Primary inclusions:</b>									
47_690_1 to 20	Bm & Bvd				601		601	68.83	No homogen <600
34_393_10	Bm	HVOD2			601		601	68.83	large trail of these
34_393_10	Bm	HVOD2			601		601	68.83	large trail of these
34_393_10	Bm	HVOD2			601		601	68.83	large trail of these
34_393_11	Bm	HVO	rare >600		601		601	68.83	rare >600
34_393_12	Bm	V>OH	rare >600		601		601	68.83	rare >600
34_393_13	Bm	LV+O				533	533		primary?
34_393_44	Bm	VO+clath	Sil melts 130		450		450	50.92	primary
34_393_45	Bm				595		595	68.03	lath remains
34_393_46	Bm				490	320	490	55.20	lath remains
34_393_42	Bvd					601	601		primary
34_393_43	Bvd					601	601		primary
34_393_48	Bh	vhj			407	281	407	46.71	primary
34_393_49	Bh	vhj			416	270	416	47.56	primary
34_393_50	Bh	vhj			420		420	47.94	primary
34_393_47	Bhvo				408	275	408	46.80	primary
34_383_7	Bvho	VHO			435	(313)	435	49.41	
34_383_8	Bvho	VHO			458	(330)	458	51.75	
34_383_9	Bvho	HV			410	(250)	410	46.99	
34_393_14	Bvho	HVO				433	433		cpy-bearing; prob primary
34_393_15	Bvho	HVO			329	383	383	40.06	cpy-bearing; prob primary
34_393_16	Bvho	HVO			340	460	460	40.92	cpy-bearing; prob primary
34_393_17	Bvho	HVO			424	390	424	48.33	cpy-bearing; prob primary
34_393_18	Bvho	HVO			337	417	417	40.68	cpy-bearing; prob primary
34_393_19	Bvho	HVO			354	485	485	42.05	cpy-bearing; prob primary
34_393_20	Bvho	HVO+cl			415	330-350	415	47.46	cpy-bearing; prob primary
34_393_21	Bvho	HVO			410	330-350	410	46.99	cpy-bearing; prob primary
34_393_22	Bvho	HVO			415	330-350	415	47.46	cpy-bearing; prob primary
34_393_23	Bvho	HVO			419	330-350	419	47.84	cpy-bearing; prob primary
34_393_24	Bvho	HVO			419	330-350	419	47.84	cpy-bearing; prob primary
34_393_25	Bvho	HVO			405		405	46.52	cpy-bearing; prob primary
34_393_26	Bvho	HVO			413	325	413	47.27	cpy-bearing; prob primary
34_393_27	Bvho	HVO			417	319	417	47.65	cpy-bearing; prob primary
34_393_28	Bvho	HVO			320	466	466	39.38	cpy-bearing; prob primary
34_393_29	Bvho	HVO			330	442	442	40.14	cpy-bearing; prob primary
34_393_30	Bvho	HVO			346	488	488	41.40	cpy-bearing; prob primary
34_393_31	Bvho	HVO			380	462	462	44.26	cpy-bearing; prob primary
34_393_32	Bvho	HVO			330	420	420	40.14	cpy-bearing; prob primary
34_393_4	LV	LV				541	541		
34_383_1	LVv		-35	7		360	360		+7 (clathrate)
34_383_2	LVv		-43			408	408		
34_393_41	VL					508	508		
Note: most primary inclusions (60-90%) do not homogenise before 600C									
<b>Secondary inclusions</b>									
34_393_33	Bm	HVD2	syv melts 107		412	384	412	47.18	
34_393_34	Bh				414	367	414	47.37	
34_393_35	Bh				410	318	410	46.99	
34_393_36	Bh				420	348	420	47.94	
34_393_37	Bh				421	351	421	48.04	
34_393_39	Bh				125	480	480	28.77	
34_393_40	Bh				410	350	410	46.99	
34_383_13	Bh	H>VL			410	(330)	410	47.00	
34_383_14	Bh	VH	-44	-19	405	(240)	405	46.52	+14 clathrate
34_383_5	2*B1	LVH	-36	-20	390	(278)	390	45.10	
34_383_16	Bh	HLV			420	(390)	420	47.94	
34_383_17	Bh	HLV				410	410		
34_383_18	Bh	HLV			400	-325	400	46.06	
47_690_1 to 4	2*Bh	VLH			360		360	42.55	
47_690_1 to 4	2*Bh	VLH			380		380	44.26	
47_690_1 to 4	2*Bh	VLH			400		400	46.06	
47_690_1 to 4	2*Bh	VLH			420		420	47.94	
47_690_4 to 8	2*Bh	VLH			532		532	60.05	
47_690_4 to 8	2*Bh	VLH			578		578	65.79	
47_690_4 to 8	2*Bh	VLH			550		550	62.24	
47_690_4 to 8	2*Bh	VLH			575		575	65.40	
34_393_38	Bvho				410	330	410	46.99	
34_393_1	2Bhvo	HVO			406	253	406	46.61	cpy bearing. Big 72nd trail
34_393_2	2Bhvo	HVO			415	254	415	47.46	cpy bearing. Big 72nd trail
34_393_3	2Bhvo	HVO			407	314	407	46.71	cpy bearing. Big 72nd trail
34_393_5	2Bhvo	HVO			428	345	428	48.72	cpy bearing. Big 72nd trail
34_393_6	2Bhvo	HVO			417	293	417	47.65	cpy bearing. Big 72nd trail
34_393_7	2Bhvo	HVO			415		415	47.46	cpy bearing. Big 72nd trail
34_393_8	2Bhvo	HVO			392	261	392	45.33	cpy bearing. Big 72nd trail
34_393_9	2Bhvo	HVO			398	266	398	45.87	cpy bearing. Big 72nd trail
34_383_4	2*7 LV	LV (o)	-32	-10		358	358	22.46	
34_383_6	2* LV	VL	-25	-8		238	238	17.10	
34_383_10	VLJ	VL	-44	-7		333	333	14.64	
34_383_11	2* VLI	VL	-38	-17		270	270	44.92	
34_383_12	2* VLI	VL	-24	-6		270	270	12.25	
34_383_15	2*LVI	LV				275	275	33.48	
34_383_3					230		230		2nd trails of LV incs that
34_383_3						240			homog -230-280
34_383_3						370			2nd trails of LV incs that
34_383_3						280			homog -230-280
34_383_3						250			2nd trails of LV incs that
34_383_3						250			homog -230-280

Stage 3- Quartz from Stage 3 quartz veins

Inclusion No#	Type	Phases	Tm first ice	Tm ice	Tm Halite	Th vapor	Th	NaCl (wt % equiv)	Comments
<i>Primary inclusions:</i>									
33_256_22	Bm & Bh	HLV (D2, O)			601		601	68.83	(80% of inclusions >600C)
33_256_15	Bm	LHD2OV			548		548	62.00	
33_256_16	Bm	HD2D3LV			420		420	47.94	(near Th)
33_256_17	Bm				551		551	62.37	
33_256_18	Bm				582		582	66.31	
33_256_19	Bm				576		576	65.53	
33_256_20	Bm				593		593	67.76	
33_256_21	Bm				594		594	67.90	
33_256_11	Bm	HD2LV			380		380	44.26	(one phase only)
33_256_6	Bh	HLV			410		410	46.99	
33_256_7	Bh	HLV			390		390	45.15	
33_256_8	Bh	HLV			433		433	49.21	
33_256_10	Bl	LHV			365		365	42.97	
33_256_12	Bl	VLH			320		320	39.38	
33_256_13	Bl	VLH			538		538	60.77	
33_256_14	Lv	LV			380		380	44.26	(small salt left)
28_223_PIXE 1A							340		halite temp?
28_223_17	Bm	LHD2	>550		601		601		
28_223_18	Bm	HD2OV	>550		591		591		
28_223_PIXE 1B						570	570		primary
28_223_PIXE 6A					440	580	580	49.91	primary
28_223_PIXE 8A						550	550		primary
28_223_(Frag 1) I	Bm	hvo		-18	Td 515	480	480		(H, D2 & O did not melt)
28_223_2	Bm	hvod2	-31	-19	Td 523	289			
28_223_3	Bm	hvod2			330	Td 530		40.14	(D2 & O did not melt)
28_223_4	Bm	hvod2			Td 490	380			(D2 & O did not melt)
28_223_5	Bm	hvod2	-30		330	Td 510			
28_508_11	Bm	hvolath			601		601	68.83	primary
28_508_12	Bm	hvolath			601		601	68.83	primary
60_529_2	bm				562		562	63.74	(co-exist with VLv)
60_529_3	bm				578		578	65.79	(co-exist with VLv)
54_468_17	Bm	hvo			548	601	601	62.00	Close to homogen at 600
54_468_1	Bm	hvo				601	601		halite starts to melt
54_468_2	Bm	hvo				601	601		at 550C, decrep at 580
54_468_3	Bm	hvo			600		600		small halite left 600
28_508_13	Bh Bm				471		471	53.12	(pseudosec?)
28_508_14	Bh Bm				462		462	52.17	(pseudosec?)
28_508_15	Bh Bm				501		501	56.43	(pseudosec?)
28_508_16	Bh Bm				540		540	61.02	(pseudosec?)
28_508_17	Bm	hvl			601		601	68.83	primary
28_508_18	Bm	hvl			601		601	68.83	primary
28_223_(Frag 2)6	Bl				542		542	61.00	(30% homog 500-550)
28_223_6	Bl				536		536	58.00	(30% homog 500-550)
28_223_6	Bl				534		534	59.00	(30% homog 500-550)
28_223_9	Bl					573	573		
28_223_10	Bl					590	590		
28_223_30	Bl				480		480	54.10	
28_223_31	Bl				447		447	49.91	
28_223_32	Bl				471		471	53.02	
28_223_33	Bl				448		448	49.91	
28_223_34	Bl				458		458	50.92	
28_223_35	Bl				490		490	55.20	
28_223_36	Bl				452		452	50.92	
28_223_37	Bl				468		468	51.96	
28_223_38	Bl				465		465	51.96	
28_223_39	Bl				472		472	53.02	
28_223_40	Bl				480		480	54.10	
28_223_41	Bl				468		468	51.96	
28_508_1 to 9	Bl & LV	(80% inclusions >600C)			>600		601	69.00	
60_529_1	Bl	vhl			570		570	64.76	
60_529_4	Bh	vhl			580	330	580	66.05	
28_223_11	Bl					540	540		
28_223_14	Bl	LHV			550		550		
28_223_15	Bl				340		340	40.90	most (6-8) Blh stable
28_223_16	Bl		>500		570		570		at 500, decrep 550
60_529_19	bl				358	207	358	42.38	
60_529_25	bl				374	174	374	43.74	
60_529_26	bl				365	224	365	42.97	
60_529_14	Bl				390	256	390	45.15	
28_508_8	Bh	vhl			601		601	68.83	primary
28_508_9	Bh	vhl			602		602	68.97	primary
28_508_10	Bh	vhl			513		513	57.81	primary
28_508_5	Bh	vth				560	560		primary
28_223_20	Bh				436		436	49.51	Probable primary
28_223_21	Bh				440		440	49.91	Probable primary
54_468_10	Bh				601	445	601	68.83	Close to melt at 600.
54_468_11	Bh				601		601	68.83	Close to melt at 600.
54_468_12	Bh				372	204	372	43.57	
54_468_15	Bh				601		601	68.83	Close to melt at 600.
54_468_16	Bh				601	395	601	68.83	Close to melt at 600.
54_468_18	Bh				601		601	68.83	Small salt & vapour at 600
54_468_20	Bh	hv				>600	601		
61_103_1	Bh	vth			450	>600	450	50.92	primary
61_103_2	Bh	vth			515	>600	515	58.04	primary
61_103_3	Bh	vth			601		601	68.83	primary
61_103_13	Bh				594		594	67.90	primary: salt still
61_103_14	Bh				590		590	67.36	stable at 600
61_103_15	Bh				515		515	58.04	probable primary
61_103_16	Bh				240	449	449	34.05	probable primary
61_103_17	Bh				560		560	63.49	probable primary
61_103_18	Bh				601		601	68.83	halite stable >600
61_103_19	Bh				601		601	68.83	halite stable >600
61_103_20	Bh				567		567	64.38	primary
61_103_21	Bh				583		583	66.44	primary
61_103_22	Bh				461		461	52.06	primary
61_103_23	Bh				528		528	59.57	primary

Stage 3- Quartz from Stage 3 quartz veins (cont.)

Inclusion No#	Type	Phases	Tm first ice	Tm ice	Tm Halite	Th vapor	Th	NaCl (wt % equiv)	Comments
<b>Primary inclusions:</b>									
28_223_22	BI					590	590		Probable primary
28_223_23	BI					365	365		Probable primary
37_87_1	BI	VLH			470		470	53.02	
37_87_2	BI	VLH			375	472	472	43.82	
28_223_PDXE 9C			-33	-18	330	380	380	40.14	
28_223_PDXE 9A	hvo		-29	-18	330	289	330	40.14	
37_322_10	Bhvo				445	200 to 260	445	50.41	Multiple gen. Some primary?
37_322_11	Bhvo				440	200 to 260	440	49.91	Multiple gen. Some primary?
37_322_12	Bhvo				430	200 to 260	430	48.91	Multiple gen. Some primary?
37_322_13	Bhvo				431	200 to 260	431	49.01	Multiple gen. Some primary?
37_322_14	Bhvo				412	200 to 260	412	47.18	Multiple gen. Some primary?
37_322_15	Bhvo				587	200 to 260	587	66.97	Multiple gen. Some primary?
37_322_16	Bhvo				577	200 to 260	577	65.66	Multiple gen. Some primary?
37_322_17	Bhvo				531	200 to 260	531	59.93	Multiple gen. Some primary?
37_322_18	Bhvo				435	200 to 260	435	49.41	Multiple gen. Some primary?
37_322_19	Bhvo				548	200 to 260	548	62.00	Multiple gen. Some primary?
37_322_20	Bhvo				590	200 to 260	590	67.36	Multiple gen. Some primary?
37_322_21	Bhvo				496	200 to 260	496	55.87	Multiple gen. Some primary?
37_322_33	Bhvo	>600			601		601	68.83	Multiple gen. Some primary?
37_322_33	Bhvo	>600			601		601	68.83	Multiple gen. Some primary?
54_468_7	Bvho				601	560	601		primary; cpy bearing; half melt
54_468_8	Bvho	hvo			601	500	601		primary; cpy bearing; half melt
60_529_13	hvo				438	610	610	49.71	
60_529_15	hvo				370	508	508	43.39	
60_529_5	hvo (2*)	hvo			420	230	420	47.94	
28_223_6	hvo				373		373	43.65	Interstitial quartz
28_223_6	hvo				385		385	44.70	Interstitial quartz
28_223_6	hvo				410		388	44.97	Interstitial quartz
37_87_3	lv				601		601	69.00	no homogen at 600,
37_87_4	lv				601		601	69.00	70% >600C
37_87_5	lv				601		601	69.00	small halite left
60_529_27	vl					440	440		
60_529_28	lv					420	420		
60_529_29	lv					610	610		
60_529_30	lv					424	424		
60_529_31	vl					420	420		
60_529_20	vl					470	470		
60_529_21	vl					410	410		
60_529_22	lv					326	326		
60_529_23	lv					342	342		
60_529_24	lv					350	350		
61_103_4	Lv	lv				483	483	26.22	primary
61_103_5	Lv	lv				414	414	26.22	primary
28_508_4	vl					570	570		primary VL
54_468_13	Lv				601		601	68.83	Close to melt at 600.
54_468_14	Lv				340	193	340	40.92	
54_468_19	Lv					>600	601		Common LV > 600C
<b>Secondary inclusions:</b>									
54_468_4	Bb	bv			364	180	364	42.88	secondary?
54_468_5	Bb	bv			240	352	352	34.05	secondary?
28_223_25	Bb				406		406	46.61	secondary, co exist with vapor?
28_223_12	BI	LHV				440	440		prob secondary
28_223_13	BI	LHV			84	330	330	27.57	prob secondary
28_508_10 % of inc	BI (sec)	VLH			460		406	51.96	
28_508_*2 trail	BI & LV	VLH				380	380		
28_508_*2 trail	BI & LV	VLH			372		372		
60_529_11	BI (2)	vlh				530	530		
60_529_12	BI (2)				350	225	350	41.72	
60_529_16	BI-silv	lvh-silvite			380	240	380	44.26	
60_529_17	BI-silv	lvh-silvite			383	246	383	44.52	
60_529_18	BI-silv	lvh-silvite			370	230	370	43.39	
61_103_6	2* vho's				462		462	52.17	secondary
61_103_7	2* vho's				464		464	52.38	secondary
61_103_8	2* vho's				465		465	52.49	secondary
61_103_9	2* vho's				465		465	52.49	secondary
61_103_10	2* vho's				470		470	53.02	secondary
61_103_11	2* vho's				470		470	53.02	secondary
61_103_12	2* vho's				489		489	55.09	secondary
37_322_1	Bhvo				420	240	420	47.94	secondary, cpy-bearing
37_322_2	Bhvo				427	304	427	48.62	secondary, cpy-bearing
37_322_3	Bhvo				432	304	432	49.11	secondary, cpy-bearing
37_322_4	Bhvo				435	260	435	49.41	secondary, cpy-bearing
37_322_5	Bhvo				440	315	440	49.91	secondary, cpy-bearing
37_322_6	Bhvo				430	310	430	48.91	secondary, cpy-bearing
37_322_7	Bhvo				398	200 to 260	398	45.87	Multiple gen. Some primary?
37_322_8	Bhvo				376	200 to 260	376	43.91	secondary, cpy-bearing
37_322_9	Bhvo				396	200 to 260	396	45.69	Multiple gen. Some primary?
37_322_22	Bhvo				445	200 to 260	445	50.41	Multiple gen. Some primary?
37_322_23	Bhvo				441	200 to 260	441	50.01	Multiple gen. Some primary?
37_322_24	Bhvo				450	200 to 260	450	50.92	Multiple gen. Some primary?
37_322_25	Bhvo				460	200 to 260	460	51.96	Multiple gen. Some primary?
37_322_26	Bhvo				390	200 to 260	390	45.15	Multiple gen. Some primary?
37_322_27	Bhvo				438	200 to 260	438	49.71	Multiple gen. Some primary?
37_322_28	Bhvo				380	200 to 260	380	44.26	Multiple gen. Some primary?
37_322_29	Bhvo				440	200 to 260	440	49.91	Multiple gen. Some primary?
37_322_30	Bhvo				415	200 to 260	415	47.46	Multiple gen. Some primary?
37_322_31	Bhvo				420	200 to 260	420	47.94	Multiple gen. Some primary?
37_322_32	Bhvo				438	200 to 260	438	49.71	Multiple gen. Some primary?
60_529_6	hvo (2*)	hvo			420	243	420	47.94	
60_529_7	hvo (2*)	hvo			413	245	413	47.27	
60_529_8	hvo (2*)	hvo			407	240	407	46.71	
60_529_9	hvo (2*)	vlh			393	570	570	45.42	(homogen to vapor)
28_223_24	LVv					468	468		secondary, co exist with brine
28_508_1	2* LV	lv				335	335		
28_508_2	2* LV	lv				340	340		
28_508_3	2* LV	lv				350	350		
28_508_6	vap (2)	vl				480	480		
28_508_7	2* LV	lv				587	587		
60_529_4b	vap (2)	v				410	410		Vapor rich (2nd)
60_529_10	VLv (2)	vl				412	412		

# Sulphur isotope results

CSL No.	Hydrothermal Stage	Sample Description	Sample ID	Mineral	Weight (mg)	Yield (mmol/g)	Delta S (wrt CDT)
6526	1A	1A (petro) cpy (+trace brn) infill of tunja/dd bio-ortho vein. (1*?)	25-273	cpy	4.2*	3.2	-3.38
6569	1A	1A ? cpy from tunja orth-bio breccia: late stage infill or distinct S iso?	54-693	cpy	8.7*	11.0	-1.98
6559	2A	2A (petro sample) brn from bahut dyke hosted peg-GK	49-644	bn	25.1	18.0	-1.45
6527	2A	2A coarse peg GK vein: fresh Cpy (later sulphide?)	28-52	cpy	15.0	22.4	-2.27
6567	2B	2B (petro sample) cpy from small glpk vein.	53-882	cpy?	15.3*	21.0	-2.15
6549	2C	2C (petro) brn from lovely gk vein	37-176	bn	10.0*	10.0	-0.91
6543	2C	2C brn from thick gk vein	37-52	bn	17.2*	17.2	-0.82
6519	2C	2C cpy in gk	3-142	cpy	16.1	12.8	-2.62
6562	2C	2C distal ('376') cpy from distal gk (petro sample)	53-396	cpy	12.0*	7.8	-2.57
6537	2C	2C distal cpy from distal. carbonate reactivated gk fissure	33-453	cpy	14.5*	14.2	-3.05
6531	2D	2D brn from intergrown ortho-brn (petro sample)	28-510	bn	17.5	13.6	-2.85
6522	2D	2D (petro sample) brn from brn-epy-ortho clot	4-96	bn	16.9	14.8	-2.82
6520	2D	2D horn-epy breccia: brn (2 Samples)	4-94B	bn	15.0	12.2	-2.99
6521	2D	2D horn-epy breccia: cpy (2 Samples)	4-94C	cpy	17.9	19.6	-3.08
6530	2D	2D cpy from disemn ortho-epy	28-395	cpy	16.0	18.0	-3.47
6566	2D	2D gk overprint ortho-sulph: brn. Drilled.	53-834	bn	16.2*	9.4	-2.22
6547	2D	2D ortho-sulph cpy. Drilled.	37-118	cpy	18.1	4.2	-0.71
6532	3A	3A distal brn from distal quartz-act vein (post distal gk)	33-62	bn	20.0*	5.2	-2.19
6544	3B	3B 3brn from sulphi infill thin qv: py later than the cpy/brn. (3 samples)	37-98B	bn	18.8	22.0	-0.73
6529	3B	3B Brn in QV	28-352	bn	19.1	14.4	-2.89
6551	3B	3B distal brn from 'distal' chl-halo shredy qtz vein (FI sample) (2 samples)	37-322B	bn	8.9*	8.8	-3.42
6523	3B	3B very hard brn from classic thick milk QV. (2 Samples)	25-86	bn	11.0*	9.8	-2.62
6568	3B	3B ? cpy in spongy balut: balut signature or bugoy? (1* or 2*). (Petro sample)	54-665	cpy	15.4	23.0	-3.36
6545	3B	3B 3cpy from sulphi infill thin qv: py later than the cpy/brn. (3 samples)	37-98C	cpy	16.0	22.0	-0.37
6536	3B	3B cpy from nice clear qv	33-371	cpy	17.4	23.2	-0.19
6556	3B	3B cpy from nice clear qv. Ortho margin.	49-479	cpy	16.1	26.2	-3.20
6550	3B	3B cpy from shredy qv	37-190C	cpy	18.0	22.0	-3.28
6571	3B	3B cpy from shredy qv	60-348	cpy	16.5	20.6	-2.02
6565	3B	3B cpy infill of planer qv	53-770	cpy	14.7	20.0	-1.58
6573	3B	3B cpy infilling clear qv in quan: qv or overprint related? [sample 60/506B]	60-506	cpy	16.9	24.8	-1.93
6534	3B	3B Cpy matrix breccia. Very tarnished.	33-257	cpy	16.1	20.0	-2.93
6542	3B	3B distal (petro) cpy from distal (chl ah) qv	37-48	cpy	16.3	14.8	-2.93
6563	3B	3B distal 53/459 qv distal: cpy. Drilled.	53-456	cpy	17.2	21.8	-2.84
6552	3B	3B distal cpy from 'distal' chl-halo shredy qtz vein (FI sample) (2 samples)	37-322C	cpy	10.0*	16.8	-3.72
6553	3B	3B distal cpy from distal milky qv/may have some gypsum in it.	49-335	cpy	16.0	17.6	-4.23
6533	3B	3B distal milky quartz-act qv. Cpy	33-94	cpy	16.7	22.0	-2.74
6525	3B	3B lovely dogtooth qv (FI sample). Cpy from core	25-223	cpy	7.7*	8.6	-2.51
6561	3B	3B potass (petro sample) cpy infilling/ assoc with white ssc ah.	49-704	cpy	16.0	22.4	-2.08
6560	3B	3B potass scc clear quartz qv - later sulphide? Tarn cpy	49-670	cpy	15.9	18.8	-2.61
6528	3B	3B qv. Cpy (tarn). drilled	28-227	cpy	18.6	25.6	-2.60
6535	3B	3B tarnished ?cpy from sulphides filling shredy quartz vein.	33-259	cpy	18.3	23.4	-2.72
6548	3B	3B tarnished cpy from shredy qv.	37-139	cpy	16.3	22.2	-0.19
6524	3B	3B vcpy from classic thick milk QV. (2 Samples)	25-86C	cpy	15.0	22.2	-2.63
6564	3C	3C cpy from bufu infill (with pyrite replacement)	53-685	cpy	16.6	19.2	-2.19
6558	3C	3C cpy in thin clear qv cutting bufu/quant	49-606	cpy	27.3	25.0	-3.77
6572	3C	3C tarn cpy infill in sulphide overprinted bufu/quant	60-435	cpy	16.1	21.2	-2.57
6540	3B	3B interstitial trails of tarn pyrite (+cpy?) in shredy quartz vein (FI sample)	34-320	py	10.6	15.0	-2.45
6546	3B	3B 3py from sulphi infill thin qv: py later than the cpy/brn. (3 samples)	37-98P	py	9.2	13.6	-0.60
6557	3C	3C (petro sample) py filled cavity from the bufu.	49-555	py	12.5	21.0	-2.76
6574	3C	3C dist xtreme distal/late stage carbonate+milk quartz vein (almost stage 4).	60-541	py?	11.5	16.4	-1.90
6541	3C	3C tarnished ?py in hugoy breccia. FI sample.	34-393	py?	16.5	18.6	-2.63
6538	3C	3C (petro sample). Late stage clay-carbonate-epy vein. Cpy (or py?).	34-256	cpy	17.4	22.2	-2.43
6554	3C	3C carbonate-hosted cpy from clay-carbonate vein.	49-407	cpy	15.4	16.8	-4.01
6555	5A	5A py from late stage fracture zone: meteoric?	49-473	py	11.7	10.0	-2.97
6539	5A	5A py. late stage carbonate vein with py and layered mud.	34-304	py	9.2	14.4	-2.31
6570	5A	5A pyrite from coarse grain py zone - late stage meteoric?	60-290	py	10.6	17.0	-1.44

\* All sample used